

FINAL STUDY REPORT

FACILITY FORM 602

N71 24337	(THRU)
(ACCESSION NUMBER)	Q3
689	(CODE)
CR-118021	30
(NASA CR OR TMX OR AD NUMBER)	(CATEGORY)

JUPITER ATMOSPHERIC ENTRY MISSION STUDY

Volume III

Supporting Technical Studies

April 1971

Reproduced by
NATIONAL TECHNICAL
INFORMATION SERVICE
Springfield, Va. 22151

MARTIN MARIETTA

DENVER DIVISION

SP
MCR-71-1

MCR-71-1 (Vol III)

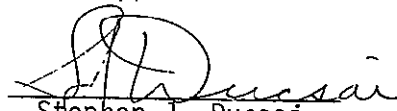
Contract JPL 952811

JUPITER ATMOSPHERIC ENTRY MISSION STUDY
FINAL REPORT

APRIL 1971

Volume III
Supporting Technical Studies

Approved


Stephen J. Ducsai
Study Manager

MARTIN MARIETTA CORPORATION
Denver, Colorado

**This work was performed for the Jet Propulsion Laboratory,
California Institute of Technology, sponsored by the
National Aeronautics and Space Administration under
Contract NAS7-100.**

FOREWORD

This report has been prepared in accordance with requirements of Contract JPL 952811 to present data and conclusions resulting from a six-month study effort performed for the Jet Propulsion Laboratory by the Martin Marietta Corporation, Denver Division. The report is divided into the following volumes:

Volume I - Management Summary

Volume II - Mission and System Evolution

Volume III - Supporting Technical Studies

The report is arranged so that Volume I (Management Summary) will provide a concise overview of the study, Volume II (Mission and System Evolution) will provide an appreciation of the major mission and system integration and trade sensitivities, and Volume III (Supporting Technical Studies) will provide the detailed supporting tradeoff studies down to the subsystem level. Volume III also includes the Appendixes with additional detailed data.

CONTENTS

	<u>Page</u>
Foreword	ii
Contents	iii thru v
I. Introduction	I-1
II. Science Studies.	II-1
A. Introduction	II-1
B. Summary of Science Objectives, Observables and Requirements	II-2
C. Instrumental Techniques.	II-8 thru II-61
III. Navigation and Trajectory Studies.	III-1
A. Launch and Interplanetary.	III-1
B. Encounter.	III-3
C. Deflection	III-6
D. Entry and Descent.	III-80
E. Navigation and Accuracy.	III-118 thru III-165
IV. Telecommunications, Data Handling and Power, Design Studies and Tradeoffs	IV-1
A. General.	IV-1
B. Data Return Optimization	IV-1
C. Trajectory Selection for Communications Optimization	IV-1
D. Relay vs Direct Link	IV-14
E. Frequency Selection.	IV-17
F. Modulation and Coding.	IV-27
G. Signal Acquisition and Tracking - Relay Link	IV-27

H.	Single Probe and Split Probe Communications Considerations	IV-37
I.	Subsystem Requirements and Selection from Available Design	IV-38
J.	Spacecraft Subsystem Performance Requirements and Changes to Present Design.	IV-57
K.	Microwave Losses in the Jovian Atmosphere.	IV-82 thru IV-158
V.	Mechanical Subsystem - Design Studies and Tradeoffs.	V-1
A.	Thermal Control.	V-1
B.	Structures and Mechanisms.	V-40
C.	Heat Shield.	V-83
D.	Aerodynamics	V-88
E.	Attitude Control and Propulsion System	V-94 thru V-114
VI.	Mission Effectiveness Model.	VI-1
A.	Introduction	VI-1
B.	Input Requirements	VI-4
C.	Effectiveness Mode Outputs	VI-20
D.	Mathematical Computations Scheme.	VI-25 thru VI-27
VII.	Trial Mission Data	VII-1
A.	Purpose.	VII-1
B.	Trial Mission Ground Rules, Criteria	VII-2
C.	Trial Mission Description.	VII-3 thru VII-44
Appendix A --	Precessing of a Spinning Probe	A-1 thru A-4
Appendix B --	Attitude Propulsion System Study for Active Control of a Descent Probe.	B-1 thru B-24

Appendix C -- Jupiter Entry Heat Shield Requirements	C-1 thru C-14
Appendix D -- Technical Memorandums Prepared by Dr. J. F. Vandrey in Support of the Study on Various Aspects of the Jupiter Environment.	D-1 thru D-57
Appendix E -- Jupiter Encounter Nomenclature	E-1
Appendix F -- Symbol Definitions	F-1 thru F-10
Appendix G -- Compendium of Parameters for all Missions	G-1 thru G-9

I. INTRODUCTION

This volume contains the parametric and technology studies which were done in support of the overall mission and system studies of Volume II and the conclusions and recommendations of Volume I. The efforts include trade studies in the areas of science, navigation and trajectory, telecommunications, and mechanical subsystems design. In addition, the mission effectiveness model is described, the Trial Mission supporting studies are discussed, and miscellaneous appendixes are included.

The science studies define the science objectives, questions to be answered, the relevant measurements, and the science instrument implementation. Results of these studies provide the basis for the science payload and support requirements, probe system design, and descent as well as encounter trajectory shaping. The navigation and trajectory studies provide the parametric data required in support of the mission design including the basic trades on available launch capability and date, trajectory type, encounter geometry, and targeting. The telecommunications and mechanical system studies provide design data for the hardware implementation for the probe, spacecraft and launch vehicle.

II. SCIENCE STUDIES

A. Introduction

The science studies were primarily concerned with (1) establishing the mission, system, subsystem and measurement requirements dictated by the scientific objectives for Jupiter, (2) investigating instrumentation and methods for performing the desired measurements from descent probes, and (3) establishing value curves for making the measurements as a function of depth, entry location, and frequency for use in the mission effectiveness modeling. The basic scientific questions defined in JPL Section Document 131-07 were first translated into observables or relevant measurements that might be performed from a descent probe. This preliminary list of observables was reviewed by five consulting scientists,* and a final list including their suggestions was compiled. The performance requirements for each of the observables (e.g., resolution, targeting, depth, etc.) were then defined, again with comments and suggestions from the consultants included. The applicability of instruments defined in JPL Section Document 131-07 (nominal payload) was reviewed and other instrumental techniques compatible with descent probes suggested by the consultants. These observables, performance requirements, and instrumental techniques were then translated into specific mission and probe system requirements (e.g., descent probe ballistic coefficients, entry sites, deployment altitude, typical payloads and approximate bit rates etc.). Concurrently, the detailed characteristics and availability of the various instruments were investigated and the performance requirements were translated into value curves for the mission effectiveness modeling. This entailed defining, for each observable, (1) the applicable instruments and their potential values for that observable, (2) the value of making a measurement with these instruments as a function of

* The five scientists were S. I. Rasool, D. M. Hunten, T. Owen, C. Sagan, and R. Goody.

pressure in the nominal model and as a function of latitude and longitude, and (3) the optimum number of measurements per scale height versus pressure. These were used as criteria for estimating the effectiveness of various mission concepts in accomplishing the scientific objectives.

B. Summary of Scientific Objectives, Observables and Requirements

The major scientific areas of interest for a first generation atmospheric descent probe to Jupiter were specified in JPL Section Document 131-07 as a set of basic questions concerning the lower atmosphere and clouds (See Table IIB-1). In order to establish specific design requirements, these questions were translated into a set of relevant measurements or observables that are compatible with the descent probe concept (See Table IIB-2). The major constraint in defining these observables was that they not be determinable by remote sensing (from earth or spacecraft). The rationale for defining the observables is discussed in Volume II, Chapter III.

TABLE IIB-1

Basic Scientific Questions for Jupiter
(JPL Section Document 131-07)

- | | |
|--|--|
| 1. | What are the relative abundances of hydrogen, deuterium, helium, neon, and other elements, and what are their isotopic compositions? |
| 2. | What are the present-day atmospheric composition and altitude profiles of pressure, temperature, and density, and what effect do they have on the radiation balance? |
| 3. | What are the chemical composition and vertical distribution of the clouds? |
| 4. | Do complex molecules exist in the atmosphere of Jupiter? |
| 5. | What are the nature and origin of the colors observed in Jupiter's atmosphere? |
| <hr/> | |
| 6. | *What is the magnetic field strength in the lower atmosphere? |
| 7. | *What is the level of turbulence in the atmosphere? |
| * Added after start of contract by direction from JPL. | |

TABLE IIB-2

Relevant Measurements or Observables
Derived from Basic Questions

Determine:

1. Relative abundances of H and He in the lower atmosphere (below the turbopause);
2. Isotopic ratios H/D; $^3\text{He}/^4\text{He}$, $^{20}\text{Ne}/^{23}\text{Ne}$, $^{36}\text{A}/^{40}\text{A}$, $^{12}\text{C}/^{13}\text{C}$ in the lower atmosphere (below the turbopause);
3. Atmospheric mean molecular weight and identify the major contributing gases (i.e., determine whether H_2 and He are indeed the only major constituents and, if not, what the other gases are);
4. Concentration profiles (versus pressure and temperature) of the minor atmospheric gases (e.g., Ne, A, N_2 , etc. and CH_4 , NH_3 , H_2O , H_2S , etc.) from above the visible cloud tops down to several hundred bars;
5. Temperature versus pressure (and time) profile from above the cloud tops down to well below the condensation level of H_2O with a precision sufficient to determine whether the lapse rate is adiabatic;
6. Vertical distribution and structure of the cloud layers with respect to pressure and temperature (particularly, locate the cloud tops);
7. Chemical composition of the cloud particles in each layer;
8. Color of each of the cloud layers;
9. Intensity distribution of the incoming solar flux (direct and diffuse) at several wavelengths as a function of pressure and temperature from above the visible clouds down to at least several tens of bars;
10. Thermal radiation (IR) flux profiles at several wavelengths from above the cloud tops down to several hundred bars;
11. Whether specific complex molecules are present in the region between the cloud tops and the condensation level of H_2O ;
12. Frequency of occurrence of electric discharges and the nature of thunder as a function of pressure and temperature down to at least the condensation level of H_2O ;
13. Physical characteristics (number density and size distribution) of the cloud particles in each layer (particularly through the cloud tops);
14. Scales and the magnitude and frequency spectra of any atmospheric turbulence from above the cloud tops down to at least several tens of bars;
15. Magnetic field strength and variations versus depth from above the ionosphere down through the lower atmosphere to as deep as possible;
16. Electric conductivity of the deep atmosphere;
17. Relative abundances and isotopic ratios of Li, Be, B;
18. Composition profiles of the ionic species through the upper atmosphere;
19. Exospheric ionospheric temperature profiles; and
20. Locate the source of decametric radiation (with respect to radius).

The ordering of the observables in Table IIB-2 is not intended to imply any strict priority but the H/He ratio is generally accepted as the most important determination for a first generation mission. The next most valuable determination for a descent probe would be the measurement of pressures and temperatures through the cloud tops down to at least several tens of atmospheres and a determination of the mean molecular weight. Some information on the clouds, at least an indication of whether there is an aerosol present at a given pressure temperature level would also be of high priority. Beyond this, the exact ordering becomes more and more subjective. Table IIB-3 indicates a priority rating that takes into account both the scientific importance and the practicality of making the desired measurements from a first generation descent probe. The priority 4 items are rated low, not because they are least important, but because they either do not uniquely require a deep descent probe (18-20) or require a very deep descent probe (17, and perhaps 16).

A summary of the performance requirements for the measurements is also shown in Table IIB-3; the rationale behind these requirements is discussed in Volume II, Chapter III. The most suitable entry site for a first generation mission is the Equatorial Zone since it is thought to be most typical or representative of the planet; the North Equatorial Belt, the Great Red Spot, and a pole follow in order of importance and difficulty. The vicinity of the subsolar point is preferred for the solar flux measurements but the weight penalties (and reduced accomplishment of other objectives) associated with the required steep entry angles argue for an entry point midway between the subpolar point and the evening terminator. This gives the best compromise for all measurements and allows adequate time for the probe to reach below the clouds before crossing the terminator.

TABLE IIB-3
SUMMARY OF PERFORMANCE REQUIREMENTS FOR OBSERVABLES

Observable	Targets	Pressure Depth	Sampling	Priority (1st Mission)
1. H/He ratio	Any	Below Turbopause	At least 4	1
2. Isotopic ratios	Any	Below Turbopause	At least 4	2
3. Mean molecular weight	Any	To 5 atm or more	At least 4	1
4. Minor constituents	Any	To 100 atm or more	2 to 5 per scale height	1 - 2
5. Temperature/pressure	EZ, NEB, TR, Poles	To 1000 atm	50 to 100 per scale height	1
6. Cloud layering	EZ, NEB, TR, Poles	To 100 atm or more	100 per scale height	1
7. Cloud composition	EZ, NEB, TR, Poles	To 100 atm or more	2 to 5 per scale height	1 - 2
8. Cloud colors	EZ, NEB, TR, Poles	To 100 atm or more	100 per scale height	2
9. Solar flux	Subsolar or LS	To 10 atm	100 per scale height	2
10. IR flux	Any	To 100 atm or more	50 to 100 per scale height	2
11. Complex molecules	GRS, Any	To H ₂ O cloud (5 to 100 atm)	2 to 5 per scale height	2
12. Lightning/thunder	Any	To H ₂ O cloud (5 to 100 atm)	10 to 20 per scale height	2
13. Cloud particle sizes	EZ, NEB, TR, Poles	To 100 atm or more	100 per scale height	3
14. Turbulence	EZ, NEB, Poles	To H ₂ O cloud (5 to 100 atm)	10 to 20 per scale height	3
15. Magnetic fields	Poles, GRS or Any	To 1000 atm or more	2 per scale height	3
16. Conductivity	Poles, GRS or Any	To 1000 atm or more	2 per scale height	3 - 4
17. Li, Be, B ratios	Any	10,000 atm	At least 4	4
18. Ionosphere composition	Subsolar, LS, DS	Pre-entry	2 per scale bit	4
19. Upper atm temperature	LS, DS	Pre-entry	2 per scale bit	4
20. Decameter radiation	Any	To 100 atm or more	—	4
Targets: EZ = Equatorial Zone GRS = Great Red Spot NEB = North Equatorial Belt LS = Lightside TR = North or South Temperate Region DS = Darkside Any = Any target except GRS				

A specification of the required depth of probe descent is strongly dependent on our present ignorance of the lower atmosphere and clouds and should not be tied to a single model atmosphere. Descent below the cloud tops to 5 or 10 atm with suitable instrumentation would provide answers to many of the most important questions concerning Jupiter (e.g., H/He, P, T structure, mean molecular weight). However, most of the other questions may or may not be answered depending on what the pressure-temperature structure actually is. Descent to below the condensation level of H₂O would answer most of what can be asked but, for the range of model atmospheres considered, this level could be anywhere between 1 and 100 atmospheres and possibly as low as 200 to 300 atm for other equally plausible models. Thus, to ensure accomplishing a majority of the objectives, descent to pressures of 100 to 300 atmospheres is required. As discussed in Volume II, Chapter III, there are reasons for attempting a descent to the 1000 atm levels, but these are of an exploratory nature and would be more appropriate to a later mission, after a specific exploration of the upper few hundred atmospheres has been accomplished.

The observables fall into several sampling interval categories: (1) those that require only a few measurements (4 for redundancy) in the mixed lower atmosphere such as the H/He and isotope ratios or the mean molecular weight; (2) those that require a few measurements (2 to 5) per scale height such as the gross pressure-temperature structure, or the cloud composition and minor constituent profiles; (3) those that require averaging or integrating over an interval such as average turbulence or lightning measurements; (4) those that require 50 to 100 measurements per scale height such as the detailed thermal and turbulence structure; and (5) those that require very detailed profiles (100 to 200 per scale height) such as the cloud structure and physical properties measurements.

These are summarized for each observable in Table IIB-3. Most of the sampling requirements can be relaxed and still give useful information. For example, a detailed pressure-temperature profile down to the 100 atm level combined with a few precise composition measurements near the 100 atm level would allow at least an inference of the probable cloud layering above the 100 atm level.

C. Instrumental Techniques

The appropriate generic instrument types were related to the observables and objectives in Volume II, Chapter III and specific instruments selected and described for the Nominal and Sample science payloads. The following sections describe the range of instrument options considered in selecting the sample payloads.

1. Instrument Performance Requirements

In general, the instruments must be able to make their intended measurements rapidly enough to meet the altitude sampling requirements shown in Table IIB-3 and, obviously, must be able to perform reliably and predictably over the required range of pressures and temperatures and in the presence of condensing clouds of unknown composition.

a. Composition Measurements

The instruments considered for this category range from a simple mass spectrometer with a limited mass range (1 to 5 m/e) for determining the H/He ratio to a complex Viking type GC/MS with a cloud particle collector and vaporizing source to search for complex molecules present in either the gas or cloud particles.

A simple 1-5 m/e mass spectrometer need only make 4 or 5 measurements between several tenths of an atm and about 5 atm to achieve its main objective. A unit resolution and a dynamic range of 10^3 should be adequate for the H/He ratio but an expanded dynamic range ($\sim 10^5$) might give indications of the NH_3 and H_2O concentrations by the increase in H fractions from these gases during descent through the clouds.

A concentration profile of the minor gaseous constituents requires a combined mass spec-gas chromatograph with columns to separate the polar and non-polar gases and to concentrate constituents in the 100 parts/billion range before presenting to the mass spec. The dynamic range of the MS should be 10^5 to 10^6 with a resolution of less than 1 amu to separate isotopes. An m/e range to 40 would be adequate but extension to 60 or 100 m/e

would allow a search for some complex organic and inorganic molecules. Extending the range further would be of little use unless the dynamic range could also be increased since the high molecular weight compounds are not expected to be present in quantities greater than parts per billion. A detailed concentration profile down to 100 to 300 atmospheres with an altitude resolution of better than 2 samples per scale height requires 20 to 30 complete cycles on the GC/MS. The amount of carrier gas and the mass spec pump must be sized accordingly.

A cloud particle collector for concentrating any complex molecules or coloring material in the particles is desirable since such material is expected to be present only in trace quantities (less than a few parts/million). A high temperature oven to vaporize the particles is unnecessary since the clouds particle of interest are condensibles and the normal increase of temperature during descent would probably be sufficient.

Since there is no fixed surface from which to reflect radar signals, any altitude scale must be derived from pressure measurements and the hydrostatic equation. This requires an accurate knowledge of either the mean molecular mass or the total mass density at each point and hence, the mass spectrometer should be capable of providing one or both of these quantities to within about $\pm 0.5\%$ (i.e., to about the same accuracy as the pressure and temperature measurements).

b. Pressure and Temperature Measurements

The pressure and temperature sensors should cover the ranges 0.1 to 1000 atm and 100°K to 2000°K, respectively, with the upper limit depending on the design depth. This will require several sensors and range switching. The absolute accuracy should be about $\pm 0.5\%$ for both pressure and temperature (± 5 mb at 1000 mb and $\pm 1^\circ\text{K}$ at 200°K). The vertical temperature gradient should be determined to within 1% or better to be useful for dynamical theories (i.e., to within 0.02°K/km). This may require temperature measurements

with a relative accuracy of $\pm 0.1^\circ\text{K}$ over a 20°K range for 15 minutes or $\pm 1^\circ\text{K}$ over a 200°K range for 60 minutes. An IR radiometer (at 10μ) can be used in conjunction with an immersion temperature sensor to obtain these relative accuracies.

c. Cloud Structure Measurements

The sidelooking nephelometer is to be preferred for determining the cloud structure or layering during descent on either the light side or dark side. A modulated light source is required to distinguish between the signal and the solar flux on the lightside. A range of about 10 to 25 meters is desired but a 1 to 5 meter range would be adequate to indicate the presence of significant amounts of aerosol.

The aerosol photometer of the nominal payload would be useful only on the light side and, even then, only for locating the cloud tops and perhaps one or two layers just below the cloud tops. The nephelometer, with its own light source, can sense the presence of aerosol at any depth below the cloud tops.

The addition of a down looking 5μ channel to the 10μ IR radiometer would permit another means of determining the cloud layering. The 10μ channel senses the blackbody radiation from the atmosphere in the immediate vicinity of the probe while the 5μ channel senses radiation from an opaque cloud layer below the probe (if it is within about optical depth 1 at 5μ). The 5 and 10 micron channel temperatures will be equal when the probe reaches the top of the cloud layer and will change again when the probe passes out the bottom of the layer.

The dual channel radiometer should be capable of resolving temperature differences of the order of 1°K or less at temperatures up to at least 350°K . This would allow the precise location of cloud layers above the condensation levels of H_2O . At greater depths, a resolution of at least 5°K at temperatures up to 500°K would be sufficient to detect a NH_4Cl cloud.

d. Cloud Properties Measurements

A determination of the cloud colors could be made by using a filter wheel in front of the nephelometer detector. At least 2 color filters (yellow and red) plus one clear would be required.

While the nephelometer might provide some information on the cloud particle size distribution, an instrument which actually detects and counts individual particles is preferred. One such instrument is currently under development at NCAR. Particles streaming through a small volume are illuminated and their shadows observed on a fiber optic background. While this would give both the number-density and size distribution of the particles, the instrumentation is complicated and requires at least 20 bps.

e. Lightning Measurements

While the flash photometer of the nominal payload would indicate whether and how frequently electrical discharges are occurring within about 10 to 20 km of the probe, no information is obtained on the magnitude or frequency of the shock waves (thunder) resulting from the discharges. The shock waves are thought to be the important factor in the production of non-equilibrium chemical species and/or complex organic molecules. For this reason a microphone is suggested to investigate the frequency and magnitude of thunder. An RF click detector would extend the range of detectable electrical discharges to the order of several hundred kilometers.

2. Instrumentation Capability

In this section the tradeoffs in regard to applicable instruments for the science subsystem are discussed. Preferred instrument types are outlined in regard to instrument characteristics and instrument operation. Information about instrument weight, power consumption, data rate and special integration requirements is provided. Requirements for science instrument R&D are also pointed out.

While a complete instrument survey and instrument tradeoff study is not within the scope of this study, this section represents an initial effort to assess science instrumentation capabilities, integration requirements and measurement accuracy for a Jupiter descent probe.

a. Atmospheric Pressure Measurements

1) Requirements

During probe descent, the atmospheric pressure between 0.1 and 1000 atmospheres is measured while the ambient temperature may increase from 100 to 2000°K. The following transducer principles were considered to determine atmospheric pressure.

2) Alternative Instrument Concepts

(a) Deformation of Elastic Membrane which Separates an Evacuated Cavity from the Unknown Pressure

To reduce hysteresis and to generate large signals, the diaphragms are near their elastic limit at full scale pressure and burst when this pressure exceeds several times the full range. The pickoffs sensing the membrane deflection can be of the strain gage, electromagnetic, capacitive, potentiometric or optical type. Transducers withstanding up to 900°F have been manufactured, but accuracy decreases when a wide temperature range is required.

(b) Pressure Effect on Electrical Resistance .

Usually a material sensitive to linear strain is sensitive also to hydrostatic pressure. A low temperature coefficient of the conductor (wire, semiconductor, carbon) is desirable and material such as manganin and gold chromium wire have been used to measure pressures of 200,000 psi and higher. Twenty-three percent resistance change for 1000 atm pressure increase has been observed for carbon composite resistors.

Transducers based on pressure effects on material can be very small but more quantitative data are needed.

(c) Damping of Vibrating Element by Gas

When a diaphragm or another mechanical element is vibrated while immersed in a gas, the vibration is damped because of mass and viscosity of the gas. If the gas composition and gas temperature are approximately known, the gas pressure can be derived. This principle has been used for low pressure measurements and the vibrating diaphragm gage developed by NASA Ames Research Center is unique because of its good accuracy (about 2% of reading) over a pressure range from 10^{-6} to 0.1 atmospheres. Extrapolating from this low pressure gage, it appears feasible to develop a similar transducer for the range of 0.1 to 1000 atmospheres. To achieve better force coupling, the electrostatic excitation of the vibrating diaphragm would probably be replaced by an electro-magnetic excitation.

(d) Absorption of Beta Particles by a Gas Column

This instrument would be based on an absorption technique in which the energy loss between a beta source and detector is measured over a known gas path. A one-millicurie Strontium 90 beta source and gas paths of one foot and one inch are considered. The instrument weight is less than one pound.

3) Preferred Instruments

For the baseline design, pressure transducers with an elastic membrane and strain gage pickoffs will be assumed. The transducer accuracy is approximately 0.5% of full scale and the signal output is 0 to 40 millivolts. Each transducer weighs 4 ounces and can be mounted outside or inside the pressure shell. During probe testing the pressure inlet(s) must be sealed to avoid bursting of the transducer diaphragms. The temperature range of the transducer is from -55°C to 100°C and the thermal shifts of sensitivity and zero are $0.01\%/^{\circ}\text{C}$. Only minor modifications of existing transducer designs are required. Further weight reductions can be achieved if the accuracy requirements are reduced.

The estimated range and weight parameters of transducers with a vibrating sensing element are 0.5 to 1000 atmospheres and 8 ounces. A measurement accuracy of 4% of reading is anticipated if the atmospheric composition is known. A considerable development effort would be required.

A pressure gage based on compression effects of resistors (metal, carbon, semiconductor) can be very small and light weight ($< 1\text{ oz}$). More information about accuracy is needed. We do not know any commercial manufacturers for this transducer type.

b. Atmospheric Temperature Measurements

1) Requirements

The atmospheric temperature between 100 and 1500°K will be measured. Measurement error before telemetry will be $\pm 0.5\%$ of the temperature intervals or $\pm 0.5^{\circ}\text{K}$ for the three low temperature intervals, and $\pm 0.5\%$ for the high temperature intervals. Further reduction in error and resolution in the order of 0.1°K are of interest.

2) Alternative Measurement Concepts

(a) Radiation Thermometer

In principle, atmospheric temperature can be determined from radiation measurements with a resolution of about 0.1°K .

The total energy radiated from a black body is proportional to the fourth power of its absolute temperature and the spectral distribution is also a function of temperature. For this discussion we will generally assume that Jupiter atmosphere layers of less than 0.5 km thickness are black bodies near a wavelength of 10μ . Radiation thermometers essentially compare the amount of radiation emitted by the target with that emitted by an internal, controlled reference source ($\sigma E_1 T_1^4 - E_2 T_2^4$). The characteristics of the infrared radiometer for the 1969 Mariner mission to Mars (Ref. 1) and the information about spectral radiant emittance at 10μ (Figure IIC-1) will be used to estimate the instrument characteristics of an IR thermometer for Jupiter which measures near 10μ wavelength.

Table IIC-2 shows major characteristics of the IR radiometers on Mariners 2, 6 and 7. The IR detectors are not cooled and the equivalent noise bandwidth for the IR radiometers on Mariners 6 and 7 is 0.68 Hz and the noise rms level is less than 0.1% of the instrument dynamic range. The digitization limit is 0.1°C for target temperatures above 250°K . Viewing of space (0°K) and a reference area are used for radiometer calibration.

For a Jupiter descent probe IR thermometer the FOV can be at least $10^\circ \times 20^\circ$. Therefore, the energy received from the target is 400 times larger than for a $0.7^\circ \times 0.7^\circ$ FOV if we assume the same aperture and target temperature. Because an instrument response time in the order of a few seconds is satisfactory, the effective noise bandwidth could be less than 0.68 Hz. We therefore conclude that sufficient instrument sensitivity to resolve 0.1°K can be readily achieved above 300°K even if the aperture of the instrument optics is only 0.5 inches in diameter.

A major difference for the instrumentation is the interface to the environment. Contrary to planetary flyby conditions, the window of an entry probe radiometer is exposed to the constantly varying ambient atmosphere. Therefore wide variations of window temperature, pressure and possible interference by condensibles and particles are encountered.

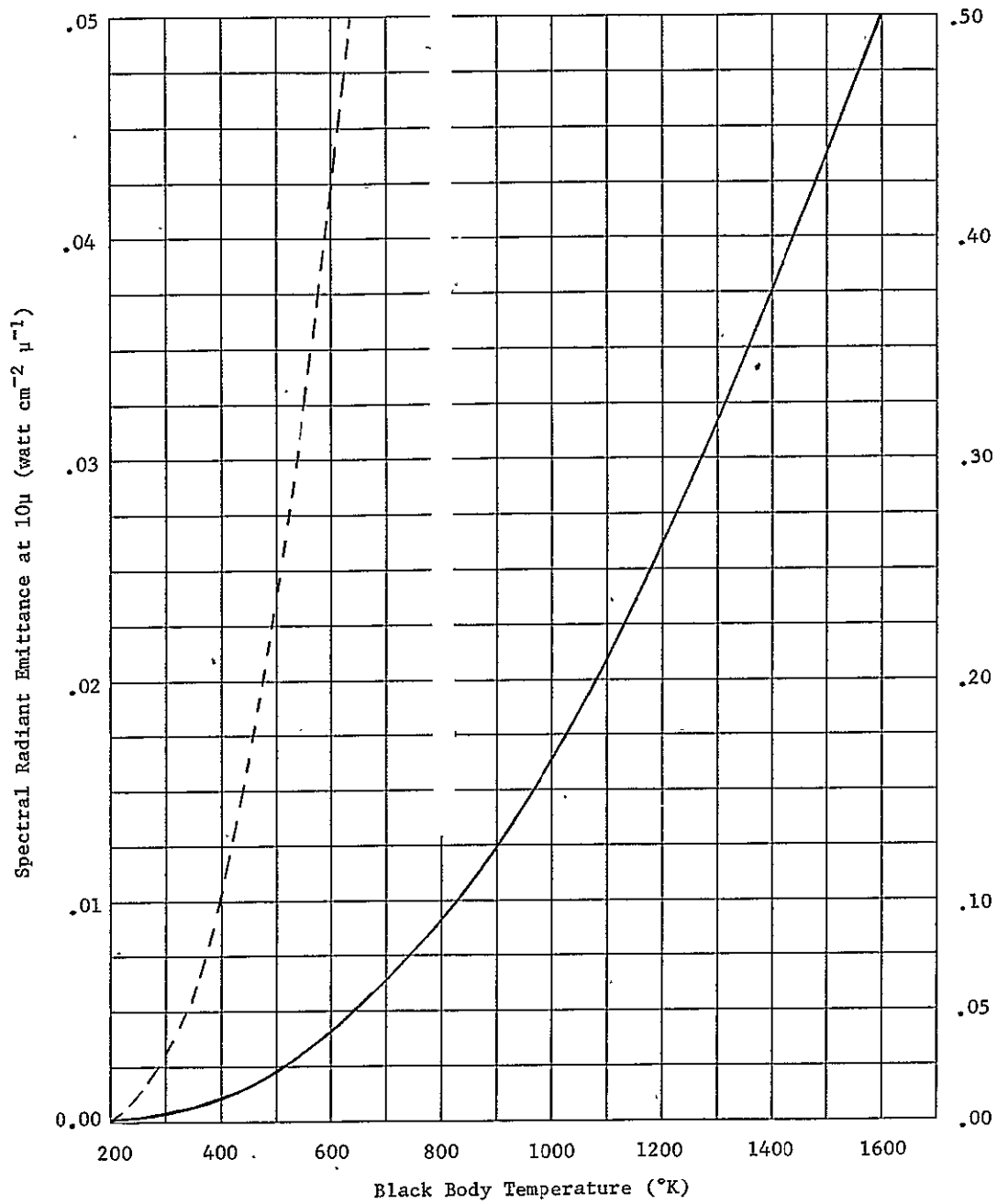


Figure IIC-1 Spectral Radiant Emittance vs Temperature at 10μ Wavelength

Table IIC-2 Characteristics of Thermal Radiometers

Radiometer Application	Weight (lb)	Power (Watts)	Spectral Range (μ)	Temperature Range ($^{\circ}$ K)	FOV	Optics	Temperature Resolution ($^{\circ}$ K)	Detector Type & Det. Area in mm ²	Inflight Calibration	Remarks
Mariner 6 & 7 (Mars)	8.25	3	8-12 18-25	140 - 325	0.7 $^{\circ}$ x 0.7 $^{\circ}$	1" dia aperture	< 0.5	Antimony-bismuth thermopile, 0.25 x 0.25	View Space & reference plate	Two telescopes
Mariner 2 (Venus)	2.88	2.4	8-9 μ 10-10.8 μ		0.9 $^{\circ}$ x 0.9 $^{\circ}$	f/2.4 f = 3"		Germanium immersed, 0.15 x 0.15	View reference plate	Two filters
Jupiter Entry Probe (estimate)	2.5	2.5	9-11	150 - 1400	10 $^{\circ}$ x 20 $^{\circ}$	0.5" dia aperture	< 0.5	Thermopile	Two reference plates	Characteristics are estimated.

FOLDOUT FRAME

FOLDOUT FRAME

2

Pressure and window temperature can be measured and only continuous changes are anticipated for these parameters. However, particles and condensibles can cause rapid fluctuations. At an atmospheric temperature of 400°K a change of 0.1% of radiation transmitted through the radiometer window corresponds approximately to a temperature change of 0.1°K. Because temperature control of the radiometer window is too power-consuming, the temperature of the external radiometer window should be close to ambient temperature and must be measured because its transmission is less than 100%.

Table IIC-2 shows the major characteristics of the IR radiometers for Mariner 2, and Mariners 6 and 7. The IR radiometer for Mariners 6 and 7 consisted basically of two radiometers. Because of the wider FOV for a Jupiter probe radiometer, the signal will be 100 to 1000 times stronger than for typical flyby radiometers. However, approximately 5 ounces of additional weight are required to adapt the radiometer to the environmental and wide temperature range requirements. In consideration of these requirements and assuming some technology improvements, weight, power, and volume requirements of 2.5 pounds, 2.5 watts and 100 cubic inches are estimated.

The signal intensity is proportional to the narrow spectral range and the temperature resolution improves with increasing target temperature. The thermopile detector used for the Mariners 6 and 7 radiometer withstood vibration levels of 50 g rms, and shock levels of 250 g.

(b) Immersion Thermometers

In these instruments the sensing element assumes the same temperature as the gas that is measured. The sensing element can be a platinum resistance wire, a thermocouple, a thermistor or some temperature dependent element that provides an electrical signal as a function of temperature. The critical design considerations for the temperature probe are:

PRECEDING PAGE BLANK NOT FILMED

Rapid temperature equalization of sensing element and atmosphere combined with low heat conduction through mechanical support structure and protection of sensing element;

High stability of the sensing element under the environmental conditions;

Interference caused by condensation, solidification or evaporation of droplets.

Thermocouples can be directly exposed and excellent thermal coupling to the atmosphere is achieved without significant interference by conductive films deposited by the atmosphere. No problems due to high acceleration are anticipated. Platinum resistance wire is used as a temperature standard up to 650°C . If protected against excessive strain and conductive deposits, excellent accuracy can be achieved. Decelerations of about 1000 Earth g's can cause problems. Inertial separation can be applied to separate atmospheric droplets and particles.

3) Preferred Instrument.

An immersion temperature probe with a platinum wire sensing element is preferred. Radiation thermometers are heavier, more costly, and no better measurement accuracy is anticipated under the environmental conditions. One immersion temperature probe weighs approximately 0.3 pound and two probes with one signal conditioner and automatic range switching are suggested for the temperature range from 100°K to 1500°K . Figure IIC-2 shows concepts of temperature probes for low and high atmospheric densities. The temperature ranges are approximately 100-200, 200-300, 300-400, 400-600 and 600-1500 $^{\circ}\text{K}$. The measurement resolution with an 8- or 10-bit digitizer will be respectively 0.4% or 0.1% of the temperature interval. When no evaporating or condensing droplets interfere, short term (15-minute intervals) temperature gradients can be determined with an accuracy that is nearly the same as the measurement resolution. However, the absolute accuracy will probably be closer to $\pm 1^{\circ}\text{K}$ rather than $\pm 0.5^{\circ}\text{K}$. The instrument weight and power consumption are approximately 1.2 pounds and 7.5 watts.

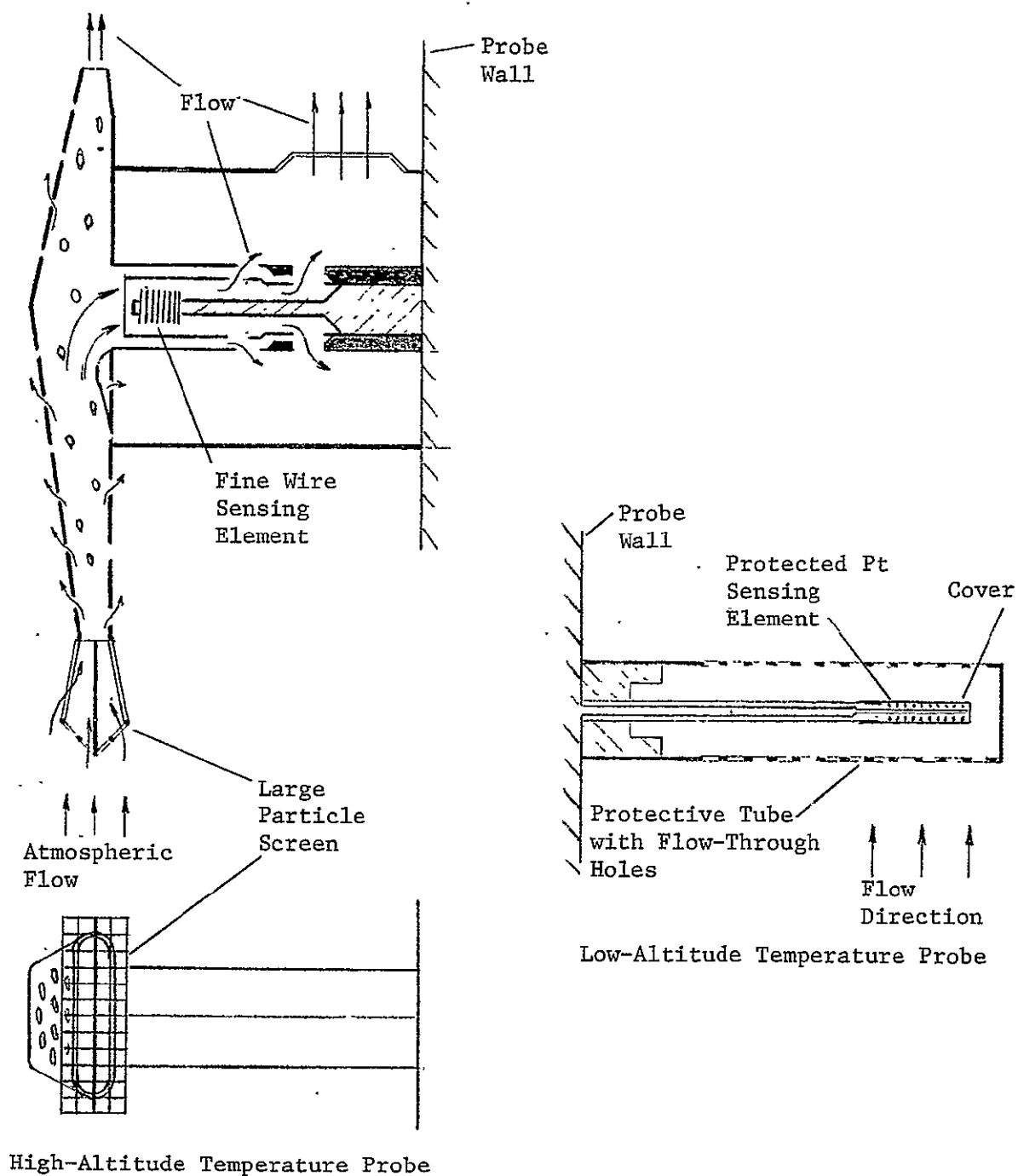


Figure IIC-2 Temperature Probe Concepts for Low and High Atmospheric Densities

If platinum wire should not be a satisfactory sensing element because of high accelerations, high pressures, and the upper temperature range, then application of thermocouples is suggested. Thermocouple measurements can have an accuracy of 2 to 5°C depending on the measured temperature.

c. Acceleration Measurement

1) Requirements

During atmospheric entry, accelerations as high as 1500 Earth g's can occur along the roll axis. The estimated maximum accelerations normal to the roll axis are less than 100 Earth g's. When the descent probe experiences a step change in horizontal wind velocity, then the accelerometers sense a horizontal acceleration.

$$a = 0.5 \rho v^2 / B_h$$

if ρ is the atmospheric density, v is the velocity step change, and B_h is the ballistic coefficient for horizontal flow conditions. A horizontal acceleration of approximately 0.001 Earth g's results for a ballistic coefficient $B_h = 1$ slug/ft², a pressure of 1 atmosphere in the Jovian environment, and a horizontal wind velocity step change of 10 miles/hour. We therefore assume a threshold no larger than 0.001 Earth g's and a resolution of 20% of the reading is required for the turbulence measurements.

2) Alternative Measurement Concepts

Most accelerometers measure along one axis. Very small accelerometers are based on electrical measurement of the displacement of an elastic element. The displacement is caused by an inertial mass. These accelerometers have an accuracy of a few percent and can readily be designed for ranges of several thousand Earth g's.

Highly accurate measurements over a wide dynamic range (10^6) are provided by force balance accelerometers. A pickoff detects minute deflections of the proof mass and the servoamplifier generates by means of a force coil a magnetic force that compensates the acceleration force exerted on the proof mass. The current through the force coil is a measure of the acceleration.

Such accelerometers that measure from 10^{-6} to 200 Earth g's are currently in use. According to information from Bell Aerosystems Inc., it looks feasible to modify a force balance accelerometer to measure the range of 10^{-3} to 1500 Earth g's.

An alternative method is to protect the sensitive instrument by immersing it in a caging fluid which is drained at parachute deployment. This concept was intended for the Ranger seismometer during a 3000-g lunar landing.

3) Preferred Instrument

An accelerometer triad is mounted in the descent probe and located at the entry capsule's center of gravity. A single axis accelerometer is mounted on the spin axis but as far away from the accelerometer triad as possible. This accelerometer is sensitive along the spin axis.

Before aeroshell separation, the pendulous force balance accelerometers measure over a dynamic range of about 10^6 . Maximum accelerations are 1500 and 100 Earth g's along and normal to the roll axis, respectively.

After aeroshell separation, some on board data evaluation is used to determine maximum accelerations within time periods of approximately 10 seconds. The dynamic measurement range is 10,000 and the transmitted signal is a logarithmic function of the maximum acceleration during the sampling period. The measurement threshold is no larger than 0.001 Earth g's. Lower thresholds can be achieved by caging the accelerometers during the high deceleration period. The mechanical structure of existing accelerometers would have to be enforced and the anticipated weight and average power consumption for each single axis acceleration measurement are approximately 1 pound and 1.5 watts, respectively. Most of the electronics associated with the accelerometers can be mounted in any location. The accelerometers should not be exposed to gas pressures above two atmospheres as long as the instrument operates. No liquid may leak into the sensor.

d. Photometer Measurements (UV to near IR)

1) Requirements

Sunlight measurements by descent probe photometers provide information about cloud tops, aerosol particles and some atmospheric constituents. Short wavelength measurements indicate cloud tops, and aerosol particles above the cloud tops are determined from comparison of measurements in the visible and near IR region. Narrow band (200 Å) measurements between 0.55 μ and 1.09 μ wavelength indicate methane and ammonia abundances and a 500 Å wide band at 4.55 μ was suggested to determine the H/D ratio. Measurements in strong and weak absorption bands provide the capability to measure a wide range of the abundances.

Above the clouds most of the light should be direct sunlight. Thorough analysis of optical absorption measurements in cloudy atmosphere is still a field of meteorological research and is beyond the scope of this study. However, there are various promising instrumentation concepts to achieve absorption measurements. Major design considerations and the trade-offs between measurement quality and instrument requirements are discussed.

2) Alternative Measurement Concepts

(a) Dynamic Range of Absorption Photometers

The dynamic range of the narrow pass band photometers is primarily limited by the filter transmission outside the transmission band. To estimate the order of magnitude, the following assumptions are made:

- (1) 100% transmissivity over a 200 Å wide transmission band.
- (2) Filter transmission outside pass band is 0.01%.
- (3) Constant light intensity over a 10,000 Å wide spectrum.
- (4) The range of the absorption spectrum is wider than the filter bandwidth.

Under these conditions, the light intensity sensed outside the transmission band is equal to the light intensity sensed in the transmission band when the atmospheric transmission is 0.5% in the absorption spectrum. Based on these considerations, a dynamic range of 100 is assumed. This result is in agreement with the dynamic ranges of actual experiments. This consideration shows that very low transmissivity outside the filter pass band is important, while transmissivities of 100% or 90% in the filter transmission band have a relatively small influence on the dynamic range.

(b) In-Flight Calibration

Another area of concern is gain drift of the photomultiplier. The following four methods to calibrate the photometers are of interest:

- (1) Initial measurements at an altitude when no significant absorption can occur.
- (2) Comparison measurements with the same photomultiplier in an optical wavelength region of no atmospheric absorption.
- (3) Use of a calibration lamp.
- (4) Photomultiplier calibration based on counting of photon pulses and comparison with analog photomultiplier output current.

(1) Initial measurements at altitudes where no atmospheric absorption in the selected wave bands can occur are limited by the technical feasibility to perform early deployment and orientation of the descent probe. To determine if this concept is practical, the tradeoffs in regard to highest possible absorption in the absorption bands vs highest practical measurement altitudes have to be evaluated. It is anticipated that when measurements are conducted in a high and a low absorption band, then conditions can be selected so that no significant absorption will occur during the initial measurements in the low absorption bands. This will be confirmed by the high absorption band measurements. If both or more filters can be applied alternatively to one photomultiplier (filter wheel photometer), then this method will also provide an inflight calibration of the photomultiplier sensitivity.

(2) Application of a filter wheel requires probably sun pointing of the photometer and moving instrument parts are needed. The advantages of a filter wheel are constant detector sensitivity for all measurements and calibration with a neutral density filter is practical.

(3) Application of a calibration lamp will provide accuracies of about $\pm 10\%$, provided that the high voltage supply for the photomultiplier changes less than 0.1% between calibration points. During calibration the ambient light may not interfere.

(4) At low light levels or with a highly absorbing filter the number of photons sensed by the photomultiplier can be counted. Comparison of the number of photon pulses and the analog photomultiplier output current provide a measure of the photomultiplier gain.

(c) Filter Characteristics

The optical characteristics of narrow band pass interference filters are affected by the angle of incidence of the light beam and by the filter temperature. These effects influence the photometer design. The band position is a function of the angle of incidence and the effective index of refraction of the spacers between the reflection stacks of the filter. Table IIC-3 shows representative values of the center wavelength ratio for light incident at angle α , normal incidence, and two spacer indexes of refraction.

Table IIC-3 Shift of Center Wavelength of Filter

Incident angle α degrees	0	5	10	20	30	45
Refractive index = 1.35	1.000	0.9979	0.9917	0.9764	0.9289	0.8518
Refractive index = 1.95	1.000	0.9990	0.9960	0.9845	0.9665	0.9319

Table IIC-3 shows that for incidence angles of 10 degrees the shift of center wavelength is less than 1%. The filter transmittance decreases significantly at incidence angles of 20 degrees and higher and when the temperature rises above 100°C. Therefore, we will assume that an incident angle variation of ± 10 to 15 degrees is acceptable for band pass filters with a bandwidth of about 200 Å. The shift of the pass band position due to temperature is roughly 0.004%/°C.

(d) Photometer Mechanization Concepts

A large number of photometer designs are possible. To point out major tradeoffs, the following three concepts will be discussed.

- (1) Accurate sun pointing and a multichannel photometer with a filter wheel.
- (2) Photometers mounted on a spinning probe and sensing in a plane parallel to the probe roll axis.
- (3) Photometers with a semispherical field of view looking upward.

(1) Sun Pointing Photometers

Figure IIC-3 shows a design concept for such an instrument. Most of the influence of light scattered or reflected by gas molecules, dust particles or droplets can be avoided by accurate sun pointing of absorption band photometers with a narrow field of view ($< 1^\circ$ cone angle). In addition, attitude variations of the descent probe do not change the sun incidence angle and the signal intensity. Measurements can be conducted at any time. As discussed previously, application of a filter wheel with one or two detectors provides more accurate correlation between measurements. Application of a filter wheel photometer is compatible with a sun pointing instrument.

The disadvantages of optical absorption measurements with accurately sun pointing instrumentation are additional weight (3 lb), less reliability (moving parts), higher power consumption (2 w) and cost.

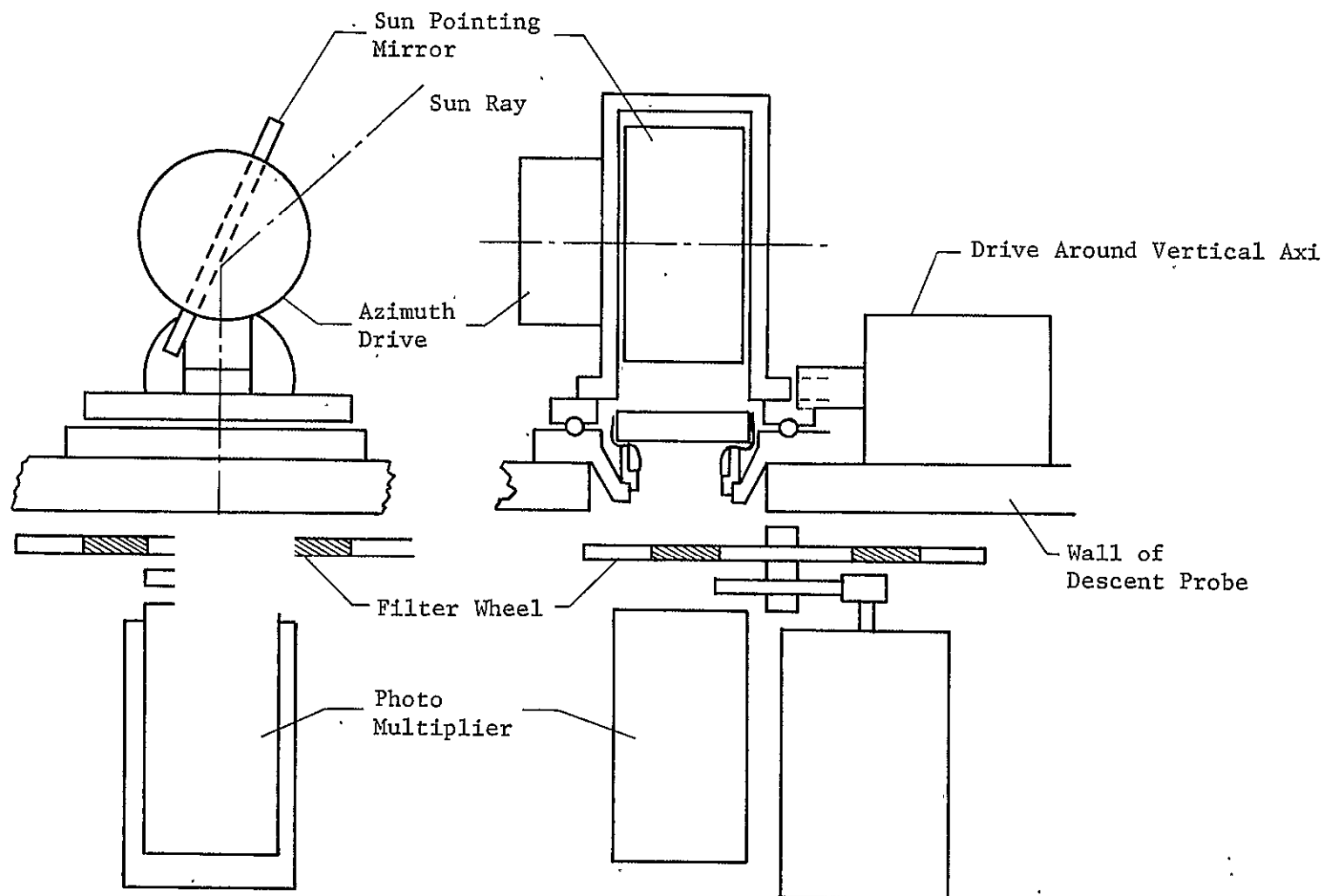


Figure IIC-3 Two Cross Sectional Views of Sun Pointing Photometer with Mirror Pointing

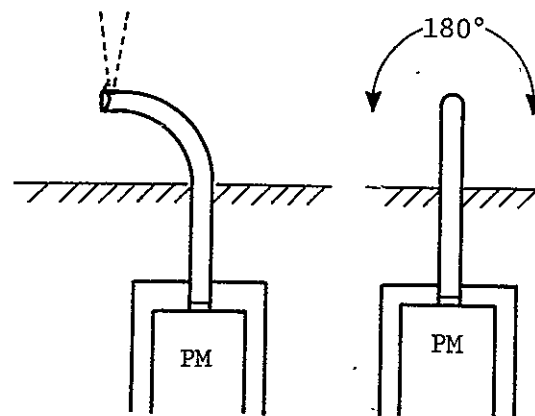
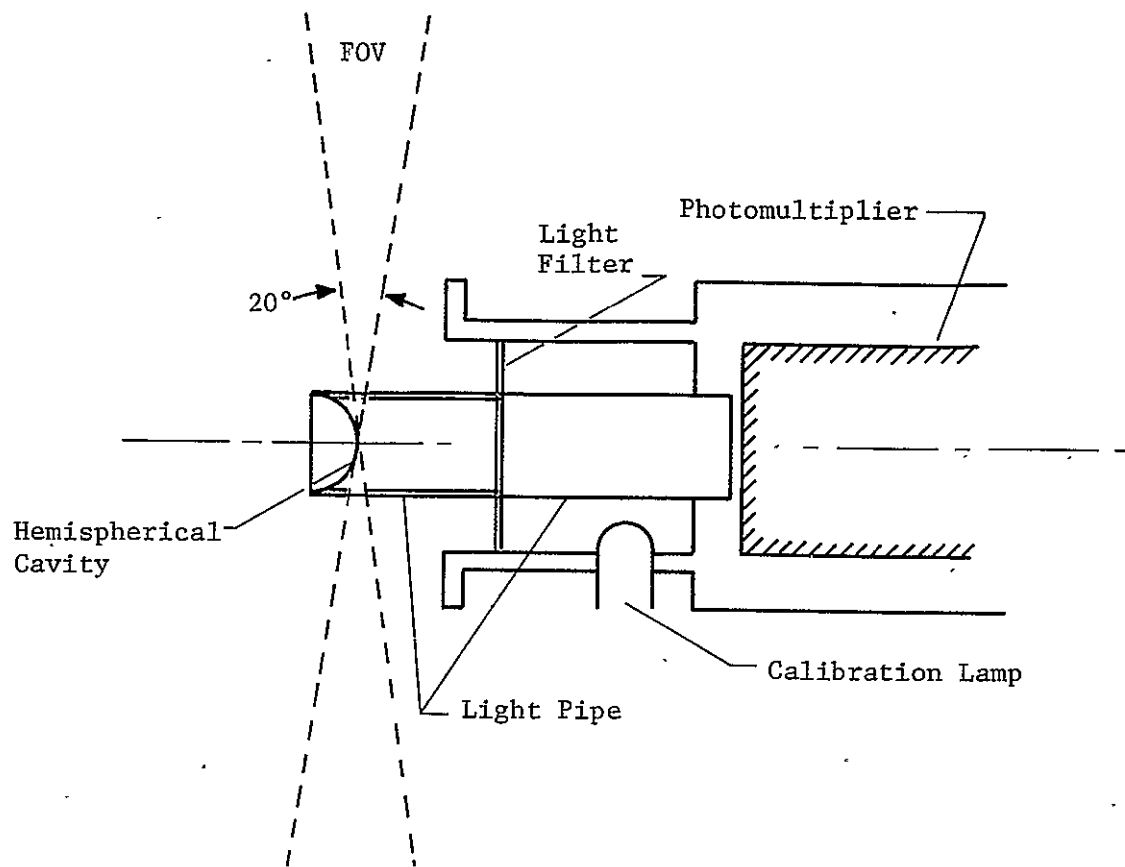
(2) Photometers which are mounted on a rotating entry capsule and sense in a plane parallel to the capsule axis.

Figure IIC-4 shows an optical arrangement which allows a uniformly sensitive field of ± 10 degrees normal to a light pipe axis and 360 degrees around the axis. Instrumentation employing this concept was used for ozone measurements with an Air Force satellite launched in polar orbit in July 1962. For the Jupiter probe a sensitivity of less than 180 degrees upward is needed. Figure IIC-4 depicts the photometer installation and the vertical FOV requirement if the probe rotates at least 180 degrees between two photometer measurements. Each photometer consists of a photomultiplier detector, a filter, a light pipe with the desired FOV and a calibration lamp. All photometers are triggered at the same time and when they point at the sun.

Unless the probe spin rate is accurately controlled by aerodynamic fin adjustment, small rocket engines or inertial equipment, a pressure or time reference is needed to determine when the absorption measurements occurred relative to the other measurements.

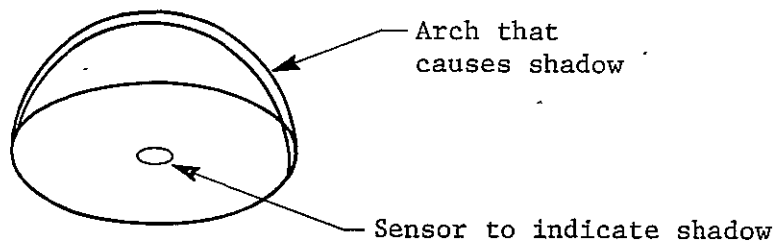
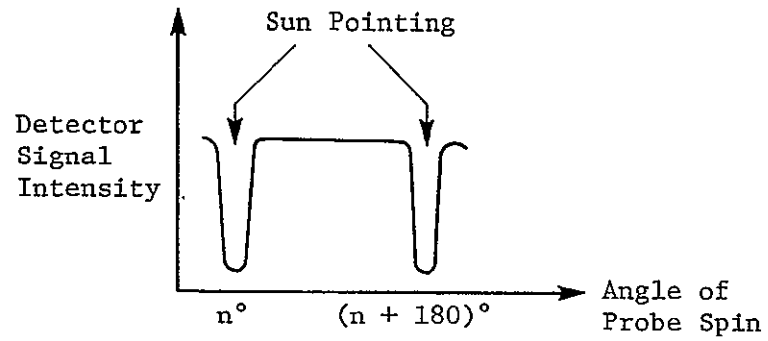
To determine when the sun passes the sensitivity plane of the photometers, concepts shown in Figure IIC-5 could be applied. An arch over a point detector provides a shadow only when the arch and the detector are in the desired plane. Then the rapid change of the light signal triggers the photometers. Another concept is to use a cylindrical lense and two light detectors as shown in Figure IIC-5. When the signal goes rapidly through zero, then the sun is in the specific plane.

The disadvantage of this photometer mechanization concept are the required probe spin rate, measurements can only be performed when photometers are sun pointing and the field of view is approximately 0.2π steradian.

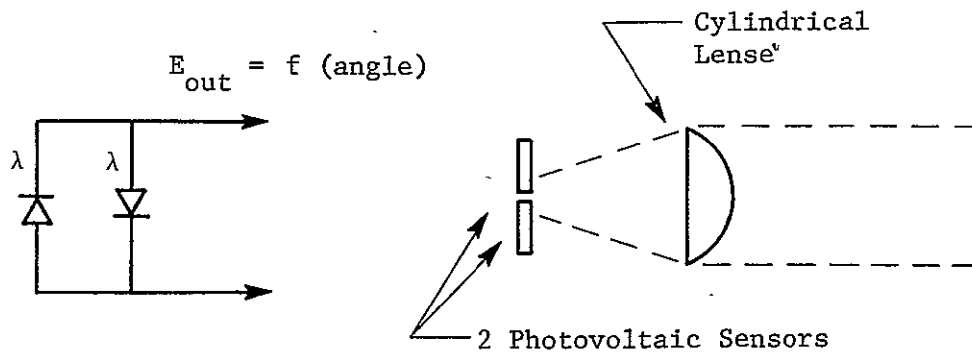


Two Cross Sectional Views
of Probe Installation
with Bent Light Pipes

Figure IIC-4 Detector with FOV 360° around Light Pipe Axis and
±10 Degrees Normal to Axis



Note: Sensor is in shadow of arch when plane of arch is sun pointing.



Note: During sun pointing, light on both detectors is balanced and electrical signal is zero.

Figure IIC-5 Concepts for Detection of Sun Pointing Direction

(3) Photometer with a 2π Steradian Field of View Looking Upward.

Figure IIC-5a shows two concepts for such an instrument. Both concepts have a light filter or a filter wheel which passes to the detector only the light with the wavelengths of interest. A photomultiplier is required to achieve the necessary narrow pass band sensitivity. Channeltron photomultipliers are most promising in regard to resistance against high acceleration.

In one concept the hemispherical diffuser scatters the incoming light and a light baffle absorbs most of the light. The light that reaches the interference filter is within $\pm 10^\circ$ degrees normal to the filter and therefore narrow (200 Å) pass band filtering is possible. It may be difficult to obtain a light diffuser that works at long wavelength as well as in the ultraviolet spectrum.

The other concept shown in Figure IIC-5a uses light pipes or fiber optics to gather light with equal sensitivity over a solid angle of 2π steradian. Baffles limit the cone angle of the incident light to achieve also approximately normal incident on the light filter.

(4) Preferred Instrument

The best instrument mechanization is a compromise between detailed measurement requirements and the instrument characteristics such as weight, reliability, quality of measurement, and cost. More detailed information about the measurement requirements is desirable. Assuming little interference from scattered light above the clouds, the simple filter wheel photometer concept with 2π steradian field of view (Figure IIC-5a) is preferred. Estimated instrument characteristics for weight and power consumption are 1 pound, and 1.5 watts, respectively.

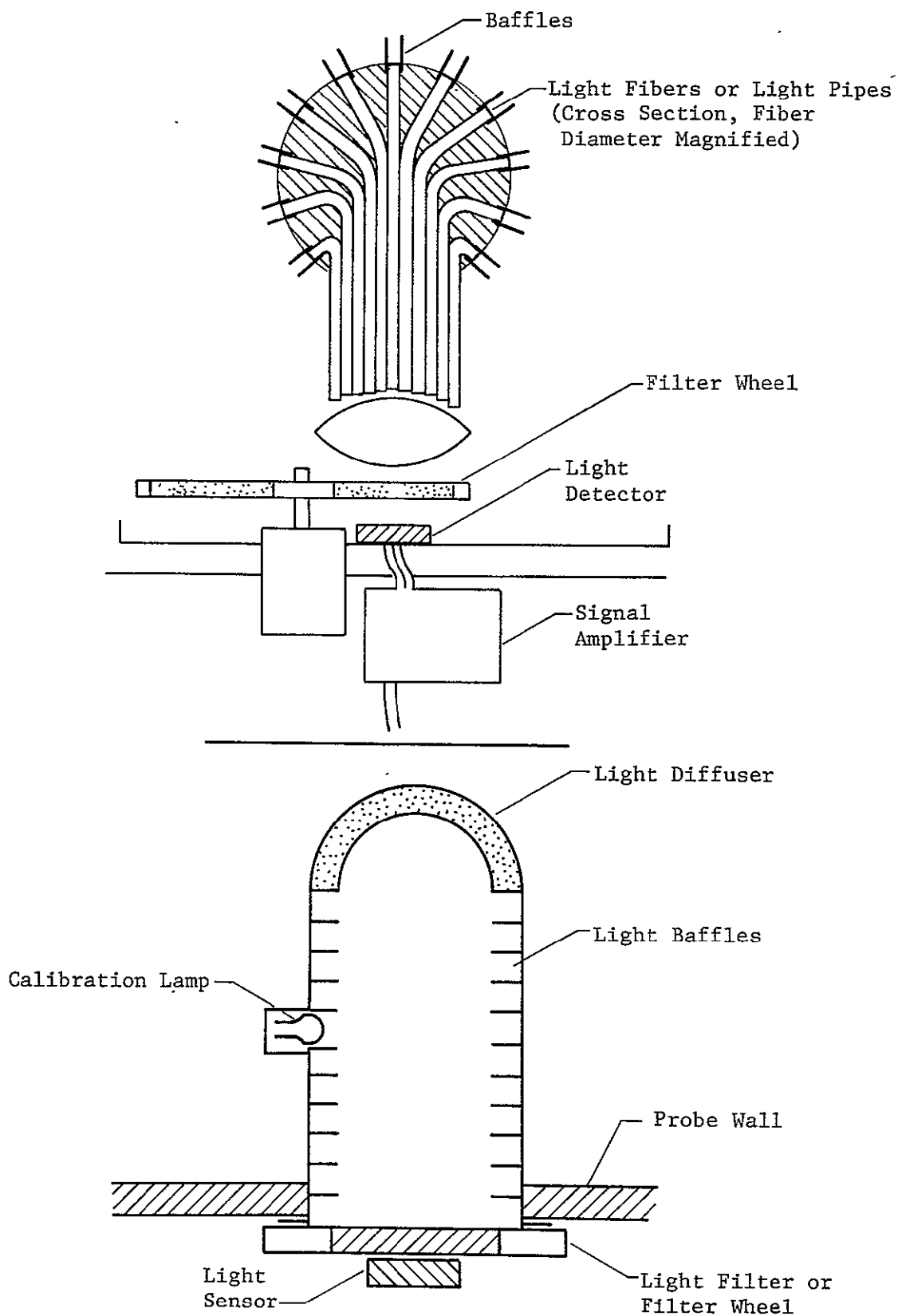


Figure IIC-5a Two Concepts for Multichannel Solar Photometers with 2π Steradian Field of View

e. Total IR Flux Measurements with Wide Field of View

1) Instrument Requirements

Below the clouds where there is little sunlight, most of the radiative energy exchange is in the IR region. Figure IIC-6 shows the black body radiation for temperatures between 200 and 6000°K. The anticipated atmospheric temperatures are between 200 and 1400°K. Therefore measurements between wavelength of approximately 0.5 and 50 μ are of interest. The measurement accuracy should be approximately $\pm 3\%$ of reading

2) Alternative Instrument Concepts

Thermal detectors such as thin film thermopiles, pyroelectric detectors, thermistor sensors and Golay cells can be designed for approximately constant sensitivity over this range. The sensor cannot be exposed to the ambient environment; and therefore, a window is required.

The ideal window has constant transmissivity from 0.5 to 50 μ and is fully compatible with the environment. A compromise is required. Some window materials (CsI, 0.3 -50 μ ; CsBr, 0.3 -40 μ) have a wide spectral transmission range but are not compatible with the environment and have poor mechanical characteristics. Large diamond windows are very costly. Hot-pressed Cadmium Telluride window material is transmittant between 1 and 30 μ at window temperatures up to 300°C.

Figure IIC-7 shows a radiometer concept. A radiation chopper and temperature control of chopper blades are anticipated. Temperature measurement instead of temperature control would reduce power consumption but increases data transmission rate. A compromise in regard to the wide (2π steradian) field of view is foreseen. About constant sensitivity over a 2π steradian range is possible in principle with bent light pipes of IR window material, but further analysis and tradeoffs of measurement objectives and instrument design may show that a 60° or 90° cone angle provides sufficient FOV for the experiment objectives.

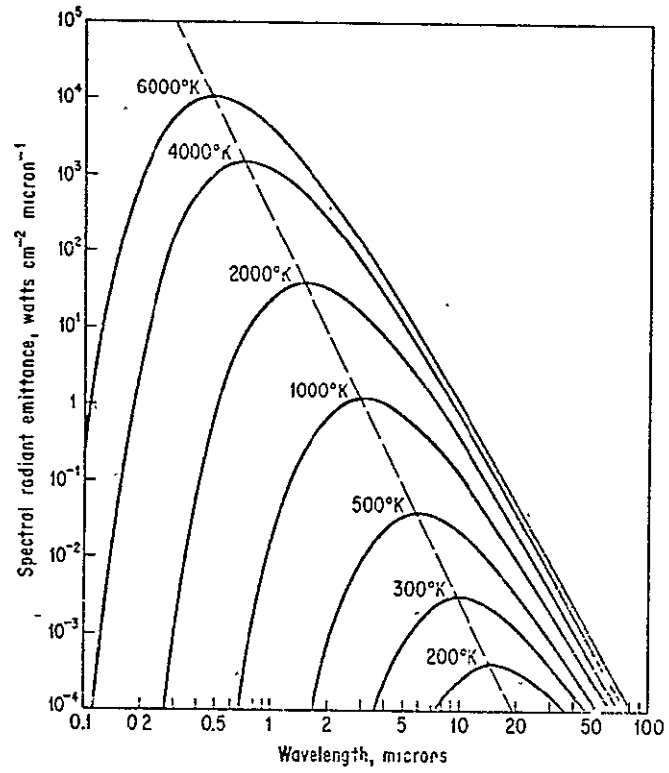
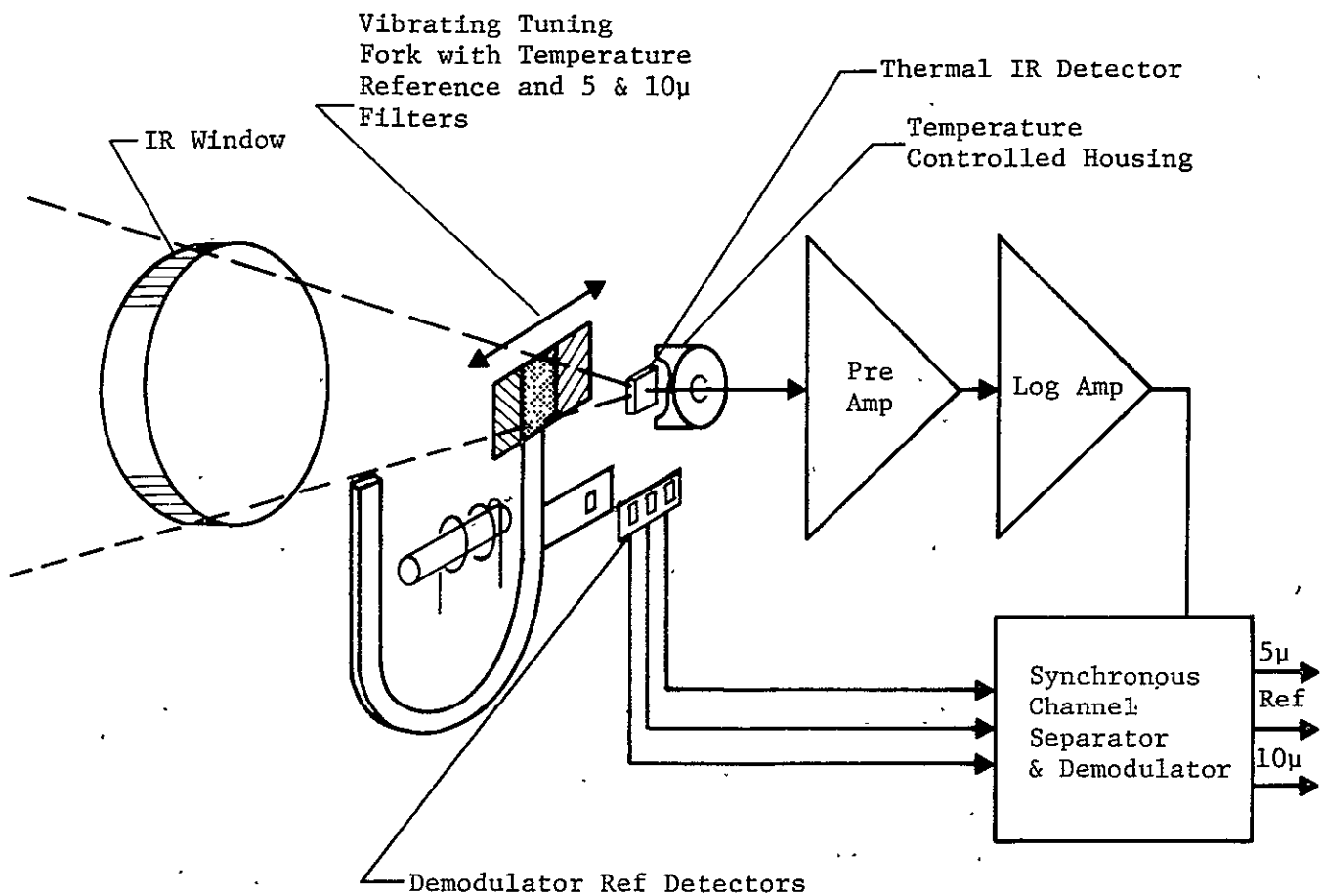


Figure IIC-6 Blackbody Radiant Emittance



Assumed Instrument Concept

Estimated Characteristics of One 5 & 10 μ Dual Channel Radiometer

Weight:	2.5 lb
Power:	2.5 w
Range:	150 to 1400°K
Accuracy:	Equivalent to $\pm 1^\circ\text{C}$ Black Body Temperature
Field of View:	Approximately 30° cone angle

Figure IIC-7 Concept and Characteristics for Dual Channel IR Radiometer

3) Preferred Instrument

The anticipated radiometer has a radiation chopper with temperature controlled chopper blades. Temperature measurement instead of temperature control reduces power consumption, but more data have to be transmitted. A compromise in regard to the wide (2π steradian) field of view requirement is anticipated. Approximately constant sensitivity over a 2π steradian range seems possible with bent light pipes of IR window material. Further analysis and tradeoff studies will probably show that a 60 or 90 degree cone angle provides sufficient field of view for this IR radiometer. Compatibility of the IR window with high temperatures would be a problem.

f. Dual Channel Radiometer for 5 and 10 Micron Wavelength

1) Instrument Requirements

Near 5μ the Jovian atmosphere is expected to be relatively transparent and near 10μ it is absorbing or opaque. Therefore, cloud particles are the main cause of short range atmospheric absorption near 5 micron and comparison of both channels yields information about cloud densities and the cloud profile.

2) Alternative Instrument Concepts

Information about high temperature tests of Irtran 2 and 3 at 1, 2 and 3 micron shows that the transmissivity of these materials changes little during the first hour at 755 and 1000°C, respectively. It is therefore assumed that a window for the range of 4 to 11μ is feasible at temperatures up to about 800°C.

Considerations in regard to IR detector and instrument electronics have been discussed in the section about radiative temperature measurements. A thermal IR detector (thin film thermopile, pyroelectric detector) is assumed because the sensitivity is sufficient and no cryogenic cooling is required.

3) Preferred Instrument

In our radiometer concept both broad band interference filters are attached to the tuning fork light chopper and are alternately put into the light path. The center part of the chopper blade is opaque and temperature controlled to provide a radiometer reference point for inflight calibration.

g. Lightning Measurements

1) Instrument Requirements

Lightning flashes in the Jupiter atmosphere may be an important source of non-equilibrium chemical species and the production of organic molecules. Generally, lightning covers an altitude range of one or several kilometers. The horizontal direction of lightnings relative to the probe is not important. It is difficult to identify with simple instruments the exact altitude range of lightning phenomena. From these considerations it is concluded that lightning measurements over an altitude range of about one kilometer can be summarized for data transmission. Because there is a wide range of possible numbers and intensities of lightnings in each altitude interval, some kind of on-board data compression is needed. In general, the horizontal direction of the lightning relative to the probe is not important. If the signal attenuation is small and omnidirectional signal propagation can be assumed, then the received optical signal intensity provides an indication of the energy released per volume of atmosphere.

2) Alternative Measurement Concepts

Following is a list of possible measurement concepts in the order of increasing information content and increasing requirements for weight and power:

- (a) Detector indicates if lightning did occur or did not occur during sampling period; 1 bit per sample is required (Figure IIC-8a).

Lightning Sensor Concepts for Jupiter Probe

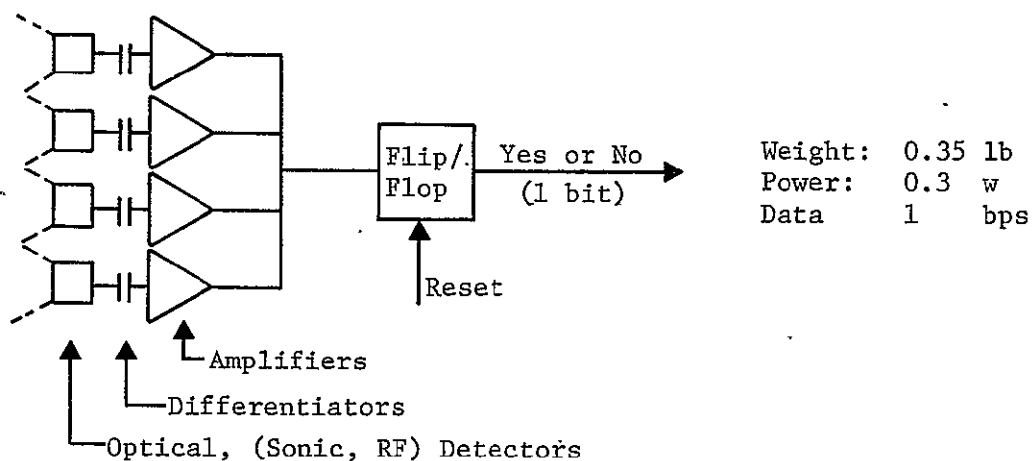


Figure IIC-8a Sensor to Detect If Lightning Occurs

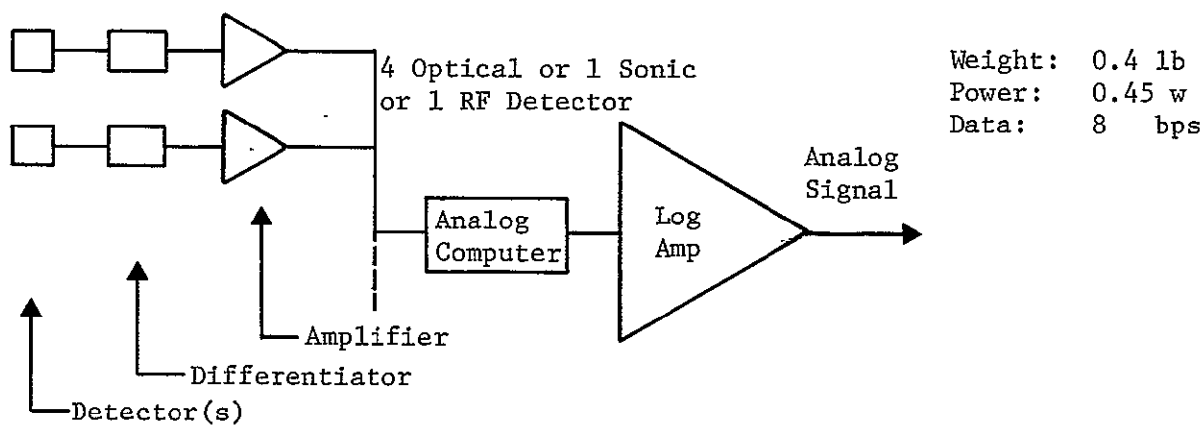


Figure IIC-8b Counter for Lightning Flashes

Lightning Sensor Concepts for Jupiter Probe (continued)

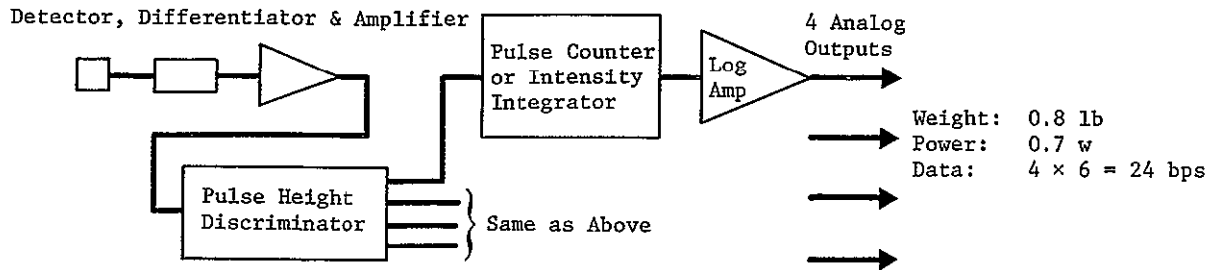


Figure IIC-8c Counting or Intensity Integration for Several Signal Intensity Levels

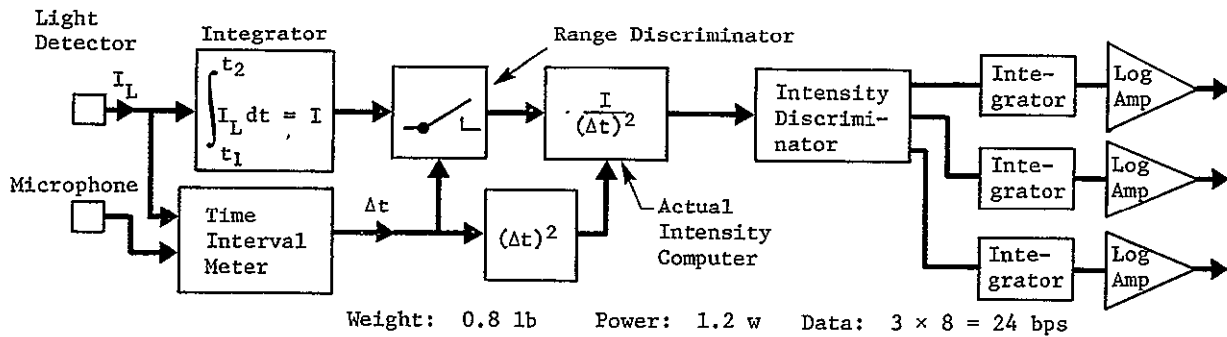


Figure IIC-8d Integration of Actual Lightning Intensities Within a Specific Distance and in Three Actual Intensity Ranges

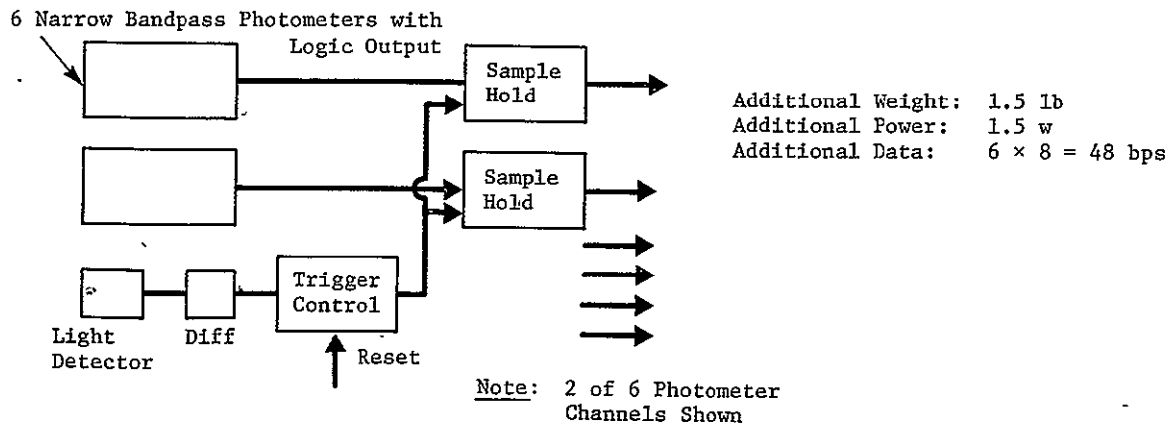


Figure IIC-8e Additional Measurements of Optical Spectra during Lightning

(b) Count number of lightnings which can be sensed during sampling period; 4 to 12 bits are required. A logarithmic counting scale with 6 to 8 bits per sample is considered a good compromise between accuracy requirement and minimum data rate (Figure IIC-8b).

(c) Count number of lightnings at several signal intensity levels (pulse height discriminator); 4 to 12 bits and 3 to 20 intensity levels can be used respectively for counting and intensity discrimination. We assume 6 bits for each counter and 4 intensity levels. Therefore 24 bits are required for each sample interval (Figure IIC-8c).

(d) Optical, sonic and radio wave effects can be used to detect lightning. Because sound travels much slower than electromagnetic waves, the difference in time of signal arrival can be used to indicate the distance between probe and lightning phenomena. Because of different attenuations, comparisons of the intensities of the radiowave and the optical signals at each lightning provide an indication of the distance to the lightning. The detectors sense the intensities of radiowave and optical signals and the sound travel time for each lightning. The degree of data compression depends on the science value. We assume that for each sample interval a measure of the total energy released within a distance of 10 km and within 3 lightning intensity ranges (0-1, 1-10, > 10, relative units) are the most important parameters and 3×8 bits are required per sample interval. Modifications such as automatic adjustment of sensed range or measurement of total lightning energy per volume are possible (Figure IIC-8d).

(e) In addition to the measurements outlined above, measurements related to the optical spectrum of the light pulses can provide information related to chemical discharge processes and atmospheric absorption. We assume that 5×6 bits are required additionally per measurement and only one measurement per sampling interval would be performed (Figure IIC-8e).

For the baseline mission it is recommended to assume the third alternative concept outlined above. If about 3 pounds of instrumentation are available, then the fourth alternative is preferred.

It is recognized that many simplifying assumptions were made and a large variety of other concepts and combinations are possible. The objective of this discussion was to outline basic concepts of lightning measurements.

Lightning is an electrical discharge phenomena. It is associated with emission of light (very hot ionized gas), radio wave signals (electromagnetic fields caused by discharge current), and sound (due to sudden thermal expansion of gas).

These three effects can be used to sense lightning. Various tradeoff factors are involved. A radio wave detector has the longest range but other phenomena may cause signals similar to lightning. The threshold of a sound detector is influenced by aerodynamic noise and thermal effects.

Because an optical lightning detector was stipulated in the RFP, optical lightning detection is discussed in more detail than a wide range radio frequency detector.

There are three major tradeoff factors for the selection of the lightning detector:

- (1) The light must be conducted to the light detector which must have a temperature below 150°C. To avoid cooling requirements, the optics should withstand the ambient temperature.

- (2) The lightning signals must be sensed in spite of the background radiation caused by the hot atmosphere.

- (3) A small, simple light detector (solid state) is preferred to evacuated and less rigid detectors (vacuum diode photo tubes, photomultipliers).

Tradeoffs between the various considerations are necessary. Glasses with softening points above 1600°K are available. A wide field of view (120° cone angle) and low heat transfer to the light detector and the thermally controlled area of the probe are desired. This can be achieved by gas spaces between optical elements. The feasibility of a light pipe consisting of hollow tubes with reflective inside surfaces is of interest. A preliminary concept for the optical arrangement of the lightning detector is shown in Figure IIC-9.

To reduce the intensity of the background signal caused by the thermal radiation of the hot atmosphere, short wavelength (blue and ultraviolet) are preferred for lightning detection. (We assume that the temperature of the lightning arc is above 4000°K). However, the sensitivity of the small and reliable solid state detectors decreases rapidly at wavelength shorter than 0.5 μ . Figure IIC-10 shows these relationships. Based on these considerations light with wavelength longer than 0.4 to 0.5 μ will be filtered out. The relative response of selenium photo detectors is better than the silicon detector response. However, silicon detectors withstand higher temperatures (150°C) and all the tradeoffs have to be evaluated. Vacuum diode photo tubes and photomultipliers have high sensitivity in the blue and ultraviolet part of the light spectrum. However, these detectors require a vacuum tube and are considered less resistant to shock and vibration. Solid state detectors can probably be exposed to 1000 atmospheres. Otherwise, they will be sealed in a small container (similar to TO 5 transistor can) with a window.

Conclusions:

The concept for optical lightning detection is to use four lightning detectors with a conical view angle of about 120 degrees. One detector looks downward and three units are equally spaced around the probe circumference. The estimated weight of each detector is 3 ounces.

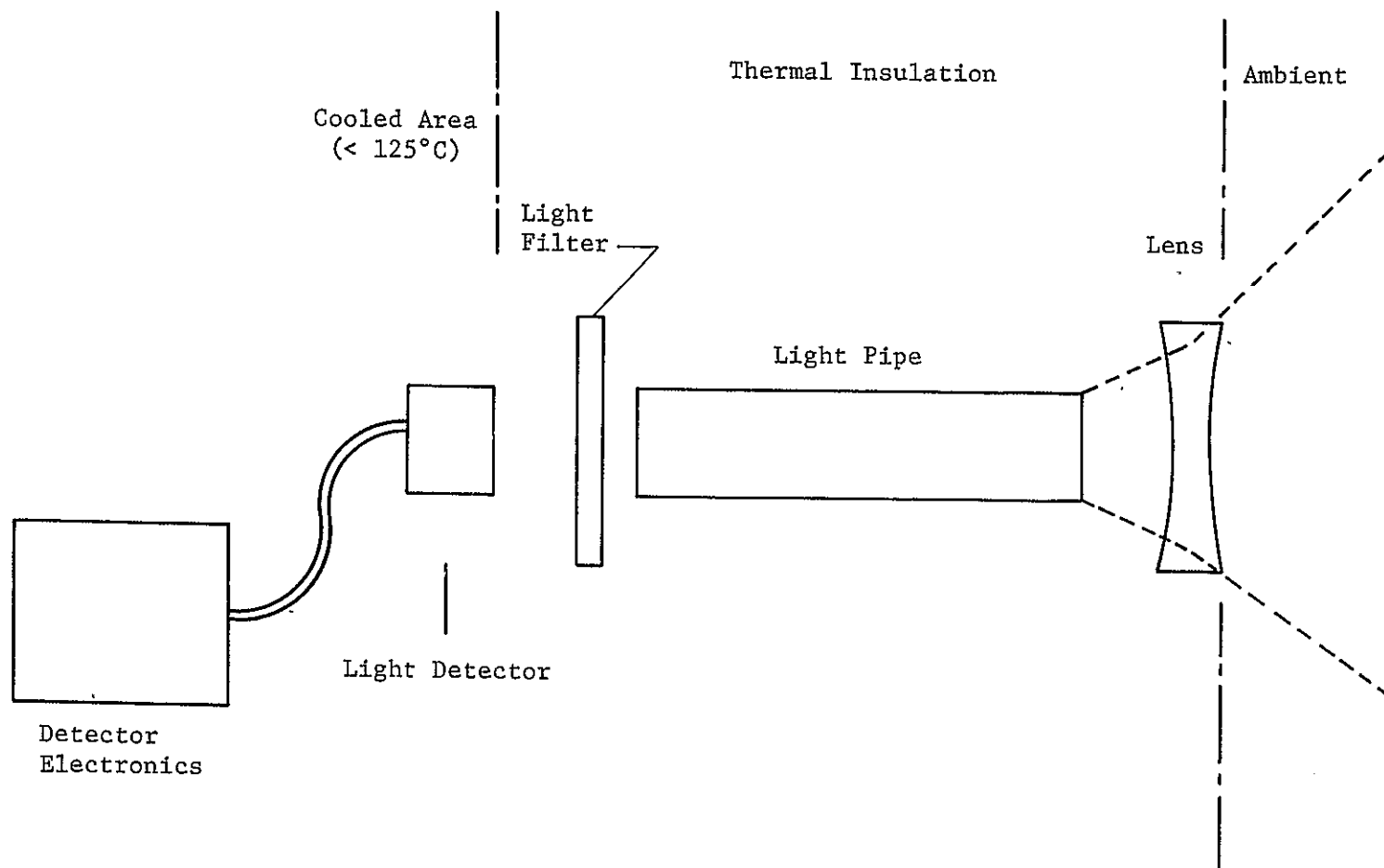


Figure IIC-9 Concept of Lightning Detector

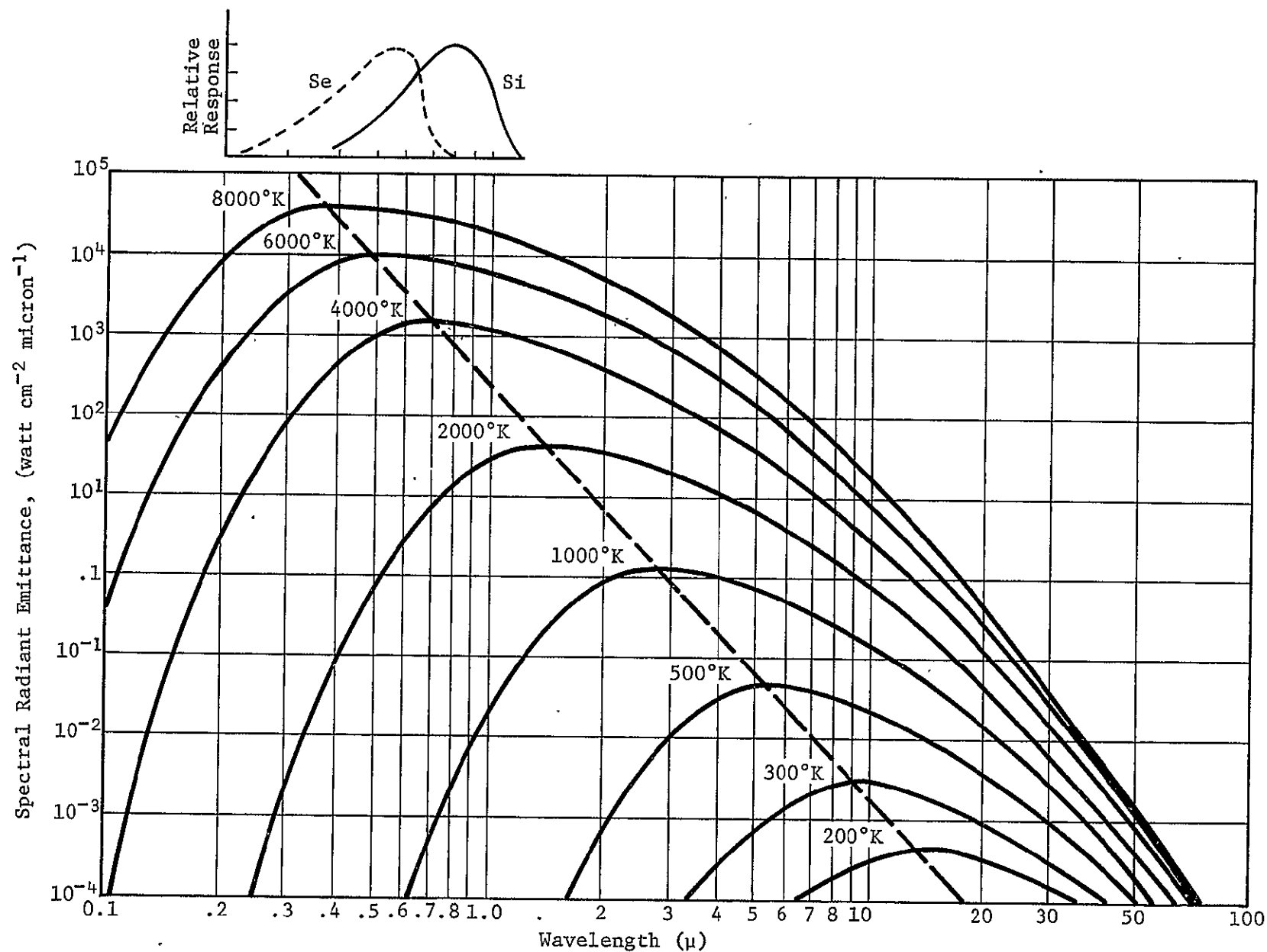


Figure IIC-10 Black Body Spectral Radiant Emittance and Relative Response of Silicon and Selenium Detectors

Figure IIC-9 depicts a design concept. All components can be designed to withstand 1000 atmospheres. The temperature of the light detector and associated electronics must be between -55 and 125°C . Lightning detection by radio or microphone will be further evaluated. Some weight savings and improvements of detector range appear possible. Should the atmospheric temperature exceed 1800°K , then the thermal radiation can jeopardize the sensitivity of optical lightning detection.

3) Preferred Instruments

Because optical and sonic detectors are limited to a range in the order of 30 kilometers, a small radio receiver is used to cover a range of more than 300 kilometers. This is important in case the probability of lightning is low. Signal handling in the receiver is arranged to filter out lightning signals.

In addition a microphone will be used for sonic lightning detection. Because of its short range, some altitude resolution is feasible. The combination of sonic and RF lightning detector can provide information about the distance to the lightning.

h. Composition Measurements

1) Requirements

As Table IIB-2 shows, atmospheric composition measurements are very important for the exploration of Jupiter. The relative abundance of H and He, the isotopic ratios of H/D , $^3\text{He}/^4\text{He}$, $^{20}\text{Ne}/^{23}\text{Ne}$, $^{36}\text{Ar}/^{40}\text{Ar}$, $^{12}\text{C}/^{13}\text{C}$, and the minor atmospheric constituents should be measured and a threshold sensitivity near 0.1 ppm is of interest. Indication of complex molecules is also desirable. These measurements have to be conducted over a wide range of ambient pressures and temperatures while the descent probe passes through clouds.

(a) Single-gas detector

These instruments usually rely on some property or effect (not always unique) of the gas which is sensed. If a radioisotope such as Kr^{85} (Krypton) can be stably embedded in a solid that reacts with a specific gas, chemical erosion will cause a proportional loss of radioactivity (0.67 Mev betas) and thus provide a measure of the reactive gas. Detection of 2 ppm was reported when the kryptonated source is heated to 1000°C . This approach is in the experimental stage.

Light weight single-gas detectors are of interest for important constituents which are not readily identified with more universal analyzers. Low humidity is a typical example. However, single-gas detectors are not expected to replace the more universal composition analyzers described below.

(b) Absorption analyzers measure the absorption of narrow wave bands in the UV, visible and/or IR spectrum. It appears possible to measure the optical absorption characteristics while the gas is near ambient temperature and pressure. Because of the wide pressure variations the instrument would have to be designed for a wide dynamic range.

(c) Mass spectrometers ionize the gas sample and measure the mass to charge ratio. Flight-type mass spectrometers are rugged, weigh 5 to 10 pounds and provide an analysis within a few seconds. However, the resolution of flight-type mass spectrometers is not much better than unit resolution. Therefore, mass spectrometer peaks at the following m/e ratios can be caused by several constituents which are listed below.

Approximate m/e Ratio	Constituents
2	H_2 , D
3	HD, He^3 , H_3
4	D_2 , He^4

To resolve these constituents, a mass spectrometer with a resolution of about 1/500 m/e at low mass numbers is required. The feasibility of developing such a mass spectrometer for space flight deserves further evaluation and study. A mass spectrometer based on time of flight measurements in a quadrupole-type analyzer ("salt shaker" type) may be a promising concept for development. Preliminary tests to distinguish between N_2 and CO by comparison of the peaks at different ionization potentials (different ionization efficiency of N_2 and CO) showed encouraging results. This approach should be of interest if it provides clues to distinguish between constituents which differ less than 0.5 amu in mass.

(d) During a gas chromatograph analysis, an atmospheric sample, together with an inert carrier gas, is injected into one or more gas chromatograph columns. The columns contain absorptive material or molecular sieves. As the gas is flushed through the column, the gas constituents take different time periods until they have passed the column and reach the detector. The duration of these time periods is a measure of the composition, and the signal intensity indicates concentration of the specific constituent. Difficulties associated with gas chromatographs are their long analysis times (minutes), isotope ratios can generally not be determined, and constituents of the hot ambient atmosphere may condense.

Condensation in the critical parts can be prevented by a "cold trap" and/or heating of the flow channels. It is apparently not practical to reduce the gas chromatograph analysis time to one minute or less when a wide range of constituents is analyzed.

(e) The gas chromatograph-mass spectrometer is considered the most universal flight instrument for atmospheric analysis within a few minutes. First the gas chromatograph separates groups of constituents. Then the mass spectrometer measures periodically the mass to charge ratio of the gas chromatograph effluent. Through the combination of the basically different gas chromatograph and mass spectrometer principles, a wide range of atmospheric constituents and isotopes can be resolved and measured accurately.

(f) Removal of hydrogen from the atmospheric sample can be used to enhance the sensitivity of the analysis when the abundance of hydrogen does not have to be measured. It is important that the hydrogen separator does not interfere with the other atmospheric constituents.

The Jet Propulsion Laboratory has developed a palladium separator which has promising characteristics for hydrogen removal. In this device a heated palladium-silver tube is generally surrounded by an oxidizing atmosphere. The hydrogen in the sample which flows through the palladium-silver tube permeates through the probe walls, and the hydrogen is therefore separated from the sample.

Further R&D efforts are recommended for the atmospheric sampling system. The difficulties are similar to those for mass spectrometer sampling in the Venus atmosphere. In principle a variable inlet leak is best, but there is doubt if a reliable design for the planetary atmosphere can be achieved. Variable leaks with suitable leak rate have been developed, but it is recommended to exclude dust, dirt, chips, moisture and other contaminants. This is difficult to achieve during actual atmospheric descent. Figure IIC-11a depicts a concept for a single variable mass spectrometer leak. Figure IIC-11b is a sampling concept with two valves.

Figure IIC-11c shows the preferred sampling concept. For analysis the inlet valve is briefly opened and the opening period is a function of ambient pressure or the pressure in V_1 . The first sintered inlet leak is relatively insensitive to contaminants and restricts the flow to the evacuated volume V_2 . The pressure in the tube V_1 is approximately 0.1 bars. The second sintered leak reduces the pressure in the mass spectrometer to less than 10^{-5} mb.

Another method uses a critical flow nozzle and a jet effluent divider to control and reduce the sample flow. However, typical inlet flow is in the order of 1 std cc/min, and a small mechanical pump is required.

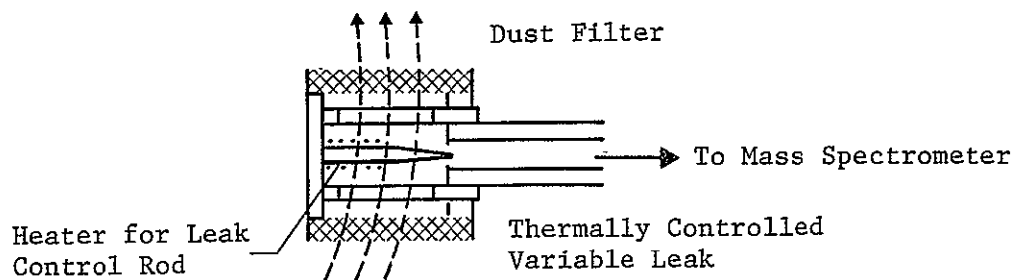


Figure IIC-11a Single Mass Spectrometer Leak

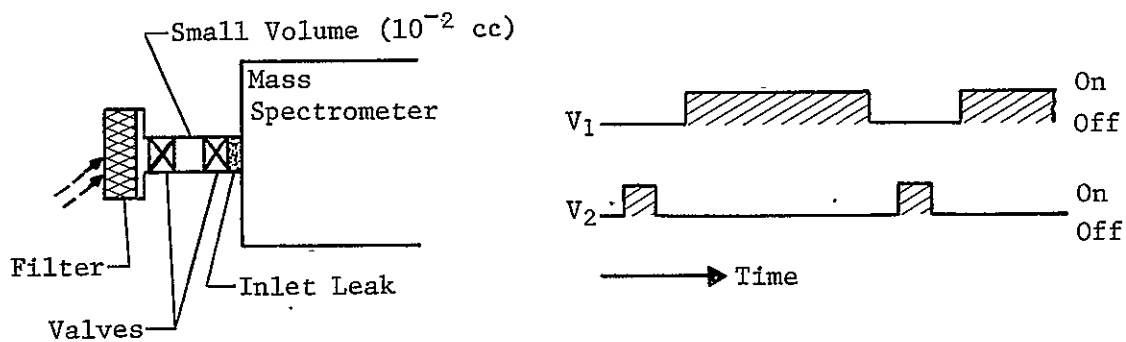


Figure IIC-11b High Pressure Sampling with Two Valves

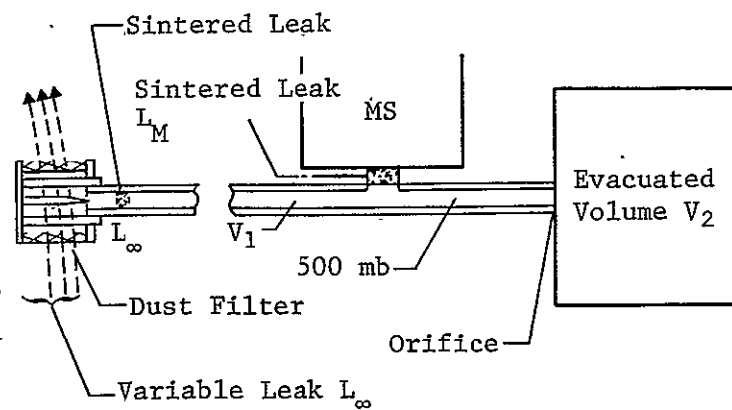


Figure IIC-11c Dual-Stage Pressure Reduction for Mass Spectrometer

3) Preferred Instrument

(a) Gas Chromatograph Mass Spectrometer

Currently a combination of gas chromatograph and mass spectrometer (GC-MS) is the most promising concept for a flight instrument to resolve atmospheric constituents that have nearly the same molecular mass or the same m/e ratio when double ionization occurs. In addition, the threshold sensitivity for a flight-type instrument can be improved from several parts per million to the fractional part per million range. Such an instrument is outlined in JPL Section Document 131-07. Reference IIA-1* shows a gas chromatographic analysis of hypothetical Jovian atmosphere with a temperature programmed (25 to 150°C at 12°/min) Poropak Q column and nitrogen carrier gas. Hydrogen, helium, neon, argon, methane, ammonia, hydrogen sulfide, water, and hydrogen cyanide are resolved. The total analysis time is approximately 10 minutes. Hydrogen, helium, argon, and neon are eluted within 1.5 minutes. Therefore, a combination of a GC with such a column and a continuously scanning mass spectrometer are a promising concept to resolve within 1.5 minutes constituents that have approximately 1, 2, 3 and 4 m/e . The assumed GC column is similar to the Poropak Q column and the MS scans continuously. The time period between the start of scan and peak measurement determines the mass numbers of the constituents. Programming of signal readout or on-board data evaluation is desirable for reduction of bit rate. Analysis of heavier molecules with up to 60 m/e , may require GC analysis periods of about 10 minutes. Assuming continuance of GC-MS development efforts, a weight of 12 pounds and power consumption of 15 watts are assumed for this GC-MS.

*IIA-1 Simmonds, P. G.: *Potential of GC-MS in the Analysis of Planetary Atmospheres*. American Laboratory, October 1970, pp 8-16.

(b) Mass Spectrometer

For minimum weight and bit rate requirement a mass spectrometer for 1, 2, 3, 4 and > 4 m/e provides some information about the atmospheric composition. Rapid analysis (< 5 sec) over a mass range of 1 to 4 m/e and with a wide dynamic range can readily be accomplished with various types of mass spectrometers. The advantages of low analyzed atomic mass numbers for mass spectrometers with magnetic sectors, quadrupole/monopole and time of flight analyzers are respectively low weight of magnet, low analyzer potentials and short time of flight analyzers. All mass spectrometer types mentioned above can provide the desired measurements. The preferred type depends on the best requirements of weight, power and reliability to achieve high resolution and a wide dynamic range.

If feasible, identification of isotopes with a slightly different mass is also of interest though a higher data rate would be required. A developmental mass spectrometer based on time of flight measurements in a quadrupole analyzer ("salt shaker") has been proposed for high resolution measurements, and separation of isotopes.

It is difficult to predict which mass spectrometer type will be the best several years from now. For this study, a quadrupole mass spectrometer is assumed. Theoretically the quadrupole mass filter is independent of the physical size and imperfections in the contours of the field forming surfaces limit the dimensions.

Figure IIC-12 shows a block diagram of the quadrupole mass spectrometer system. During cruise the ion pump operates for 10 minutes every three days. At aeroshell staging the mass spectrometer inlet is opened and the ion source and pump work continuously. The quadrupole analyzer has flat peaks (100% transmission) and the quadrupole excitation potentials are applied in steps (no continuous scan) for 1, 2, 3, 4 and > 4 amu as controlled by the probe sequencer. To obtain a

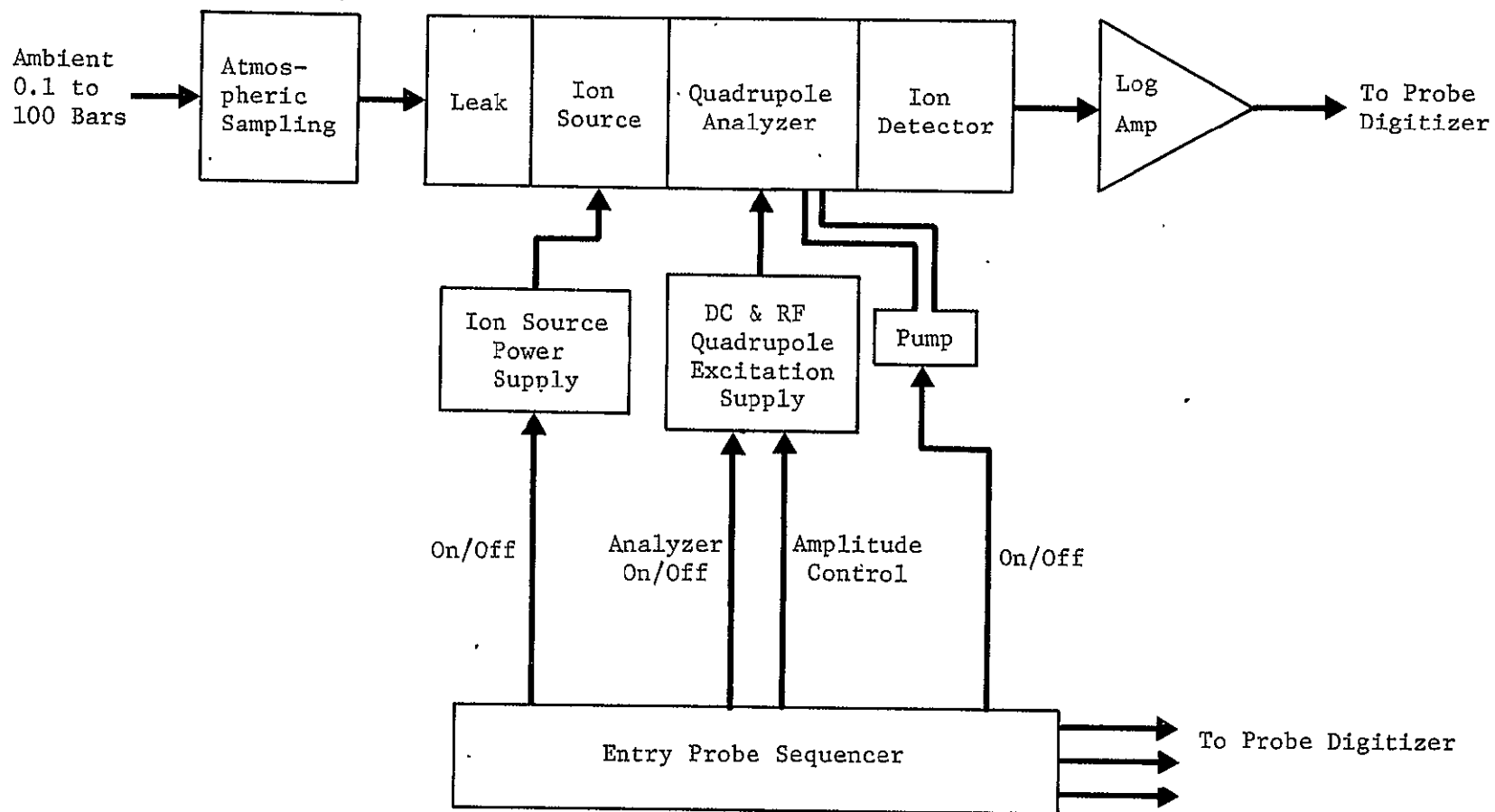


Figure IIC-12 Block Diagram for Quadrupole Mass Spectrometer System (1, 2, 3, 4, > 4 amu)

measure of the concentration of constituents with more than 4 amu, only a fixed RF potential is applied to the quadrupole analyzer and the ions with more than 4 amu (single ionization is assumed) reach the detector. The measurements are repeated in intervals of about 30 seconds. A period of one second per amu step is assumed; however, shorter or longer analysis steps are feasible. The detection threshold improves with increasing analysis periods (noise filtering). The quadrupole power supply is turned on only during measurements.

The estimated total instrument weight and power requirements are 3.5 pounds and 6 watts. Typical characteristics for the quadrupole analyzer are hyperbolic rods which are 2 inches long and 0.15 inch in diameter. Ion source and analyzer have a weight of 0.5 pound. A 0.5 liter/second ion pump weighs 0.5 pound. Half a pound and 2 pounds are estimated for the sampling system and the instrument electronics respectively.

Because of the long measurement periods a dynamic range of 10^5 or 10^6 can be achieved with an ion collector (Faraday cup) and an electrometer amplifier. To obtain a higher dynamic range a less stable but very sensitive photomultiplier is required.

i. Magnetic Field Measurements

1) Measurement Requirements

The magnetic field intensity near the Jovian equator is assumed to be about 7.5 gauss during the measurements of the entry probe. Because of various uncertainties a range of 0.2 to 20 gauss will be assumed.

2) Alternative Instrument Concepts

Table IIC-5 lists various magnetometer concepts. In principle any magnetometer which has a range of 20 gauss or less can be used because the magnetometer can serve as a null indicator while compensating

Table IIC-5 Alternative Magnetometers for Jupiter Descent Probes

Row No.	Measurement Techniques	Previous Use of Technique	Evaluation
1	<u>Proton precession magnetometer</u> Polarizing field excites protons. When field is removed, protons emit signal with a frequency proportional to field intensity. Scalar, absolute. Range 10^{-2} to about 20 gauss. Accuracy: $\pm 10\gamma$, about 10 lb	Vanguard 3	Used only in early spacecraft measurements, heavy. Very accurate, standard.
2	<u>Rubidium vapor magnetometer</u> <u>Helium magnetometer</u> Optically pumped rubidium or helium atoms are de-excited by electromagnetic field, whose frequency is proportional to magnetic field. Scalar, absolute. A range of 0 to 1 gauss is considered feasible.	Explorer 18: 3.1 lb 3.5 w Mariners 3 & 4: 5.5 lb 7 w Range ± 360 gamma	These magnetometers are very sensitive but because of the high weight and power requirement other magnetometers are preferred for the descent probe.
3	<u>Fluxgate magnetometer</u> Ambient field biases magnetic characteristics of saturable core. Even harmonics in secondary winding are proportional to magnetic field vector intensity. Vector measurement, not absolute. Typical ranges: $\pm 64 \times 10^{-5}$ up to ± 2 gauss; Accuracy: 0.6×10^{-5} gauss and 0.001 gauss respectively. 3.5 lb 1.2 w (IMP); 6 lb, 0.7 w Pioneer 6	Mariner 2: 4.7 lb 6 w Range: 5 to 3000 gamma Accuracy: 1 gamma Sensitivity: 1 gamma Pioneer 6, IMP: 3.5 lb 1.2 w Ranges: $\pm(0-25)\gamma$, $\pm(25-500)\gamma$ $\pm(500-10,000)\gamma$ Others: Explorers 12 & 15 Sputnik 3.	Preferred when magnetometer can be mounted inside descent probe. Fluxgate magnetometers measure vector components of the magnetic field and are used in many space applications for measurements below ± 2 gauss. This range can be extended to ± 20 gauss with compensating field. With corrosion protection the Curie point (500 to 1000°C) of the magnetic material causes a basic upper temperature limit. A sensor design for about 400°C appears possible.
4.	<u>Hall Effect Magnetometer</u> Electrical charge carriers experience a force mutually perpendicular to electric and magnetic fields. This force results in an e.m.f. in the direction of the force. The Hall generator applies this phenomenon to measure magnetic fields. Typical range: 10^{-2} to 3×10^4 gauss Accuracy: $\pm 0.5\%$ Estimated weight & power: 1 lb, 0.5 w	Used in many industrial applications. Probably not used for space science measurements because of relatively low accuracy for measurements below 0.5 gauss. Sensor temperature: -269 to +230°C Temperature Coef: $-0.1\%/^{\circ}\text{C}$	Preferred when magnetometer must be outside probe and ambient temperature is below 500°C. The Hall generator is less accurate ($\pm 1\%$) than other sensors but the weight for thermal control is small because the size of the Hall generator is less than 1 cm ³ .
5.	<u>Magnetoresistive Magnetometers</u> The resistance of both metals and semiconductors changes when they are placed in a magnetic field either transverse or longitudinal to the direction of the current flow. Typical range: 500 to 7000 gauss Temperature coef: -0.05 to $0.4\%/^{\circ}\text{C}$	Used in industry and laboratories for measurements of high (>500 gauss) magnetic fields. Temperature range: cryogenic to +110°C.	Not selected because of poor sensitivity near 5 gauss.
6.	<u>Search Coil Magnetometer</u> Spinning coil cuts magnetic field lines and generates e.m.f. proportional to change of magnetic flux through coil(s). Typical ranges: ± 1 to $\pm 10^5$ gauss	OGO 1 Sensitivity: $10\mu\text{V}/(\text{gamma}/\text{s})$ Pioneer 1 and Explorer 6 Range: 10^{-5} to 10^{-2} gauss	Preferred when sensor must be deployed outside pressure shell and ambient temperature is above 500°C. Induction coils for temperatures up to 1400°K are feasible without thermal protection. The coil(s) can be rotated by aerodynamic forces or by the spinning probe (aerodynamic fins spin probe).

electromagnetic coils (Helmholtz coils) are used to expand the measurement range. The compensating coils provide also information about the magnetic field vector even when an absolute magnetic sensor is used. Requirements of weight, power, cost and accuracy are other selection requirements. A consideration of general importance for the magnetic field measurements is thermal protection of the sensor. Only one sensor candidate (search coil) withstands more than 230°C and development of other sensors for several hundred degrees centigrade is difficult. When practical, the sensor should be mounted inside the temperature controlled area of the probe with a nonmagnetic pressure shell. If the pressure shell is magnetic and measurements inside the probe are not possible, then the sensor must be mounted or deployed outside the probe and a weight or power tradeoff in regard to thermocontrol requirements is needed. Only the search coil (or spin coil) magnetometer appears to be feasible for sensor operation over the full environmental range (100 to 1400°K, 0.2 to 1000 bars). Unless the probe spin is used, a drive is necessary to spin the pickup coil(s). Aerodynamic forces can be used to spin the coils. Fixed coils would provide information about attitude and oscillations of the probe.

Spin precession magnetometers (proton precession, rubidium or helium or cesium vapor magnetometers) are absolute scalar magnetometers whose operation depend upon magnetically split, atomic energy states (Zeeman effect). The signal frequency is 4.26, 700 and 2300 kHz/gauss for proton precession, rubidium, and hydrogen magnetometers, respectively. Similar to the Mariner-3 helium magnetometer, Helmholtz coils can be applied to compensate for vectors of the ambient magnetic field. In this manner spin precession magnetometers can be used to measure magnetic field vectors.

Spin precession magnetometers have been used to measure deep space ($\pm 10^{-2}$ gauss) and Earth magnetic fields (0.5 gauss) by spacecraft, however spin precession magnetometers for ranges up to 1 or 20 gauss are considered feasible.

Fluxgate magnetometers provide vector information and the sensor (0.35 in.³/axis) is much smaller than a sensor for spin precession magnetometers. These instruments measure generally below one gauss but a range of ± 20 gauss is practical if compensating Helmholtz coils are applied. Development of a sensor for a few hundred degrees centigrade (400°C) appears possible, but a considerable development effort is required.

Magnetoresistors are nonlinear and are generally used above 500 gauss. Hall effect generators are also very small sensors (0.1 x 0.2 x 0.006 in.) and are available for temperatures up to 230°C. Their low sensitivity (30 μ V/gauss) is a disadvantage which limits accuracy. But simple inflight calibration and measurements near 5 gauss with an accuracy of about $\pm 1\%$ appear practical.

The sensor of a search coil or spin coil magnetometer can be designed to withstand the ambient environment without thermal protection. A spinning probe and/or aerodynamic (propeller) drives for the spin coils are assumed.

3) Preferred Instruments

All listed types of magnetometers except the magnetoresistive sensor can be developed to measure the anticipated Jovian magnetic field. However there are significant tradeoffs in regard to requirements of weight, thermal control, accuracy, and electrical power. The Earth magnetic field intensity is less than 1 gauss and the magnetic fields of Venus, Mars and space are less than 0.01 gauss. Therefore all developed spacecraft magnetometers measure less than 1 gauss.

Ambient temperature and magnetic conductivity of the probe shell have a decisive influence on the magnetometer instrumentation requirements. Thermal control of the magnetometer sensor outside the pressure shell is probably not practical at ambient temperatures above 500°C. Then the search coil magnetometer is the only promising sensor candidate unless a fluxgate magnetometer can be developed for very high temperatures. The fluxgate magnetometer is preferred for sensor mounting inside a non-magnetic pressure shell of the probe unless the weight saving of about 1 pound is worth a considerable sacrifice in accuracy ($\pm 0.1\%$ for fluxgate, $\pm 1\%$ for Hall generator). Precession magnetometers are not preferred because of the high weight (5 lb) and power (5 w) requirements.

When a magnetic pressure shell is necessary for measurements at ambient temperatures below 500°C, then the small Hall effect sensor (0.1 in.³, -70° to +230°C) is preferred because of the minimum weight for thermal control of the small sensor.

j. Measurement of Electrical Conductivity in the Atmosphere

1) Measurement Requirements

The range of atmospheric conductivity measurements by a descent probe is limited by the high conductivity which causes black-out of radio communications and the low conductivity which can be reliably detected with the descent probe instrumentation.

A maximum conductivity of $10^{-8} \text{ (ohm)}^{-1} \text{ cm}^{-1}$ and a sensor with an effective electrode area of 100 cm² spaced 1 cm apart are assumed. Then for a 10 volt electrode potential an electrometer with a threshold of 10^{-14} amps detects a minimum conductivity of $10^{-17} \text{ (ohm)}^{-1} \text{ cm}^{-1}$.

2) Alternative Measurement Concepts

Gases are insulators but they become ionized and conductive because of interactions with phenomena such as radiation, energetic particles (electrons, nuclei), high temperatures and electric fields.

Figure IIC-13 shows various regions of gas discharge. For conductivity measurements the current is sustained by external agents. The most frequent cause of atmospheric ionization is radiation. The minimum ionization energy is in the order of 20 electron volts but depends also on the gas composition. The energy of radiation quanta is proportional to their frequency and UV light or radiation with shorter wavelength (x-rays, γ -rays, cosmic rays) is required for ionization.

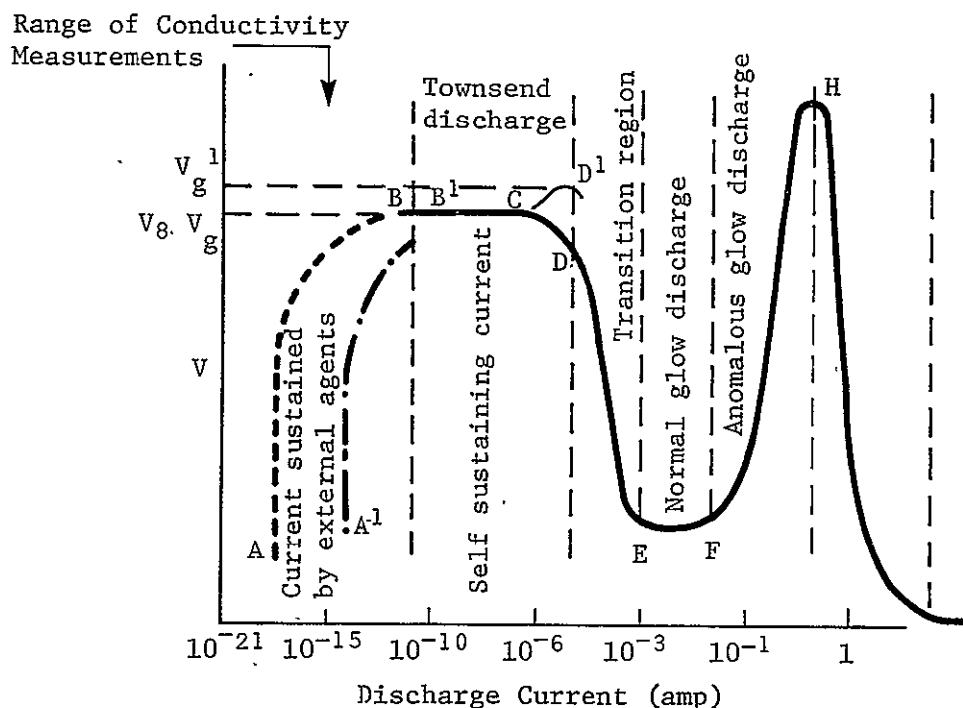


Figure IIC-13 Schematic Characteristics of Gas Discharges

Apparently, conductivity measurements of the Earth atmosphere are not conducted on a routine basis. The concept of atmospheric conductivity measurements is simple, but because of the high instrument sensitivity, interference by condensing vapors and particles can cause difficulties. The descent probe or conductivity sensor may not interfere significantly with any phenomena (radiation, particles, ion recombination) which are related to gas ionization. Electrometers have a threshold current in the order of 10^{-14} amperes. On Mariner 2 and Pioneer 6, a Neher integrating ionization chamber was used to measure very low currents.

3) Preferred Instrument

Figure IIC-14 shows a concept of a conductivity sensor. Further study and evaluation of the best practical instrumentation is recommended because we found no evidence of similar airborne measurements in the Earth atmosphere.

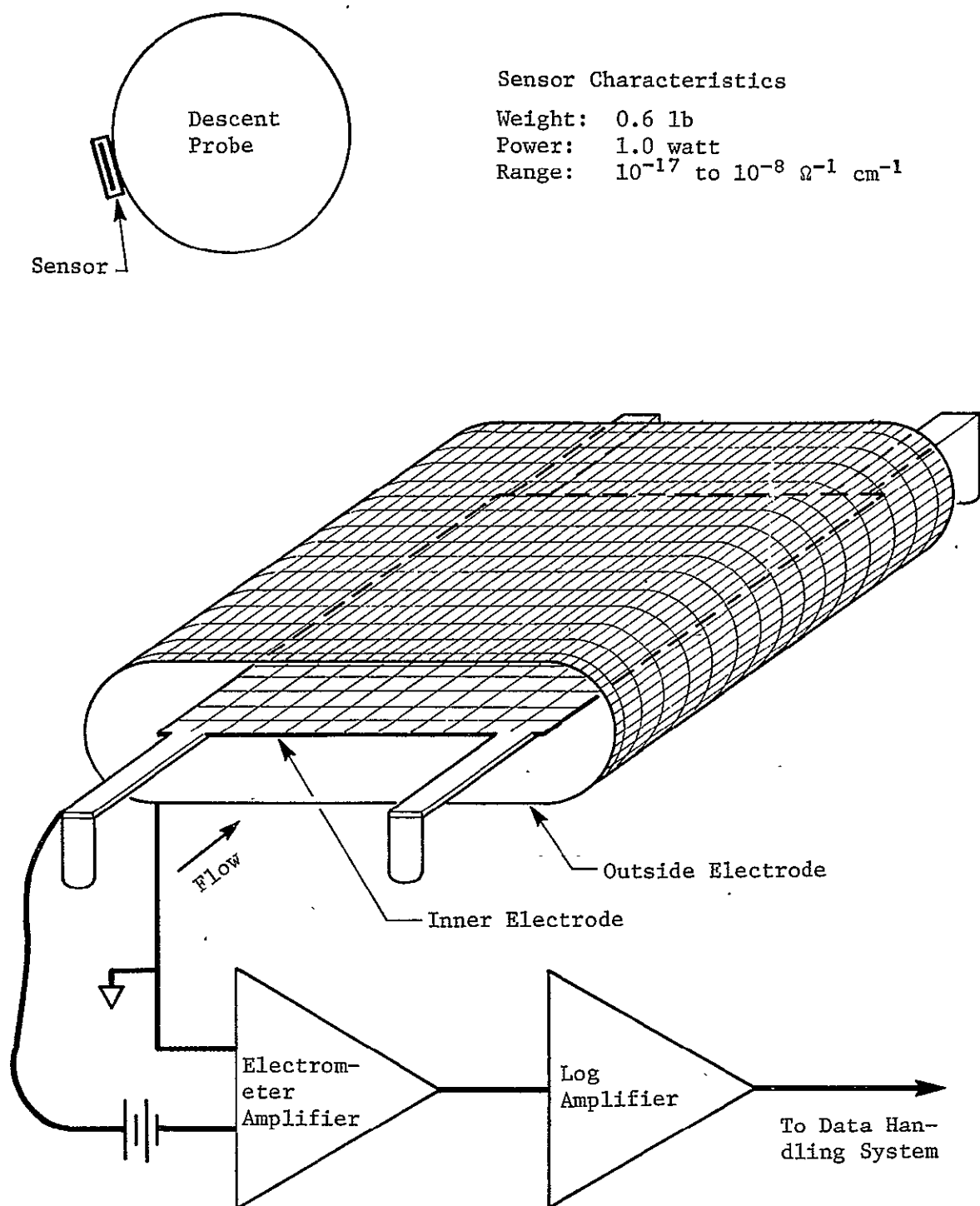


Figure IIC-14: Sensor Concept for Measurement of Atmospheric Conductivity

III. NAVIGATION AND TRAJECTORY STUDIES

A. Launch and Interplanetary

The major trajectory requirements for a Jupiter mission launched in 1978, 1979 or 1980-1981 are presented in Figures IIIA 1, 2 and 3 respectively. Contours of twice the total energy per unit mass, C_3 , are presented and the hyperbolic excess velocity at Jupiter, V_{HP} , is noted. The values of V_{HP} can be related directly to inertial entry velocities, V_E , as noted in Figure IIIA-4. For this figure entry is assumed to occur at a radius of 71908 km, well above any significant atmospheric effects. Zero altitude is assumed to be at a radius of 71420 km (the nominal radius yielding a pressure of 1 atmosphere). The variation in velocity as the planet is approached is shown in Figure IIIA-5. It should be noted that a very large variation in V_{HP} results in small variations in V_E .

Certain launch parameters constrain our choice of mission dates. The declination of the launch asymptote, DLA, is limited to ± 36 deg as a result of range definition and safety and tracking considerations. The nominal range azimuths are limited to between 90 and 115 deg. Azimuths outside of these limits involve relocation of tracking ships and a waiver of land over-flight rules or significant trajectory yaw steering. The DLA limit of $+36$ deg is shown in the Figures (IIIA1-3) and eliminates a significant portion of the Type I launch opportunities for 1978 launches. For 1980 launches this is not a significant constraint. The -36 deg limit occurs in the high energy region between Type I and Type II opportunities and does not constrain the choices.

Allowing northerly launches but avoiding major land mass overflight will yield acceptable maximum DLA's between $+33$ and $+40$ deg. In 1980 these values do not show significantly different capability from the $+36$ deg value used in the study. In 1979 the $+36$ case exhibits a launch period of 1 to 3 days more than the $+33$ and $+40$ deg conditions which have nearly identical capabilities. Going to $+40$ deg in 1978 adds about 2 days to the launch period capability for the same C_3 value. Reducing the maximum DLA to $+33$ deg, however, will reduce the launch period by 7 to 12 days and severely restrict the payload. Type I trajectories are the only

ones affected by this constraint.

Similarly the DLA must be greater than ± 2 deg to achieve good tracking data for the near earth correction maneuvers. This constraint is noted on the figures and divides the Type II launch opportunities into two regions. While this constraint is more restrictive in 1980 than in 1978 and 1979 it does not present any real mission problems.

The launch vehicle is another source of constraints. The launch vehicle choices for this study are defined in Ref. IIIA-1 and the launch period is constrained to 20 days for 5 segment Titan IIID vehicles and 30 days for 7 segment Titan IIID vehicles. The significance of this constraint is the need for variable arrival dates during the launch period. A single arrival date would require C_3 values too large to yield a worthwhile payload weight.

Generally the C_3 values for Type I trajectories are greater than those for Type II trajectories. Similarly the V_{HP} values of Type I trajectories are large (near 9 km/sec) while those of Type II trajectories are small (near 6 km/sec). The higher V_{HP} values affect the entry velocity only slightly; increasing it by about 0.3 km/sec.

With these parameters in mind the effect of launch period on energy requirements can be examined. It can be readily seen that Type II trajectories are not penalized by the 20 and 30 day launch period constraints. Values of C_3 of less than $100 \text{ km}^2/\text{sec}^2$ can be achieved for 1978 launches. The energy requirements decrease in 1979 and again in 1980. Type I trajectories in 1978 and 1979 are constrained by the DLA constraints and present a more restrictive case. For these years C_3 values between 100 and $110 \text{ km}^2/\text{sec}^2$ will be required to achieve 30 day launch periods. Further mission constraints discussed in Section IIIB tend to magnify this effect.

Another launch vehicle constraint is the maximum coast time limit for the upper stage in a parking orbit. The allowable parking orbit coast time in Ref. IIIA-1 is one half hour or less. In 1978 this constraint eliminates Type I trajectories from consideration as noted in Figure IIIA-1. However refinements already considered for Centaur make this a rather "soft" constraint and the time has been extended to one hour for this study. By extending the maximum allowable coast time to one hour this parameter no

longer constrains the mission design in any way.

The payload data for the launch vehicles considered is shown in Figure IIIA-6. The basic contract data are shown as well as a stretched Centaur version on the 5 segment vehicle. Although the stretched Centaur vehicle has less capability than the 7 segment vehicle for the same C_3 values it can operate with the shorter 20 day launch period and lower attendant C_3 requirements; thus achieving very nearly equal performance.

Other factors influencing our choice of mission dates involve the interplanetary trajectory and encounter geometry. Figure IIIA-7 shows the communication range as a function of arrival date. Since the range varies from its minimum to maximum in six months and the arrival date probably will vary by at least 6 months to accommodate a 30 day launch period with reasonable payload weights it appears that the system design must accommodate the maximum range. These data are typical for any launch year arrival year combination. The encounter parameters are discussed in the next section of this report.

B. Encounter

At encounter, a good earth-probe communication link depends, among other criteria, upon having the position of the sun sufficiently displaced from the earth-probe line to avoid interference. JPL has suggested that the angle between the earth-probe line and the earth-sun line should exceed 15 deg. Figure IIIB-1 presents the angle, measured at the sun, between the vectors to the earth and to Jupiter. By limiting the angle, ϕ , to less than 160 deg or more than 200 deg we achieve the equivalent of the suggested separation between the sun and the communication link. The impact of this constraint on the launch-arrival date choices is to eliminate three bands of arrival dates centered about late September 1980, early October 1981 and late November 1982. For subsequent years the dates eliminated due to communication geometry occur at approximately 13 month intervals.

Looking at the launch-arrival date opportunities in light of these constraints yields Figures IIIB-2, IIIB-3 and IIIB-4. The Type I payload capabilities for a given launch period are 400 to 700 lbs less than the Type II capabilities. For 20 day launch periods the Type II C_3 requirement is less than the minimum achievable value for any Type I path. The Type I

capability would match the Type II 30 day launch period capability if the Type I launch period could be reduced to 12 days for 1978 launches and 25 days for 1980 launches. In 1979 the minimum Type I C_3 is greater than the 30 day Type II requirement and Type I paths will always exhibit less payload than Type II. The total flight time for Type I trajectories, however, would be reduced from the 3 to 4 years at Type II paths to $1\frac{1}{2}$ years.

The encounter geometry is our next consideration. Figure IIIB-5 presents the Sun-Jupiter-Probe angle at encounter, ZAP, and it should be noted that for 1978 launches arrivals after late August 1981 will approach Jupiter on the darkside. Therefore the available Type II arrival dates result in approaches to Jupiter on the darkside moving from near the terminator to approximately 35 deg from the terminator as the arrival falls on later dates.

Accuracy is affected by the encounter geometry also. Usually the Earth-Jupiter probe angle should not be near 90 deg for good tracking data. This angle, ZAE, is presented in Figure IIIB-6. Again the available arrival dates for 1978 launches move away from the 90 deg condition. Recent accuracy studies have indicated that the large gravity effects of Jupiter reduce the significance of this parameter as compared to approaches to Venus and Mars. Also as noted in Figure IIIB-6, the approach should be near the ecliptic plane (noted by the celestial attitude LAP) and near the geocentric equatorial plane (noted by the declination at the V_{HP} , DPA). Throughout the mission opportunities these criteria are met.

Targeting opportunities can now be defined. Figure IIIB-7 presents the displacement between the V_{HP} position and the entry position for various entry flight path angles. It should be noted that a -10 deg entry will be on the light side of the planet for the available arrival (Type II) opportunities, varying between more than 30 deg from the terminator and 65 deg from the terminator as the arrival becomes later in the opportunity window. Type I trajectories would approach Jupiter from the light side and a -10 deg entry path angle would yield entry at a point located near the terminator to 10 deg into the darkside. The path curvature due to the gravitation effect of Jupiter is noted in Figure IIIB-7 also. This curvature coupled with the probe deflection angle in the case of a flyby spacecraft is significant to the definition of the angle of attack at entry if no means of reorientation is provided after probe deflection.

Several other targeting parameters are of interest. The impact parameter required for direct targeting is presented in Figure IIIB-8 as a function of entry path angle and V_{HP} . The periapsis radius resulting from a given impact parameter is presented in Figure IIIB-9 and IIIB-10. In the case of a flyby or orbiting spacecraft these parameters describe the path that must be achieved by the deflection maneuver to target the probe to a given entry condition. The angle the approach asymptote makes with the orbit plane of Jupiter, GP, varies with launch and arrival date. In general for Type I trajectory opportunities available this angle varies from -3 deg to less than -1 deg as the launch date gets later for a given arrival date. The line of constant approach angle shows an increasingly late launch. A negative sign means that the approach is from above or in the northern hemisphere. Type II trajectory opportunities available exhibit angles from +2.5 to +12 deg as the launch date gets later for a given arrival date. These positive angles indicate an approach from below. The actual surface position at entry depends on trade-offs of the science objectives, the communications geometry, the deflection maneuver implementation, accuracy and the entry heating advantages of utilizing planetary rotation to reduce the entry velocity.

One other aspect of the encounter parameters is the possible post encounter objectives. A direct impact mission can not pursue post encounter objectives not related to atmospheric and surface exploration. Therefore, the spacecraft has limited use as a relay communications link and direct communications to the Earth are generally used. Deflection of a probe may or may not be required and, if used, the deflection energies are small.

An orbiter mission will be payload limited by the need for substantial injection propulsion and possibly unique encounter geometry to achieve a specific orbit alignment. A probe deflected from the spacecraft can best be utilized if its mission is completed prior to orbit injection. The spacecraft can then be a good relay communications link and the probe targeting can be simplified. Probe missions are relatively short in duration and can easily be deflected ahead of the spacecraft to complete their mission prior to spacecraft periapsis passage.

Multiple planet missions such as the Grand Tour have the encounter geometry set by the mission year and the other target planets. The periapsis radius at a given planet is a function of the mission year and the path energy and is a very important parameter in probe missions. As noted in the deflection strategy and communications sections the periapsis radius may limit the useful time that the spacecraft can act as a relay communication link for an atmospheric probe. The weight of the deflection system and the dispersion at entry are both functions of the periapsis radius, increasing with larger flyby radii.

For example, a 1978 Jupiter-Uranus-Neptune mission is considered with a Jupiter flyby radius of 1.6 planet radii or as close to the 2.0 radii utilized in the basic study as possible. A 1979 Jupiter-Uranus-Neptune mission is also considered. The flyby radius for this mission is 6.8 Jupiter radii. Both of these missions have C_3 values near $112 \text{ km}^2/\text{sec}^2$ and are Type I paths to Jupiter. Figures IIIB-11 and IIIB-12 show how the periapsis radius varies with date and path energy. From these figures it can be seen that the periapsis radius at Jupiter increases with the later dates and is closest to Jupiter in 1978 for Jupiter-Uranus-Neptune missions and in 1976 for Jupiter-Saturn-Pluto missions.

The cost of reducing periapsis radius is great. In 1979 reducing the payload by 230 pounds reduces the flyby radius from 6.8 to 6.4 Jupiter radii. To reduce the flyby radius from 6.8 radii to 5 radii requires a reduction of 650 pounds. In 1978 the flyby radius can be increased easily from 1.6 radii to 2.0 radii by reducing the path energy and thus adding 200 pounds to the payload capability.

C. Deflection

This study is concerned primarily with a Jupiter entry probe utilizing a flyby-spacecraft as a relay communications link. For some time (1-4 hours) after probe entry the spacecraft must be in a position to receive radio signals from the probe. This is most effectively accomplished by separating the probe and spacecraft at a considerable distance from Jupiter. The "deflection strategy" is to effect this separation so as to produce geometry favorable for relay communications. Considerations of entry targeting, weight requirements, and accuracy of implementation affect this strategy.

Either of two deflection modes can be adopted. One mode is to target the spacecraft-probe combination to achieve a desired periapsis radius and at the separation point apply a velocity increment only to the probe. The path of the probe then intersects the Jupiter atmosphere with a specified flight path angle at entry. The spacecraft remains in the flyby trajectory. An alternate mode is to target the spacecraft-probe combination to achieve an impacting trajectory with the specified flight path angle at entry and at the separation point apply a velocity increment only to the spacecraft so as to alter its path to achieve a desired flyby periapsis radius. The probe path remains undisturbed on its previous impacting trajectory. Velocity requirements for deflection are similar; therefore, deflecting the spacecraft will require more weight in propellant. Quarantine requirements will be an important factor in selecting the deflection mode. The results presented here will be mainly based on the probe being deflected from the flyby spacecraft trajectory, thus avoiding major quarantine considerations.

The hyperbolic excess velocities at Jupiter are small compared to the planet's escape velocity of about 60 km/s. Therefore, the escape velocity approximates the inertial velocity at entry. Because of its large size and a rapid rotation rate of $36.57^\circ/\text{hour}$, the equatorial velocity of Jupiter is about 12.6 km/s. Therefore entry in the direction of Jupiter's rotation and in the vicinity of the equatorial plane can reduce the relative entry speed with respect to the atmosphere to about 47 km/s, as shown in Figure IIIC-1. In addition to the reduction of relative velocity, entry in the direction of the planet's rotation can be utilized to extend the useful life of the probe-spacecraft relay communications link.

"Entry with rotation" has been studied in detail for the reasons given above. The deflection maneuver required to produce "entry with rotation" is essentially an in plane maneuver. That is, the plane of the probe path after deflection coincides with the trajectory plane of the probe - spacecraft combination before deflection. Variants to this approach deserve consideration and are discussed.

The impulsive velocity requirements are relatively small at deflection so that the time of application of the thrust is relatively short.

For this reason the study considers impulsive velocity increments and does not consider finite burning time effects. These impulse requirements and the direction of application are independent of the type of deflection system.

Entry is assumed to occur at a radius of 71907 KM, 488 KM above the equatorial reference radius of 71420 KM. The reference radius corresponds to a pressure of 1 atmosphere in all the atmospheric models considered in the study.

Because the oblateness of Jupiter is pronounced, the radius varies markedly with latitude. The polar radius of Jupiter is approximately 67000 KM. Because entry latitudes are small this study neglects the effect of radius variation with latitude and assumes that entry always occurs at 71907 KM.

The rotation rate of Jupiter's bands also vary slightly with latitude. This variation has also been neglected, so that a constant rotation rate has been assumed.

1. Basic Considerations

During the approach phase to Jupiter, in which the spacecraft-probe is in the sphere of influence of Jupiter the path of the vehicle is hyperbolic with respect to a Jupiter centered coordinate system. The hyperbolic excess velocity vector has magnitude V_{HP} and direction and is computed by subtracting the velocity vector of Jupiter from the arrival velocity of the spacecraft. This is an important quantity in the deflection strategy as it yields the energy and the direction of approach to Jupiter. The impact parameter, B , which is orthogonal to the V_{HP} vector, and the arrival date complete the specification of the hyperbolic orbit in the Jupiter centered coordinate system.

The selection of the impact parameter, B , is essentially independent of the heliocentric path. Its selection strongly influences the path inclination and the periapsis radius.

Since Jupiter rotates so rapidly and since we are not attempting to target to a specific longitude on Jupiter, but only a specific latitude (5°) just the magnitude of the V_{HP} and its declination with

respect to Jupiter's equator are of direct concern to the deflection problem.

The application of an impulsive velocity increment to the probe at some radius within the sphere of influence of Jupiter is generally called the deflection point. The radius of the sphere of influence is about 48 million kilometers. Deflection radii of 10 to 40 million kilometers have been studied, with a nominal value chosen to be 10 million. The effects of changes in deflection radius on the minimum deflection velocity for various flight path angles are shown in Figure IIIC-2 for a periapsis radius of $2 R_J$. Figure IIIC-3 illustrates the effect of deflection radius on deflection velocity requirements for various peripasis radii and an entry-flight path angle of -10° . The radius at which the deflection of probe from spacecraft path is executed is dependent upon considerations of (1) communication requirements and (2) velocity increment limitations. The deflection maneuver should be performed in view of earth and large velocity increments reduce the useful payload.

The deflection of the probe path from the path of the spacecraft should be accomplished so that two independent effects are produced. One requirement is to displace the probe path from the spacecraft path so that the probe trajectory intersects the planet's "entry surface" at a prescribed flight path angle.

The other effect produced by the deflection velocity is to change the magnitude of the velocity vector of the probe from that of the spacecraft by applying a deflection impulse approximately tangential to the approach velocity vector of spacecraft. This change in magnitude of the probe velocity speeds up or slows down the probe with respect to the spacecraft and directly affects the lead time (t_L) or equivalently lead angle at probe entry.

If we restrict the application angle to a range of values around -90° we can accomplish the -10° entry specified and significantly reduce the deflection velocities which need be considered. This means, that by applying a deflection impulse approximately normal to the approach velocity (V_{HP}) vector so that the approach velocity of the probe is equal

to that of the spacecraft at the deflection point, only the direction of the velocity vector is changed.

These quantities implicitly determine the position of the spacecraft relative to the probe at the instant of probe entry. The lead time is defined as the time required for the spacecraft to travel from its position at the instant of probe entry to periapsis. The lead angle (λ) is the central angle between probe and spacecraft at the instant of probe entry, the angle being positive if the spacecraft leads the probe.

The direction of application of the deflection velocity impulse generally establishes the orientation of the probe in inertial space, because the thrust axis is usually aligned with the probe longitudinal spin axis. However without any subsequent orientation after the deflection impulse the angle of attack at entry resulting from this orientation will be large, on the order of 45° for a -10° entry flight path angle. Figure IIIC-4 illustrates the magnitudes of the angles of attack resulting from no reorientation after deflection. This preliminary consideration has dictated that the probe have a self-contained system to yield the desired orientation to give a zero angle of attack at entry. This orientation is then maintained by spin stabilization during the coast phase from deflection to probe entry. Hence pre-entry probe aspect angles reflect this assumption in the parametric data which follows.

Due to the rapid rotation rate of Jupiter it is possible to select a periapsis radius for the spacecraft so that over an extended communication interval the average angular motion of both probe and spacecraft is approximately the same. This rotation rate averaging has an advantageous affect on the probe aspect angle time history. Figure IIIC-5 illustrates time histories of spacecraft angular rate for various periapsis radii, with the corresponding effect on probe aspect angle variations during the encounter. The range of periapsis radii which will produce an angular rate greater than 36.57 deg/hour (Jupiter's rate) is from 1 to 2.82 Jupiter radii. This is illustrated in Figure IIIC-6, which summarizes some of the relationships involved.

In summary, the governing parameters which characterize the spacecraft-probe-Jupiter encounter are the magnitude and direction of V_{HP} vector, radius of deflection, radius of periapsis, the probe flight path angle at entry, and the lead time (or the lead angle).

A particular choice of the above parameters will dictate a value of the deflection velocity magnitude and the application angle required. In addition, time histories of the following variables are important in considerations of the relay communications link.

- Communications Range
- First time derivative of range (affects doppler)
- Second time derivative of range (affects doppler rate)
- Probe Aspect Angle
- Spacecraft Aspect Angle

Other parameters of interest are

- Entry Latitude
- Entry Longitude (with respect to a sun pointing reference system.)
- Time on the light side
- Down range angle at entry
- Coast time
- Communications interval

The communications range is the distance between spacecraft and probe. It is desirable to have this range as small as possible for relay communications purposes. The first and second time derivatives of range vary quite significantly during the encounter phase and variation must be accommodated by relay communications system design. An attempt is usually made to keep these variations within reasonable limits. The probe aspect angle is the angle between the probe antenna centerline and the line of sight between spacecraft and probe. (The probe antenna centerline is assumed to be coincident with the longitudinal axis of the probe.) The spacecraft aspect angle is the angle between the line of sight between spacecraft and probe and the spacecraft-Earth line. The coast time is defined as the time from deflection to entry.

2. Parametric Analysis

The parametric data was generated to show how the probe-spacecraft relative geometry is affected by variations in the parameters governing the deflection strategy. In this respect the data serves as supporting information useful in the design and analysis of the relay-link communications system. To this extent this parametric analysis supported the design of the relay-link communications. A close coordination between communications studies and trajectory parameterization has necessarily resulted in a good deal of data. Only trajectory oriented data has been included herein. The effect of these variations on communications parameters is presented in other sections of the report.

a. General considerations which apply in the parameter selection process.

Deflection Radius (R_{EJ})

The nominal value of the deflection radius chosen for the parametric analysis was set at 10^7 KM from Jupiter. This point is well within the sphere of influence of Jupiter. As outlined in the previous section the effect of an increase in the value of the deflection radius (R_{EJ}) is a decrease in the value of the deflection velocity required to achieve equivalent entry and descent geometry and a corresponding increase in the coast time from deflection to entry. These effects are illustrated in Figures IIIC-2 & IIIC-3. The velocity increment varies approximately as the inverse of the deflection radius. Deflection velocity requirements together with communication considerations of the deflection maneuver will very probably result in the selection of a radius other than 10^7 KM. However the encounter geometry is relatively independent of the deflection radius so that the parametric data to follow is independent of the value selected.

Entry Flight Path Angle (γ_E)

The nominal value of the inertial flight path angle of the probe at entry was set at -10° for the deflection maneuver parametric study. We would like to know the effects of entry flight path angle variations from -10° to -85° on the other parameters of the encounter, and this is done in the parametric data. Some general considerations

should be kept in mind in studying these effects.

- (1) Shallow entry angles result in minimizing the relative velocity of the entry probe when entry is close to the equator in the direction of rotation. This observation is illustrated by Figure IIIC-1.
- (2) Steep entry angles can produce extended intervals of relay-link communication. The increase in communication time corresponds to the increase in lead time requirements for steeper angles, as illustrated in Figure IIIC-7.
- (3) Probe entry location can be adjusted by variations in γ_E , thus varying the amount of time on the light side and moving the latitude of entry slightly. Figure IIIC-9 illustrates this effect for a V_{HP} magnitude of 5.476 km/s. Figure IIIC-9 illustrates this for V_{HP} of 10 km/s.
- (4) Deflection velocity requirements increase as steeper entry angles are required. Figure IIIC-10 gives the minimum deflection velocity requirements for various entry angles and various periapsis radii.

Periapsis radius R_p

The nominal value of the periapsis radius of the spacecraft was set at 2 Jupiter radii for the parametric analysis. In the parametric data the periapsis radius is varied from $1.5 R_J$ to $10 R_J$, with emphasis placed on the range from $1.75 R_J$ to $2.5 R_J$. Due to the nature of the encounter properties it is logical to define a small periapsis radius as between 1.5 and 2.82 Jupiter radii, and a large radius from 2.82 to $10 R_J$. As described in the previous section rotation rate averaging effects can be advantageously utilized when a small periapsis radius is chosen. For long time periods the probe aspect angle can be held within acceptable limits while small communication ranges result. When a large periapsis radius is selected, spacecraft aspect angle variations are reduced but correspondingly longer communications ranges are required, and shorter total communication times result. The following considerations also apply to the selection process.

- (1) Accuracy requirements may dictate a small R_p . The minimum may be affected by planetary quarantine requirements.
- (2) The first and second time derivatives of Range between spacecraft and probe have time variations during encounter which must be considered as to their effect on doppler and doppler rate in the design of the relay communications link. The variations rise drastically as the periapsis radius is reduced below $1.75 R_p$. Communications considerations will place a limit on the acceptable minimum value of R_p . Figure IIIC-11 shows how range rate varies as a function of time for various R_p selections. The time variations of the second time derivative of range is shown in Figure IIIC-12 for various R_p .
- (3) Radiation intensity is more severe as the planet is approached. The requirements to shield the spacecraft equipment may dictate to some extent the value of R_p selected.
- (4) Deflection velocity requirements increase as larger periapsis radii are selected for a fixed deflection radius. Figure IIIC-10 illustrates the effect of an increase in periapsis radius on velocity requirements.

Lead Time (t_L)

The nominal value of lead time selected during the parametric analysis was chosen so that the spacecraft was directly over the probe at periapsis passage. The lead times required to satisfy this condition are consequently a function of the periapsis radius chosen and the probe entry flight path angle selected. The reason this nominal value was chosen was that in all cases this "rule" produced satisfactory time histories of range and probe aspect angles during the communication period. While a detailed analysis of the communications considerations may indicate a slightly different value as more acceptable, the change will be small. Figure IIIC-13 defines the nominal lead time values required to produce the condition at periapsis that the spacecraft be directly over the probe. This figure is for an entry angle of -10° , and shows the regions of possible interest for small periapsis radii.

Also the related deflection requirements are noted for easy reference. If, for example, we require that the probe aspect angle at entry be no more than 45° we restrict our interest to a much smaller domain. Note that the rule of putting the spacecraft directly over probe at periapsis results in a locus of points well within the 45 degree probe aspect angle lines. Clearly the rule chosen for selection of nominal values of lead times can be justified from this plot.

It should be noted that lead angle at entry or spacecraft true anomaly would be acceptable substitutes to lead time as a governing parameter in characterizing the position of the spacecraft at the instant of probe entry. However, lead time has proven very useful since time is a critical parameter in the encounter.

The value of lead time selected has a first order effect on probe aspect angle, spacecraft aspect angle, and communications range time histories after entry. Its value is critical when "rotation rate averaging" of the probe aspect angle time history is made for small periapsis radii.

The value of t_{LEAD} (or t_L) can be selected by an appropriate choice of application angle of the deflection velocity, together with slight changes to the minimum velocity requirements. Figure IIIC-14 illustrates this for various periapsis radii from 1.75 to $10 R_2$.

The effect of variations in lead time on all the parameters of encounter are shown in parametric data that follow.

The following set of graphs, Figure IIIC-15 thru IIIC-26 all illustrate relationships which apply when a lead time is selected so that the spacecraft is directly over the probe at periapsis passage. As mentioned before, this choice of lead time as a nominal is reasonable, and representative of practical relay-link geometries when small periapsis radii are being considered. A different choice of lead time would lead to a similar set of graphs, all of which will display similar trends.

Figure IIIC-15 is a plot of periapsis radius versus flight path angle at probe entry, and summarizes the relationships which apply when the lead time is selected so as to position the spacecraft directly over the probe at periapsis passage. Lines of constant lead time, deflection velocity, and deflection application angle are presented. Lead time requirements vary but slightly with the magnitude of the periapsis radius, and are essentially a function of the entry angle only. The increase in deflection velocity required as steeper entry angles are desired is illustrated. The increase in deflection velocity required as periapsis radius is increased is also shown in Figure IIIC-15. Deflection application angle requirements are displayed also for a range of conditions.

Figure IIIC-16 illustrates the region of interest with regard to deflection requirements for a -10° entry and a small periapsis radius. For practical considerations we are concerned with the maximum value of probe aspect angle attained during the communications interval rather than its value at probe entry. For example, if we select a deflection angle of about -93° so that the probe aspect angle at entry is 90° we will find that for a long time thereafter the probe aspect angle will grow greater than 90° and will therefore be unacceptable. This increase in aspect angle is due to the fact that Jupiter is rotating more rapidly than the spacecraft at entry. This increase continues until the spacecraft's rotation rate about Jupiter equals Jupiter's (or the probe's) rotation rate. The dotted lines indicate the maximum values of 90° , 60° and 45° attained on the probe aspect angle for at least 2 hours after entry, so that practical considerations limit the region of concern to within these limits. Note the locus of points where spacecraft is directly over probe at periapsis lies well within the 45° limits on maximum probe aspect angle. Note also the increase in velocity requirements as periapsis radius is increased.

Figure IIIC-17 illustrates the region of interest with regard to deflection requirements for a -20° entry, while Figure IIIC-18 shows the effects of a -30° entry.

Figure IIIC-19 is a plot of deflection angle versus true anomaly of entry point for various periapsis radii, and various entry flight path angles. Steeper entry angles require larger lead times because the true anomaly of the entry point becomes larger for steeper entries. Note also that for the positive lead times considered the large periapsis radii require more negative deflection angles than the smaller radii. Figure IIIC-13 also illustrates this effect for positive lead times.

Figure IIIC-20 is a plot of deflection angle versus probe flight path angle at entry for various periapsis radii and deflection velocities. The same trends previously mentioned are illustrated here.

Figure IIIC-21 is similar to Figure IIIC-20 except that communication range and probe aspect angle are shown. Range at entry increases as entry angles are made steeper. The region that produces small probe aspect angles at entry is illustrated.

Figure IIIC-22 plots deflection velocity versus flight path angle at entry for various periapsis radii and deflection angles.

Figure IIIC-23 relates communications range at entry to the entry flight path angle for various small periapsis radii. Essentially this shows that steeper entries require longer ranges at entry. Figure IIIC-24 relates lead angle at entry to flight path angle at entry, for various periapsis radii. Figure IIIC-25 is a plot of lead time versus flight path angle at entry for a few small periapsis radii. Figure IIIC-26 gives probe aspect angle at entry versus flight path angle at entry for various periapsis radii. In the range of shallow entry angles the probe aspect angles at entry increase as periapsis radii decrease. For example if a -20° entry is required and the maximum probe aspect angle is limited to less than 30° , the plot shows that a periapsis radius of 2 or greater would satisfy these constraints. The lead times shown result from positioning the spacecraft directly over the probe at periapsis passage.

b. Parametric Data related directly to relay-link communications analysis

In general the data to be described here are time histories of encounter parameters a few hours prior to and a few hours after entry. These data directly support the analysis and design of the relay communications link.

Figure IIIC-27 shows spacecraft aspect angle variations with time for various probe flight path angles at entry, when the periapsis is 2 Jupiter radii. The cusp at entry for each curve results from the probe being decelerated from an inertial velocity of 60 km/s down to 12.6 km/s over a short time interval. The lead times were chosen so as to place the spacecraft directly over the probe at periapsis, except for the -10° entry curve. Each case results in good communication geometry. Figure IIIC-28 describes the time variations of this angle for various values of periapsis radii and for an entry angle of -10° . Here it is easily seen that the effect of large periapsis radii is to slow down the angular rate at which the spacecraft moves past Jupiter, and results in less time variation of spacecraft aspect angle. Figure IIIC-29 illustrates the effect of lead time selection on the spacecraft aspect angle for a -10 degree entry and a periapsis radius of 2.

Figure IIIC-30 shows the probe aspect angle variations with time for various probe flight path angles at entry, when the periapsis radius is 2 Jupiter radii, and the lead time for each curve is selected such that the spacecraft is directly over the probe at periapsis. It is assumed that during the coast period from deflection to entry the probe is oriented so that the angle of attack at entry is zero. After entry it is assumed that the probe is aligned along the probe radius vector. The re-alignment which takes place at entry appears as a discontinuity due to the short interval of deceleration. The rotation rate averaging effects of a periapsis radius of 2 are evident in this plot, where limited variations of probe aspect angle occur around zero to produce favorable geometry for extended periods. These periods are extended as the entry angle is increased. Figure IIIC-31 illustrates the effect of different periapsis radii for an entry angle of -10° . As R_p is increased above $2.82 R_J$, there is no change in direction of motion of this probe aspect angle. Figure IIIC-32 describes the effect of lead time variations

on probe aspect angle for a periapsis radius of 2 and a -10° entry.

Figure IIIC-33 shows the effect of variations in entry angle on communications range for a fixed periapsis radius and a lead time selected so as to position spacecraft directly over probe at periapsis. This condition at periapsis delays the time at which the steeper entries produce a minimum range. Figure IIIC-34 illustrates the effects of changing periapsis radius on the entire history of communication range, for an entry angle of -10° and with the lead time selected to place the spacecraft over the probe at periapsis. Figure IIIC-35 shows the effect of lead time variations on communications range for a -10° entry and a periapsis radius of $2 R_4$.

Figure IIIC-36 shows probe aspect angle time history variations for four cases to evaluate their value to communications. Entry is at -10° . Figure IIIC-37 shows communications range for these four cases. These data were generated in search of a typical trajectory for the pioneer spacecraft, and curve No. 2 represents the trajectory illustrating this type of spacecraft. Pioneer is a spinning spacecraft with very limited antenna pointing capability.

Figure IIIC-38 shows spacecraft aspect angle time histories for various periapsis radii and flight path angles when a pre-periapsis communication scheme is studied where the ability to receive signals from the probe is limited to variations of a few degrees in aspect angle. The pre-periapsis communications scheme refers to choosing the communications interval so that relay communications is completed well before periapsis passage. This condition has been used for all pioneer spacecraft applications.

Figure IIIC-39 illustrates the resulting probe aspect angle time histories when a condition of pre-periapsis communication is imposed on the same set of cases as described for Figure IIIC-38.

Figure IIIC-40 shows the probe aspect angle "to Earth" as a function of time from entry for an October 2nd arrival. A -40° entry would start out with the Earth directly overhead. For a 2 hour mission, a -60° entry would exhibit the smallest aspect angle history, being less than 36° at all times. Arrival at Jupiter on

on dates later than October 2, 1981 would shift the entry set of curves to the right and make shallower entry conditions more favorable.

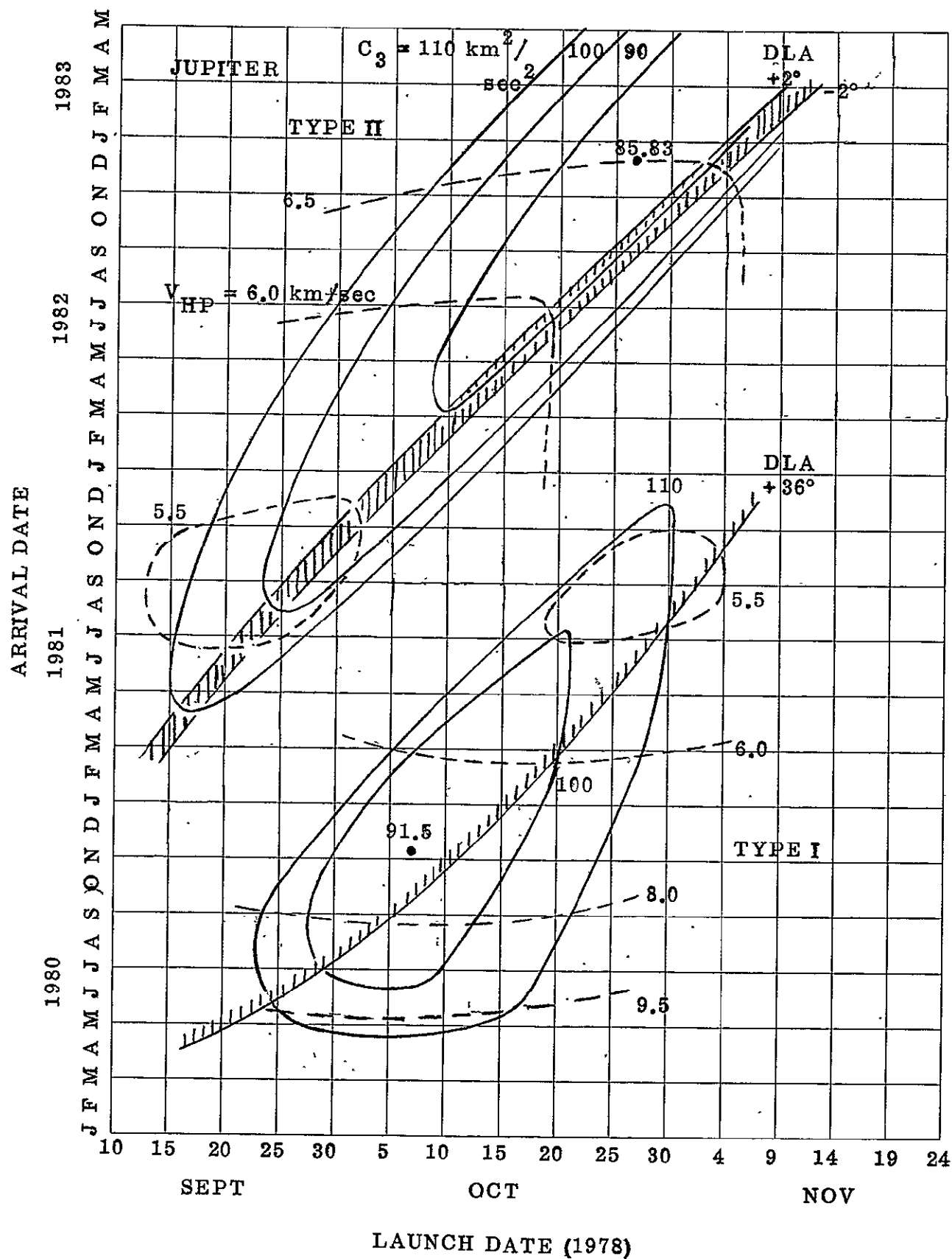


Figure IIIA-1

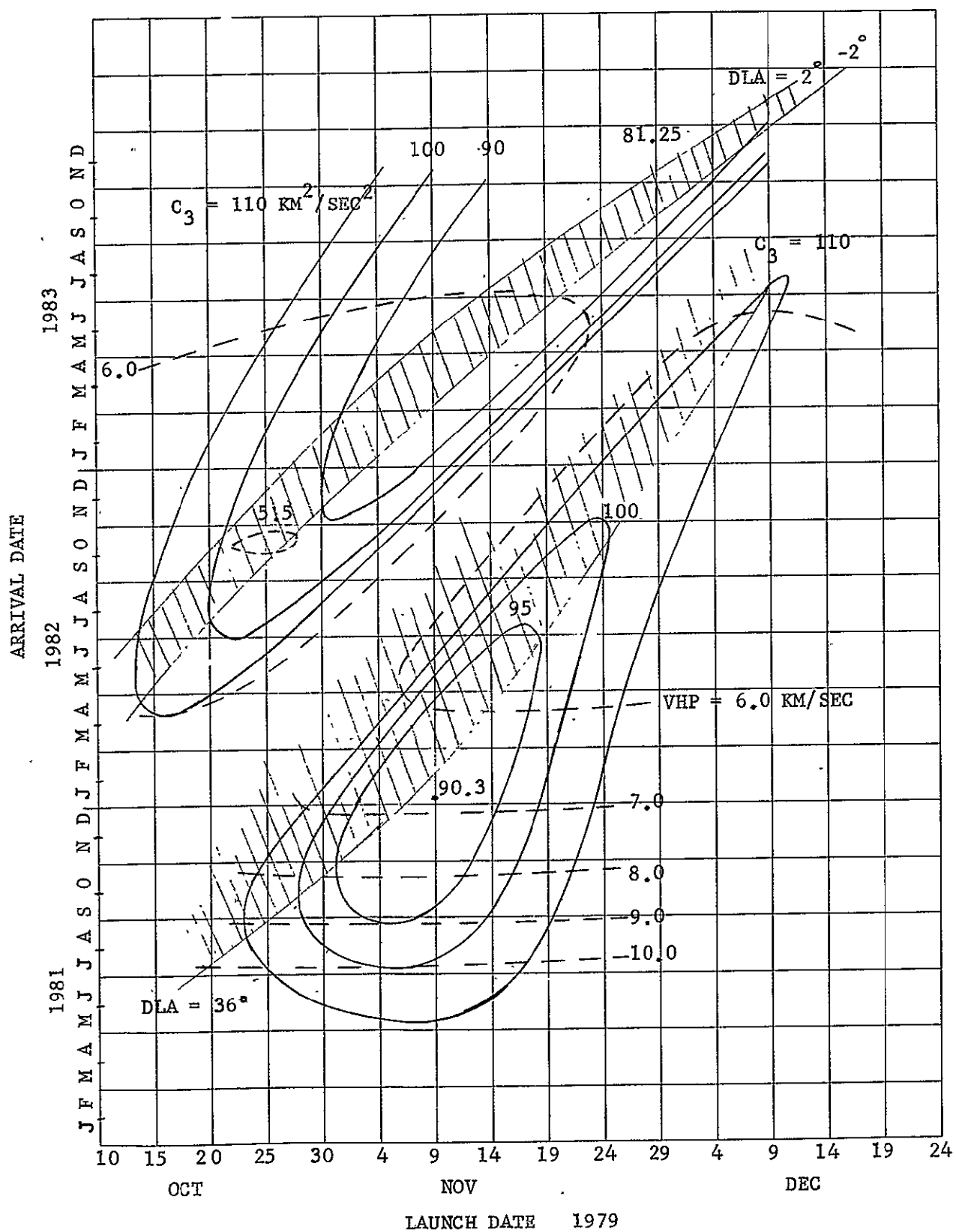


Figure IIIA-2 1979 JUPITER LAUNCH OPPORTUNITIES

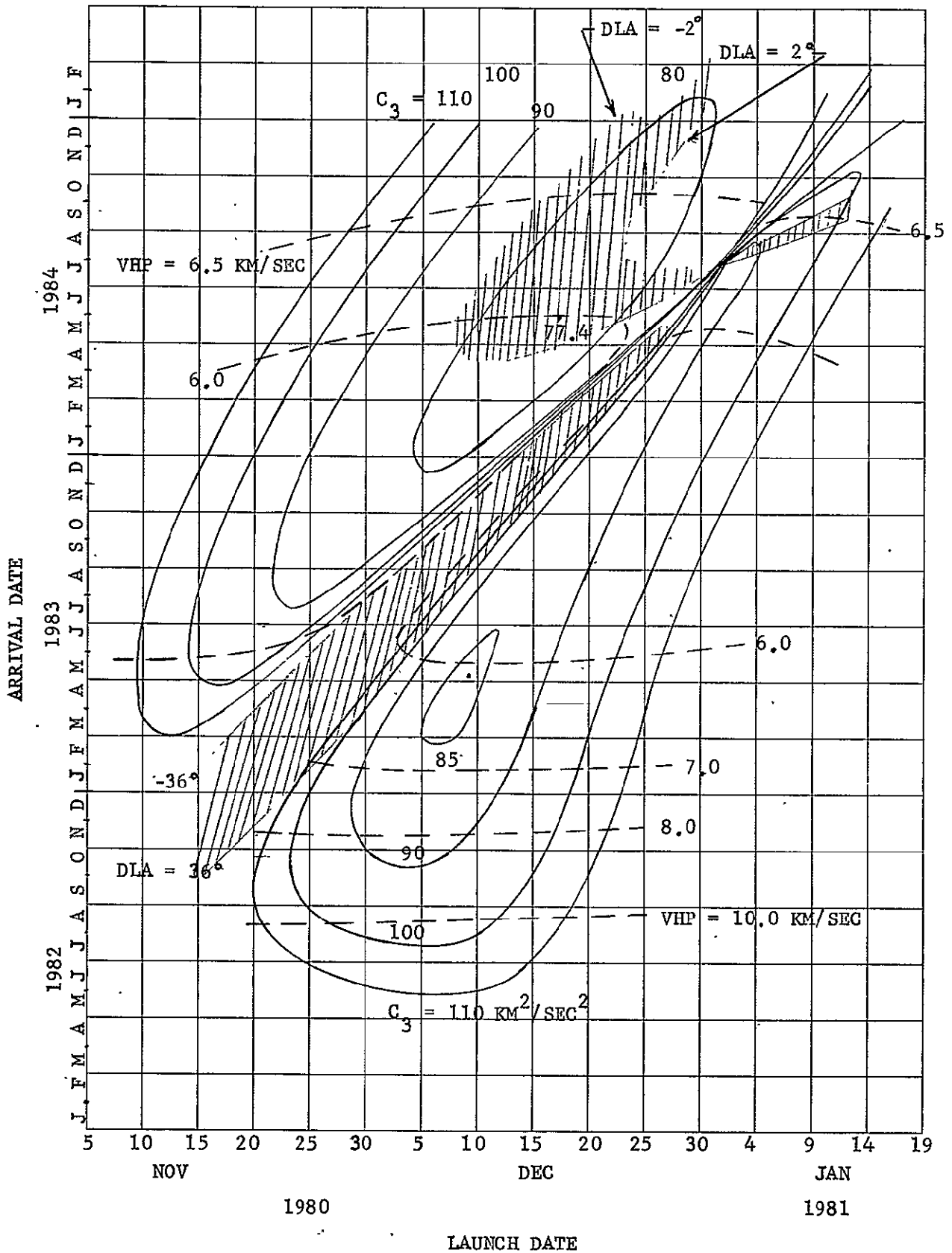


Figure IIIA-3 1980 JUPITER LAUNCH OPPORTUNITIES

$$\mu = 1.267077 \times 10^8 \text{ km}^3/\text{sec}^2 \quad R = 71908 \text{ km} \quad V_C = 41.977 \text{ km/sec} = 137,720 \text{ fps}$$

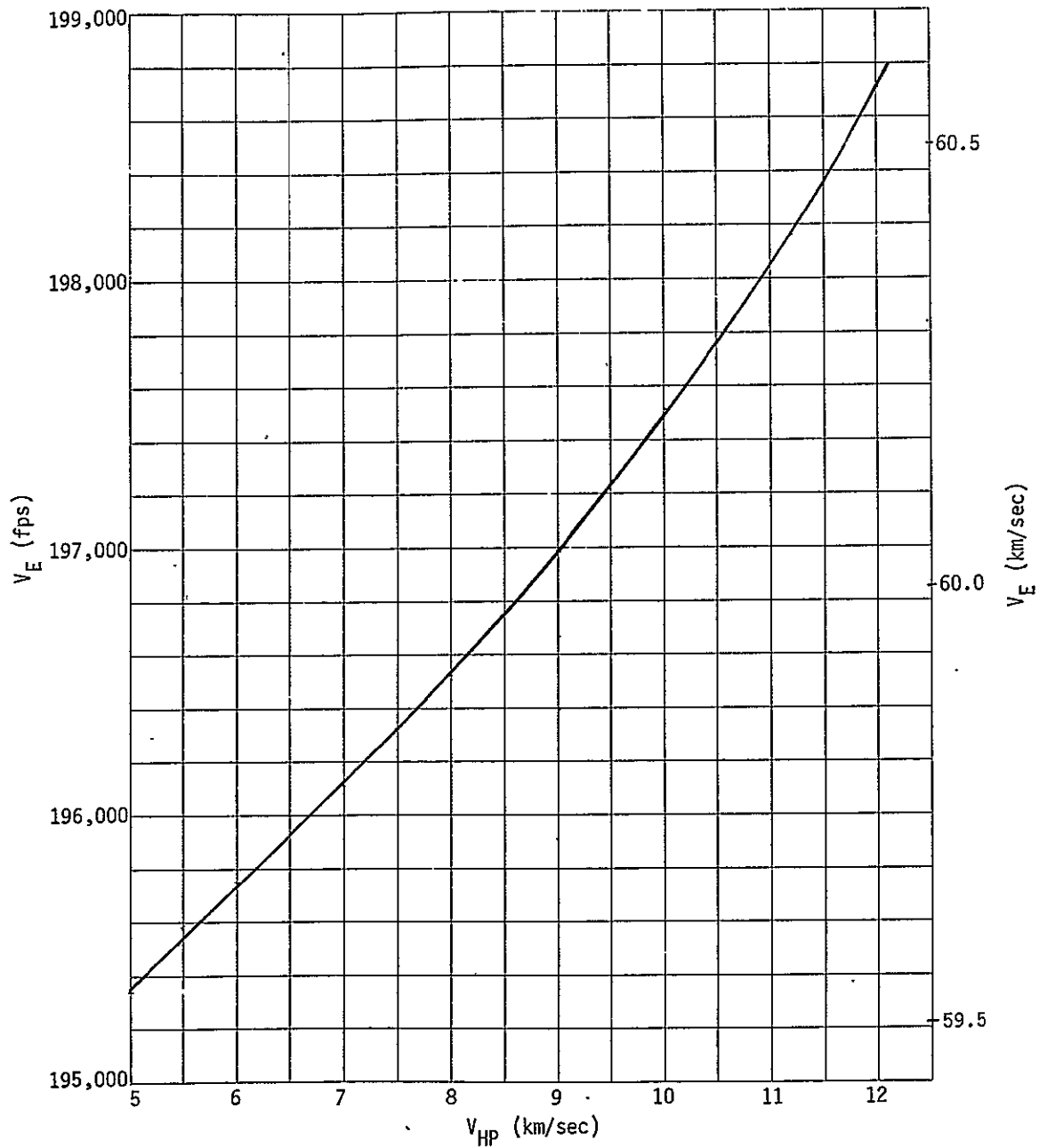


Figure IIIA-4

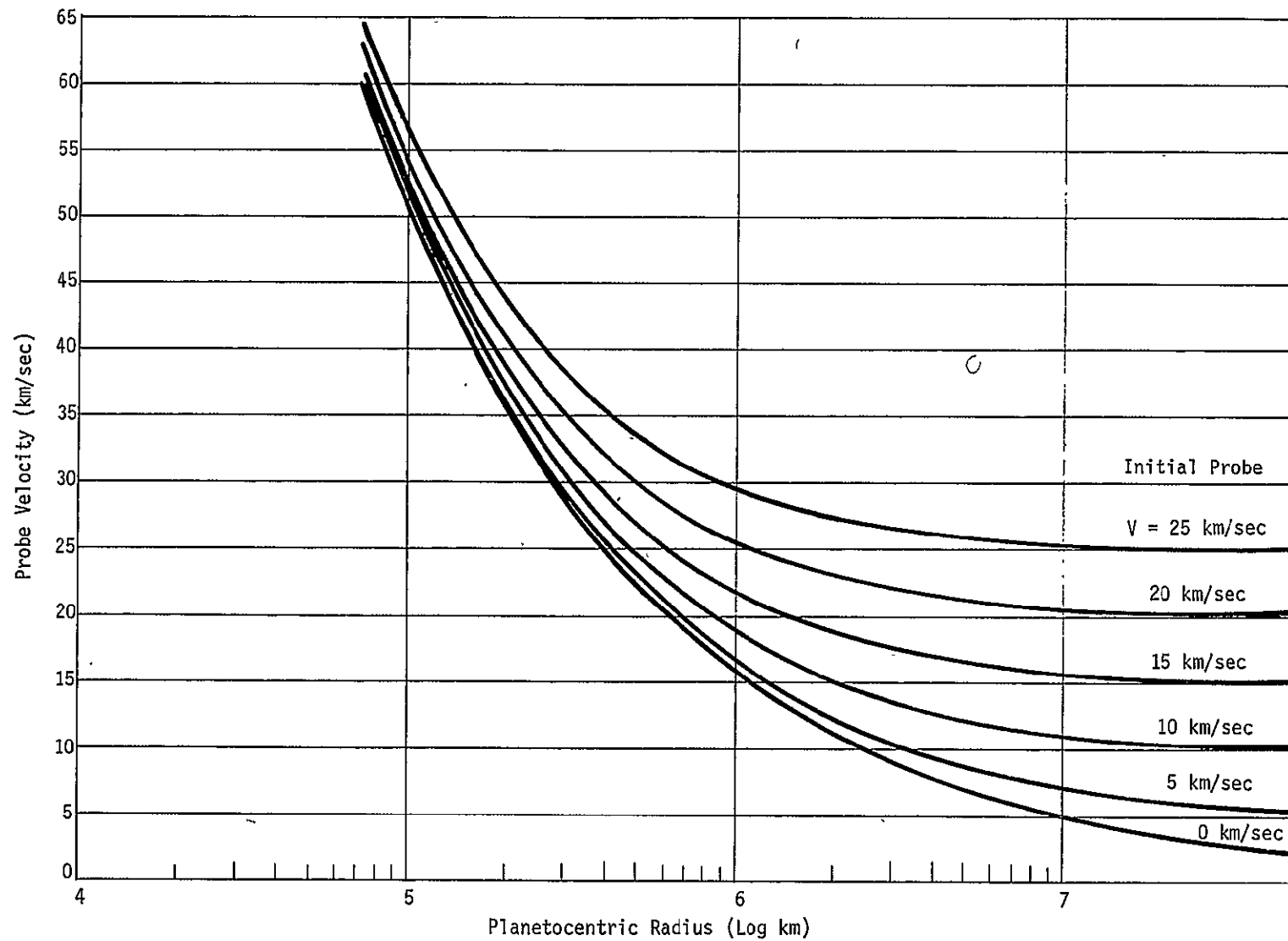


Figure IIIA-5

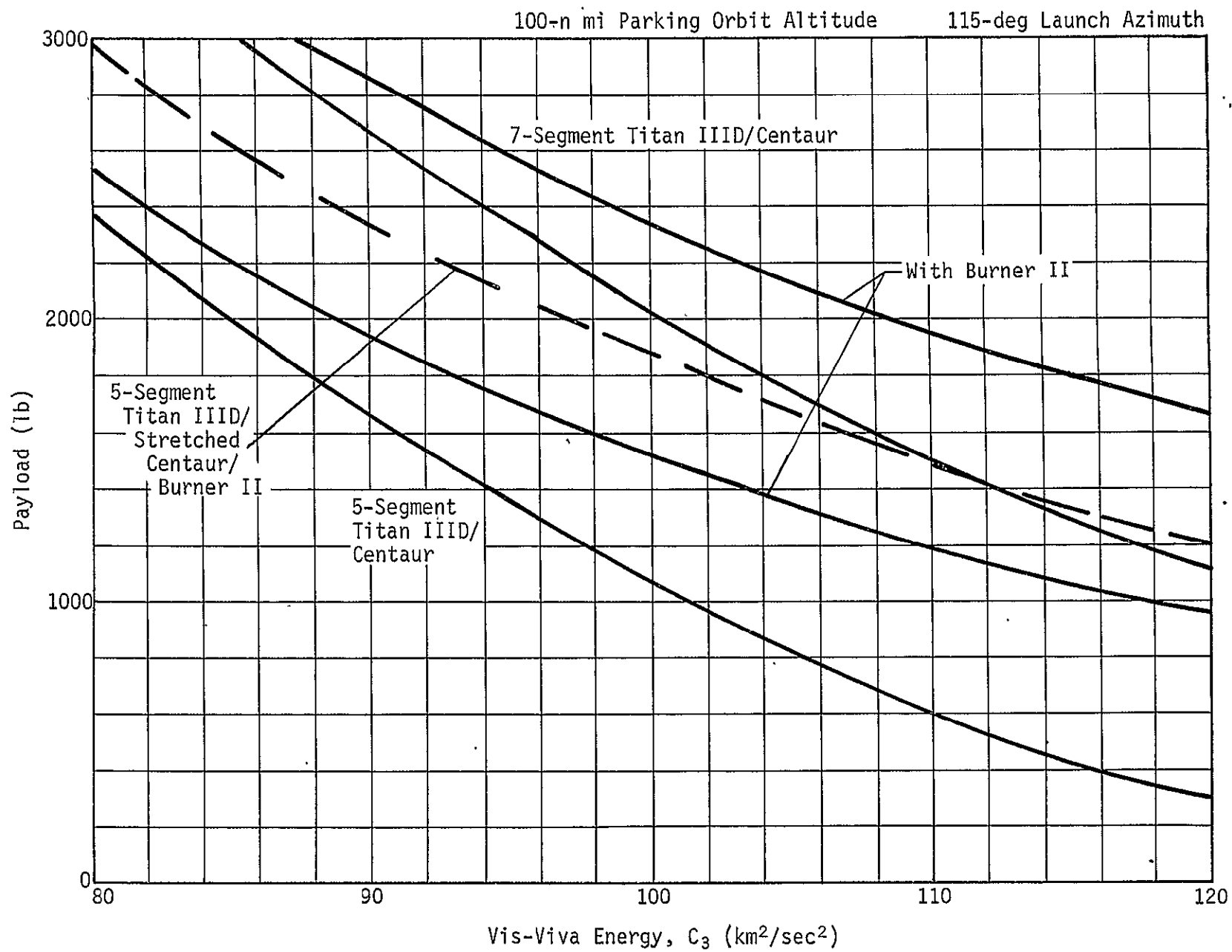
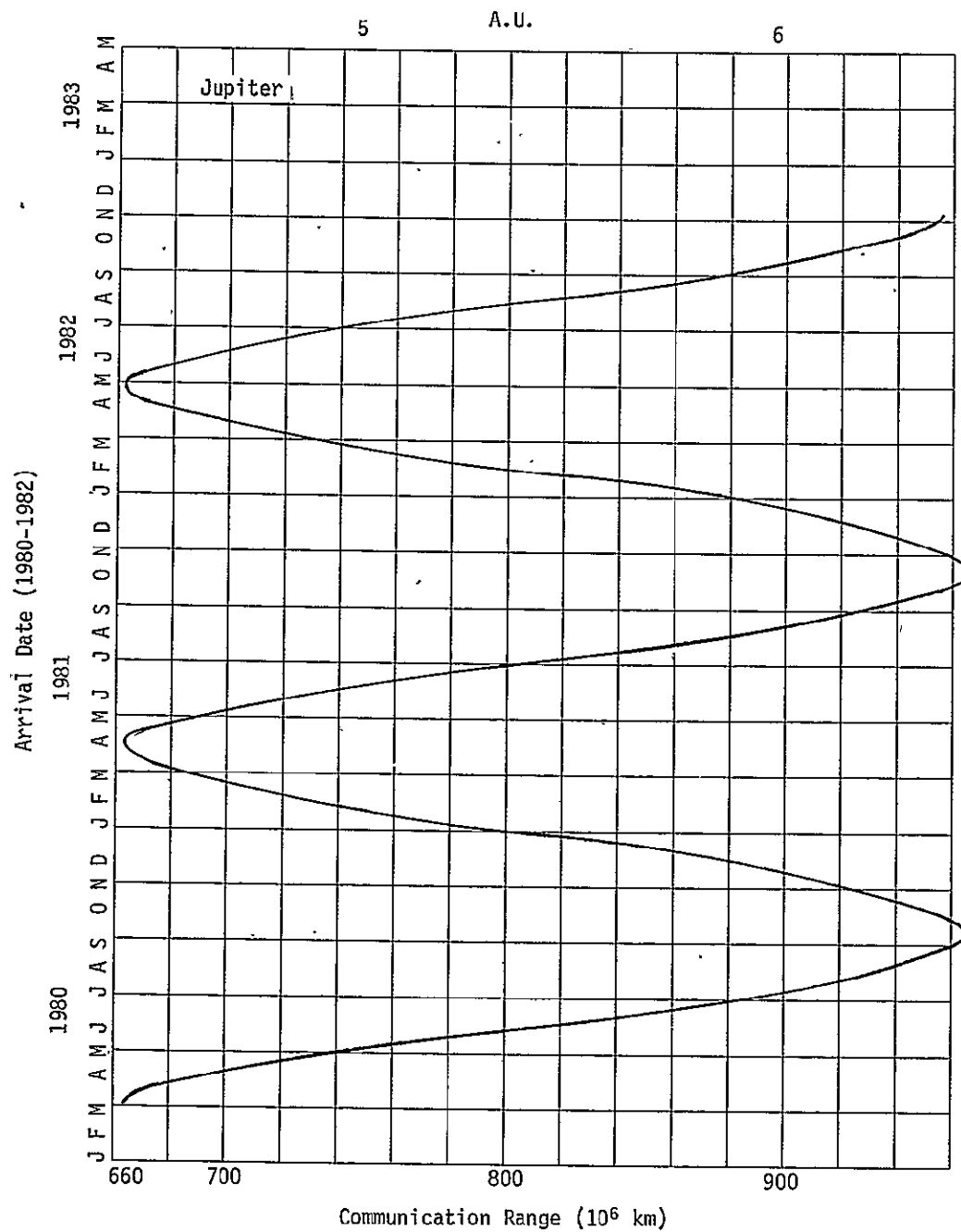


Figure IIIA-6



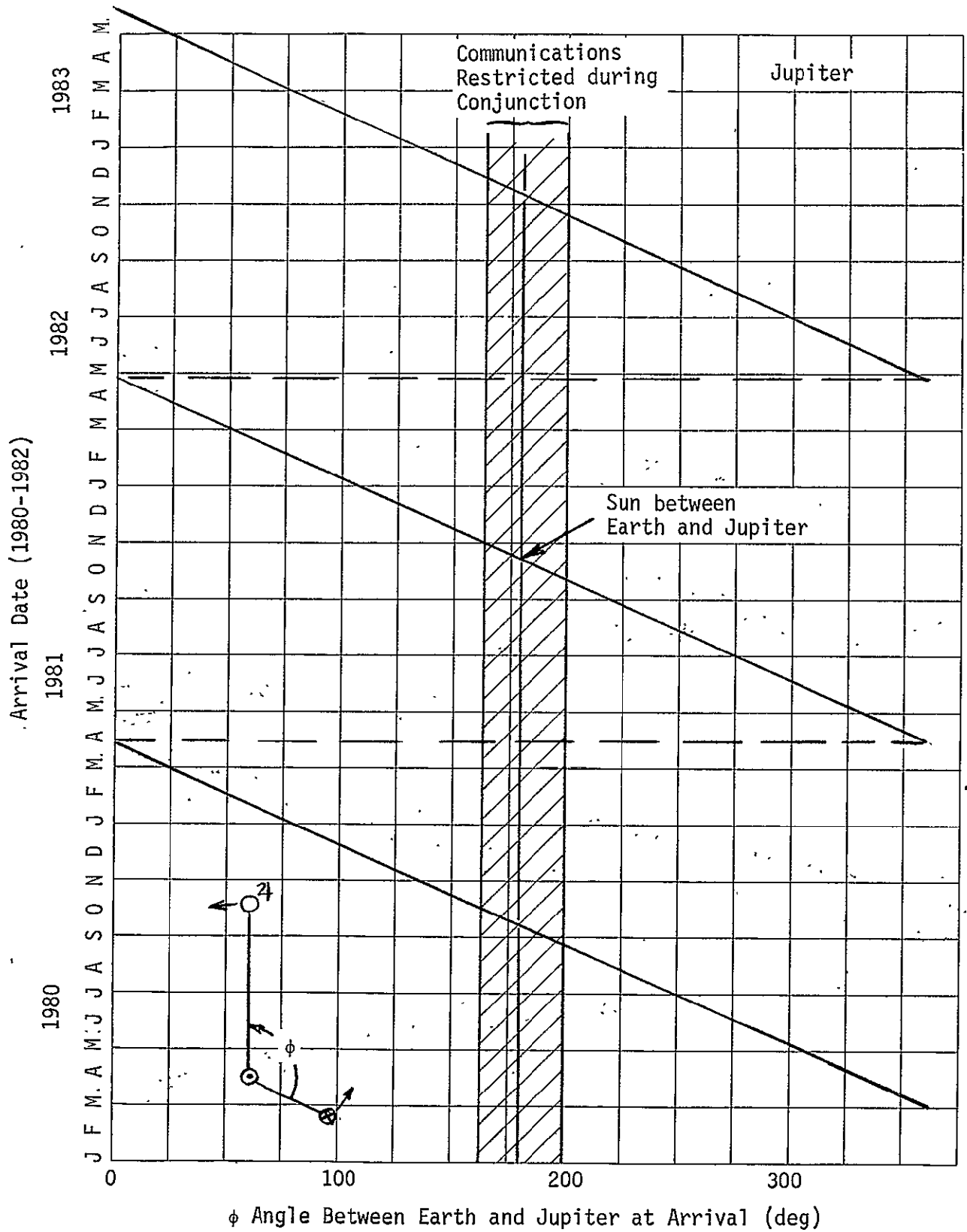


Figure IIIB-1

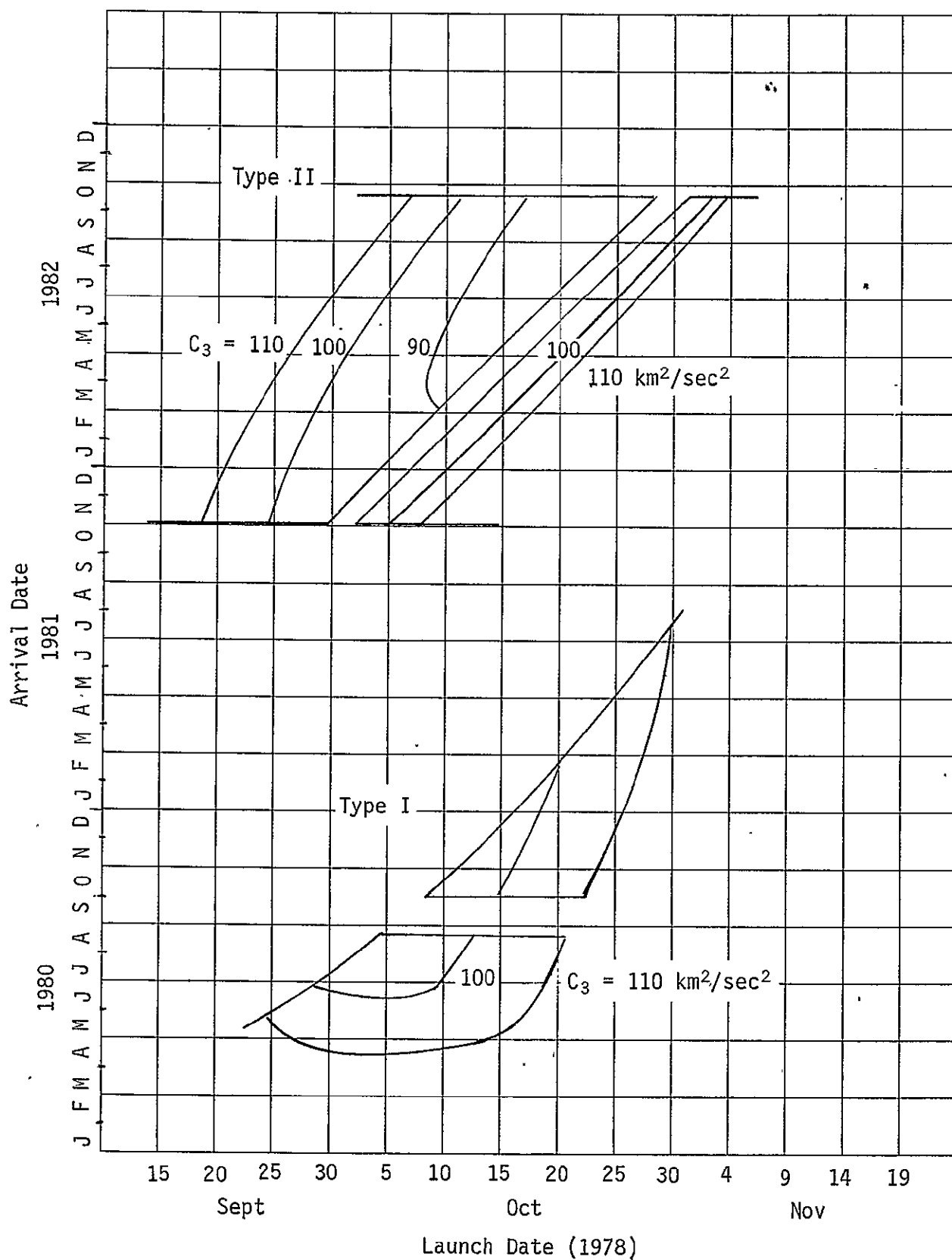


Figure III B-2

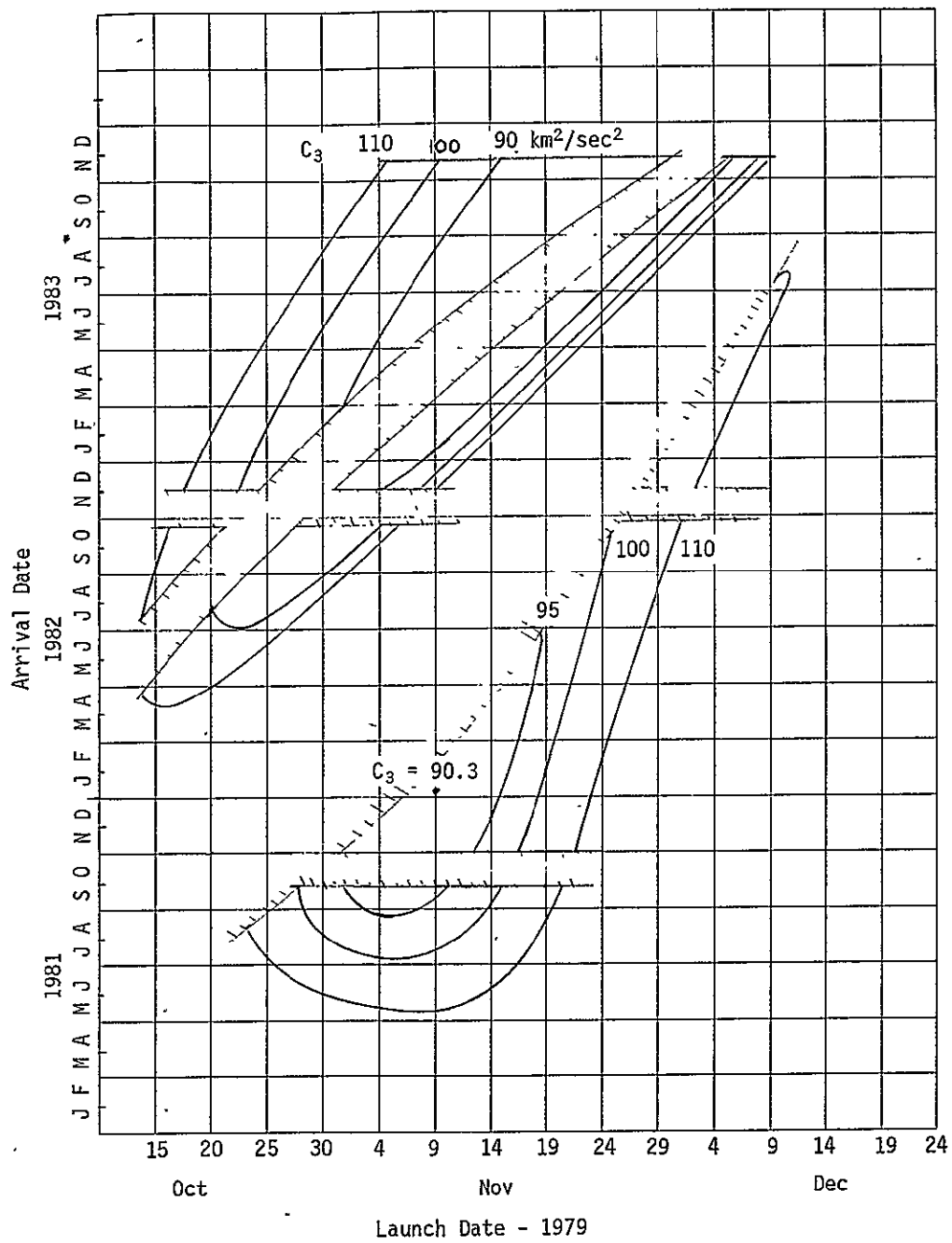


Figure IIIB-3

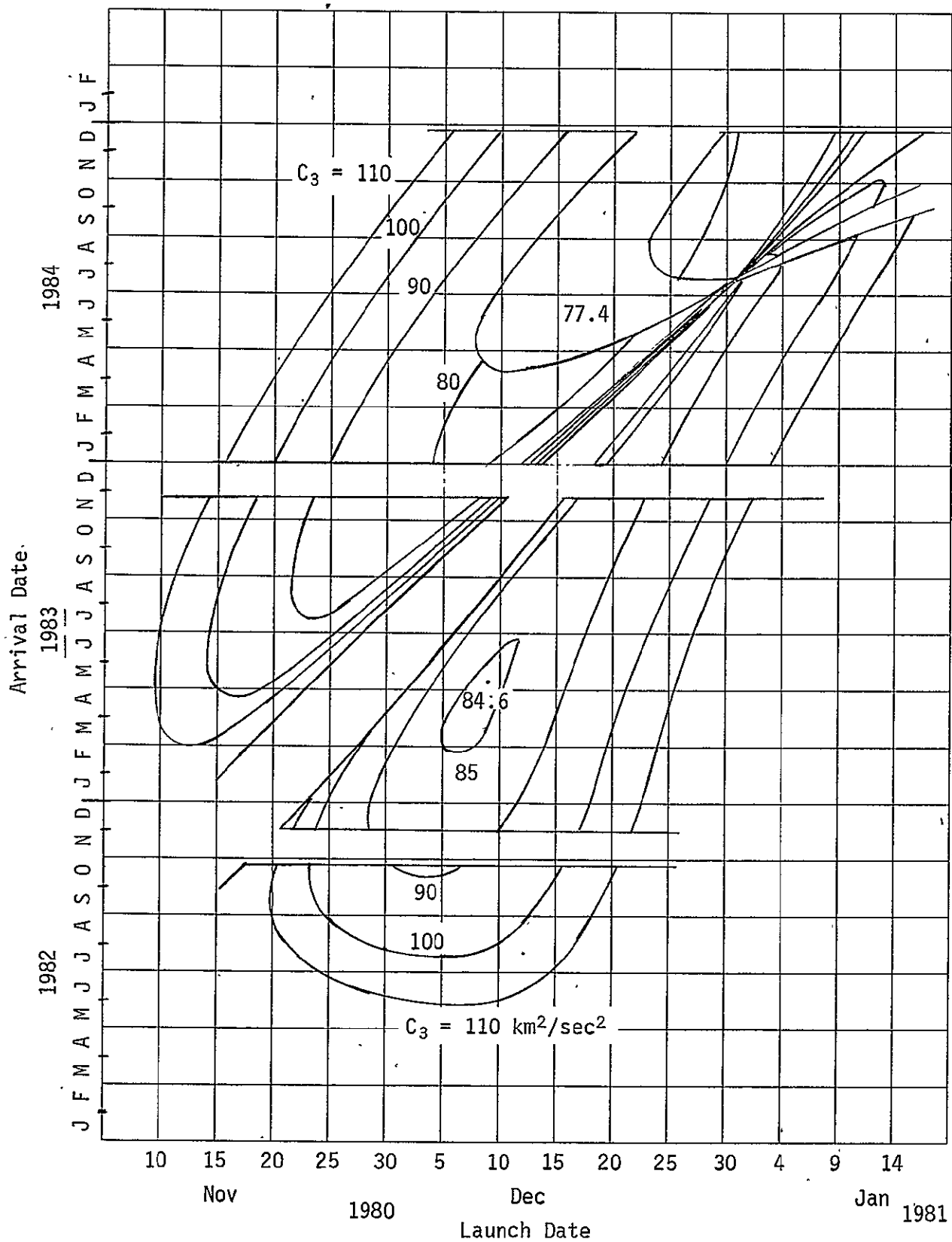


Figure IIIB-4

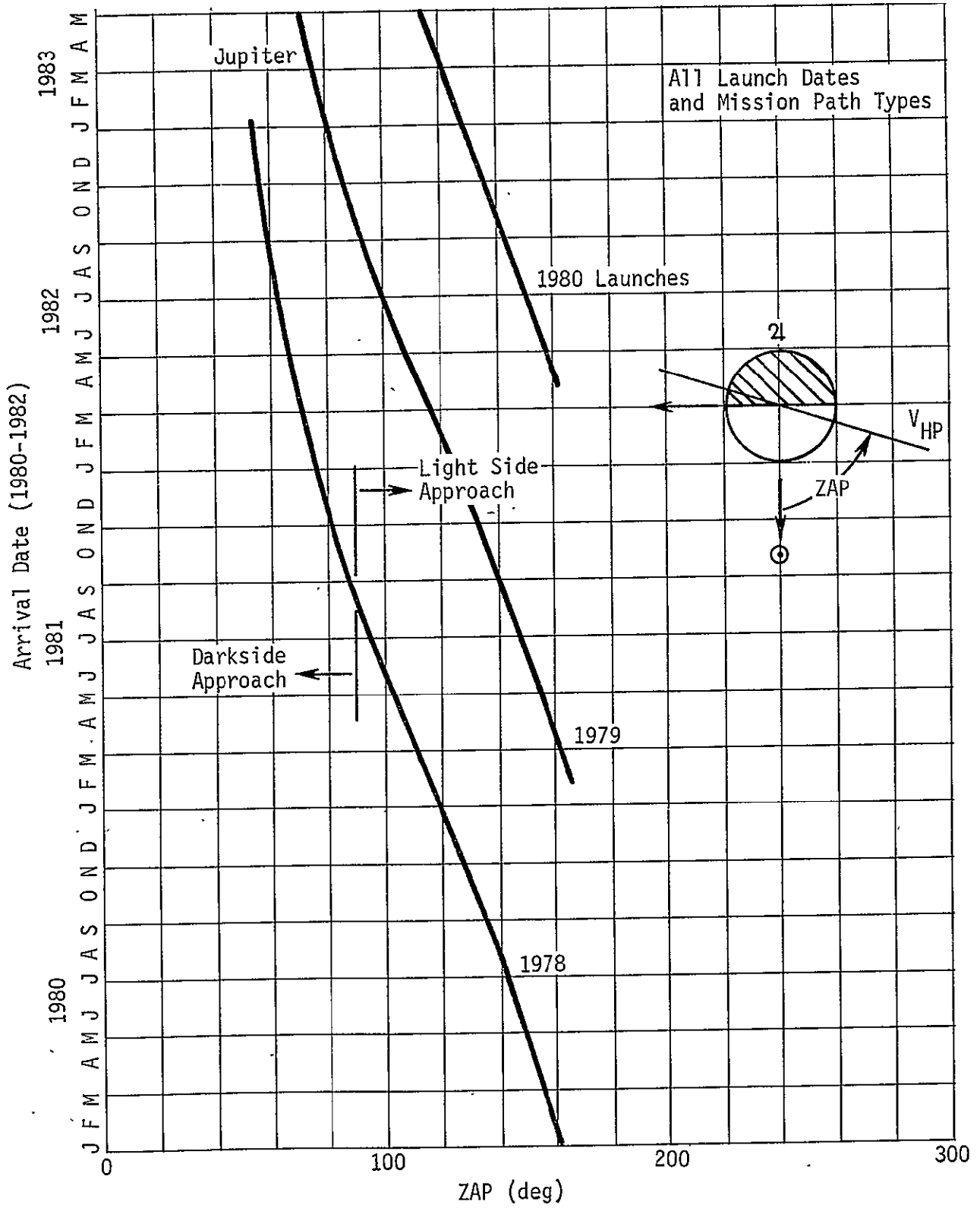


Figure IIIB-5

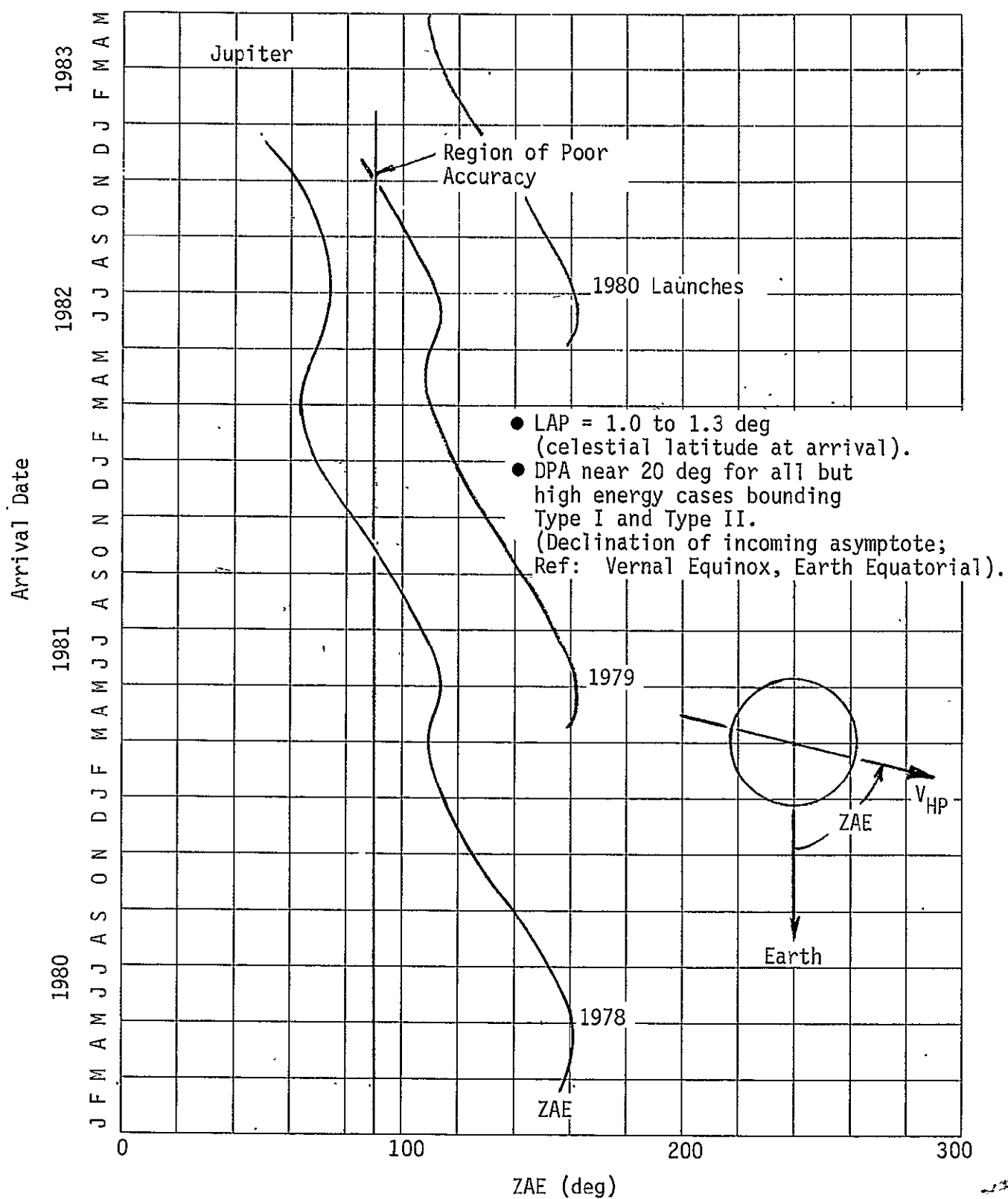


Figure IIIB-6

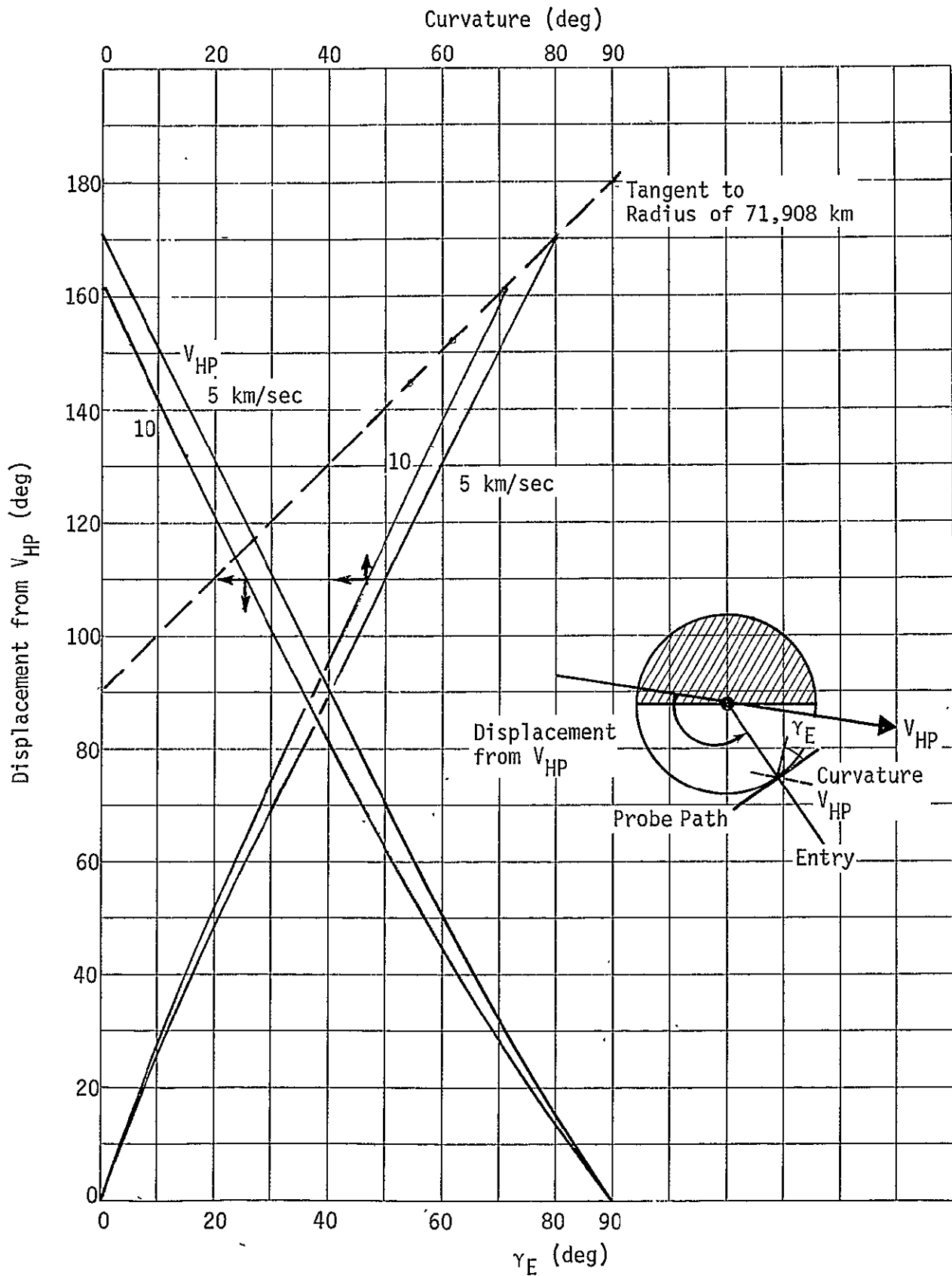


Figure IIIB-7

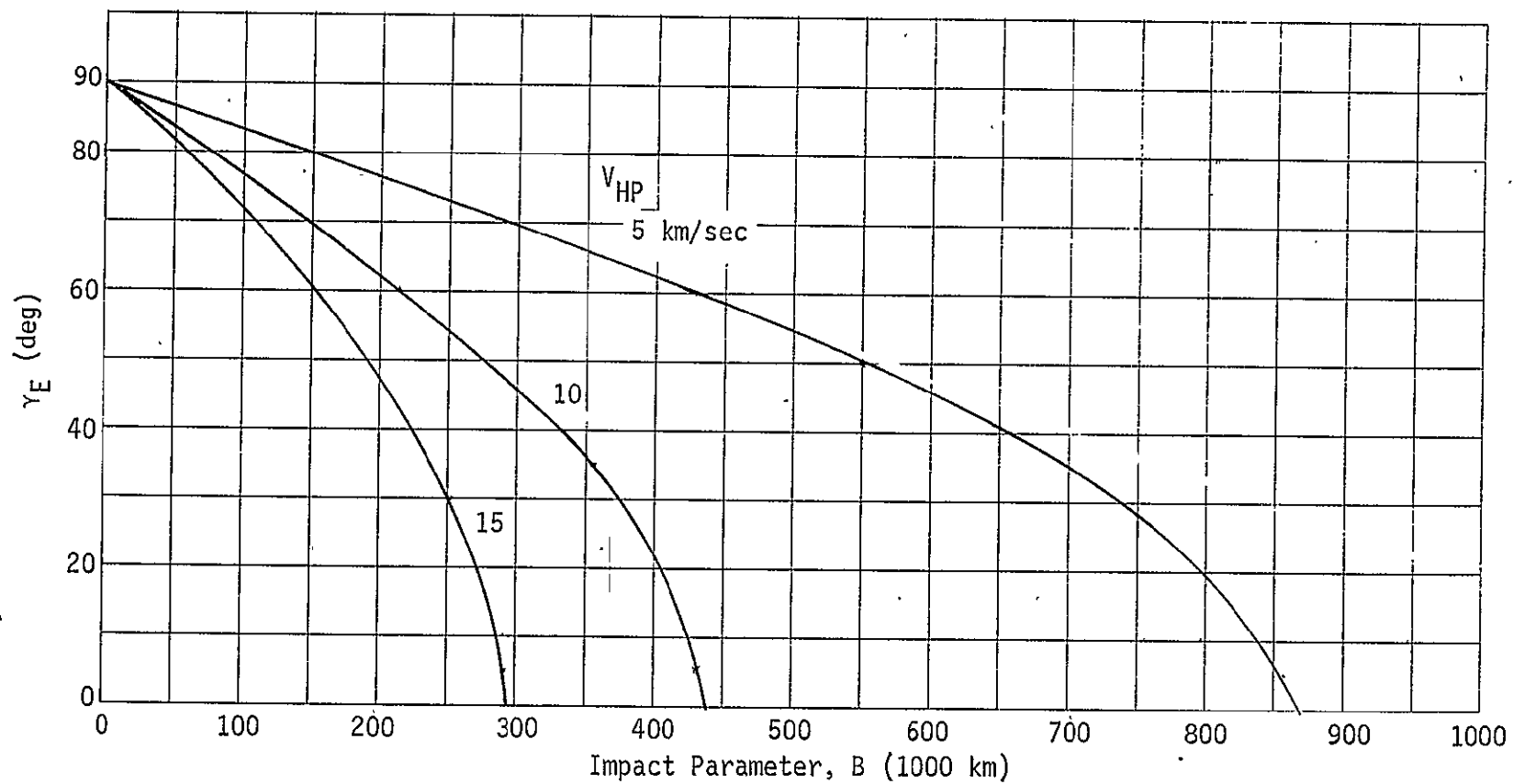


Figure IIIB-8

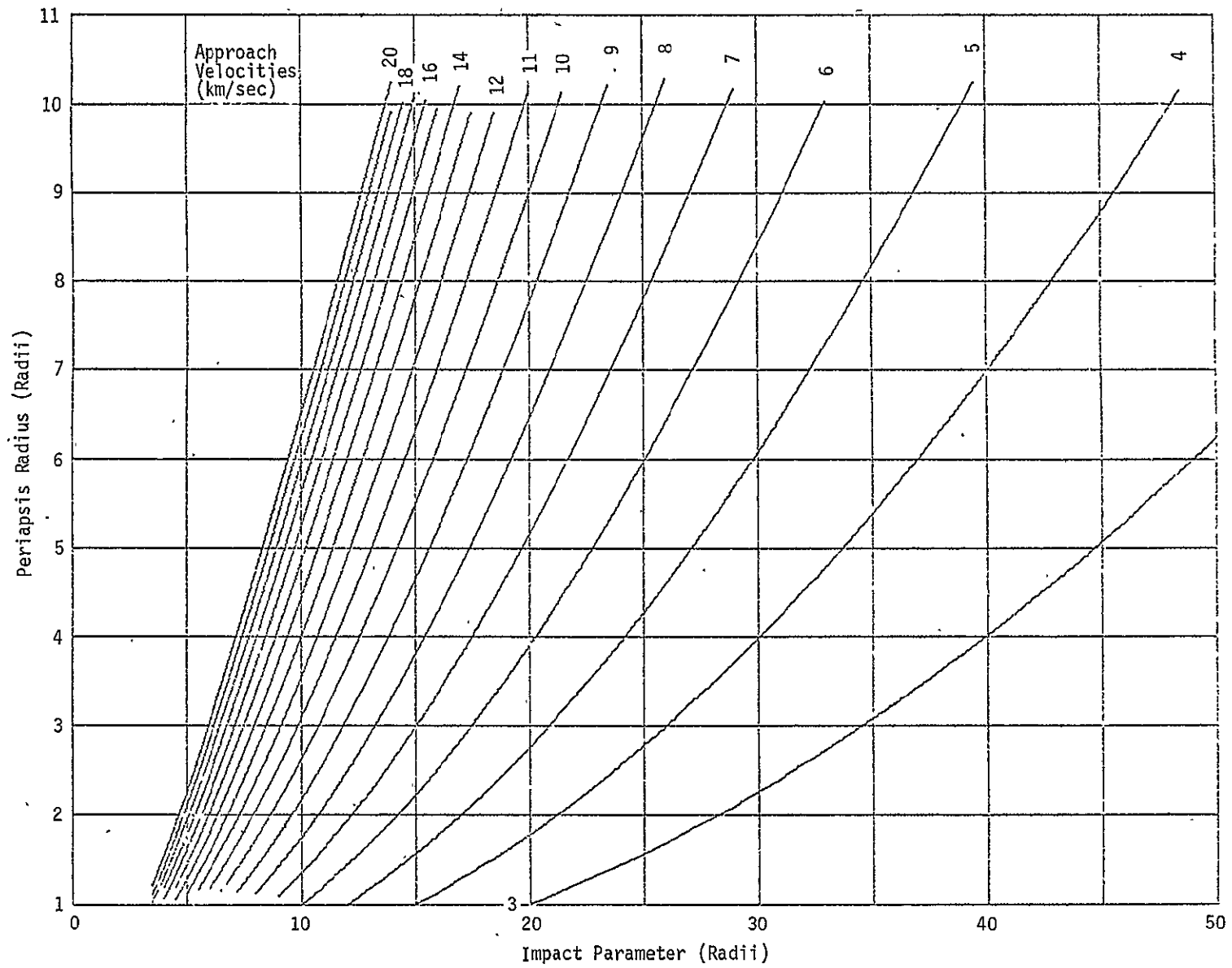


Figure IIIB-9 Periapsis Radius vs Impact Parameter - Jupiter

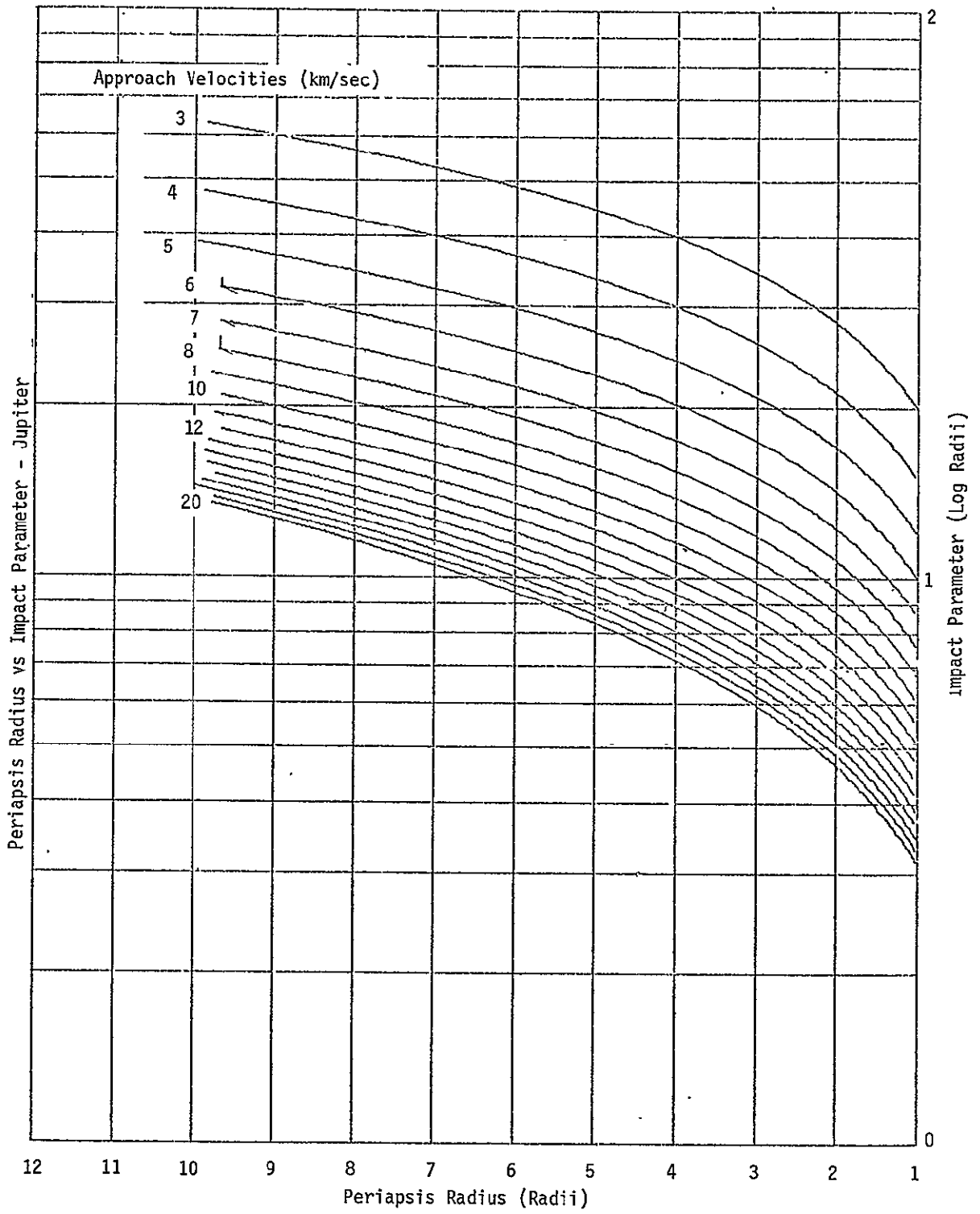


Figure IIIB-10

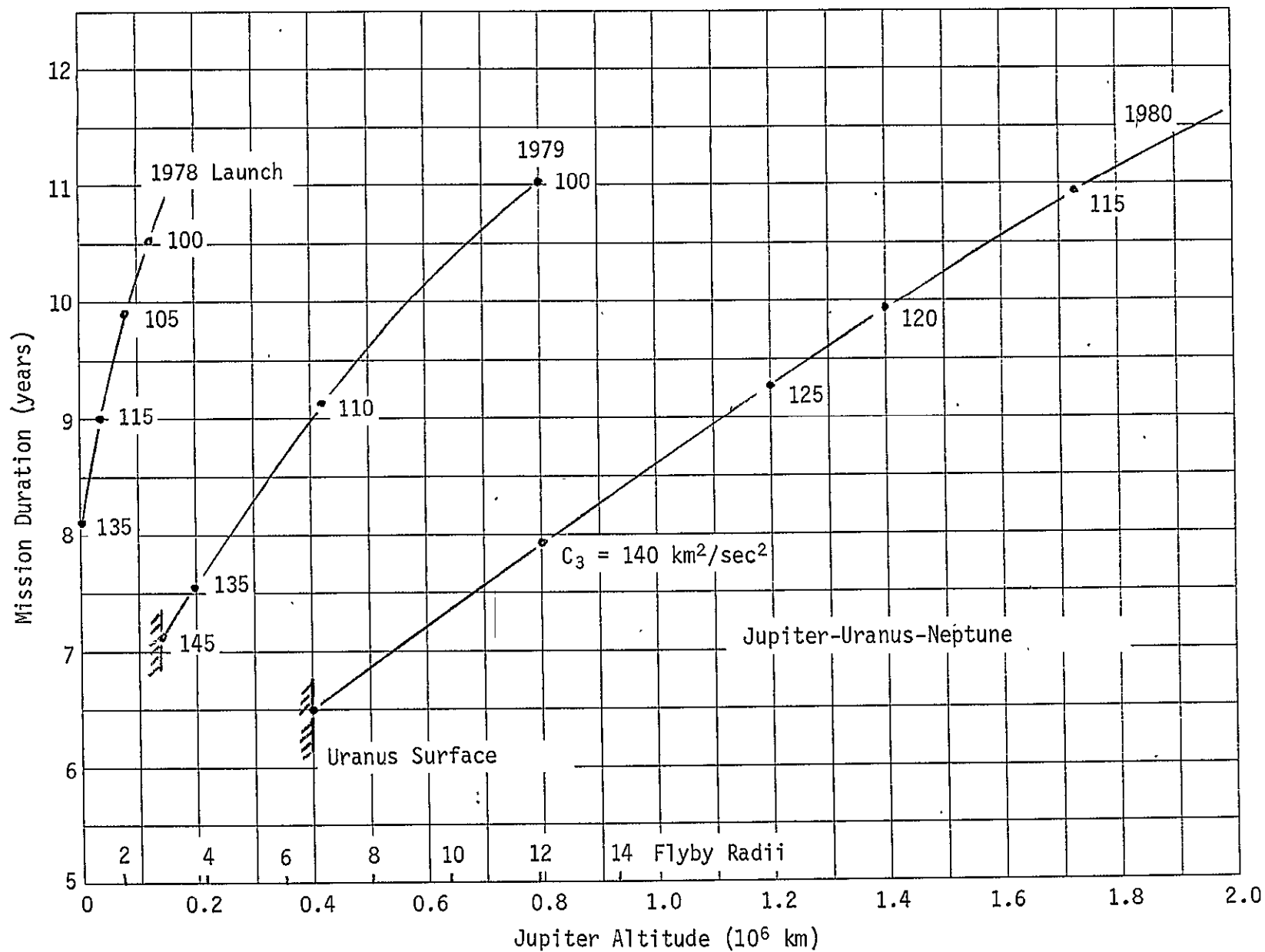


Figure IIIB-11

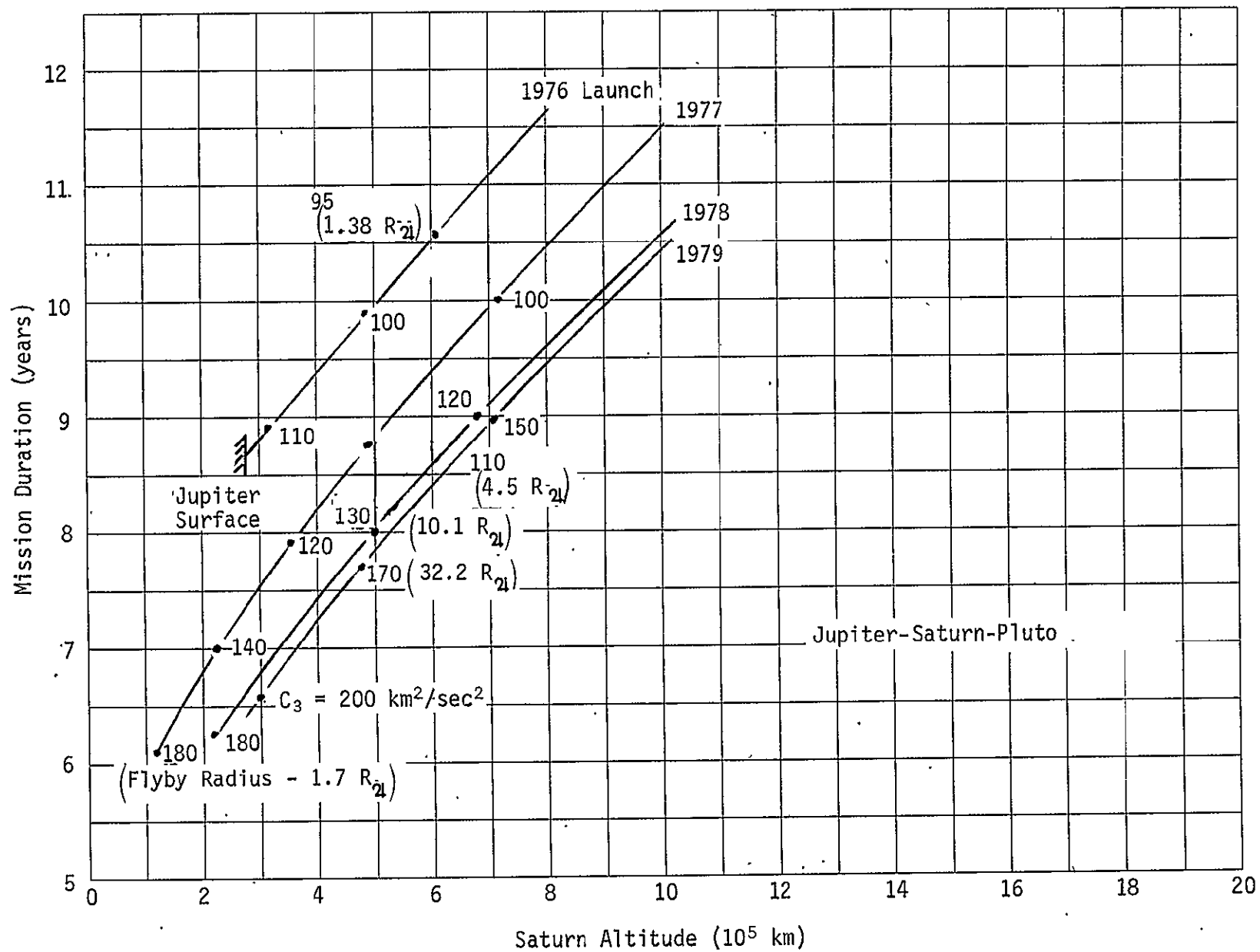


Figure IIIB-12

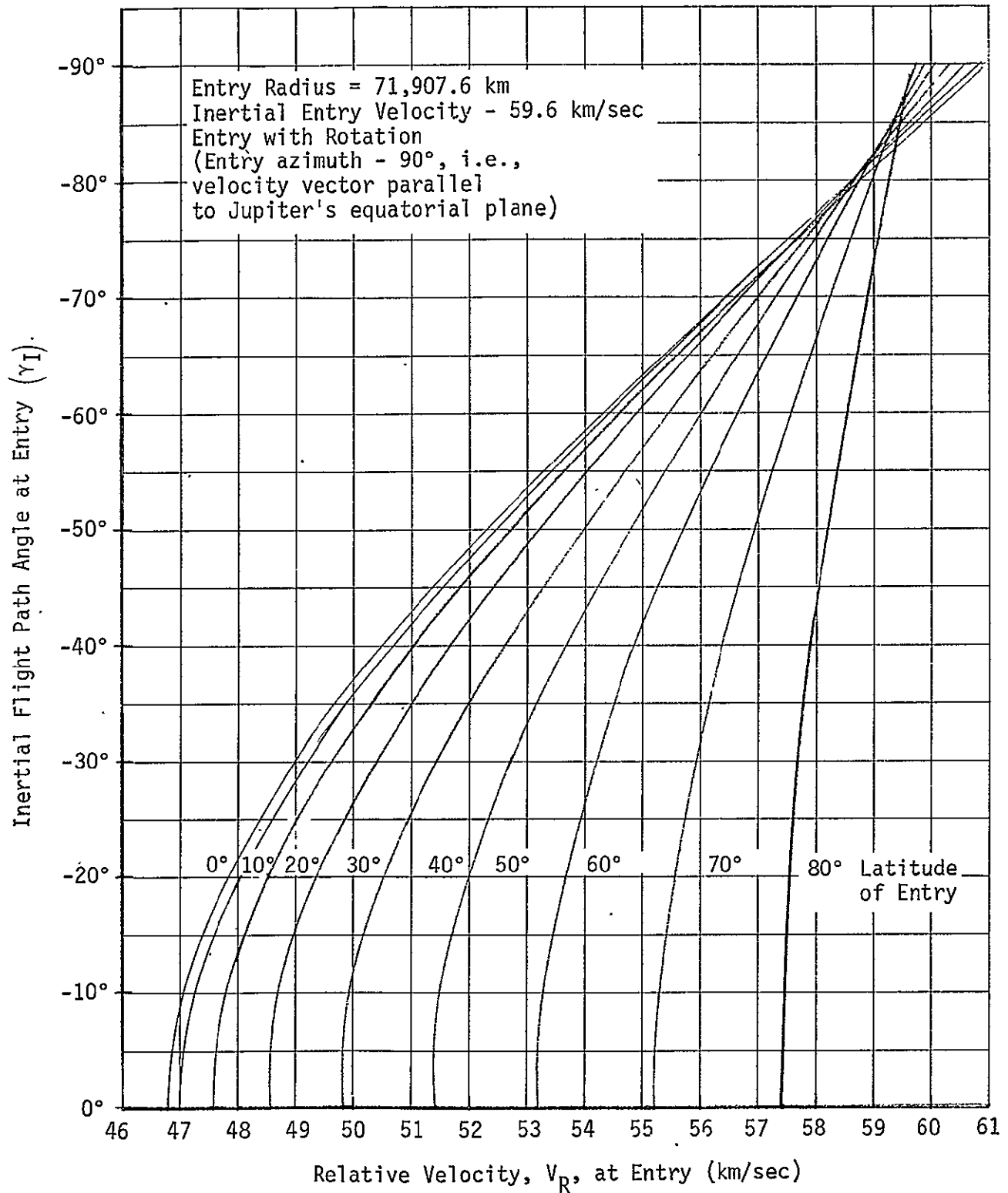


Figure IIIC-1 Effect of "Entry with Rotation" on Entry Velocity

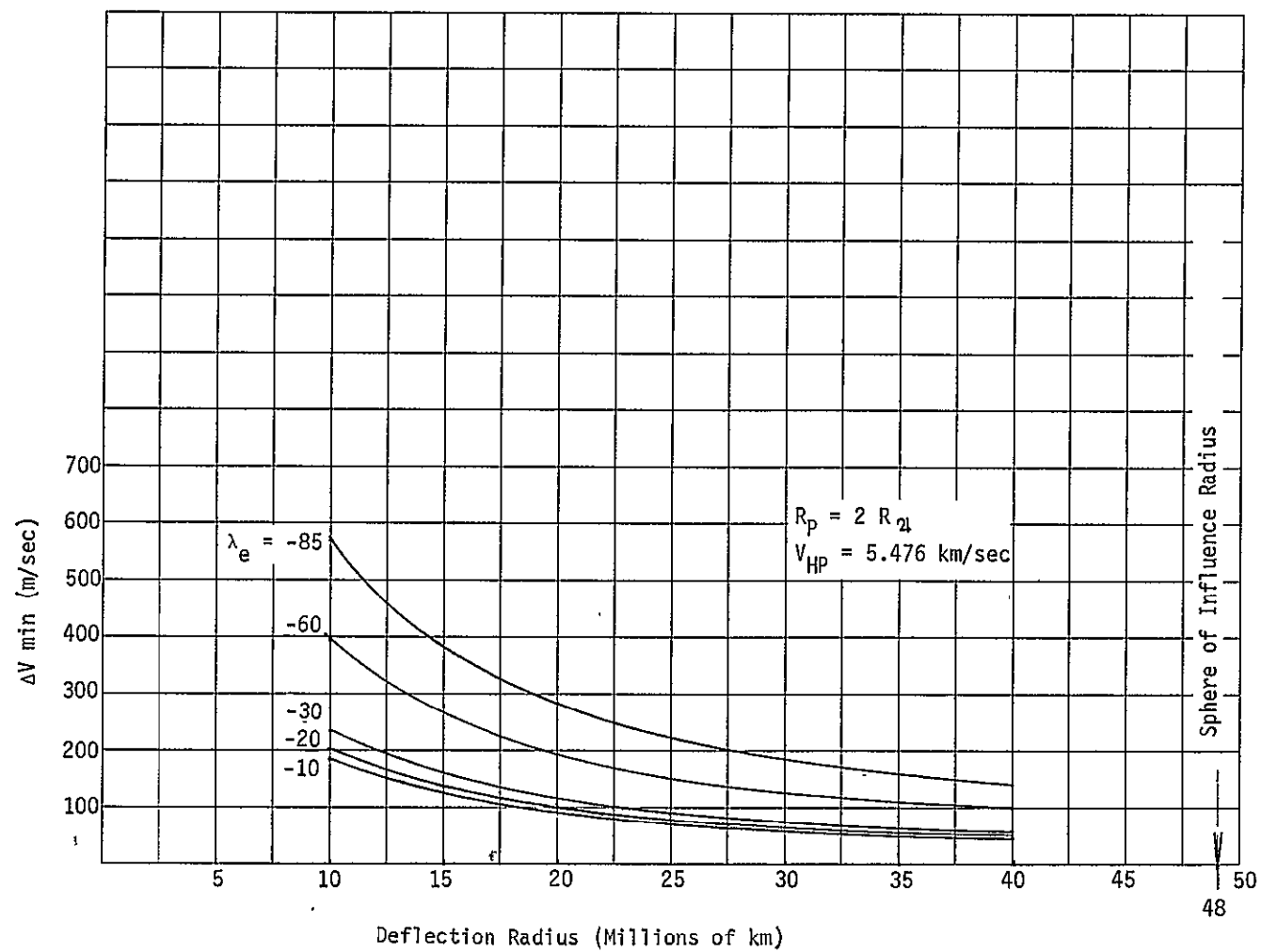


Figure IIIC-2

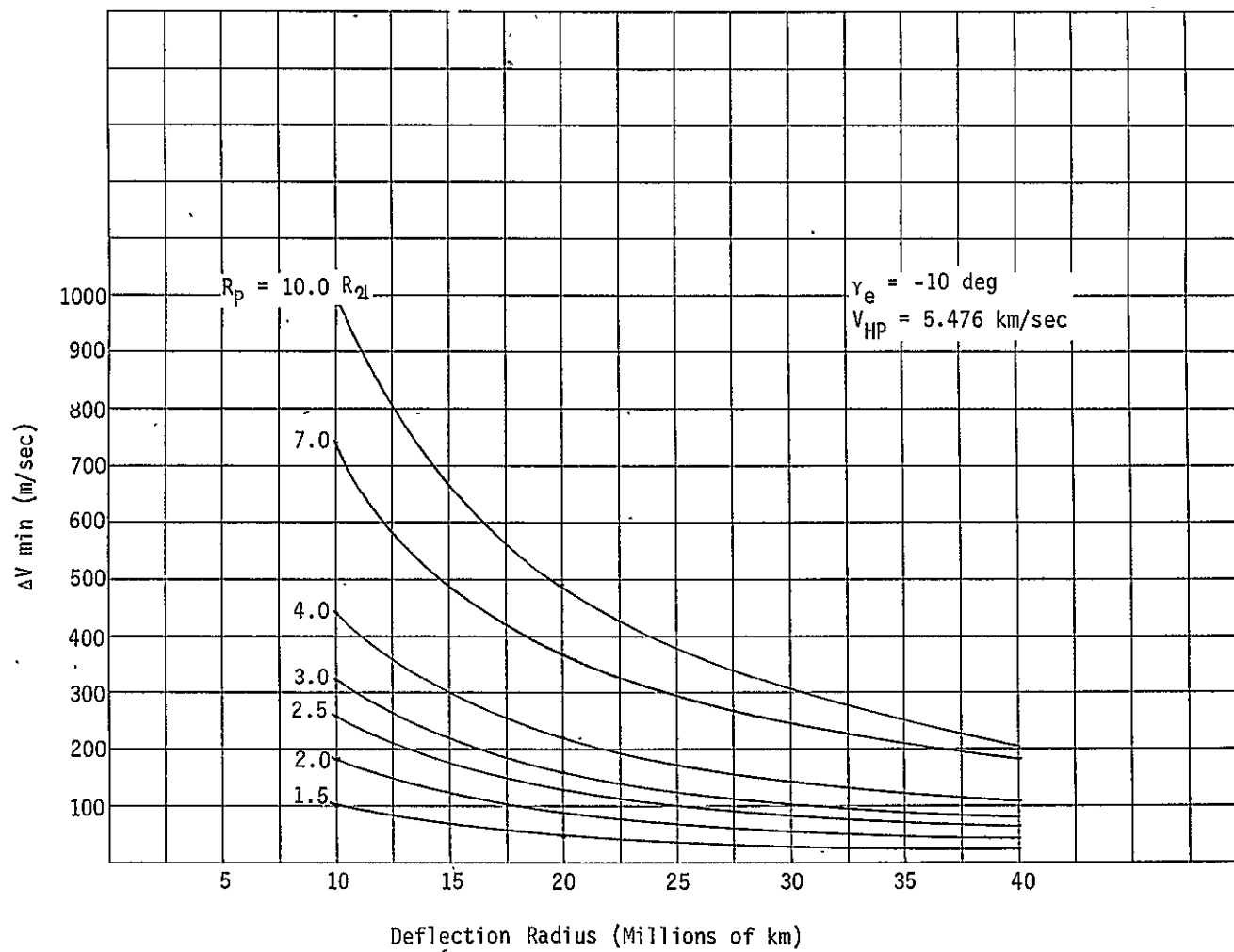


Figure IIIC-3

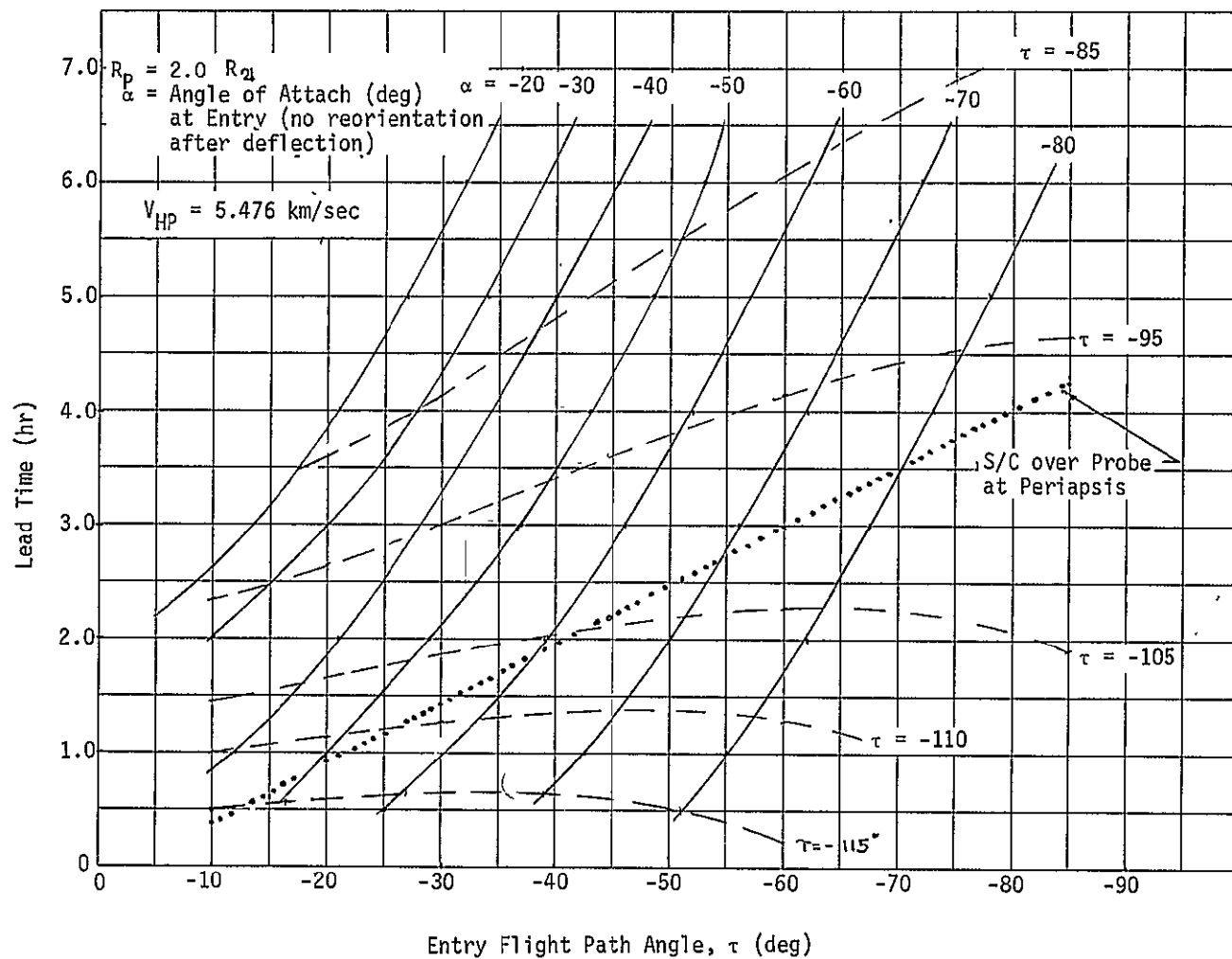


Figure IIIC-4 Lead Time vs Entry Flight Path Angle

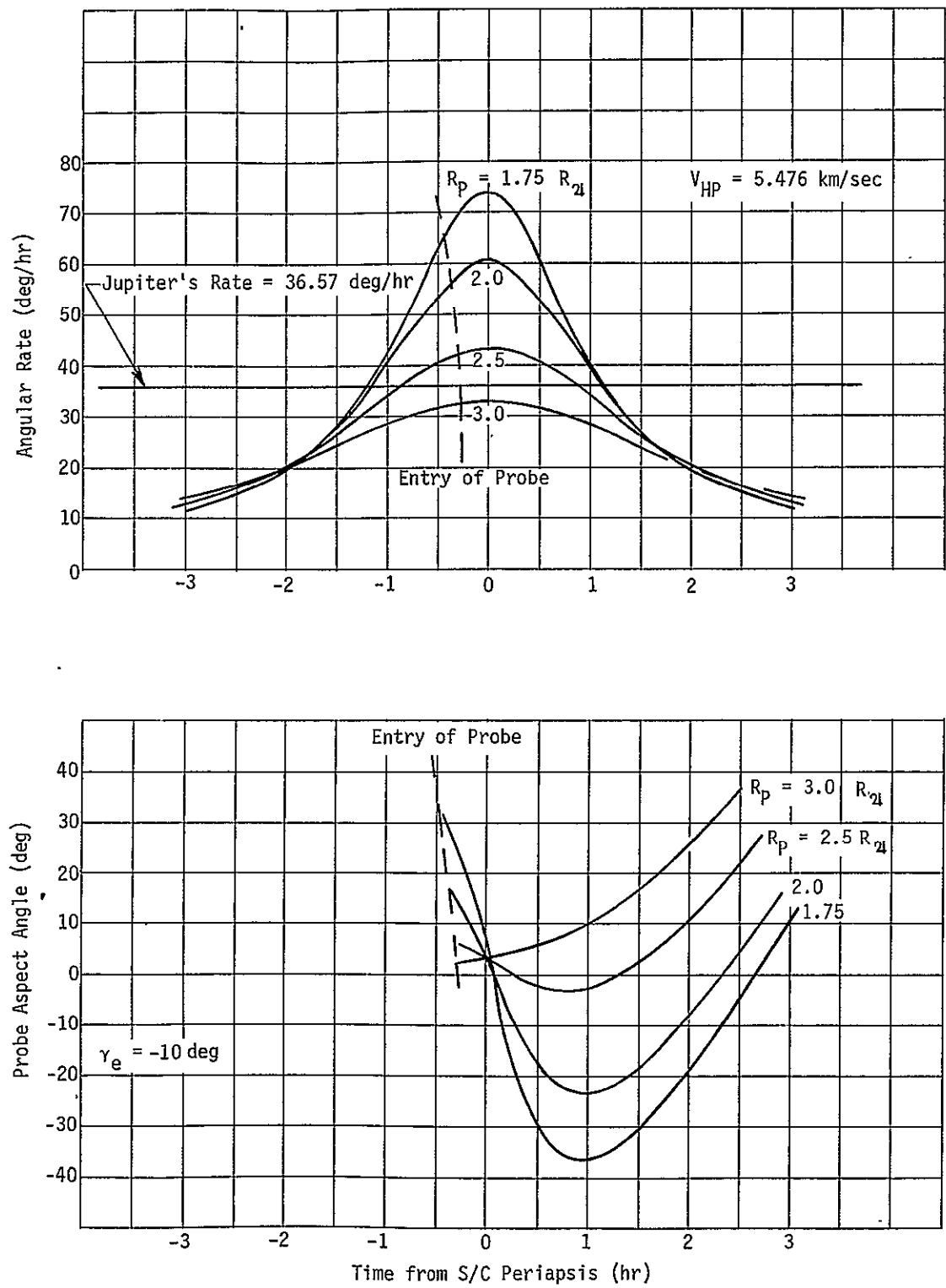


Figure IIIC-5 Rotation Rate Averaging Effects

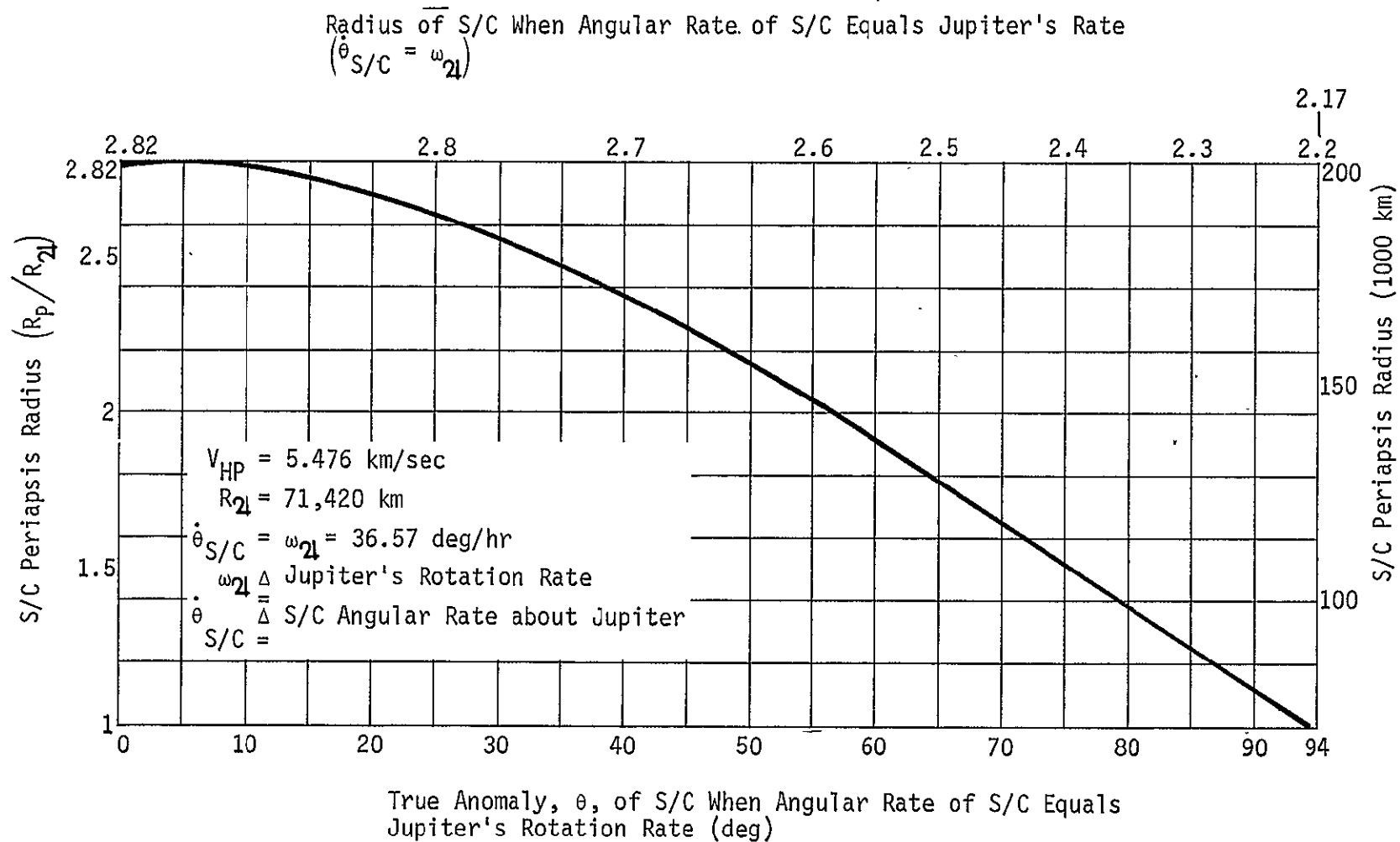


Figure IIIC-6 Angular Rate Matching of Jupiter and S/C

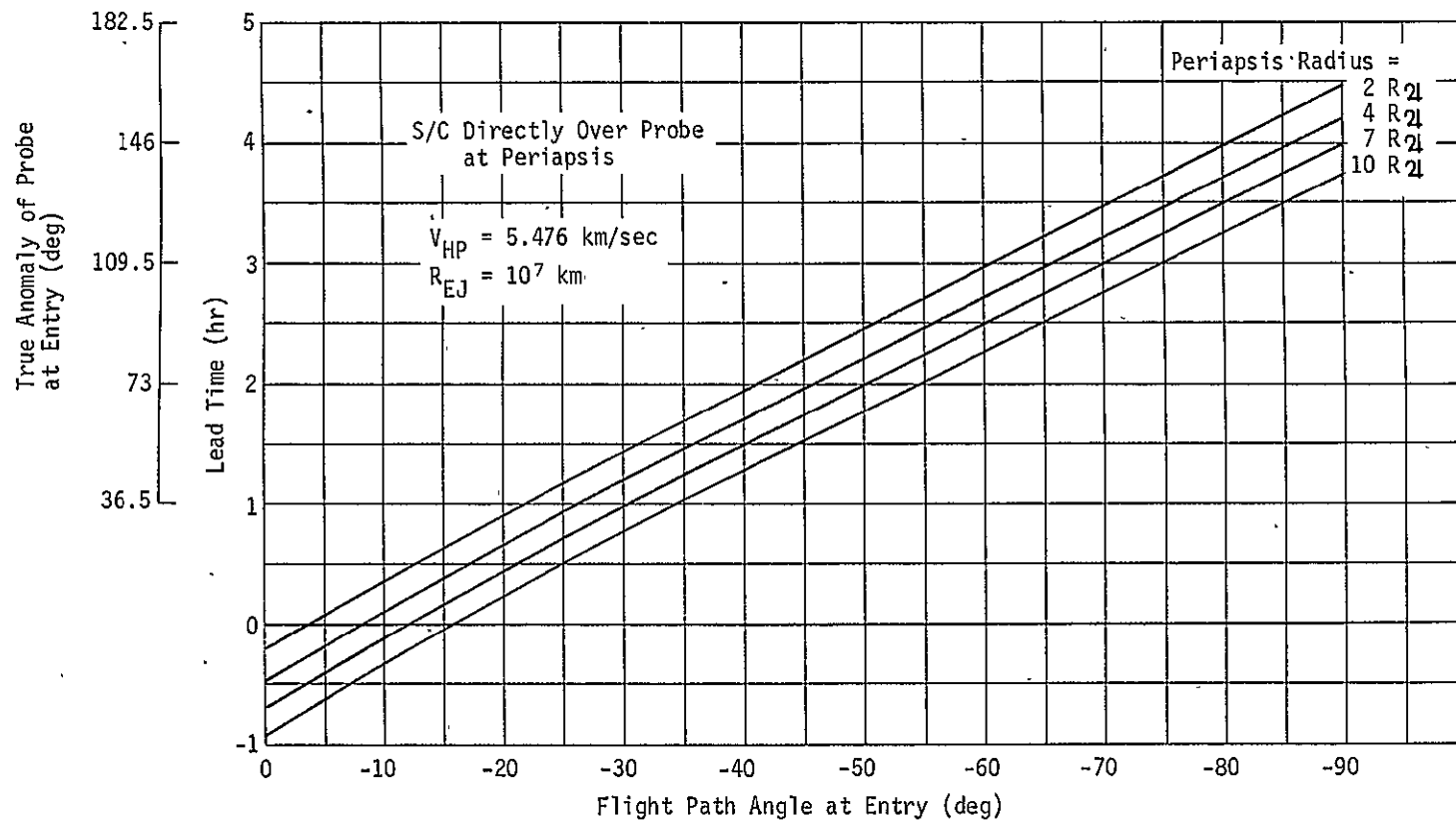


Figure IIIC-7

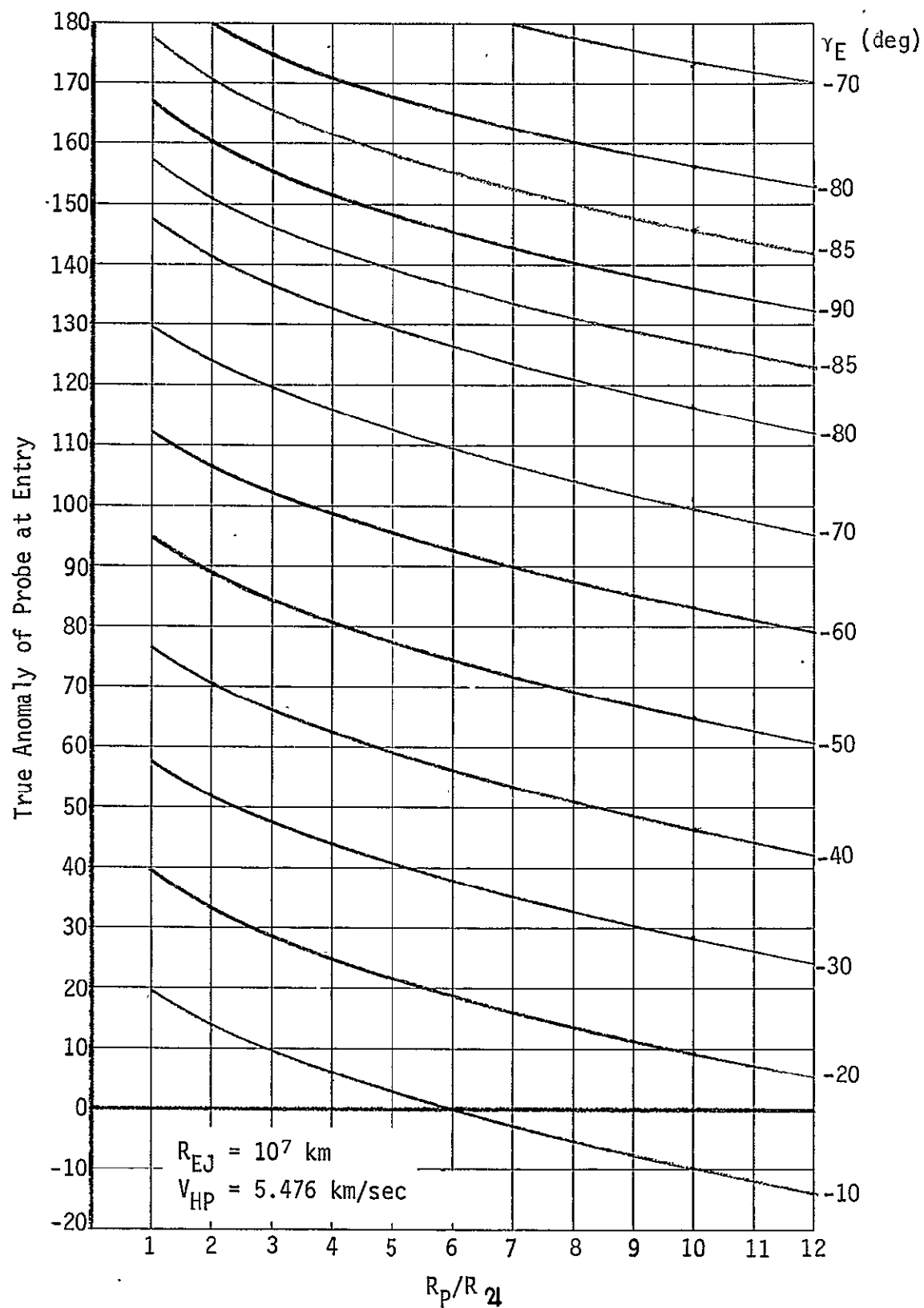


Figure IIIC-8

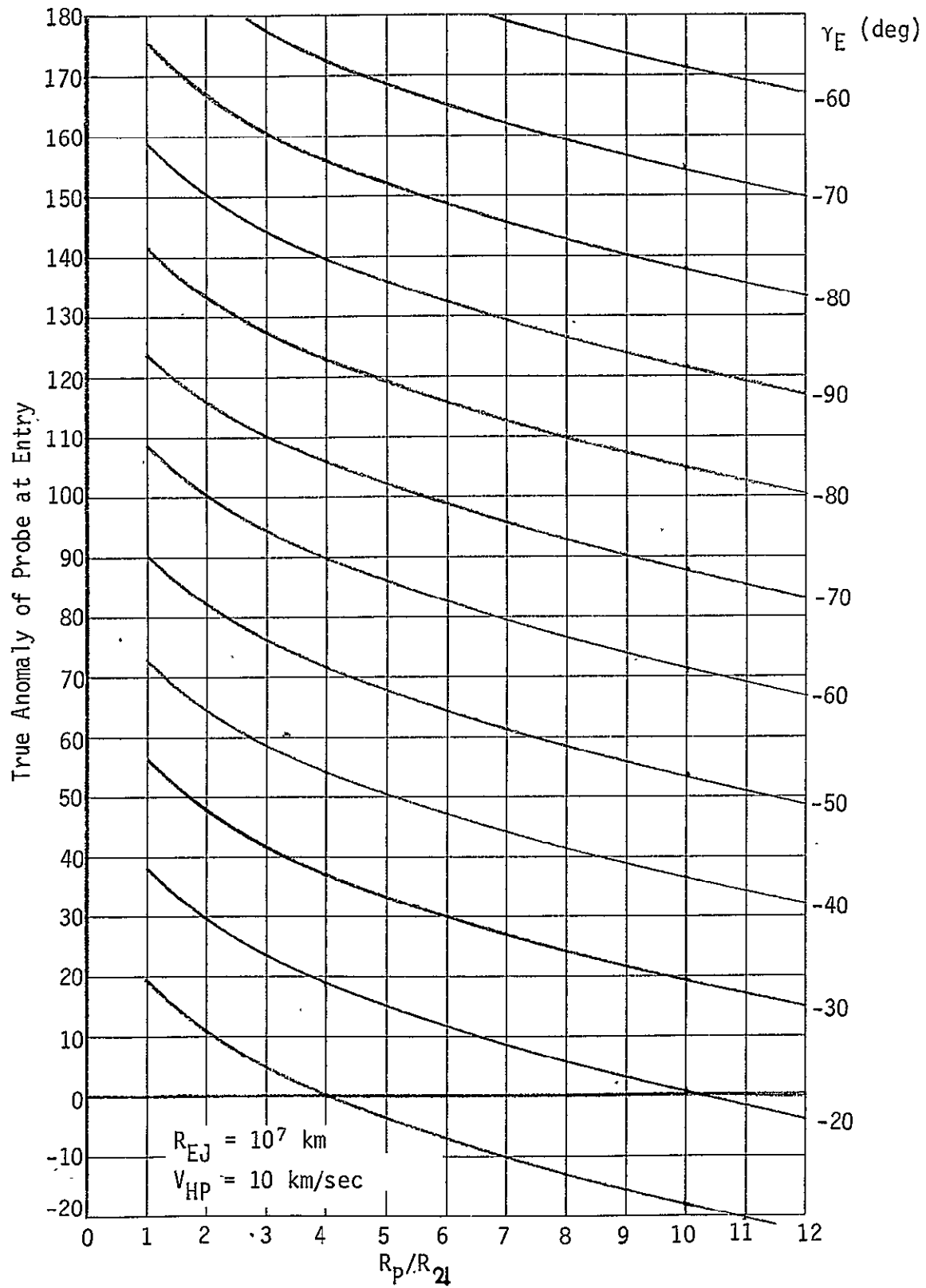


Figure IIIC-9

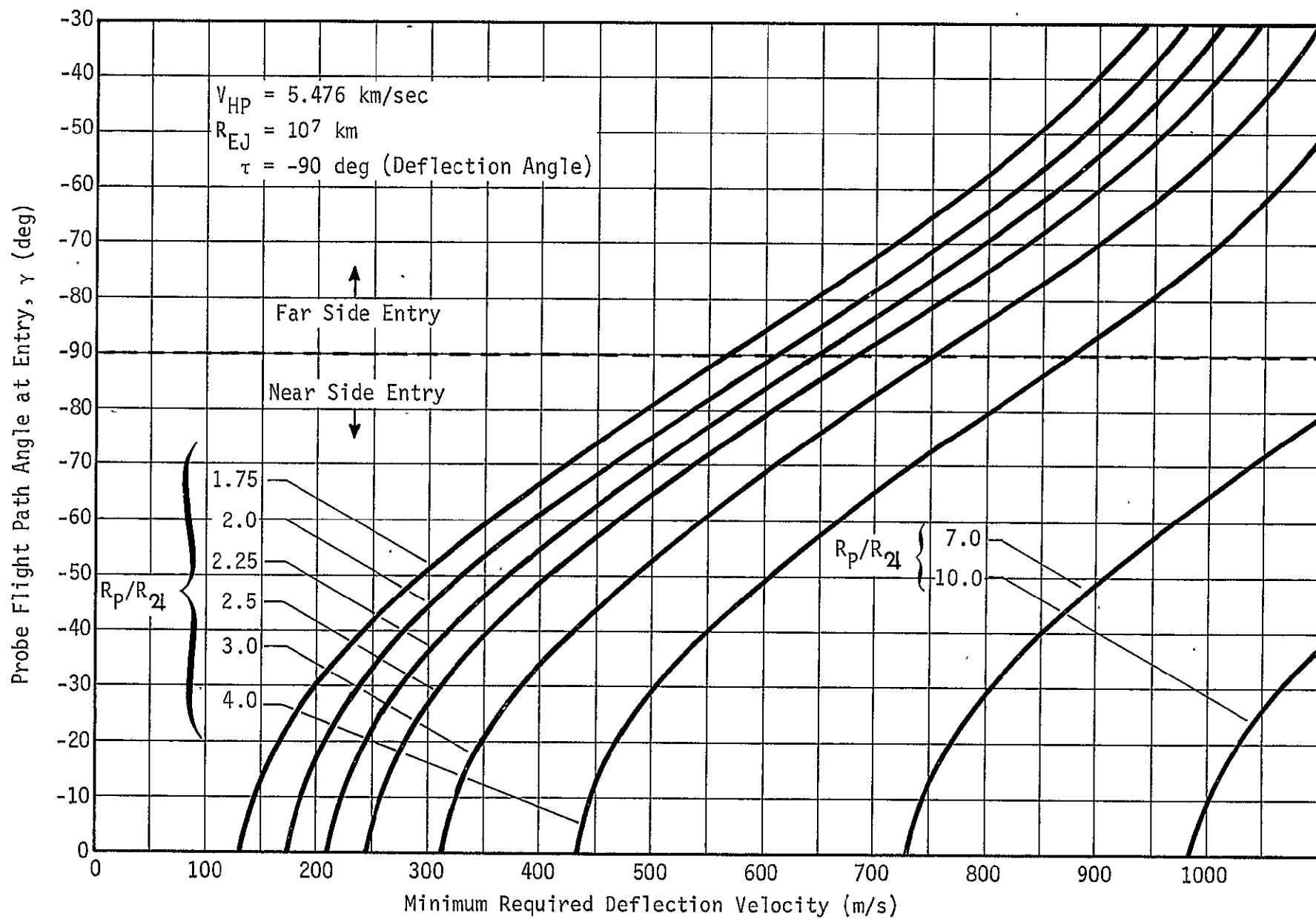


Figure IIIC-10 Deflection Velocity Requirements

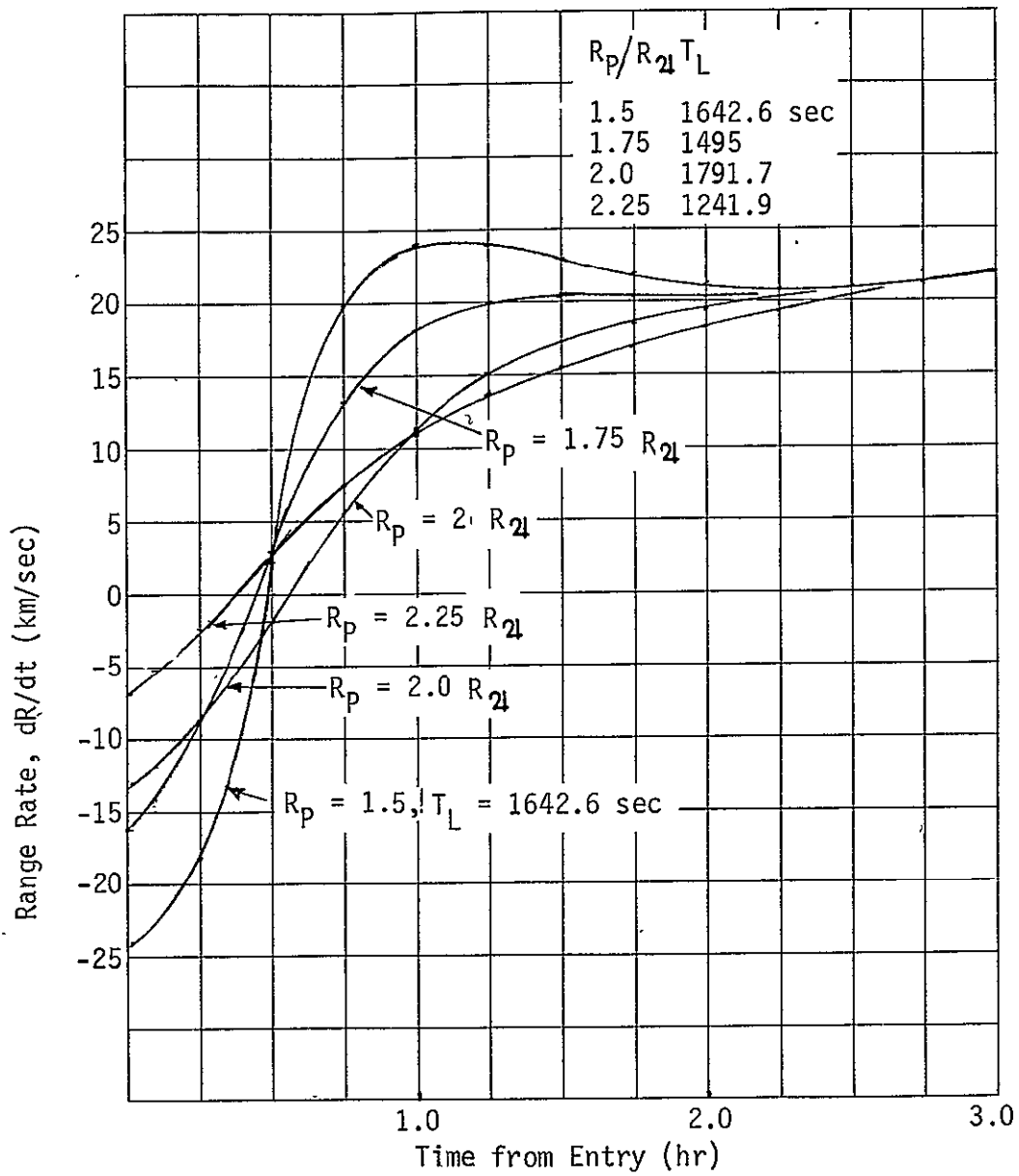


Figure IIIC-11 Range Rate vs Time

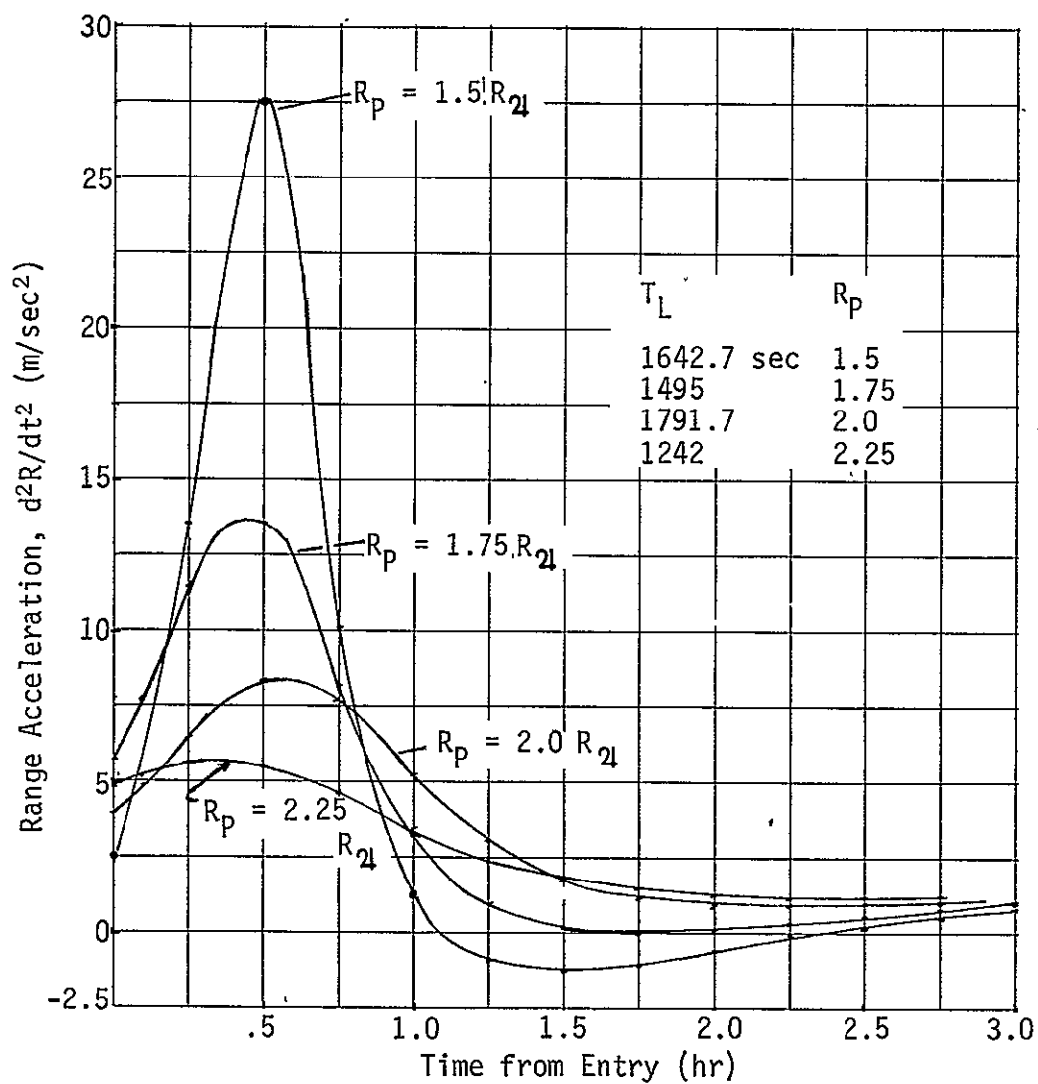


Figure IIIC-12 Range Acceleration vs Time

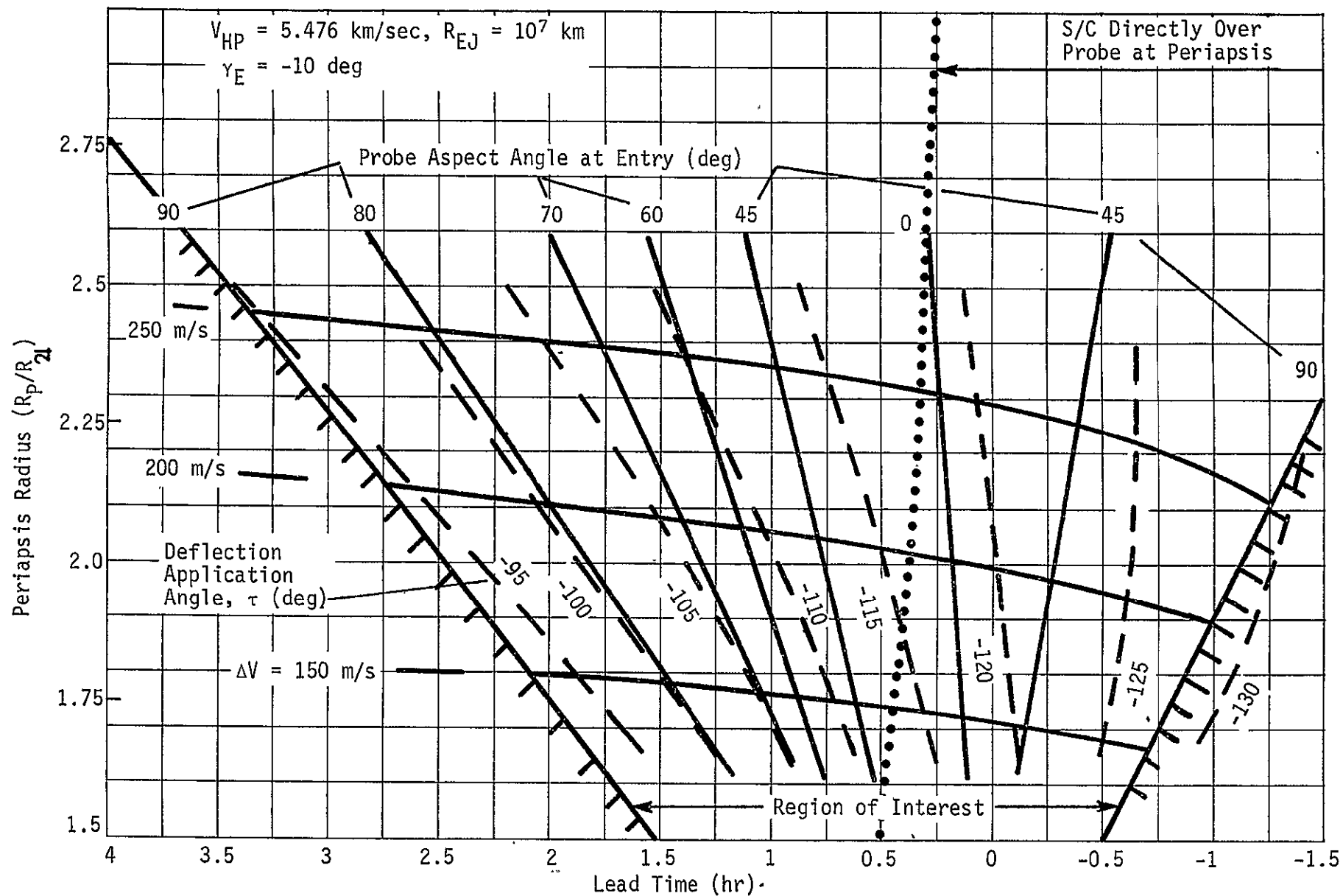


Figure IIIC-13 Lead Time Selection Relationships

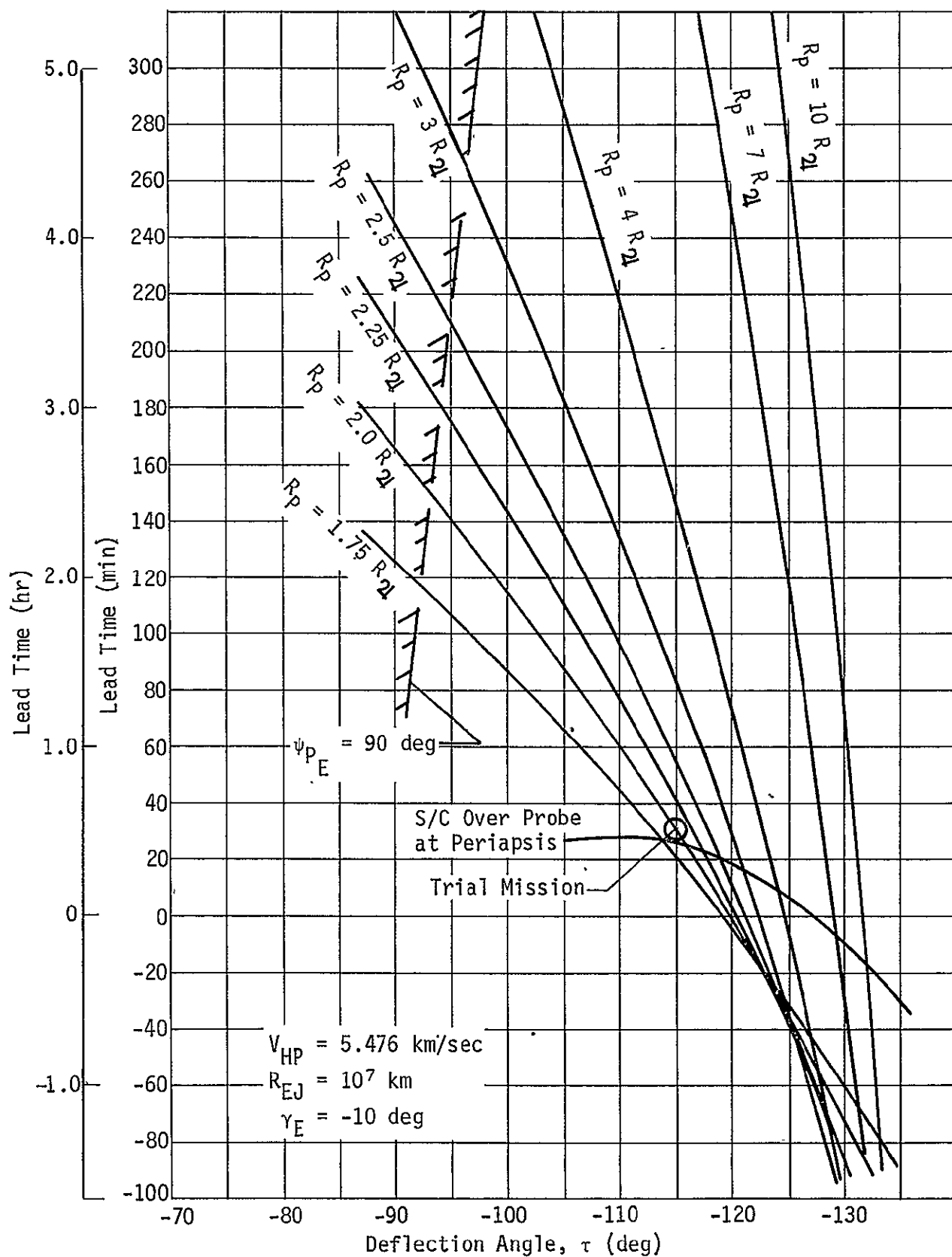


Figure IIIC-14

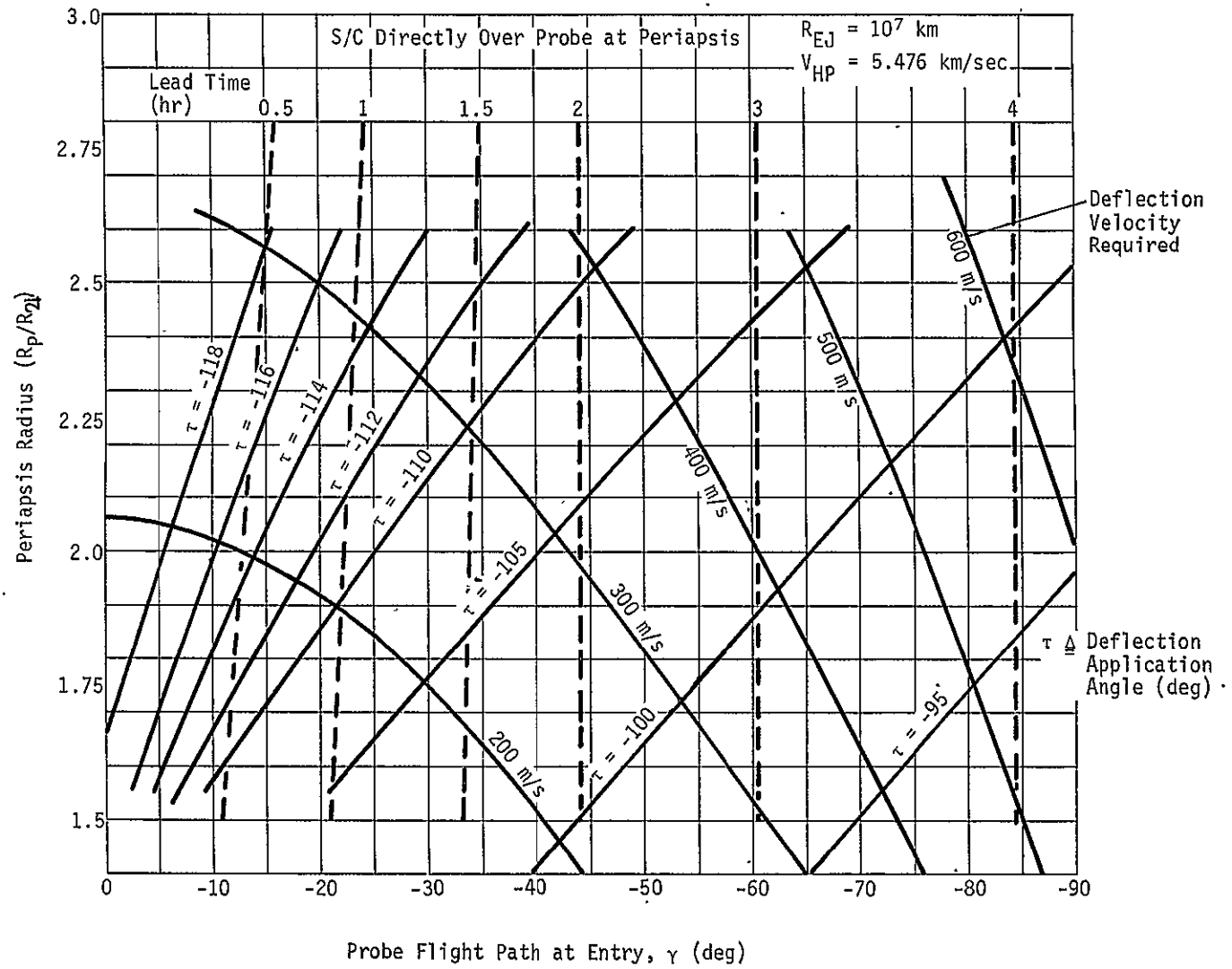


Figure IIIC-15

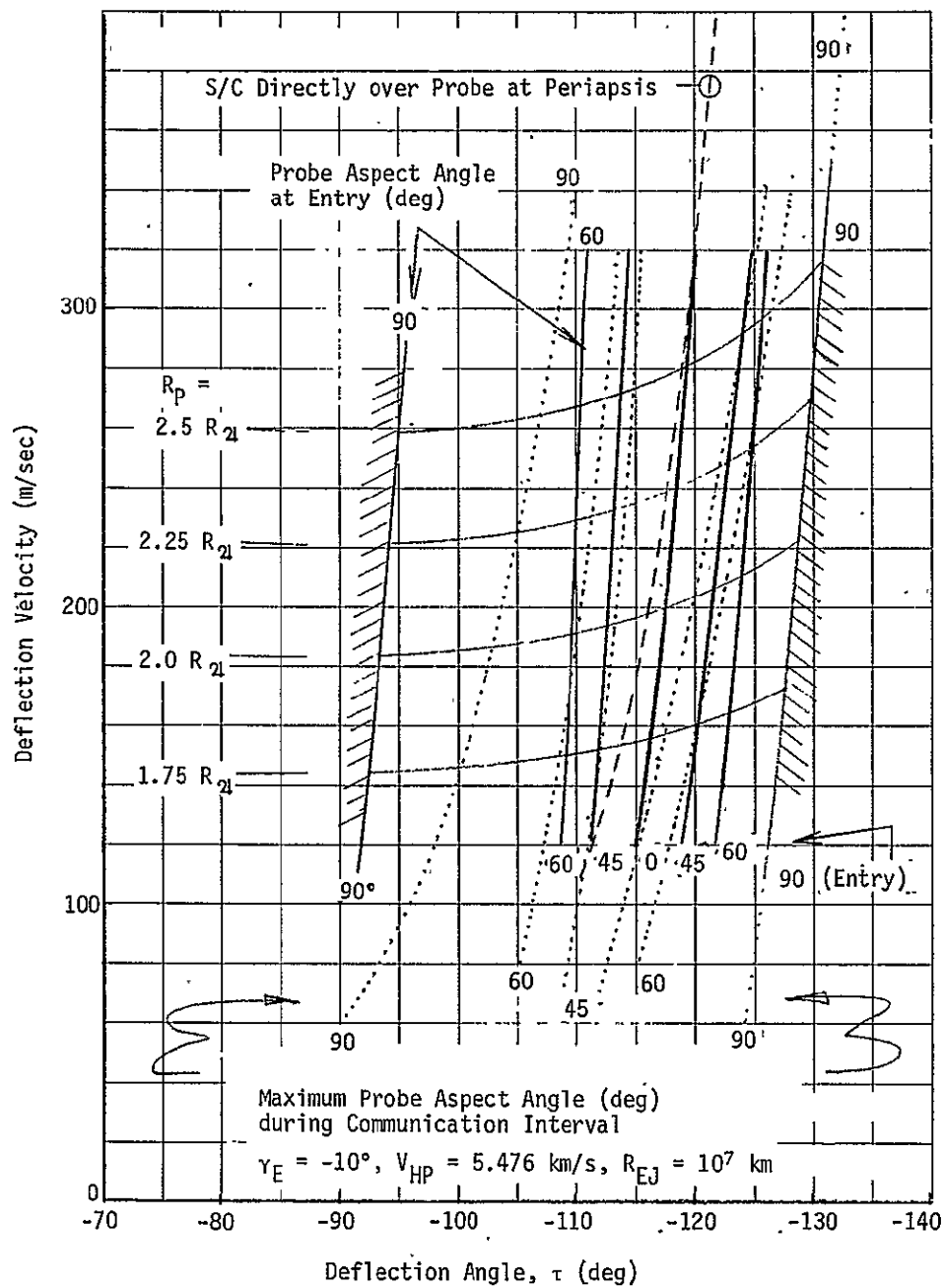


Figure IIIC-16

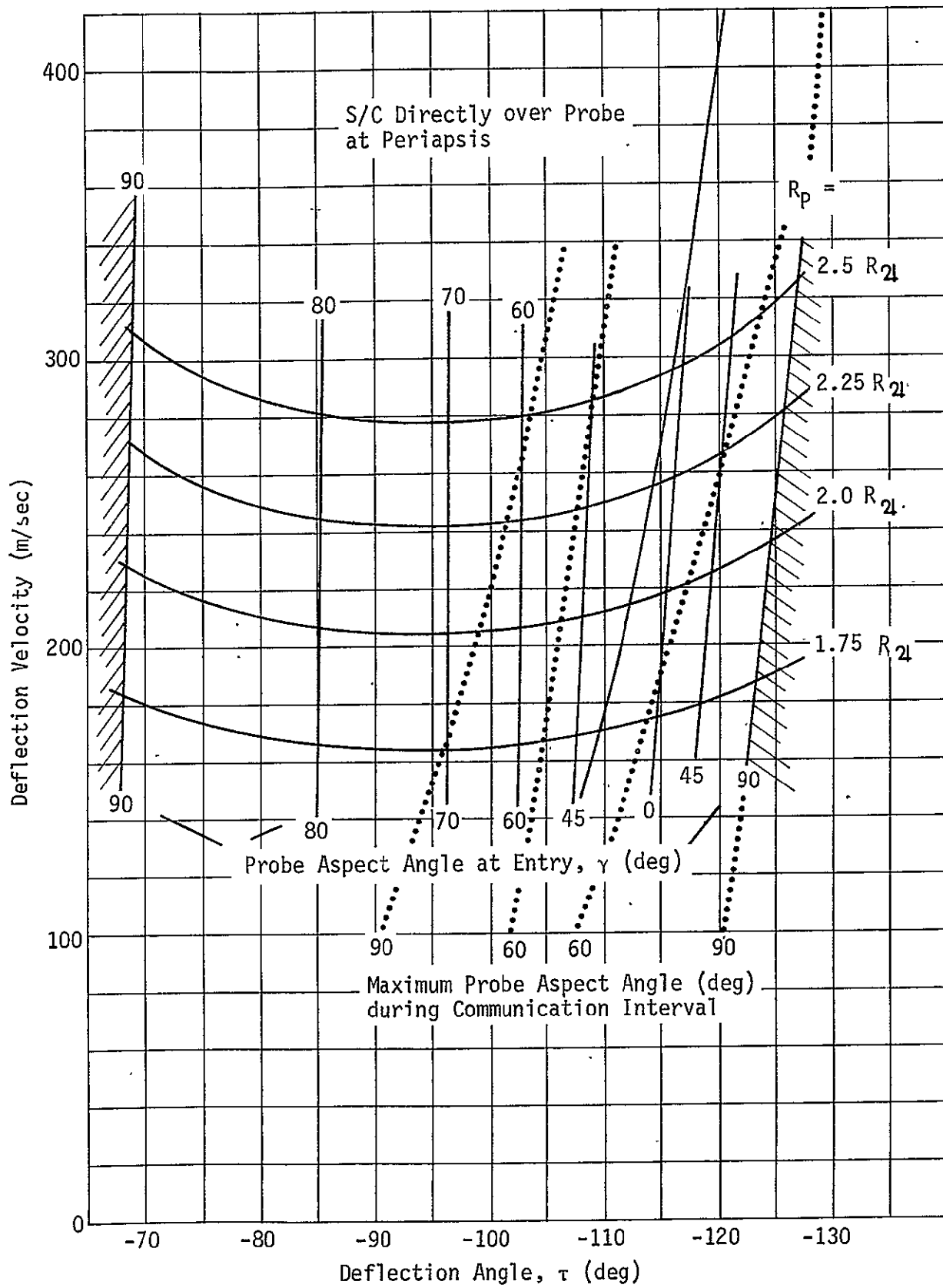


Figure IIIC-17

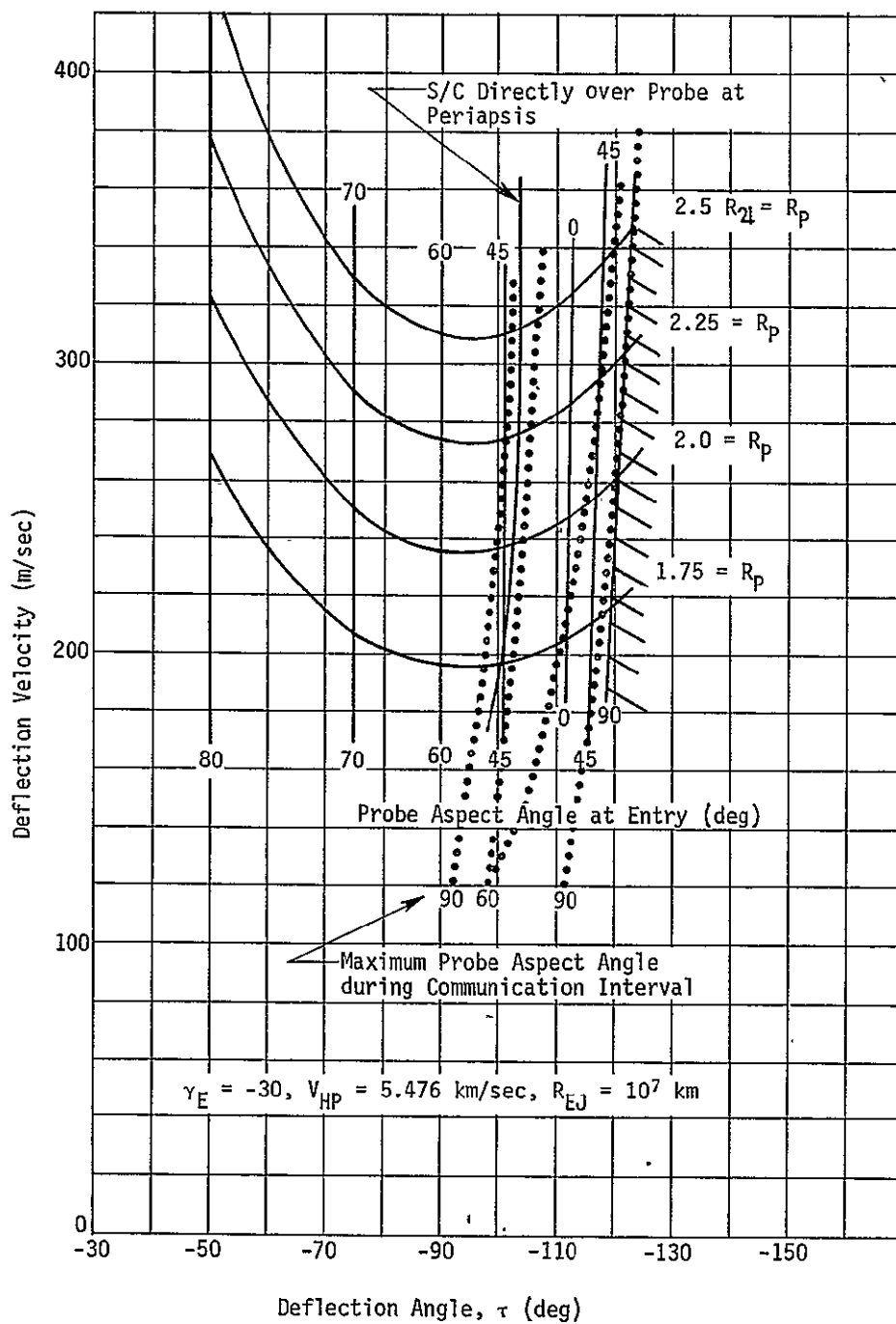


Figure IIIC-18

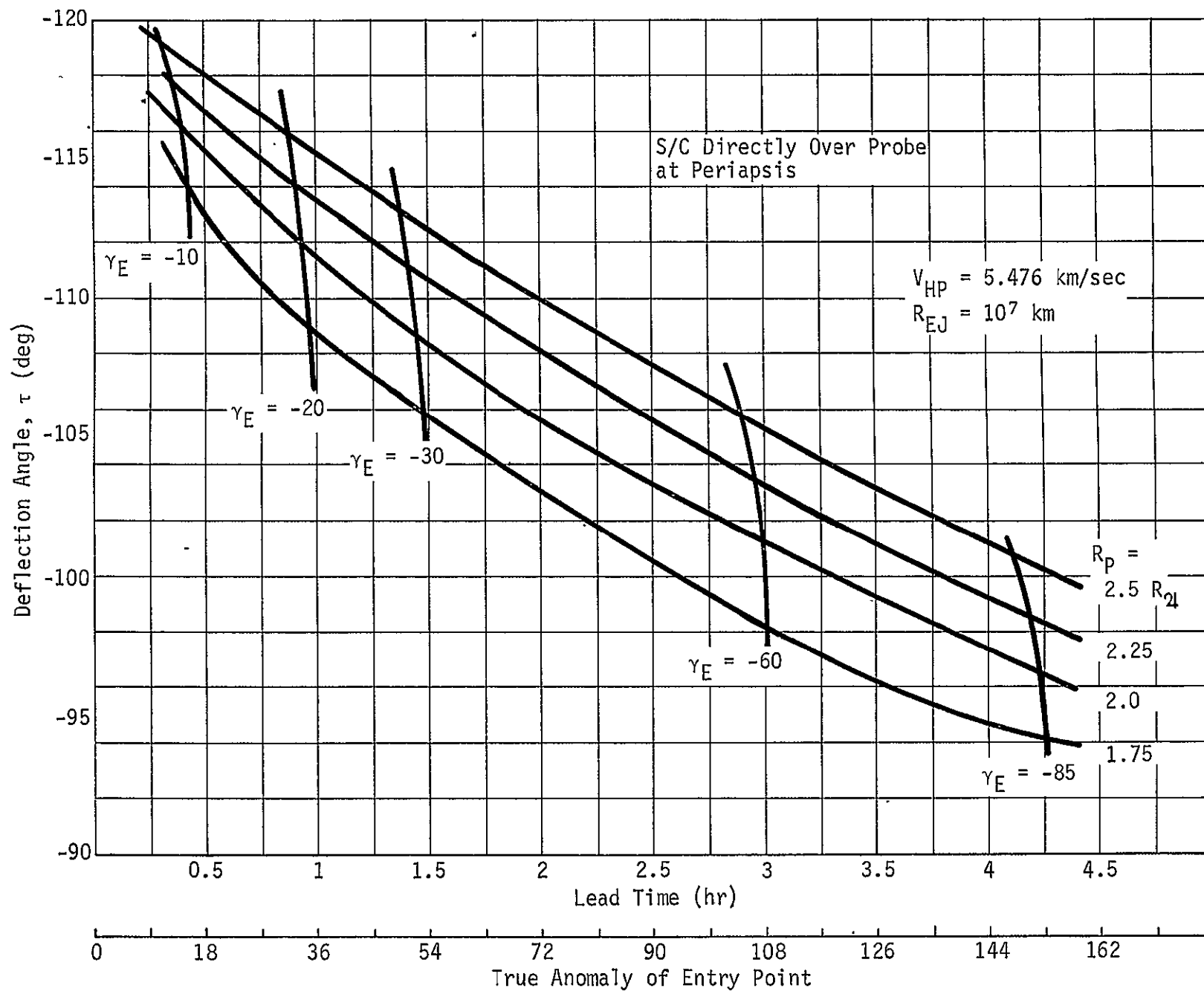


Figure IIIC-19

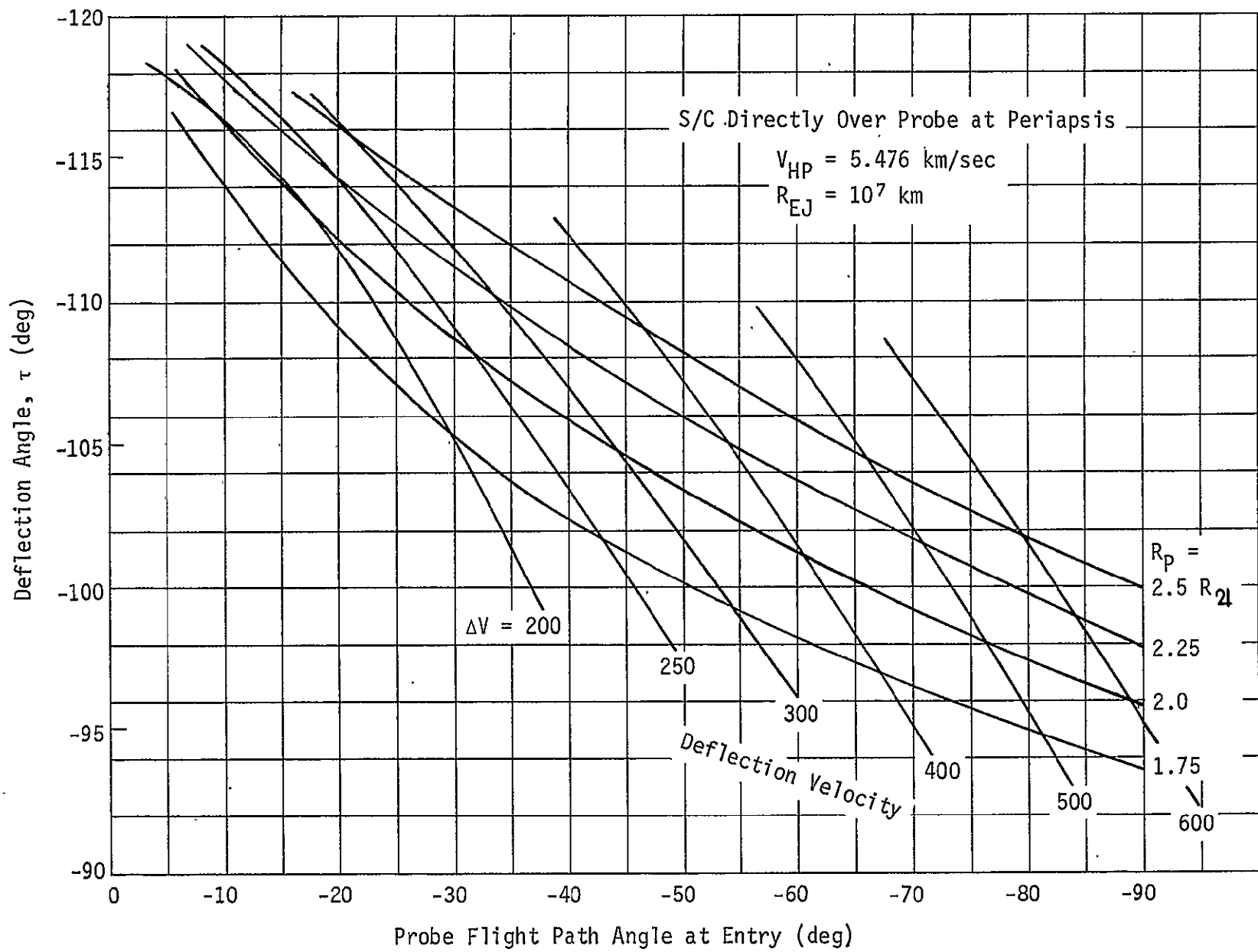


Figure IIIC-20

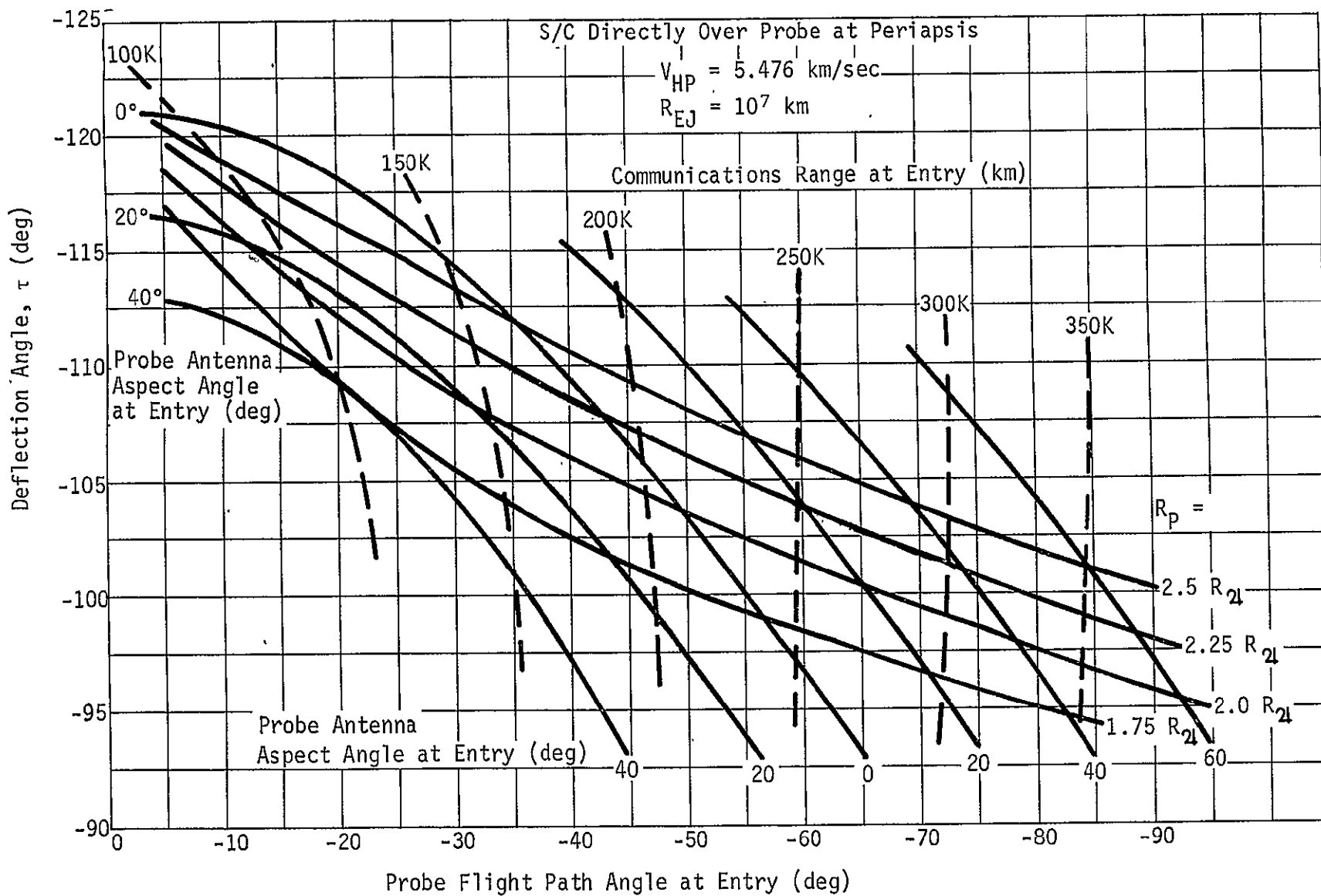


Figure IIIC-21

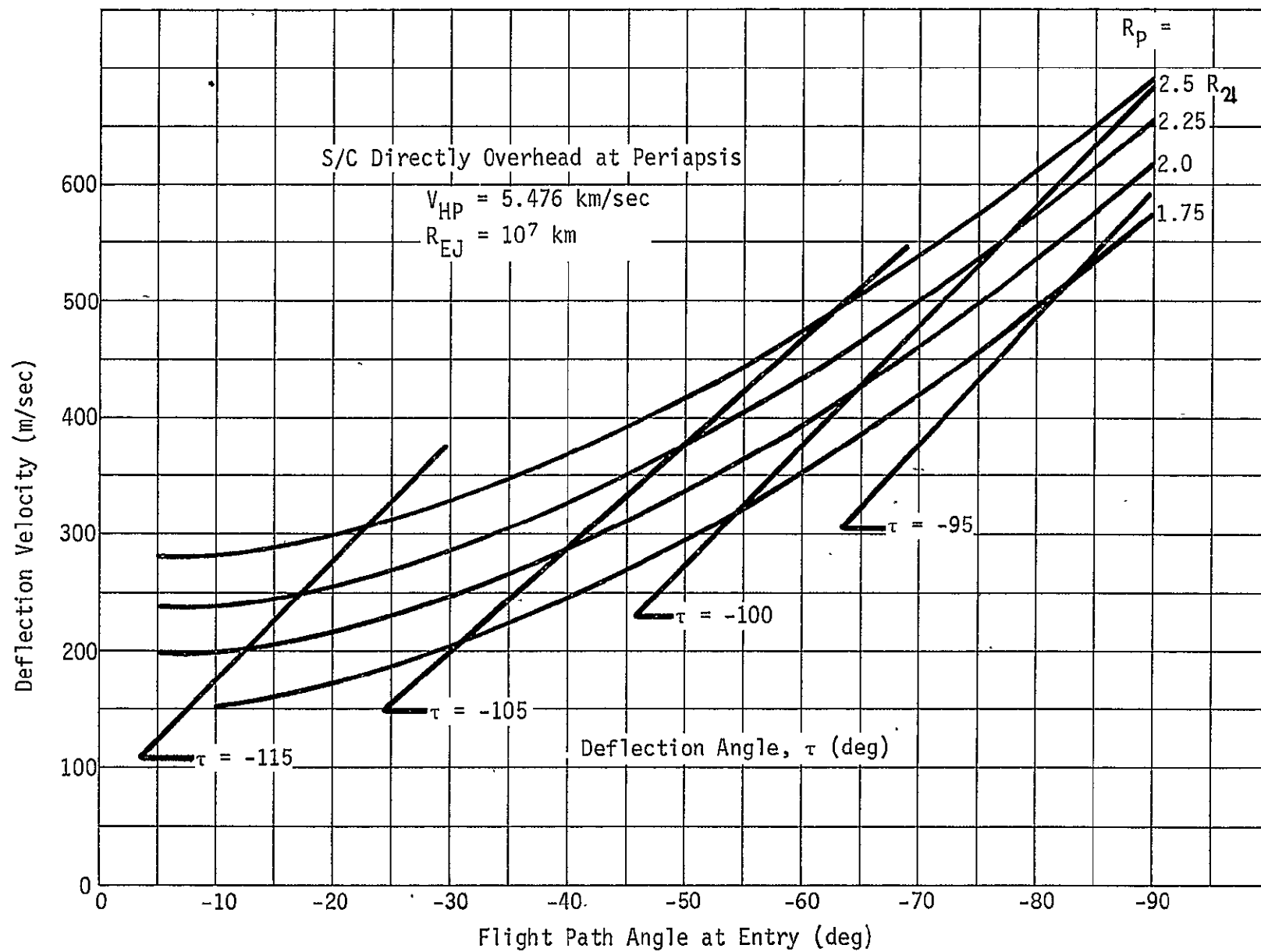


Figure IIIC-22

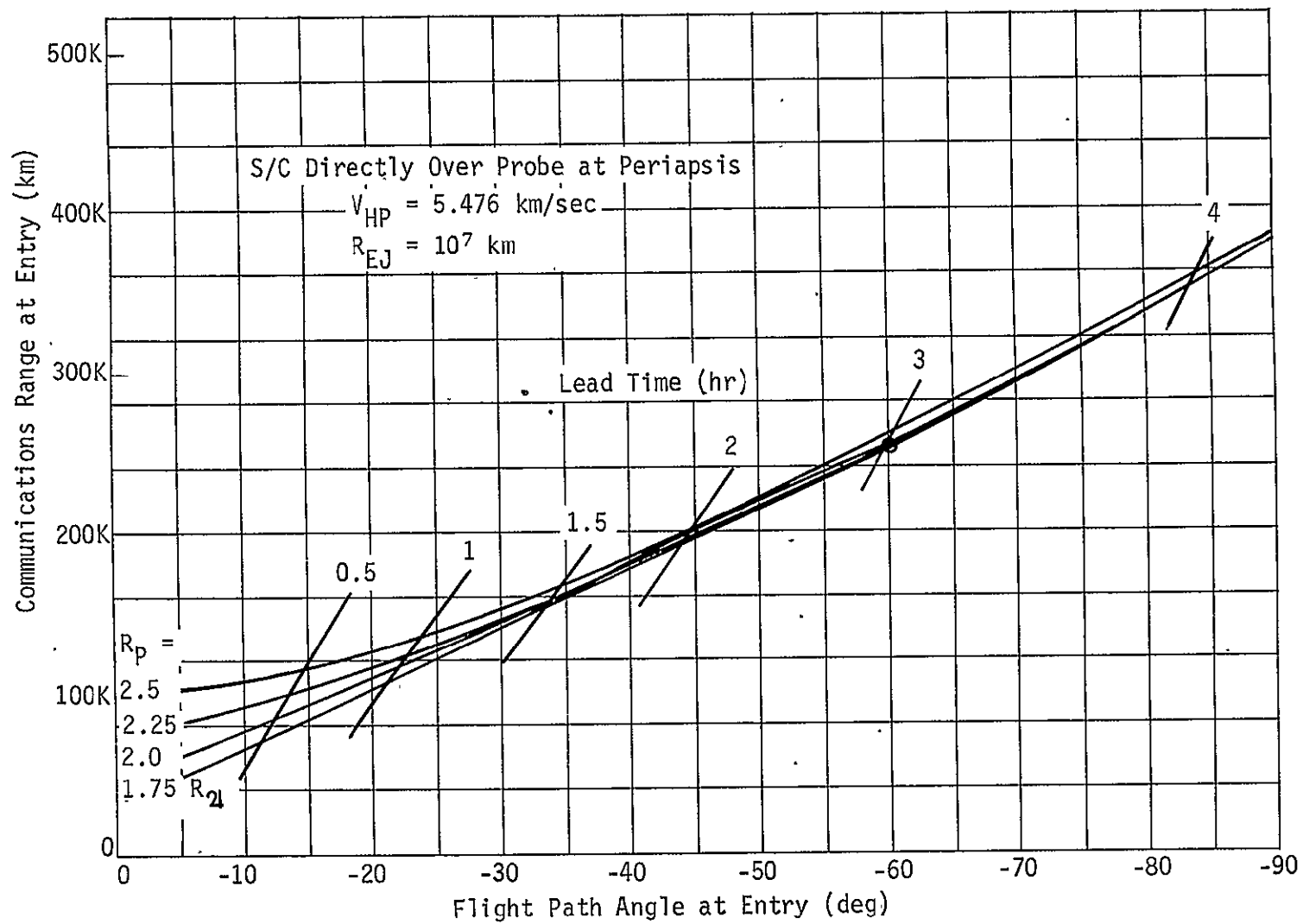


Figure IIIC-23

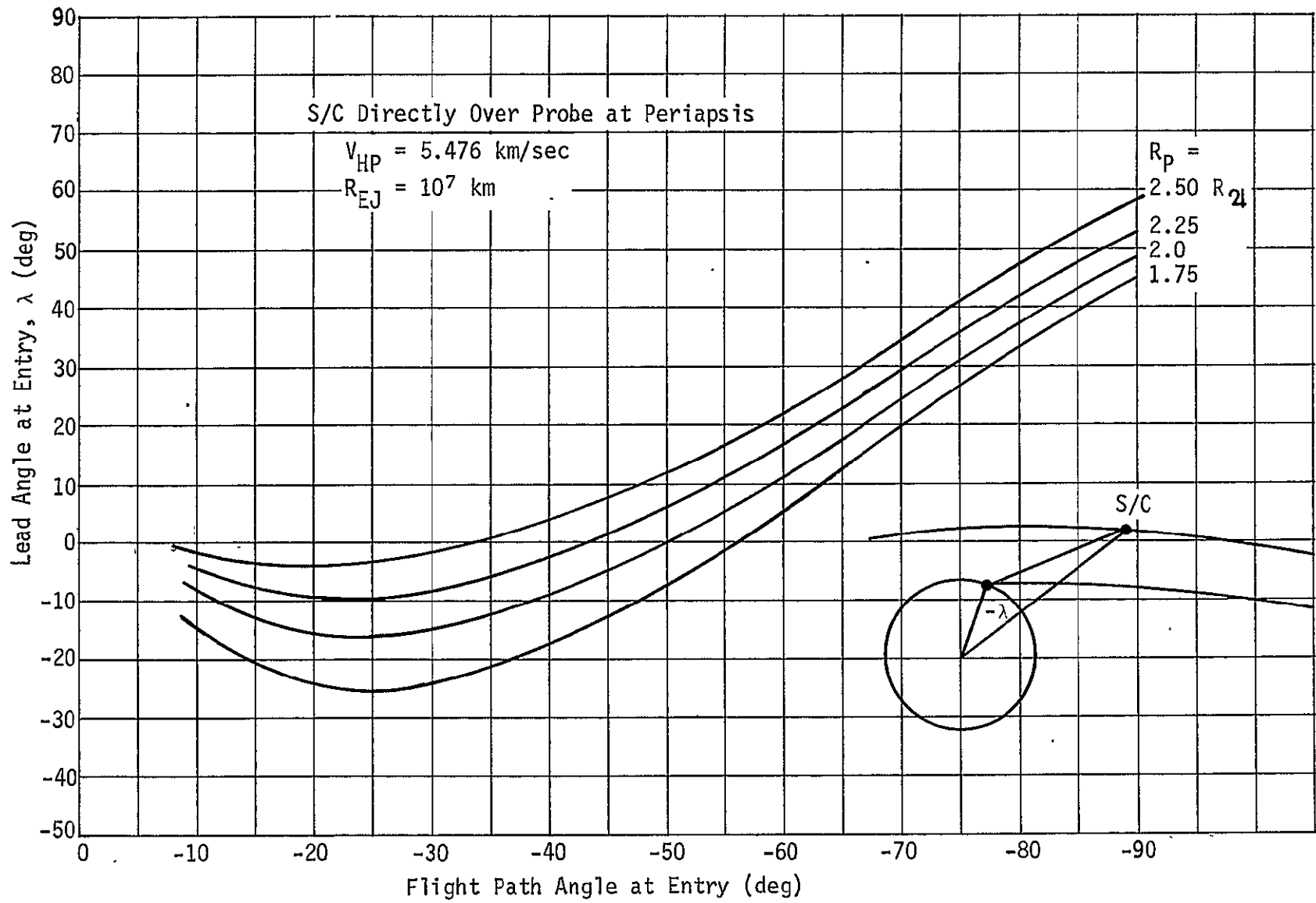


Figure IIIC-24

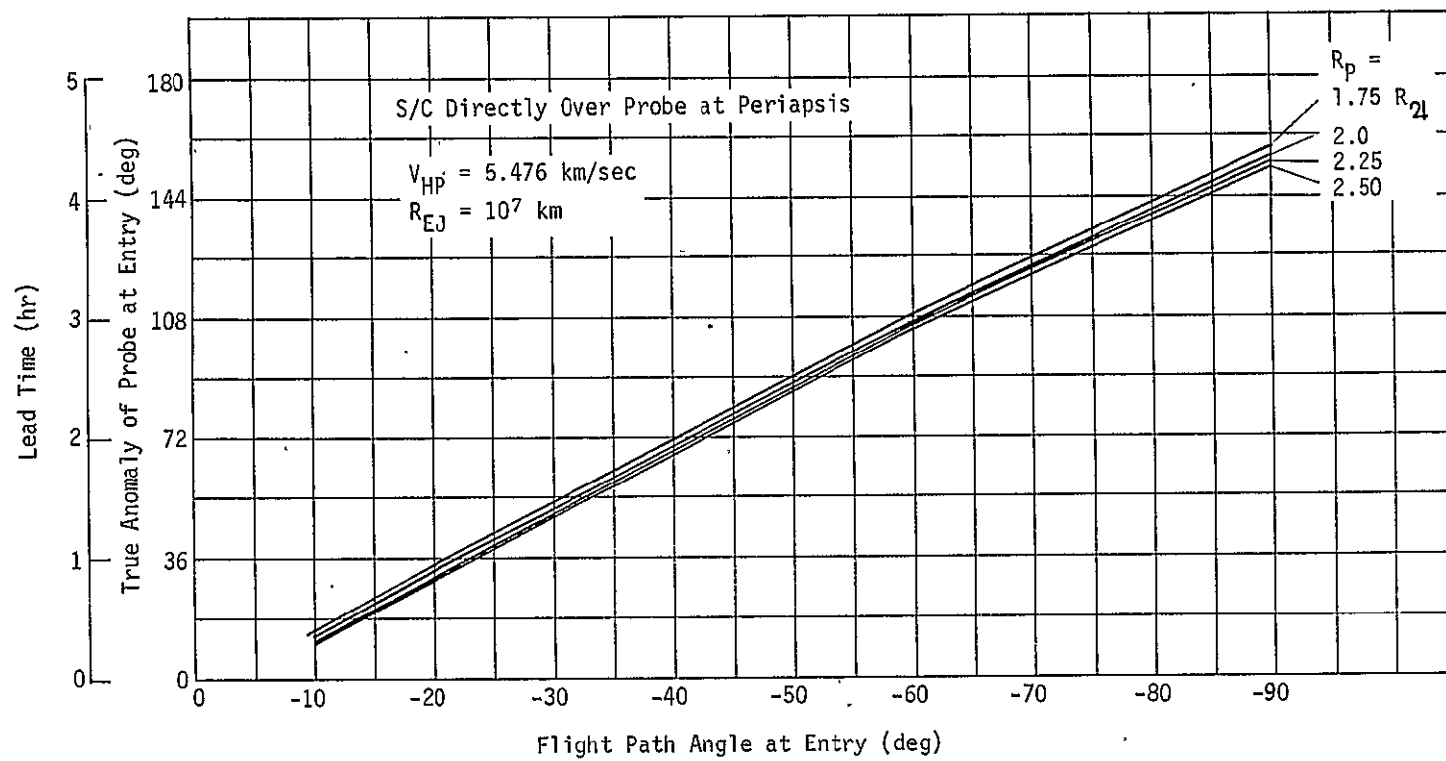


Figure IIIC-25

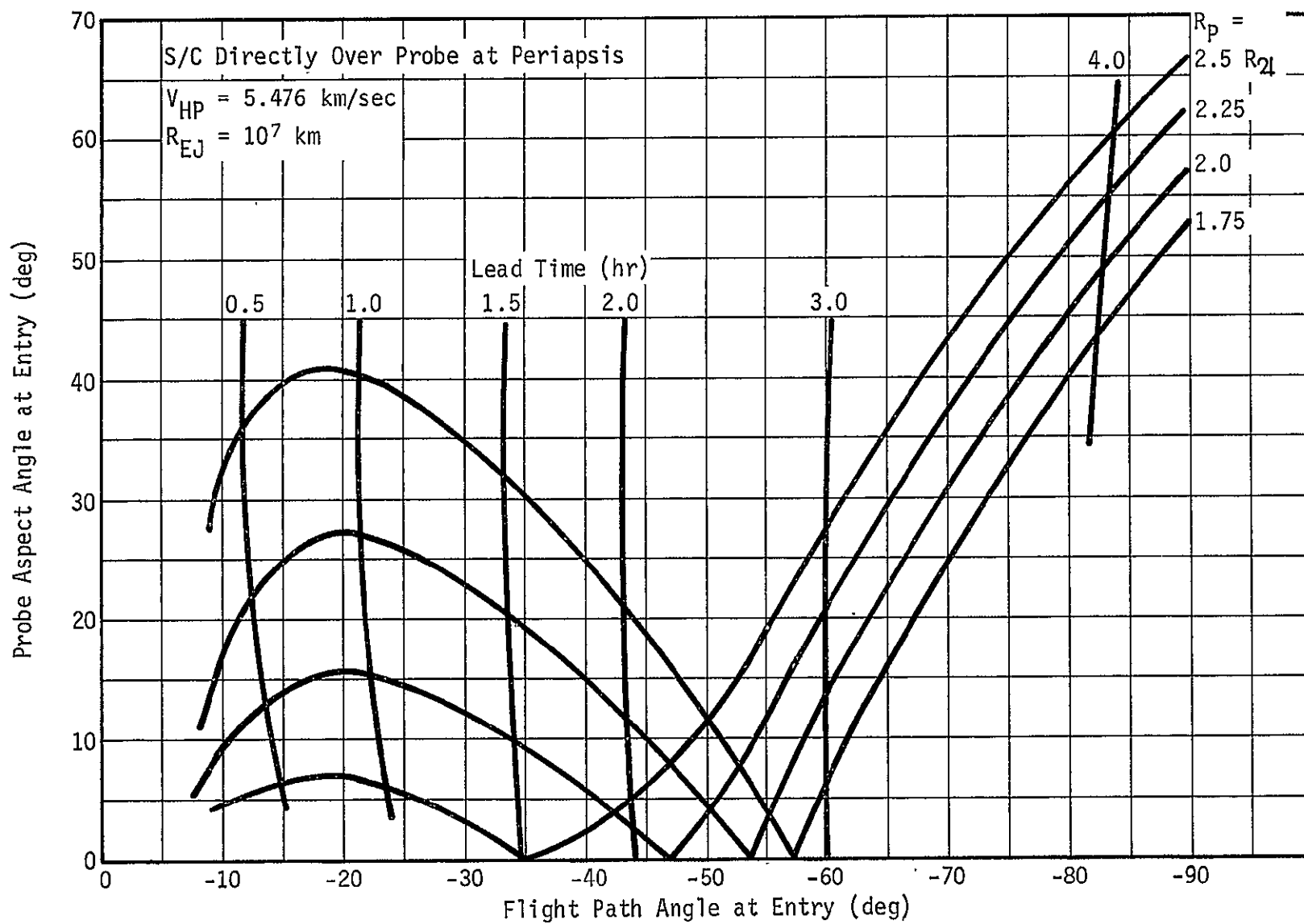


Figure IIIC-26 Entry Probe Aspect Angle vs Flight Path Angle

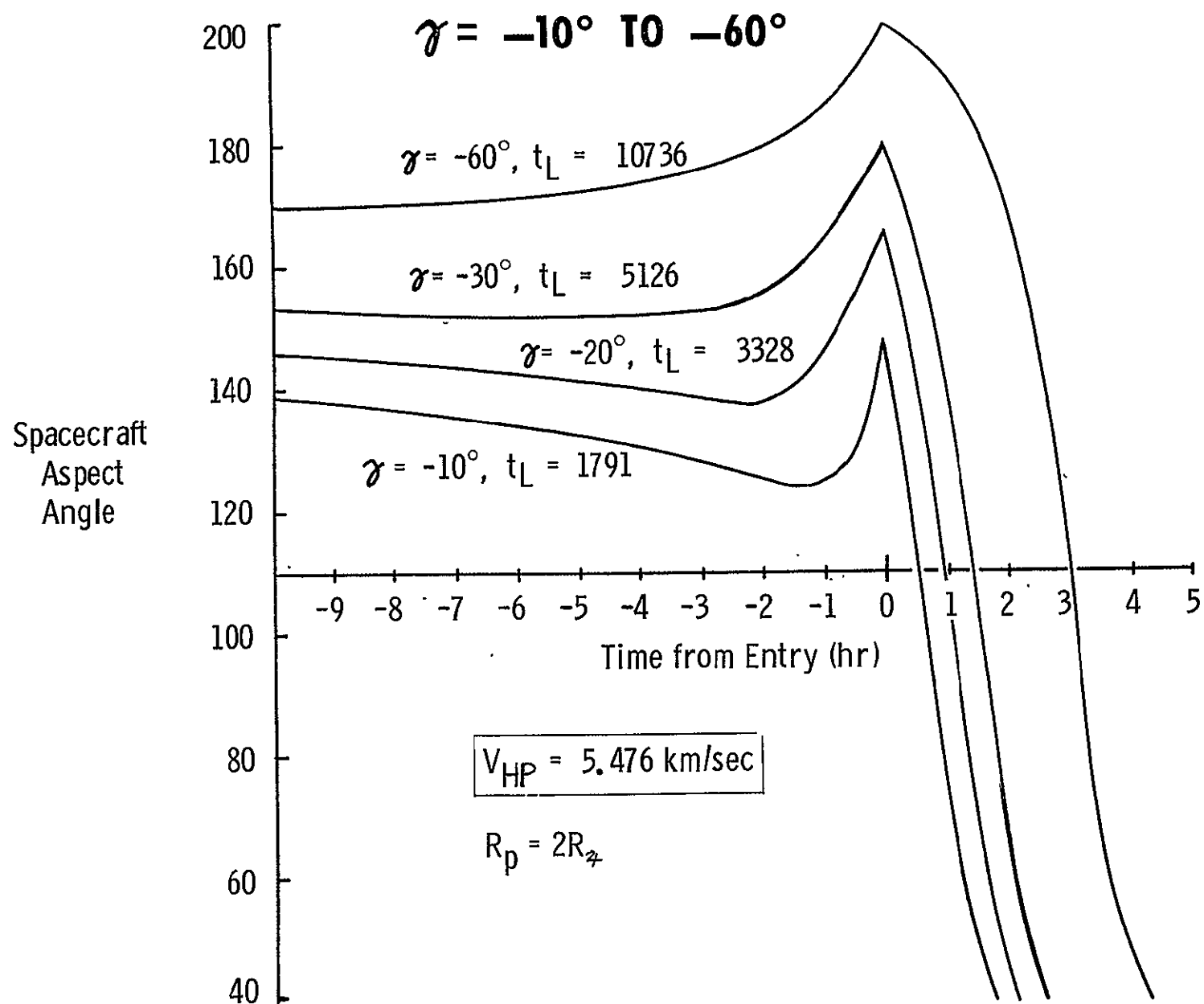


Figure IIIC-27 S/C Relay Antenna Aspect Angle

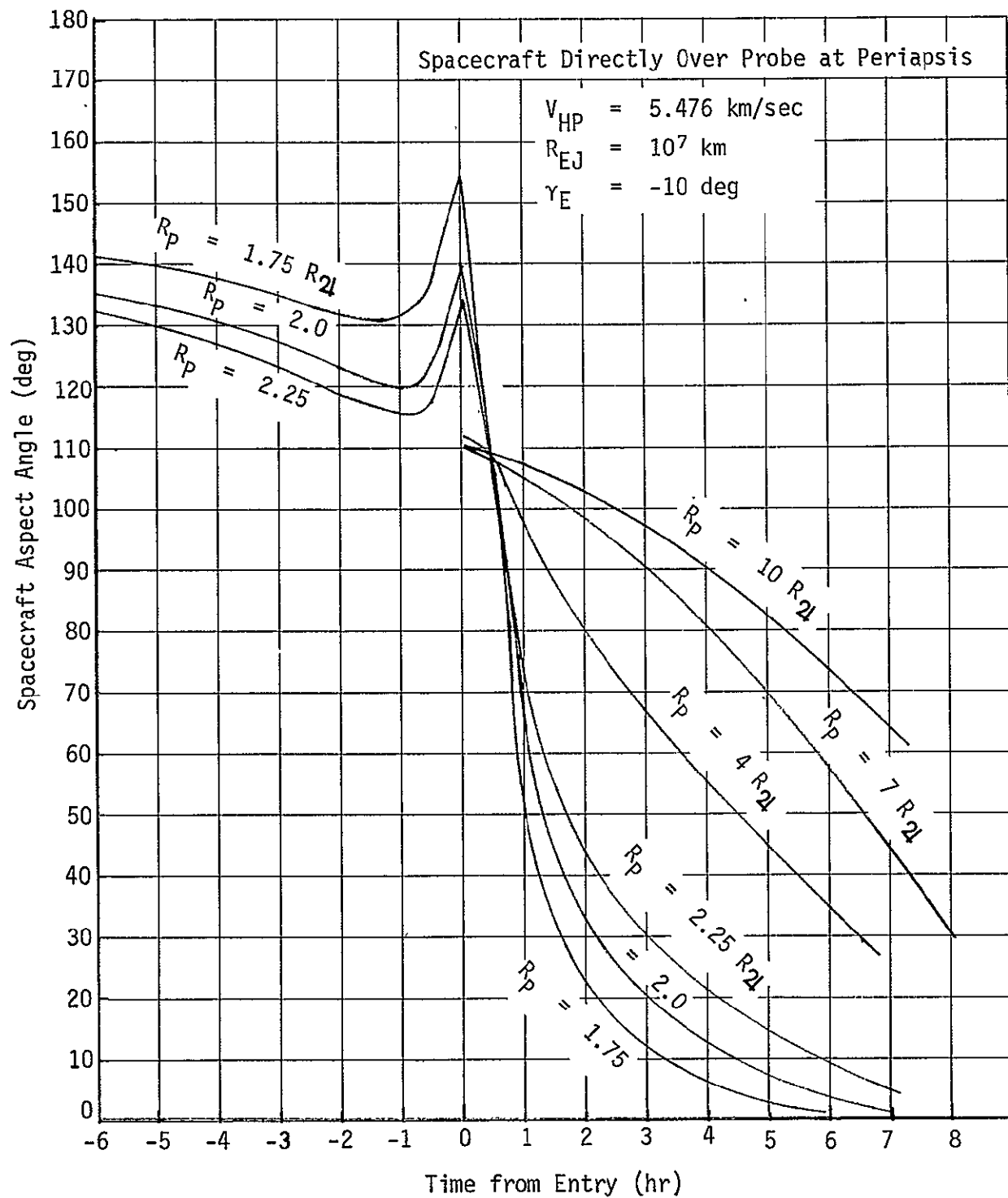


Figure IIIC-28

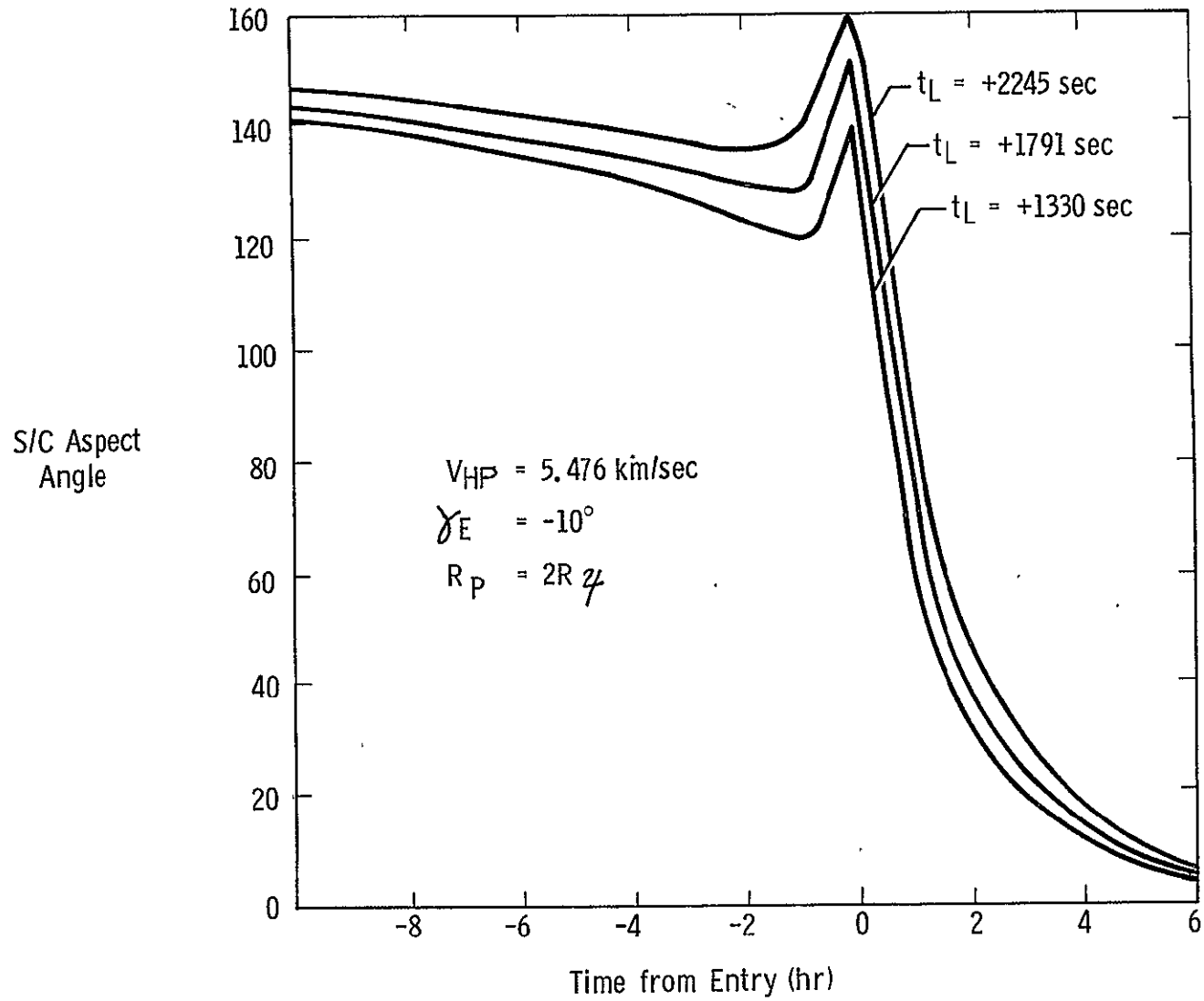


Figure IIIC-29 S/C Aspect Angle $R_P = 2$

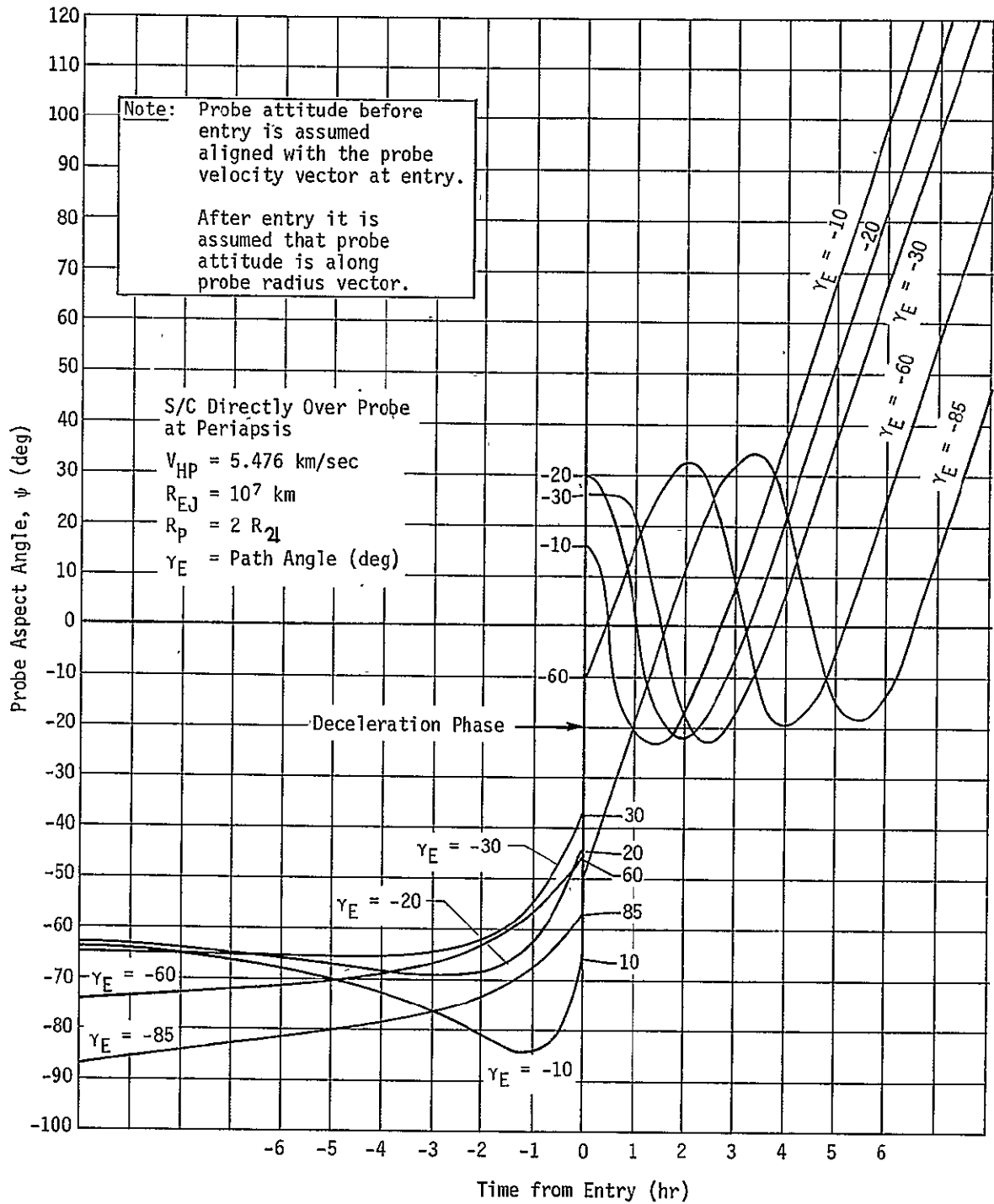


Figure IIIC-30

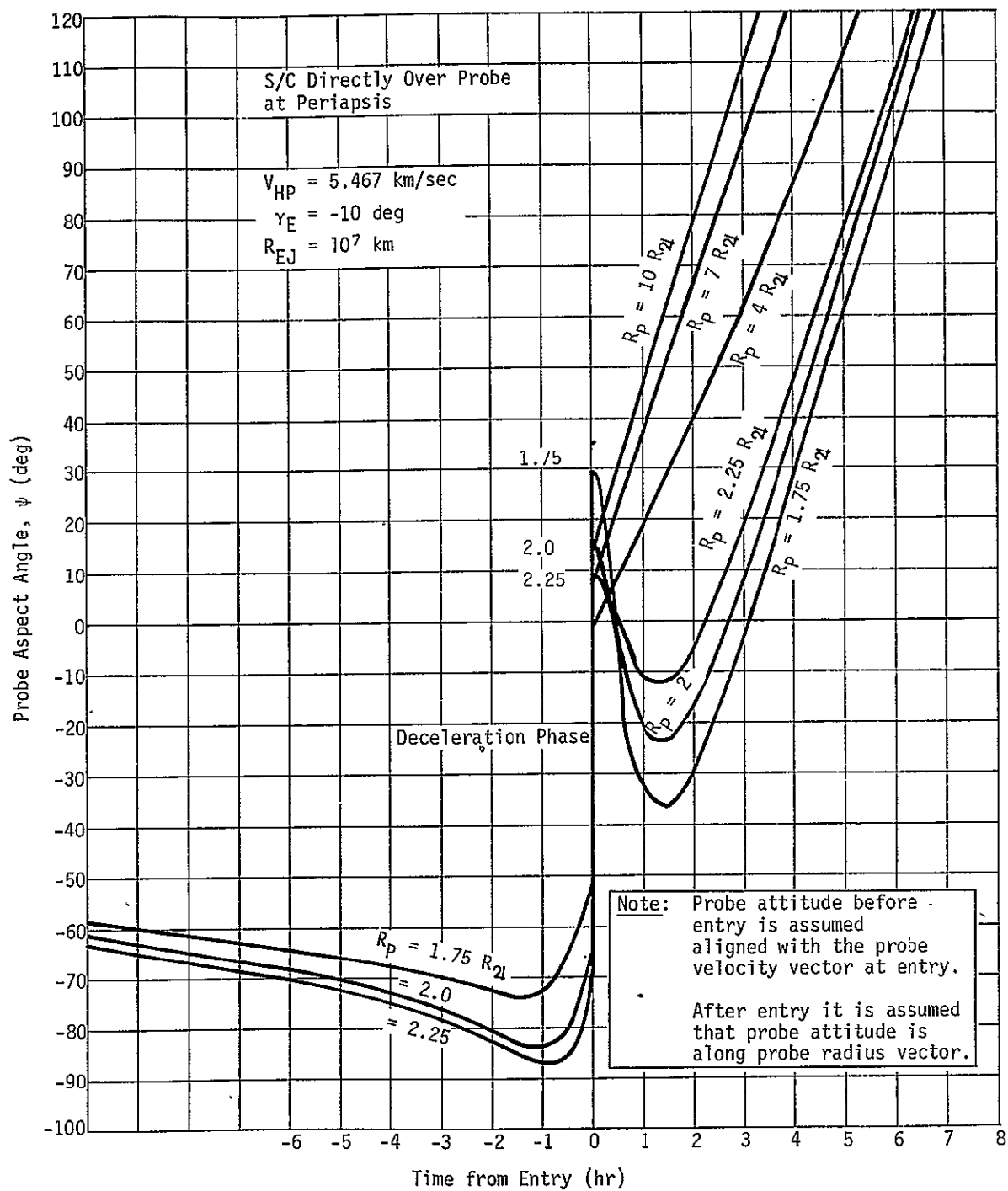


Figure IIIC-31

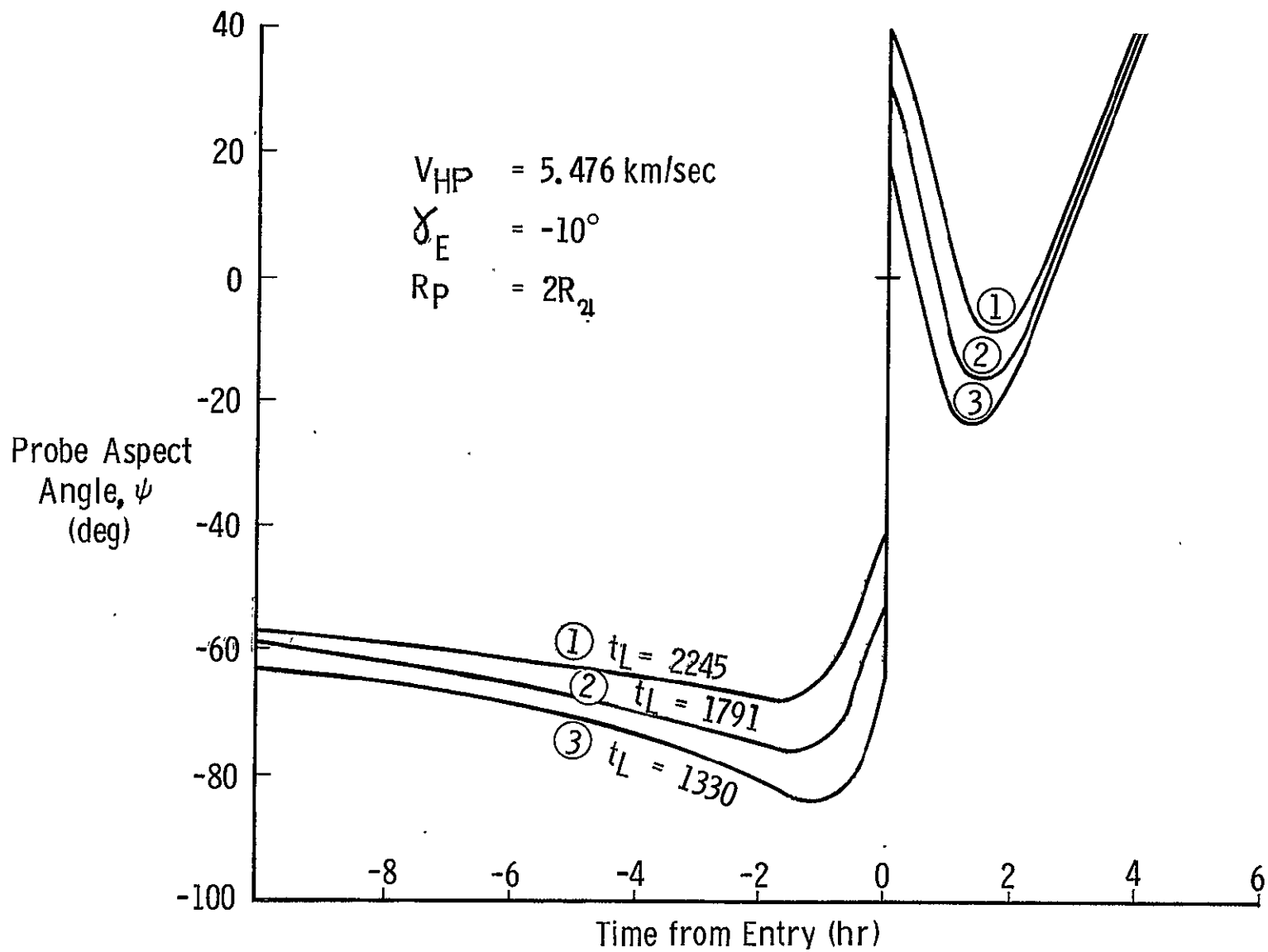


Figure IIIC-32 Probe Aspect Angle

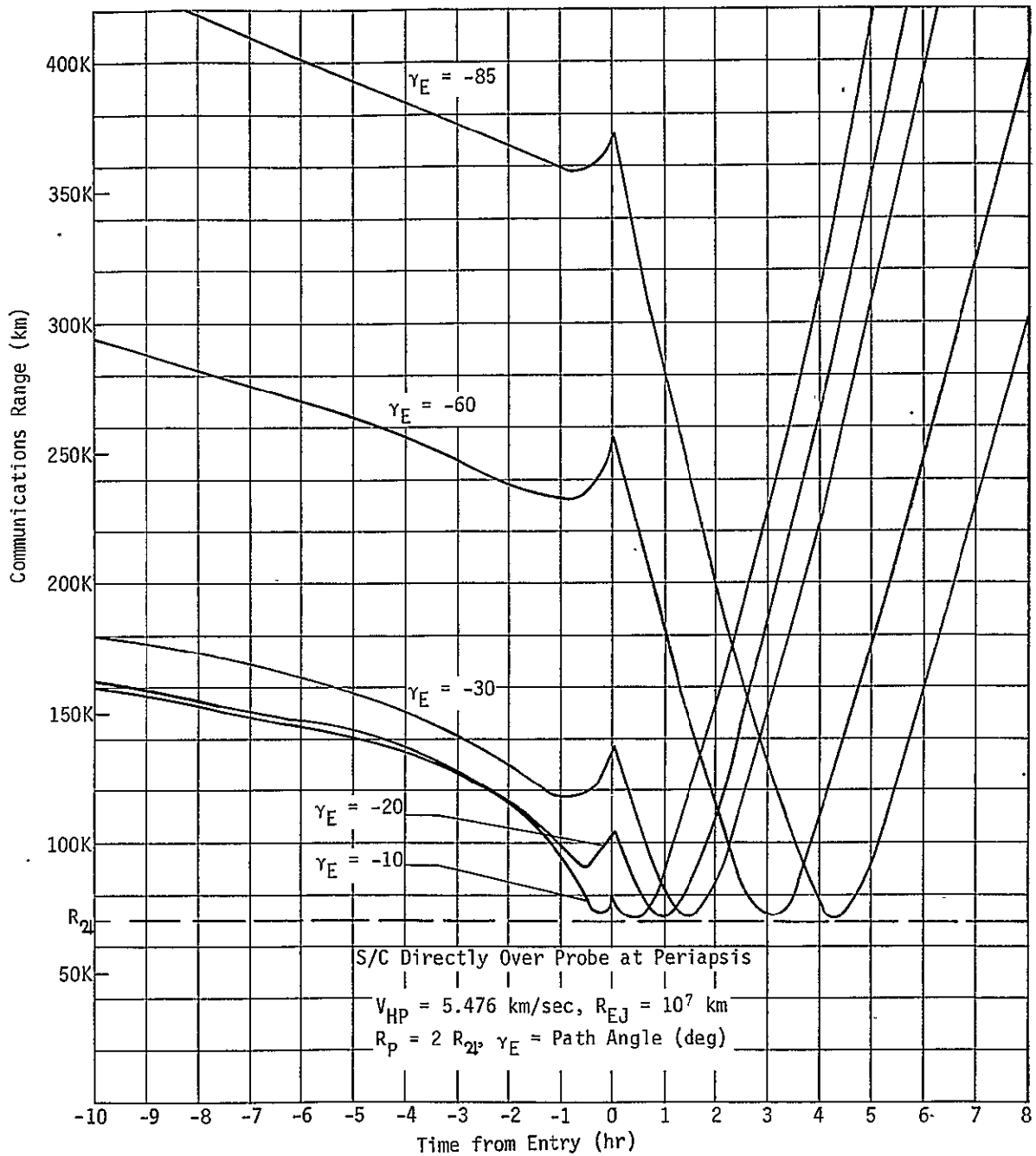


Figure IIIC-33

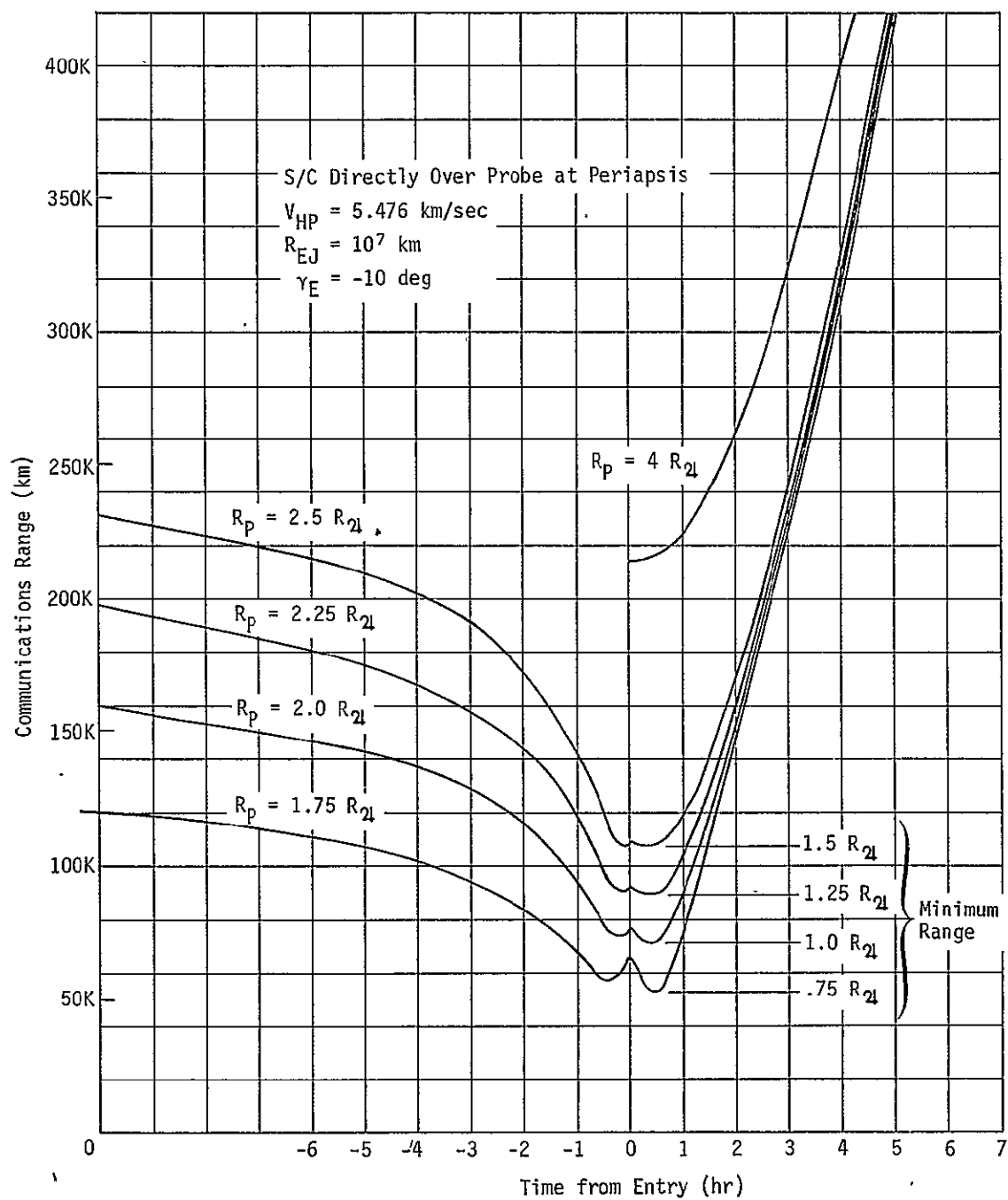


Figure IIIC-34

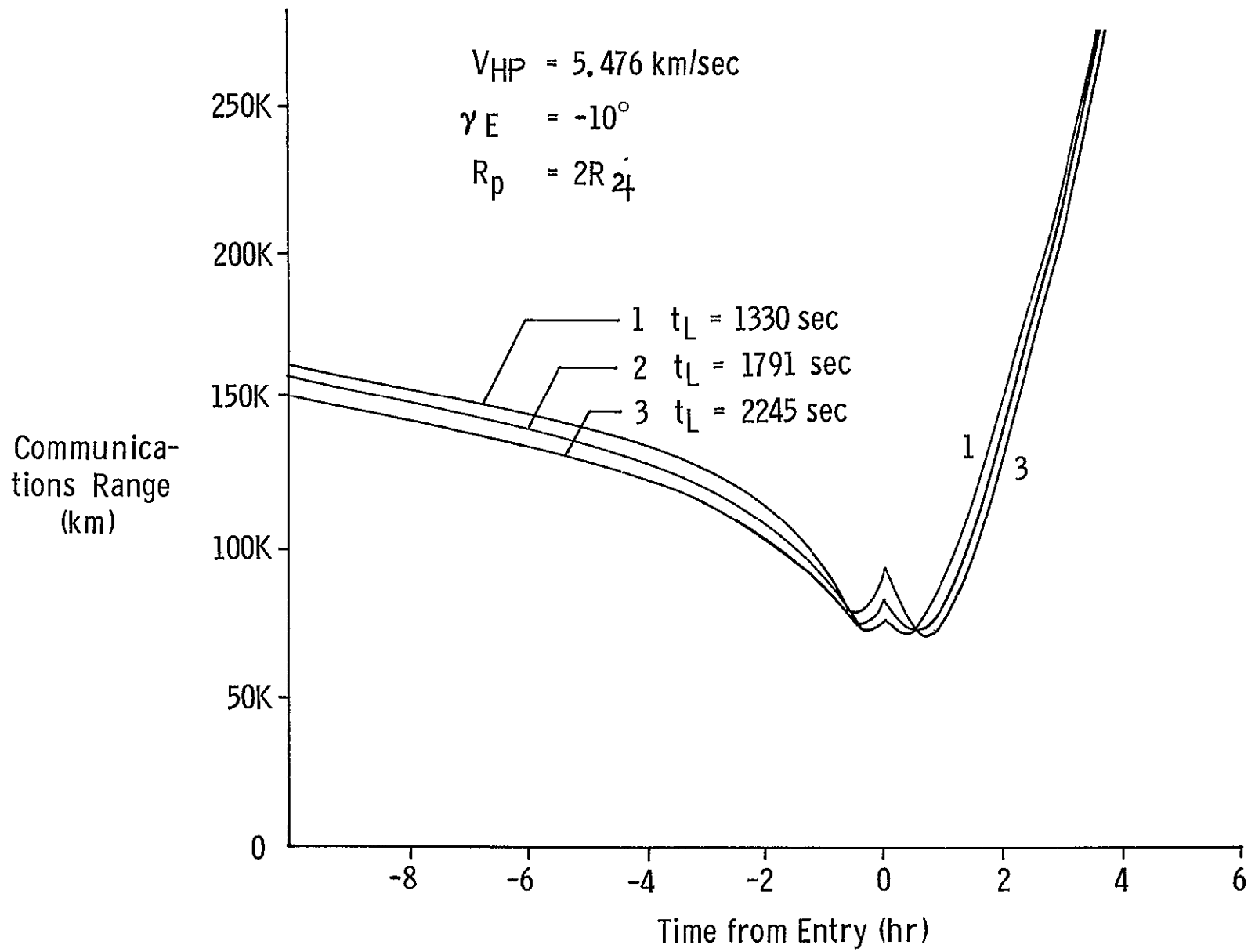


Figure IIIC-35 Relay Communications Range vs Time ($R_p = 2$)

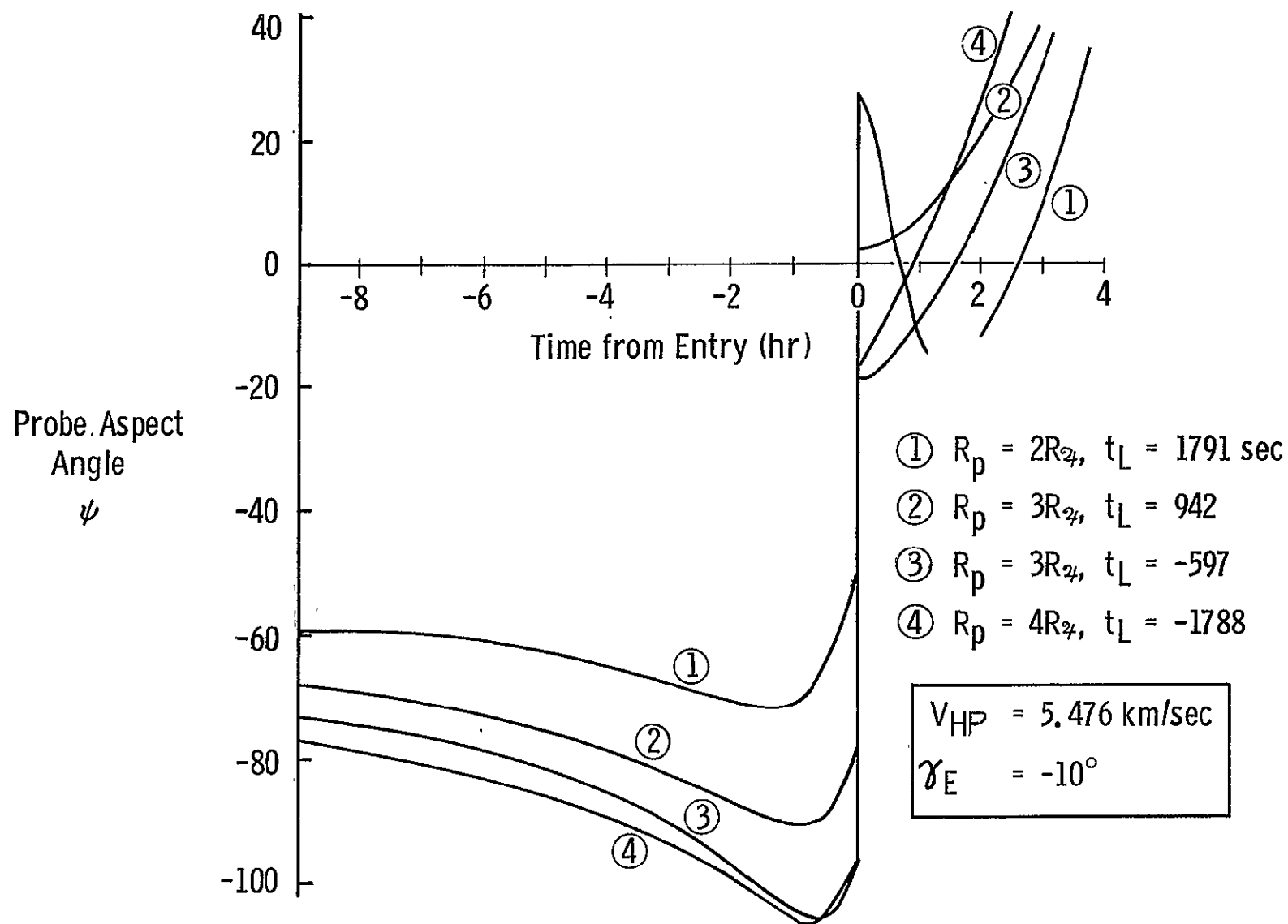


Figure IIIC-36 Descent Probe Antenna Aspect Angle

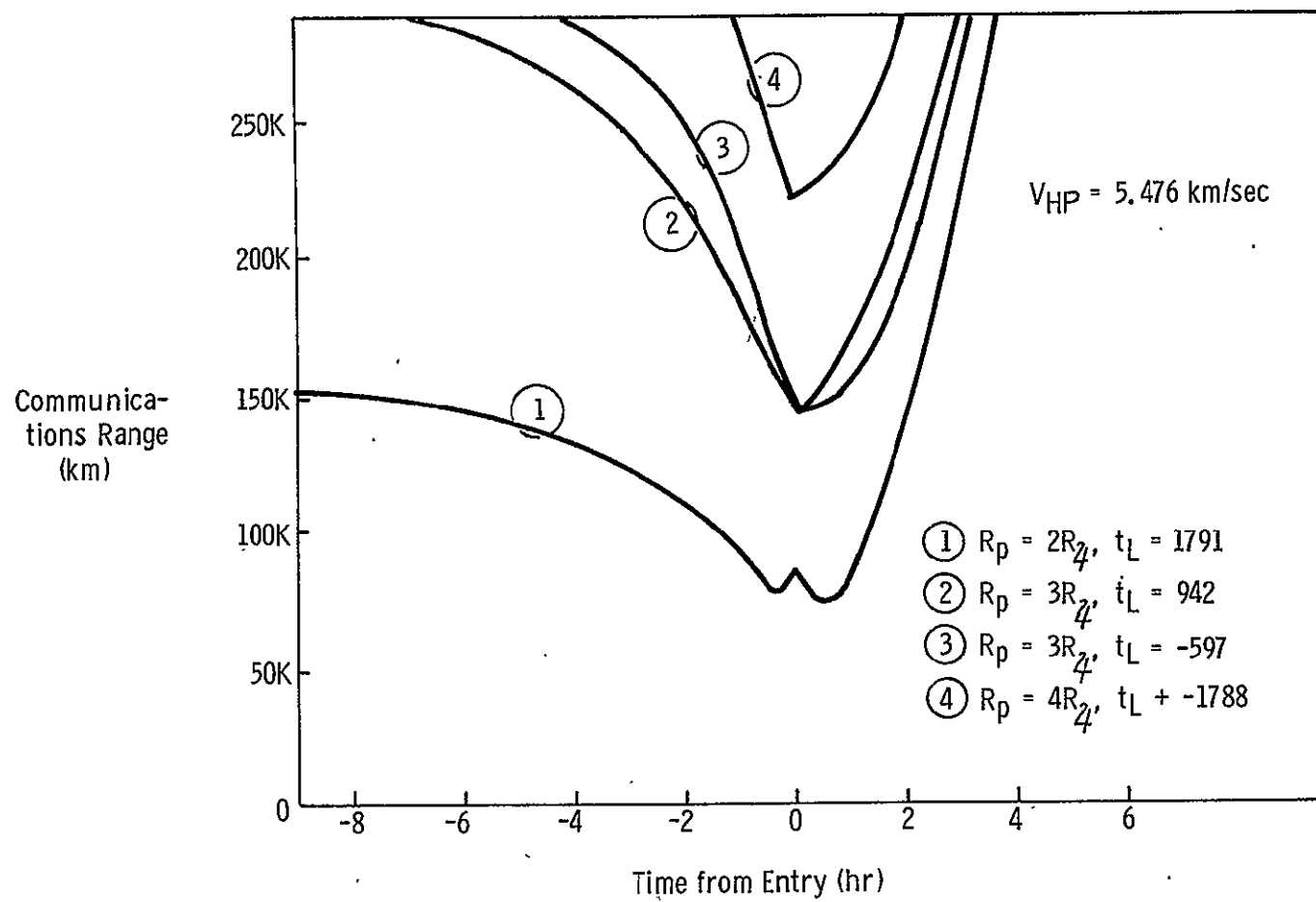


Figure IIIC-37 Relay Communications Range ($R_p = 2$ to 4)

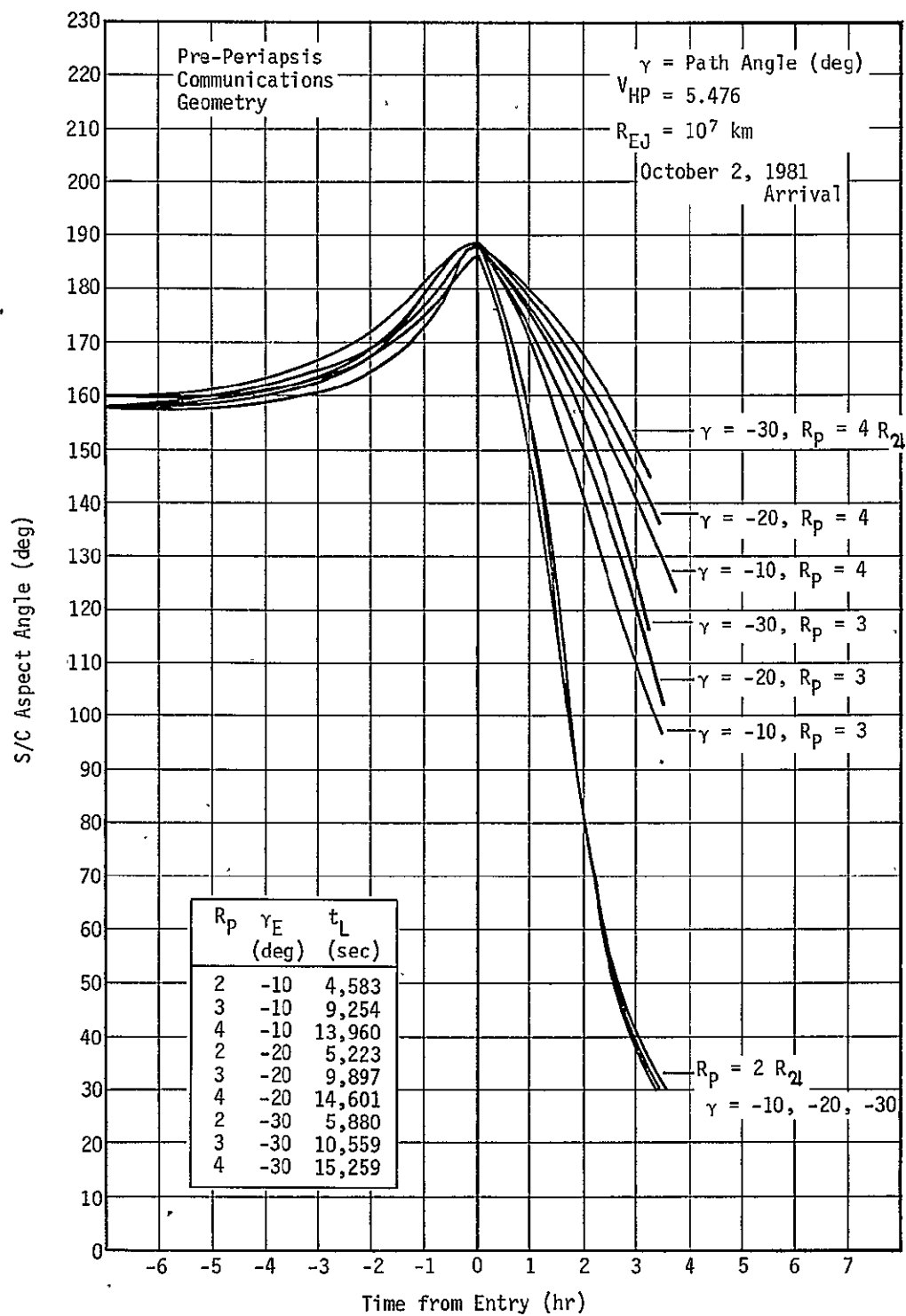


Figure IIIC-38

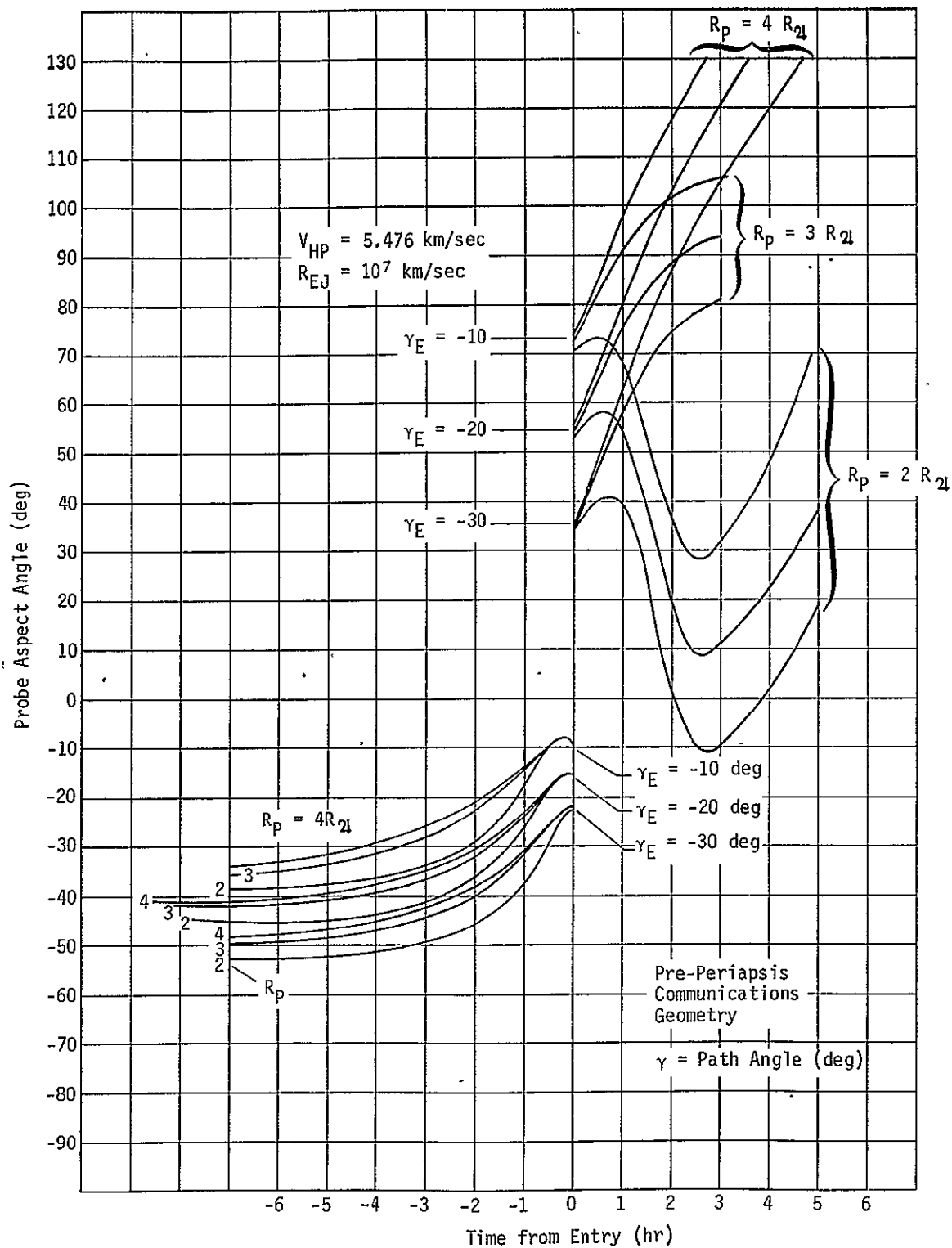


Figure IIIC-39

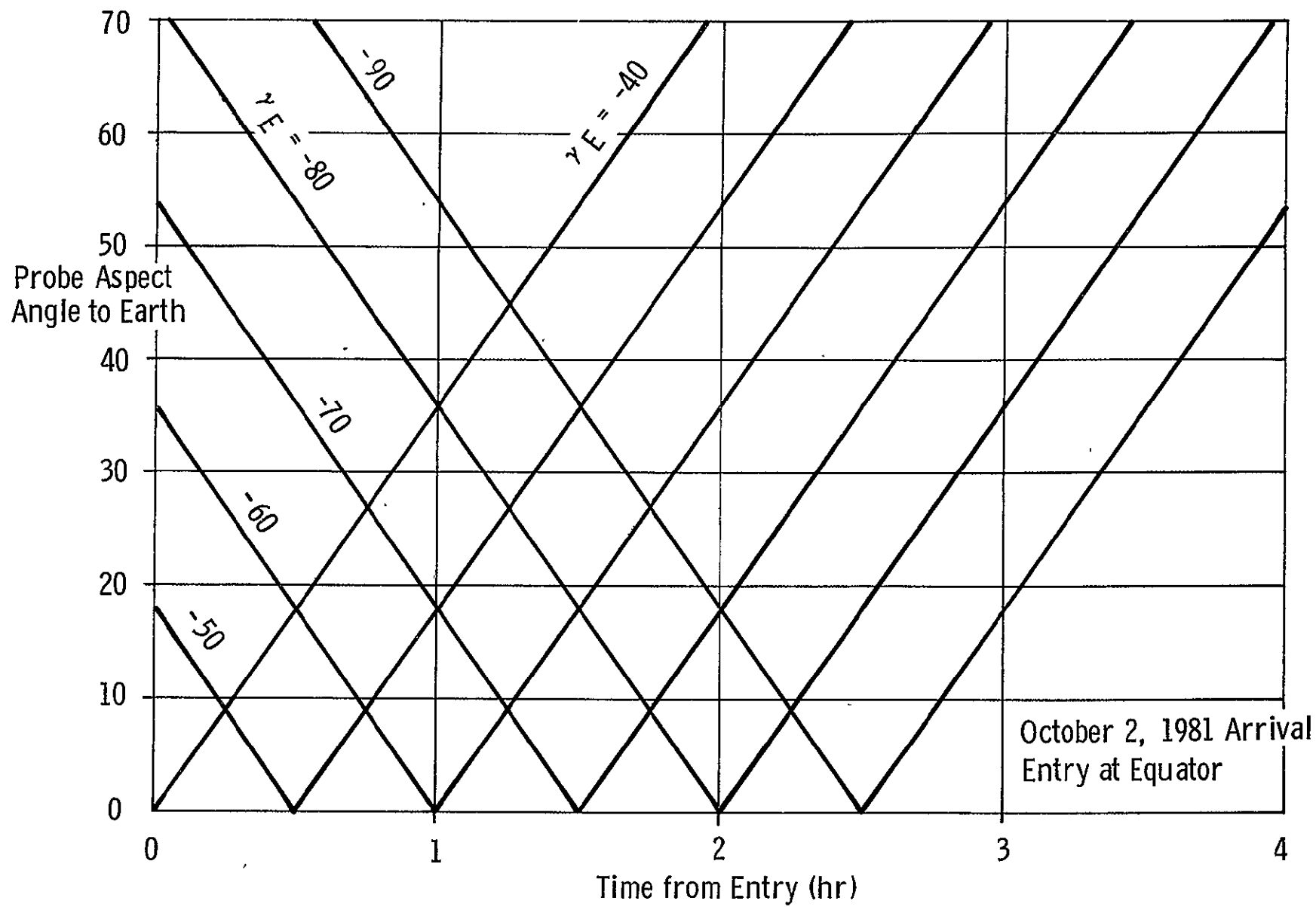


Figure IIIC-40 Direct Link Communications

D. Entry and Descent

To provide adequate sampling of the Jovian atmosphere by the science instruments on board the descent probes, the entry aeroshell should be staged in the region of 200 mb pressure. Since staging should be initiated at subsonic velocities, parametric entry studies were conducted to enable a selection of entry parameters which will permit staging near 200 mb while meeting other mission requirements; i.e., tolerable decelerations and realistic ballistic coefficients. The entry data were generated using the Martin Marietta Corporation's UD208 entry program modified to model ablation of the aeroshell's heat shield.

Entries into the nominal atmosphere, as defined in JPL Section Document 131-10 "Preliminary Model Atmospheres for Jupiter", were investigated for entry ballistic coefficients (Be) of 78.5, 157.1 and 235.6 kg/m^2 (.5, 1.0, and 1.5 slug/ft²), inertial entry flight path angles (γ_{Ie}) from -10° to -85° , and an inertial entry velocity (V_{Ie}) of 59.61 km/sec (195,570 fps). This entry velocity corresponds to the hyperbolic approach velocity of 5.476 km/sec and an entry altitude of 488 km (1.6×10^6 ft) above the one atmospheric pressure level. The effects of variations in the atmospheric model and entry velocity were studied for selected cases. Near equatorial entries in the direction of planetary rotation were considered in order to take advantage of the high rotational rate of Jupiter and thus minimize the entry velocity of the aeroshell relative to the atmosphere. Entering at latitudes other than equatorial results in increased relative entry velocity. The effect of this condition on entry is briefly noted for entry latitudes of 45° , 60° , and 90° . Also noted is the sensitivity of staging altitude to errors in entry ballistic coefficient. The entry ballistic coefficient is defined as $m_e/C_D A$ and is based on an entry drag coefficient of 1.51 and a reference area of 0.0019 m². With this reference area, the entry ballistic coefficient is equal to the entry weight, thus simplifying computer input. Since the equations of motion are dependent solely on ballistic

coefficient, this assumption in no way affects the descent trajectory. Aerodynamic research on hypersonic entries of sphere cone configurations has shown that for the configurations considered in this study, a good approximation to the variation of drag coefficient with Mach number is

<u>M</u>	<u>C_D</u>
100	1.51
5	1.51
3	1.53
2	1.52
1.5	1.48
1.0	1.25
.5	1.02
0	1.0

Because of vehicle stability requirements, it was assumed that the angle of attack during entry was nearly zero and could be neglected. Entry calculations were terminated at a Mach number of .5.

After the aeroshell is staged, the probes quickly attain terminal velocity and the remainder of the trajectory is completed under terminal conditions, i.e., vertical descent and atmospheric drag equaling the probes' weight. Parametric data relating terminal velocity to ballistic coefficient and planetary radius are included. Also descent times to various atmospheric depths under terminal conditions are given.

The extremely high entry velocities experienced at Jupiter result in a substantial portion of the heat shield being ablated. Assuming the reference area and drag coefficient of the vehicle are essentially unchanged during entry, this mass loss is reflected in a corresponding decrease in ballistic coefficient. To determine what effects this has on the entry trajectory, a mass ablation model as outlined in Appendix C, was incorporated in the Martin Marietta entry program.

According to this model, the mass at any time is given by

$$m(t) = m_e \left\{ 1 - \frac{m_a}{m_e} \left[1 - f \left(\frac{V_R(t)}{V_{Re}} \right) \right] \right\}$$

where m_e = mass at entry
 m_a = total mass ablated
 $V_R(t)$ = velocity at time t relative to Jovian atmosphere
 V_{Re} = relative velocity at entry

The function $\left[1 - f \left(\frac{V_R(t)}{V_{Re}} \right) \right]$ relates the fraction of the total mass ablated to the instantaneous ratio of velocities $V_R(t)/V_{Re}$. At entry its value is zero, no mass is yet ablated, and when $V_R(t) \ll V_{Re}$ the value of the function is one; i.e., the fraction of total mass ablated is unity. The value of the function is also dependent on the entry angle, and the size, shape and weight of the vehicle. Figure D-1 reproduced from Appendix C, illustrates the variation of $\left[1 - f (V_R(t)/V_{Re}) \right]$ with entry angle for a vehicle having a cone angle of 60° , base radius of .8 m, and a mass of 250 kg. While the shape of the curves in Figure D-1 may vary with ballistic coefficient, they were considered to be typical and were employed for all ballistic coefficients studied. The ablation mass fraction (m_a/m_e) is shown in Figure D-2 as a function of inertial entry flight path angle and entry ballistic coefficient.

For the trial mission, the entry velocity at 488 km above the one atmosphere level is 59.61 km/sec (195570 fps). This is nearly the minimum entry velocity over the launch period and at no time should it exceed 59.73 km/sec (195930 fps). For the range of entry velocities encountered, entry flight path angles must be greater than about -4° to avoid skipout from the Jovian atmosphere. The uncertainties in entry angle arising from tracking limitations, execution errors, etc. dictate that a margin be applied to this skipout limit. Moreover, at low entries the dispersions in descent

path arising from errors in entry angle as excessive. Because of these factors, the lower limit on entry angle for this study was taken to be -10° while the maximum was assumed to be -85° .

To minimize the severity of the entry environment, entries in the direction of planetary rotation and along the equator were considered. This takes advantage of the high rotational rate of the Jovian atmosphere (12.7 km/sec at 488 km) and minimizes the entry velocity of the aeroshell relative to the atmosphere.

To determine what effect the modeling of mass ablation has on the descent trajectory, several computer simulations were conducted at entry angles of -10° and -60° without mass ablation. The constant mass runs were made using ballistic coefficients corresponding to those at entry (B_e) and those after all mass is ablated ($B_e \left[1 - m_a/m_e \right]$). The entry analysis (Figures D-3 thru D-6) indicated that the altitude-velocity history of an ablating vehicle is approximately equal to that of a vehicle with constant mass and having a ballistic coefficient given by $B_e \left[1 - m_a/m_e \right]$. However, the peak dynamic pressure (Figures D-7 thru D-10) of an ablating vehicle tends to be the average of that experienced by constant mass vehicles with ballistic coefficients of B_e and $B_e \left[1 - m_a/m_e \right]$. Since the maximum deceleration shows little dependence on ballistic coefficient, the modeling of mass ablation has no appreciable effect on this quantity.

Before atmospheric measurements can be initiated by the probes, it is required that the probe/aeroshell configuration be decelerated to subsonic velocities and the aeroshell staged. For entries into the nominal atmosphere with mass ablation, Figures D-11 thru D-13 illustrate the altitudes at which subsonic velocities are attained for entry ballistic coefficients of 78.5, 157.1 and 235.6 kg/m^2 (.5, 1.0,

and 1.5 slug/ft^2). Above approximately $M = .7$, vehicles with steeper entry angles tend to penetrate to lower altitudes for a given velocity. Below $M = .7$, the pronounced crossing of the descent profiles at low entry angles ($<30^\circ$) is primarily due to the modeling of mass ablation. For instance, vehicles entering at -20° compared to -10° experience greater mass ablation and, thus, effectively have lower ballistic coefficients. For entries greater than -30° , changes in the ballistic coefficient are usually not sufficient to prevent vehicles entering at steeper angles to penetrate deeper.

While entry calculations were initiated at 488 km, the aeroshell does not begin to experience atmospheric deceleration until altitudes in the region of 250 km are reached. The values of maximum deceleration and dynamic pressure, Figures D-14 and 15 are nearly proportional to $V_{Re}^2 \sin \gamma_{Re}$. The relative entry velocity (V_{Re}) is found by the vector subtraction of the velocity of the atmosphere from the aeroshell's inertial entry velocity; the angle the resultant vector makes with the local horizontal is the relative entry flight path angle (γ_{Re}). The maximum deceleration exhibits little dependence on entry ballistic coefficient, increasing slightly with increasing B_e . However, peak dynamic pressure is directly proportional to ballistic coefficient, because of mass ablation it is not a function of B_e but of an effective ballistic coefficient that is approximately the average of entry and final ballistic coefficients. The extremely high entry velocities at Jupiter result in much larger peak decelerations than those encountered in previous entry studies for other planetary atmospheres. At an entry angle of -85° and a B_e of 157.1 kg/m^2 (1.0 slug/ft^2), peak deceleration is 3600 earth g's while at -10° it is 430 g's.

For the instruments on board the upper and lower probes to adequately sample the Jovian atmosphere, the aeroshell should be staged at altitudes between 200 and 100 mb pressure. For a given entry ballistic coefficient, this dictates that the proper entry angle be selected which will decelerate the aeroshell to subsonic velocities at the desired altitude. For entry angles of -10° , -20° , and -30° Figures D-16 thru D-18 detail the entry ballistic coefficients required to attain subsonic velocities at the desired pressure levels. Packaging of the entry payload in the desired aeroshell configuration results in entry ballistic coefficients of 188.5 to 235.6 Kg/m^2 (1.2 to 1.5 slug/ft^2). With this range of B_e , entries of -10° and -20° permit staging at the 200 mb level with Mach numbers of .7 or less. Staging at 100 mb is possible for an entry of -10° although higher Mach numbers are required. For entries at -30° or higher, staging of the aeroshell at the desired pressures is precluded for ballistic coefficients of 188.5 to 235.6 Kg/m^2 (1.2 to 1.5 slug/ft^2). Only by accepting higher pressure levels at staging can steeper entries be considered.

Over the thirty day launch period being studied, the geocentric hyperbolic excess velocity will not exceed 6.5 km/sec; this corresponds to a maximum entry velocity at 488 km of 59.73 km/sec (195930 fps). For the maximum and nominal entry velocities, a comparison of pertinent entry parameters is shown in Tables III D-I and III D-II for entries of -10° and -60° . Over the range of entry velocities, the peak deceleration and dynamic pressure, which are functions of the square of V_{Re} , are essentially unchanged. Similarly, the altitudes and times of occurrence of major events do not vary greatly. The values shown are for the nearest .5 sec printout of the UD208 program and may not be the absolute maximums.

The effects of atmospheric model variation on the descent profile have been analyzed for an entry angle of -10° and an entry ballistic coefficient of 235.6 Kg/m^2 (1.5 slug/ft^2). Entries into the nominal, cool and warm atmospheres,

Table IIID-I Effects of Entry Velocity Variation on Entry

ENTRY CONDITIONS	$\gamma_{Ie} = -10^\circ$	$B_e = 235.6 \text{ kg/m}^2$ (1.5 slug/ft ²)	$m_a/m_e = .25$	NOMINAL ATMOSPHERE
Inertial Entry Velocity (fps, km/sec)	195,570 = 59.61	195,930 = 59.72		
Max Deceleration (g)	449	451		
Max Dynamic Pressure (psf)(nt/m ²)	17,235 = 825,216	17,300 = 828,328		
Altitude of Max Deceleration and Dynamic Pressure (ft, km)	279,314 = 85.1	278,083 = 84.8		
Time of Max Deceleration and Dynamic Pressure (sec)	42.0	42.0		
Altitude of $g = .1$ (ft, km)	903,847 = 275.5	902,662 = 275.1		
Time of $g = .1$ (sec)	21	21		
Maximum Relative Velocity (fps, km/sec)	154,882 = 47.2	155,241 = 47.3		
Altitude of Max Relative Velocity (ft, km)	807,196 = 246.0	805,864 = 245.6		
Time of Max Relative Velocity (sec)	24	24		
Altitude of $M = 1.0$ (ft, km)	145,342 = 44.3	145,273 = 44.3		
Time of $M = 1.0$ (sec)	79.0	79.0		
Mach Number at 200 mb	.67	.67		
Time at 200 mb	103.5	103.5		

Table IIID-II Effects of Entry Velocity Variation on Entry

ENTRY CONDITIONS	$\gamma_{Ie} = -60^\circ$	$B_e = 235.6 \text{ kg/m}^2$ (1.5 slug/ft ²)	$m_a/m_e = .22$	NOMINAL ATMOSPHERE
Inertial Entry Velocity (fps, km/sec)		195,570 = 59.61		195,930 = 59.72
Max Deceleration (g)		-3,016		-3,046
Max Dynamic Pressure (psf)(nt/m ²)		131,546 = 6.3×10^6		132,506 = 6.34×10^6
Altitude of Max Deceleration and Dynamic Pressure (ft, km)		189,467 = 57.7		187,799 = 57.2
Time of Max Deceleration and Dynamic Pressure (sec)		8.5		8.5
Altitude of $g = .1$ (ft, km)		922,207 = 281.2		920,961 = 280.7
Time of $g = .1$ (sec)		4.0		4.0
Maximum Relative Velocity (fps, km/sec)		178,693 = 54.5		179,052 = 54.6
Altitude of Max Relative Velocity (ft, km)		667,891 = 203.6		751,108 = 228.9
Time of Max Relative Velocity (sec)		5.5		5.0
Altitude of $M = 1.0$ (ft, km)		71,403 = 21.8		70,116 = 21.4
Time of $M = 1.0$ (sec)		16.5		17.0
Mach Number at 200 mb		6.02		5.95
Time at 200 mb (sec)		10.5		10.5

as defined in JPL section document 131-12 "Preliminary Model Atmospheres for Jupiter", were investigated. Entry into the Lewis cool atmosphere, JPL IOM 2947-617, was also simulated.

For each of these atmospheres, Table III D-III details the time and altitude at which the major events occur during descent. The altitudes at which each of these events occur are largest for the warm model and decrease by approximately 50% for the Lewis cool model. Conversely, the maximum deceleration and dynamic pressure experienced by the entry probe is approximately 55% greater for the Lewis cool than for the warm model. Despite the wide variation in the entry environment for each of the atmosphere models, the Mach number at the staging pressure of 200 mb is essentially unchanged. However, the time from .1 g to the staging altitude exhibits a variation of 39 seconds between the atmosphere models.

Entries at latitudes other than near equatorial can be accomplished at the expense of increasing the severity of the entry environment. For inclinations of the probe trajectory other than 0° (equatorial), the high rotational velocity of Jupiter is not used to full advantage to reduce the entry velocity of the probe relative to Jupiter's atmosphere. While equatorial orbits are usually not obtainable (the declination of the VHP vector with respect to Jupiter's equator determines the minimum inclination) the minimum inclination is usually less than 10° ; this permits entries nearly in the direction of Jupiter's rotation and results in a substantial decrease in the relative entry velocity. For an inertial entry velocity of 59.6 km/sec and an inertial entry angle of -10° , the relative entry velocity (V_{Re}) is 47.1 km/sec for a 0° inclination; polar entries and equatorial entries against the planet's rotation (180° inclination) result in relative entry velocities of 59.6 and 72.1 km/sec respectively.

Table IIID-III Effects of Atmospheric Model Variation on Entry

ENTRY CONDITIONS	Flight Path Angle $\gamma_{Ie} = -10^\circ$	Ballistic Coefficient			Fraction of Mass Ablated $m_a/m_e = .25$
		$V_{Ie} = 195570 \text{ fps}$ $= 59.62 \text{ Km/sec}$	$B_e = 1.5 \text{ slug/ft}^2$ $= 235.6 \text{ Kg/m}^2$		
Atmosphere		Warm	Nominal	Cool	May 8 Cool
Max Deceleration (g)		393	449	552	718
Max Dynamic Pressure (psf, nt/m ²)		15,110 = 7.234×10^5	17,235 = 8.252×10^5	21,293 = 10.20×10^5	27,878 = 13.35×10^5
Altitude of Max Decel- eration and Dynamic Pressure (ft, km)		327,122 = 99.7	279,314 = 85.2	268,113 = 81.7	189,182 = 57.7
Time of Max Decelera- tion and Dynamic Pressure (sec)		40.5	42	42	44.5
Altitude of $g = .1$ (ft, km)		1,364,170 = 415.8	903,847 = 275.5	759,117 = 231.4	584,370 = 178.1
Time of $g = .1$ (sec)		7	21	25.5	31.0
Maximum Relative Veloc- ity (fps, km/sec)		154,702 = 47.2	154,882 = 47.2	154,946 = 47.2	155,029 = 47.3
Altitude of Max Rela- tive Velocity (ft, km)		1,082,947 = 330.1	807,196 = 246.0	679,401 = 207.1	521,416 = 158.9
Time of Max Relative Vel (sec)		15.5	24	28	33
Altitude of $M = 1.0$ (ft, km)		168,926 = 51.5	145,349 = 44.3	140,878 = 42.9	99,452 = 30.3
Time of $M = 1.0$ (sec)		81.5	79	78.5	73.5
Mach Number at 200 mb		.65	.66	.66	.66
Time at 200 mb (sec)		108	104	103.5	93

The maximum deceleration and dynamic pressure experienced during entry are proportional to the product of V_{Re}^2 and the sine of the relative entry angle γ_{Re} . While γ_{Re} decreases slightly as the inclination of the probes orbit increases, the product $V_{Re}^2 \times \sin \gamma_{Re}$ and, therefore, the maximum deceleration and dynamic pressure increase as the probe's inclination increases. This effect is shown in Table III D-IV for entries at latitudes of 0° , 60° , and 90° . For an inertial entry angle of -10° , polar entries result in approximately a 25% increase in the severity of the entry environment over an equatorial entry with the rotation of the planet.

After the aeroshell is staged, the rate of descent of the upper and lower probes is dictated by the communications requirements and the sampling rates of the science instruments. The descent velocity of the probes and the time required to reach various pressure depths is shown in Figures D-19 and D-20 as a function of ballistic coefficient and altitude. In generating these figures it was assumed that the probes descend at terminal velocity, i.e., their descent is nearly vertical and the atmospheric drag equals the probe's weight. In actuality, there is a brief time span after staging of the probes in which they accelerate or decelerate to terminal conditions. However, for the range of ballistic coefficients and pressure levels being considered this time span (~ 2 minutes) is negligible compared to the total mission time of approximately 155 minutes. The altitude descended during the brief period of acceleration or deceleration is approximately equal to the distance that would have been covered had the descent during this period been at terminal velocity. Figures D-19 and D-20 can therefore be used to design descent profiles for a variety of ballistic coefficients, descent times and descent depths. The errors introduced by assuming terminal velocity at all times will be negligible.

Table IIID-IV Effects of Entry at Various Latitudes

ENTRY CONDITIONS	$\gamma_{Ie} = -10^\circ$	$h_e = 488 \text{ km}$
	$V_{Ie} = 195570 \text{ fps}$	$B_e = (1.5 \text{ slug/ft}^2)$
	$= 59.61 \text{ km/sec}$	235.6 kg/m^2
	$m_a/m_e = .25$	
	Nominal Atmosphere	

ENTRY LATITUDE	INERTIAL* HEADING	V_{Re} (fps, km/sec)	γ_{Ie}	MAXIMUM DECELERATION (g)	MAXIMUM DYNAMIC PRESSURE (psf)(nt/m ²)	ALTITUDE AT M = .5 (km)
0°	0°	154,536 = 47.1	-12.6°	449	17,235 = 8.252×10^5	22.5
60°	60°	186,110 = 56.7	-10.51°	532	20,415 = 9.775×10^5	21.2
90°	90°	195,570 = 59.6	-10°	557	21,371 = 10.23×10^5	20.8

*Inertial heading is the azimuth of the inertial velocity vector at entry measured from the local east direction.

For the Lewis cool atmosphere, the terminal velocities are descent times are shown in Figures III D-21 and III D-22. The terminal velocities at a given pressure level are smaller for this model. Although the depth of the atmosphere is much smaller for the Lewis cool model, for the nominal atmosphere there are 636 km between the 200 mb and 1000 atmosphere pressure levels and only 265 km for the Lewis cool, the descent times are longer for this model.

From this parametric analysis, it is obvious that a probe entering the Jupiter atmosphere will encounter an extremely hostile Aerothermodynamic environment. Therefore, entry parameters should be chosen which will minimize the severity of the entry environment while satisfying other mission requirements. Because of the high entry velocities the use of steep entry angles should be avoided. Only at the shallower entries (-10° to 30°) are the maximum decelerations kept within tolerable limits (430 to 1500 g's). For the ballistic coefficients under consideration, shallow entry angles are also preferred if the aeroshell is to be staged in the vicinity of the 200 mb pressure level. Entry along the equator in the direction of the planet's rotation produces the most benign trajectory by minimizing the velocity of the aeroshell relative to the Jovian atmosphere.

Ablation of the aeroshell's heat shield during entry causes significant altering of the descent profile over that predicted by a constant mass simulation. However, in the event a constant mass simulation is employed, the altitude-velocity history of an ablative vehicle can be approximated using a ballistic coefficient of $B_e (1 - m_a/m_e)$ while the peak dynamic pressure is adequately modeled using an average ballistic coefficient. Since peak deceleration shows little dependence on ballistic coefficient using the value associated with B_e should provide results accurate enough for preliminary planning purposes.

For each of the missions defined in this study the entry aeroshell will be staged in the vicinity of the 200 mb pressure level, approximately 33 km above the one atmosphere level. Errors in the atmospheric model and entry conditions will cause errors in the staging altitude. The effect of atmospheric model variations on the descent profile were detailed in Table III-D III. The entry parameters that will affect the staging altitude include flight path angle, ballistic coefficient, quantity of mass ablated, time of staging, and magnitude and direction of the entry velocity.

During entry, a deceleration of 0.1 g is sensed and after a predetermined time has elapsed (based on preflight entry analyses) the entry aeroshell is staged. The time of staging will be in error if the deceleration of 0.1 g is not sensed accurately or if timing errors exist. Tracking limitations and inaccuracies in the deflection maneuver can cause deviations in the entry flight path angle and the entry velocity vector. Uncertainties in the aeroshell's drag coefficient may result in variations in the ballistic coefficient, and lack of knowledge of the aero/thermodynamic processes occurring during descent may result in errors in the quantity of heat shield mass ablated.

Sensitivity coefficients were developed to determine the extent each of these error sources affects the staging altitude (h_s). The sensitivity coefficients are approximately linear except for errors in the entry flight path angle for changes in the entry conditions of up to 10%. Since the design example entry angle is -20 deg and skip-out is approximately -4 deg, the relation between errors in the entry flight path angle and staging altitude is extremely nonlinear. Because the expected variations in entry angle are rather large, the usefulness of a sensitivity coefficient for entry angle is doubtful. For this reason, the staging altitude is shown in Figure IIID-23 for entry angles from -10 to -30 deg; the 10 deg variation in entry angle about the nominal causes staging altitude errors from 7.5 to 20.5 km. The sensitivity coefficients for the other error sources are summarized in Table IIID-V.

Table IIIDV

<u>Error Source</u>	<u>Sensitivity Coefficient</u>
Ballistic Coefficient, B_e	$\Delta h_s / \Delta B_e = -18 \text{ km/slug/ft}^2$
Entry Velocity Magnitude, V_e	$\Delta h_s / \Delta V_e = -0.2 \text{ sec}$
Ablated Mass Fraction, (m_a/m_e)	$\Delta h_s / \Delta (m_a/m_e) = 19.5 \text{ km}$
Time of Staging, t_s	$\Delta h_s / \Delta t_s = -0.38 \text{ km/sec}$
Azimuth of Entry Velocity, A_V	$\Delta h_s / \Delta A_V \sim 0$
$B_e = 0.9 \text{ slug/ft}^2$ $\gamma_{Ie} = -20 \text{ deg}$ $V_{Ie} = 195586 \text{ fps}$	
$\frac{m_a}{m_e} = 0.2$ $t_s = 57.5 \text{ after } 0.1 \text{ g}$	

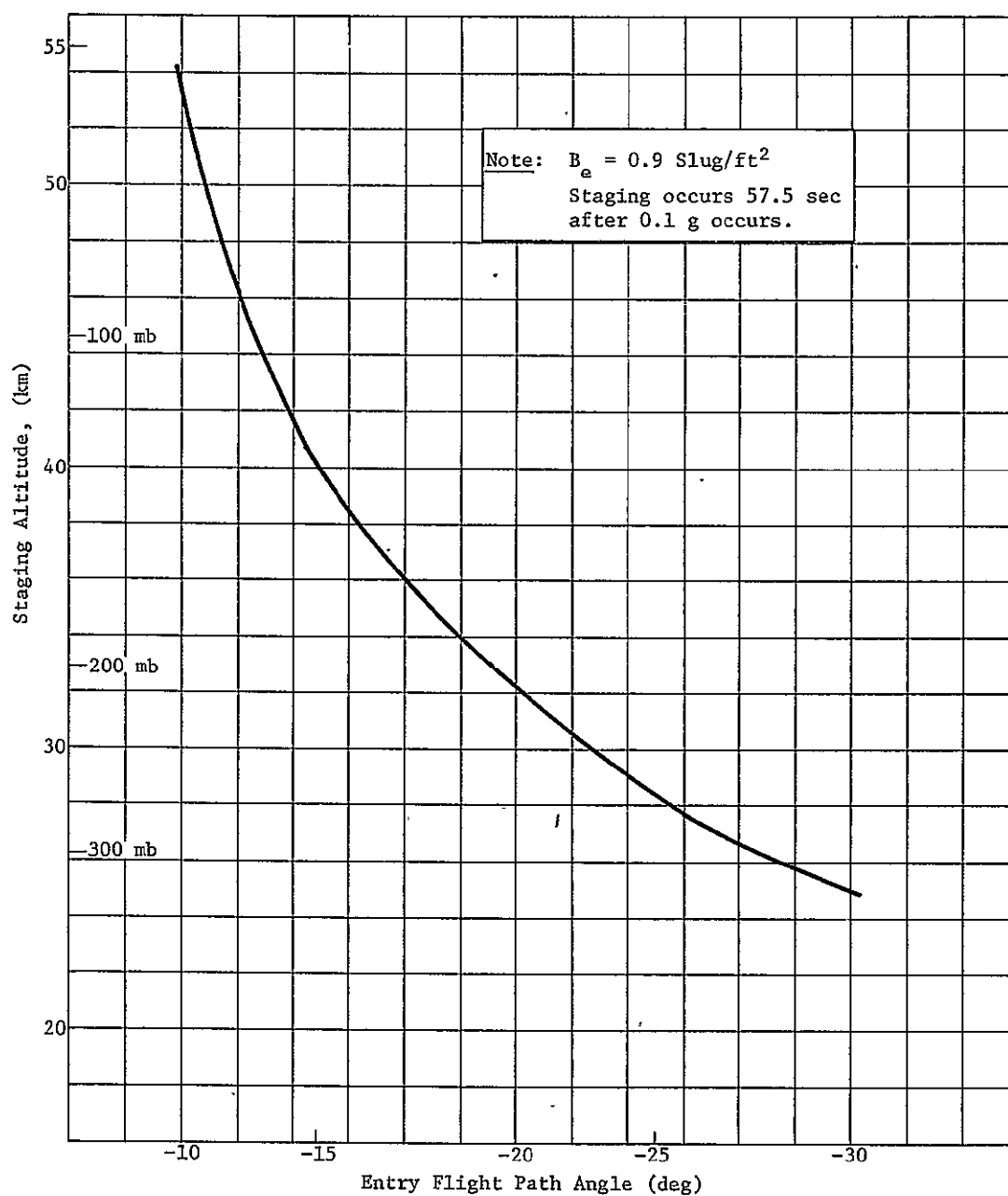


Figure IIID-23 Effect of Entry Angle Errors on Staging Altitude

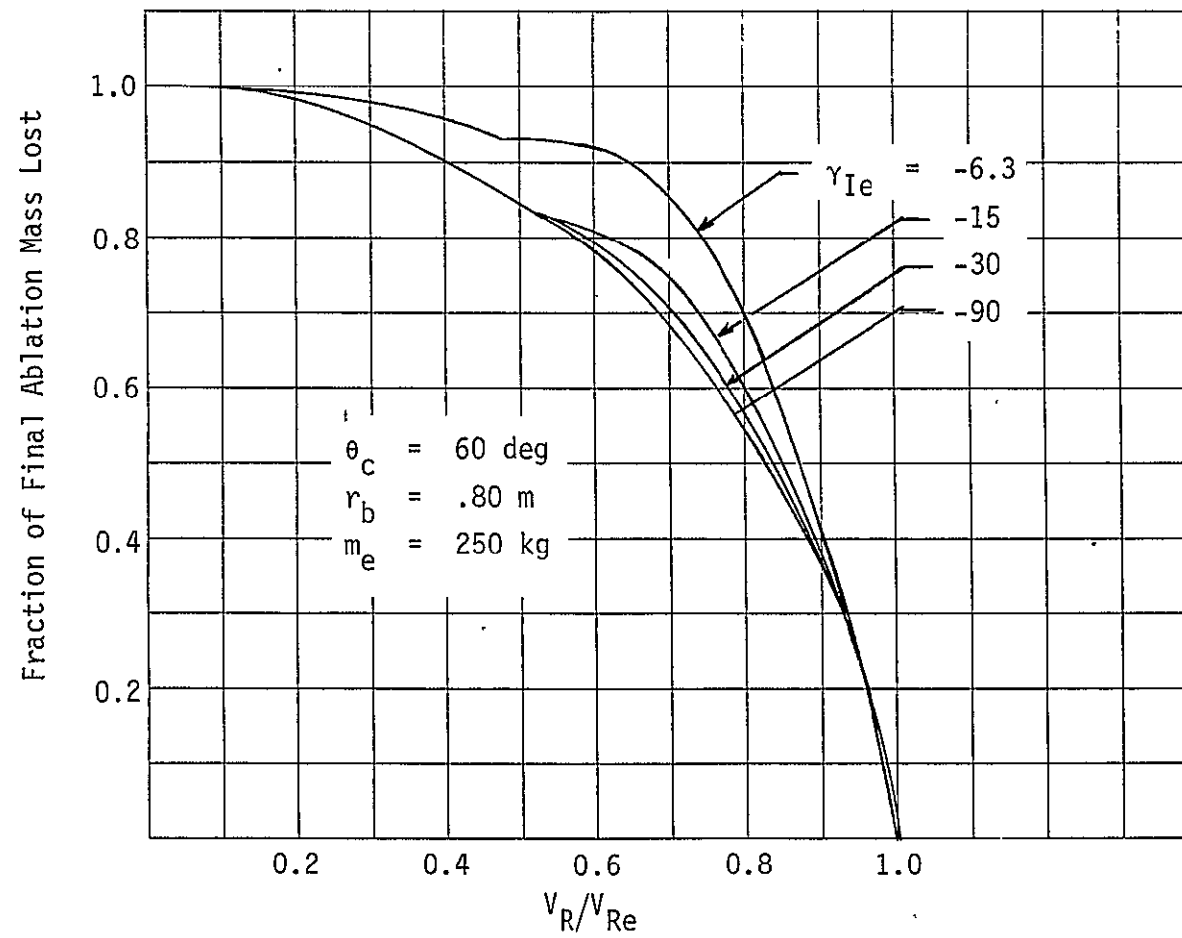


Figure IIID-1 Variation of Mass Loss with Velocity

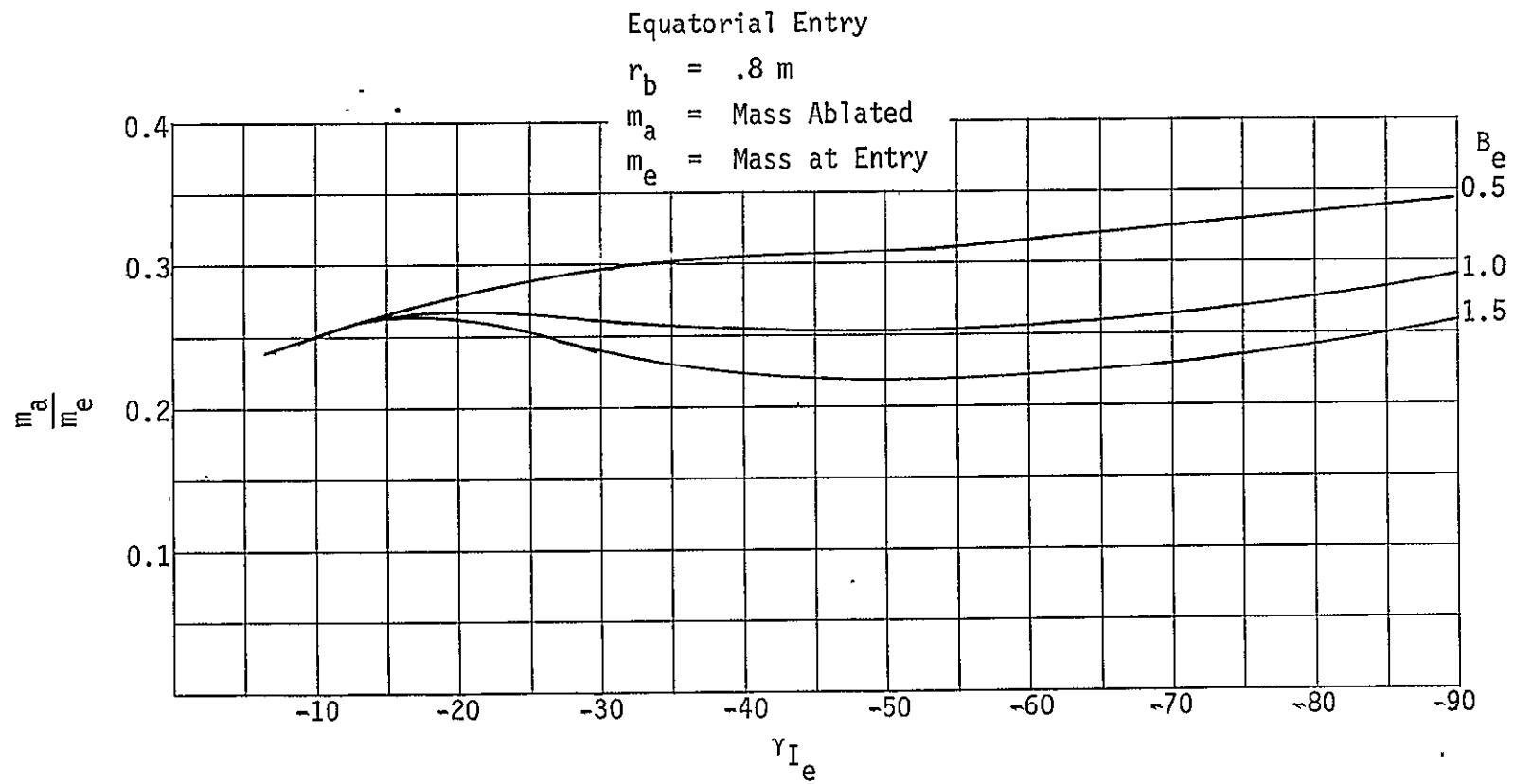


Figure IIID-2 Variation of Ablated Mass with Entry Angle

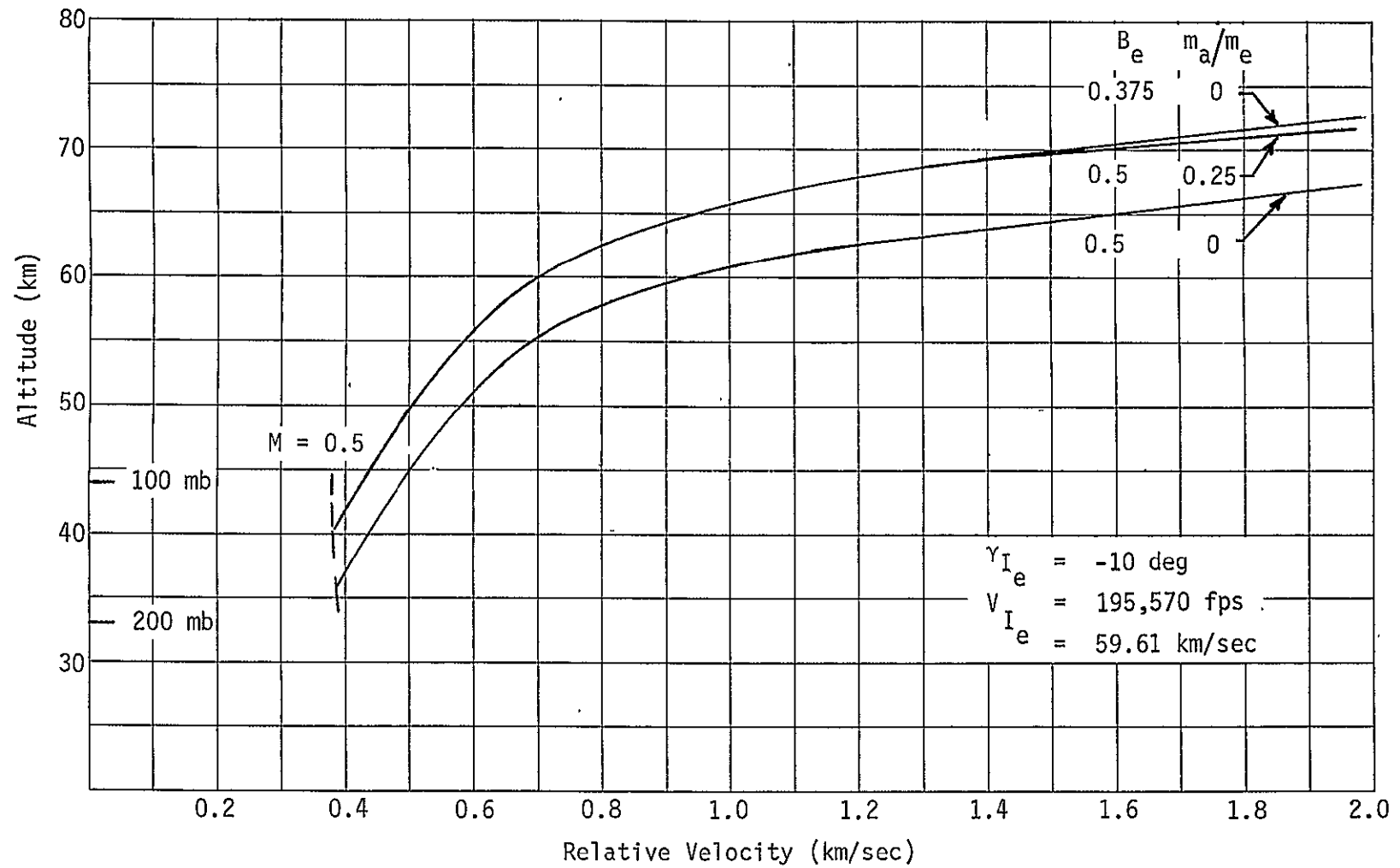


Figure IIID-3 Effects of Modeling Ablation on Entry

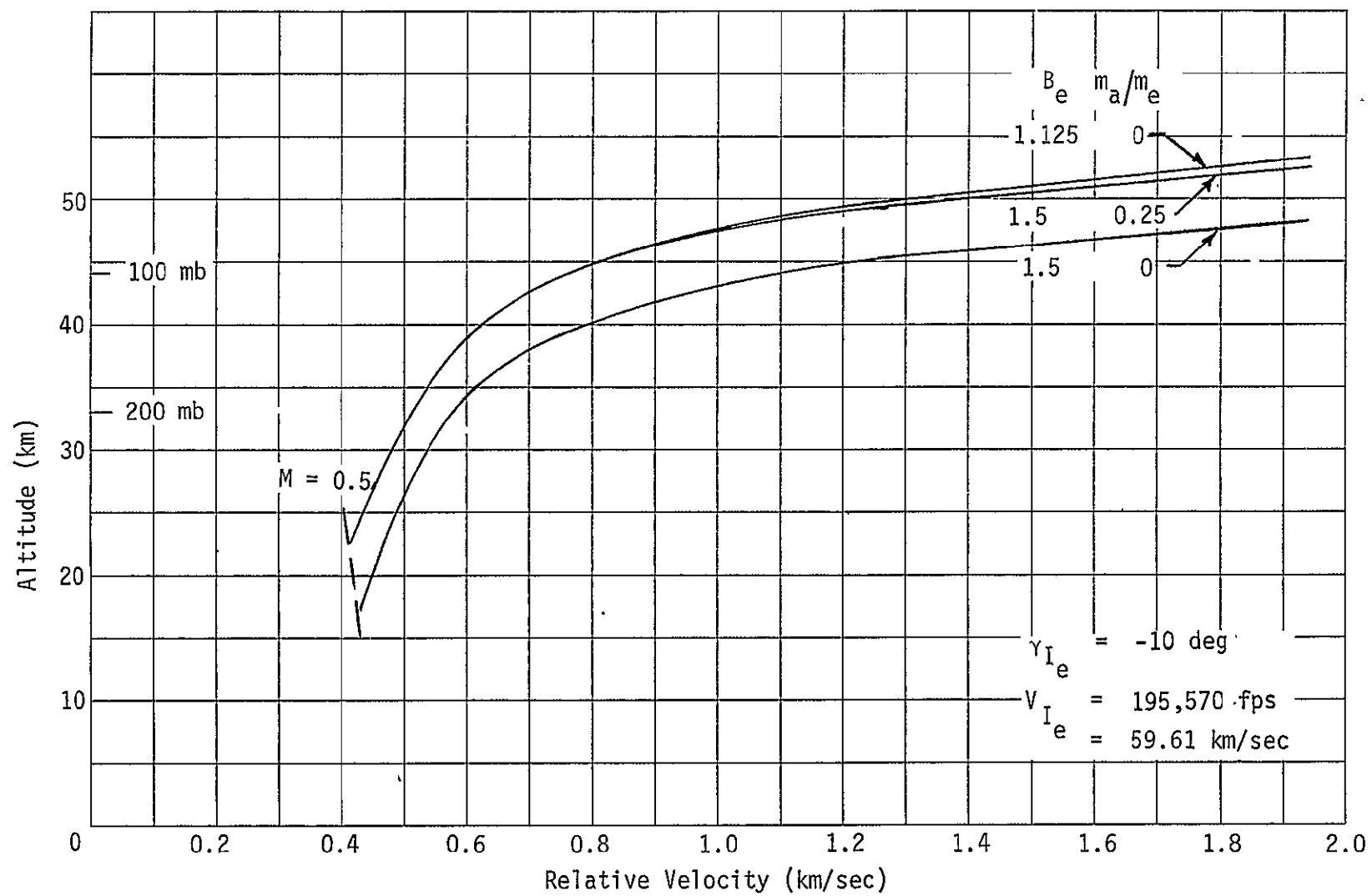


Figure IIID-4 Effects of Modeling Ablation on Entry

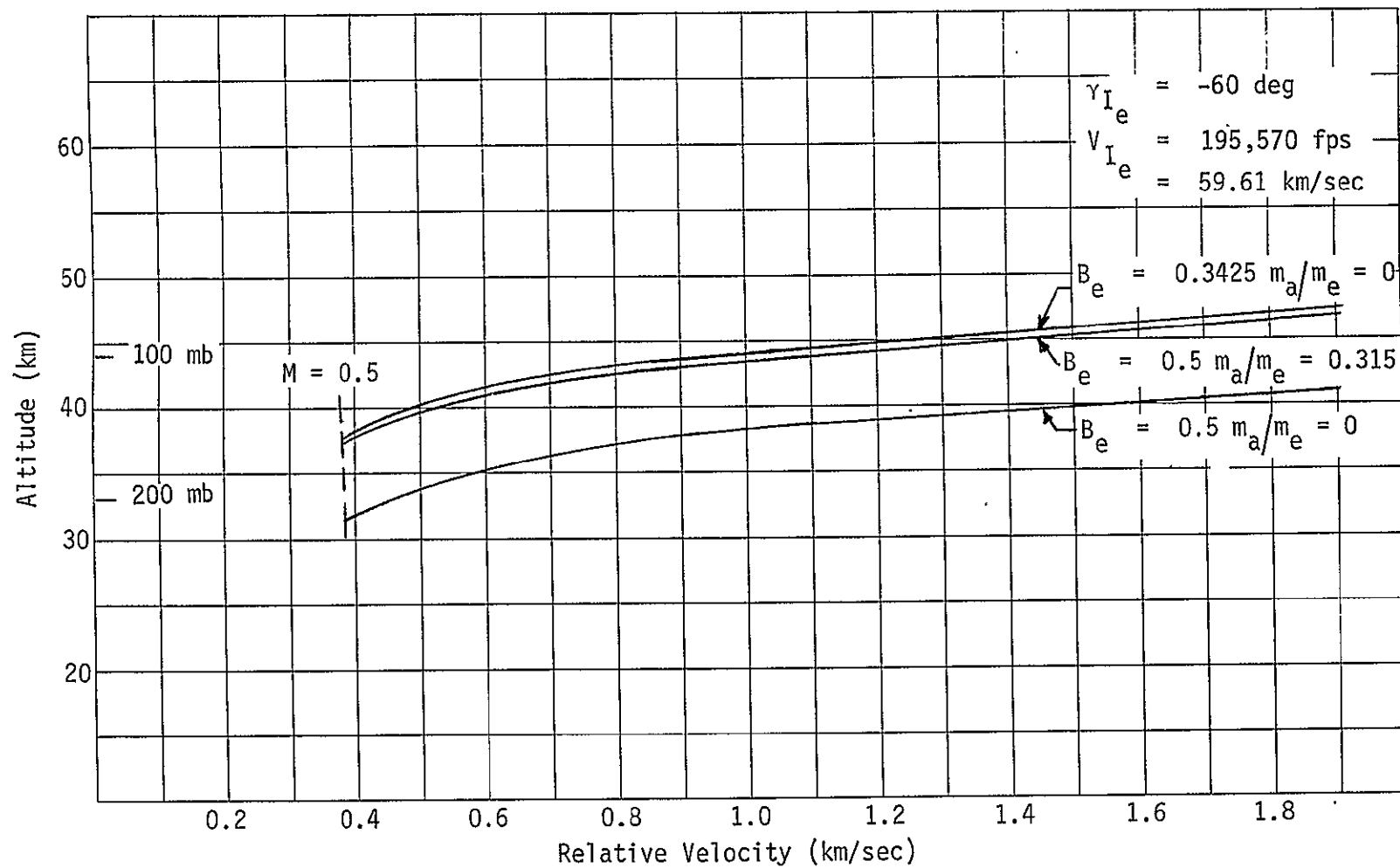


Figure IIID-5 Effects of Modeling Ablation on Entry

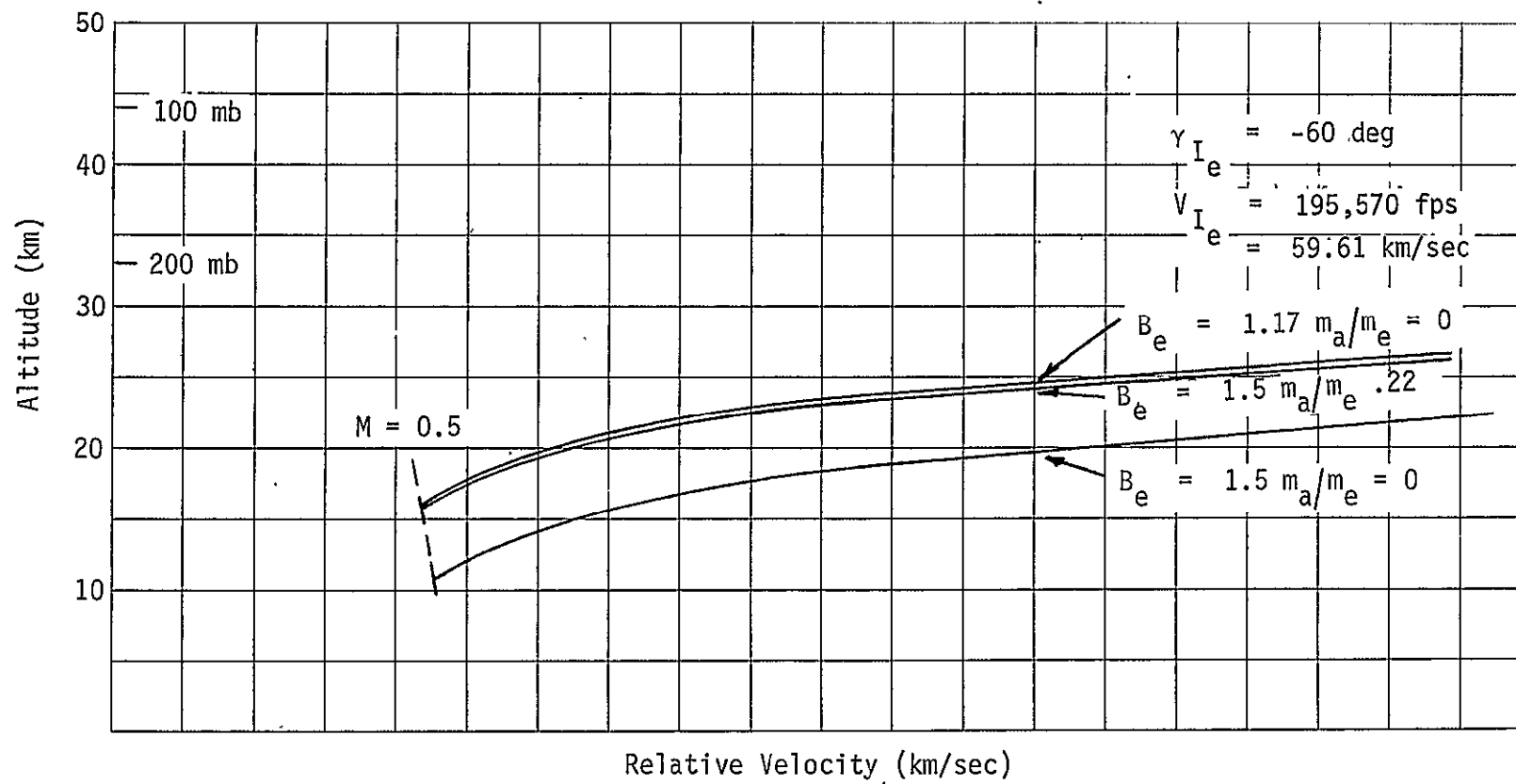


Figure IIID-6 Effects of Modeling Ablation on Entry

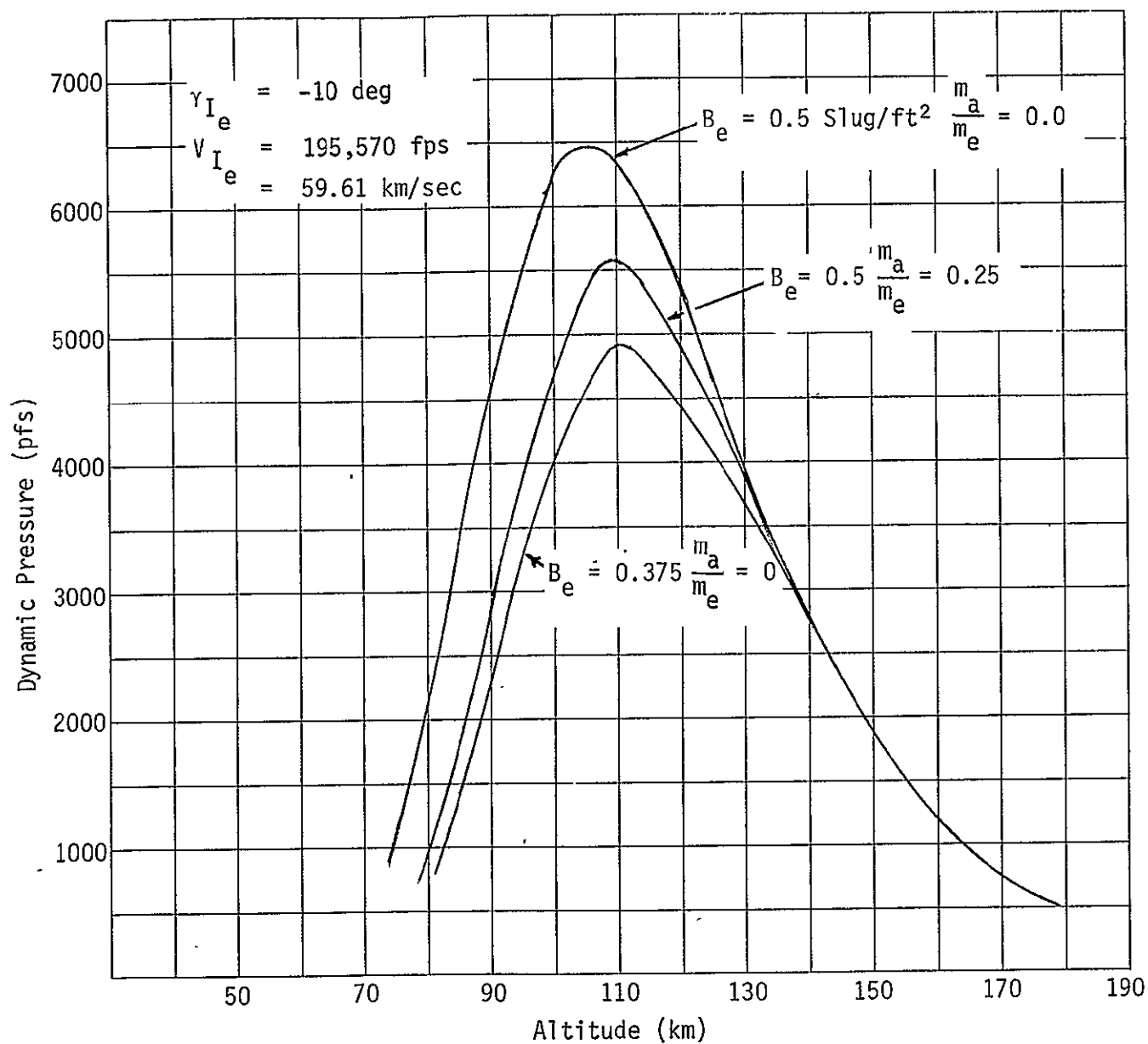


Figure IIID-7 Effect of Modeling Mass Ablation on Dynamic Pressure

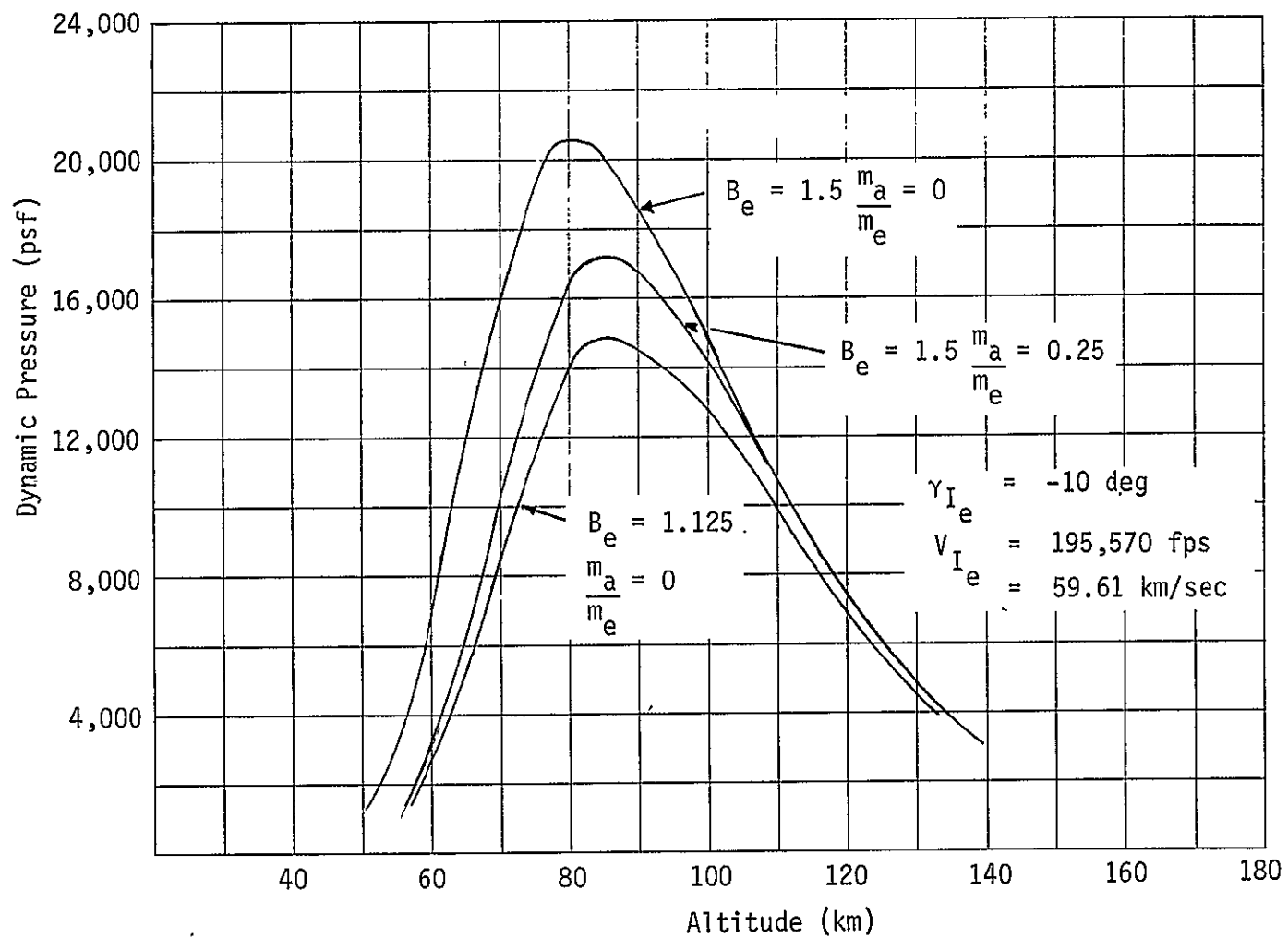


Figure IIID-8 Effect of Modeling Mass Ablation on Dynamic Pressure

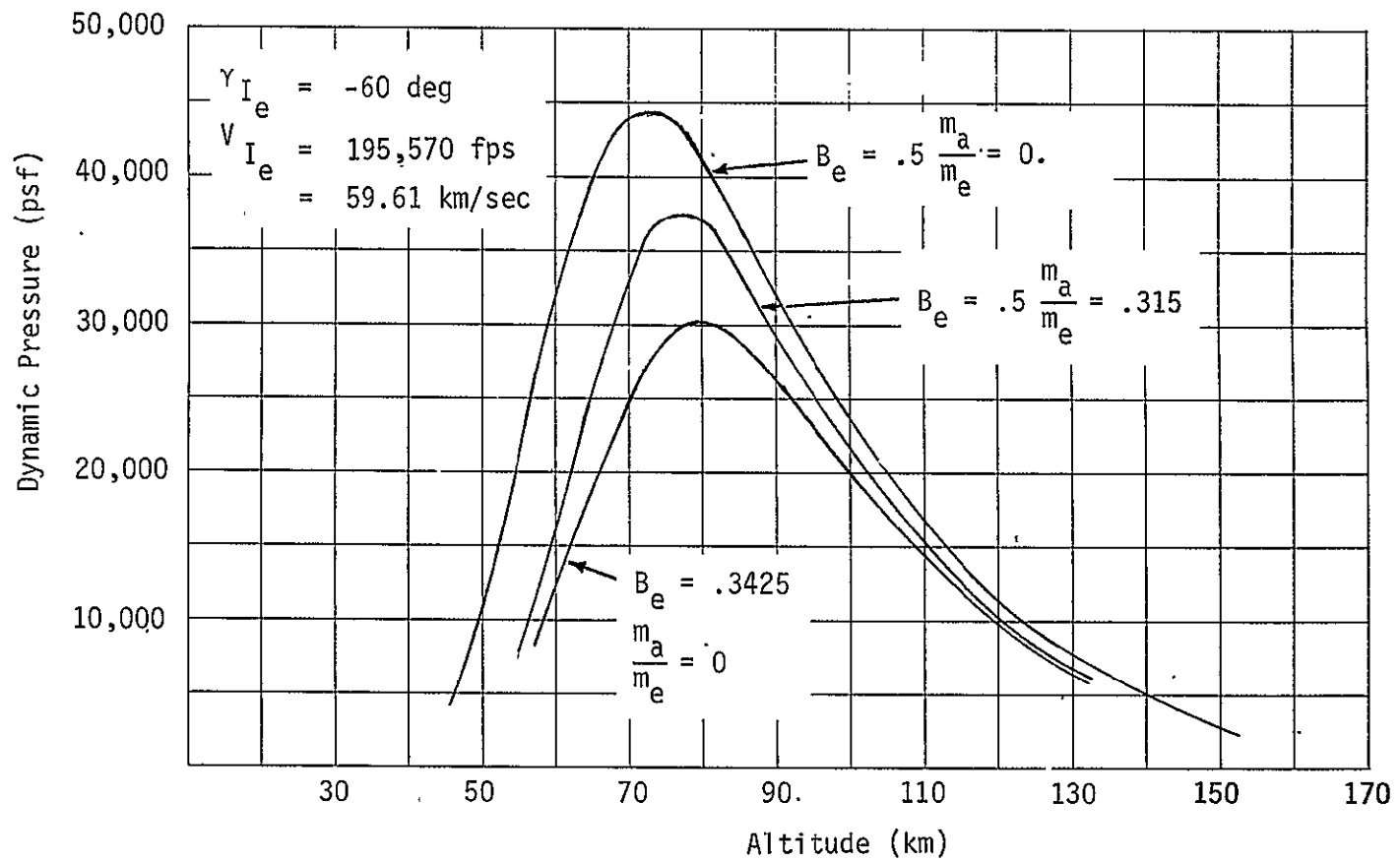


Figure IIID-9 Effect of Modeling Mass Ablation on Dynamic Pressure

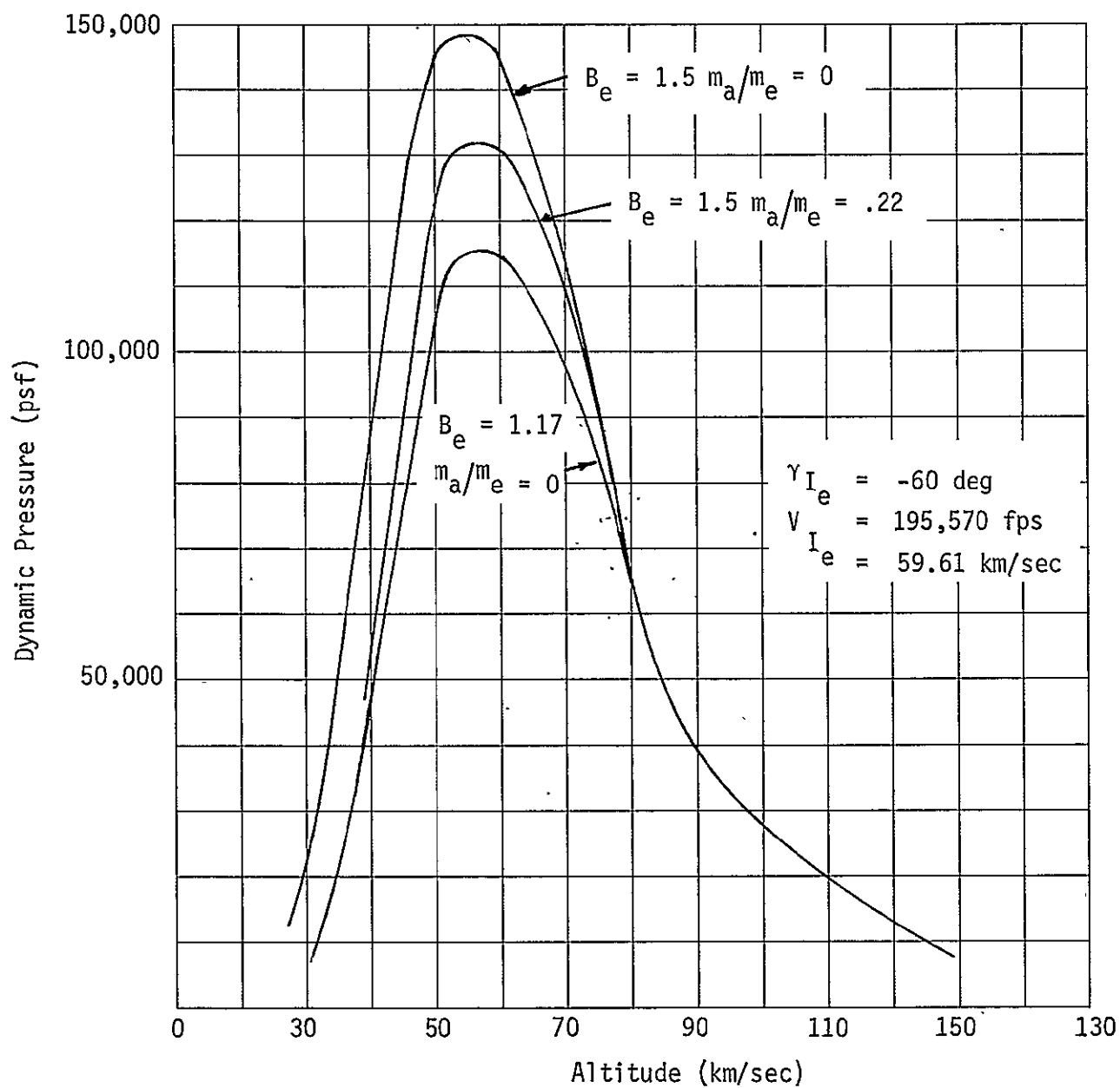


Figure IIID-10. Effect of Modeling Mass Ablation on Dynamic Pressure

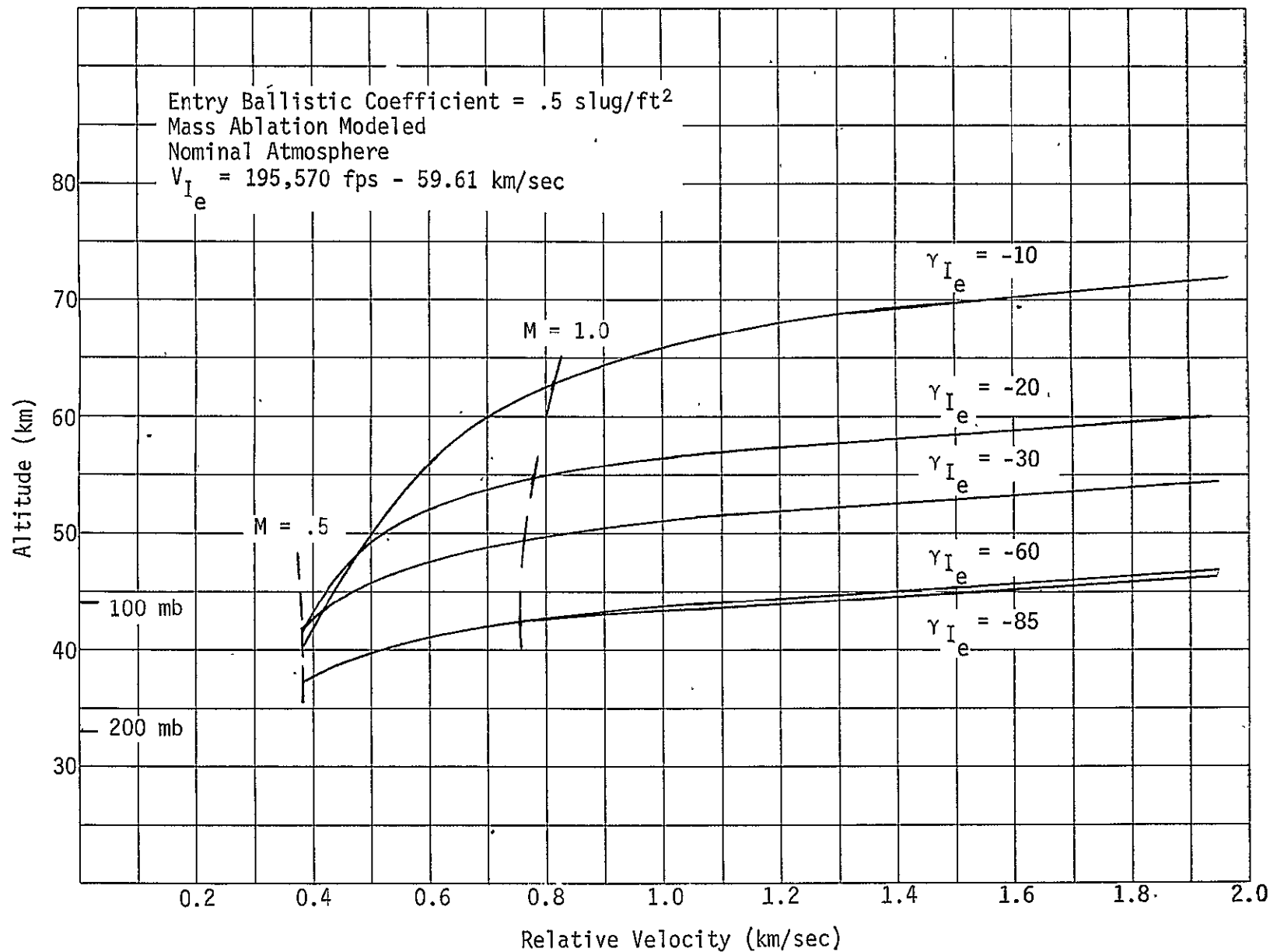


Figure IIID-11 Descent Profile for $B_p = .5 \text{ Slug/ft}^2$

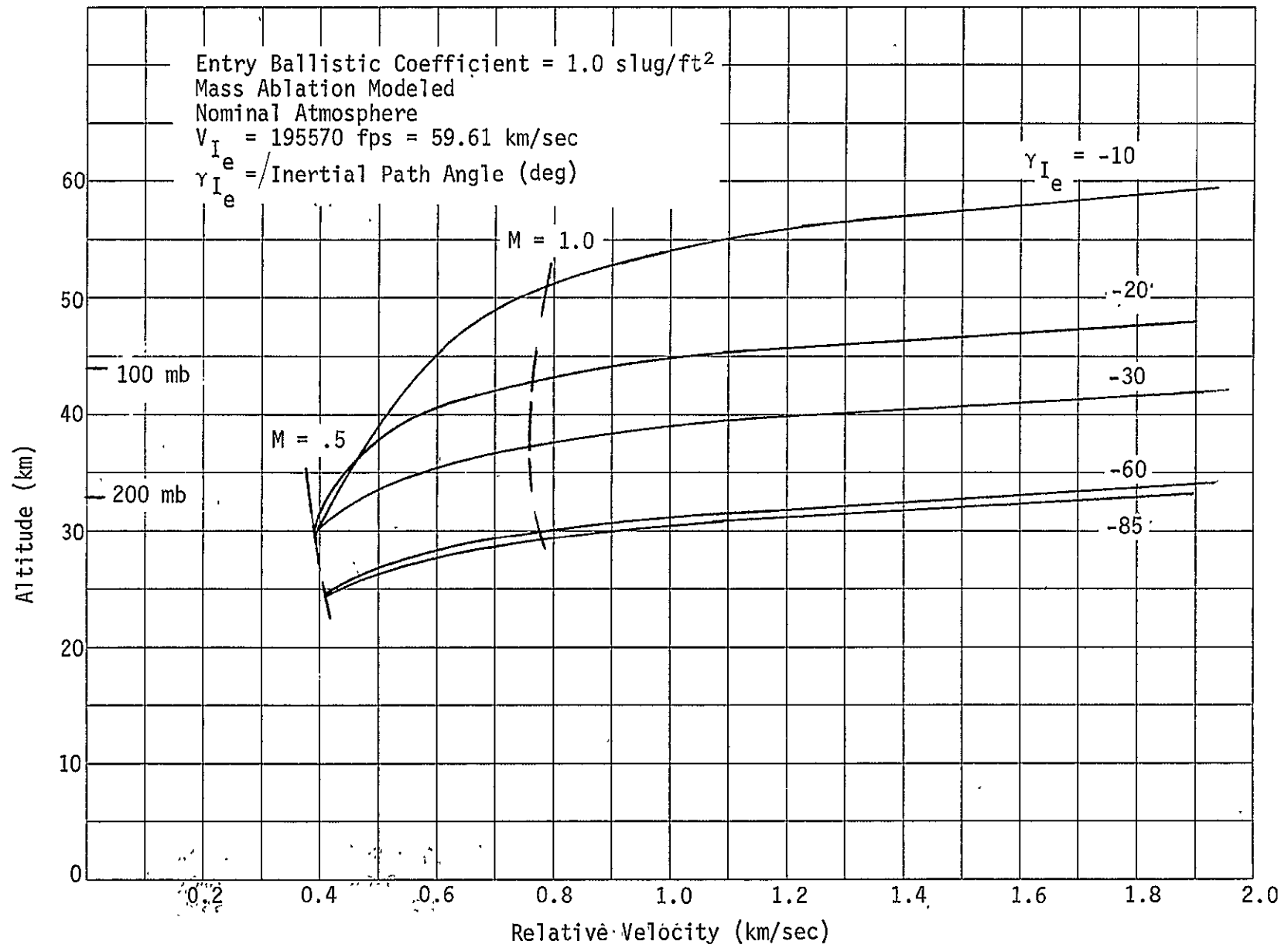


Figure IIID-12 Descent Profile for $B_e = 1.0 \text{ Slug/Ft}^2$

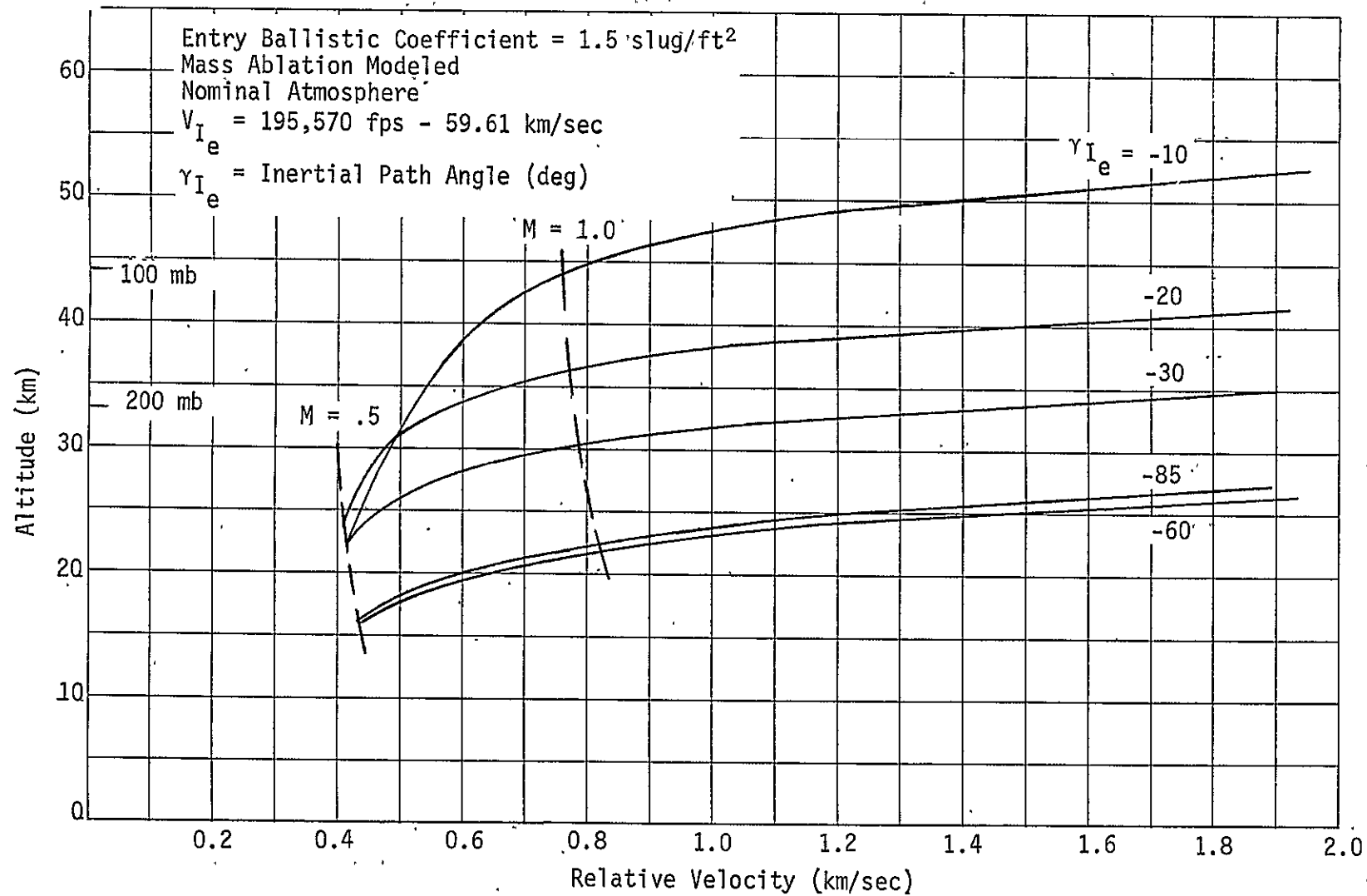


Figure IIID-13 Descent Profile for $B_d = 1.5 \text{ Slug/Pt}^2$

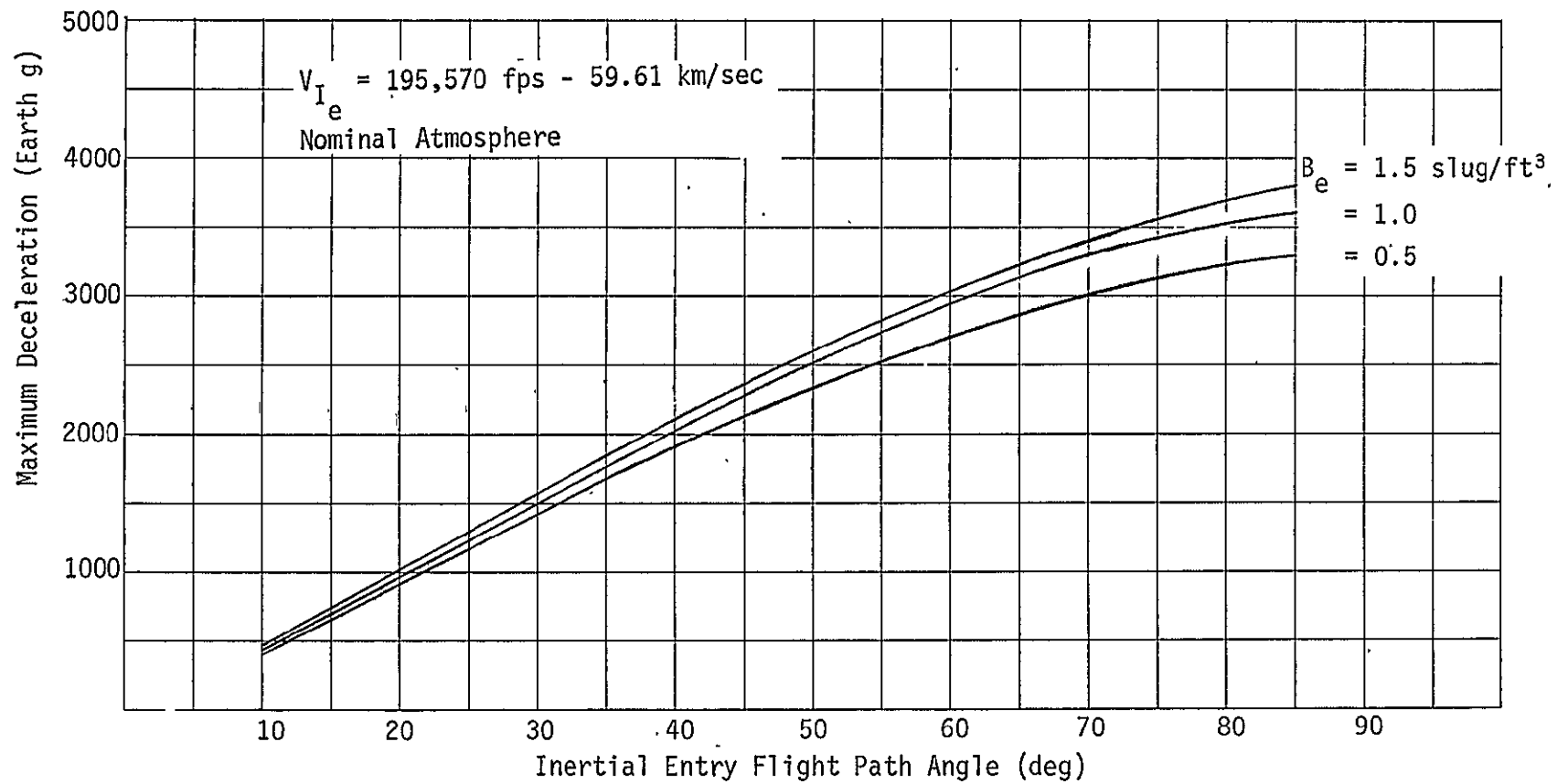


Figure IIID-14 Variation of Peak Deceleration with Entry Angle

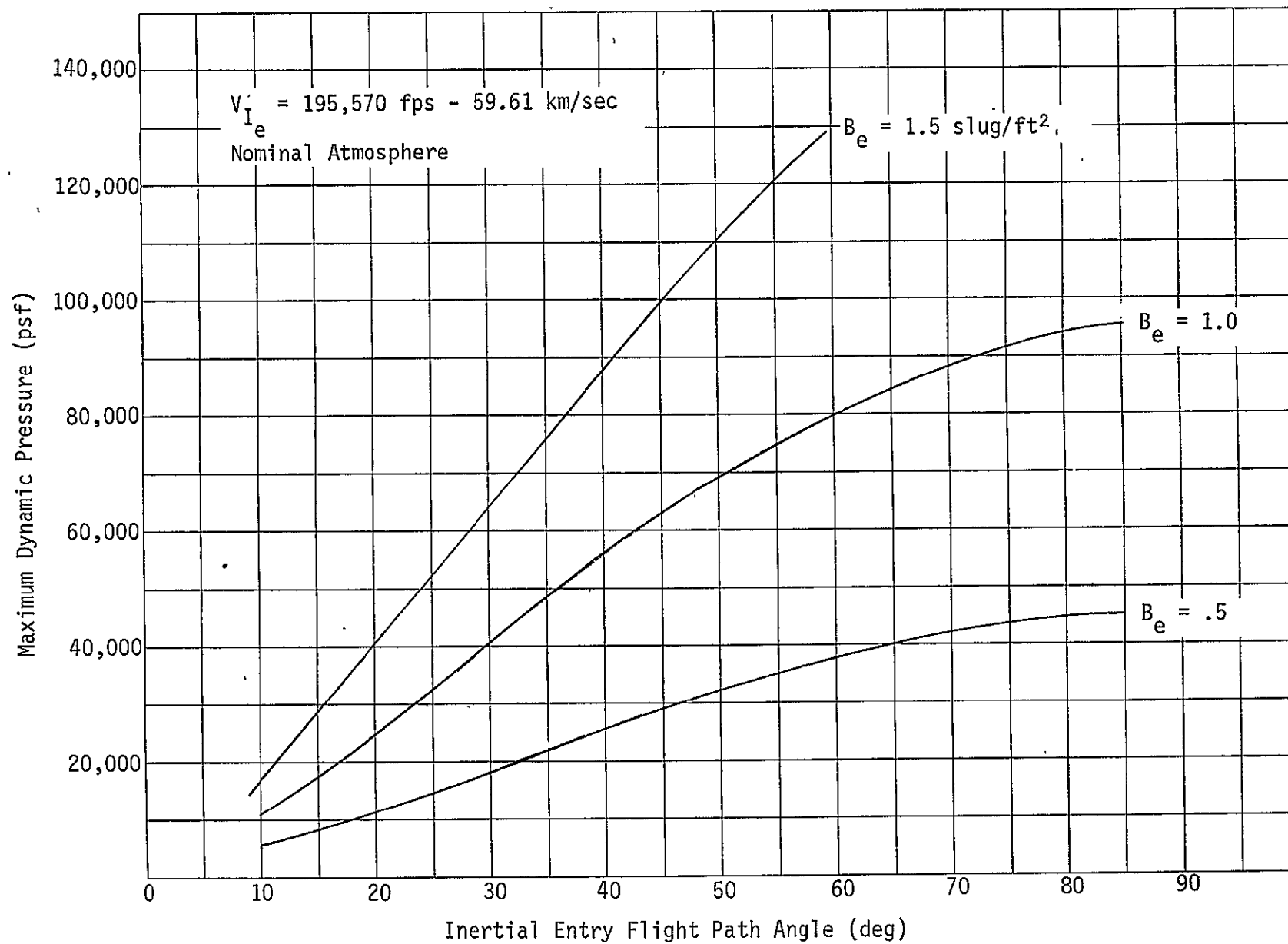


Figure IIID-15 Variation of Peak Dynamic Pressure with Entry Angle

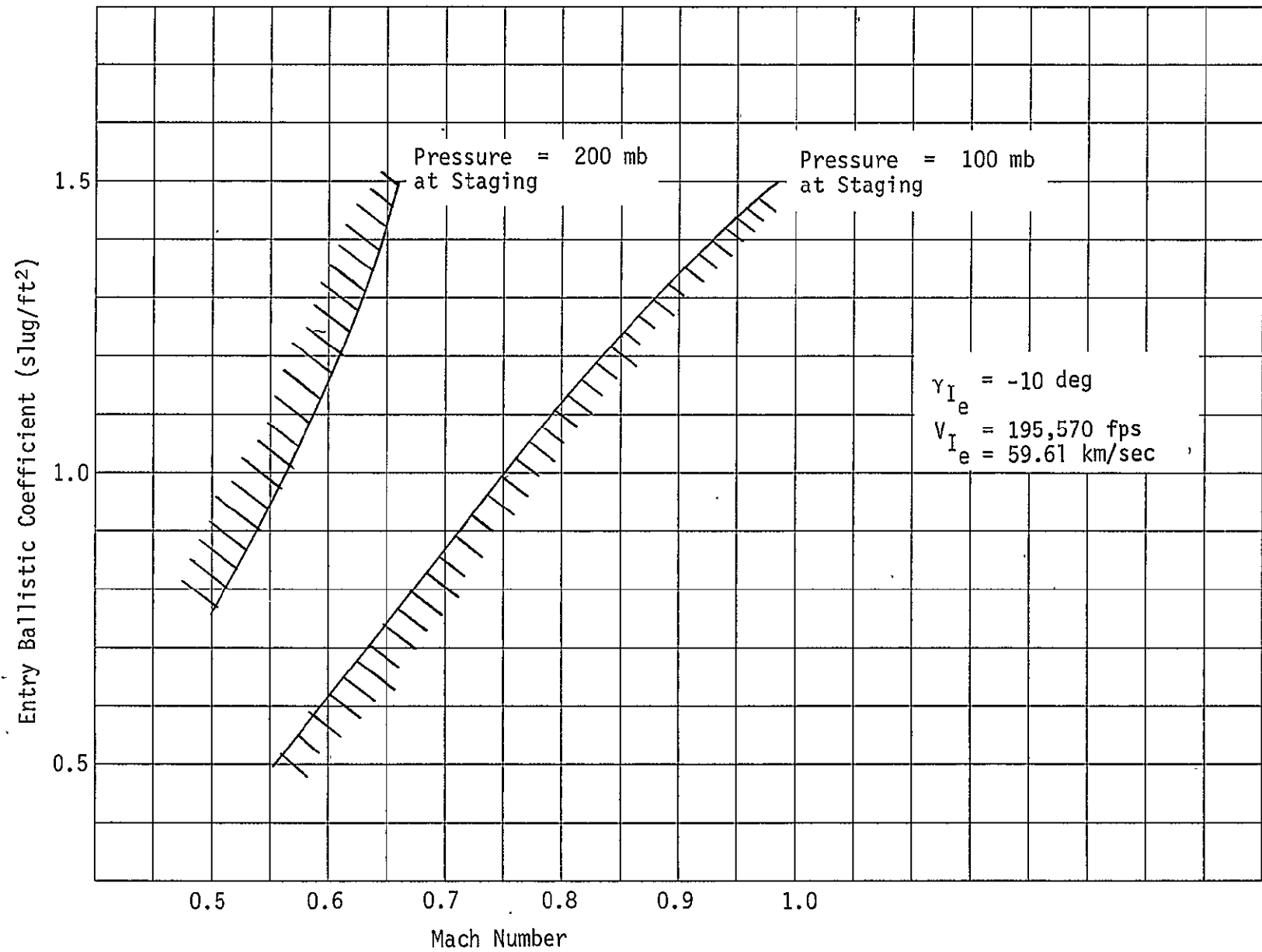


Figure IIID-16 Mach Number at Staging Pressures of 100 & 200 mb

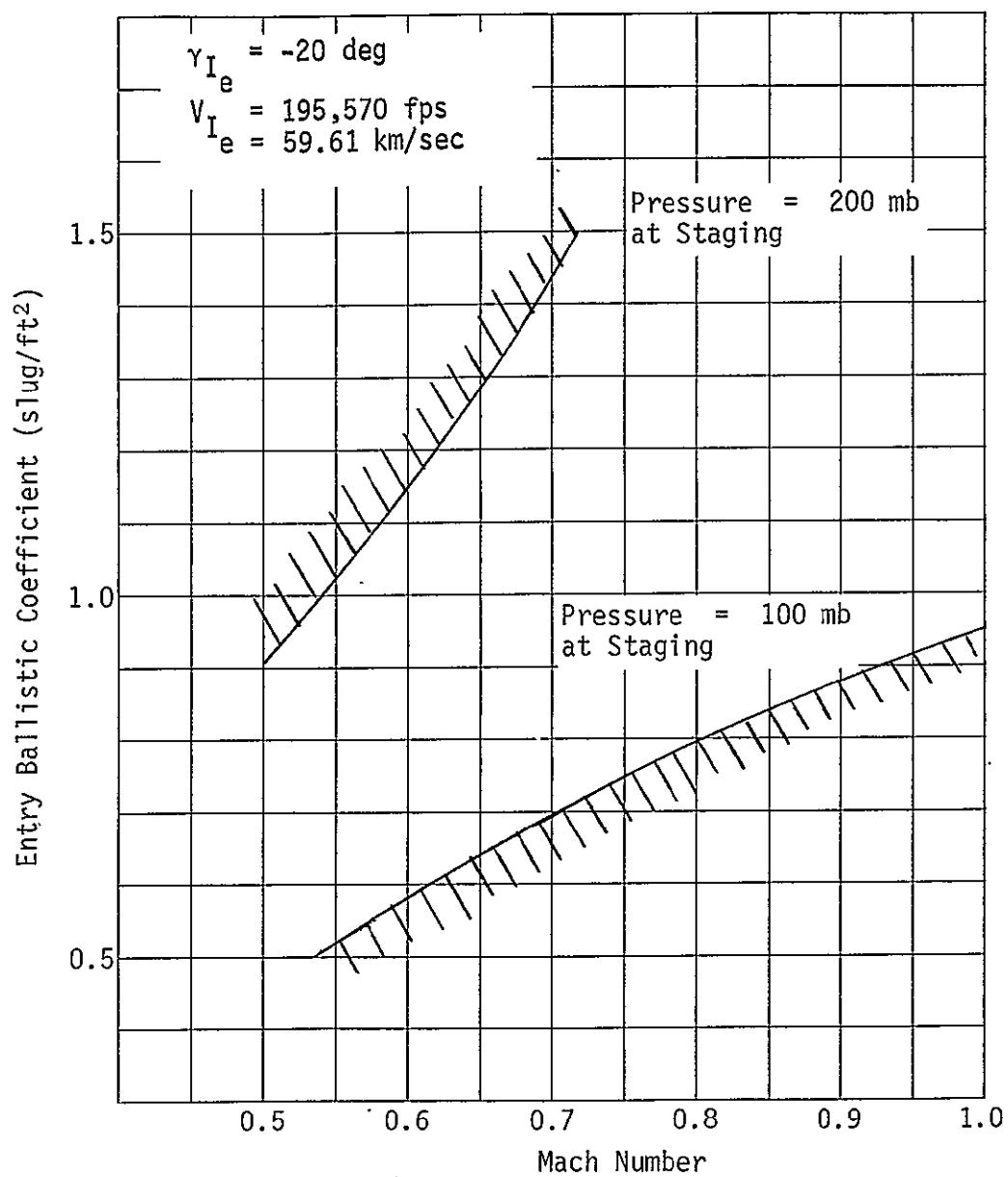


Figure IIID-17 Mach Number at Staging Pressures of 200 & 100 mb

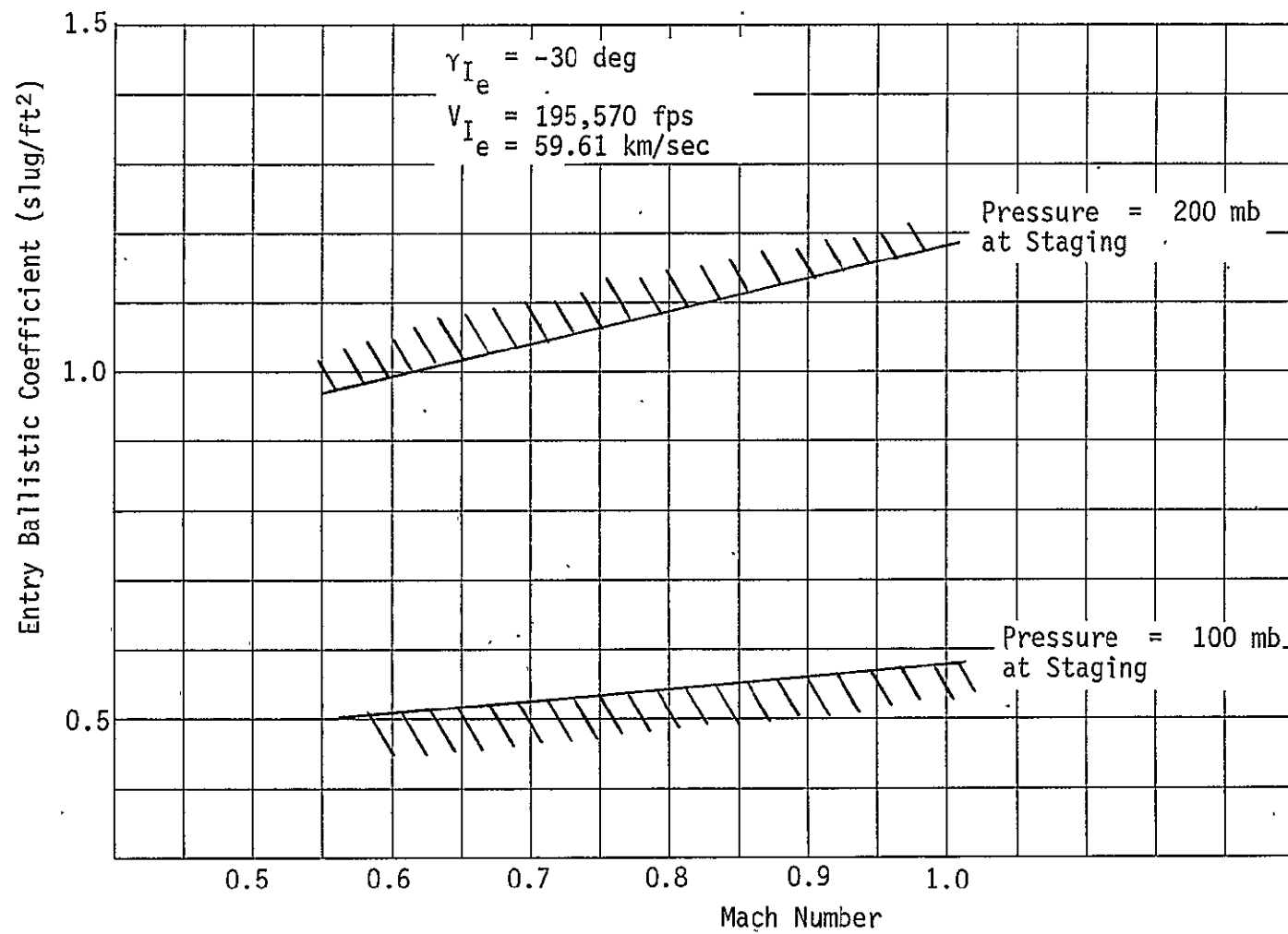


Figure IIID-18 Mach Number at Staging Pressures of 100 & 200 mb

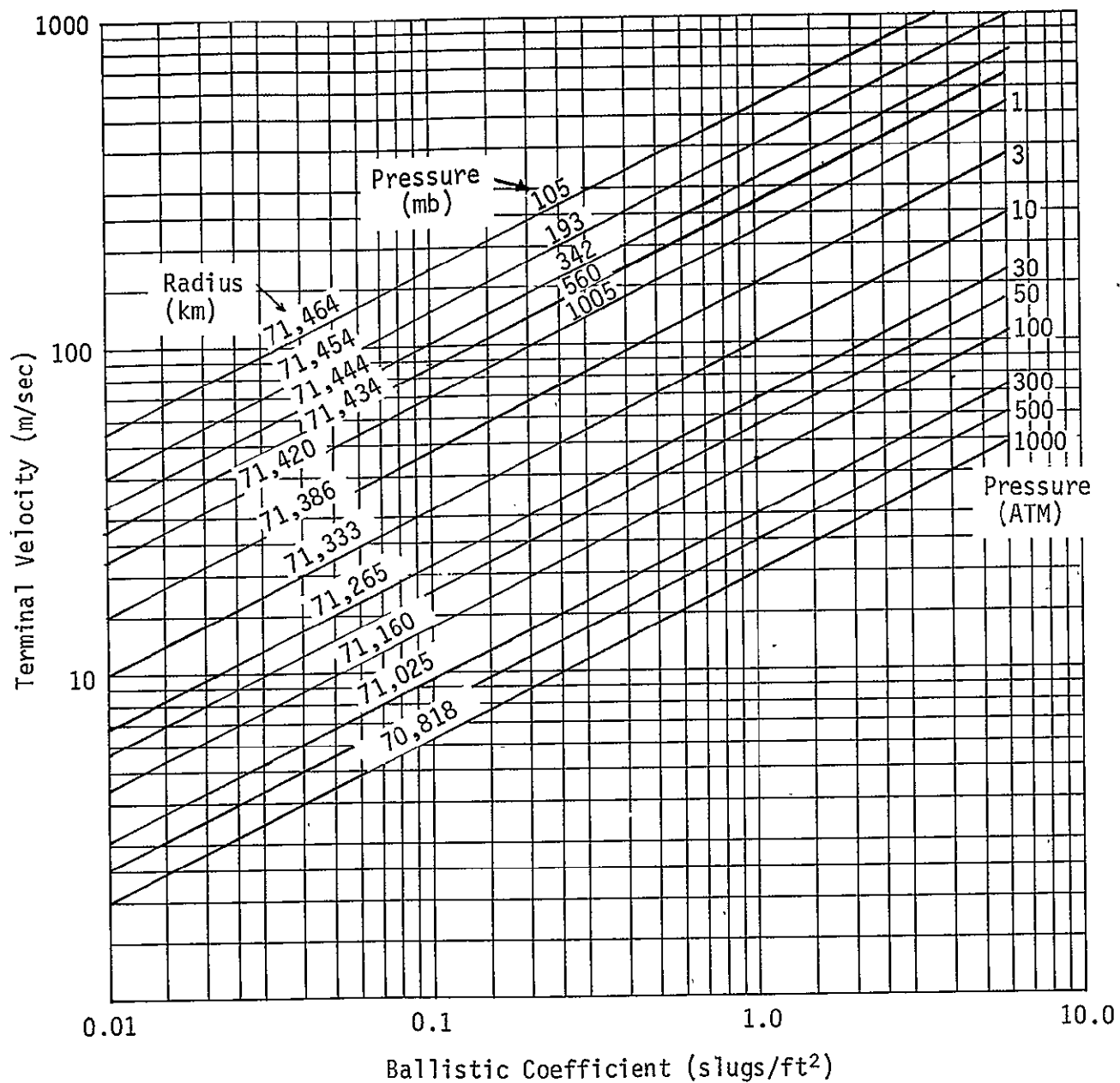


Figure IIID-19 Terminal Velocities for Nominal Atmosphere

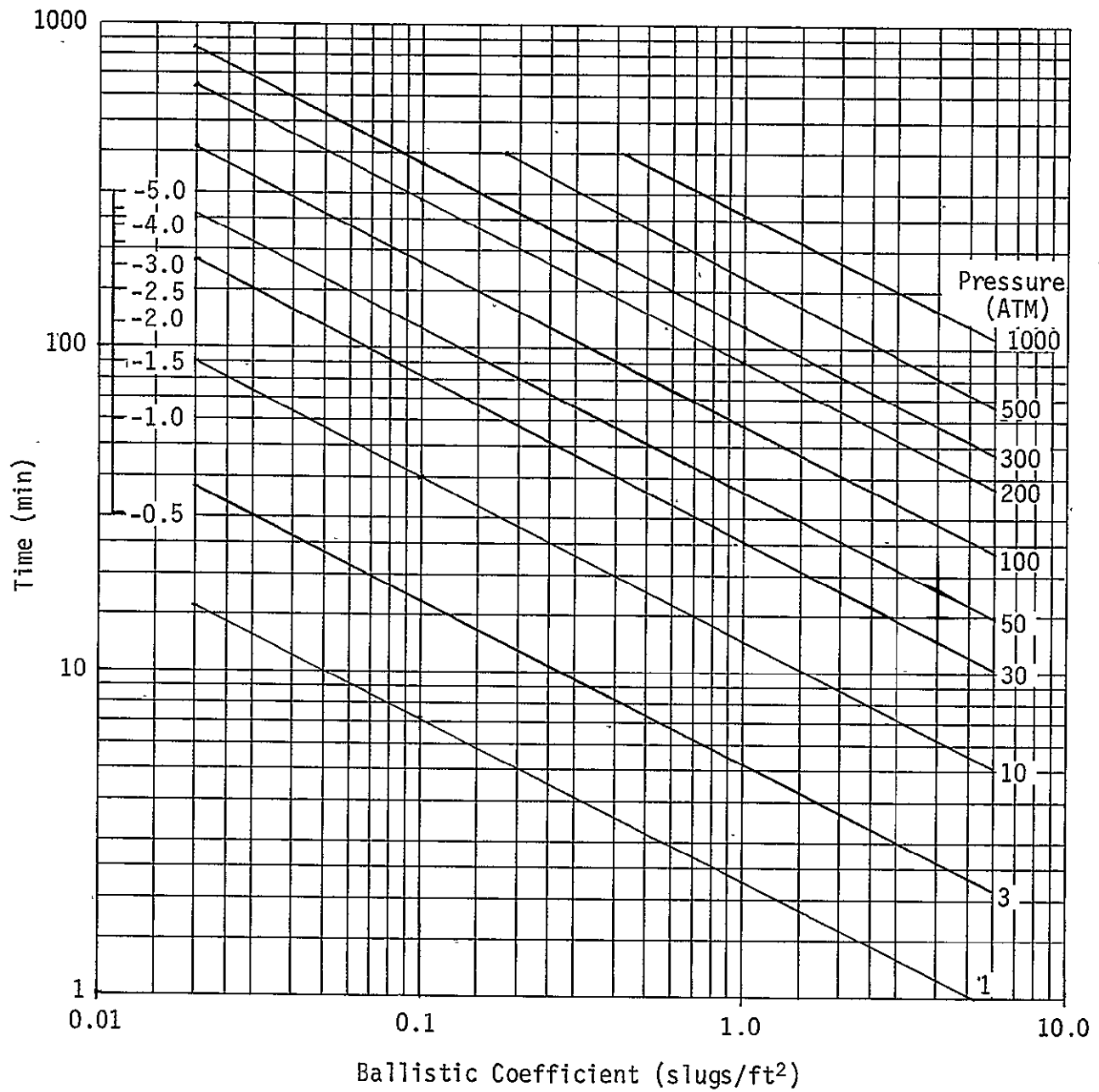


Figure IIID-20 Descent Times from 100 mb for Nominal Atmosphere

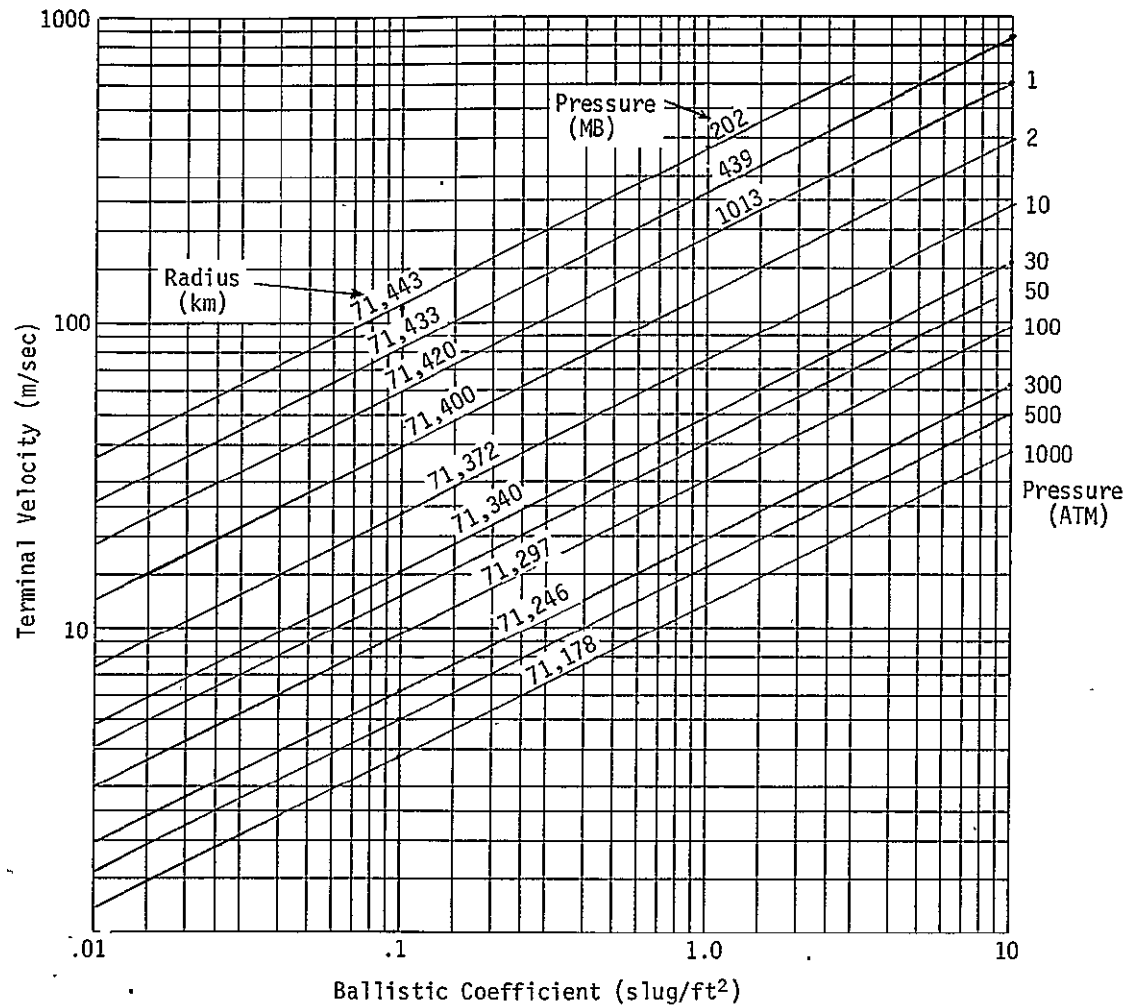


Figure IIID-21 Terminal Velocities for Lewis Cool

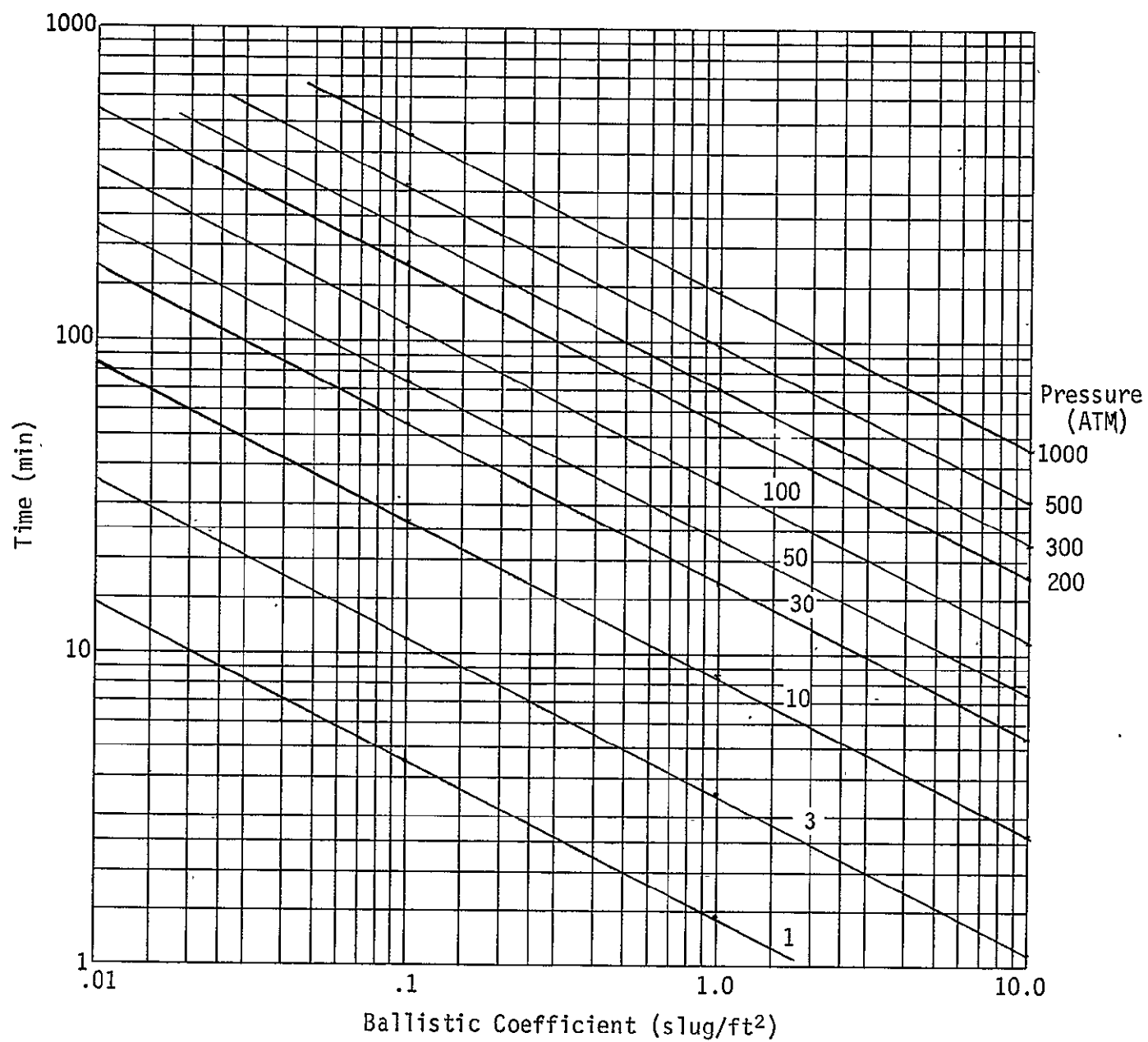


Figure IIID-22 Descent Times from 200 mb for Lewis Cool

E. Navigation and Accuracy

An accuracy analysis was conducted for three of the Jupiter atmospheric probe missions considered in this study. Monte Carlo techniques were employed to obtain the dispersions in the probe entry parameters, probe spacecraft communication geometry, and communications power requirements. Four sources of error were evaluated: errors in the maneuver which deflects the probe from the spacecraft, uncertainties in the spacecraft and probe states due to orbit determination errors, uncertainties in the radial location of the one atmosphere pressure level of the Jupiter atmosphere and uncertainties in the Jupiter gravitational constant. The effects and relative importance of each of these error sources are described for the three missions considered.

Probe Deflection System Errors

Deviations in the implemented deflection velocity from the commanded are generated using a three parameter error model. The first error source is the proportionality error and is in the direction of the deflection velocity with magnitude determined by the proportionality factor k . The second error source, in the direction of the deflection velocity but independent of its magnitude, is the resolution error s that corresponds to a thrust tailoff error from the deflection engine. The deflection velocity pointing error is the third error source. These errors are assumed uncorrelated and normally distributed with zero mean values.

The accuracy analyses assumed proportionality errors of 1%, 2%, 4.5% (3 σ); pointing errors of 1 deg., 1.5 deg., 2. deg., and 4.5 deg., (3 σ); and resolution error of .152 m/sec (3 σ). Proportionality and pointing errors of 1% and 1 deg., are representative of the accuracy that can be achieved with a sophisticated probe guidance system⁽¹⁾ (strapdown inertial measurement unit an onboard computer) and a three axis stabilized spacecraft such as TOPS. Somewhat poorer performance can probably be expected for deflection from a spinning spacecraft (see Chapter V, Section E for discussion).

NAVIGATION

The navigation analysis is concerned with determining the uncertainties associated with the spacecraft state vector at probe deflection time as a result of processing subsequent tracking measurements. The navigation analysis was conducted for alternate mission B. The type II approach trajectory was targeted using the targeting mode of the Simulated Trajectories Error Analysis Program⁽²⁾ (STEAP). The properties of the resulting n-body trajectory* are listed in Table III E1.

The first phase of the analysis generated the navigation uncertainty covariance matrices at probe deflection assuming a large a priori navigation uncertainty matrix at 50 days before spacecraft periapsis or encounter (E). Probe deflection was assumed to take place at E-13 days. The second phase of the navigation analysis examined the implication of deflecting the probe at an earlier time.

For the first phase, navigation uncertainties were generated assuming two types of measurements--range-rate (doppler) measurements from the DSN tracking stations, and Jupiter/Canopus angle measurements made by a sensor onboard the spacecraft.

Uncertainties in the approach trajectory due to tracking accuracy, injection errors, midcourse maneuver implementation errors and unmodeled accelerations are given in terms of the control and knowledge covariance matrices. The probabilistic dispersions of deviations in the estimated spacecraft state about the actual is given by the 6 x 6 knowledge covariance matrix P_k , which is a function of the orbit determination process only. The probabilistic dispersion of deviations in the actual spacecraft state about the nominal is given by the 6x6 control covariance matrix P_c . P_c is a function of the tracking process, injection errors, midcourse maneuver implementation errors and unmodeled accelerations.

This analysis assumes that the control uncertainties at probe deflection time are entirely due to knowledge uncertainties (tracking uncertainty) at the time of the last midcourse maneuver which precedes the probe deflection maneuver. Experience in orbit determination problems has shown this to be a good assumption especially when the knowledge uncertainties are large.

*Gravitational bodies included: Sun, Earth, Earth's Moon, Jupiter, Saturn.

Table III E1 Approach Trajectory Parameters

Launch Data - 9-25-78

Launch Energy - $99 \text{ km}^2/\text{sec}^2$

Arrival Date - 11-4-81

 θ (clockwise angle from T axis to B) - -7.5 deg Inclination to Jupiter Equatorial Plane - 10 deg B (miss parameter) - $1,110,000 \text{ km}$ V_{HE} (hyperbolic excess velocity at Jupiter) - 5.47 km/sec Periapsis Radius - $143,000 \text{ km}$ (2 Jupiter radii)

Table III E2 Doppler Measurement Errors

<u>Station Location Errors</u>		<u>Doppler Noise</u>
$\sigma_{r_s} \text{ (m)}$	$\sigma_{r_s \Delta\lambda} \text{ (m)}$	(mm/sec for a 1 minute count time)
0.5	1.0	0.3
1.5	3.0	1.0
2.5	5.0	

Notes: 1. r_s is the station's distance from the Earth's spin axis.2. $\Delta\lambda$ is the station's longitude deviation from nominal

Since only short-tracking arcs (37 days) are considered, unmodeled accelerations during the encounter phase are not included in this analysis.

The navigation analysis was performed using the error analysis mode of STEAP which is based on Kalman recursive filtering theory.⁽³⁾ The STEAP consider recursive estimation algorithm extends the basic Kalman filter equations to consider bias uncertainties in parameters that affect the spacecraft dynamics such as planet ephemeris information. Reference 1 describes the STEAP program in detail. Briefly, the consider parameters are augmented to the state vector and the Kalman filter equations are modified to prohibit any decrease in the consider parameter covariance. However, the consider parameter uncertainties still influence the weighting assigned to the measurements. The state vector can also be augmented to include solve for parameters which are related to the measurements or the system dynamics. The uncertainties associated with these parameters are reduced in the filtering process.

A P_c matrix was calculated for the approach trajectory at probe deflection time. An *a priori* orbit determination uncertainty matrix at encounter (E) minus 50 days was assumed. The *a priori* covariance matrix used uncorrelated spherical position and velocity errors of 1σ magnitude 5000 kilometers in position and 100 m/sec in velocity. Starting with this initial covariance matrix, measurements were processed from E-50 days to E-25 days when the last midcourse maneuver was assumed to take place. P_c was determined by mapping the orbit determination uncertainties at E-25 days along the nominal trajectory to the deflection time t_D which was E-13 days.

P_k was determined by continuing the tracking process from E-25 days to E-14 days and then mapping the uncertainties to E-13 days. Tracking was stopped at one day before probe deflection to allow sufficient time for Earth based computation of the required probe deflection velocity direction and magnitude, sending the deflection command to the spacecraft and confirming the command.

Jupiter ephemeris errors were included in the navigation analysis by augmenting uncertainties in the mean Jupiter ecliptic orbital elements, a , the semi-major axis, i , the inclination and, ω , the argument of periapsis,

to the state vector as consider parameters. The a , i and ω bias uncertainties used in the analysis were derived by evaluating the partial derivatives of Jupiter position with respect to a , i , and ω at probe deflection time. The a , i and ω uncertainties were chosen to produce a spherical 500 km (15') uncertainty⁽⁴⁾ in the position of Jupiter. The uncertainties in a , i and ω used were

$$\delta a = 475 \text{ km}$$

$$\delta i = .127 \text{ arc sec}$$

$$\delta \omega = .127 \text{ arc sec}$$

The navigation analysis was performed assuming DSN doppler data as the sole observable and with DSN doppler data combined with Jupiter/Canopus angle measurements made by a sensor onboard the spacecraft. It was assumed that doppler data was provided from the DSN tracking stations at Madrid, Goldstone and Canberra with each station taking one full pass of data per day. Jupiter/Canopus angle measurements were assumed to take place four times per day.

Results for Doppler Measurements

Table IIIE2 lists the three sets of equivalent station location errors and two values of doppler noise used for the runs made with no onboard sensor measurements. The smallest set of station location errors are the values predicted for DSN performance in the late 1970s⁽⁵⁾ while the largest set is typical of the performance expected for spacecraft with S-band doppler only--lack of X band limits calibration of charged particle effects. The low doppler data noise level is the value predicted for the late 1970s while the larger is the value for the early 1970s.

Navigation results are presented in terms of the knowledge and control position uncertainties in B plane coordinates. The approach trajectory incoming asymptote S is one axis of the orthogonal system. The second axis T is defined by the intersection of the ecliptic plane and the plane normal to S . The third axis R is defined by the vector cross product of S and T .

Table III E3 lists the geocentric navigation uncertainties for the DSN doppler tracking only cases. The 1σ position uncertainty in the S direction is shown as σ_s . SMMA and SMIA denote the semi-major and semi-minor axes of the projection of the position uncertainty ellipsoids on the T R plane. For all cases, the semi-major axis is nearly aligned to the R axis. The navigation uncertainties are insensitive to the doppler data noise level over the 0.2 mm/sec to 1.0 mm/sec range and the results of Table 3 are valid for both noise levels. As shown in Table III E3, the position uncertainties are very sensitive to the DSN equivalent station location errors. Figures III E1 and III E2 show the B plane control and knowledge position uncertainty ellipses for the three sets of equivalent station location errors.

Results for Doppler and Onboard Sensor Measurement

The navigation analysis for the Jupiter/Canopus angle onboard sensor measurement cases was done using DSN equivalent station location errors of $\sigma_{r_s} = 1.5$ m, $\sigma_{r_s \Delta \lambda} = 3.0$ meters, and doppler noise of 0.3 mm/sec. Onboard sensor measurement errors were modeled as noise--random variations uncorrelated between measurements--and bias--a random variation perfectly correlated between measurements. Noise levels from 5 arc sec to 50 arc sec were assumed. When bias uncertainties from 100 arc sec to 400 arc sec were considered, absolutely no improvement in the navigation uncertainties was produced. These bias uncertainty levels cause the filtering process to ignore the onboard sensor measurements. When the bias uncertainty was treated as a solve-for parameter, the bias uncertainty was reduced to approximately 5 arc sec after a few days of measurements and the onboard sensor measurements caused considerable reduction of the navigation uncertainties. As long as the onboard sensor bias is a solve-for parameter, the performance of the sensor is independent of the initial bias uncertainty over the 100 arc sec to 400 arc sec interval.

Table III E4 presents the geocentric navigation uncertainties for the onboard sensor analysis. The major effect of the Jupiter/Canopus angle measurements is the reduction of the position uncertainty in the direction normal to the approach trajectory plane of motion. The semi-minor axis

Table IIIE3 Position Dispersions (1σ) -- Doppler Measurements Only

EQUIVALENT STATION LOCATION ERRORS (m)	CONTROL UNCERTAINTY			KNOWLEDGE UNCERTAINTY		
	SMMA (km)	SMIA (km)	σ_s (km)	SMMA (km)	SMIA (km)	σ_s (km)
$\sigma_{r_s} = 0.5, \sigma_{r_s \Delta\lambda} = 1.0$	1068	125	763	775	92	587
$\sigma_{r_s} = 1.5, \sigma_{r_s \Delta\lambda} = 3.0$	1950	146	994	1561	114	848
$\sigma_{r_s} = 2.5, \sigma_{r_s \Delta\lambda} = 5.0$	2556	168	1075	2021	125	919

Table IIIE4 Position Dispersions (1σ) -- Doppler and Onboard Sensor Measurements

JUPITER/CANOPUS ANGLE MEASUREMENT NOISE (arc sec)	CONTROL UNCERTAINTY			KNOWLEDGE UNCERTAINTY		
	SMMA (km)	SMIA (km)	σ_s (km)	SMMA (km)	SMIA (km)	σ_s (km)
5	370	149	781	260	113	719
20	990	149	832	485	112	725
30	1294	149	877	657	113	735
50	1625	148	929	939	113	759

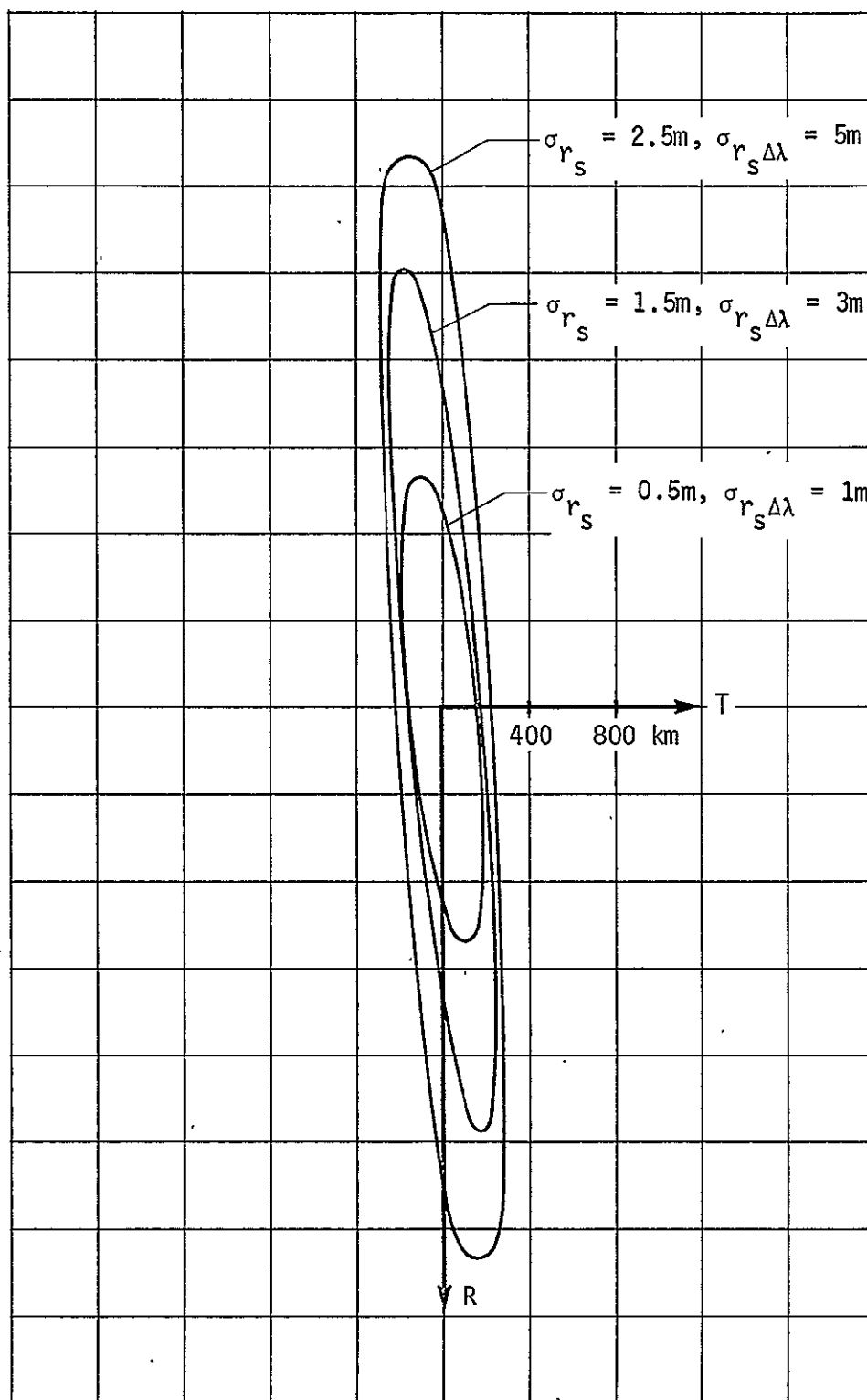


Figure III E1 B Plane Control Uncertainty (1σ) Ellipses -
Doppler Measurements Only

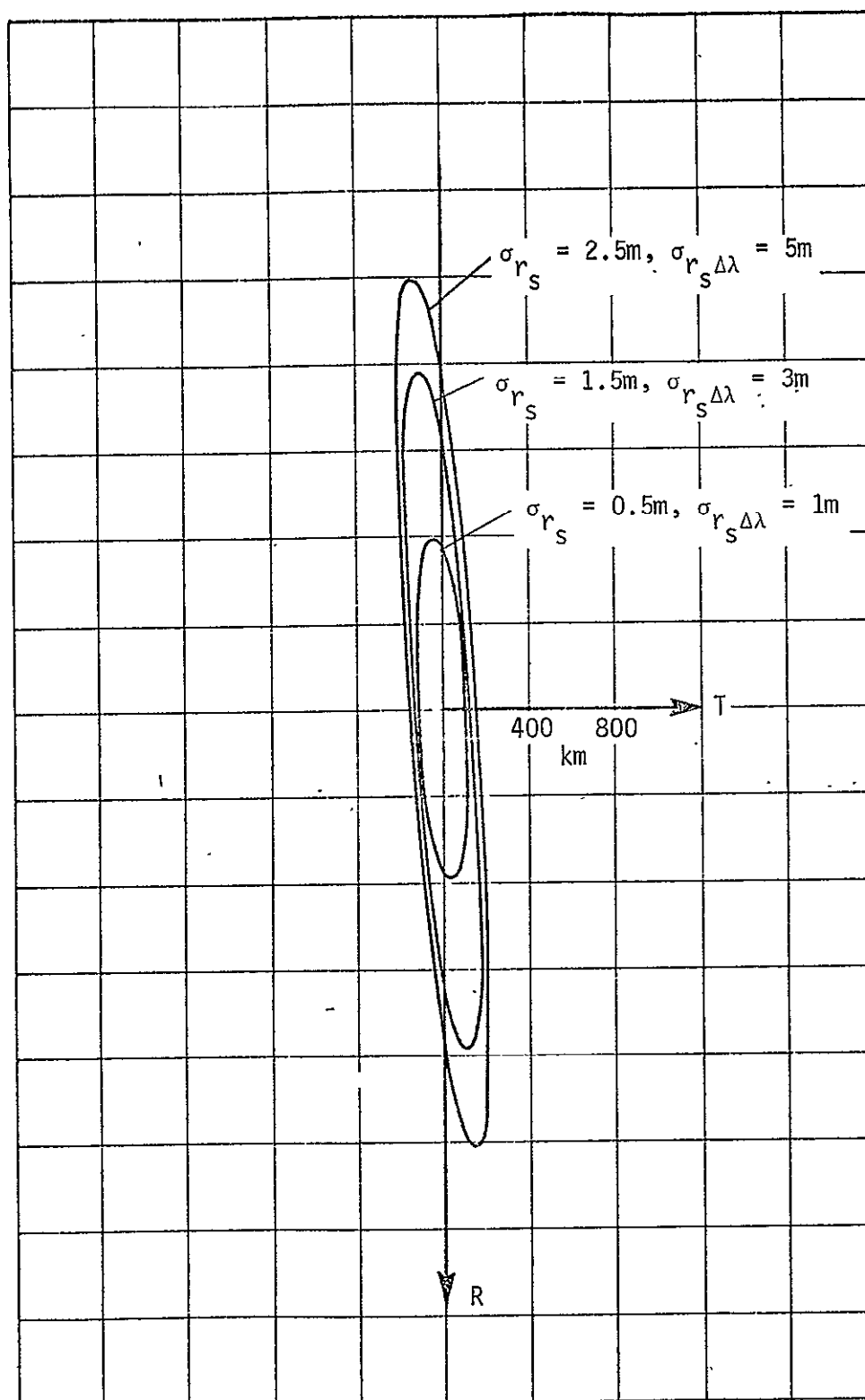


Figure III E-2 B Plane Knowledge Uncertainty (1σ) Ellipses - Doppler Measurements Only

position uncertainty which is nearly ~~the~~ position uncertainty along B is not significantly influenced by the addition of the onboard sensor measurements. Position uncertainty normal to the impact plane is reduced slightly. Figure IIIE3 and IIIE4 show the control and knowledge B plane position uncertainty ellipses for the onboard measurement cases.

The second phase of the navigation analysis establishes the efficacy of DSN doppler data in reducing the orbit determination uncertainties as a function of tracking time and the distance of the spacecraft from Jupiter. This information is one consideration in establishing the probe deflection radius. Since the probe deflection velocity is approximately proportional to the distance from Jupiter for a given entry flight path angle and lead angle, a large deflection radius is desirable from a deflection system weight standpoint. However, orbit determination uncertainties are reduced as the spacecraft approaches the planet due to the increased curvature of the trajectory. Thus a small deflection radius is desirable from a navigation standpoint.

To establish the effects of distance from Jupiter on orbit determination errors, tracking was started at 99, 82 and 50 days before entry. These times correspond to spacecraft/Jupiter distances of 5.7×10^7 km, 4.8×10^7 km, and 3×10^7 km. The a priori covariance matrix, doppler measurement schedule, ephemeris error and doppler noise discussed earlier were used for each case. No onboard sensor measurements were assumed. DSN station locations of $\sigma_{r_s} = 2.5$ m and $\sigma_{r_s \Delta\lambda} = 5.0$ m were used.

At several times after the start of tracking, the covariance matrices were propagated to E-13 days allowing comparison of the uncertainties at the same time point for a given tracking length. Figure IIIE5 shows the navigation uncertainties at E-13 days as a function of the number of days of tracking for each of the tracking start times. Comparison of the B plane position uncertainties for tracking started at E-50 days and E-99 days shows that the E-50 day tracking is almost twice as effective in reducing SMMA uncertainties and 5 times more effective in reducing SMIA uncertainties. The σ_{λ} uncertainties are smaller for the earlier tracking since the spacecraft velocity vector is more nearly aligned to S so that the earlier doppler data contains more S direction information.

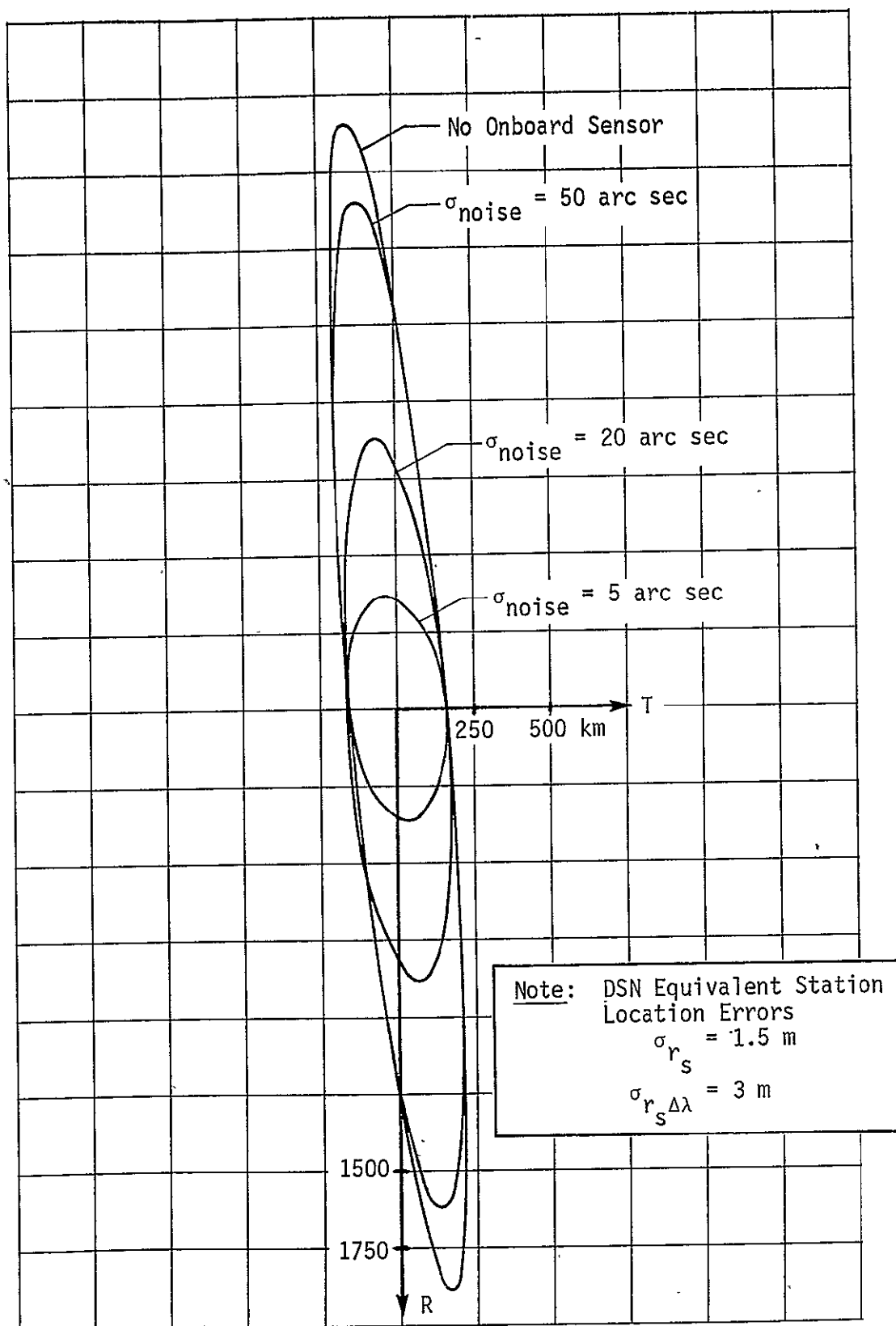


Figure III E-3 B Plane Control Uncertainty (1σ) Ellipses - Doppler and Onboard Sensor Measurements

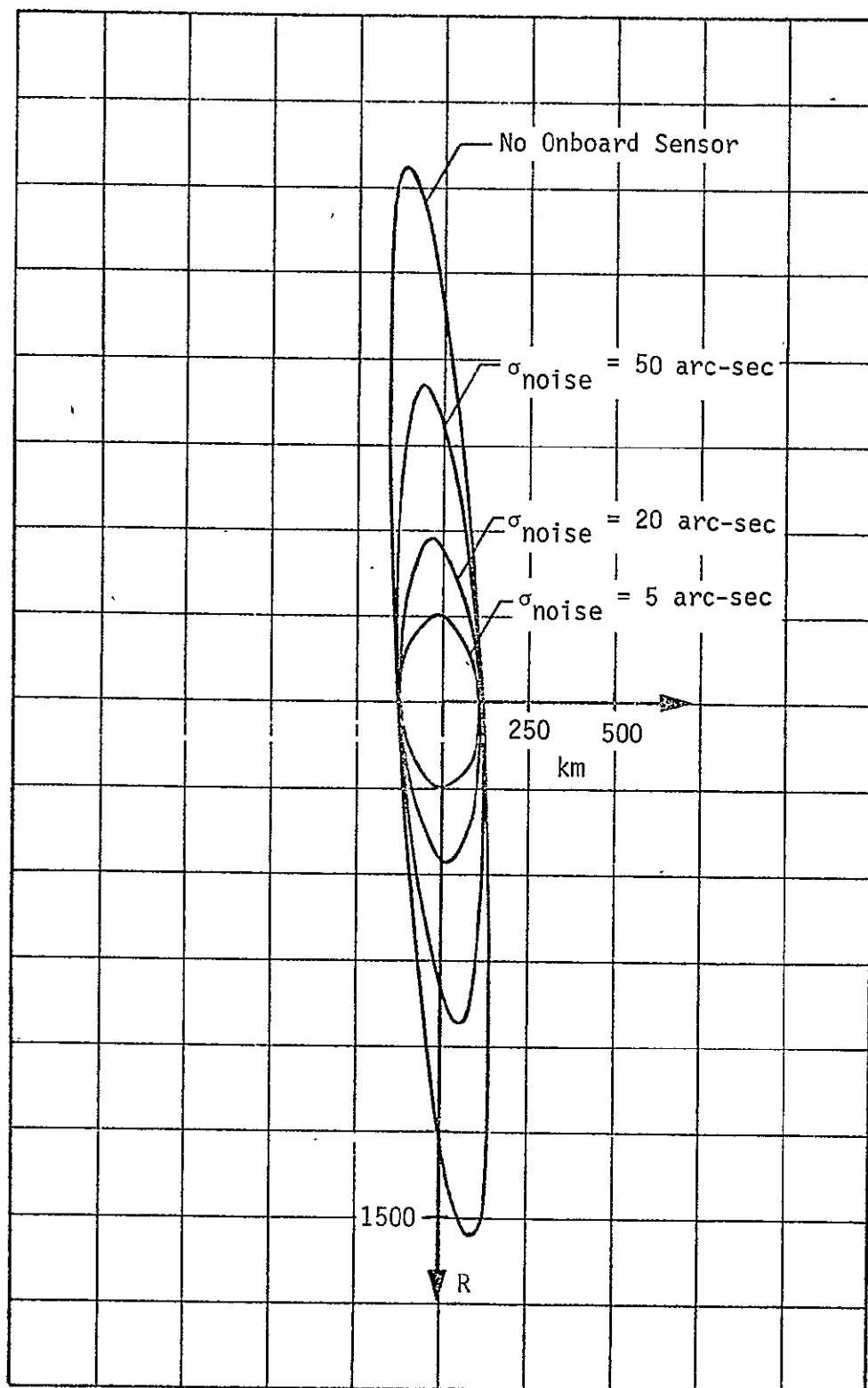
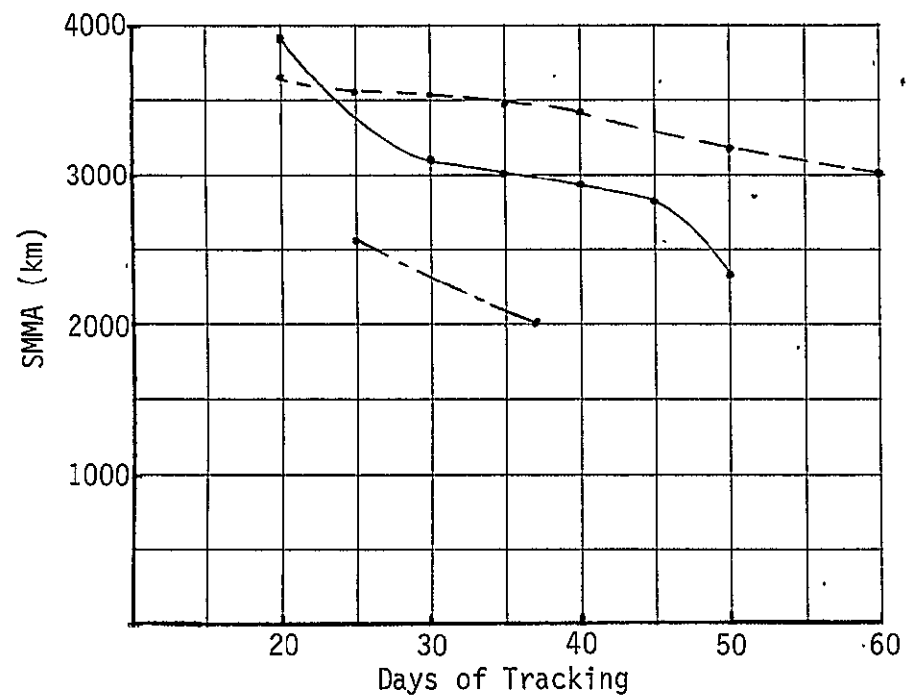


Figure IIIE-4 B Plane Knowledge Uncertainty (1σ) Ellipse - Doppler and Onboard Measurements



Tracking Initiated at
 S.O.I. ~ E-82.4 Days
 E-50 Days
 E-99.2 Days

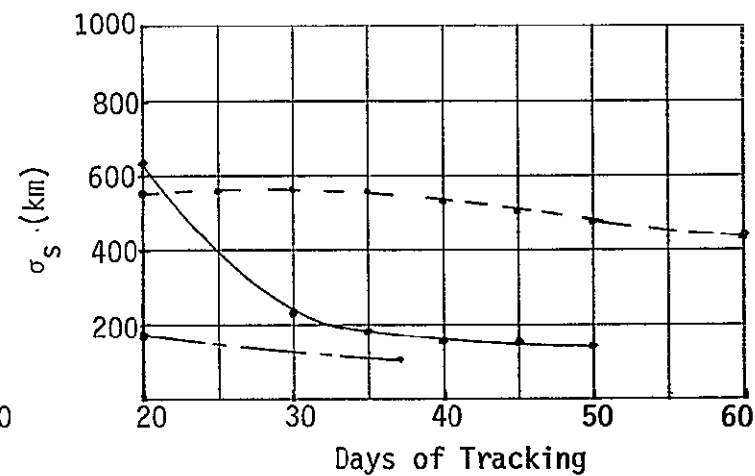
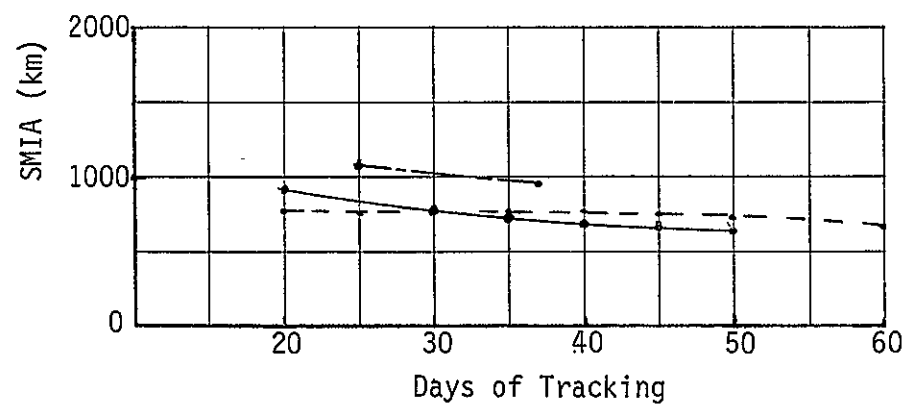


FIGURE III E-5 B Plane Uncertainty at E-13 Days

Atmospheric Radius Uncertainty

The nominal Jupiter atmosphere was used in the analysis with the one atmosphere reference level assumed to be uncertain by 1000 km (3σ). This seems to be a realistic number since the planet radius estimates are based on optical observations whose resolution is limited to approximately .1 arc sec. This compounds to a radius uncertainty of approximately 400 km.

In addition, the distance between the one atmosphere level and the visible cloud tops is not well known. The analysis does not include the various atmosphere models. The impact of this uncertainty is discussed with the Monte Carlo results.

Gravitational Constant Uncertainty

In accordance with Ref 6, the uncertainty in the Jupiter gravitational constant (μ_J) expressed in terms of the Jupiter reciprocal mass ratio (mass of Sun/mass of Jupiter) is $1047.3908 \pm .07$. Then $\mu_J = 1.267077188 \times 10^8 \pm 8470$ (1σ) km^3/sec^2 . This uncertainty is only .0066% of the nominal μ_J . Results of the Mission B Monte Carlo analysis indicate that the impact of errors in the Jupiter gravitational constant are negligible.

Monte Carlo Analysis

A Monte Carlo analysis was used to determine the dispersions in critical mission parameters due to the previously described error sources. The parameters of interest are:

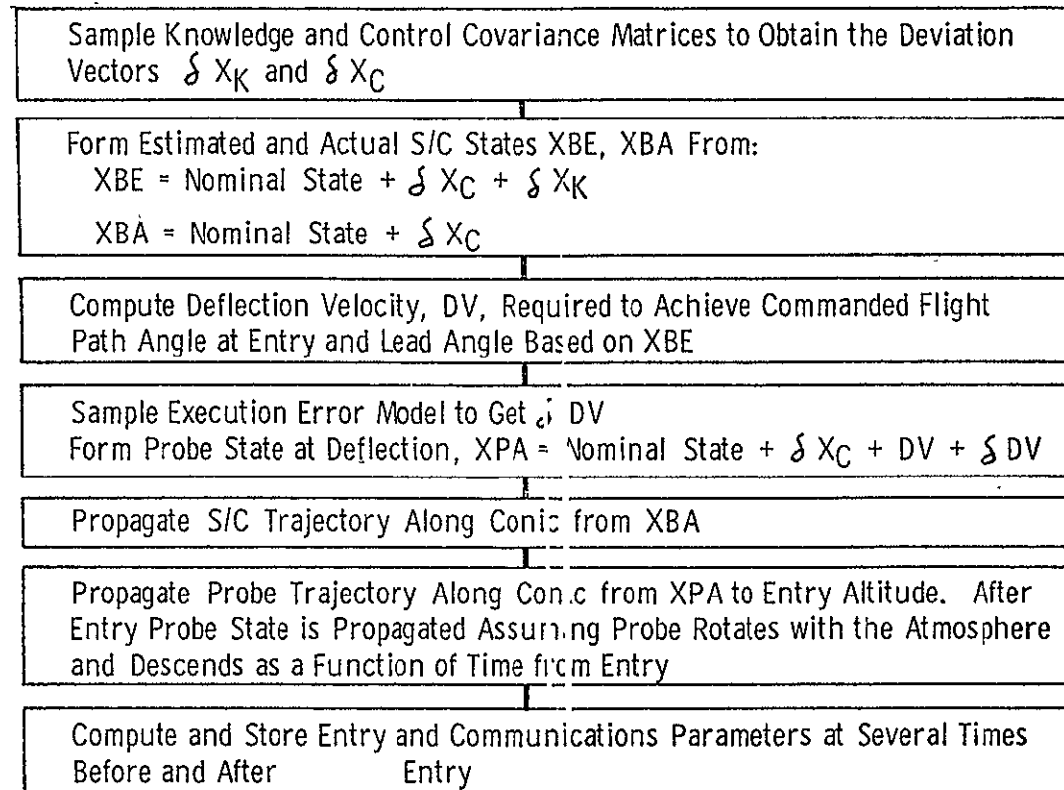
1. Probe flight path angle at entry
2. Probe deflection velocity
3. Lead time (time from probe entry to spacecraft periapsis)
4. Latitude and longitude of probe entry
5. Probe/spacecraft range, range rate, range acceleration
6. Probe/spacecraft communication power losses
7. Spacecraft antenna pointing angles

Figure III-E-6 illustrates the Monte Carlo sampling procedure. In the first block of Figure III-E-6, the knowledge and control matrices are samples to produce random deviations δX_k and δX_c . The sampling is done as follows:

Let P represent P_K or P_c then since P is positive definite it may be diagonalized.

$$P = T^T D T$$

④ SAMPLING PROCEDURE



⑤ CALCULATE STATISTICS BASED ON THE COMPUTED PARAMETERS FROM 250 MONTE CARLO SAMPLINGS

Figure IIIE6 Monte Carlo Analysis

where $D = \text{diag} (d_{11}^2, d_{22}^2, d_{33}^2, d_{44}^2, d_{66}^2)$ and T is the orthonormal matrix of the eigenvectors of P . The elements of D are written as squares to indicate they are necessarily positive numbers. T defines a transformation from the original cartesian coordinate system to a new system in which the covariance matrix is uncorrelated, thereby allowing the individual components to be sampled independently. A vector random variable from a distribution of mean zero and covariance D is given by:

$$\xi_z = (e_1 d_1, e_2 d_2, \dots, e_6 d_6)^T$$

where each of the e_i is a scalar random variable sampled from a normal distribution of mean zero and standard deviation unity. The e_i are computed from the formula:

$$e_i = (-2 \ln \alpha_i)^{1/2} \cos (2 \pi \beta_i)$$

where α_i and β_i are random numbers generated from a uniform distribution over the interval $(0, 1)$. The correlated deviation in the original cartesian coordinates may now be computed using the transformation matrix T as

$$\xi_x = T \xi_z$$

A statistically consistent estimate of the spacecraft state at probe deflection time is then given by the vector sum of the nominal spacecraft state, the control deviation and the knowledge deviation. The actual state of the spacecraft is the nominal state plus the control deviation.

The commanded probe deflection velocity is computed as a function of the estimated spacecraft state at deflection, the desired probe flight path angle at entry γ_c and the desired lead angle λ_c . The lead angle is the angle between the radius vector to the probe at entry and the radius vector to the spacecraft at the time of entry. The lead angle is negative when the probe leads the spacecraft. The deflection velocity is determined by iterating on the value of $\Delta\theta$, the true anomaly increment of the probe in going from deflection to entry. The true anomaly of the probe at entry f_{PE} can be expressed as:

$$f_{PE} = f(\gamma_c, R_{EJ}, \Delta\theta, R_A)$$

where R_{EJ} is the radius of the bus at deflection and R_A is the radius of the atmosphere. f_{PE} , R_{EJ} , $\Delta\theta$, R_A are used to compute the time of flight T from deflection to probe entry using the universal form of Kepler's Equation as presented in Ref. 7. The spacecraft state is then propagated forward for time T , again using the universal form of Kepler's Equation, and the angle λ is computed from the state of the spacecraft and the state of the probe at time T . The angle λ is compared with the desired λ_c and $\Delta\theta$ which causes λ to be within .01 degrees of λ_c is found the orbital elements of the probe are known and the required deflection velocity vector is calculated. The commanded deflection velocity is in the spacecraft plane of motion.

The deviations in the implemented deflection velocity from the commanded are generated using the model developed in Ref. 2. This model assumes the implementation error is given by three sources: proportionality error K , resolution error S , and pointing angle error α . These errors are assumed uncorrelated and normally distributed. The standard deviation of each error (σ_K , σ_S , σ_α) is input to the program. The error used in each Monte Carlo sample is generated by:

$$(K, S, \alpha) = (e_1 \sigma_K, e_2 \sigma_S, e_3 \sigma_\alpha)$$

where each e_i is a scalar random variable sampled from a normal distribution of mean zero and standard deviation unity.

The state of the probe at deflection is then given by the actual state of the spacecraft plus the actual deflection velocity. The actual deflection velocity is the commanded plus the implementation errors obtained by sampling the error sources described above.

Jupiter gravitational constant uncertainties are incorporated by sampling a normal distribution with mean zero and standard deviation σ_μ , the uncertainty in the gravitational constant. The sum of the sample deviation and the nominal gravitational constant is used as the gravitational constant in propagating the probe and spacecraft states from deflection to entry time. Atmospheric radius uncertainties are included by sampling from a normal distribution

with standard deviation $\sqrt{R_A}$, the uncertainty in the radius and adding the sample value to the nominal to form the actual radius for each sample.

The spacecraft state at any time after deflection is found by propagating the actual state at deflection along the conic whose elements are defined by the actual spacecraft state at deflection. The probe state at any time before entry is determined by propagating the state along the conic defined by the actual probe state at deflection. After the probe reaches actual entry altitude, the probe velocity is set to that of the Jupiter atmosphere and the position is computed by assuming the probe rotates with the atmosphere and descends as a function of time from actual entry.

The probe antenna axis orientation is computed assuming the antenna is aligned to the negative roll axis of the probe and that during flight from deflection to entry, the roll axis is aligned to the direction of the velocity vector at entry (zero angle of attack). After entry the antenna orientation is local vertical.

The standard deviation of the entry flight path angle $\sqrt{\gamma}$, the probe deflection velocity DV and lead time are calculated as follows. Let γ_i be the value of γ from the i^{th} Monte Carlo sample and N be the total number of samples. Then

$$\sigma_{\gamma} = \left[\sum_{i=1}^N \frac{\gamma_i^2}{N} - \frac{1}{N^2} \left(\sum_{i=1}^N \gamma_i \right)^2 \right]^{\frac{1}{2}}$$

σ_{DV} and $\sigma_{\text{lead time}}$ are calculated in the same way.

Entry site dispersions are determined by computing the covariance of the entry latitude and longitude. Let x_i and y_i be the latitude and longitude of the probe at entry (probe radius vector magnitude = R_A) for the i^{th} Monte Carlo sample. Longitude is referenced to the subsolar meridian. Then the covariance of the latitude and longitude P_{LL} is the 2×2 matrix whose elements are given by

$$\begin{aligned}
\left(P_{LL}\right)_{1,1} &= \sum_{i=1}^N \frac{x_i^2}{N} - \frac{1}{N^2} \left[\sum_{i=1}^N x_i \right]^2 \\
\left(P_{LL}\right)_{2,2} &= \sum_{i=1}^N \frac{y_i^2}{N} - \frac{1}{N^2} \left[\sum_{i=1}^N y_i \right]^2 \\
\left(P_{LL}\right)_{1,2} &= \left(P_{LL}\right)_{2,1} = \sum_{i=1}^N \frac{x_i y_i}{N} - \frac{1}{N^2} \sum_{i=1}^N x_i \sum_{i=1}^N y_i
\end{aligned}$$

For each Monte Carlo sample, probe/spacecraft communication power losses and spacecraft antenna pointing angles are calculated at five times in the interval from two hours before entry to entry and at ten time points after probe entry. The time points can be referenced to nominal or actual entry. The communication power losses are those due to range attenuation, atmospheric attenuation and probe aspect angle*. The method used to determine the standard deviation of the power loss at each time point is the same as that used for σ_y .

Spacecraft antenna pointing is prescribed in terms of cone and clock angles referenced to Earth and Canopus. The antenna pointing dispersions are found by computing the covariance of the cone and clock angles at each time point. The method used is the same as that used for the latitude and longitude covariance.

*Probe aspect angle is the angle between line of sight from probe to spacecraft and the probe antenna axis.

MONTE CARLO RESULTS - ALTERNATE MISSION A

Alternate mission A has a type I grand tour approach trajectory with a 6.8 Jupiter radius closest approach distance. The probe is deflected when the spacecraft is 3×10^7 km from Jupiter. Since the dispersions in the probe trajectory due to navigation errors are much smaller than those due to probe deflection maneuver errors, no navigation uncertainties are included in this analysis. The rationale for the dominance of the deflection maneuver errors is presented under the alternate mission B discussion. As shown in Table III E-5, nine sets of probe deflection conditions were examined. The last column of Table III E-5, lists the probability that the probe will enter the Jovian atmosphere for the given conditions. All of the cases run with the large set of deflection errors fail to provide sufficient reliability even for a nominal -20 degree flight path angle entry. Even with the small deflection errors, entry with a -10 degree flight path angle is not feasible.

The probe flight path angle, lead angle, lead time and entry site dispersions for the 99% reliable cases are presented in Table III E-6 in terms of mean values, standard deviations, maximum and minimum values. The statistics are computed from 250 Monte Carlo samples for each case. The shallowest possible entry angle for alternate mission A is about -15 degrees for the case A3 deflection errors. The effect of atmospheric radius uncertainty is seen by comparison of cases A5 and A6.

The entry site 3σ ellipses are given in terms of the semi-axes and their orientation relative to the latitude and longitude directions. The rotation angle Θ is defined by Figure III E-7.

The nominal entry flight path angle is -15 degrees and the nominal lead angle is 19.5. Accordingly, the communication parameter dispersions are calculated for case A5. Table III E-7 shows the nominal probe/spacecraft communication parameters for case A5. The communication power losses are expressed in db referenced to an arbitrary zero level. The power loss expressed in db is useful because the probe transmitter power requirements are directly related to this power loss for a given data transmission rate and signal to noise ratio. The last column shows the probe transmitter power requirement in watts for one system configuration.

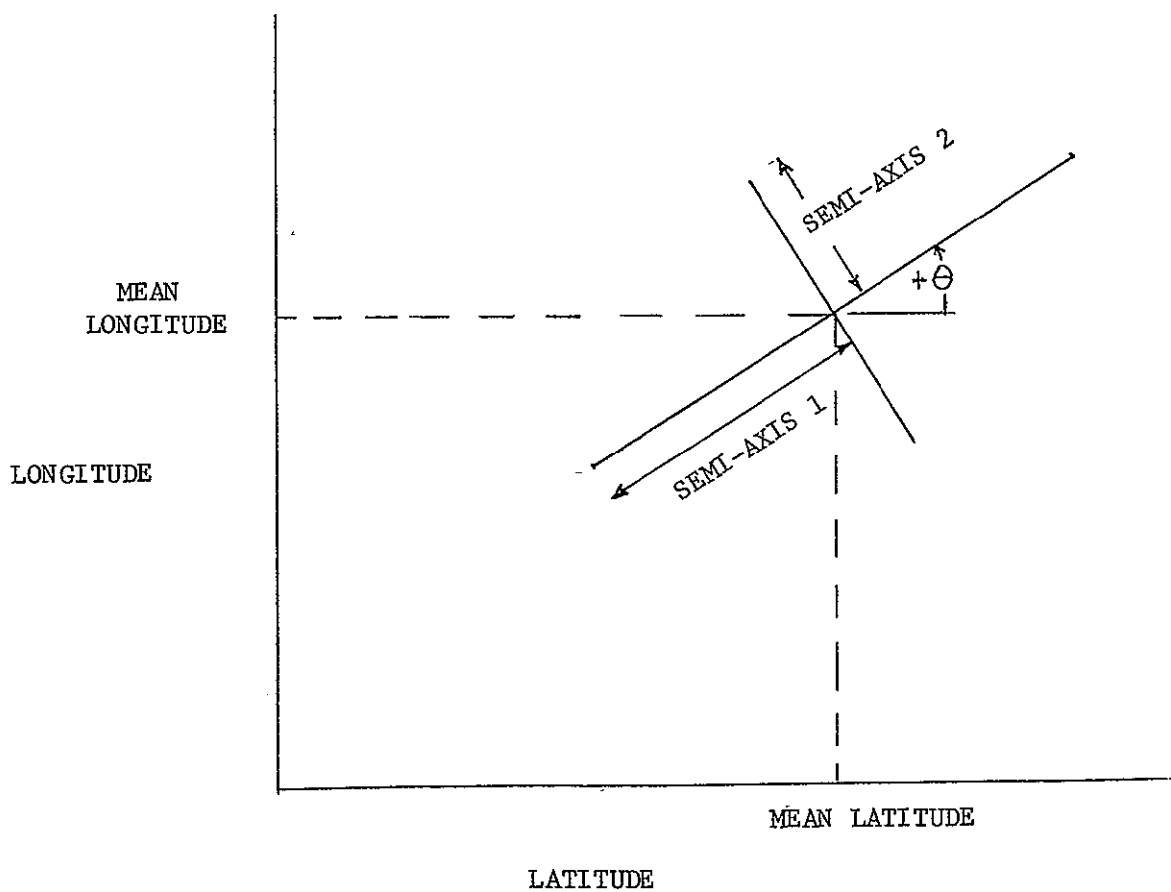


Figure III E-7 Entry Site Dispersion Geometry

Case	γ_c (deg)	λ_c (deg)	3σ Deflection Errors *		3σ RA (km)	Probability of Entry
			Prop.	Pointing		
A1	-10	11	1%	1 deg	0	.94
A2	-10	11	4.5%	4.5 deg	0	.58
A3	-15	11	1%	1 deg	0	.996
A4	-15	11	4.5%	4.5 deg	0	.80
A5	-15	19.5	1%	1 deg	0	.996
A6	-15	19.5	1%	1 deg	1000	.992
A7	-20	11	1%	1 deg	0	1.0
A8	-20	11	4.5%	4.5 deg	0	.94
A9	-20	19.5	1%	1 deg	1000	1.0

* Deflection velocity resolution errors of .152 m/sec (3σ) used for all cases.

TABLE III E-5 ALTERNATE MISSION A CASE DEFINITION

Case	Entry Flight Path Angle (deg)				Lead Angle (deg)			
	Mean	3σ	Min	Max	Mean	3σ	Min	Max
A3	-14.96	6.39	-19.4	-5.8	11.06	9.42	-4.08	18.0
A5	-14.8	6.84	-19.5	-6.97	19.1	10.80	6.38	26.6
A6	-14.8	7.62	-20.9	-6.23	19.1	11.61	5.81	28.8
A7	-20.0	4.59	-23.4	-13.5	11.16	6.36	2.78	16.4
A9	-19.9	5.34	-24.6	-14.9	19.3	7.68	12.1	27.0

Case	Lead Time (min)				Entry Site (deg)				
	Mean	3σ	Min	Max	Mean lat	Mean long	Semi-axis 1 (3σ)	Semi-axis 2 (3σ)	θ
A3	-66.8	18.99	-89.5	-50.8					
A5	-114.3	18.5	-133.6	-98.6	-.56	106.6	1.98	12.6	-.8
A6	-114.5	21.7	-133.8	-95.9	-.51	106.7	1.77	14.1	-.9
A7	-16.5	18.0	-37.5	-2.35					
A9	-62.2	20.1	-80.0	-44.8	-.62	97.3	2.02	9.72	-1.0

TABLE III E-6 ENTRY PARAMETER DISPERSIONS - ALTERNATE MISSION A

Pre-entry probe/spacecraft communication is not planned for this mission because of the large pre-entry range and probe aspect angles. The post entry cone and clock angle dispersions and total power loss dispersions are shown in Tables III E-8 and 9. The 3 σ cone and clock angle dispersions are specified in the same way as the entry site dispersion described earlier with a zero Θ corresponding to semi-axis 1 aligned to the cone angle axis and semi-axis 2 aligned to the clock angle axis. The cone and clock angle dispersions are small compared to the other missions considered. This is due to the large distance between the probe and spacecraft. The worst dispersion occurs at entry and is approximately 5.6 degrees by 1.1 degrees. The spacecraft antenna pattern is large enough to cover this area so that programming the spacecraft antenna pointing angles as a function of time from nominal entry is feasible. The power loss dispersion at 300 sec. (.0833 hr) and .25 hr after entry are very large. This is due to the lead time dispersions in that actual entry occurs over a \pm 18 min time from nominal entry. Thus, for some cases the probe has not yet entered at 300 seconds or .25 hours after the nominal entry time, so the probe aspect angle is greater than 90 degrees and the losses are very large. Power loss dispersions should be computed relative to the actual probe entry time in order to remove the effect of the abrupt probe aspect angle change at entry.

At the end of the mission (1 hour after nominal entry) the power loss dispersions are tolerable. The maximum power loss is .9 db greater than the nominal so that a 23% increase in nominal probe power is required.

Time From Entry (hr)	Range (1000 Km)	Range Rate (Km/Sec)	Range Acceleration (M/Sec ²)	Cone Angle (deg)	Clock Angle (deg)	Aspect Angle (deg)	Total Power Loss (db)	Power Required (watts)
-1.6	531	-15.2	-1.34	37.5	-105.2	104.8		
-1.2	508	-17.2	-1.44	37.3	-105.2	105.0		
-.8	482	-19.1	-.98	37.8	-105.2	104.5		
-.4	454	-18.5	3.14	39.7	-105.1	102.5		
0	436	-11.5	25.0	44.6	-104.7	97.6		
.0833	437	2.74	1.99	44.3	-104.7	19.2	-17.2	40.6
.24	439	3.94	2.03	43.3	-104.7	14.1	-18.1	32.8
.5	443	5.79	2.06	41.9	-104.8	6.3	-17.2	40.6
.75	450	7.65	2.07	40.6	-104.8	1.6	-16.8	45.0
1.0	457	9.50	2.05	39.2	-104.9	9.4	-16.1	53.1

TABLE III E-7 NOMINAL COMMUNICATIONS PARAMETERS - ALTERNATE MISSION A

Time From Nominal Entry	Mean Cone Angle (deg)	Mean Clock Angle (deg)	3 σ Ellipse		
			Semi-axis 1 (deg)	Semi-axis 2 (deg)	θ (deg)
.0833	44.0	-104.7	2.82	.564	3.3
.25	43.3	-104.7	1.62	.532	4.5
.5	41.9	-104.8	1.58	.525	5.0
.75	40.6	-104.9	1.56	.517	5.2
1.0	39.3	-104.9	1.52	.509	5.4

TABLE III E-8 CONE AND CLOCK ANGLE DISPERSIONS - ALTERNATE MISSION A

Time From Nominal Entry (hr)	Mean (db)	Standard Deviation (db)	Minimum Value (db)	Maximum Value (db)
.0833	-13.7	6.83	-17.6	-1.51
.25	-17.2	1.32	-17.6	-2.00
.5	-17.2	.118	-17.5	-16.9
.75	-16.8	.181	-17.3	-16.2
1.0	-16.0	.269	-16.7	-15.2

TABLE III E-9 TOTAL POWER LOSS DISPERSION - ALTERNATE MISSION A

Monte Carlo Results - Alternate Mission B

Alternate Mission B has a Type II approach trajectory with a 2.0 Jupiter radius closest approach distance. The probe is deflected when the spacecraft is 10^7 km from Jupiter. The design entry flight path angle is -30 degrees and lead angle is -20.8 degrees.

Table IIIE-10 lists the Monte Carlo runs made for alternate Mission B. Best case navigation errors refer to the uncertainties generated for doppler and onboard sensor measurements with station location errors of $\sigma_{r_s} = 1.5$ m, $\sigma_{r_s \Delta \lambda} = 3.0$ m, onboard sensor noise of 5 arc sec., and sensor bias solved for. Worst case navigation errors are those generated for doppler measurements only with equivalent station location errors of $\sigma_{r_s} = 2.5$ m, and $\sigma_{r_s \Delta \lambda} = 5.0$ m. For all cases except B2, the probability of probe entry is greater than 99.6%. The probability of entry for case B2 is 95%. Thus, for alternate Mission B, a -10 degree probe entry angle is feasible.

TABLE IIIE-10
ALTERNATE MISSION B - CASE DEFINITIONS

Case	γ_c (deg)	λ_c (deg)	Deflection Errors		Navigation Errors	$3\sigma_{RA}$ (km)	$3\sigma_{\mu}$ (km ³ /sec ²)
			Proportionality (3 σ)	Pointing (3 σ)			
B1	-10	- 8.0	1%	1 deg	Worst Case	0	0
B2	-10	- 8.0	4.5%	4.5 deg	Worst Case	0	0
B3	-10	-20.8	1%	1 deg	Worst Case	1000	0
B4	-10	- 8.0	1%	1 deg	Worst Case	0	25410
B5	-30	-20.8	1%	1 deg	Best Case	0	0
B6	-30	-20.8	4.5%	4.5 deg	Best Case	0	0
B7	-30	-20.8	1%	1 deg	Worst Case	0	0
B8	-30	-20.8	4.5%	4.5 deg	Worst Case	0	0
B9	-30	-20.8	1%	1 deg	Worst Case	1000	0

TABLE IIIE-11
ENTRY PARAMETER DISPERSIONS - ALTERNATE MISSION B

Case	Entry Flight Path Angle (deg)				Lead Angle (deg)				
	Mean	3 σ	Min	Max	Mean	3 σ	Min	Max	
B1	-10.0	1.88	-11.4	- 8.05	- 8.03	5.22	-14.9	- 3.05	
B3	- 9.9	2.79	-12.7	- 7.50	-20.9	5.61	-25.5	-16.1	
B4	-10.0	1.91	-11.6	- 8.08	- 8.01	5.31	-14.9	- 3.11	
B5	-30.0	.68	-31.0	-29.3	-20.8	2.80	-24.4	-17.5	
B6	-29.9	3.09	-34.2	-26.6	-20.7	12.8	-34.7	- 3.57	
B7	-30.0	.75	-30.9	-29.2	-20.8	2.83	-24.6	-17.6	
B8	-29.9	3.12	-34.1	-26.6	-20.7	12.8	-34.8	-37.0	
B9	-30.0	.96	-31.1	-29.3	-20.8	3.15	-23.6	-17.9	

Case	Lead Time (Min.)				3 σ Entry Site (deg.)				
	Mean	3 σ	Min.	Max.	Mean Lat.	Mean Long.	Semi-axis 1	Semi-axis 2	θ
B1	21.4	6.96	15.2	29.4					
B3	36.0	7.05	29.6	41.8					
B4	21.4	6.99	15.1	29.4	6.62	35.4	.59	2.74	.8
B5	98.0	7.32	90.2	106.7	7.03	16.4	.62	1.29	- .4
B6	97.9	32.9	62.9	137.0	7.06	16.5	2.79	5.85	- .1
B7	98.0	7.32	90.2	106.0	7.03	16.4	.83	1.42	-8.1
B8	97.9	33.0	63.0	136.2	7.07	16.5	2.84	5.90	- .8
B9	98.0	7.62	91.6	104.2	7.04	16.4	.79	1.86	-3.4

Table IIIE-11 presents the entry parameter statistics. Comparison of cases B1 and B4 shows that the gravitational constant uncertainty of $8500 \text{ km}^3/\text{sec}^2$ (1 σ) has very little effect on the entry dispersions. Comparison of cases B5, B6, B7 and B8 shows the entry parameter statistics are dominated by the deflection maneuver errors even when the errors are small.

The nearly complete dependence of the entry parameter statistics on deflection maneuver errors is explained by the following analysis. Due to conservation of angular momentum, the probe hyperbolic excess velocity v_{HP} , impact parameter B_P , radius vector r_p , velocity v_p , and flight path angle γ are related by

$$v_{HP} B_P = r_p(t) v_p(t) \cos \gamma(t) \quad (\text{III E } 1)$$

The probe radius and velocity satisfy the equation (7)

$$v_p^2 = v_{HP}^2 + 2\mu/r_p \quad (\text{III E } 2)$$

Manipulation of these two equations yields

$$\frac{\partial \gamma_{\text{entry}}}{\partial B_P} = \frac{-v_{HP}}{R_A \sqrt{v_{HP}^2 + 2\mu/R_A} \sin \gamma_{\text{entry}}} \quad (\text{III E } 3)$$

Uncertainty in B_P is the dominant γ_{entry} error source with the linear approximation to the relationship given by Eq. III E 3. There are two sources of uncertainty in B_P . One is due to navigation uncertainty and the other is due to deflection velocity errors. It will be shown that the uncertainty in B_P due to deflection velocity error is much greater than that due to navigation error. The following equation is easily derived from Eq. III E 1 and III E 2.

$$\frac{B_P}{B_s} = \cos \gamma_{\text{entry}} \frac{R_A \sqrt{1 + \frac{2\mu}{R_A v_{HP}^2}}}{R_{PS} \sqrt{1 + \frac{2\mu}{R_{PS} v_{HS}^2}}}$$

where B_s is the impact parameter of the spacecraft. R_{PS} is the peria-
 sis radius of the spacecraft, and v_{HS} is the spacecraft hyperbolic
 excess velocity. Since $v_{HP} \approx v_{HS}$ and $\frac{2\mu}{R_{PS} v_{HS}^2} \gg 1$,

the following approximation is valid:

$$\frac{B_P}{B_s} = \cos \gamma_{\text{entry}} \sqrt{\frac{R_A}{R_{PS}}}$$

The value of $R_A/R_{PS} \approx .5$, $\gamma_{\text{entry}} = -30$ degrees, and $B_s = 1.1 \times 10^6$ km so $B_p \approx 680000$ km. The deflection velocity must change the B of the probe trajectory by 420000 km. As a rough approximation, the B_p uncertainty should be this change multiplied by the $1\frac{1}{2}\%$ maneuver error, i.e., $420000 \text{ km} \times .015 = 6300 \text{ km}$, a distance far greater than the position uncertainty due to navigation. The value of $\frac{\partial \gamma_{\text{entry}}}{\partial B_p}$ for the probe trajectory is 1.46×10^{-4} degrees/km so the γ dispersion due to the deflection error should be approximately

$$\sigma_\gamma = \frac{\partial \gamma_{\text{entry}}}{\partial B_p} \times \sigma_{B_p} = 0.92 \text{ degrees}$$

This is in good agreement with the Monte Carlo generated σ_γ (1.03 deg).

A comparison of these results with the results of similar analyses conducted for a Mars atmospheric probe illustrates the effects of Jupiter's tremendous mass. For a typical Mars mission ⁽⁸⁾ the sensitivity of γ to errors in B is .02 degrees/km vs the .00015 degrees/km for Jupiter. For a Mars mission with a spacecraft periapsis radius of twice Mars' radius and a -30 degree entry flight path angle, the deflection velocity must produce a change in B of approximately 5000 km vs the 420000 km change required for a similar Jupiter mission. Since the B change for the Mars mission is only 5000 km, a 1.5% deflection error will produce only 75 km of uncertainty in B . Thus the relative importance of navigation uncertainties is much greater for a Mars mission.

For alternate Mission A the difference in B of the spacecraft and B of the probe is 680000 km. So for a deflection maneuver accuracy of 1% (3 σ) the 3 σ error in B_p is 6800 km, a distance far greater than the navigation expected navigation uncertainties.

Comparison of cases B1 and B3 shows that the atmospheric radius uncertainty increases the flight path angle dispersion by about 40 percent for a -10 degree entry angle. Since the atmospheric radius uncertainty is independent of the deflection errors, the 40% increase implies that the flight path angle dispersions due to atmospheric radius uncertainty alone is about equal to the dispersions due to deflection

velocity errors alone. A 1000 km (3σ) uncertainty in radius has the same effect as a 1%(3) deflection velocity uncertainty. When the targeted flight path angle is increased to -30 degrees, the atmospheric radius uncertainty becomes somewhat less important (cases B7 and B9). Atmospheric radius uncertainties have little effect on lead angle and lead time dispersions (case B1 vs B3 and B7 vs B9). Entry site longitude dispersions are increased by approximately 30% due to atmospheric radius uncertainty while latitude dispersions are unchanged.

The nominal communications parameters for alternate Mission B design case (B7) are shown in Table IIIE-12. Since probe/spacecraft communication during the pre-entry phase of alternate Mission B is desired, the pre-entry probe/spacecraft geometry dispersions were calculated and are presented in Table IIIE-13. Range rate and acceleration dispersions are important in establishing spacecraft tracking loop bandwidth requirements. Probe aspect angle and range dispersions contribute to the total power loss dispersions. The standard deviations of all these variables increase as nominal entry time is approached since range and probe antenna axis orientation change rapidly at entry. The spacecraft antenna pointing angle dispersions are shown in Table IIIE-14. The size of the cone and clock angle dispersion makes acquisition of the probe difficult. The half power beam width of a typical spacecraft antenna is on the order of 11 degrees so that prior to entry some sort of a search procedure is required. Additional work is required in this area to establish methods of prescribing spacecraft antenna pointing angles after the probe has been acquired. Implications of the cone and clock angle dispersions are discussed in Chapter IV, Section G.

TABLE IIIE-12
NOMINAL COMMUNICATIONS PARAMETERS - ALTERNATE MISSION B

Time (hr)	Range (1000 km)	Range Rate (km/sec)	Range Acceleration (m/sec ²)	Cone Angle (deg)	Clock Angle (deg)	Aspect Angle (deg)	Total Power Loss (db)
-1.6	129.0	- 2.04	.425	168.8	316.1	50.68	-23.64
-1.2	126.7	- 1.00	1.13	170.3	334.3	47.09	-24.25
- .8	126.9	1.69	2.87	170.3	4.1	42.12	-24.79
- .4	133.5	8.62	7.54	167.1	33.1	35.69	-24.96
0	157.1	27.0	18.9	162.5	47.5	29.82	-24.00
.14	148.6	-18.1	.386	164.5	42.6	33.31	-24.22
.33	136.2	-17.9	.451	167.6	30.9	36.2	-24.65
.5	125.6	-17.5	.642	170.1	12.0	37.8	-25.05
1.02	94.6	-14.7	2.85	161.5	284.8	36.5	-26.23
1.25	83.4	-11.5	5.01	148.8	271.2	31.3	-25.42
1.5	75.6	- 5.76	7.54	130.9	263.5	22.4	-24.50

TABLE IIIE-13
PRE-ENTRY COMMUNICATIONS GEOMETRY DISPERSIONS - ALTERNATE MISSION B

RANGE

Time (hr)	Mean (1000 km)	Standard Deviation (1000 km)	Minimum (1000 km)	Maximum (1000 km)
-1.6	129.1	.772	127.1	131.0
-1.2	126.8	1.20	124.0	130.1
- .8	127.1	2.04	121.7	132.9
- .4	133.8	3.72	123.6	144.9
0	154.5	4.29	137.7	164.4

RANGE RATE

Time (hr)	Mean (km/sec)	Standard Deviation (km/sec)	Minimum (km/sec)	Maximum (km/sec)
-1.6	-2.02	.277	- 2.81	-1.31
-1.2	- .968	.464	- 2.28	.310
- .8	1.73	.841	- .612	4.18
- .4	8.67	1.71	4.14	14.3
0	5.09	21.2	-18.4	27.7

RANGE ACCELERATION

Time (hr)	Mean ₂ (m/sec ²)	Standard Deviation (m/sec ²)	Minimum (m/sec ²)	Maximum (m/sec ²)
-1.6	.429	.0954	.161	.704
-1.2	1.14	.182	.639	1.70
- .8	2.88	.386	1.88	4.22
- .4	7.55	.947	5.31	11.1
0	9.94	8.70	.319	19.2

PROBE ASPECT ANGLE

Time (hr)	Mean (deg)	Standard Deviation (deg)	Minimum (deg)	Maximum (deg)
-1.6	50.6	1.70	46.6	56.0
-1.2	47.0	1.86	42.8	53.0
- .8	42.1	2.00	37.5	48.6
- .4	35.7	1.98	31.2	42.3
0	27.5	7.67	.514	52.1

TABLE IIIE-14
CONE AND CLOCK ANGLE DISPERSIONS - ALTERNATE MISSION B

Time From Nominal Entry (hr)	Mean Cone Angle (deg)	Mean Clock Angle (deg)	3 σ Ellipse		
			Semi-Axis 1 (deg)	Semi-Axis 2 (deg)	θ (deg)
-1.6	168.8	-43.10	1.41	23.2	- 6.43
-1.2	170.2	-24.90	1.30	32.2	- 2.34
- .8	170.1	3.85	1.31	34.3	2.31
- .4	167.0	32.50	1.44	21.0	10.6
0	162.9	46.64	.999	7.39	19.9
.14	164.5	42.78	.818	6.78	14.6
.33	167.6	31.22	.741	11.0	8.68
.5	170.0	12.46	.669	18.2	3.45
1.02	161.7	-74.8	1.21	9.81	-29.3
1.25	149.0	-88.6	7.74	1.19	30.8
1.5	131.2	-96.4	8.46	.996	15.80

TABLE IIIE-15
TOTAL POWER LOSS DISPERSIONS - ALTERNATE MISSION B

Time From Nominal Entry (hr)	Mean (db)	Standard Deviation (db)	Minimum (db)	Maximum (db)
-1.6	-23.7	.192	-24.1	-23.0
-1.2	-24.3	.157	-24.6	-23.7
- .8	-24.8	.090	-25.0	-24.4
- .4	-25.0	.088	-25.2	-24.6
0	-24.2	.398	-25.1	-21.8
.14	-24.2	.224	-25.6	-23.6
.33	-24.6	.242	-25.3	-23.9
.5	-25.0	.278	-25.8	-24.2
1.02	-26.7	.622	-27.8	-24.6
1.25	-25.4	.731	-27.5	-23.6
1.5	-24.5	.861	-26.4	-21.9

Total power loss dispersions are shown in Table IIIE-15. The largest dispersions occur at the end of the mission. The 2.6 db (3 σ) power loss requires an 80% increase in nominal probe transmitter power to insure communication 1.5 hours after nominal entry.

Monte Carlo Results - Design Example

The design example mission approach trajectory is the same approach trajectory used for alternate Mission B. Probe deflection takes place at 2.6×10^7 km from Jupiter with a targeted entry flight path angle of -20 degrees and lead angle of -16.5 degrees.

Table IIIE-16 lists the Monte Carlo runs made for the design example mission. Since the alternate Mission B analysis showed that the navigation uncertainties are dominated by the deflection velocity implementation errors, no navigation uncertainties were included in the design example runs. The communication parameter dispersions calculated for alternate Missions A and B were referenced to the nominal entry time. If the spacecraft could sense the time at which the probe enters the atmosphere the spacecraft antenna pointing angles might then be pre-programmed as a function of time from actual entry instead of nominal entry or equivalently time from deflection. If the cone and clock angle dispersions are smaller when referenced to actual instead of nominal entry the probe tracking problem after entry would be simplified. Cases DE2 and DE5 were run to determine if the dispersions are reduced when actual entry is used as the time reference.

The entry parameter dispersions are given in Table IIIE-17. Comparison of cases DE1 vs. DE3 and DE4 vs. DE6 shows that the atmospheric radius uncertainties influence the flight path angle dispersions but have little effect on the lead time and lead angle dispersions. Entry site longitude dispersions are increased by the radius uncertainty. Comparison of cases DE1 and DE7 shows that increasing the pointing angle error while holding the proportionality error fixed has little effect on the flight plane angle dispersion but the lead time dispersion increases proportionally.

Probe aspect angle, range, range rate and range acceleration dispersions are shown in Tables IIIE-17 thru IIIE-21. Atmospheric radius uncertainty has little effect on the dispersions. The dispersions are roughly proportional to the deflection errors in that those for case DE4 are twice as large as the dispersions for DE1. The dispersions are sensitive to the 50% pointing angle error increase between cases DE7 and DE1.

The spacecraft antenna pointing angle dispersions, shown in Table IIIE-22 are extremely sensitive to probe deflection system errors. Comparison of cases DE1 and DE2 shows that the dispersions referenced to actual entry time are somewhat worse than when referenced to nominal entry so pre-programming the angles as a function of time from actual entry would not simplify the probe tracking problem. The cone and clock-angle dispersions are insensitive to atmospheric radius uncertainty.

The total power loss dispersions shown in Table IIIE-23 are roughly proportional to the deflection system errors during the pre-entry phase of the mission. From entry to about an hour after entry the power loss dispersions are very sensitive to deflection errors. During the last hour of the mission the sensitivity is reduced. Atmospheric radius uncertainties have little effect.

TABLE IIIE-16
DESIGN EXAMPLE - DEFINITION OF CASES

Case	3 σ Deflection Errors		3 σ RA (km)	Time Reference
	Proportionality %	Pointing (deg)		
DE1	1	1.5	0	Nominal Entry
DE2	1	1.5	0	Actual Entry
DE3	1	1.5	1000	Nominal Entry
DE4	2	3.0	0	Nominal Entry
DE5	2	3.0	0	Actual Entry
DE6	2	3.0	1000	Nominal Entry
DE7	1	1.0	0	Nominal Entry

TABLE IIIE-17
ENTRY PARAMETER DISPERSIONS - DESIGN EXAMPLE

Case	Entry Flight Path Angle (deg)				Lead Angle (deg)			
	Mean	3 σ	Min.	Max.	Mean	3 σ	Min.	Max.
DE1	-20.0	1.03	-20.8	-18.9	-16.5	10.5	-28.5	-6.32
DE3	-20.0	1.52	-21.3	-18.5	-16.5	10.4	-28.0	-6.93
DE4	-20.0	1.94	-21.4	-17.9	-16.3	20.9	-37.7	5.75
DE6	-20.0	2.26	-21.8	-17.8	-16.2	20.9	-36.9	5.15
DE7	-20.0	.95	-20.8	-19.0	-16.6	7.08	-25.2	-9.96

Case	Lead Time (Min.)				3 σ Entry Site (deg)				
	Mean	3 σ	Min.	Max.	Mean Lat.	Mean Long.	Semi-axis 1	Semi-axis 2	θ
DE1	59.3	17.5	43.2	79.8	6.69	33.1	.758	2.00	-2.17
DE3	59.4	17.6	42.9	80.1	6.69	33.1	.754	3.00	.079
DE4	59.5	34.8	27.1	100.6	6.71	33.2	1.30	3.75	-.082
DE6	59.5	35.0	26.8	101.0	6.71	33.1	1.30	4.41	.499
DE7	59.3	11.6	48.5	72.7	6.69	33.1	.60	1.83	-2.17

TABLE IIIE-18
ASPECT ANGLE DISPERSIONS - DESIGN EXAMPLE

Time From Entry (hr)	Nominal (deg)	Case	Mean (deg)	Standard Deviation (deg)	Minimum Value (deg)	Maximum Value (deg)
-1.6	67.7	DE1	67.4	5.08	47.8	79.9
		DE2	67.6	4.70	50.0	80.3
		DE3	67.4	5.06	48.3	79.5
		DE4	66.7	9.99	28.0	89.1
		DE5	67.4	9.23	34.5	91.7
		DE6	66.8	9.96	28.5	88.6
		DE7	67.5	3.43	54.6	76.2
-1.2	65.7	DE1	65.3	6.12	42.9	80.4
		DE2	65.7	5.34	46.2	80.3
		DE3	65.4	6.10	43.4	80.0
		DE4	64.7	11.8	22.6	91.1
		DE5	65.6	10.4	30.4	93.8
		DE6	64.7	11.8	23.0	90.7
		DE7	65.5	4.15	50.6	75.9
- .8	61.6	DE1	61.1	7.54	36.1	80.0
		DE2	61.5	6.05	40.6	78.7
		DE3	61.2	7.53	36.6	79.6
		DE4	60.7	14.1	17.9	93.2
		DE5	61.7	11.8	25.2	95.4
		DE6	60.7	14.0	18.4	92.8
		DE7	61.3	5.19	44.3	74.3
- .4	53.5	DE1	53.3	8.81	28.8	77.2
		DE2	53.6	6.34	33.1	72.7
		DE3	53.4	8.79	29.3	76.8
		DE4	54.3	15.4	9.5	95.1
		DE5	54.2	12.5	19.9	93.8
		DE6	54.4	15.4	6.96	94.7
		DE7	53.3	6.17	35.9	69.6
0	43.0	DE1	39.9	11.7	6.87	68.5
		DE2	43.2	5.11	27.4	59.4
		DE3	39.6	12.2	22.8	68.2
		DE4	45.1	16.4	1.04	95.0
		DE5	44.1	10.5	17.4	81.9
		DE6	45.5	16.0	1.49	94.6
		DE7	38.0	11.7	1.42	63.2

TABLE IIIE-19
RANGE DISPERSIONS - DESIGN EXAMPLE

Time (hr)	Nominal (km)	Case	Mean (km)	Standard Deviation (km)	Minimum Value (km)	Maximum Value (km)
-1.6	117653	DE1	118002	3136	112105	128359
		DE2	117985	1242	115707	123014
		DE3	118002	3137	112105	128359
		DE4	119494	6045	111203	144182
		DE5	119053	3003	114963	133698
		DE6	119494	6045	111203	114182
		DE7	117735	2297	112314	124867
-1.2	109838	DE1	110429	2527	105997	119720
		DE2	110252	802	108638	113477
		DE3	110429	3527	105997	119720
		DE4	112547	5486	106036	136428
		DE5	111511	2618	107777	126962
		DE6	112547	5486	106036	136428
		DE7	110038	1890	106071	116522
- .8	102310	DE1	103405	1847	100482	114444
		DE2	102820	1615	100482	112094
		DE3	103405	1848	100482	114443
		DE4	106647	6547	100411	156321
		DE5	104274	3921	99623	131322
		DE6	106647	6547	100411	156231
		DE7	102783	1149	100481	107191
- .4	98923	DE1	101083	5790	93751	130159
		DE2	99477	4122	91460	118127
		DE3	101083	5791	93751	130158
		DE4	105779	12767	94509	164484
		DE5	100947	8240	90320	144202
		DE6	105768	12731	94510	163510
		DE7	100044	3632	94274	114734
0	113017	DE1	108530	7281	89699	128574
		DE2	113435	7583	94483	142771
		DE3	108482	7232	89699	127634
		DE4	107612	10657	88189	140772
		DE5	114374	14839	83381	175081
		DE6	107567	10598	88189	139190
		DE7	109254	5476	93490	125306

TABLE IIIE-20
RANGE RATE DISPERSIONS - DESIGN EXAMPLE

Time (hr)	Nominal (km/sec)	Case	Mean (km/sec)	Standard Deviation (km/sec)	Minimum Value (km/sec)	Maximum Value (km/sec)
-1.6	-5.25	DE1	-5.13	.401	-5.76	-2.64
		DE2	-5.20	.447	-6.13	-3.11
		DE3	-5.13	.401	-5.77	-2.64
		DE4	-4.81	1.06	-5.78	2.86
		DE5	-5.08	.893	-6.39	- .596
		DE6	-4.81	1.06	-5.78	2.86
		DE7	-5.20	.250	-5.69	-3.78
-1.2	-5.52	DE1	-5.28	.921	-6.61	- .661
		DE2	-5.45	.784	-7.25	-2.12
		DE3	-5.28	.921	-6.61	- .662
		DE4	-4.71	2.18	-6.85	8.58
		DE5	-5.31	1.52	-8.08	1.30
		DE6	-4.71	2.18	-6.85	8.58
		DE7	-5.40	.589	-6.44	-2.78
- .8	-4.56	DE1	-4.06	2.26	-7.65	4.85
		DE2	-4.50	1.40	-8.07	.823
		DE3	-4.06	2.26	-7.65	4.85
		DE4	-3.02	4.79	-8.08	20.9
		DE5	-4.39	2.68	-10.4	5.25
		DE6	-3.02	4.79	-8.08	20.9
		DE7	-4.28	1.52	-7.08	1.17
- .4	1.29	DE1	2.28	5.63	-7.89	20.98
		DE2	1.27	2.32	-5.46	8.83
		DE3	2.28	5.63	-7.89	20.98
		DE4	2.22	2.45	-17.1	27.5
		DE5	1.12	4.48	-11.7	13.7
		DE6	2.22	9.45	-17.1	27.5
		DE7	1.93	4.05	-5.76	15.5
0	21.3	DE1	-.260	15.8	-10.9	23.3
		DE2	21.1	2.18	13.8	27.2
		DE3	-.419	15.7	-17.0	22.5
		DE4	-4.23	13.9	-17.0	23.3
		DE5	20.6	4.60	2.57	30.4
		DE6	-4.23	13.9	-17.0	23.2
		DE7	1.23	16.5	-16.9	23.7

TABLE IIIE- 20
 RANGE RATE DISPERSIONS - DESIGN EXAMPLE (Continued)

Time (hr)	Nominal (km/sec)	Case	Mean (km/sec)	Standard Deviation (km/sec)	Minimum Value (km/sec)	Maximum Value (km/sec)
.0833	-16.1	DE1	-8.57	13.3	-16.8	20.9
		DE2	-16.0	.695	-17.0	-13.0
		DE3	-8.72	13.1	-16.8	20.9
		DE4	-8.19	12.2	-16.7	21.1
		DE5	-15.6	1.74	-17.1	-6.31
		DE6	-8.49	11.9	-16.7	21.0
		DE7	-9.51	13.2	-16.8	21.0
.25	-14.9	DE1	-14.4	3.10	-16.2	13.4
		DE2	-14.7	1.11	-16.7	-10.2
		DE3	-14.4	3.10	-16.3	13.4
		DE4	-12.3	7.27	-16.3	15.3
		DE5	-14.1	2.58	-16.8	-1.94
		DE6	-12.3	7.29	-16.3	16.0
		DE7	-14.8	.532	-16.3	-13.2
.5	-11.8	DE1	-11.6	.951	-14.2	-8.6
		DE2	-11.6	1.98	-15.9	-4.45
		DE3	-11.7	.953	-14.3	-8.64
		DE4	-11.5	1.59	-14.7	1.22
		DE5	-10.9	4.08	-16.5	4.82
		DE6	-11.5	1.59	-14.7	1.22
		DE7	-11.7	.920	-14.2	-8.96
1.0	- .205	DE1	- .091	1.68	-5.68	4.49
		DE2	- .262	3.38	-10.9	8.64
		DE3	- .083	1.69	- 5.58	4.49
		DE4	- .0927	2.08	-7.55	5.58
		DE5	- .275	6.10	15.3	13.8
		DE6	- .085	2.08	-7.51	5.57
		DE7	- .0895	1.61	-5.17	4.09
1.5	11.7	DE1	11.7	1.01	7.66	14.0
		DE2	11.4	2.15	1.14	15.5
		DE3	11.7	1.02	7.80	14.0
		DE4	11.7	1.25	5.39	14.4
		DE5	10.7	4.36	-9.49	16.8
		DE6	11.7	1.25	5.48	14.3
		DE7	11.7	.969	8.15	13.9

TABLE IIIE-20
 RANGE RATE DISPERSIONS - DESIGN EXAMPLE (Continued)

Time (hr)	Nominal (km/sec)	Case	Mean (km/sec)	Standard Deviation (km/sec)	Minimum Value (km/sec)	Maximum Value (km/sec)
2.0	17.0	DE1	17.0	.356	15.7	17.9
		DE2	16.9	.660	12.7	17.8
		DE3	17.0	.356	15.6	17.9
		DE4	17.0	.386	15.4	18.0
		DE5	16.4	1.73	2.88	17.9
		DE6	17.0	.385	15.4	18.0
		DE7	17.0	.350	15.7	17.9
2.5	19.1	DE1	19.1	.365	18.2	20.2
		DE2	19.1	.106	18.2	19.3
		DE3	19.1	.367	18.2	20.3
		DE4	19.1	.623	17.6	21.0
		DE5	18.9	.460	13.9	19.4
		DE6	19.1	.623	17.6	21.0
		DE7	19.1	.289	18.4	20.0

RANGE ACCELERATION DISPERSIONS - DESIGN EXAMPLE

Time (hr)	Nominal (m/sec ²)	Case	Mean (m/sec ²)	Standard Deviation (m/sec ²)	Minimum Value (m/sec ²)	Maximum Value (m/sec ²)
-1.6	-.325	DE1	-.272	.233	-.640	.757
		DE2	-.315	.169	-.733	.347
		DE3	-.272	.233	-.640	.757
		DE4	-.153	.524	-.700	2.65
		DE5	-.296	.324	-.991	.895
		DE6	-.153	.524	-.700	2.65
		DE7	-.297	.153	-.582	.286
-1.2	.004	DE1	.164	.566	-.776	2.40
		DE2	.052	.315	-.785	1.16
		DE3	.164	.566	-.776	2.40
		DE4	.397	1.17	-.925	5.69
		DE5	.060	.593	-1.40	1.85
		DE6	.397	1.17	-.925	5.69
		DE7	.114	.385	-.061	1.50
- .8	1.64	DE1	1.92	1.47	-.696	7.00
		DE2	1.63	.564	-.008	3.27
		DE3	1.92	1.47	-.696	7.00
		DE4	2.33	2.72	-1.26	11.9
		DE5	1.56	1.07	-1.67	3.90
		DE6	2.33	2.72	-1.26	11.9
		DE7	1.82	1.06	-.149	5.52
- .4	7.71	DE1	8.02	3.37	.871	16.5
		DE2	7.61	.600	5.20	8.64
		DE3	8.02	3.37	.871	16.5
		DE4	7.48	4.99	-1.66	16.4
		DE5	7.30	.137	1.09	8.71
		DE6	7.48	4.99	-1.66	16.4
		DE7	7.99	2.63	2.43	15.5
0	18.9	DE1	9.91	8.16	.603	20.2
		DE2	18.9	1.11	15.1	22.0
		DE3	9.85	8.16	.619	20.2
		DE4	7.85	7.48	-.656	20.1
		DE5	18.9	2.04	12.6	23.3
		DE6	7.86	7.47	-.656	20.1
		DE7	10.5	.832	.752	19.7
.0833	1.72	DE1	5.88	7.32	.780	20.3
		DE2	1.78	.589	.382	3.95
		DE3	5.81	7.28	.796	20.3
		DE4	6.23	7.13	.373	21.3
		DE5	1.98	1.26	-.043	6.85
		DE6	6.10	7.04	.373	21.3
		DE7	5.18	6.94	.940	20.7

TABLE IIIE-21
RANGE ACCELERATION DISPERSIONS - DESIGN EXAMPLE (Continued)

Time (hr)	Nominal (m/sec ²)	Case	Mean (m/sec ²)	Standard Deviation (m/sec ²)	Minimum Value (m/sec ²)	Maximum Value (m/sec ²)
.25	2.54	DE1	2.80	2.09	1.3	21.9
		DE2	2.61	.814	.608	5.36
		DE3	2.81	2.09	1.32	21.9
		DE4	4.37	5.31	.876	21.8
		DE5	2.80	1.58	.0485	7.61
		DE6	4.37	5.31	.877	21.8
		DE7	2.58	.357	1.49	3.66
.5	4.37	DE1	4.43	.539	2.64	5.97
		DE2	4.41	1.08	1.32	7.31
		DE3	4.44	.541	2.67	5.98
		DE4	4.57	1.66	2.06	21.4
		DE5	4.42	1.84	.111	7.73
		DE6	4.57	1.65	2.06	21.4
		DE7	4.43	.507	2.9	5.83
1.0	7.79	DE1	7.71	.111	6.89	7.82
		DE2	7.50	.418	4.72	7.83
		DE3	7.72	.110	6.95	7.85
		DE4	7.66	.196	6.07	7.83
		DE5	6.83	1.15	1.53	7.83
		DE6	7.66	.193	6.10	7.85
		DE7	7.73	.0937	7.14	7.82
1.5	4.67	DE1	4.65	.541	3.22	6.59
		DE2	4.72	1.07	2.09	7.76
		DE3	4.65	.542	3.23	6.56
		DE4	4.66	.712	2.84	7.15
		DE5	4.71	1.79	.749	7.71
		DE6	4.66	.713	2.84	7.15
		DE7	4.65	.504	3.37	6.31
2.0	1.67	DE1	1.69	.258	1.11	2.94
		DE2	1.77	.544	.733	4.56
		DE3	1.69	.258	1.11	2.89
		DE4	1.71	.420	.795	3.86
		DE5	1.97	1.15	.348	7.49
		DE6	1.71	.419	.834	3.82
		DE7	1.69	.216	1.19	2.64
2.5	.899	DE1	.904	.114	.607	1.44
		DE2	.930	.172	.641	1.94
		DE3	.903	.114	.631	1.41
		DE4	.910	.225	.344	1.96
		DE5	1.02	.438	.535	4.46
		DE6	.909	.224	.369	1.94
		DE7	.903	.0788	.701	1.28

TABLE IIIE-22
CONE & CLOCK ANGLE DISPERSIONS - DESIGN EXAMPLE

Time (hr)	Case	Mean Cone Angle (deg)	Mean Clock Angle (deg)	3 σ Ellipse (deg)		
				Semi-Axis 1	Semi-Axis 2	Θ
-1.6	DE1	150.9	- 82.86	19.74	3.93	43.6
	DE2	150.7	- 83.1	17.8	3.43	41.1
	DE3	150.9	- 82.9	19.7	3.93	43.6
	DE4	151.1	- 79.5	16.0	50.4	-26.9
	DE5	150.6	- 81.1	13.6	40.7	-35.1
	DE6	151.1	- 79.5	16.0	50.4	-26.9
	DE7	150.8	- 83.32	12.7	2.13	40.0
-1.2	DE1	152.7	- 80.8	5.98	26.2	-39.0
	DE2	152.5	- 81.4	4.45	21.5	-43.7
	DE3	152.7	- 80.8	5.98	26.2	-39.0
	DE4	152.7	- 75.3	19.5	68.7	-20.5
	DE5	152.1	- 78.4	16.2	50.3	-29.6
	DE6	152.7	- 75.3	19.5	68.8	-29.6
	DE7	152.7	- 81.6	16.3	2.62	44.9
- .8	DE1	156.4	- 75.1	9.76	41.6	-25.4
	DE2	156.1	- 76.9	6.65	29.3	-32.1
	DE3	156.4	- 75.1	9.76	41.6	-25.4
	DE4	155.4	- 66.4	23.3	96.7	-14.3
	DE5	155.3	- 71.9	19.3	68.7	-21.0
	DE6	155.4	- 66.4	23.3	96.8	-14.3
	DE7	156.5	- 77.0	4.38	24.8	-33.2
- .4	DE1	162.4	- 58.9	12.1	75.1	-11.9
	DE2	162.8	- 63.0	7.97	49.9	-15.0
	DE3	162.4	- 58.9	12.1	75.1	-11.9
	DE4	159.4	- 49.3	24.5	126.2	-10.2
	DE5	160.7	- 55.7	20.5	98.8	-11.8
	DE6	159.5	- 49.3	24.5	126.1	-10.2
	DE7	163.0	- 62.4	6.98	50.4	-14.3
0	DE1	167.9	- 39.5	6.1	60.3	- 8.9
	DE2	168.8	- 27.5	5.1	72.9	- 3.3
	DE3	167.9	- 39.6	6.1	60.1	- 8.9
	DE4	164.7	- 41.1	16.7	91.9	-14.5
	DE5	166.1	- 25.2	15.0	115.5	- 4.5
	DE6	164.7	- 41.2	16.7	91.7	-14.5
	DE7	168.7	- 38.3	3.14	46.0	- 6.76
.0833	DE1	167.7	- 46.4	4.3	42.8	- 9.9
	DE2	167.7	- 39.8	5.9	68.6	- 5.9
	DE3	167.7	- 46.5	4.3	42.6	-10.0
	DE4	165.0	- 48.3	14.7	71.4	-17.2
	DE5	165.1	- 35.2	16.9	112.9	- 6.5
	DE6	165.0	- 48.3	14.7	71.3	-17.2
	DE7	168.2	- 45.3	1.92	33.0	- 7.68

TABLE IIIE-23
TOTAL POWER LOSS DISPERSIONS - DESIGN EXAMPLE (Continued)

Time (hr)	Nominal (db)	Case	Mean (db)	Standard Deviation (db)	Minimum Value (db)	Maximum Value (db)
.25	-24.25	DE1	-24.17	.63	-25.53	-21.13
		DE2	-24.19	.978	-26.50	-20.37
		DE3	-24.17	.64	-25.53	-21.21
		DE4	-23.42	1.80	-25.92	-12.91
		DE5	-24.04	1.82	-27.07	-16.80
		DE6	-23.39	1.87	-25.92	-13.10
		DE7	-24.24	.424	-25.34	-22.17
.5	-25.55	DE1	-25.52	.54	-26.70	-22.49
		DE2	-25.46	.95	-27.23	-21.30
		DE3	-25.51	.55	-26.68	-22.61
		DE4	-25.27	1.27	-26.93	-16.77
		DE5	-25.15	1.76	-27.28	-17.02
		DE6	-25.25	1.27	-26.92	-16.91
		DE7	-25.53	.414	-26.53	-23.40
1.0	-27.11	DE1	-27.05	.258	-27.33	-25.04
		DE2	-26.94	.380	-27.26	-23.94
		DE3	-26.99	.27	-27.31	-25.06
		DE4	-26.76	.86	-27.37	-18.88
		DE5	-26.34	1.17	-27.25	-18.25
		DE6	-26.68	.89	-27.34	-18.77
		DE7	-27.03	.167	-27.27	-25.93
1.5	-23.73	DE1	-23.89	.728	-25.86	-21.94
		DE2	-23.84	.774	-24.96	-21.12
		DE3	-23.68	.75	-25.72	-21.71
		DE4	-23.69	.94	-25.73	-19.08
		DE5	-23.45	1.50	-25.06	-17.90
		DE6	-23.50	.95	-25.57	-19.02
		DE7	-23.70	.706	-25.73	-21.86
2.0	-18.47	DE1	-18.64	.532	-20.40	-17.29
		DE2	-18.69	.872	-21.17	-16.19
		DE3	-18.40	.54	-20.24	-17.05
		DE4	-18.52	.600	-20.31	-16.54
		DE5	-18.58	1.62	-21.28	-13.77
		DE6	-18.28	.60	-20.14	-16.48
		DE7	-18.43	.531	-20.18	-17.12

PRECEDING PAGES BLANK NOT FILMED
(161-162)

Conclusions

The probe deflection system errors are the dominant source of dispersions in the critical mission parameters. For the missions considered, the maximum allowable 3 σ deflection errors are about 1% in proportionality and 1.5 degrees in pointing. The entry flight path angle dispersions associated with larger deflection errors can be tolerated by going to steeper nominal entry angles but the affects of larger deflection errors on the spacecraft antenna pointing angle dispersions and required probe transmitter power are intolerable.

Since the probe deflection errors are the dominant error source, there is little to be gained by reducing the navigation uncertainties with onboard sensor measurement. Increasing the probe deflection radius to the neighborhood of 3×10^7 km is feasible from a navigation standpoint. The resulting increase in the navigation uncertainties are not large enough to affect the dominance of the deflection errors. However, the lead time dispersions for given probe deflection errors increase with probe deflection radius so communications geometry dispersions are increased.

For shallow probe entry angles, uncertainties in the Jovian atmospheric radius are a significant source of entry flight path angle dispersion. The atmospheric radius uncertainty has very little effect on the communication parameter dispersions.

The uncertainty in the Jupiter gravitational constant has very little effect on the missions considered.

References

1. Myers, J. E., "Guidance and Control Subsystem Calibration and Initialization Studies," Martin Marietta Corporation, Denver, Colorado, (Contract NAS1-9000), June 1970.
2. Lee, B. G., et al, "Simulated Trajectories Error Analysis Program, Volume II - Analytical Manual, Volume III - Supplementary Manual," Martin-Marietta Corporation, Denver, Colorado, (Contract NAS1-8745), June 1969.
3. Kalman, R. E., "New Methods and Results in Linear Prediction and Filtering Theory," RIAS TR 61-1, Martin Marietta Corporation, Research Institute for Advanced Studies, Baltimore, Maryland, 1961.
4. Melbourne, W. G., "Planetary Ephemerides," Astronautics and Aeronautics May 1970.
5. Curkendall, D. W. and Stephenson, R. R., "Earthbased Tracking and Orbit Determination," Astronautics and Aeronautics, May 1970.
6. Telephone conversation with Louis Friedman (JPL) on August 4, 1970.
7. Battin, R. H., "Astronautical Guidance," McGraw-Hill, New York, 1964.

IV. TELECOMMUNICATIONS, DATA HANDLING AND POWER, DESIGN STUDIES AND TRADEOFFS

A. General

Design studies and general tradeoffs for telecommunications, data handling and power systems are presented in this chapter. For individual mission tradeoffs and baseline parametric tradeoffs see Volume II.

B. Data Return Optimization

Optimization of data return from Jupiter descent probes entails giving consideration to establishing appropriate data rate versus time profiles, selecting optimum trajectories for the required or desired mission duration, storing data during critical periods to guard against data loss and optimizing data link parameters such as radio frequency and signal acquisition capability to provide adequate link margin.

In general, as the desired depth of probe penetration increases, mission duration must be increased to allow time for the probe to descend at a slow enough rate to acquire the desired number of samples. Therefore, one must select an appropriate trajectory, radio frequency, etc. to provide the mission duration, antenna aspect angles, atmospheric losses, data rate and margins required to give the most data return. Discussion of the selection of these parameters are given in detail in following sections.

Comparison of the data return for missions treated in Volume II will also give the reader further insight into the data return optimization process.

C. Trajectory Selection for Communications Optimization

In the early part of the study contract, during the Trial Mission trade-off study phase, it was determined that proper selection of trajectory parameters was of utmost importance in optimizing a relay communications link between an entry probe and a flyby spacecraft. Obviously, important communications parameters such as probe antenna aspect angle, communications range and atmospheric losses as a function of time play important roles. In some cases spacecraft antenna look angles restrictions must also be considered.

The probe entry flight path angle also plays an important role since it has an affect on communications range and in many cases has an affect on probe aspect angle both before and immediately after entry.

Aspect angles and communications range variations for a variety of trajectory conditions are shown in Figure IVC-1 to IVC-9. Variable parameters include entry flight path angle, radius of periapsis of the flyby spacecraft and lead time.

Figure IVC-1 shows the effect on range vs time of increasing the entry flight path angle γ_E at a R_p of $2 R_J$. For these cases the lead time was chosen to place the probe under the spacecraft when the spacecraft is at periapsis. In general the effect of increasing γ_E is to increase range at entry and cause the minimum range point to occur later in the mission.

Figure IVC-2 shows probe aspect angle vs time for various γ_E at R_p of $2 R_J$ for the same conditions as above.

Figure IVC-3 shows spacecraft aspect angle variation with time as a function of γ_E . Spacecraft aspect angle is measured clockwise from the Earth oriented spacecraft axis to the spacecraft probe line assuming the Earth spacecraft axis and probe are in the same plane.

Figure IVC-4 shows communications range as a function of time for various R_p for a γ_E of -10° . Note the ratio of ranges for the pre-entry phase is higher than for the post entry. For example the ratio of ranges for R_p of $3 R_J$ compared to $2 R_J$ is approximately 2.34 at 1 hour before entry and 1.5 at 2 hours post entry. These represent additional power losses of 7.36 db and 3.5 db respectively when computing radio link power requirements thus the effect on preentry and entry range is more severe but the effect is felt over the entire period.

Figure IVC-5 shows probe aspect angle variations with time as a function of R_p . Note that both the preentry and post entry aspect angles are better for the R_p of 2 case in that for a $2\frac{1}{2}$ hour mission, probe aspect angle is zero at missions end giving maximum antenna gain and minimum atmospheric path length at a time when the probe is deepest in the atmosphere. For pre-entry, probe antenna aspect angles greater than 90° present a more difficult design problem.

FIGURE IVC-1
COMMUNICATIONS RANGE VS TIME

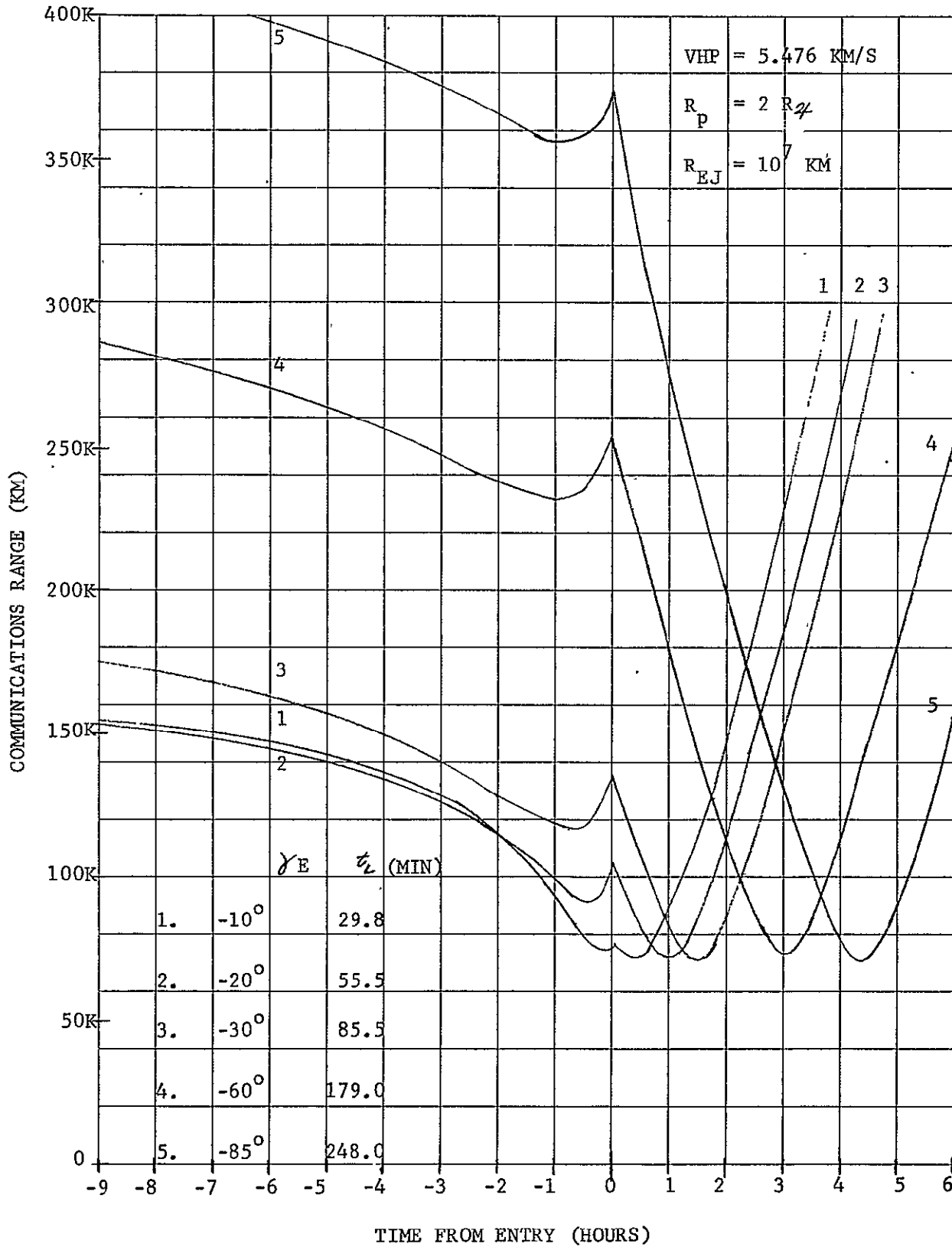


FIGURE IVC-2
PROBE ASPECT ANGLE VS TIME

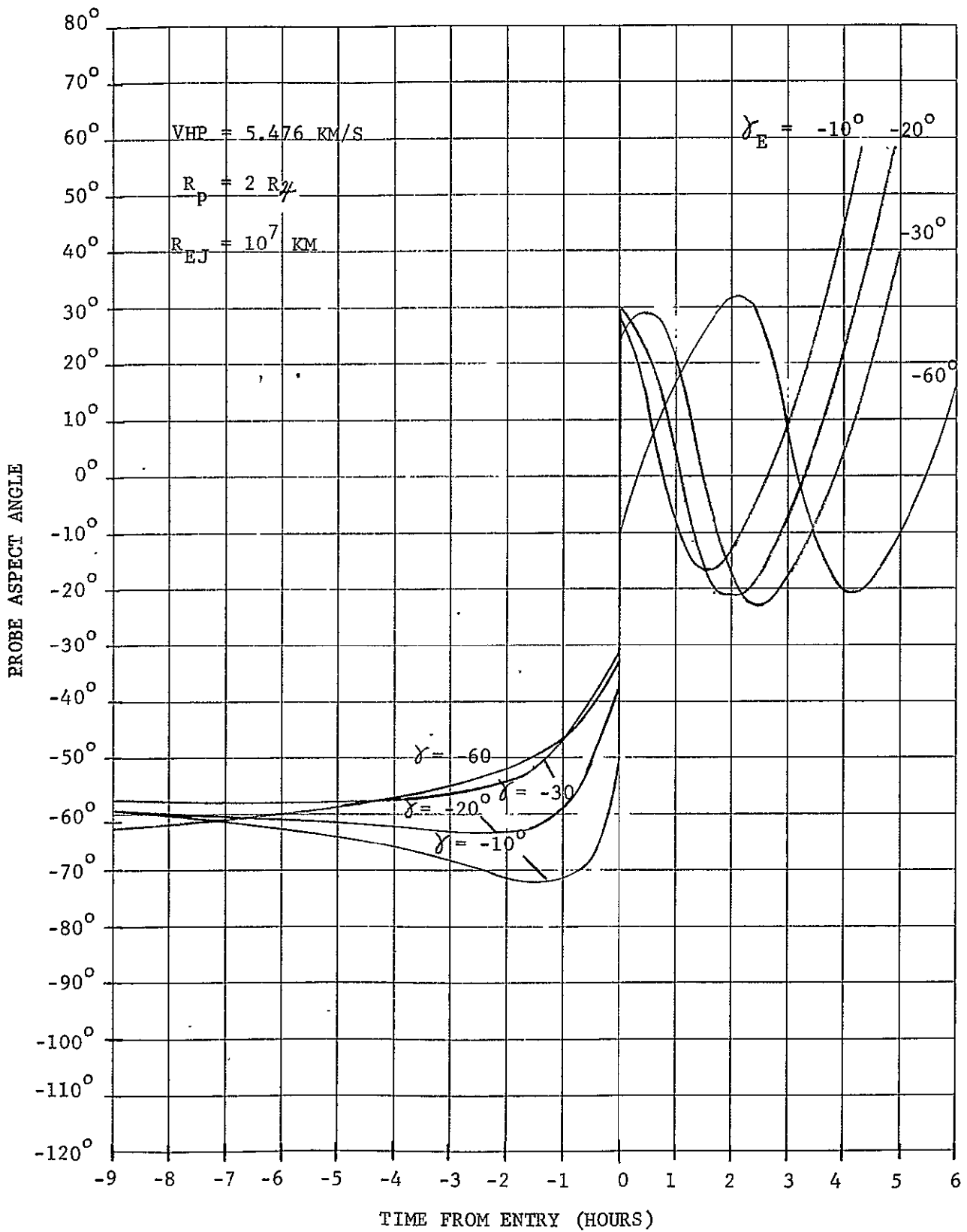


FIGURE IVC-3
SPACECRAFT ASPECT ANGLE VS TIME

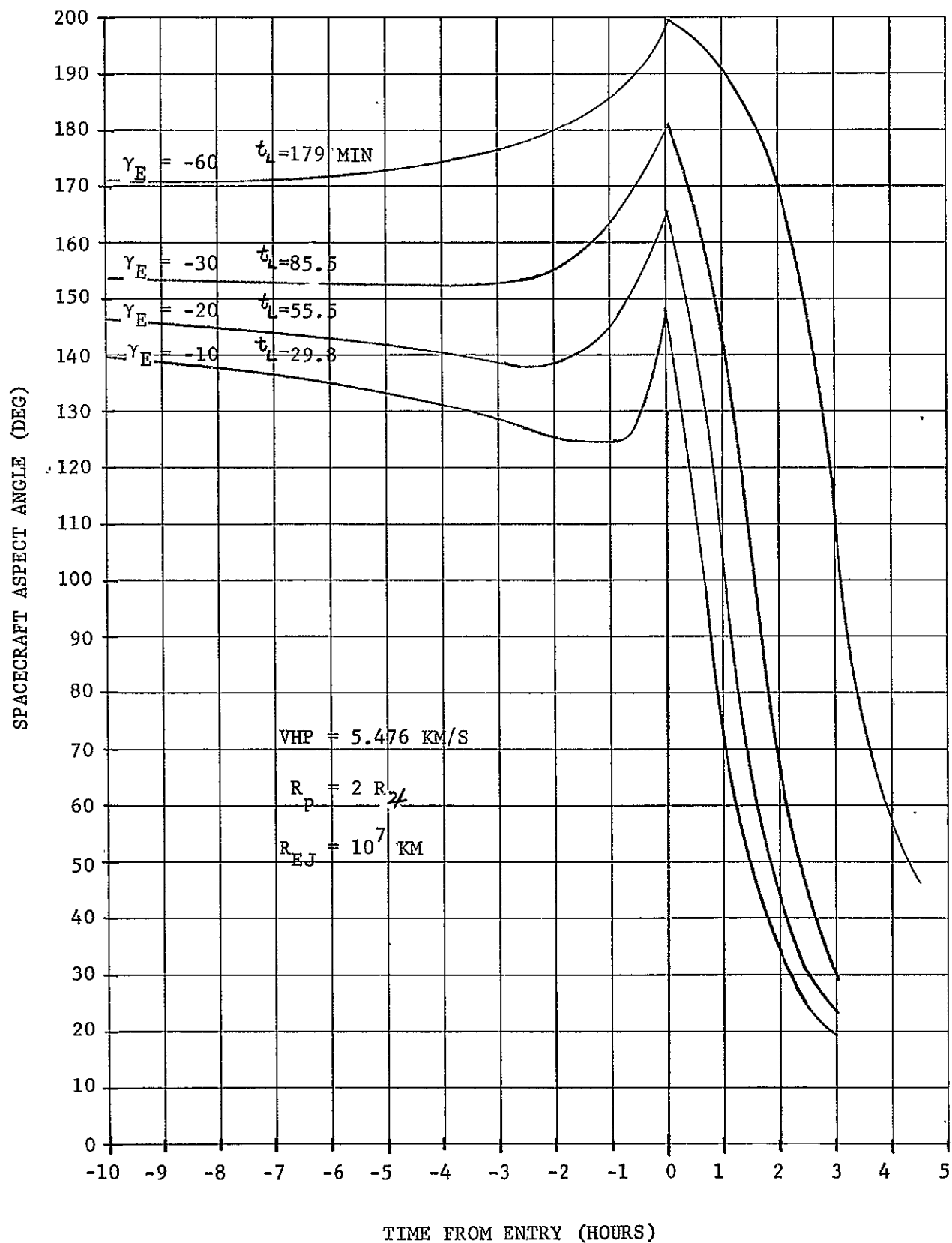


FIGURE IVC-4
COMMUNICATIONS RANGE VS TIME

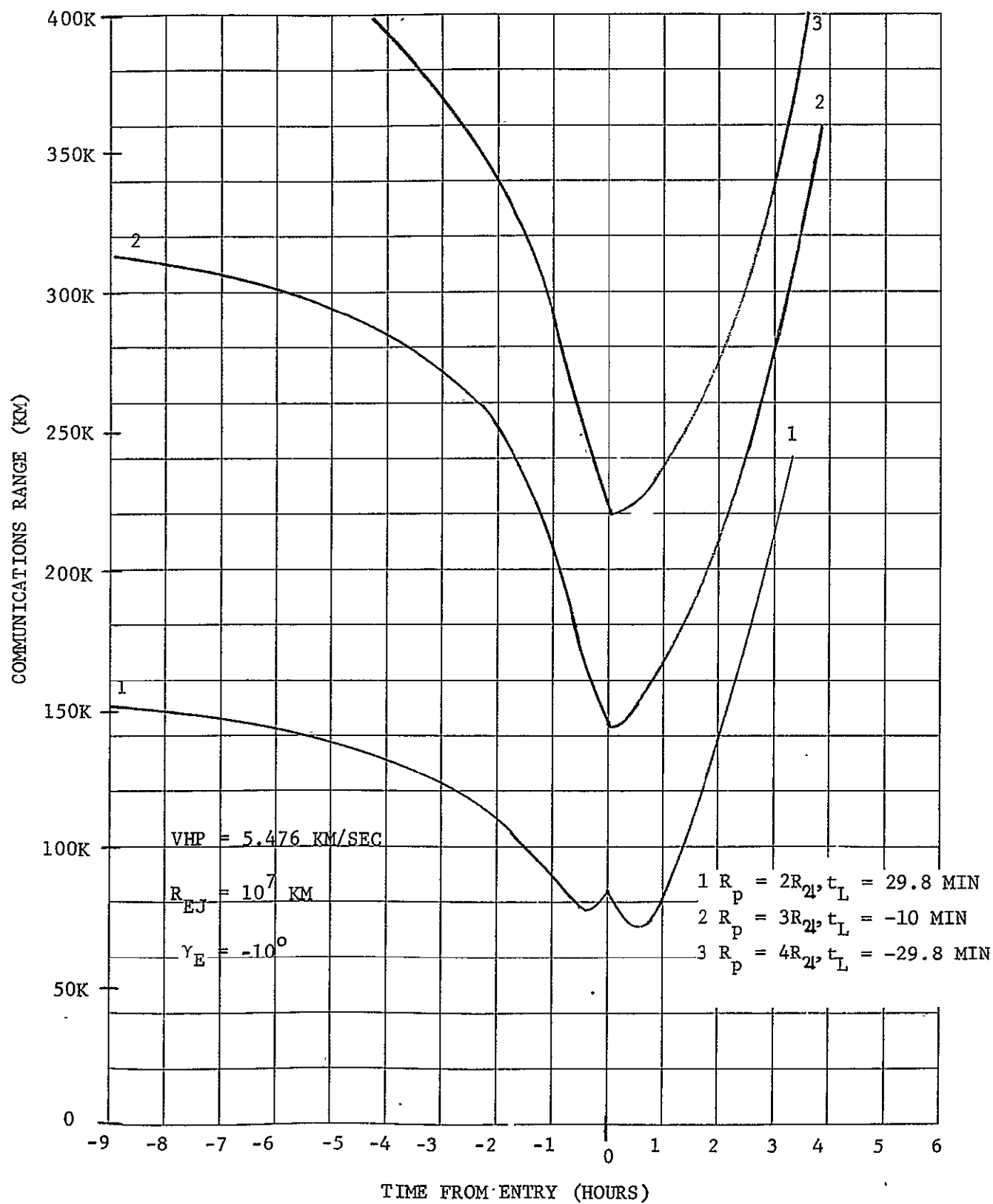


FIGURE IVC-5
PROBE ASPECT ANGLE VS TIME

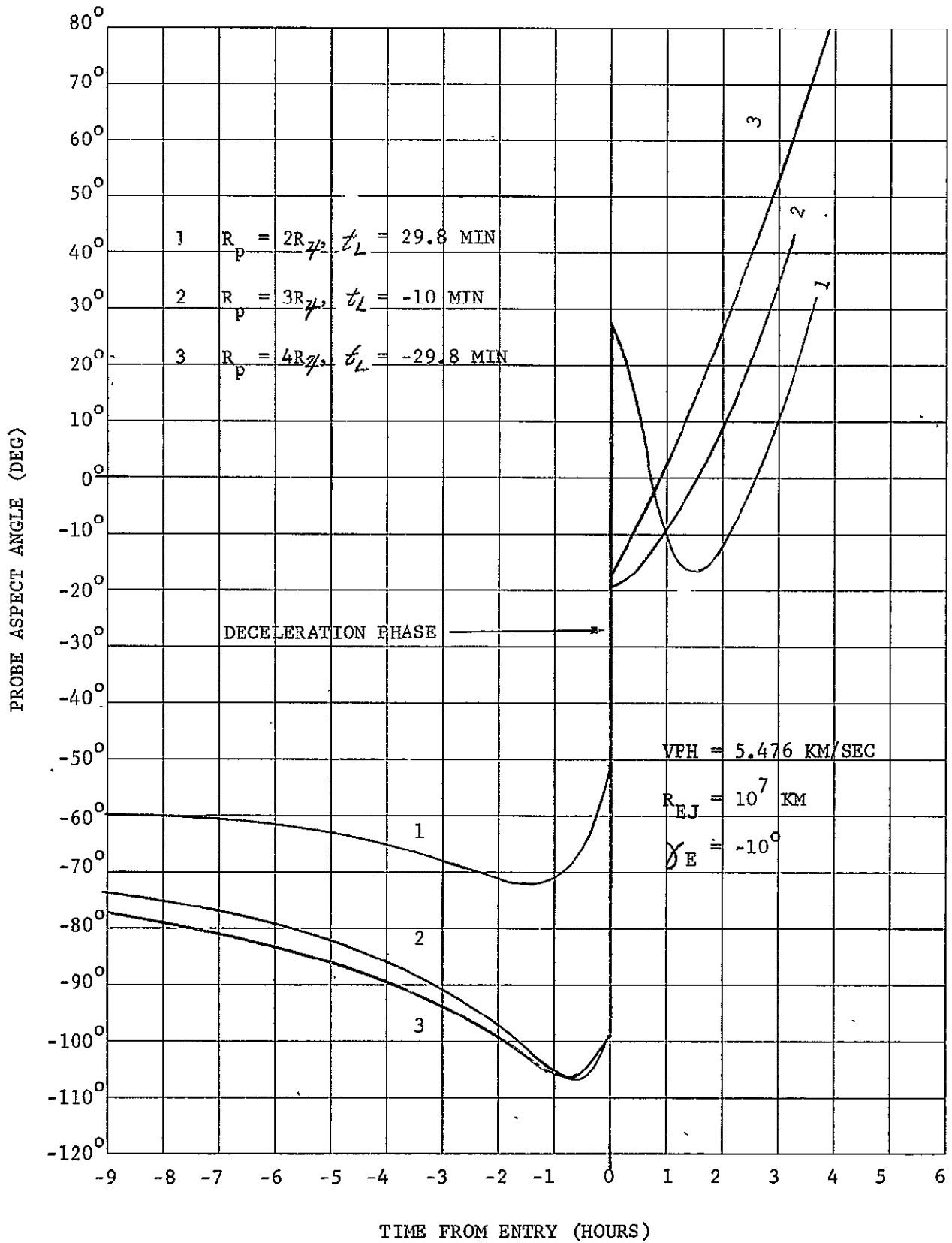


FIGURE IVC-6
SPACECRAFT ASPECT ANGLE VS TIME

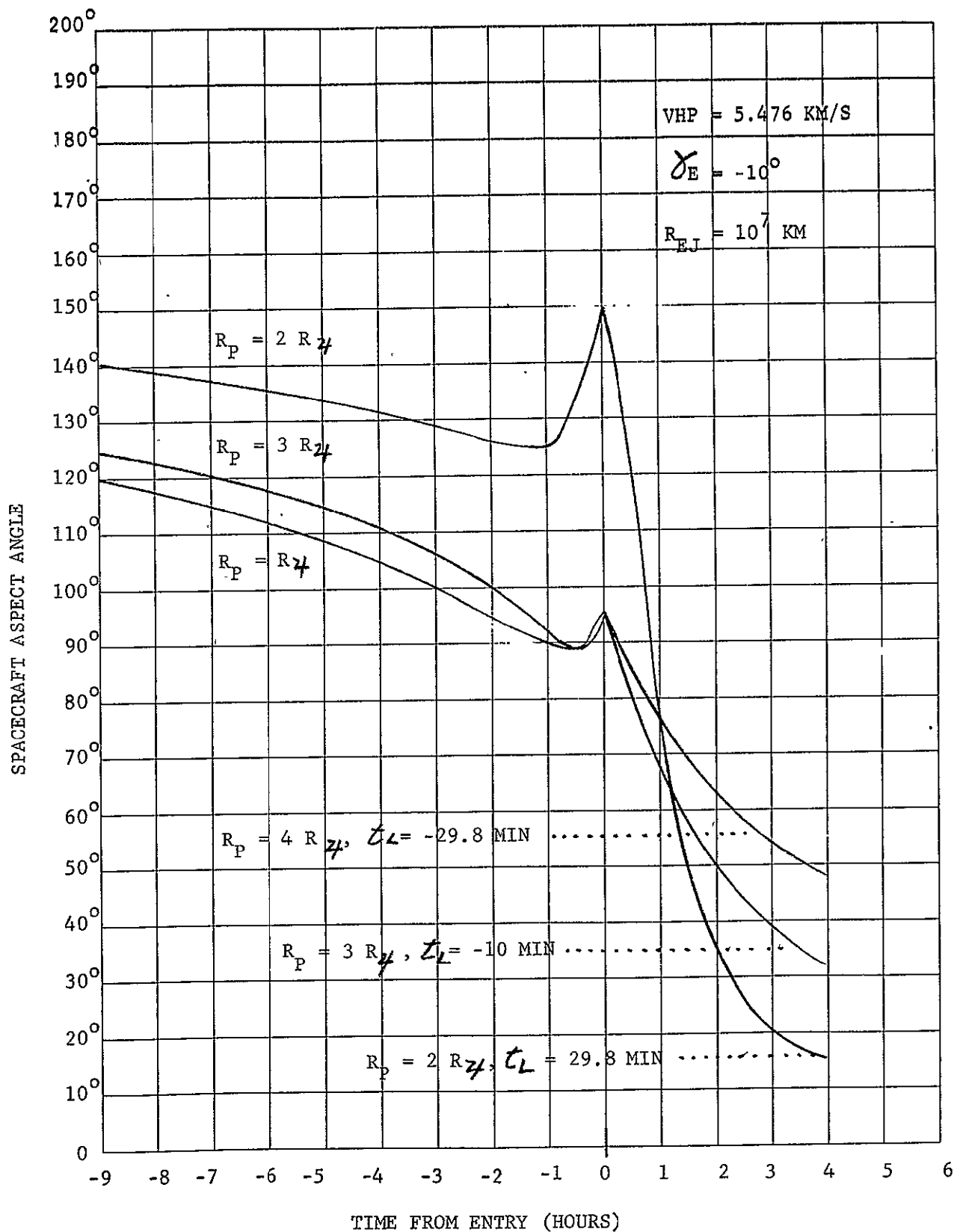


FIGURE IVC-7
COMMUNICATIONS RANGE VS TIME

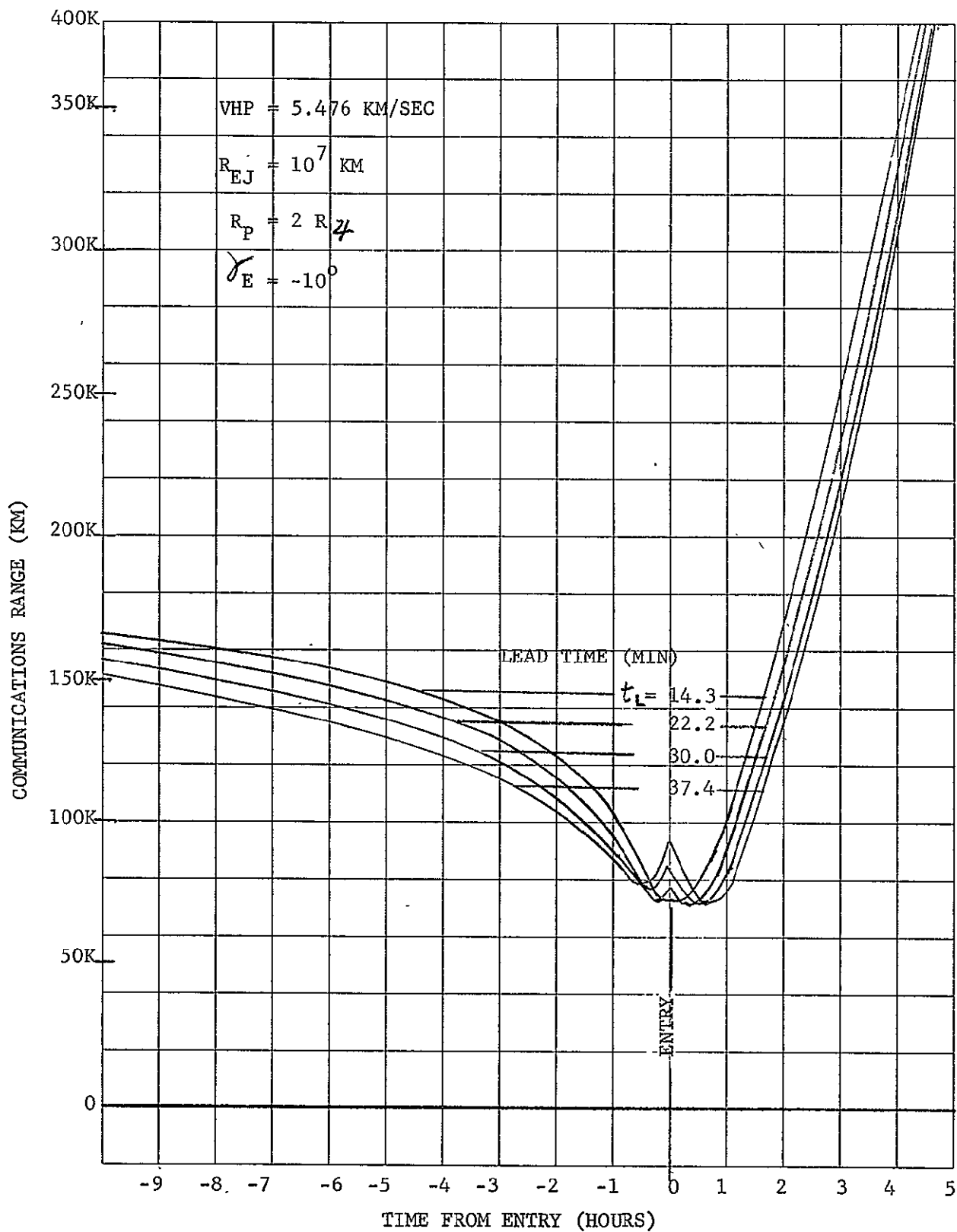


FIGURE IVC-8
PROBE ASPECT ANGLE VS TIME

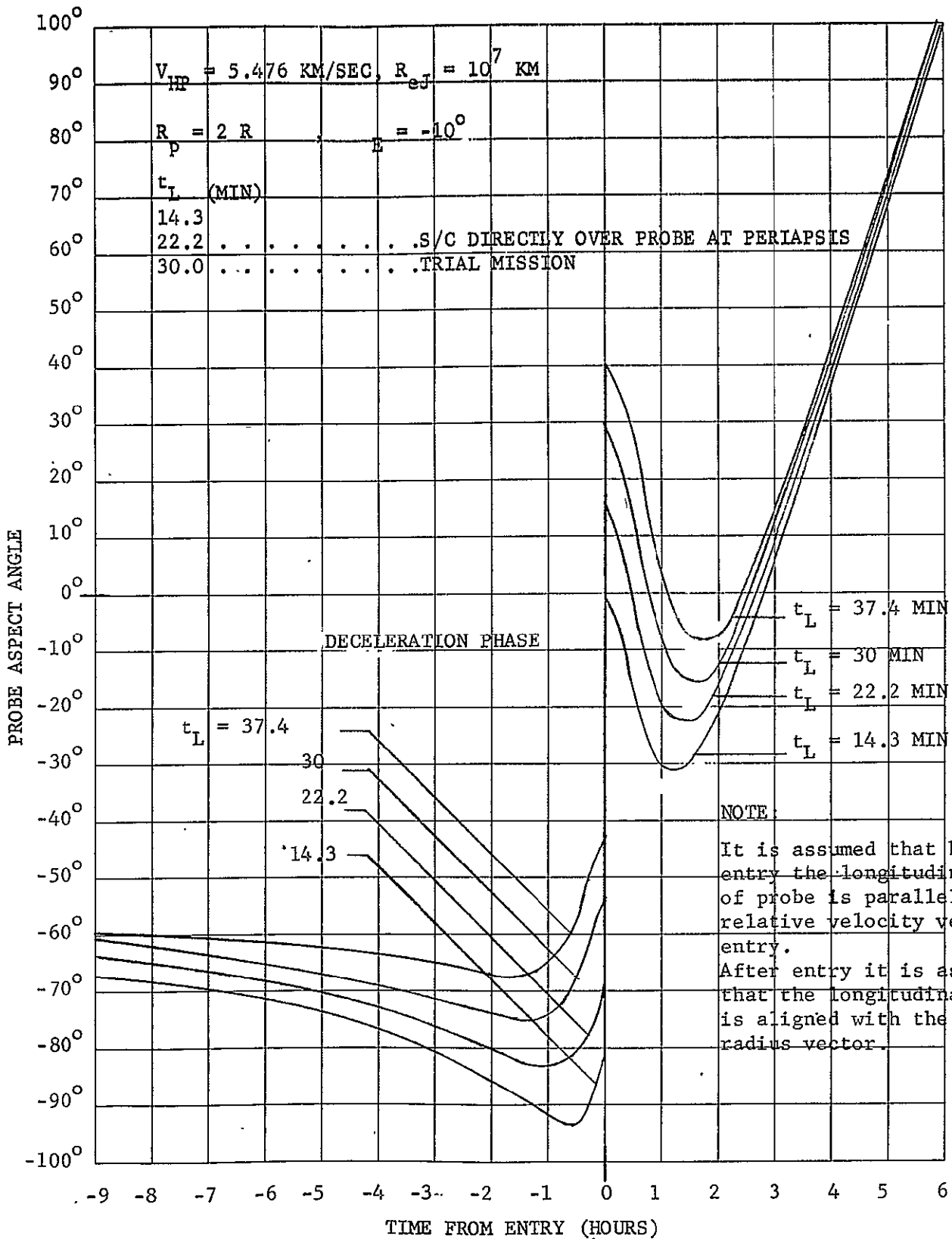


FIGURE IVC-9
SPACECRAFT ASPECT ANGLE VS TIME

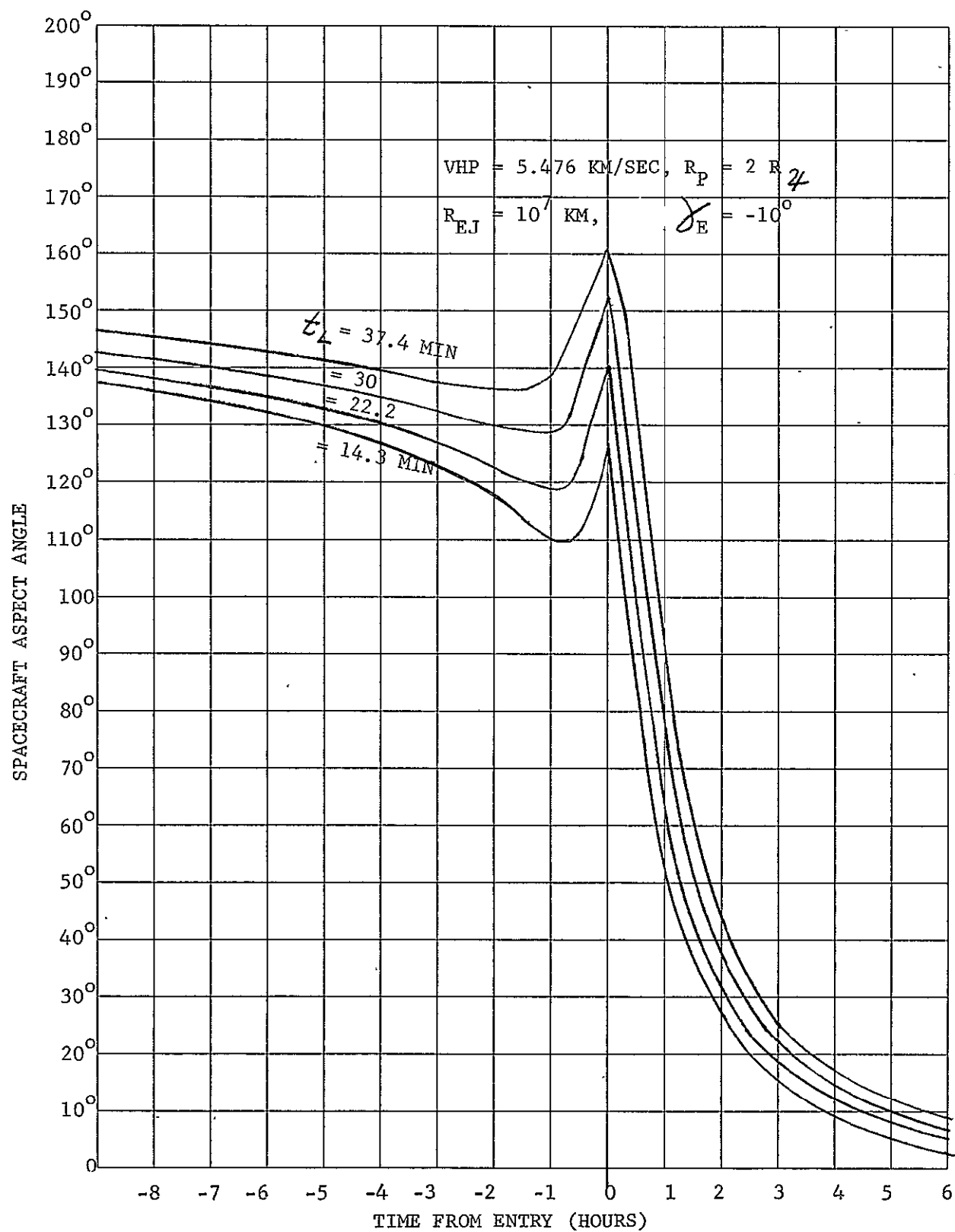


Figure IVC-6 shows spacecraft aspect angle variations for R_p of 2, 3 and 4. As R_p is increased the angular excursion decreases for a given mission duration.

Figure IVC-7 shows the effect of lead time variations on range at an R_p of 2 and γ_E of -10° . A 1.8 db difference in space loss occurs at 2.5 hours past entry for the extremes of lead time shown.

Figures IVC-8 and IVC-9 show antenna aspect angle variations of the various lead times considered in previous figures.

Relative communications gains and losses in the relay link as a function of time are shown in Figure IVC-10 for a frequency of 1.80 GHz using variables for radius of periapsis and lead times. Flight path entry angle (γ_E) is constant at -10° . Terminal descent depth is 19.3 Earth atmospheres.

Conclusions that can be reached from the above figures and from the baseline parametric study which is detailed in Volume II are generally as follows for probe entry near the planets equator which is the only case considered here.

1. A radius of periapsis of approximately 2 planet radii maximizes the communications period for entry flight path angles of interest.

This is primarily illustrated by the loss curves of Figure IVC-10 which combine effects of range and antenna angles for R_p of 2, 3 and 4 R_J . For comparison of these data with data for a trajectory having an R_p of less than 2 R_J ($R_p = 1.6 R_J$) see the description of mission E in Volume II.

2. Lead time should be such as to put the entry probe at subperiapsis as the spacecraft reaches periapsis. This is true for R_p of about $1 \frac{3}{4}$ to 4 R_J . Beyond an R_p of 4 R_J , optimum lead time for post entry optimization places the spacecraft progressively past periapsis point as the R_p is increased.
3. Generally, as γ_E is increased communications range for pre-entry and entry is increased. See Figure IVC-1.
4. As R_p is increased to 4 and beyond, pre-entry communications becomes more and more difficult in relation to post entry due to adverse entry vehicle antenna aspect angle before the probe turns to descend vertically. This is apparent from Figure IVC-5 and IVC-10.

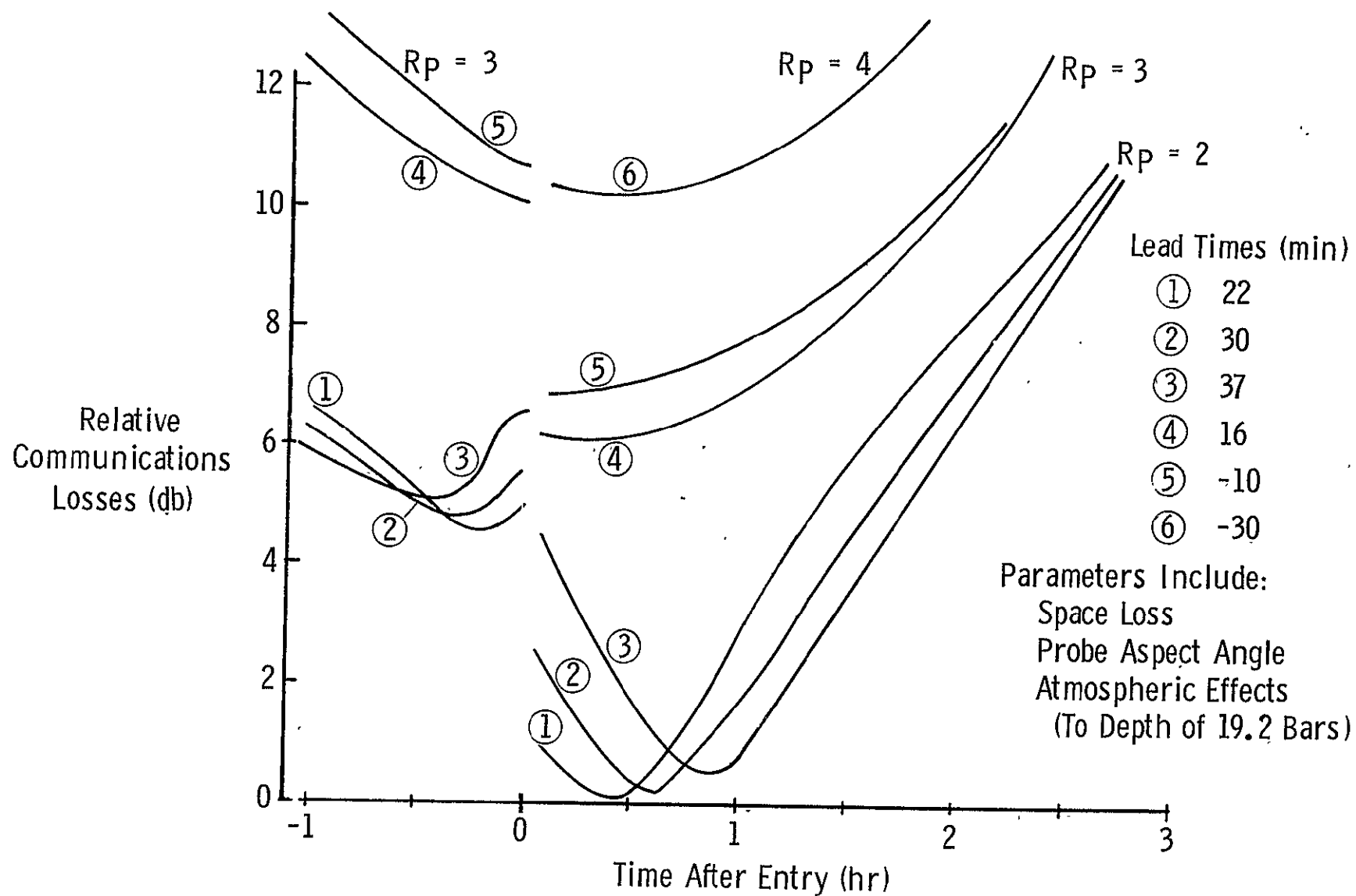


Figure IVC-10 Communications - Losses Vs Trajectory & Lead Time

5. As R_p is increased beyond $2 R_J$, mission durations must be progressively shortened due to adverse post entry probe antenna aspect angles and longer communications ranges (Figure IVC-10).
6. As probe depth into the atmosphere is increased the optimization of antenna aspect angle to near zenith becomes more and more important. This is apparent from the fact that the atmospheric attenuation increases approximately by the factor of the secant of the transmission angle off zenith times the zenith attenuation in db. See Chapter IV K Vol III.

A baseline parametric study further illustrating the sensitivity of communications parameters to trajectory, γ_E and depth into the atmosphere was performed during the course of this study. The reader is referred to Volume II for the ground rules and results of that study.

D. Relay vs Direct Link

In general it can be said that probe targeting for a direct link option required probe entry angles (γ_E) of from approximately -45 to 90° and restricted targeting such as to keep the probe within roughly 25° of the sub Earth point for the duration of the mission. The former (γ_E of -45 to 90°) occurs due to launch constraints and the latter (remain within 25° sub Earth) due to restrictions on both probe antenna aspect angle and increase in atmospheric attenuation as a function of angle off zenith. Mission F is a detailed example of what can be done to communicate directly with Earth under the above constraints. See Volume II for the mission description.

It has been found that for optimum relay links relatively shallow entry angles (-10 to -30°) and a flyby R_p near $2 R_J$ give good Pre and Post entry results. However, one case considered in the parametric baseline study Volume II included an entry at -50° and a flyby R_p of $2 R_J$. Descents to depths down to 300 Earth atmospheres were treated parametrically. Communications parameters for these cases are shown in Table IVD-1 along with data for the direct link case to give a comparison. These data were taken from Volume II baseline parametric and Mission F description which should be consulted for details and sensitivities.

It can be concluded that from the communications standpoint, disregarding the physical entry problem, a relay link provides the greater flexibility for selection of mission and targeting. In general, higher bit rates and longer mission durations are attainable with relay links with much less

complexity in the probe subsystems, but at the expense of added spacecraft complexity required by the relay link terminal equipment.

Direct links can be considered only for high entry gammas.

Relay links become less practical for cases where the probe entry near the equator is more than about 60° from subperiapsis point for an R_p of $2 R_J$. As the R_p is increased the entry point must be closer to the subperiapsis point to provide a reasonably good relay link. Consult Volume II baseline parametric data for sensitivities of relay links to R_p , γ_E and depth of descent.

Table IVD-1 shows a comparison of relay and direct link transmitter power and antenna requirements for various depths into the atmosphere. A 3.4 ft diameter antenna is assumed for the spacecraft relay antenna and a 22 db retrodirective phased array is used for the direct link. Required transmitter power is increased as required as the depth of penetration is increased.

Weights for the relay communications case are given in the baseline parametric study Volume II. Weight for the direct link case for a 15 watt transmitter and mission depth of 17 atmospheres corresponds to Mission F as described in Volume II.

Direct link weight for other cases was not determined due to lower priority of interest in missions requiring the high weight penalties for higher γ_E .

TABLE IVD-1

COMMUNICATIONS SYSTEM PARAMETERS, DIRECT VS RELAY LINKS, ENTRY ANGLE $\gamma = -50^\circ$

Link Type	Periapsis Radius, R_J	Penetration Depth Atm	Transmitter Power, Watts	Relay Dish Size, Ft	Frequency, GHz	Probe Antenna	Bit Rate, bps
Relay	2	17	15	3.4	2.3	Omni	40
Relay	2	25	20	3.4	2.3	Omni	40
Relay	2	31	20	3.4	2.3	Omni	40
Relay	2	50	20	3.4	1.6	Omni	40
Relay	2	300	30	3.4	1.6	Omni	20
Direct	-	17	15	-	2.3	Phased Array, 22 db Gain	20
Direct	-	31	25	-	2.3		20
Direct	-	50	46	-	2.3		20
Direct	-	17	25	-	2.3		40
Direct	-	31	43	-	2.3		40
Direct	-	50	76	-	2.3		40

E. Frequency Selection

There are 3 factors that in general have carried the most weight in selection of a probe to spacecraft relay link radio frequency to be used for the missions considered in this study. These are the system temperature, the atmospheric attenuation and the signal acquisition and tracking problem which entails s/c antenna beamwidth and frequency uncertainty due primarily to doppler

1. Spacecraft Receive System Temperature

Spacecraft receive system temperature as a function of frequency for all relay missions for this study are based on the simplifying assumption that antenna temperatures, including effects of decimeter radiation, correspond to the microwave brightness curves given in Reference IVE-1. See Figure IVE-1. These are a compilation of measurements resulting from microwave radiometry studies made over a number of years from Earth. The source of the decimeter radiation appears from Earth to be spread over a region approximately equal to 3 planet diameters. This places the spacecraft in the outer edge of the system for all R_p of 3 R_J or more and for the latter part of missions with trajectories having R_p of 2 R_J , thus such an assumption appears valid since the source is distributed over the entire 3 db beamwidth of the spacecraft relay antennas used in this study. For portions of the $R_p = 2 R_J$ trajectory where the spacecraft is near periapsis and well inside the distributed source with the spacecraft antenna looking at the planet the antenna temperature should drop. This improvement in system temperature will be considered a plus in the tolerance column for our design control table and will not otherwise be considered. A noise figure of 3 db has been assumed for the spacecraft receiver(s) for all frequencies under consideration. The resulting spacecraft receive system temperature as a function of frequency is shown in Figure IVE-1. No other contribution to system temperature is considered significant.

2. Atmospheric Attenuation

Another dominant factor to be considered along with system temperature is atmospheric losses. These include atmospheric attenuation due

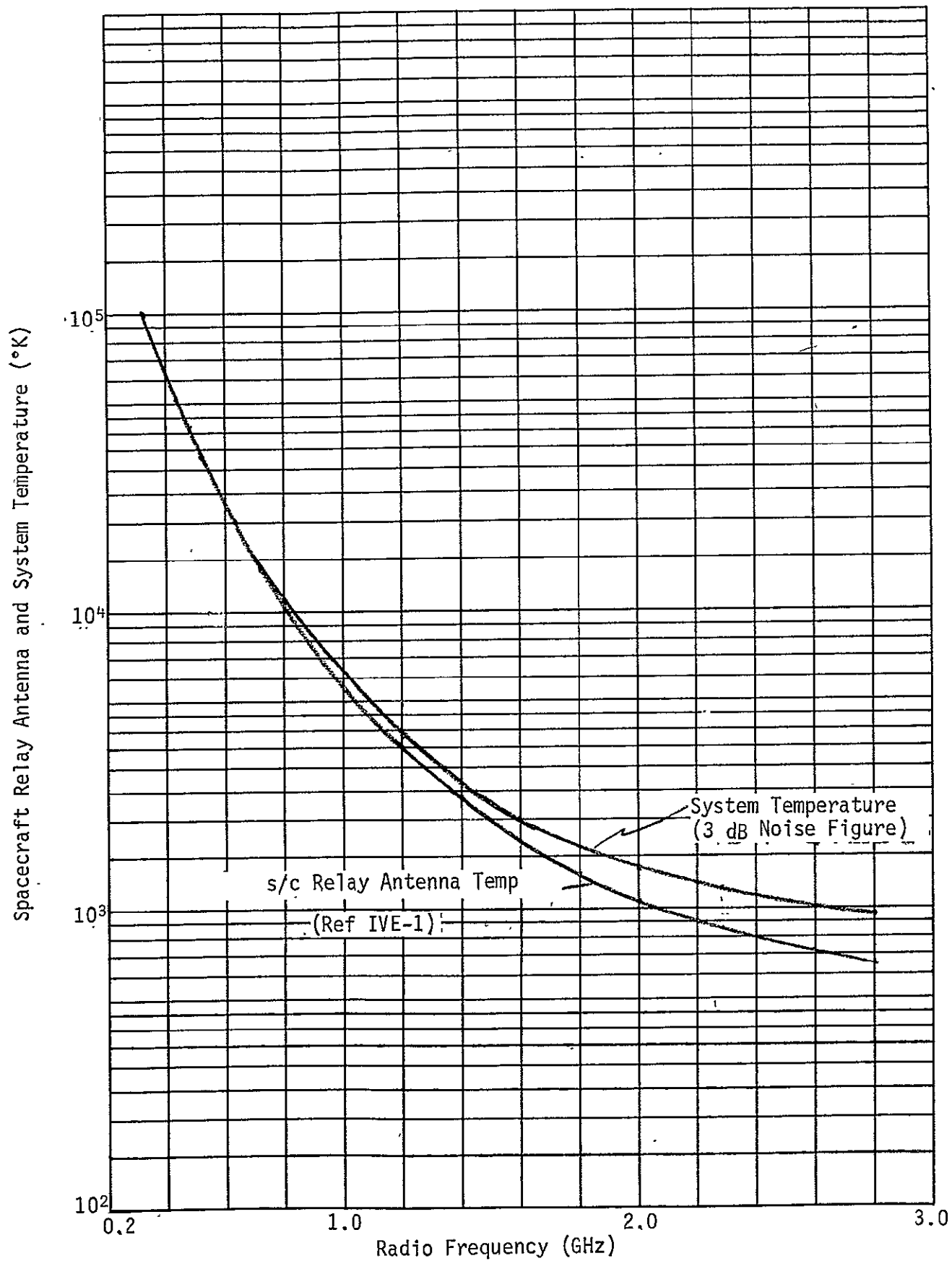


Figure IVE-1 Spacecraft Relay Receive System and Antenna Noise Temperatures Versus Radio Frequency

to the atmospheric constituents as well as defocussing losses. Detailed discussion of these losses for the various atmospheric models and how the losses were estimated are covered in Chapter IVK. Figure IVE-2 shows the relative combined effect on a communications link of spacecraft system temperature plus atmospheric losses at zenith for various descent depths as a function of the radio frequency where relative required power gain in db represents the additional link power gain required to overcome the combined effect of system temperature and zenith atmospheric attenuation for conditions other than a frequency of 2.3 GHz and zero depth into the atmosphere. It is further assumed that the probe antenna gain is constant for all frequencies and the spacecraft antenna aperture is constant such that the product of space-loss and spacecraft antenna gain at any frequency of interest is constant.

The no atmosphere curve (zero depth) represents $10 \log_{10}$ of the ratio of system temperature at any frequency to the system temperature at a frequency of 2.3 GHz.

The curve for any depth of penetration at any frequency is then equal to the sum in db of the no atmosphere value plus the atmospheric attenuation in db for the depth and frequency selected.

Also shown is an example of a 30° off zenith propagation path from the descent probe to the spacecraft at a descent depth of 1000 atmospheres where attenuation is approximately equal to the zenith attenuation in db multiplied by the sec of the angle off zenith.

These curves are useful as tools in estimating the suitable frequency for the relay link keeping in mind that, as the frequency is decreased to reduce atmospheric losses near the end of the mission, the system temperature is increased for both pre-entry and initial post entry conditions where atmospheric attenuation is negligible and bit rate requirements are in general higher.

3. Frequency Acquisition and Tracking

The third consideration in selecting a relay link radio frequency is the signal acquisition and tracking problem. The probe radio signal must be acquired prior to entry as well as after staging from the

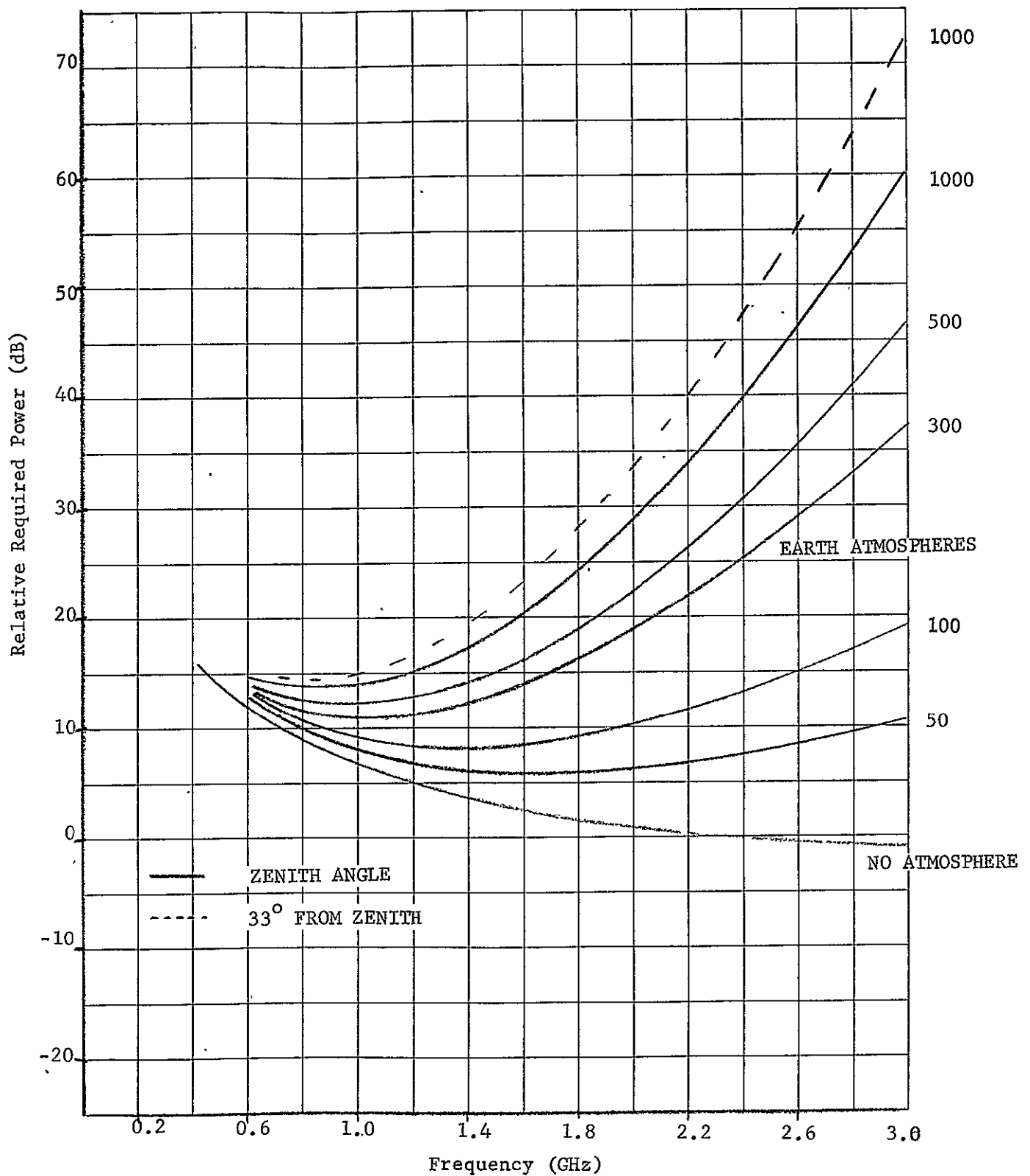


Figure IVE-2 Relative Power Gain Required Versus Frequency for Various Depths into Atmosphere and Constant S/C Antenna Aperture Fixed Probe Antenna Gain

aeroshell for acquisition of pre-entry data and post entry data. Doppler and Doppler rates of the order of 80 KHz and 82 Hz/sec are encountered at 1.2 GHz at pre-entry for spacecraft flyby trajectories in the region of $2 R_p = 2 R_j$. These vary depending upon the flyby geometry as shown in Figure IVE-3 A&B for a frequency of 1.8 GHz.

Spacecraft antenna apertures of from 3.4 ft diameter to 4.9 ft have been considered for the category of missions investigated since the midterm contract report. Antennas of this size result in half power beamwidths of from $6 \frac{1}{4}$ to 20° depending upon the combination of frequency selected and the antenna aperture. Since there is an uncertainty in both the relay link frequency and the spacecraft antenna aspect angle at the time we wish to acquire the signal and, further, since there is a limited time in which we have to acquire the signal we must also consider the consequences of the frequency selection on acquisition time and antenna pointing requirements.

In general the acquisition procedure for pre-entry is to point the antenna at the most likely location of the probe and search in frequency over the 3σ range of unknown frequencies then move the antenna successively to cover the unknown regions in space searching each time over the unknown range of frequencies until the signal is acquired. See Section IVG for further discussion.

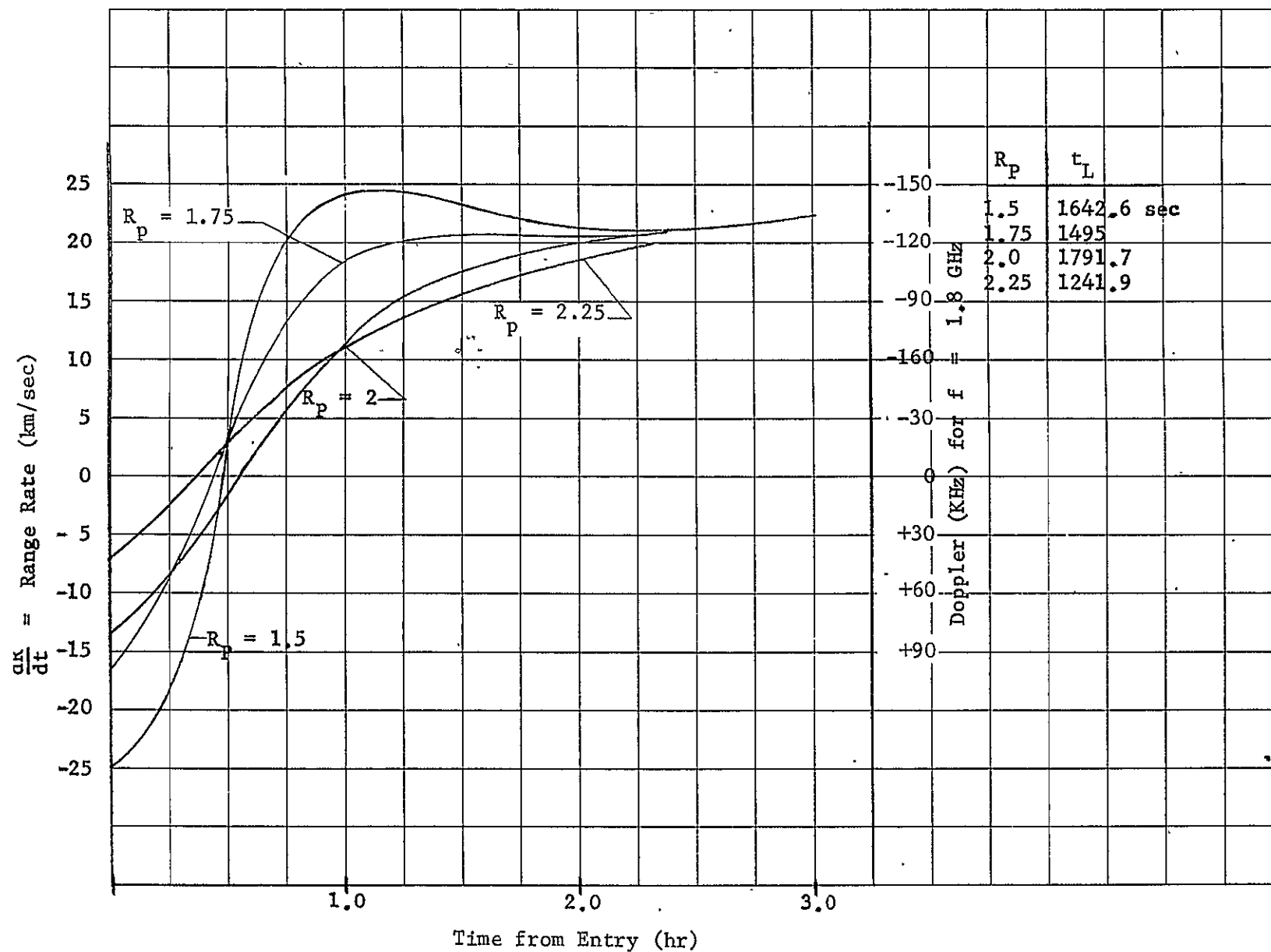


Figure IVE-3A Typical Relay Communications Range Rate and Doppler vs Time

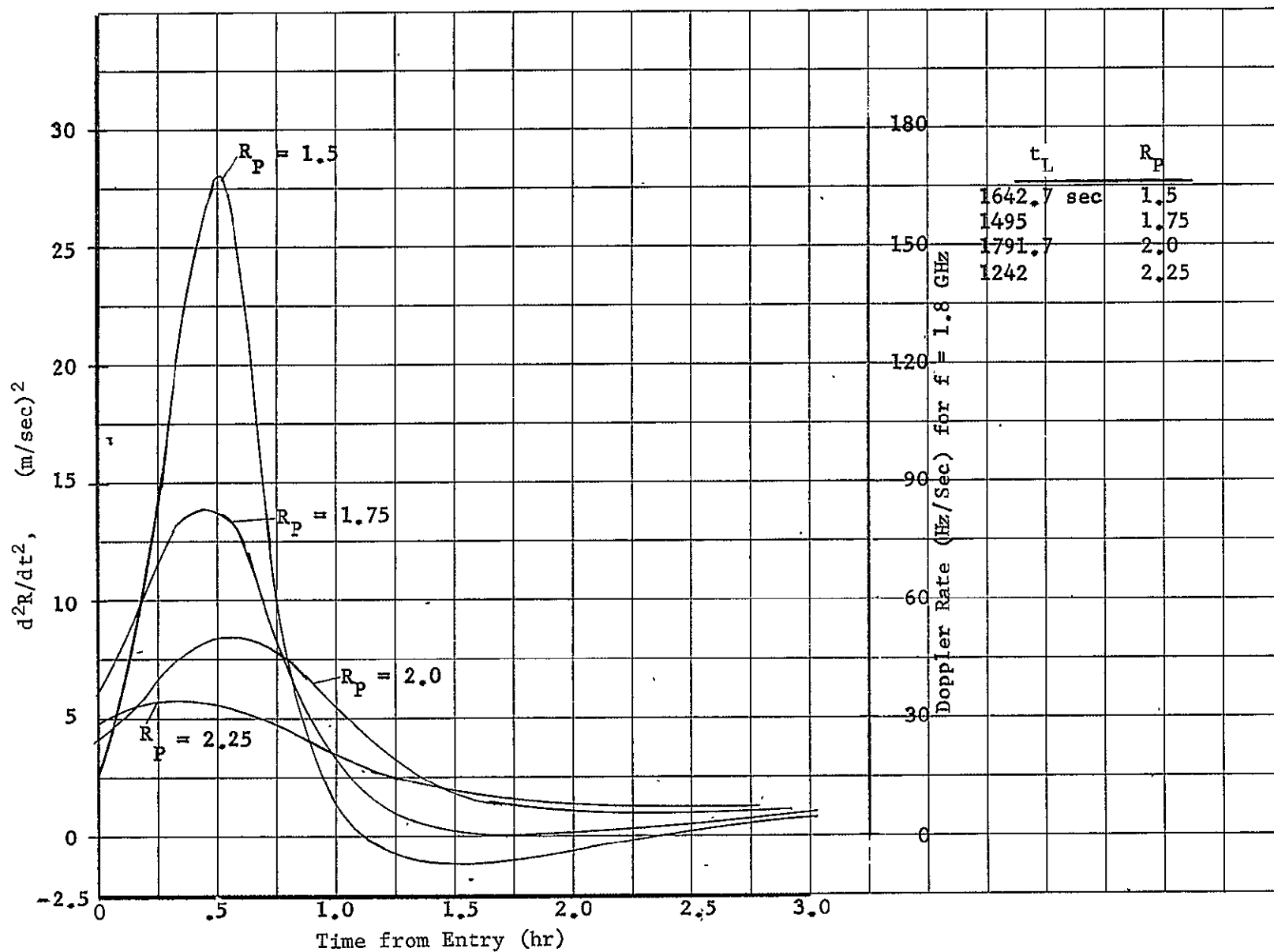


Figure IVE-3B Typical Relay Communications Range Acceleration and Doppler Rate Time

4. Frequency Selection Example

The Design Example mission will be used as an example of the sensitivity of the relay communications system to frequency selection. This mission requires probe entry at a γ_E of -20° followed by a descent to 300 atmospheres in a period of 2.47 hrs after entry. The flyby spacecraft trajectory carries the spacecraft by the planet at an R_p of 2. Assuming a lead time of 57.2 minutes, the resulting relative power requirements for a total signal to noise ratio of one in a one hz noise bandwidth for three relay link radio frequencies is shown in Figure IVE-4. These data consider the receive system temperature, the space loss and the gains of both the spacecraft antenna and the entry vehicle or probe antenna as the case may be.

These data indicate that for a given bit rate over the entire mission, and if one ignores frequency acquisition, the best frequency of the 3 is 1.2 GHz since lower power gain is required in the link. When relative bit rates are considered [100 bps pre-entry, 40 bps initial post entry and 10 bps for the last 0.72 hours of the mission] as well as carrier tracking loop bandwidths compatible with the Doppler rates the curves of required transmitter power versus time change to those shown in Figure IVE-5.

These results show that, for the conditions assumed, the best frequency of the 3 for minimizing transmitter power requirements is still $f = 1.2$ GHz since at $f = 1.6$ approximately 2.5 db additional power is required at mission end and at $f = 0.8$ approximately 2.8 db additional power is required for pre-entry.

It is obvious that for other conditions such as a shallower depth into the atmosphere, and shorter mission duration that initial post entry conditions for example may be the most important period of the mission for frequency selection. In such a case, relative weights must be given to pre-entry and post entry objectives for one to make an intelligent selection.

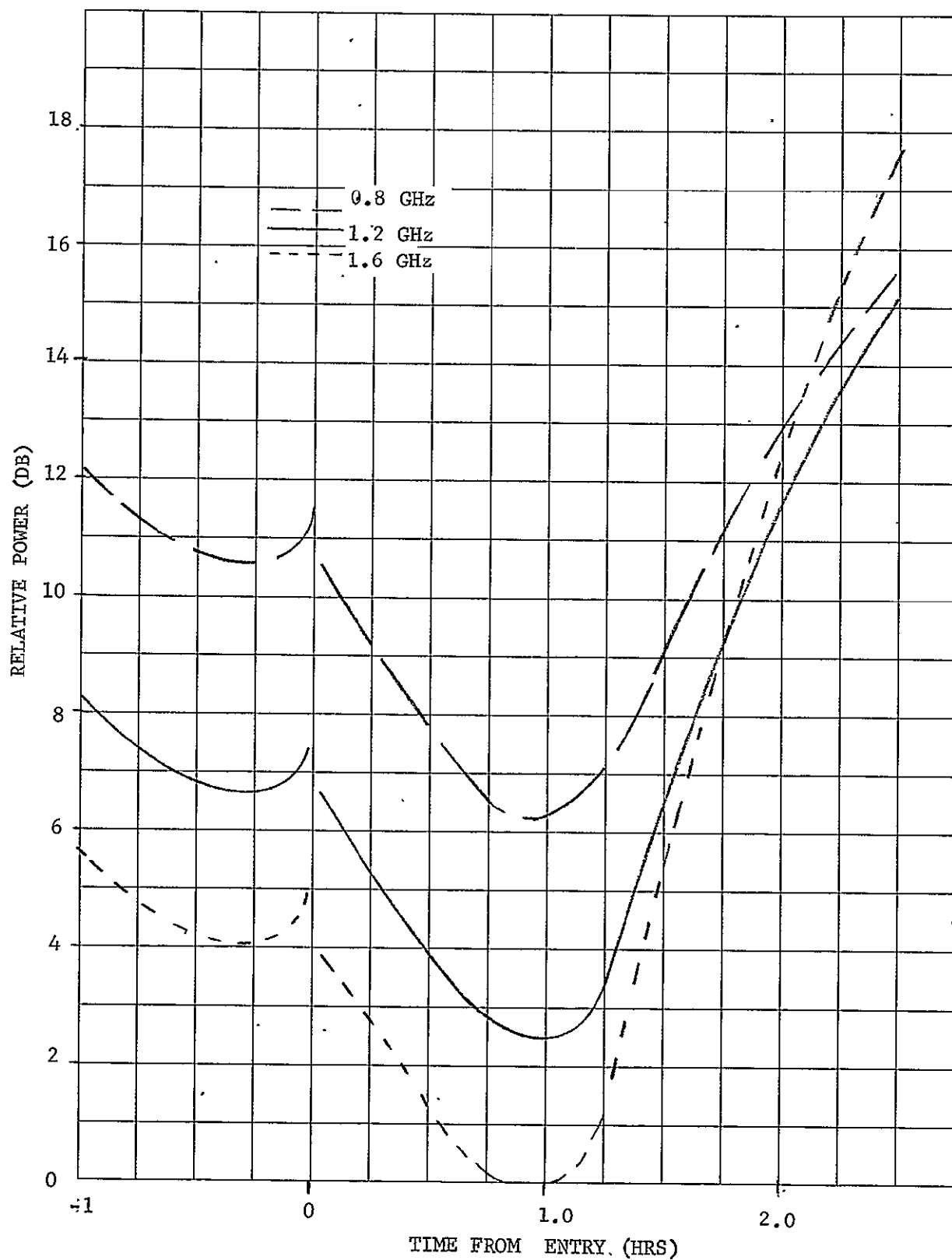


Figure IVE-4 Relative Signal Power Requirements Versus Time
Three Radio Frequencies Constant Bit Rate

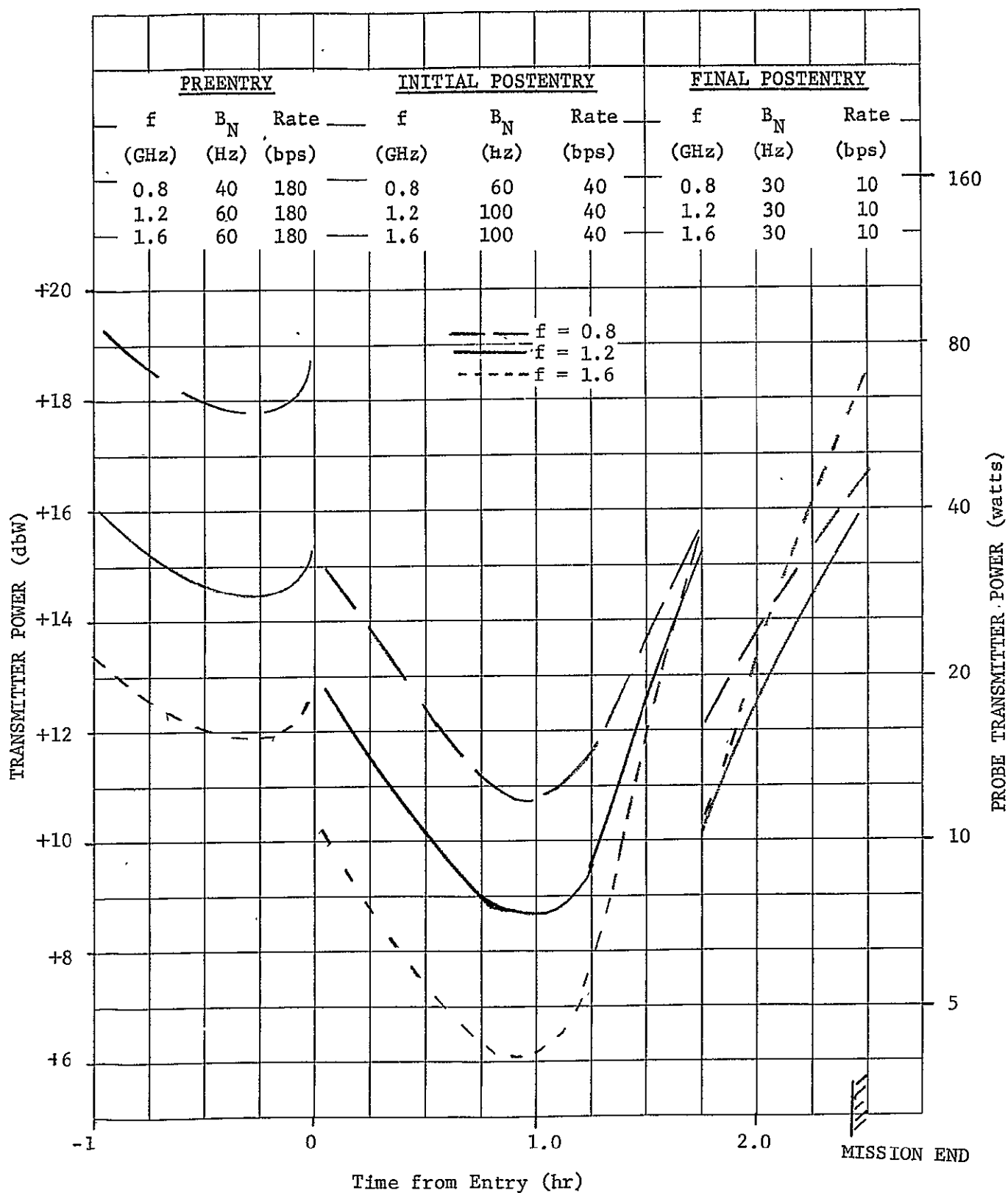


Figure IVE-5 Required Transmitter Power Versus Time for Three Radio Frequencies

F. Modulation and Coding

Only coded PCM/PSK/PM modulation was considered for probe to spacecraft relay links due to the more efficient operation. Large frequency uncertainties prohibited consideration of multiple frequency shift key operation especially since the receiver is located aboard a spacecraft.

Convolutional as opposed to biorthogonal coding was selected on the basis of superior performance by as much as one db plus the fact that both the required number of symbols per bit and the bandwidth are less for the convolutional system. This results in more energy per symbol for better symbol synchronization. The above are based on comparison of the following. In the first case, a rate $1/3$, constraint length four convolutional code and a Viterbi's algorithm decoder using soft decision, 3 bit symbol quantization. Output is delayed three constraint lengths.

This is compared with both a constraint length 4 and constraint length 7 code generator and biorthogonal decoder. Comparative estimates of performance are given in Figure IVF-1 (Reference IVF-1).

For the missions considered in this study an E_b/N_0 of 4.0 db was used for a bit error probability of $5/10^4$.

G. Signal Acquisition and Tracking - Relay Link

Special signal acquisition and tracking procedures are required for probe to spacecraft relay links due to the combination of high doppler rates, high doppler frequencies, high spacecraft antenna gains and narrow band carrier tracking loops.

The problem is to acquire the entry vehicle radio signal at least an hour before entry and maintain the link to the point of entry which is defined here as the time when the entry vehicle experiences 0.1 Earth g. At this time the transmitter power is turned off until the descent probe is separated from the aeroshell. This occurs approximately one minute after entry.

The spacecraft system must again acquire the probe signal and track in antenna angle and phase for the duration of the mission.

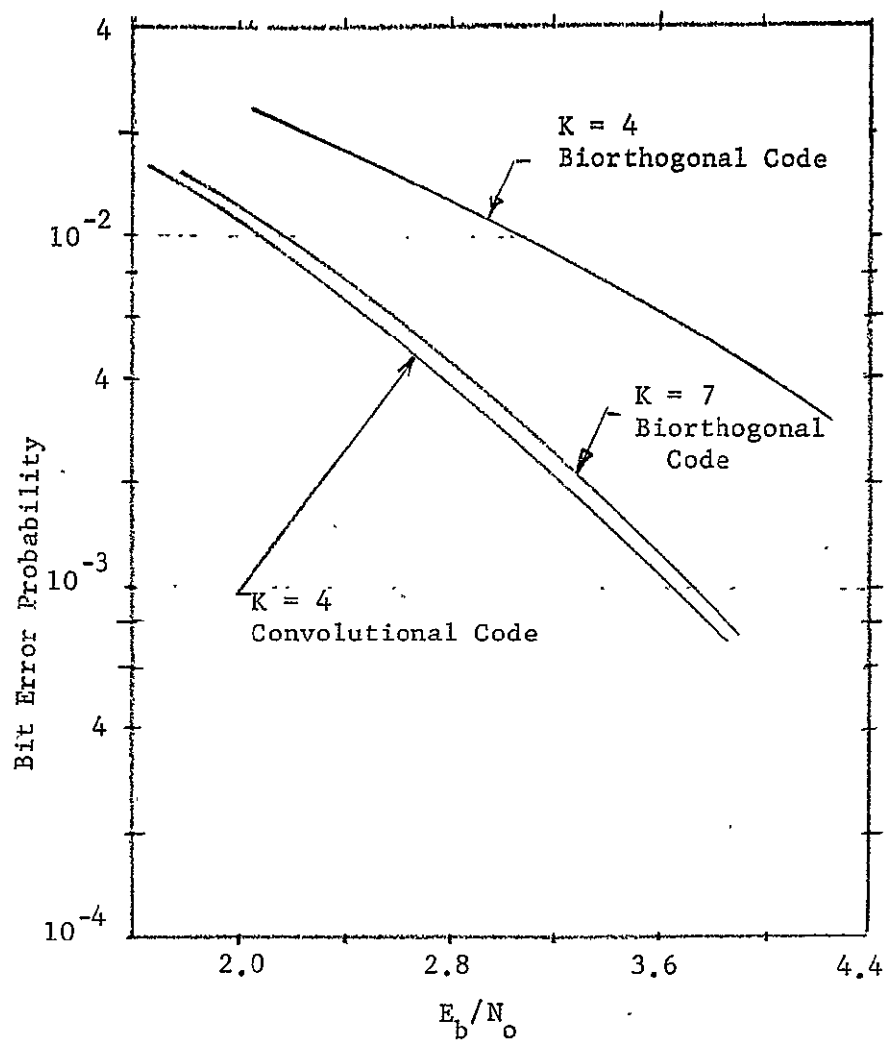


Figure IVF-1 Bit Error Probabilities for K = 4 Codes and a Comparison with a K = 7 Biorthogonal Code.

Uncertainties in the relay link radio frequency to be acquired by the spacecraft receive system and uncertainties in the direction of the incoming signal will exist due primarily to probe deflection and reorientation maneuvers when the spacecraft and probe are separated. The probe transmitter frequency drift due to aging, temperature, entry shock, etc. also contributes to the frequency uncertainty. Uncertainties due to deflection maneuvers are treated in Chapter III E for various errors in deflection maneuvers including error in pointing for the deflection. Our interest for the following discussion is in case DE-1 and DE-2 both of which correspond to 3σ deflection errors of 1% in proportionality and 1.5 degrees in pointing during the deflection burn period. However, case DE-1 references all dispersions in communications geometry to the nominal entry time of the probe and DE-2 treats all time references to actual entry time of the probe for each of the runs in the Monte Carlo program described in Chapter III E.

These statistical data for Doppler, Doppler rate and antenna pointing parameters obtained in the trajectory error analysis studies as reported in Chapter III E will be used here. These data which are for the Design Example mission are shown in Tables III E-20, III E-21 and III E-22 respectively.

Plots vs time, of conversions of these data to correspond to Doppler and Doppler rate for a frequency of 1.2 GHz are shown in Figures IV G-1, 2 & 3. In Figure IV G-1 the spacecraft is essentially at its nominal position at the time of nominal probe entry with the probe position being variable due to deflection errors. In some cases the probe will not have entered and in other cases the probe will have entered. This can be compared to Figure IV G-2 in which at actual time of Probe entry the spacecraft can be displaced over a range of ± 17 minutes along its nominal trajectory. For the initial acquisition and search phase Figure IV G-1 should be used.

For a frequency of 1.2 GHz the mean Doppler varies over a range of minus 57.5 KHz to plus 80 KHz during post entry and somewhat less for pre-entry. The Doppler rate mean based on actual entry time is always positive and varies over a range of 1.28 Hz/sec to 79.6 Hz/sec. The maximum of any run was 82.5 Hz/sec which occurred at entry. Figure IV G-4 shows 3σ relay antenna

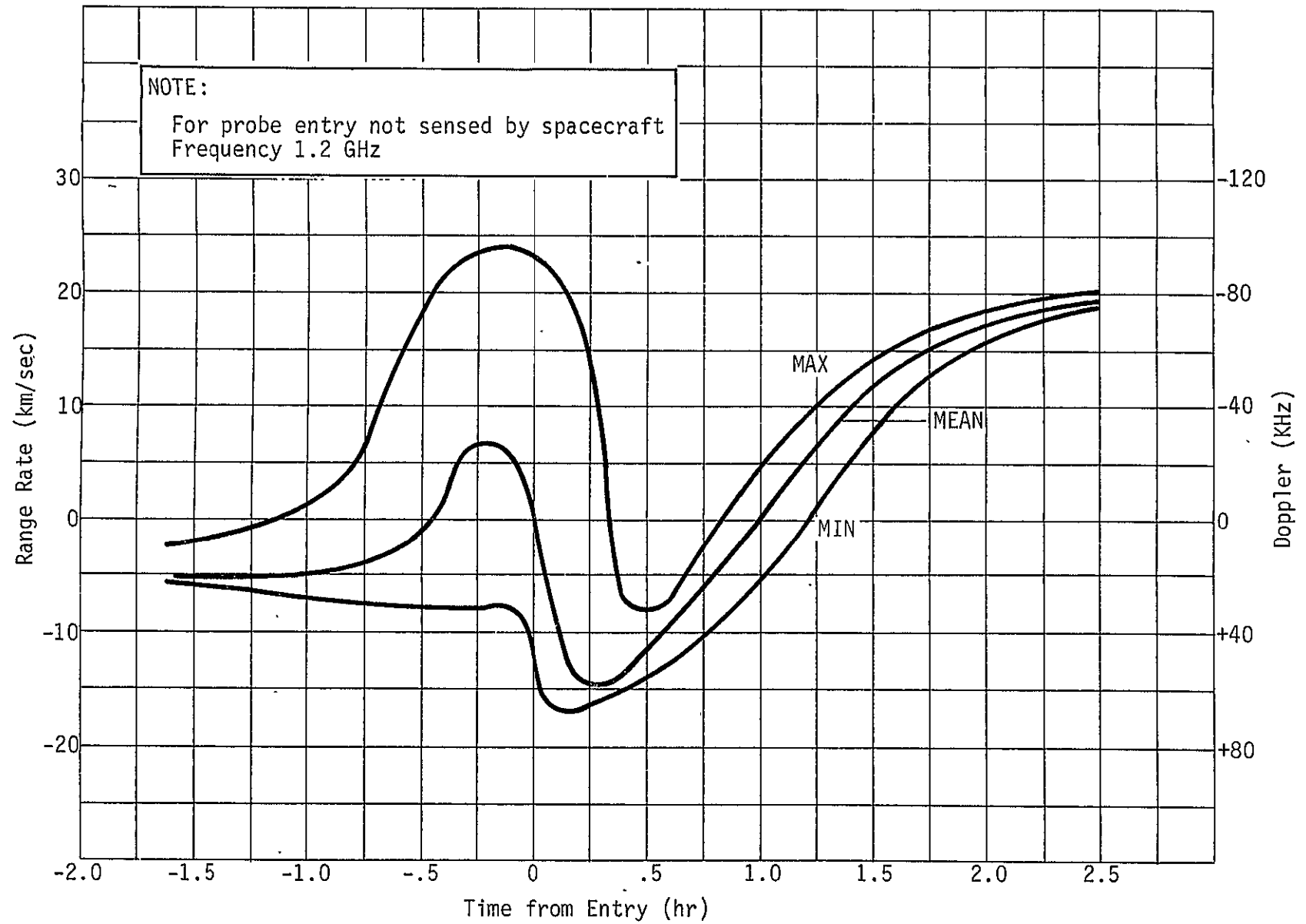


Fig. IVG-1 Design Example Mission Range Rate and Doppler vs Time

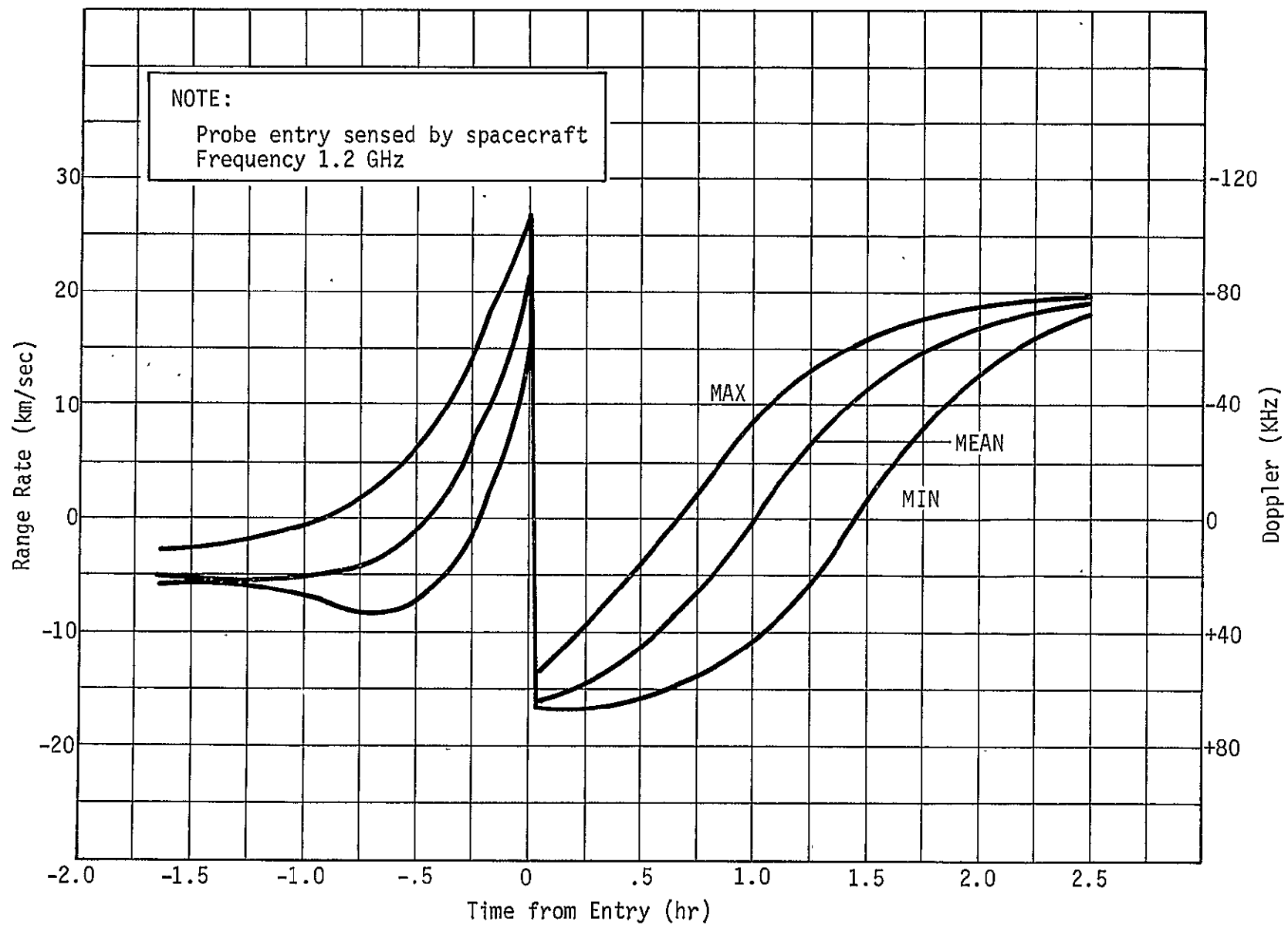


Fig. IVG-2 Design Example Mission Range Rate and Doppler vs Time

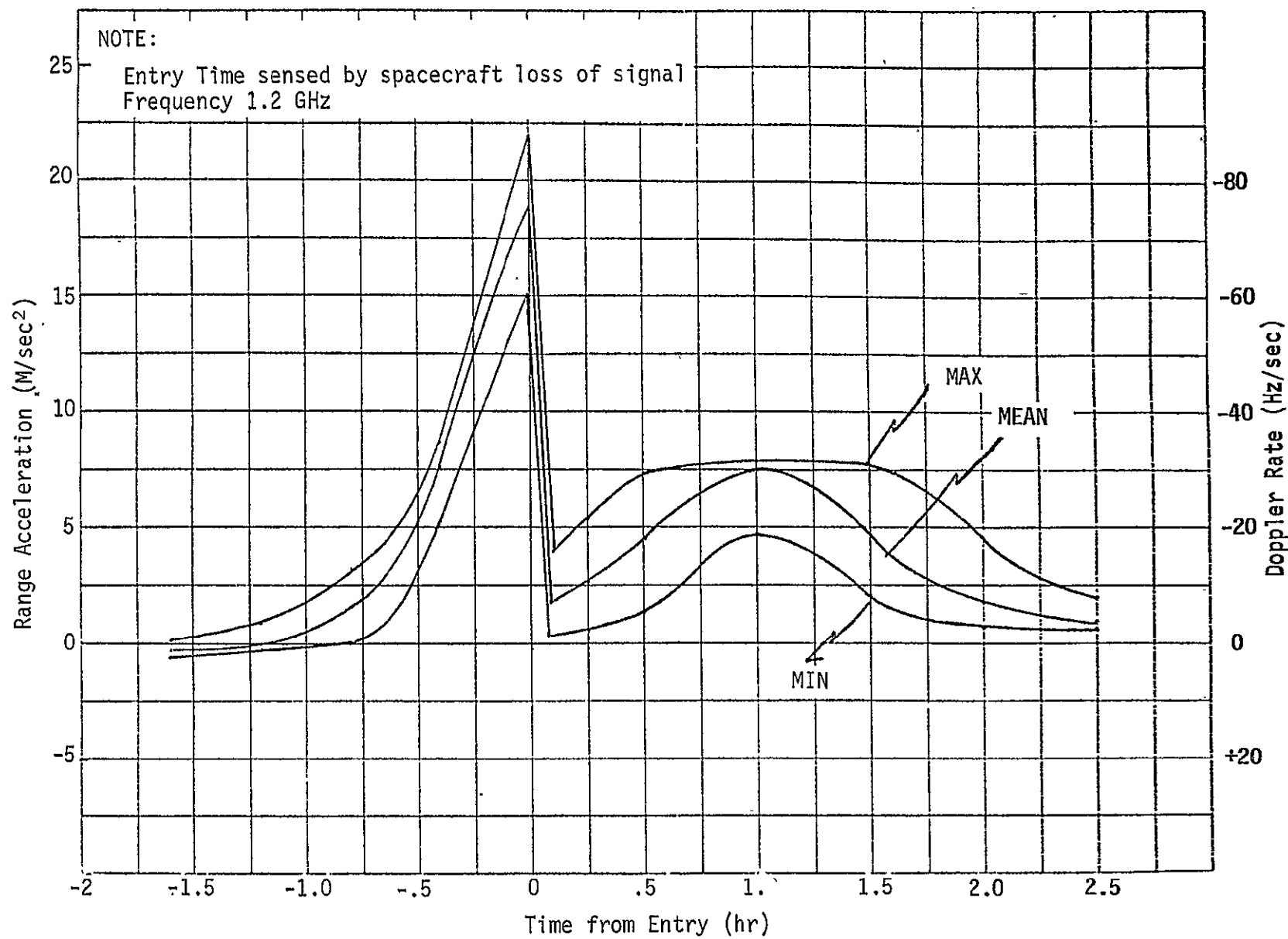


FIG. IVG-3 Design Example Mission Range Acceleration and Doppler Rate

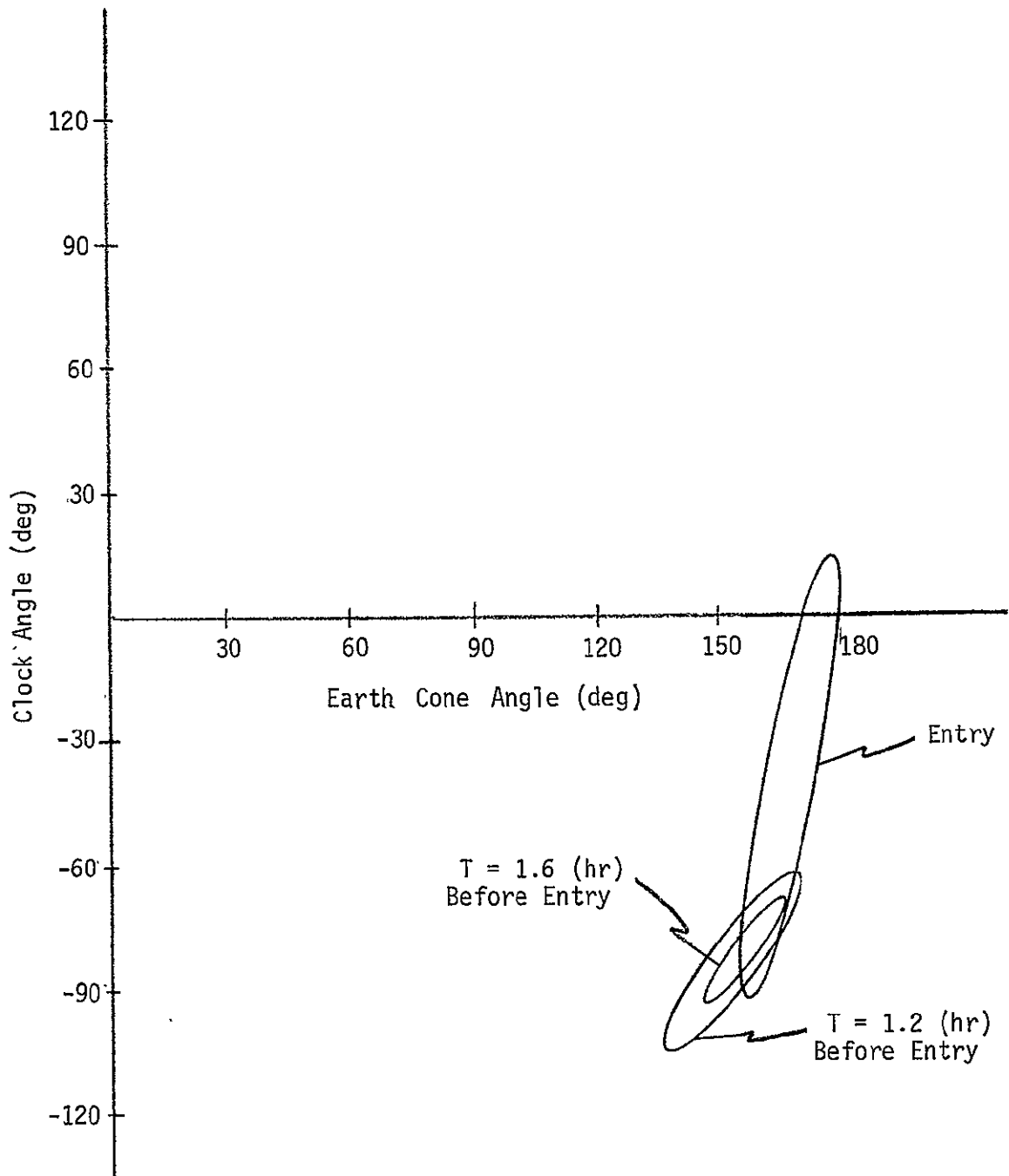


Figure IVG-4 Design Example Mission Spacecraft Relay Antenna 3 α Cone and Clock Angle Error Ellipses for Preentry and Entry Times

Earth/spacecraft/probe cone and clock angle dispersions for the 3 acquisition cases to be considered in detail. These data are taken from Table IIIE-22 for case DE-1 at the nominal entry time as well as for 1.2 and 1.6 hours before nominal entry time. Cone and clock angles in this case are defined the same as conventional spacecraft cone and clock angles except that the spacecraft longitudinal axis is assumed pointed to Earth and Earth is the reference in each case instead of the Sun as in conventional nomenclature.

Consider the case for attempted acquisition at a time 1.6 hours prior to entry when a coherent modulation system (PCM/PSK/FM) is used. The acquisition procedure is to point the antenna at the estimate mean location and search through the frequency limits successively for each antenna beam position until the signal is located. Antenna pointing angles and frequency search limits are program controlled by an acquisition programmer. Frequency search and acquisition is accomplished in this case by a VCO and noncoherent detection using a predetection bandwidth equal to $1/2$ that of the carrier tracking loop to be used after acquisition of the signal. When the signal is acquired the search is halted and the carrier tracking loop locks on the carrier. The loop stress is relieved by programmed tuning of the receiver as a function of time or by other means. For this example assume a predetection noncoherent bandwidth of 30 Hz and a 60 Hz carrier tracking loop bandwidth. Assuming that for the initial acquisition period an unmodulated carrier is used giving a carrier SNR of 12 db in the 30 Hz bandwidth. Then, a frequency search rate equal to the 900 Hz/sec can be used with a probability of detection of 99% (Reference IVG-1). At 1.6 hours before entry the antenna pointing 3σ error ellipse is such that it requires a maximum of 4 antenna positions for an antenna half power beamwidth of 14.5° . Assuming a frequency uncertainty of $\pm 4.8 \times 10^3$ Hz for transmitter and receiver (± 2 Parts in 10^6 for each) plus a total Doppler uncertainty of 12.5 KHz (the difference between maximum and minimum values for that time period) the maximum search time is $(22.1/0.9) \times 4 = 98.3$ seconds. In contrast the time required at a period 1.2 hours prior to entry is approximately 152 seconds because the maximum

Doppler uncertainty has increased to 23.8 KHz. Thus it is apparent that acquisition becomes more difficult as the probe approaches entry. It should be noted that the distribution of range rate and acceleration data is not normal and that use of values less than the difference between the maximum and minimum values is appropriate. This would reduce the calculated time of acquisition.

When acquisition has occurred the 60 Hz tracking loop locks to the signal. Under these conditions the initial frequency offset from the design point frequency is less than $1/2$ the carrier tracking loop bandwidth. Assuming a 9 db carrier to noise ratio and performance similar to the DSN type of receiver (Reference IVG-1), a static phase error of less than 5° can be held for frequency offsets to at least 0.4×10^{-5} of design frequency or ± 48 KHz. Doppler rates (Hz/sec) = $(1/30) \times (2 b_{LO})^2$ can be tracked at static phase errors of 5° even at frequency offsets of ± 48 KHz.

The maximum doppler rate up to the entry period is less than $(1/30) \times (2 b_{LO})^2$. At rates of $(1/10) \times (2 b_{LO})^2$ the static phase error would approach 15° .

After acquisition, the autotrack spacecraft antenna will track the signal in angle thus maximizing the signal level. Here we assume a 2 gimbal simultaneous lobing tracking system. At no later than 1 hour prior to entry the modulation of the carrier with data begins and the system should track to the entry point.

Post entry acquisition begins 2 minutes after entry. If one ignores the fact that the spacecraft system can detect time of entry then the statistics for doppler and angle dispersion parameters are as given in case DE-1 in the tables otherwise the Doppler variations due to lead time uncertainties would be reduced to that of case DE-2.

Considering the case where we ignore entry updating and search over the wide doppler range and antenna dispersion area. It is estimated that a maximum of 3 beam positions would cover the 3σ region. The maximum frequency uncertainty at 1.2 GHz is 169.6 KHz. If we use a 50 Hz bandwidth for search, the maximum search rate is $(50)^2$ or 2500 Hz/sec ignoring doppler rate. At this rate 63 seconds is required to search each antenna position for a maximum of 189 seconds. If the frequency range is covered by 2 receivers, a period of $189/2$, or ≈ 95 seconds is required.

Maximum doppler rate is 80 Hz/sec.

In this case, after lock on is accomplished, the ratio of $\frac{\dot{f}}{B^2} = \frac{80}{10^4} = 8 \times 10^{-3}$ due to doppler rate. This is well below the maximum for a 5° static phase error.

Thus it appears that in the worst case a two receiver search would be required to minimize post entry data storage time or loss of data during reacquisition. For redundancy the receivers could be designed to search over either the upper or lower end of the uncertainty band so that in case of failure of one receiver the good receiver could operate in an emergency mode to cover the entire band.

For the case where the spacecraft detects probe entry by loss of relay communication signal, total doppler uncertainty is reduced from 169.6 KHz ($f = 1.2$ GHz) to a value of 53.5 KHz. For this case the search time per beam position for a single receiver would be approximately $(53.5 + 9.6)/2.5$ or 25.2 seconds. The total for 3 beam positions is 75.6 seconds. Thus use of the knowledge that entry occurred drastically cuts the frequency uncertainty immediately after entry.

For the antenna autotrack function a single error channel receiver could be time shared for both X and Y error channels. The sum channel receivers for a dual receiver search mode could be used for both the angle tracking and data receiving functions.

Some consideration was given to relying only on preprogramming the spacecraft antenna pointing, and eliminating the autotrack requirement; however, the magnitude of antenna pointing uncertainty indicated by the trajectory error analysis precludes one giving serious consideration to such a configuration for the range of frequencies and antenna sizes required for most of these missions.

For missions in which entry depth is shallow and small diameter spacecraft antennas are feasible, preprogrammed pointing without autotrack may prove feasible.

H. Single Probe and Split Probe Communications Considerations

The split probe concept (see Mission A-2 and the Trial mission for definition) was first explored in this study when it was learned that the atmospheric attenuation of radio signals in the frequency region of interest for either relay or direct radio links was much greater than anticipated. The attenuation estimate at the time the single probe concept was conceived was 25 db at 2.3 GHz at 1000 atmospheres and a zenith angle for the nominal atmospheric model. This was the attenuation model used for the Trial Mission. A few weeks later this model was upgraded to 37 db attenuation under identical conditions. The upgraded model is the model used for mission A-2 and all missions other than the trial mission.

The split probe concept has several advantages over the single probe system: Generally for any depths beyond 300 atmospheres the same depth can be sampled by the combination of upper and lower probes in a much shorter time than a single probe. The upper probe transmitter power can be kept within reasonable bounds as opposed to the single probe system. (See the baseline parametric study - Volume II) The split probe concept appears to be the only practical approach to descending to 1000 atmospheres and obtaining adequate sampling because of the adverse affect of atmospheric attenuation on a high power link.

How does the split probe concept conquer the atmospheric attenuation problem? It is simply that a relay of data between lower and upper probe is required over quite a short range compared to the upper probe to spacecraft communications range; thus, the atmospheric attenuation loss is applied initially against a low power transmitter requirement. Further, a lower radio frequency can be used because the decimeter radiation that influences receive system temperature on the spacecraft has much less influence on the upper probe antenna temperature since it is "looking" away from the noise source and is shielded somewhat by the attenuation of the upper atmosphere as the upper probe descends.

For a direct comparison of communications systems for single and split probes using the latest atmospheric attenuation model see the results & observations for the baseline parametric study in Volume II, Chapter V.

I. Subsystem Requirements and Selection from Available Design

1. Data Handling - Probe Subsystems

Several basic design tradeoffs are presented below to reduce the large number of system and circuit designs available within the different component families and combinations of component families to one or two that are best suited to this mission. These tradeoffs are also presented to define in a general sense those designs that are expected to be the state of the art designs of 1975.

The available device families which will be suitable for design include the complementary MOS (COS/MOS), P channel-MOS and low power TTL. Any one or combination of these could be used and satisfy the mission power, weight, and size requirements. However, only the P MOS and low power TTL at this time would meet the reliability requirements of a Jupiter mission. Current development plans and the announcement of a high reliability line by RCA on January 1, 1971 indicate that the COS/MOS family will be in use for Jupiter type missions by mid 1975. Several advantages of the COS/MOS line make it very attractive for this type of application. The most important is the extremely low quiescent power, independent of output state ("1" or "0"), .01 uw for currently used simple devices. This device, due to its simple basic structure and low power, is also easily used in large scale integrated circuits. A comparison of device speeds or delay times is unnecessary as all three families will operate at speeds in excess of a thousand times higher than is required for a low speed data system. However, the device power dissipation comparison is, for this type system, very important. This comparison can be started by comparing the 1 MW per simple inverter gate of the low power TTL family to the 9 MW (50% duty cycle) of the P MOS family to the .5 uw (one COS/MOS load) of the COS/MOS family operating at 1000 Hz, 10 volt supply. This is a very rough and hardly complete comparison of the total system power consumption. The COS/MOS system design should be compared to a power switched TTL or P MOS design because the data rates and usage times do allow power switching and provide increased power economy for the TTL and P MOS designs. This is not possible to do accurately unless all three systems are completely designed.

However, the decrease in power consumption is between 25 and 50% and does not produce a design which is competitive with an equivalent COS/MOS design. This does indicate that such a design (TTL low power or P MOS) could be used at a penalty of increased power, but within available power limits, and with, in the case of the TTL design, a larger percentage of proven designs and flight experience.

The use of COS/MOS memories is attractive for low power consumption and small physical size, even with logic elements of another family providing the remainder of the system. There is also the advantage of the economy obtained in parts count, power supply voltages and system compatibility when the COS/MOS memory is used with COS/MOS logic elements. This type memory which would include all semiconductor memories have the disadvantage of being volatile. This could cause a partial or complete loss of data depending upon where in the mission the memory was lost and the available technique(s) for restoring the memory content. Use of this type of memory would then require that a power supply system be used that would be independent of all other components and have the redundancy and reliability to guarantee mission success. Due to the low quiescent power dissipation of the COS/MOS a redundant battery system could be used. Alternately, the plated wire or core memories which are nonvolatile could operate at approximately the same power levels because at these low data rates power switching could be used. The plated wire memory is now starting to be recognized for space flight usage and some amount of development and qualification must be accomplished before it can be used on Jupiter type probe missions. It is expected that this development work will have been done by mid 1975 and that all three memories - plated wire, core, and semiconductor with redundant power source; will be design candidates. Due to the volatility and the extra required weight of the redundant power source, the semiconductor memories are considered a third choice. The plated wire system has certain advantages over the core. Weight and power requirements of the plated wire memory are less because the system can be operated in the read only mode after launch. This is due to the nondestructive readout feature of the plated wire. This will also provide the additional system flexibility of permitting a system design

using either a memory load before launch and read only thereafter or with read-write electronics installed and power switching the write electronics. This system design flexibility and power saving are sufficient reasons to use the plated wire system rather than the core system.

As yet this COS/MOS family has not been proven to be as reliable as the TTL devices. This will, as noted above, not be the case in mid 1975 if the development of this family proceeds as predicted by the vendors now engaged in this development. With this development, the COS/MOS design will be the only logical choice for probe data systems after 1975. Under a more accelerated program this development could well occur by the end of 1973. This time table is consistent with the development of a plated wire memory system. Therefore, a system using COS/MOS logic elements, a plated wire memory and low power IC linear elements would be compatible, realizable and satisfy the system requirements.

Quite independent of the device family used, several data system tradeoffs are presented below to provide system flexibility, a maximum of transmitted data and total data handling efficiency.

The general data system block diagram is shown in Figure IVI 1-1. Several modifications to this diagram can be made under certain system design conditions, however, all the various system design tradeoffs can be described using this very general diagram. Preliminary indications of the required analog channel sample rates and analog data rates of change tend to eliminate the need for sample and hold (S/H) circuitry. The tradeoff is in time correlation of all analog data channels i.e. all channels sampled simultaneously, the S/H sequentially interrogated and transmitted within a large combined data format. Time correlation of the engineering data does provide considerable high priority information during diagnostic analyses. The flexibility in using multiple output formats is increased with S/H circuits because the data channels can be interrogated at any time during the major time frame and relative data channel time correlation preserved. Alternately, reduced accuracy of data channel time correlation could be obtained using a very fast ADC

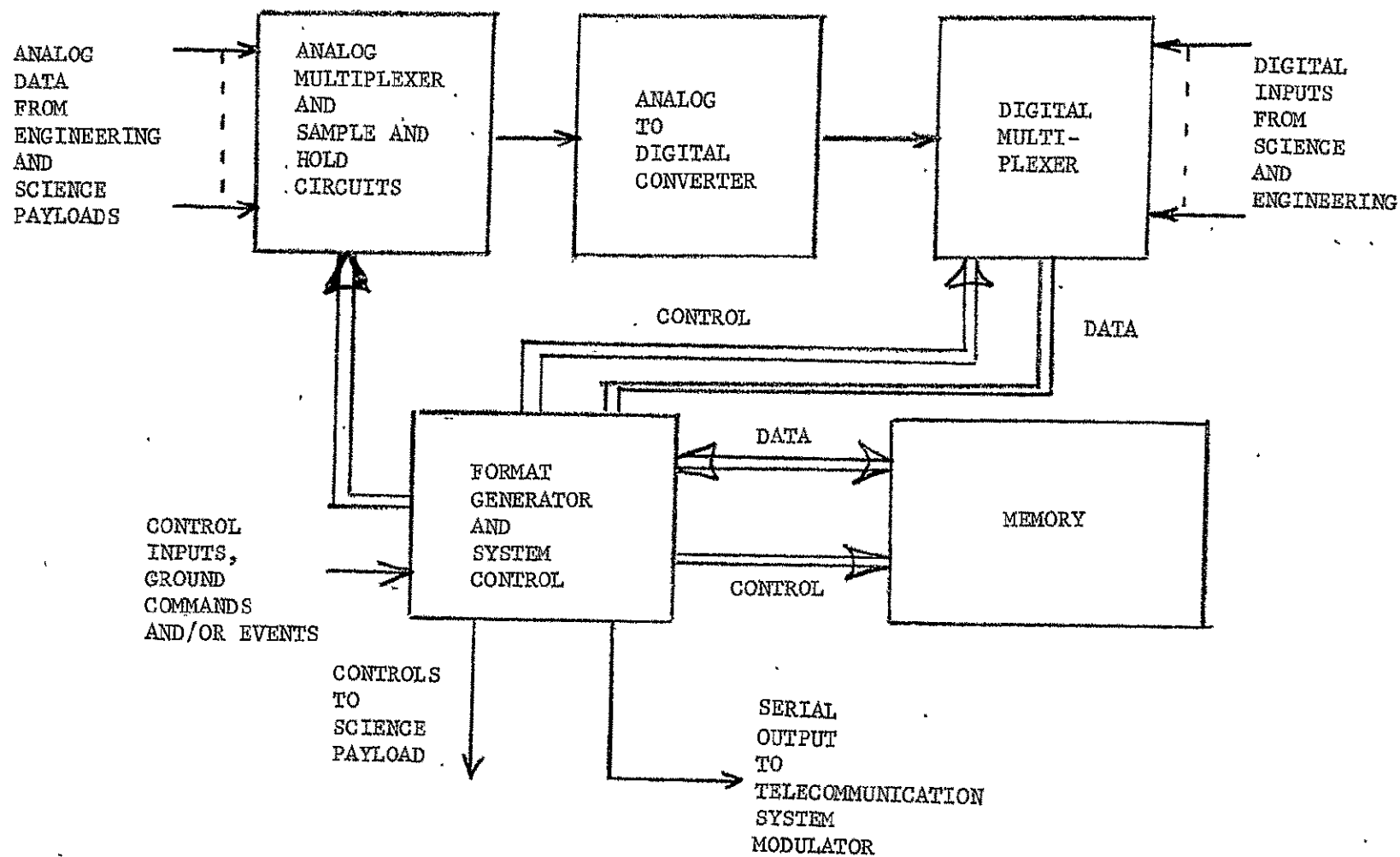


Figure IV11-1
Data System Block Diagram

and knowledge of the set of specific data channel interrogation formats. This error could be quite large at very low data rates and long main frame lengths with sub-commutated channels. Therefore, the S/H circuitry is not considered a high price to pay for accuracy in this high priority information.

The block diagram (Figure IV 11-1) shows two multiplexers, an analog and digital unit. Most all data systems built to date tend to combine both units into one larger unit using MOS switching circuitry. This requires the use of a larger control word but is justified in reduced hardware and system complexity. Memory word size is usually not effected because the total number of addressed data channels is usually within the data word (memory word) size, and most all system use the same length control word as data word.

The analog-to-digital converter (ADC) requirements provide for the use of any of several types of converters. The low conversion rate and low power requirements would indicate the use of the dual slope converter. However, the recent and continuing development of low power, stable and fast response operational amplifiers with COS/MOS logic elements indicate that a successive approximated device using power switching of the analog circuitry would provide a better design. This is especially true if the S/H circuitry were not used because a successive approximation unit is orders of magnitude faster than the dual slope converter and would reduce the time correlation errors considerably. However, the elimination of the sample and hold circuits would still reduce the flexibility in using multiple output formats, as discussed above. The dual slope converter also provides inherent smoothing of the input at no cost in parts or power. Therefore, the best choice is the use of S/H circuitry, a dual slope converter and power switching of the converter.

Efficient data system design would indicate that system control and data formatting be done within the same unit. Furthermore, that data format(s) should be stored in memory to obtain system flexibility and permit the use of multiple formats. Hard wired format generators are an acceptable compromise if the number of formats is small and few changes

are required. However, a stored format generator provides the maximum flexibility at a small cost in memory hardware. This is especially true if some amount of data storage is also a system requirement. Changes to any or all formats is a simple memory update and can be done on the ground at any time before flight. This as mentioned elsewhere would, when using a plated wire memory, reduce the required memory electronics to only those required for readout. A stored program format generator would also allow the changing of formats (within the stored set) on either a time or event basis. This flexibility would permit descent phase changes in the format to compensate for multiple atmospheric and/or system conditions.

The COS/MOS logic elements also provide several advantages when used in timer and sequencer designs. Currently mechanical timers are used that contain a dedicated battery power source which reduces main battery drain to zero during the power down conditions of space flight. The near zero power requirements of the COS/MOS elements permit a trade off in size, system compatibility and weight vs the small amount of current required for operation over a long space flight. Several design economies are also available, such as designing the timer and sequencer from the same element and sharing digital comparators to decode time functions for probe control and sequencing. However, even without using the element sharing techniques a COS/MOS design of a timer unit provides a shock resistant, low power, logic compatible, small and light design. A complete counter to operate from a 1 MHz source would require less than 1 mw. This would require about 1 w hour for a 40 day flight. This magnitude of standby battery drain is acceptable for Jupiter type missions. Decoding the time functions with dedicated or shared digital comparators also provides flexibility in the changing of time functions and the multiple use of system hardware.

2. Telecommunications - Probe Subsystems

Primarily the telecommunications components for entry vehicles and probes considered for the missions in this study consist of the following items:

Solid State Transmitter	40 watts output
Entry Vehicle Antenna	Hemispheric or Butterfly Pattern
Descent Probe Antenna	Hemispheric Pattern
Antenna Switch	Solid State
Subcarrier Oscillator/Modulator	Square Wave/Biphase
Convolutional Encoder	1/3 Rate - Constraint Length 4

Certainly basic designs exclusive of environmental conditions exist for each of the above with exception of the 40 watt solid state transmitter which at present day technology is pushing the art somewhat. In the case of the transmitter it is expected that the art will progress to the point where an efficient 40 watt output in the range of 0.8 to 2.3 GHz is practical before mid 1975. If not, there are basically but 2 alternatives -- reduce transmitter power requirements or go to a tube type power amplifier.

Depending upon the mission, lower transmitter power may be compensated for by increasing the spacecraft aperture. This is generally true for optimum trajectories near an R_P of $2 R_J$ where the target descent depth is moderate. Table IVI2-1 shows basic design requirements for a solid state transmitter.

TABLE IV-I-2-1

Basic requirements for a Solid State Transmitter:

Frequency	1.2 GHz (0.8 to 2.3 GHz)
Frequency stability	4 parts in 10^6 long term
Output power	40 watts minimum
Efficiency	30% minimum
Weight	Less than 8 lb
Size	Less than 75 cu. in.
Input Voltage	24 volts DC nominal
Type Modulation	Phase to 1.25 radians
Other characteristics	To be determined

A tube type amplifier has the disadvantage of apparently being more difficult to design for high G entry and requiring a high voltage supply.

The circularly polarized antenna designs may be chosen from any of several basic types such as the following:

For Hemispherical Coverage

Crossed dipole in a cup
Curved crossed dipole
Cavity backed crossed slots

For Butterfly Pattern

Four-arm conical beam
(Reference IV-I2-1)

Care must be taken to choose materials which will endure the immersion in the Jupiter environment and which will best circumvent multipaction and breakdown conditions encountered during preentry or post entry operation as the case may be. The entry vehicle operates from approximately one hour prior to entry to 0.1 g increasing at entry. The descent probe antenna is required to function after separation of the probe from the aeroshell beginning at an atmospheric pressure of approximately 0.2 Earth atmosphere continuing on to the final design pressure depth.

Table IV-I2-2 gives basic entry vehicle and probe antenna requirements assuming a "butterfly" pattern for the entry vehicle antenna and an on-axis hemispherical pattern for the probe antenna.

The subcarrier oscillator/modulator and convolutional encoder designs of today are adequate, but final designs should take advantage of state of the art in digital circuitry and frequency stability.

TABLE IV-I2-2

Typical basic requirements for Entry Vehicle and Probe Antennas.

Entry Vehicle Relay Antenna

Type	4 arm Conical Beam
Type Patterns	Max gain at 60° from zenith (Butterfly pattern)
Max Power Gain	4.5 db above isotropic
Half Power Beamwidth	50°
Frequency	1.2 GHz
Polarization	Circular
Power Handling Capability (Preentry environment)	50 watts (continuous)
Other characteristics	To be determined

Descent Probe Relay Antenna

Type (typical)	Curved crossed turnstile
Type Pattern	Omni (hemispherical)
Max Power Gain	7 db
Half Power Beamwidth	100°
Polarization	Circular
Frequency	1.2 GHz
Power Handling Capability (Post entry environment)	50 watts (continuous)
Other characteristics	To be determined

3. Power

a. Battery Requirements for Probe Mission Design Example

The battery shall survive an unoperable interplanetary phase of three years while subjected to an ambient temperature range of 0 to 100°F.

Prior to separation from the spacecraft the probe shall be heated by RTS power until the probe temperature attains 115°F. The probe shall then be released and have a maximum course period of 40 days by which time the temperature is expected to be 50°F. The entry temperatures shall be 40°F to 120°F.

A typical power profile during the cruise and entry phase will be similar to that shown in Figure IV I3-1. The profile represents an energy requirement of 640 watt hours with a peak load of 180 watts in one duty cycle. It is the profile for the Design Example Mission as described in Volume II.

b. Alternate Power System Configurations

Within the usual constraints of optimum energy density it is obvious that power source selection must be limited to electrochemical sources. These sources may be primary or secondary and the individual attributes of each are described.

1) Secondary Batteries

Secondary electrochemical systems are those that are manually activated prior to launch and must survive in the wet state throughout prelaunch periods, the interplanetary phase and the probe entry phase. The batteries would be capable of being charged and discharged at any time. Within the state of the art expected by 1975 and energy densities required for a successful mission, only three systems may be considered; Silver-Zinc, Silver Cadmium and Nickel Cadmium.

Silver Zinc Batteries - A two-year wet-stand life has been demonstrated by three major vendors for secondary silver zinc batteries. However, when cell degradation with time is accounted for the more stable electrochemical systems such as nickel cadmium and silver cadmium become competitive on energy density.

Failure modes are usually the result of electrical shorts through the separator material either by Zinc dendrite penetration or oxidation of the separator from the positive plate. Other modes of failure are loss in capacity of the negative plate by redistribution of active material and increased current

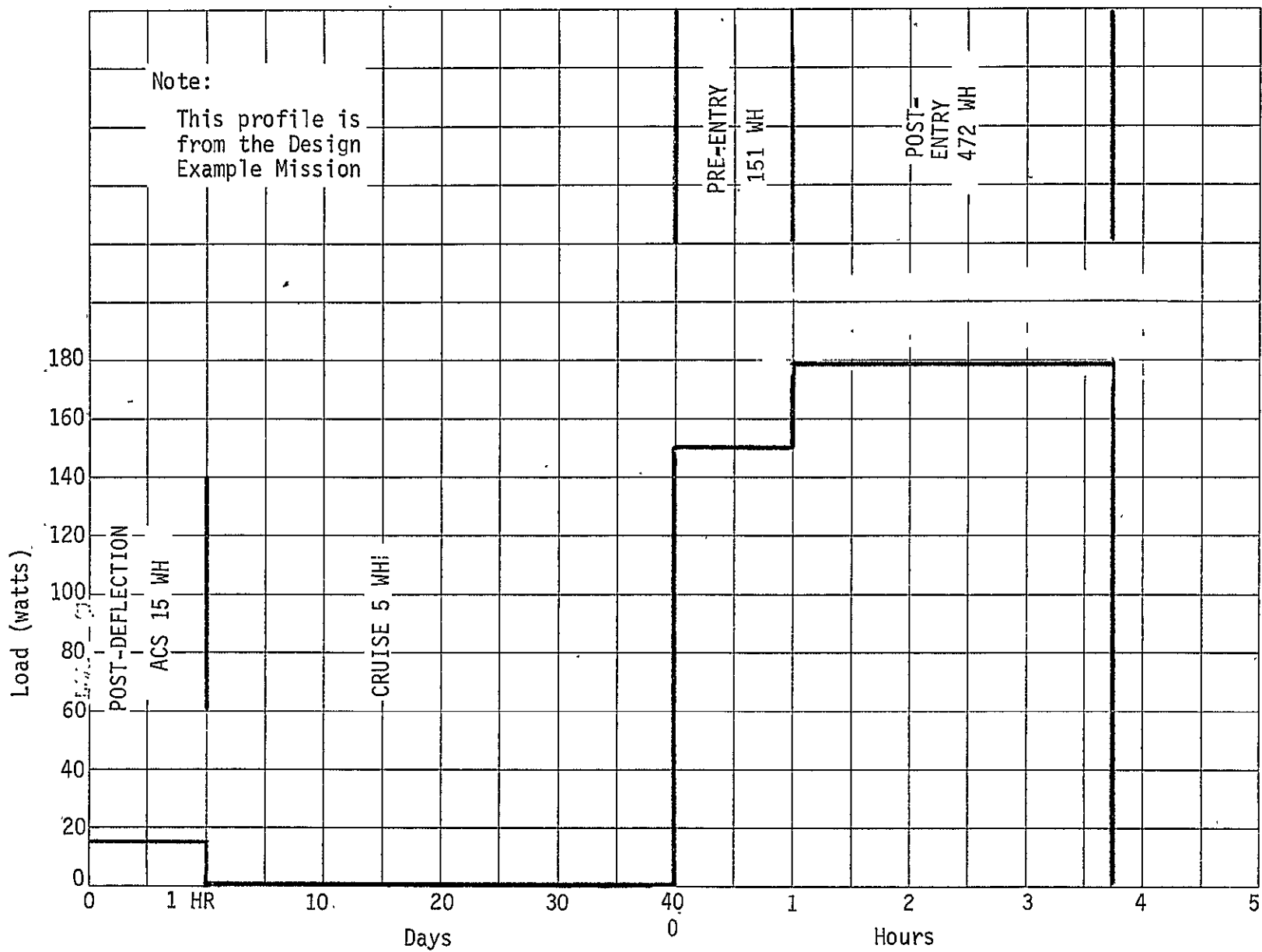


Fig. IV13-1 - Typical Probe Power Profile

density by reduction in effective plate surface area. Supersaturation of electrolyte with Zincate also results in precipitation of Zinc between separators further aggravating the electrical shorting problems.

Research on irradiated and grafted separators is continuing to improve the oxidation resistance and penetrability of the separator material. Current developments for the Viking Program indicate a silver zinc secondary with a reliable two year capability will be available by 1975. Continuing evaluations of zinc plate additives and manufacturing techniques will substantially increase the life capability of the silver zinc system.

The existing energy density of 80 watt hours per pound for new batteries cannot be expected to improve significantly by 1975. However, improved separator materials and more stable negative plates will reduce degradation with respect to activated life. In spite of these improvements it must be anticipated that permanent losses in the order of 50% during the interplanetary phase will occur. An additional loss during the 40 day cruise period of 25% should also be expected considering the degraded state of the separators at this time.

With a final requirement of 640 watt hours it would be necessary to design a battery with a 2600 watt hour capability which would weigh 33 pounds.

Silver Cadmium Batteries - These batteries would have the same separator oxidation problem as the silver zinc battery but would have the advantage of a more stable negative cadmium plate.

Existing cell design offers energy densities up to

34 w-hr/lb, but with techniques used in silver zinc cell design to increase energy density a design goal of 40 w-hr/lb is immediately possible.

It is anticipated that capacity degradation during the interplanetary phase of 30% will occur and another 15% during the cruise period. The battery design would have an energy requirement of 1160 watt hours and at an energy density of 40 watt hours per pound the battery would weigh 29 pounds.

Nickel Cadmium Batteries - It is well known that Nickel Cadmium batteries are extremely reliable and have many years of service life provided the correct charge control regime is selected and the ambient temperature is low.

Available capacity decreases with increasing temperature and decreasing current to the extent that only 65% of the maximum possible capacity would be available if the charge was c/10 and occurred at 90°F. Degradation with life is also a function of temperature and 100°F would be prohibitive for a three year period.

Assuming the temperature can be idealized at 70°F, the decay rate during the interplanetary phase would be in the order of 30% but during the 40 day cruise would be negligible. Based on these factors, the initial design would be for a 915 watt hour battery, which at 16 watt hours per pound would weigh 57 pounds.

Providing the temperature does not exceed 70°F the Nickel Cadmium battery would provide a reliable system within the present state of the art.

2) Primary Batteries

Primary batteries for this mission would be defined as

one shot devices that would be remotely activated.

Activation would be by way of an electrical input, from the RTG spacecraft power which initiates a gas generator which in turn forces the electrolyte into the cells.

Since optimization of weight is considered in this proposal, only zinc silver oxide batteries are considered.

Zinc Silver Oxide Remote Activated Batteries - A remotely activated zinc silver oxide battery for this application would comprise a cell configuration of dry charged plates and secondary microporous separators capable of a wet stand life of 40 days. Electrolyte would be stored in a container so designed that gas generated from an electrically activated double base propellant would eject the electrolyte into the cells. Many activation mechanism designs exist and the optimum for the particular configuration would be selected.

The major problem area is in the cell filling mechanism which must be so designed that each cell is isolated from each other after activation. Electrolyte paths between cells would result in high resistance shorts on initial activation followed by low resistance shorts when Zinc is precipitated along the electrolyte paths.

The present state of the art in separator materials is well capable of handling the 40 day activated life. Further developments of the inactivated materials will increase the wet stand capability by 1975.

Although present zinc silver oxide remote activated batteries offer average energy densities of 15 w-hr/lb, it is not uncommon to achieve 40 w-hr/lb when optimizing energy densities. It is not unreasonable to assume a battery

designed for this application would be capable of achieving this energy density. An unactivated dry stand loss of 3% per year can be expected. Once activated a conservative degradation rate would be 15% over 40 days. The initial design would have an energy requirement of 840 watt hours and the battery weight would be 20 pounds.

The reliability of the design would be proven by extensive ground tests as is usual with one shot devices. However, these battery types are used in many weapon systems and reliabilities of 99-90% at 50% confidence are expected.

c. Charge Control and Storage Methods

With all secondary batteries it will be necessary to periodically check the capacity and charge control system during the interplanetary phase.

With the wide temperature range imposed it would be preferential to have the charge voltage regulated, temperature dependent to obtain maximum capability at all temperatures. The charge rate should also be selected that will provide the maximum required capacity at the maximum operating temperature where minimum charge acceptance is available.

A number of options are available for storage during the interplanetary phase. Of major importance are the three extremes. Fully charged with continuous trickle charge, fully charged with open circuit stand and fully discharged.

It is well known that cell degradation, i.e. oxidation of separator, zinc penetration, electrolyte crystalization, etc. occurs more rapidly at the highest electrochemical state of activity, and particularly in the Silver alkaline system.

Float charge at best retains full capacity but provides almost 100% thermal dissipation which becomes a system problem.

The individual cell in the charged state or trickle charged state, even if closely watched initially, will gradually get out of step with each other further aggravating the available capacity problem. Under these conditions the charge control by necessity cannot be optimized because of concern for driving poor cells negative producing Hydrogen or overcharging individual cells producing oxygen.

By leaving the battery in the discharged state, i.e. 1.0 volts per cell on load, the least electrochemical reaction would result and battery degradation reduced. When stored in the discharged state the cells will get out of step to a lesser degree thus increasing capacity available by permitting optimum charge rates and control limits.

d. Power Source Selection

It is possible to provide mission success utilizing a Nickel battery with restricted high temperature operating range and storing the battery in the discharged state during the interplanetary phase. Since the battery is not required during this phase, however, it is more reasonable to use a remotely activated Ag/Zn battery. This selection removes the complexity of a charge regulation system and the guesswork involved in evaluating degradation rates and reliability of the secondary batteries.

The remotely activated Zinc Silver Oxide battery will satisfy the mission requirements with the minimum weight and minimum state of the art improvement.

e. Probe Active Thermal Control Considerations

Active probe thermal control during the 40-day post-separation cruise is required in the case of use of the Pioneer S/C. An estimated 33 lb of additional battery is required in this case to provide the added energy.

REFERENCES FOR CHAPTER IV

- IVG-1 "A Feasibility Study of An Experiment for Determining the Properties of the Mars Atmosphere", Final Report, Volume II, Book I, Section 3, NASA Contract NAS2-2970, 1 Sept 66, P. 630.
- IVG-2 "Deep Space Network/Flight Project Interface Design Handbook"- DSN Standard Practice, JPL Report 810-5, March 1, 1970, pp. 2-36 through 2-41.
- IVE-1 Michaux, C. M., et al, "Handbook of the Physical Properties of the Planet", NASA SP-3031, 1967.
- IVF-1 Heller, J. A., "Sequential Decoding:- Short Constraint Length Codes", Space Programs Summary 37-54, Volume III, Jet Propulsion Laboratory, December 31, 1968, pp. 171-177.
- IVI-1 Dyson, John D., Maves, Paul E., "New Circularly Polarized Frequency Independent Antennas with Conical Beam or Omnidirectional Patterns", Antenna Technical Laboratory Report #46, Contract No. AF33(616)6079, University of Illinois, June 20, 1960.

J. Spacecraft Subsystem Performance Requirements Tradeoffs and Changes to Present Design -- Telecommunications, Data Handling and Power

Major differences in presently defined "existing" subsystems for TOPS and PIONEER spacecraft make separate treatment of tradeoffs and changes for each spacecraft necessary. A major tradeoff exists in selection of the type of despin relay antenna for the Pioneer spacecraft. Discussion of this tradeoff follows the requirements and changes given below.

1. Spacecraft Performance Requirements and Changes to Present Electrical Design

The basic performance requirements and changes to present design for the TOPS spacecraft are shown in Tables IVJ1-1 through IVJ1-4. Specific antenna diameter and other requirements directly related to each mission are discussed in Volume II in the mission description.

Basic performance requirements and changes to present design for the PIONEER spacecraft are given in Tables IVJ1-1 and IVJ1-5 through IVJ1-7.

TABLE IVJ1-1 TELECOMMUNICATIONS AND DATA HANDLING REQUIREMENTS FOR TOPS AND
PIONEER SPACECRAFT IN SUPPORT OF RELAY COMMUNICATIONS

Post Launch to Probe Deflection

<u>Function</u>	<u>Requirements</u>
Entry Vehicle Monitoring	Accept low rate PCM data train from entry vehicle intermittently to monitor temperatures and status. Relay data to Earth.
Receive Data for Probe Deflection	Receive probe deflection data from Earth immediately prior to deflection maneuver. Deflection and coast time via Earth to spacecraft radio link. Transfer data to probe data handling system.

Probe Deflection to 1.3 Hr Prior to Probe Entry

Updating Spacecraft Programs for Support of Probe Pre-Entry Phase	Spacecraft relay antenna pointing and frequency acquisition programs may be updated at this time if available. Mean relay antenna position and frequency as well as search limits are required as a function of time.
---	---

TABLE IVJ1-1 TELECOMMUNICATIONS AND DATA HANDLING REQUIREMENTS FOR TOPS AND
PIONEER SPACECRAFT IN SUPPORT OF RELAY COMMUNICATIONS - Continued

Pre-Entry and Entry Phase

<u>Function</u>	<u>Requirements</u>
Acquire Relay Radio Signal and Track in Angle and Frequency	Perform relay signal search and acquisition function as discussed in Chapter IV. This requires several antenna beam positions and frequency search for each beam position -- See Volume II mission descriptions.
Demodulate, Decode and Store Data	Demodulate subcarrier and establish symbol and bit sync. Decode convolutional code using Viterbi algorithm for 1/3 rate, con- straint length 4 code. Store data in space- craft memory or integrate into real time TOPS telemetry.

Probe Entry to Final Loss of Probe Relay Signal

Reacquire Relay Signal	Same as for pre-entry phase.
Demodulate, Decode and Store Data	Same as for pre-entry phase except change in bit rate immediately after entry and in some cases later in the descent profile.

TABLE IVJ1-1 TELECOMMUNICATIONS AND DATA HANDLING REQUIREMENTS FOR TOPS AND
PIONEER SPACECRAFT IN SUPPORT OF RELAY COMMUNICATIONS - Concluded

IV-60

Final Loss of Probe Relay Signal to End of Probe Mission

<u>Function</u>	<u>Requirements</u>
Transmit Stored Probe Relay Data to Earth	Transmit all probe data to Earth over spacecraft to Earth Communications Links at appropriate time and rate.

TABLE IVJ1-2

TYPICAL REQUIRED CHANGES TO TOPS SPACECRAFT
(Telecommunications & Data Handling)

TELECOMMUNICATIONS

ADD

Relay Antenna
2 gimbal antenna mount
Servo system for autotrack
Monopulse antenna feed
Antenna Pointing Programmer Interface
Antenna position indicating sensors

Sum channel Preamplifier and Receiver
Tracking x & y Receiver
Frequency search programmer interface
Subcarrier demodulator
Viterbi decoder and bit synchronizer

NOTE:

Antenna diameter varies with mission. See Volume II mission descriptions.

DATA HANDLING

ADD

Interface relay link decoder output with TOPS data storage system

Interface TOPS Central Programing & control to accept & transfer probe deflection & coast time to probe system via umbilical when transmitted by Earth.

Interface TOPS central programing & control to accommodate spacecraft attitude programing for probe separation phase. Also accommodate antenna and frequency search program storage.

Accommodate retrieval of stored data in TOPS data formats for transmission to Earth.

Add engineering channels to TOPS telemetry to accommodate added telecommunications equipment.

Add umbilical for transfer of data between probe and S/C.

TABLE IVJ1-3
 REQUIREMENTS - TOPS SPACECRAFT POWER SUBSYSTEM

<u>FUNCTION</u>	<u>WATTS</u>	<u>TIME PERIOD</u>
Power for probe thermal control	0 to 2.3	Launch to 3 days before
Power for added spacecraft support equipment	5	probe deflection
Power to pre-heat probe for coast	100	3 days continuously prior
		to deflection
Power up probe for separation	10	Prior to separation
Power for Telecommunication and Data Handling support equipment.	40	1.3 hours before entry to 2.5 hours after probe entry.

TABLE IVJ1-4
 MODIFICATIONS TO TOPS POWER SYSTEM

ADD

Power distribution and protection for probe support equipment
 Interface power control with TOPS central programmer
 Add engineering sensors for added power system monitoring

TABLE IVJ1-5
REQUIRED CHANGES TO PIONEER SPACECRAFT
TELECOMMUNICATIONS & DATA HANDLING

TELECOMMUNICATIONS

ADD

Same as for TOPS except relay antenna mounted on boom and despun.

If use phased array instead of mechanically despun antenna see next section of report.

DATA HANDLING

ADD

Same as for TOPS except must add data storage capacity for 360 K bits of pre entry data and 300 K bits of post entry probe data unless one chooses to integrate the relay data into PIONEER telemetry in near real time.

Antenna pointing programmer must accommodate need for despin reference if mechanical despin used.

If despun phased array used see next report section.

TABLE IVJ1-6
PIONEER SPACECRAFT - POWER SUBSYSTEM REQUIREMENTS

<u>FUNCTION</u>	<u>REQUIREMENT</u>
Provide power for same functions as shown for TOPS spacecraft Table IVJ1-3.	Same as for Table IVJ1-3 except for 0 to 3.0 watts for probe thermal; delete 100 watts for probe pre-heating.
Provide for despinning a boom mounted relay antenna.	Provide power for electric motor and control servo for despun antenna.
	Provide slip rings for power transfer across despun interface.
If electronically despun array is desired (see next section of report)	Provide power for phased array beam pointing including programing computer.

TABLE IVJ1-7
CHANGES TO PIONEER SPACECRAFT POWER SUBSYSTEM

According to the data available on the proposed PIONEER Spacecraft only 15 watts of excess power (over and above presently defined spacecraft requirements) is available for probe and probe support equipment. To accommodate probe support equipment during probe pre and post-entry phase addition of a zinc silver oxide remote activated battery could handle the additional power of approximately 50 watts. Otherwise, the functions can be supplied from the PIONEER source.

2. SPACECRAFT SUBSYSTEM TRADEOFFS

a. Telecommunications

The Pioneer telecommunications system must be augmented to serve as a relay for the probe data for all missions except F, which uses a direct link. These changes consist of an antenna, a receiver, and suitable storage and interface electronics to put the probe data into the existing telecommunications system. The principal problem area is the antenna, whose narrow beam must be despun and pointed toward the probe. This was initially examined for Mission B, which has a limited scan range, and the resulting mechanically despun design was then extended to give essentially unrestricted coverage, allowing any of the missions to be worked from the Pioneer.

A tradeoff between a mechanically and an electrically despun system for Mission B is given below. The mechanical details of both the Mission B system and the unrestricted coverage system are discussed in Chapter V.

1) Spacecraft Antenna, Mission B

(a) Introduction

Mission B (pre-periapsis) requires a high-gain spacecraft receiving antenna whose nominal beam position is along the vehicle spin axis, directed backwards. However, it must be scanned as far as 45° off axis, and when it is off-axis it must be despun. This can be accomplished mechanically, using a gimbaled dish on a despun platform, or electrically, using a phased array whose aperture is centered on and normal to the spin axis. Both of these options will be examined.

Link analysis and frequency optimization indicate an aperture of around 3.5 ft diameter with a frequency of around 1.2 GHz for an array and 1.8 GHz for a despun dish. At 1.2 GHz the gain should be 20 db for the minimum signal part of the mission, but can be 19 db at the maximum scan angle of 45° which does not coincide with the minimum signal part of the mission. A planar array would lose 3 db gain when scanned to 45° , so it would need a boresight gain of 22 db to give the desired 19 db at a 45° scan angle. Given a fixed aperture, the weight of a dish is nearly independent of frequency, while that of an array rises sharply with increasing frequency because the number of elements goes as f^2 . This is the reason for selection of a lower frequency for an array-based system.

(b) Phased Array Antenna

An aperture efficiency of 80% can **conservatively** be assumed for a uniformly illuminated array. At 1.2 GHz and 22 db, this gives an area of 10.63 ft^2 . A hexagonal array of 61 elements on a triangular grid, sketched in figure 1, will be assumed. Element type is a crossed dipole in a $\lambda/4$ depth ($= 2.46''$) hexagonal cup, fed for circular polarization. The dipoles will be printed on the overlying radome, and fed from below. The cups form a honeycomb structure as shown in figure 1. The cups serve to increase the element directivity and reduce interelement coupling. Figure 2 shows details of the element design. Aperture area assigned to each element is $\frac{10.63 \times 144}{61} = 25.1 \text{ in}^2$. This results in the dimensions shown in figures 1 and 2 for the array and the elements. The effective minimum spacing for grating lobe formation shown in figure 2, 0.475λ , will give complete suppression of grating lobes over the desired 0 to 45° scan range. This aperture will give the desired gain of 22 db at boresight and 19 db at 45° . Beamwidth will be 12° at boresight, increasing to an elliptical beam, $17^\circ \times 12^\circ$, when the beam is scanned to 45° .

The suggested electronic configuration of the array includes a low-noise RF amplifier at each element. This is required to overcome losses in the feed network and achieve a noise figure commensurate with that achievable using a dish antenna. A corporate feed with 3-bit diode phase shifters is recommended. Amplifiers, phase shifters, and baluns would all be realized in a minimum-weight microelectronics and microstrip configuration.

The received signal will not be strong enough to use self-focusing techniques on a per-element basis. A multilobing approach is recommended for auto-tracking the beam. This requires the division of the aperture into several subapertures. The sum pattern will be used to drive the data receiver, and difference patterns will be formed to generate error signals for beam tracking, using a second receiver.

The spacecraft is Earth-Canopus stabilized, with the Canopus sensor giving an indication each time its window rolls past Canopus. This Canopus signal will be used as an angular reference for the despun system. The angular distance of the despun beam from Canopus will be dependent on the arrival date, and will be time-varying through the mission. This tra-

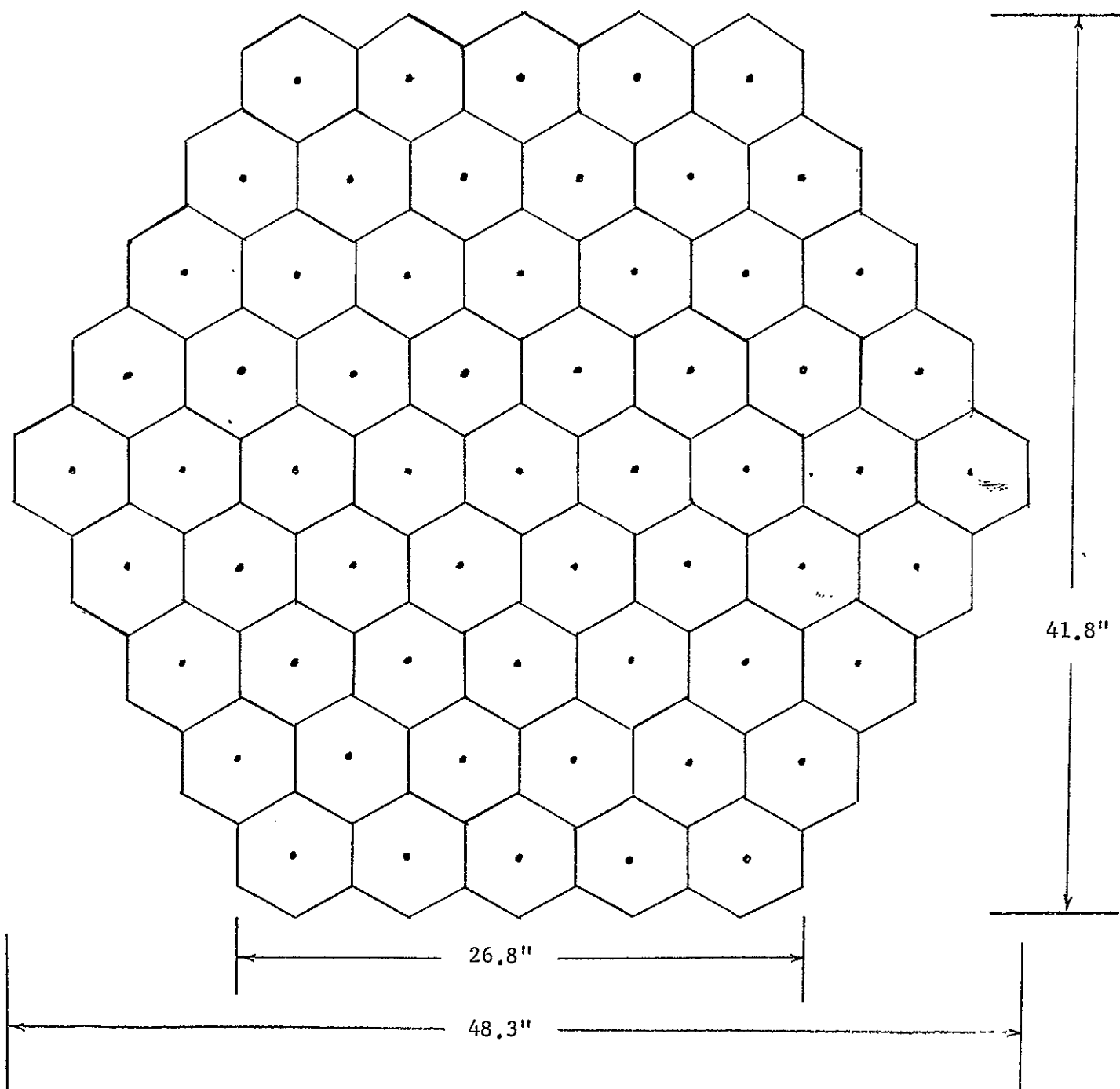


Figure IVJ-2.a-1

Element Locations, 61 Element Hexagonal Array, 1.2 GHz

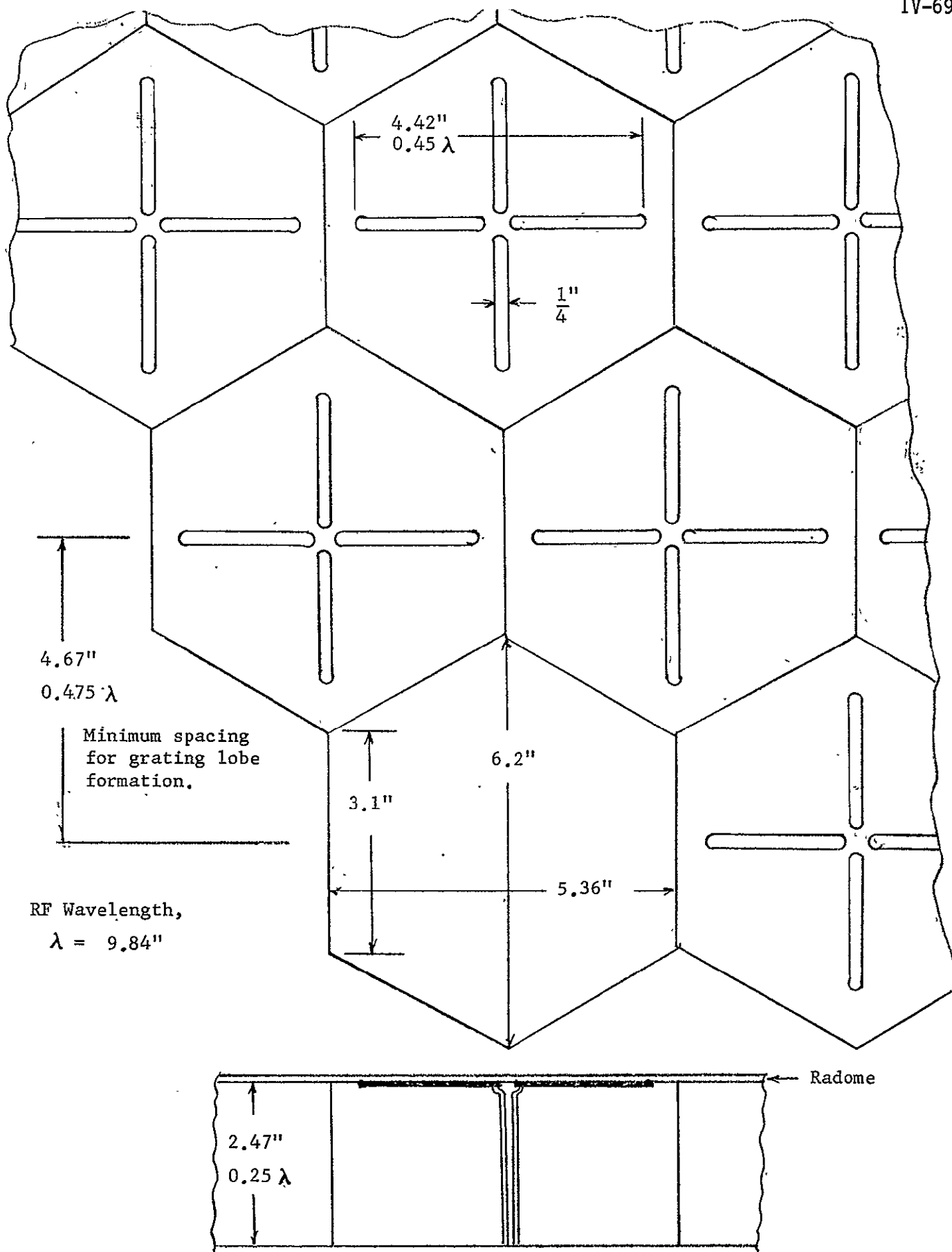


Figure IVJ-2.a-2

Element Detail, Array of Crossed Dipoles in Hexagonal Cups, 1.2 GHz

jectory will be stored in a read-write memory, loaded just prior to launch, when the scheduled arrival date is fixed. The predicted scan angle away from boresight will also be stored and used by the tracking system.

These predicted angles will not be exactly correct, so a search mode will be required for initial acquisition and an autotrack mode will be used after the signal has been acquired. Three-sigma dispersions from these predicted angles give an uncertainty ellipse that can be adequately covered by four beam positions.

The search mode will have to be programed so that the beam stays in one position long enough to complete the required frequency search. This frequency search must be repeated for each beam position until the signal is acquired.

There are two acquisitions required for this mission, one pre-entry and one post-entry. $3-\sigma$ doppler and oscillator stability uncertainty for the pre-entry acquisition is 12 KHz. Assuming a 40 Hz PLL with a scan rate of 160 Hz/sec, search time is 75 sec per beam, giving a total search time of 300 sec or 5 minutes. This assumes a scan rate of $0.1 B_N^2$, where B_N is the loop noise bandwidth. At this scan rate, the loop can lock onto the signal as it goes by. Search rates as high as B_N^2 can be used with a somewhat more elaborate system. This requires an envelope detector to trigger a "signal present" indicator which would stop the sweep. Loop acquisition would then occur within a few seconds. Ideally, this would reduce the total search time to about 0.5 minutes. However, the envelope detection requires a fairly high SNR, +12 db or better, to reduce the false-alarm probability to an acceptable level. Also, sideband energy could cause false alarms. If this system is used, it would be desirable to send carrier-only for an initial acquisition period of perhaps 2 minutes to increase the carrier SNR and eliminate the possibility of false alarms due to sideband energy. A further improvement in the SNR at the envelope detector could be realized by reducing the bandwidth at this point. A 30 Hz bandwidth would give a sweep rate of 900 Hz/sec and a total acquisition time of around 1 minute. Post-entry uncertainties are almost twice as large so acquisition time would be around 2 minutes.

Computation of the necessary phase shifter settings for each of the 61 elements, and the switching to form the multilobing aperture combinations, will require a small special-purpose digital computer. This computer will also have the capability to scan the beam through a predetermined search pattern when the antenna is operating in the search mode.

The Pioneer spins at a nominal rate of 4.8 RPM. At a scan angle of 45° , one revolution represents 21 beamwidths. It would be desirable to step the beam in smaller than 3 db beamwidth steps. 54 steps per revolution have been assumed for the maximum scan angle, giving steps about 5° apart. If we assume a maximum spin rate of 6 RPM, this would be a maximum of 324 beam steps per minute, or $\frac{324 \times 61}{10} = 330$ three-bit phase shifter commands per second. This is not a high computation rate. Commands could be computed serially, stored in a $3 \times 61 = 183$ bit buffer storage, and then transferred simultaneously to the 61 phase shifters. This transfer would be done at a low power level, to higher power diode drivers located at each element of the array.

The electronic de-spin is accomplished by controlling the phasing to the various elements of the antenna array. This phasing is synchronized to the output of the Canopus Detector which is used as a reference.

The two operating modes are search and track. In the search mode the antenna pattern is electronically despun and scanned through a search pattern that is $\pm 10^\circ$ in azimuth and $\pm 45^\circ$ in elevation. A signal from the command receiver is used to start a preprogramed azimuth pattern to enable the antenna to track various entry profiles.

When a signal is received the antenna tracks the entry spacecraft by comparing the signals received by the antenna after despin correction. Tracking is provided in both azimuth and elevation by comparing the combined signals received from the six antenna segments.

Figure 3 shows the basic precepts used to electronically despin and track the antenna. The basic idea is to utilize a READ ONLY Memory (ROM) to store the element phasing data for each of the 271 beam directions

desired. The 271 beam directions consist of a central beam surrounded by 9 concentric rings. There are 54 azimuth positions in the outer ring, decreasing by 6 in each ring to 6 in the inner ring. Beam separation is approximately 5° . Since each of these is stored in a particular memory address, all that needs to be done to despin and point the antenna is to address the memory and insert the phase shifts described into each antenna element.

The azimuth portion of the address is obtained as follows: A sync signal from the Canopus detector reads an azimuth address from the Preset Storage Register into the Despin Register to indicate the starting address (which determines the basic angle from Canopus). The control circuit decodes this address and provides either a correction signal in the track mode or an increment signal in the search mode to an up-down counter. The contents of the counter is used to modify the address received from the despin register by means of an adder, and inserts this into the azimuth portion of the address register.

The elevation portion of the address is obtained entirely from the control circuitry. It consists of either an error signal or an increment signal to the elevation up-down counter. The contents of the elevation up-down counter is used to provide the elevation portion of the address. This system has the advantage that the contents of the up-down counters are the proper modification signals when signal is acquired.

The control circuit is shown in Figure 4. In the search mode, the search clock increments the azimuth up-down counter with each pulse and presets it every fourth pulse. Every fourth pulse also increments the elevation up-down counter. Every ninth one of these (36 search pulses) sets the elevation counter to a preset value. The preset values in the counters are necessary for tracking in both directions and are known when the ROM data is determined.

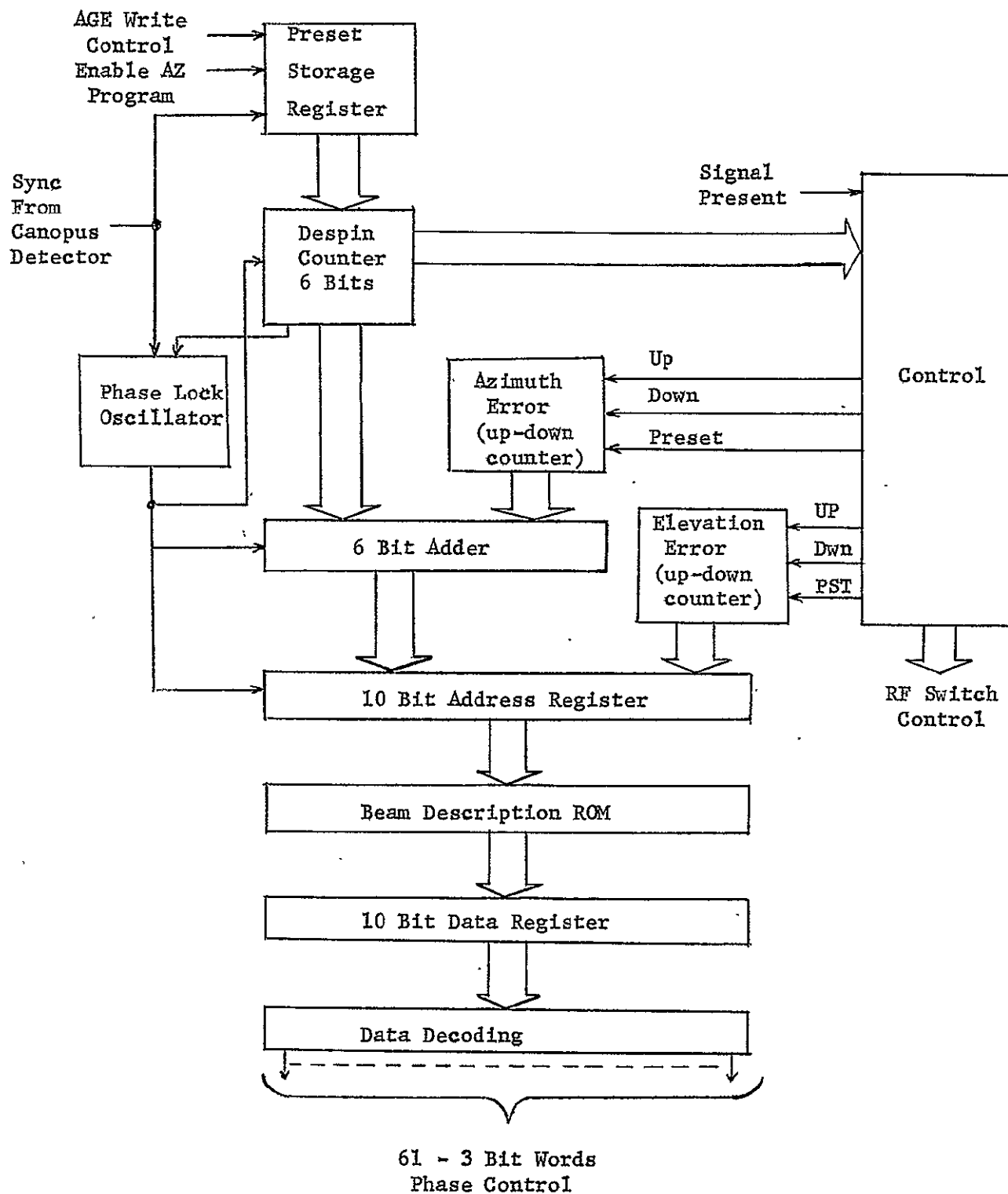


Figure IVJ-2.a-3
Despin Electronics Block Diagram

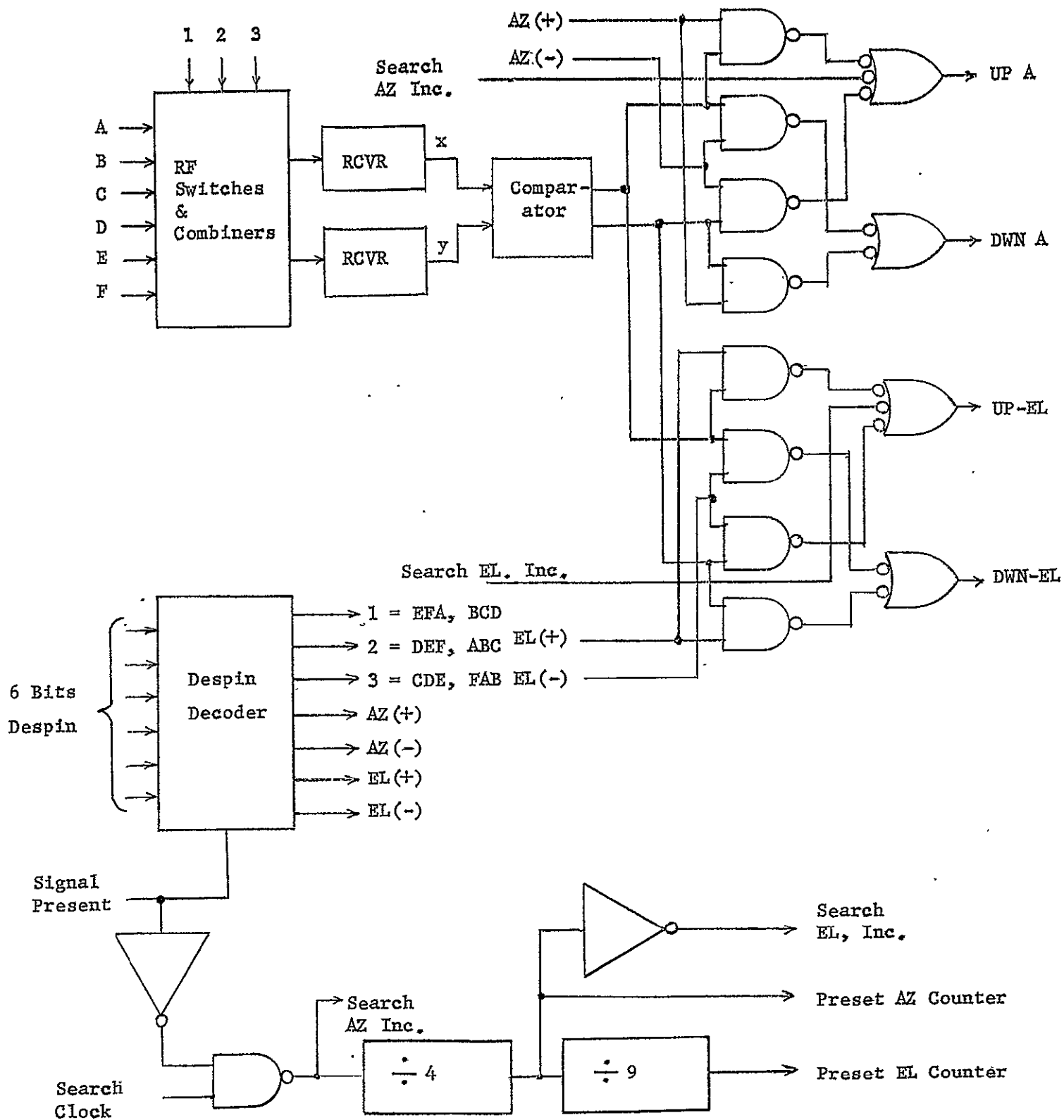


Figure IVJ-2.a-4

Control

In the track mode, the despin decoder determines which antenna segments are to be compared. There are only three basic comparisons available from the six segments. These three comparisons with the proper timing and the proper polarity can be used to determine the required pointing corrections. The timing is indicated by 1, 2, and 3 and by the presence of one of the four polarity signals AZ (+), AZ (-), EL (+) and EL (-). The pattern in Table IVJ-2.a-1 is followed.

TABLE IVJ-2.a-1
COMPARISON SEQUENCE

Seq. Pos.	No.	Polarity	Seq. No.	No.	Polarity
1	1	AZ (+)	7	1	AZ (-)
2	3	EL (+)	8	3	EL (-)
3	2	AZ (+)	9	2	AZ (-)
4	1	EL (-)	10	1	EL (+)
5	3	AZ (+)	11	3	AZ (-)
6	2	EL (-)	12	2	EL (+)

The signal comparator shown has three possible states: $x > y + \Delta$, $y > x + \Delta$, and neither of these. The comparator outputs are gated to the proper up-down counter by the AZ (+), AZ (-), EL (+) and EL (-) signals.

The phase lock oscillator, Figure IVJ-2.a-5, is a digital phase lock oscillator that provides 36 pulses to the despin register for each sync pulse from the Canopus detector. This will point the antenna within ± 5 degrees of the desired angle.

Power and weight estimates for the array are summarized in Table 2.

The power consumption would only occur during the active mission, 2.5 hours. This will consume 178 watt-hours of energy.

If we assume that a battery power system will be added to the spacecraft for this purpose, and assuming 25 watt-hours/lb, power system weight would be 7.2 lbs, giving a total weight for the system of 74 lbs. The data receiver and associated demodulation and data processing equipment is not

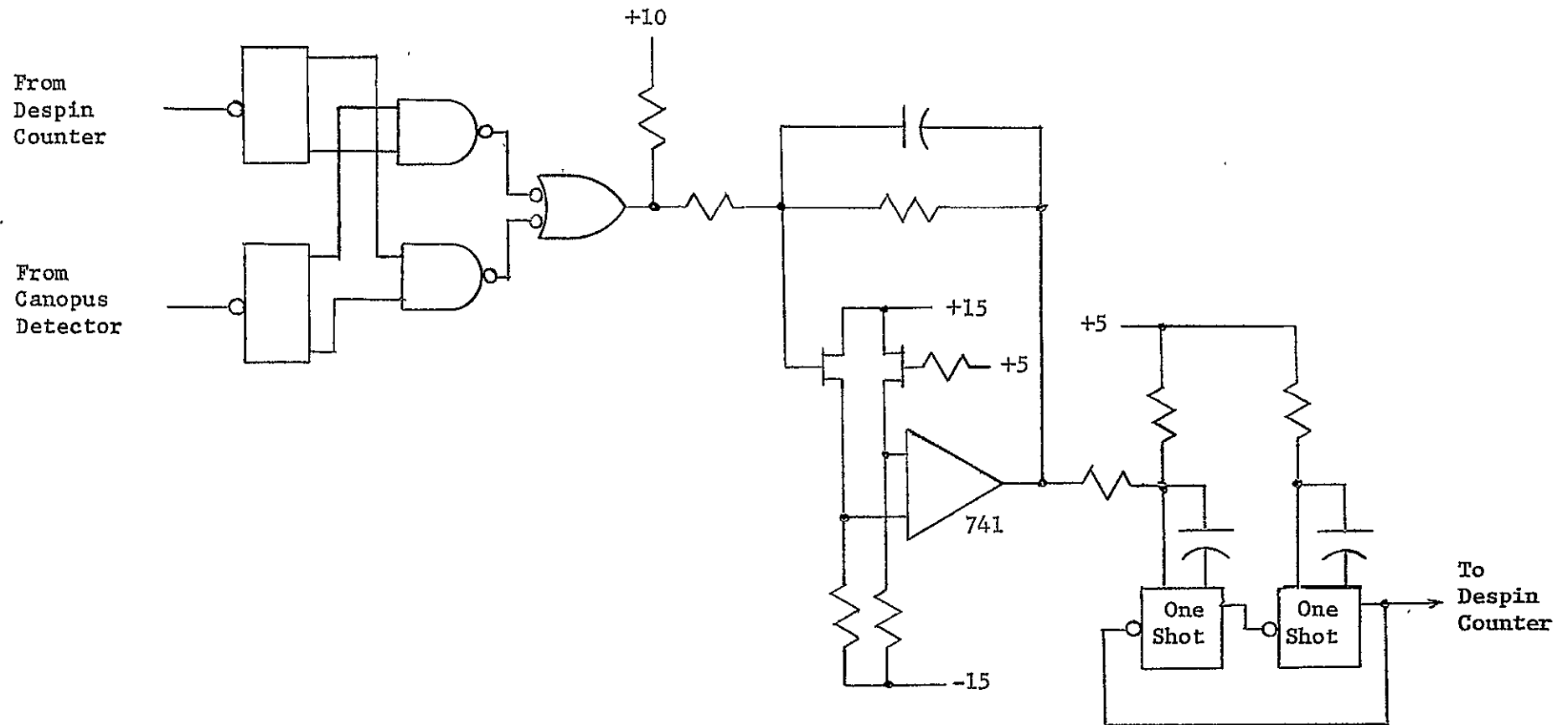


Figure IVJ-2,a-5

Phase Lock Oscillator

included in this summary because it would be required with any antenna and therefore it is not considered to be part of the antenna system.

TABLE IVJ-2.a-2

POWER AND WEIGHT ESTIMATES, PHASED ARRAY ANTENNA

Item	Power, watts	Wt, lbs
Supporting Structure	-	12
61 elements	-	16
61 RF preamplifiers	30	12
61 digital phase shifters, including diode drivers.	37	12
Corporate Feed and DC Power Distribution	-	9
Multilobing receiver and switching	3	3
Computer	2	3
Battery	-	7
Totals	72	74

(c) Despun Dish Antenna

The dish antenna, in contrast to the array, does not lose gain as it is scanned off the roll axis, so a 3.5 ft dish can be used. Optimum frequency for a dish-based system is found to be around 1.8 GHz. This will increase acquisition time by a factor of about 2, but performance thereafter will be around 3 db better.

The mechanically despun system functions in essentially the same way as the electrically despun system. The Canopus reference is used to despin a platform, with the reference point adjusted to match a pre-programmed variable angular distance \emptyset (t) from the Canopus direction. A two-axis x-y gimbal is then driven by either a search or an autotrack command. It would be possible to use a single axis gimbal and get the other degree of freedom by placing some additional control on the despun mechanism to vary \emptyset , giving an az-el tracking system. However, it was found that at one point in the mission a gimbal-lock geometry is encountered with an az-el system, so the two-axis gimbal system is recommended.

The mechanically despun system has one significant advantage over a phased array. It can be designed to give much wider angular coverage, approaching complete coverage, with only a nominal increase in system weight and complexity. To do this with an array while retaining the specified gain would require a many-fold increase in system size. However, the comparison for this mission will be based wholly on the assumed 45° cone angular coverage. This despun dish system is well within current state-of-the-art capabilities and no major implementation problems are seen.

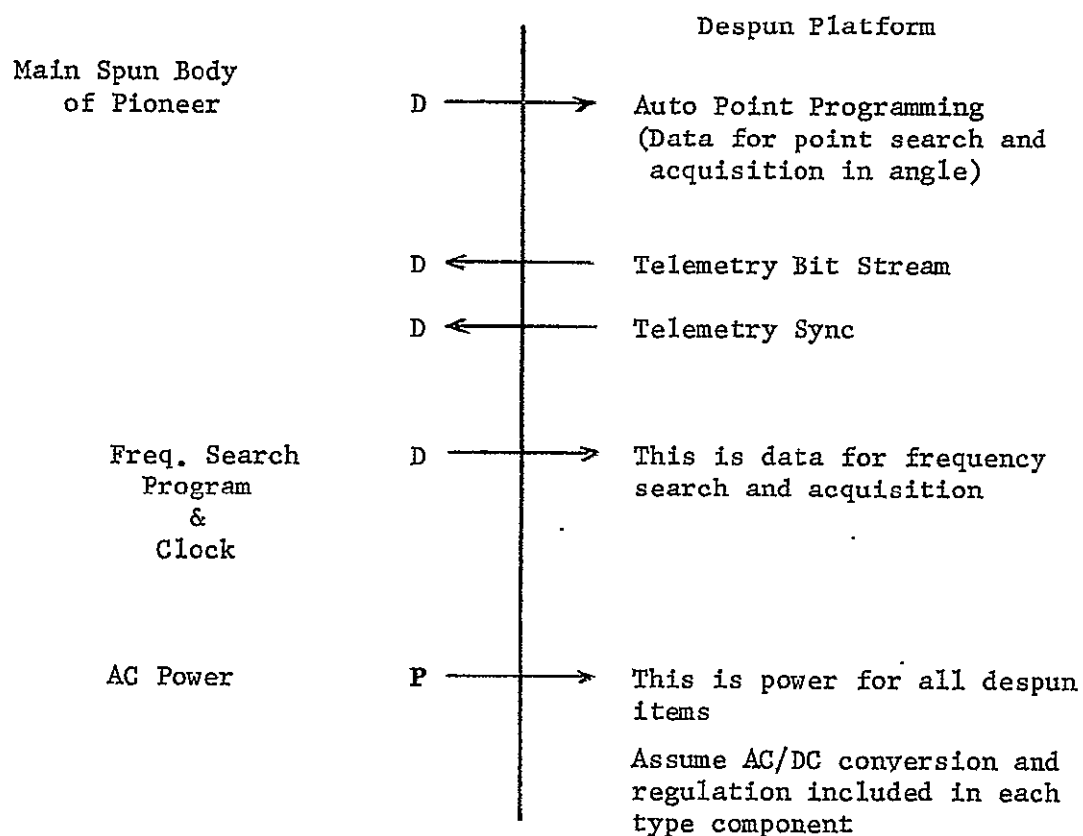
The despun platform will carry sufficient electronics equipment so that the slipring interface will transfer only digitized information and prime power. The complete autotrack system, including the autotrack receiver, associated servos, and gimbal motors, will be on the platform. Also, the data receiver, with demodulator and bit synch system, will be on the platform and will transmit the reconstructed binary data stream across the slipring interface. Table 3 shows the signals crossing the slipring interface. A conductive self-lubrication system is proposed to avoid the cold welding problem.

A magnetic pickup system on the spacecraft body, in conjunction with a magnet on the platform, is used to detect the spin rate. This and the Canopus sensor signal are the inputs to the spin rate control system. The gimbal servo is of conventional design. Brushless torque motors are recommended. Dry film lubrication is recommended for gimbal and platform bearings. Block diagrams of the servo systems are shown in Figure 6.

Weight and power estimates are given in Table 4. As with the array system, battery weight is sized on the basis of a 2.5 hour mission.

TABLE IVJ-2.a-3

ELECTRICAL SIGNALS AT THE SLIPRING INTERFACE



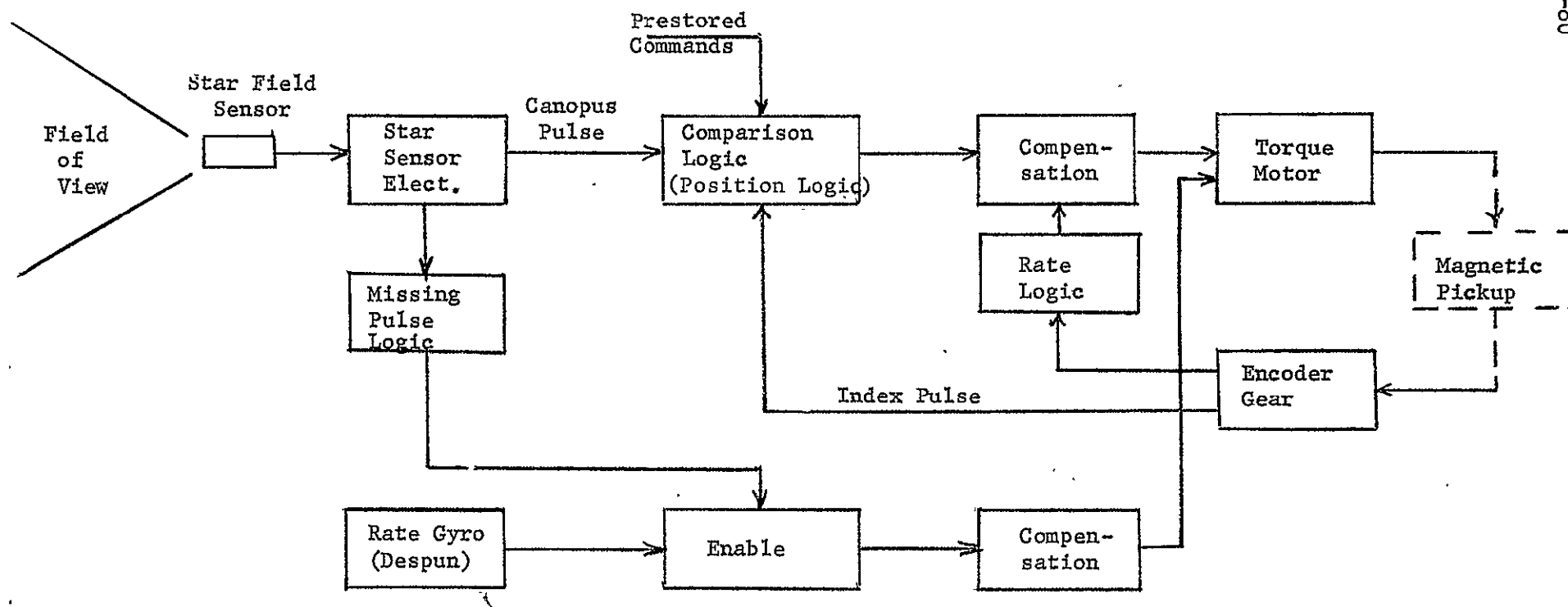
Notes:

D digital bit stream

P AC power for all items

Figure IVJ-2.a-6 Functional Diagram of Despun Dish Servo System
Despin Drive

IV-80



Gimbal Drive
(Two required for 2-axis Gimbal)

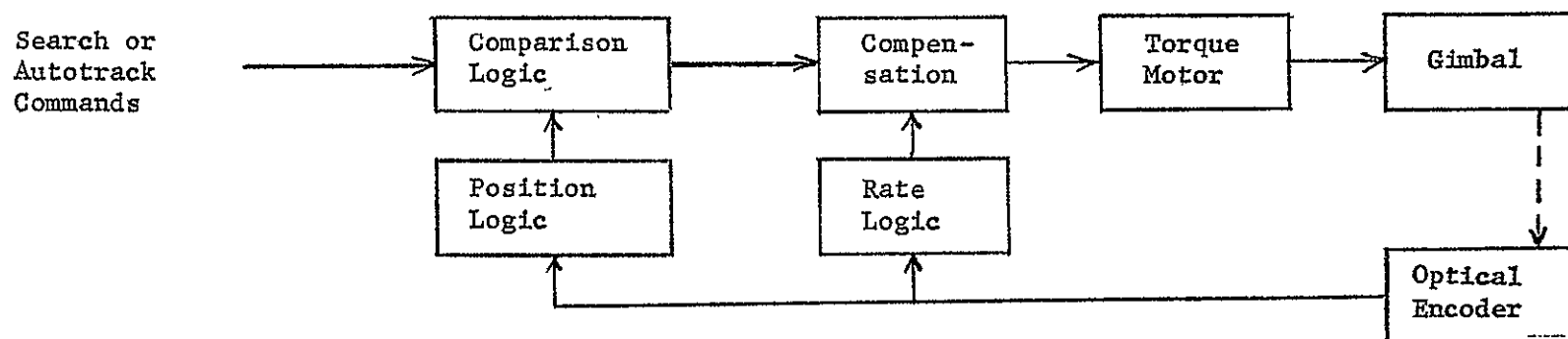


TABLE IVJ-2.a-4

POWER AND WEIGHT ESTIMATES, DESPUN DISH ANTENNA

Item	Pwr, watts	Wt, lbs
Dish	-	5
Monopulse Feed & RF Circuitry	-	3
Two Gimbals with motors	10	14
Despin Drive	4	17
Supporting Structure and Balance Weight	-	8
Servo Systems	5	4
Frequency and Beam Search Programmer	3	2
Multilobing Receiver and Switching	2	3
Battery	-	3
	<hr/>	<hr/>
Totals	24	59

(d) Conclusions

Based wholly on the estimated weight totals, the mechanically despun dish is seen to be the preferred choice. As stated earlier, this system can be designed to give essentially complete coverage with only a moderate increase in system weight. This is seen as an approach to using the Pioneer spacecraft for any Jupiter probe mission, not just the limited scan Mission B considered in this section. Mechanical details of both the limited scan system and the wide scan system are discussed in Chapter V.

It should also be noted that although both approaches are considered to be technically feasible, development costs for the mechanically despun system are expected to be lower because the technology is all current use on several space programs, notably the Intelsat Program.

K. Microwave Losses and Antenna Temperatures in the Jovian Atmosphere

1. Introduction

The sources of absorption in the Jovian atmosphere are 1) pressure broadening of absorption lines in the polarizable gasses NH_3 and H_2O , 2) absorption in the clouds, 3) pressure-induced losses in the nonpolarized gasses that comprise the bulk of the atmosphere, and 4) losses in the ionosphere. These will all be considered below. The computation of antenna temperature is closely related to the computation of absorption. This is also treated here. Total attenuation, of course, increases as the communications angle is moved away from zenith. This is computed and plotted as a function of elevation, z , and ψ , the communications angle measured from zenith.

A second source of signal loss is defocussing loss caused by ray-bending in the dense atmosphere. This loss is also computed as a function of z and ψ . Computation of the trap elevation z_t and the trap angle θ_t is also carried out. z_t is the elevation at which the radius of curvature of a horizontal ray equals the planet radius, and thus is the maximum depth that can be penetrated with an occultation experiment. θ_t , a function of z , is the angle at which ray-trapping or superrefractivity occurs.

The possibility of turbulence-induced fading of microwave signals is also considered briefly.

Our atmosphere models are derived from the contractual document JPL Section Document 131-10, "Preliminary Model Atmospheres for Jupiter", Dec 31, 1969, [1]. We have also examined some of the models described in [2] and [3]. The "nominal" in [1] is used as the basis for our mission design. It is identical to the "nominal" in [2], and is identified simply as "nominal" in this document. "Cool" and "warm" in [1] are fairly close to "nominal",

while "cool" and "warm" in [2] have a wider spread from "nominal". These will be identified herein as "cool [1]", "warm [1]", "cool [2]", "warm [2]". The Lewis models A and B are described in [3]. A Lewis modification to the cool [2] atmosphere, given to us informally, has also been examined. It was used for a worst case design in the design example mission. It will be identified herein as "cool/dense." This model retains the pressure-temperature profile from the cool [2], but has slightly lower abundances of NH_3 and H_2O and a less massive solution cloud. Atmospheres worked in detail are the nominal, warm [1], cool [1], cool [2], and cool/dense.

2. Absorption Losses

a. General

NH_3 has a large group of absorption lines (the "inversion spectrum") centered around 25 GHz. These lines, very narrow at low pressure, are broadened by increasing pressure, merging into a single line for pressures greater than 1 atm. Although 25 GHz is remote from the frequency band of interest for telecommunications (around 1 to 2 GHz), line broadening due to the very high pressures encountered in the mission is sufficient to cause substantial attenuation even at these relatively low frequencies. It was found that even the rotational spectrum of NH_3 , extending upward from 600 GHz, gives an absorption at 1000 atm that is not completely negligible. Similarly, H_2O has an absorption line at 22 GHz, but lines as high as 380 GHz were included in the computation.

b. Line Shapes

In the past, most workers in microwave spectroscopy have used the Van Vleck [4] shape factor, given by

$$SF_{\nu} = \frac{\Delta\nu}{(\nu_0 - f)^2 + \Delta\nu^2} + \frac{\Delta\nu}{(\nu_0 + f)^2 + \Delta\nu^2}$$

where ν_0 is the line resonant frequency, $\Delta\nu$ is the linewidth parameter, and f is the applied signal frequency. For $\nu_0 \gg f$, the case of interest to us, this reduces to

$$SF_v \cong \frac{2\Delta\nu}{\nu_0^2 + \Delta\nu^2} \quad (\text{IVK-1a})$$

$\Delta\nu$ is proportional to density. At low pressures $\Delta\nu \ll \nu_0$ and at very high pressures $\Delta\nu \gg \nu_0$. These conditions give

$$SF_v \cong \frac{2\Delta\nu}{\nu_0^2} \quad (\text{low pressures}) \quad (\text{IVK-1b})$$

$$SF_v \cong \frac{2}{\Delta\nu} \quad (\text{high pressures}) \quad (\text{IVK-1c})$$

It was found that SF_v gives a good match to observed data at high pressures. At lower pressures agreement is good for frequencies near ν_0 , but poor for frequencies remote from ν_0 . Recently Ben-Reuven [5] devised a shape factor in which the single linewidth parameter $\Delta\nu$ is replaced by two parameters γ and β . This additional degree of freedom permits a good match to observed data over the whole range of pressure and frequency of interest. The Ben-Reuven shape factor is given by

$$SF = \frac{2(\gamma - \beta)f^2 + 2(\gamma + \beta)(\nu_0^2 + \gamma^2 - \beta^2)}{(f^2 - \nu_0^2 - \gamma^2 + \beta^2)^2 + 4f^2\gamma^2}$$

Again, $f \ll \nu_0$. γ and β are also proportional to density. This gives

$$SF \cong \frac{2(\gamma + \beta)}{\nu_0^2 + \gamma^2 - \beta^2} \quad (\text{IVK-2a})$$

$$\cong \frac{2(\gamma + \beta)}{\nu_0^2} \quad (\text{low pressures}) \quad (\text{IVK-2b})$$

$$\cong \frac{2}{\gamma - \beta} \quad (\text{high pressures}) \quad (\text{IVK-2c})$$

ν_0 , $\Delta\nu$, γ , β , and f are all in GHz.

The Ben-Reuven shape factor was used in our computations. Since the Van Vleck factor gives good agreement with experimental data at high pressures, equating (1c) to (2c) gives $\Delta\nu = \gamma - \beta$ (IVK-3)

At low pressures, the Ben-Reuven shape factor is greater than the Van Vleck factor by $\frac{\gamma + \beta}{\gamma - \beta}$.

Computation of absorption $\alpha(z)$ km^{-1} was done for each line and summed. This was then integrated over the atmosphere profile to give the total zenith absorption. $\alpha(z)$ and $\int_{z_0}^{\infty} \alpha(z) dz$ are converted to db per km and db by the factor $10 \log_{10} (e) = 4.35$.

$\alpha(z)$ is computed from

$$\alpha(z) = k_1 \cdot A \cdot SF(z) \cdot f^2 \cdot \frac{P(z)}{T(z)^2} \text{ km}^{-1} \quad (\text{IVK-4})$$

(from Maryott [6]),

where A is the abundance of ammonia or water, P is the pressure in atm, T is the temperature in degrees K. $SF(z)$ is defined in (2), f is the applied frequency, and k_1 is matched to experimental data. As stated earlier, γ and β are proportional to density, giving

$$\gamma(z) = k_2 \frac{P(z)}{T(z)} \quad (\text{IVK-5})$$

$$\beta(z) = k_3 \frac{P(z)}{T(z)} \quad (\text{IVK-6})$$

where k_2 and k_3 are matched to experimental data, and are a function of the foreign gasses (H_2 and H_e) as well as the absorbing gas (NH_3 or H_2O). $P(z)$ and $T(z)$ are taken from the model atmospheres specified in the contract.

c. Ammonia Vapor

Our principal sources of information for NH_3 absorption are Maryott [6] and Wrixon [7]. For the 25 GHz inversion line at high

pressures, Maryott's results can be reduced to

$$\Delta\nu^{\text{NH}_3} = 231.4 (A_{\text{H}_2} + 0.24 A_{\text{He}}) \frac{P(z)}{T(z)} \text{ GHz} \quad (\text{IVK-7})$$

where A_{H_2} and A_{He} are the abundance of hydrogen and helium. For the 0.867, 0.133 composition of the nominal atmosphere, (7) reduces to

$$\Delta\nu^{\text{NH}_3} = 207.9 \frac{P(z)}{T(z)} \text{ GHz.}$$

$$\text{The value } K_1^{\text{NH}_3} = 2.028 \times 10^6 \quad (\text{IVK-8})$$

was also taken from Maryott. It includes the effects of all of the lines clustered around 25 GHz after they are merged into a single line by pressure broadening.

Using these values it is found that at $f = 2.3$ GHz and at the 1000 atm level in the nominal atmosphere, attenuation due to this source is 0.0482 db/km. Total zenith attenuation from 1000 atm up due to this source is 32 db at 2.3 GHz. This of course scales with frequency as f^2 .

Wrixon [7] uses an elaborate computation for γ and β in which k_2 and k_3 in (4) and (5) are not quite constant but are functions of temperature. However, the corrections are small and have been neglected in our computation. His values for γ and β give

$$\frac{\gamma}{\beta} \cong 2.0 \quad (\text{Ammonia}) \quad (\text{IVK-9})$$

Again, this is a function of temperature, but the effect of his departures from (8) on the computed absorption is small. Using (3), (7) and (9) in (5) and (6) gives

$$k_2^{\text{NH}_3} = 462.8, \quad k_3^{\text{NH}_3} = 231.4 \quad (\text{IVK-10})$$

Wrixon's values of k_2 and k_3 range on both sides of these, depending

on temperature, but in such a way that the value of α is never altered by more than about 10%. It was decided to use Maryott's value because it is based on unpublished experimental data which was presumably not available to Wrixon.

Maryott also gives a computation for the contribution due to the rotational spectrum of ammonia. This is quite small. In the nominal atmosphere it is about 5% of the inversion spectrum contribution at high pressures and less at low pressures. However, it was included in our computation. It follows a relationship quite different from (4). Maryott's expression can be reduced to

$$\alpha_{\text{rot}} = 71.1 A (A_{\text{H}_2} + 0.267 A_{\text{He}}) f^2 \frac{P(z)^2}{T(z)^{2.5}} \text{ km}^{-1} \quad (\text{IVK-11})$$

d. Water Vapor

Information on absorption due to water vapor is taken from Bean [8] and Gallet [9]. Bean, writing in the Radar Handbook, treats effects observed on Earth. He uses the Van Vleck shape factor, and then observes that this underestimates the effects of lines higher than the first (22 GHz) by a factor of about 4. His method of compensating for this would not give the correct result at high pressures. This can be corrected by using the Ben-Reuven shape factor in (4), with

$$\frac{\gamma}{\beta} = 1.667 \quad (\text{water}) \quad (\text{IVK-12})$$

on all of these lines. The lines of interest are the first line at 22 GHz and the higher lines at 183, 325 (2 lines) and 380 GHz. The higher lines are stronger than the first line. They were arbitrarily given the same strength in our computations. While this and (12) may not be exactly correct for all of these higher lines, the error

should not be large since the water contribution to the absorption is less than 10% of the total.

Bean gives $\Delta \nu^{\text{H}_2\text{O}} = 2.61$ GHz for all of these lines at $P = 1$ atm and $T = 318^\circ\text{K}$. Converting this into the form of (5) and (6) and using (3) and (12) gives

$$k_2^{\text{H}_2\text{O}} = 2070., \quad k_3^{\text{H}_2\text{O}} = 1242. \quad (\text{IVK-13})$$

Bean gives

$$k_1^{\text{H}_2\text{O}} (\text{first line}) = 1733. \quad (\text{IVK-14})$$

Partitioning his nonresonant term among the four higher lines gives

$$k_1^{\text{H}_2\text{O}} (\text{higher lines}) = 57400. \quad (\text{IVK-15})$$

for each line.

From discussions with Gallet [9] it was concluded that this approach should give reasonably accurate results even though the Jupiter foreign gasses (H_2 , He) are not the same as those on Earth (N_2 , O_2).

e. Clouds

All of the JPL atmospheres ([1] and [2]) have an NH_3 ice cloud and an H_2O ice cloud. The cool [2] and cool/dense [2] atmospheres add a liquid NH_3 - H_2O solution cloud below the two ice clouds. The cool/dense [2] also has a solid NH_4 SH cloud just below the solid NH_3 cloud. All of these clouds will cause absorption of RF signals passing through them. This is in addition to the attenuation caused by gaseous absorption. There is sufficient information on H_2O ice clouds, measured on Earth, to quickly determine the effects of these

clouds. They will be considered first. Absorption due to the NH_3 ice and solution clouds will also be estimated, based on modifications of analysis done on Earth clouds.

H_2O ICE CLOUDS

Data from Bean [8], will be used here. Since these effects are small, and decrease with decreasing frequency, no data exists for frequencies below around 10 GHz. These data will be extrapolated into our region of interest, around 1 to 2 GHz.

Attenuation is calculated from

$$B = B_1 M \quad (\text{IVK-16})$$

where B = absorption, db/km,

B_1 = absorption coefficient, db/km/g/m³, a function of frequency and temperature, and

M = water content, g/m³

Extrapolating the data tabulated for B_1 in ice clouds gives the following empirical approximation:

$$B_1(2.3 \text{ GHz}, 253^\circ\text{K}) = 1.38 \times 10^{-4} \quad (\text{H}_2\text{O ice}) \quad (\text{IVK-17a})$$

$$B_1(f, T) = 1.38 \times 10^{-4} \cdot \left(\frac{f}{2.3}\right) \cdot \left(\frac{T}{253}\right)^{19.4} \quad (\text{IVK-17b})$$

Taking the temperature and water content data from the "nominal" model as given in [2] and integrating B_1 thru the H_2O ice cloud give a total zenith attenuation of 0.0037 db at 2.3 GHz. This decreases linearly with decreasing f . This is completely negligible. The other atmospheres have similar H_2O ice cloud thicknesses and densities, and would have comensurate absorption.

NH₃ ICE CLOUDS

The absorption in clouds is a strong function of the dielectric constant of the cloud material. Thus, for example, clouds of liquid water, which has a dielectric constant of 81.1 (at 291°K), give markedly more absorption than clouds of water ice. (Ice dielectric constant = 3.20). The very high dielectric constant of liquid water is due to its high polarizability. This polarizability is "frozen out" in the solid form, giving a dielectric constant for ice near that of many other crystalline solids. Similarly, ammonia, which is also polarizable in liquid form, has a relatively high dielectric constant in its liquid form of around 23. We have not been able to find a value for the dielectric constant of ammonia ice. However, it is reasonable to assume that effects similar to those occurring in water also occur in ammonia, with the high polarizability eliminated in the frozen material, giving a dielectric constant roughly commensurate with that of water ice. Since the NH₃ ice clouds are much more tenuous than the H₂O ice clouds, absorption due to these clouds should be completely negligible, much less than that due to the H₂O ice clouds. The solid NH₄ SH cloud in the cool/dense [2] atmosphere is also assumed to give negligible absorption, for the same reasons.

NH₃ - H₂O SOLUTION CLOUDS

Among the five JPL model atmospheres, the solution cloud layer is present only in the cool [2] model. The cool/dense model also has a solution cloud. The cloud in the cool [2] model will be examined first. Figure 1 shows the mass vs elevation plot for this cloud, taken from [2]. This integrates to a total mass of 79.2 gm/cm². This compares to 39 and 50 gm/cm² for the solution clouds in the Lewis models A

and B [3] and 48 gm/cm^2 for the cool/dense model, so it can presumably be taken as a worst case. It should be noted that this is an enormous cloud by Earth standards. Its maximum density of 68.8 mg/liter can be compared to a typical earth value of 1 mg/liter . 4 mg/liter is the maximum density normally encountered on Earth. Earth clouds are rarely more than a few km thick, while this Jupiter cloud is 40 km thick. The total mass is around two orders of magnitude greater than that of heavy clouds on Earth. Significant absorption would be expected from this cloud even if it were pure water. The conductivity introduced by the NH_3 in solution will increase this attenuation somewhat, as will be shown below. Solution strength vs elevation is not given in [2]. An estimate for solution strength vs elevation, based on Lewis' results [3], is also shown in Figure 1.

In order to determine the effect of these clouds, it is necessary to determine the dielectric constant and conductivity as a function of temperature and solution strength. Conductivity, σ , $\text{ohm}^{-1} \text{m}^{-1}$, as a function of solution strength, at 291°K , shown in Figure 2, is taken from [10].

This varies with temperature approximately as

$$\sigma(T) = \sigma(291) \cdot \left(\frac{T}{291}\right)^{6.2} \quad (\text{IVK-18})$$

$\text{NH}_3 - \text{H}_2\text{O}$ solutions are characterized in [10] as weak electrolytes, so this conductivity is quite low relative to that of strong electrolytes such as KCl or NaCl solutions.

Dielectric constant, ϵ_r can be taken as that of water, 81.1 at 291°K , with adequate accuracy. This varies with temperature approximately as [11]

$$\epsilon_r(T) = 81.1 \left(\frac{291}{T}\right)^{1.4} \quad (\text{IVK-19})$$

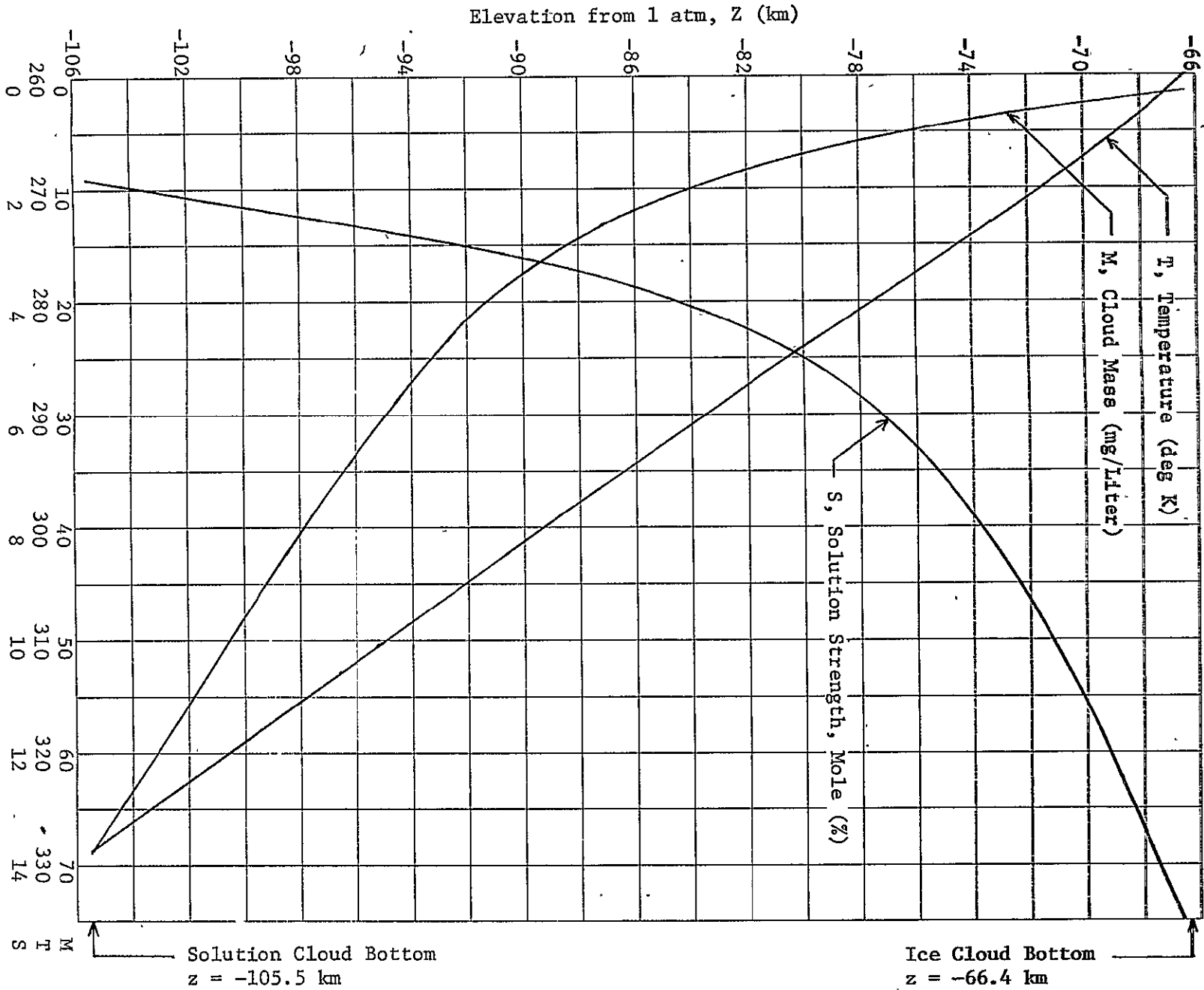


Figure IVK-1 The NH_3 - H_2O Solution Cloud, Cool [2] Atmosphere

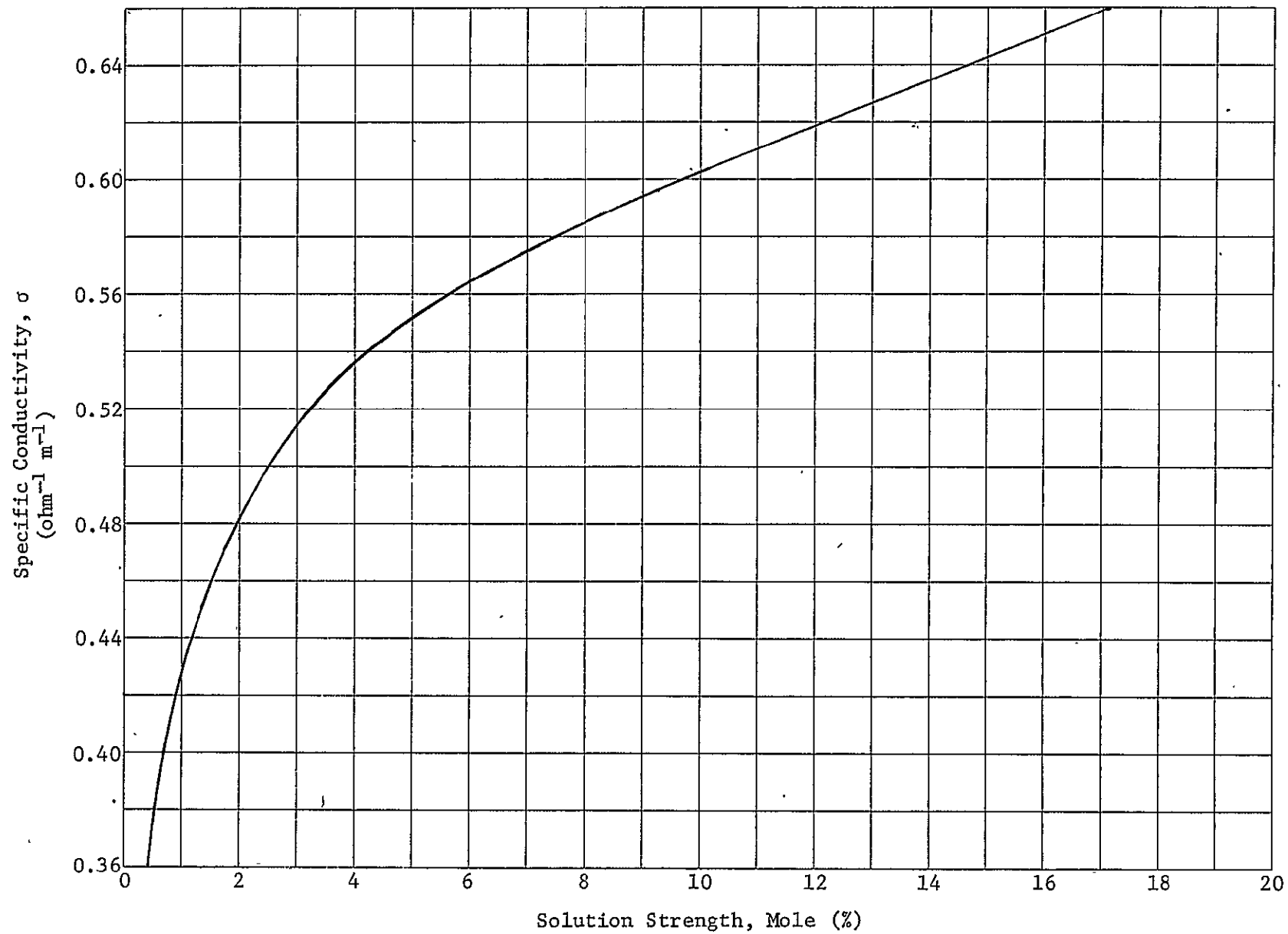


Figure IVK-2 Specific Conductivity of $\text{NH}_3 - \text{H}_2\text{O}$ Solutions

The complex dielectric constant ϵ_j is defined by

$$\epsilon_j = \epsilon_r - j \frac{\sigma}{\omega \epsilon_0}, \quad (\text{IVK-20})$$

where

σ = conductivity, $\text{ohm}^{-1} \text{m}^{-1}$

ω = radian frequency

$\epsilon_0 = 8.854 \times 10^{-12}$ farads/meter

This can be used to calculate B_1 using an expression from Bean ([8], p 24-22),

$$B_1 = 0.4343 \frac{6\pi}{\lambda} \cdot \text{Im} \left(-\frac{\epsilon_j^{-1}}{\epsilon_j + 2} \right) \quad (\text{IVK-21})$$

where λ is the wavelength in cm. (= 13 at 2.3 GHz)

First, however, it will be necessary to determine a value for ϵ_j for pure water using (21) and an extrapolation of tabulated values for B_1 . The imaginary part of this will then be augmented by the $-j \frac{\sigma}{\omega \epsilon_0}$ term in (5). As with ice clouds, tabulated data for B_1 do not extend into the frequency range of interest because the effects are relatively small. Extrapolation of these data gives the empirical results

$$B_1(2.3 \text{ GHz}, 291^\circ\text{K}) = 0.00314 \quad (\text{H}_2\text{O liquid}) \quad (\text{IVK-22a})$$

$$B_1(f, T) = 0.00314 \left(\frac{f}{2.3} \right)^2 \cdot \left(\frac{291}{T} \right)^{8.35} \quad (\text{IVK-22b})$$

Using (22a) in (21), and assuming $\text{Re}(\epsilon_j) = 81.1$, ϵ_j (2.3 GHz, 291°K) is found to be $81.1 - j 11.50$. The imaginary part of this quantity is not caused by conventional conductivity, since pure water is assumed, but by molecular absorption effects. It differs from that due to conductivity in that it increases with increasing frequency as f^2 while that due to conductivity decreases with increasing frequency as shown in (20).

Now let us calculate the imaginary part of (20) for some typical numbers. Assume $f = 2.3$ GHz, $T = 291^\circ$, $A = 2$ mole %. From Figure 2 this gives $\sigma = 0.48$, and

$$\text{Im}(\epsilon_j) = - \frac{0.48}{2\pi \times 2.3 \times 10^9 \times 8.854 \times 10^{-12}} = -3.76, \text{ which is}$$

about 1/3 that for pure water calculated above. For $\text{Im}(\epsilon_j) \ll \text{Re}(\epsilon_j)$, K_1 given by (21) is directly proportional to $-\text{Im}(\epsilon_j)$. Combining the two components of $\text{Im}(\epsilon_j)$ and scaling K_1 accordingly implies that the solution cloud is about 1 1/3 times as bad for attenuation as a pure water cloud. This factor increases with increasing NH_3 concentration, increasing temperature, and also with decreasing frequency.

It will be sufficiently accurate to approximate B_1 with

$$B_1(f, T, \sigma) = 0.00314 \left(\frac{f}{2.3}\right)^2 \left(\frac{291}{T}\right)^{8.35} + 0.00214 \sigma \left(\frac{2.3}{f}\right) \left(\frac{T}{291}\right)^{4.8}, \quad (\text{IVK-23})$$

where σ is taken from Figure 2, given that the NH_3 concentration is known. The $T^{4.8}$ dependency in the last term reflects the $T^{6.2}$ dependency in (3) and the $T^{-1.4}$ dependency in (4).

Integrating MB_1 through the cloud of Figure 1 will give the total absorption of this cloud at the selected frequency. Figure 3 shows the results at $f = 2.3$ GHz. Total attenuation is found to be 2.71 db. Figure 4 shows total attenuation as a function of frequency. This has a minimum of 2.53 db around 1.8 GHz. It is dominated by the $\frac{1}{f}$ term (conductivity loss) for lower frequencies and the f^2 term (molecular absorption) for higher frequencies.

A similar computation was made for the solution cloud in the cool/dense model. Absorption was found to be approximately 60% of that in the cool [2] cloud. It is 1.636 db at 2.3 GHz.

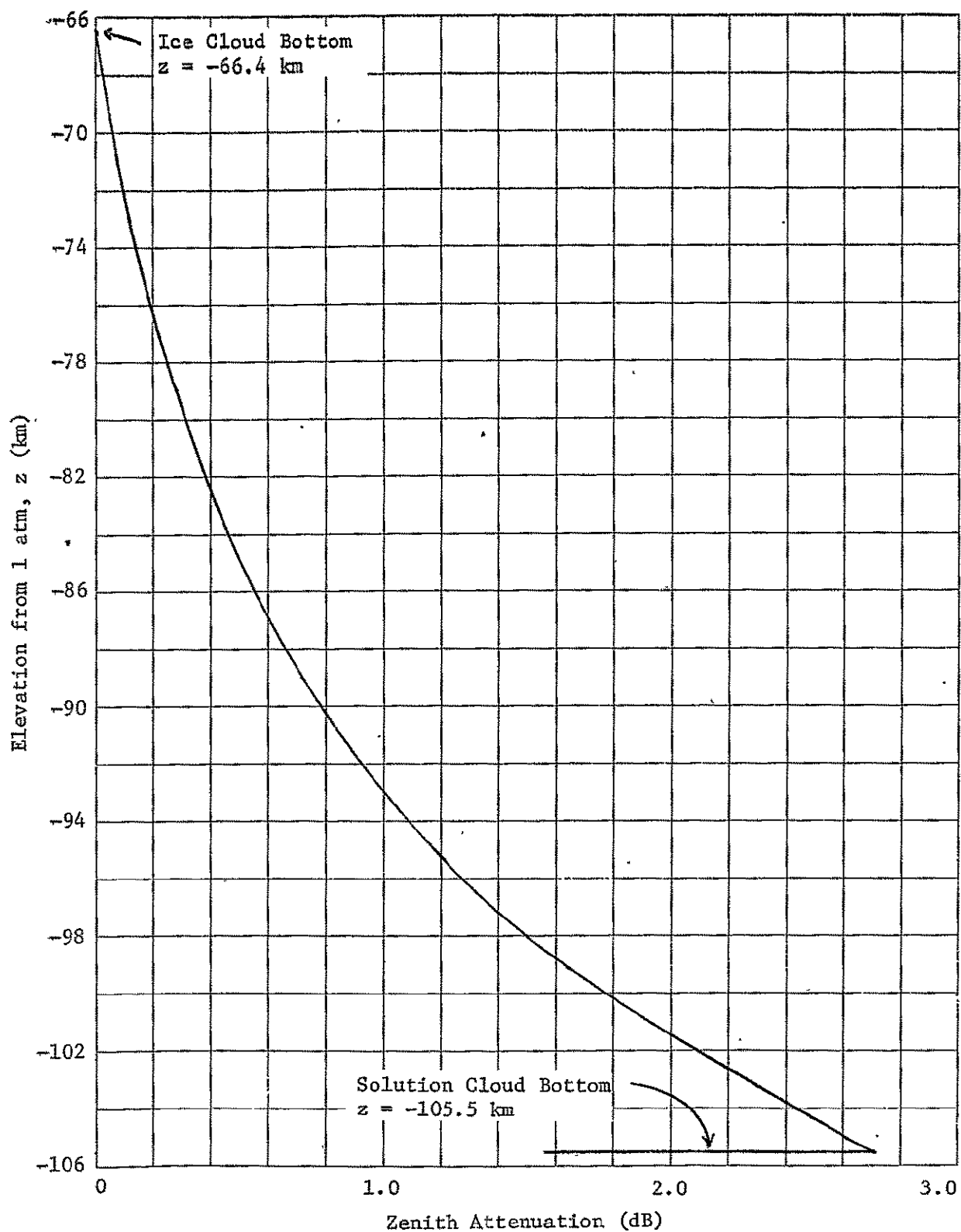


Figure IVK-3 Zenith Attenuation at 2.3 GHz, Solution Cloud, Cool [2]
Atmosphere

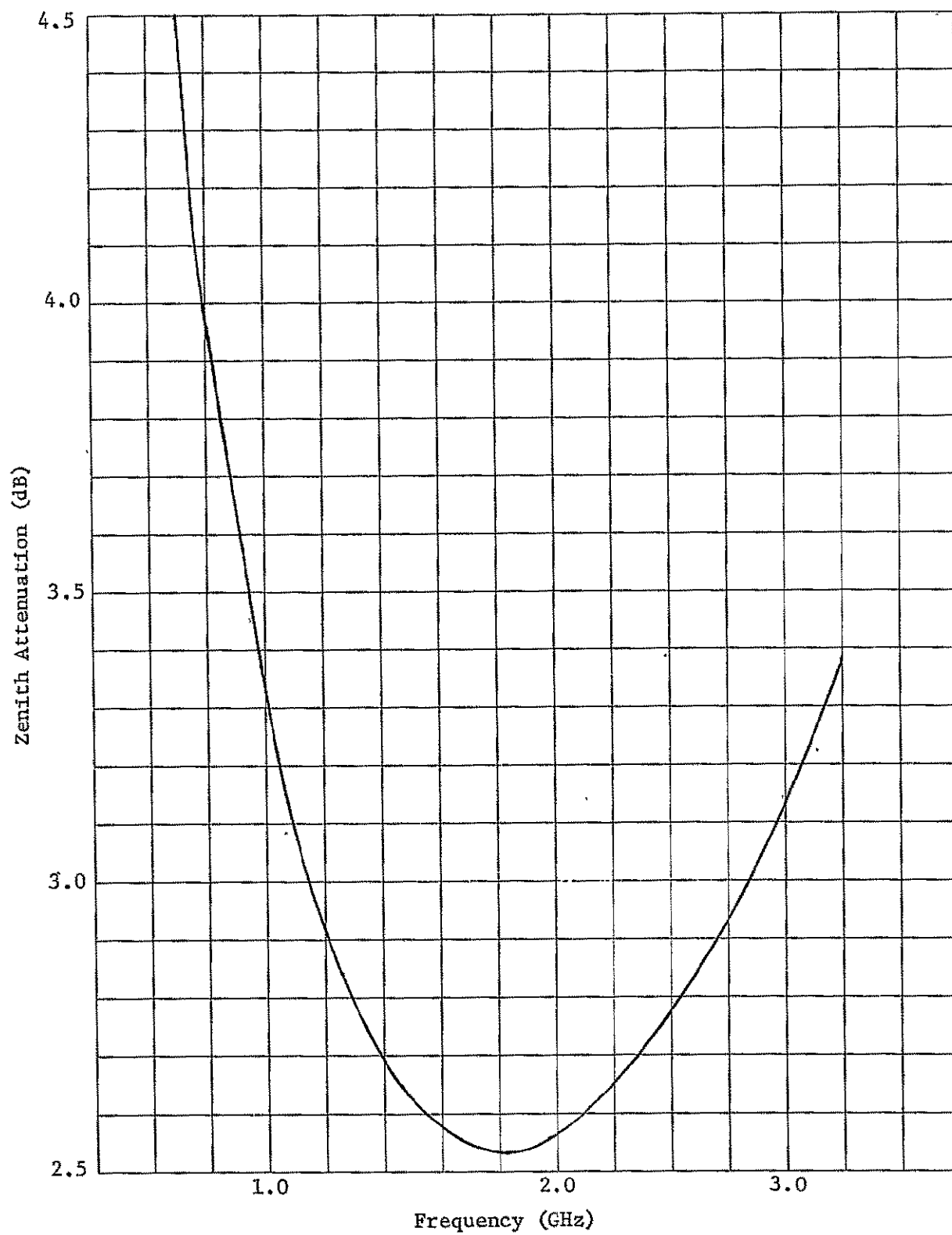


Figure IVK-4 Solution Cloud Loss vs Frequency, Cool [2] Atmosphere

f. Pressure-Induced Absorption

This phenomena, which occurs in non-polarized gasses at high pressures, is the principal loss mechanism in the CO_2 atmosphere of Venus. It has the form (from [12])

$$\alpha_{PI} = C f^2 \frac{P^2}{T^5}, \quad (\text{IVK-24})$$

where C is of the form

$$C_{aa} A_a^2 + C_{bb} A_b^2 + C_{cc} A_c^2 - - - + C_{ab} A_a A_b + C_{ac} A_a A_c + \dots, \quad (\text{IVK-25})$$

where the C's are experimental coefficients and the A's are abundances of the component gasses. Apparently, the cross term coefficients C_{ij} are generally smaller than the single-gas coefficients C_{jj} . This, together with the abundances, suggests that we only need consider H_2 and He in calculating C for the Jovian atmosphere. We make this assumption even though we were not able to find any data on terms of the type $\text{H}_2 \times \text{CH}_4$ which will occur in the Jovian atmosphere.

Hydrogen-Helium mixtures have been studied by Copla [13]. He found that the loss in Hydrogen is lower than that in CO_2 by better than three orders of magnitude. The loss in helium is much smaller than that in hydrogen, so it simply acts as a dilutant of the hydrogen. The total zenith attenuation due to this source in the nominal atmosphere from the 1000 atm level up is found to be about 0.02 db at 2.3 GHz, completely negligible compared to the other losses. It has not been included in our computation.

g. Losses in the Ionosphere

Information on the Jupiter ionosphere is quite limited. Perhaps the best model is given by Hunten [14]. He shows an upper bound on n_e , the electron density, between 10^5 and 10^6 cm^{-3} , or about

equal to the maximum density found on Earth. He states that this upper bound may be high by as much as two orders of magnitude. The Jupiter ionosphere is about 10 times as thick as the earth's ionosphere due to the greater scale height on Jupiter. Without making a detail calculation, an upper bound on the loss due to this ionosphere can be estimated as 10 times that due to the Earth's ionosphere. This would be around .02 db at 1 GHz, scaling as f^{-2} for higher frequencies. Therefore, in the frequency band of interest to this program (~1 to 2.3 GHz) ionospheric effects can be neglected. Lower frequencies have been considered for a lower probe to upper probe link. However, this link does not penetrate the ionosphere.

h. Results, Absorption

The equations cited above were programmed to compute absorption and the integral of absorption versus depth of penetration into the atmosphere. The model atmosphere data was put into the computation using a data deck of P, T, and z with 5 km intervals on z. Some initial computations were made using (from [15])

$$A'_{\text{NH}_3}(z) = \begin{cases} A_{\text{NH}_3}, & T(z) > T_{\text{SAT}} \\ \frac{A_{\text{NH}_3} \cdot T_{\text{SAT}} \cdot P_{\text{SAT}}}{P(z)T(z) \cdot \left[\exp \left(25.88 \left(\frac{T_{\text{SAT}}}{T(z)} - 1 \right) \right) \right]}, & T(z) < T_{\text{SAT}} \end{cases} \quad (\text{IVK-25})$$

where A'_{NH_3} = Ammonia Abundance

z = Elevation above pressure = 1 atm., measured in km
(radius = 71,420 km in our model)

T = Temperature, °K

P = Pressure, atm

T_{SAT} = NH_3 Saturation temperature in the given atmosphere model

P_{SAT} = NH_3 Saturation pressure in the given atmosphere model,

A_{NH_3} = The below-saturation abundance of NH_3 specified in the model atmosphere.

to compute A'_{NH_3} in and above the clouds. However, it was found that the abundance computed from (25) dropped so rapidly in and above the clouds that adequate accuracy is given by

$$A'_{\text{NH}_3} = \begin{cases} A_{\text{NH}_3}, & T(z) \geq T_{\text{SAT}} \\ 0, & T(z) < T_{\text{SAT}} \end{cases} \quad (\text{IVK-26})$$

A similar expression was used for water. The cool/dense tables show the variation in abundances within the cloud zone, so these values were used in lieu of (26) in the computation of absorption in this model.

Zenith absorption vs elevation at 2.3 GHz in the nominal atmosphere is shown in figure 5. This scales as f^2 . The NH_3 and H_2O components of the absorption are also plotted. Absorption is plotted vs pressure in figure 6. Figure 7 shows the absorption in the cool [2] atmosphere for several frequencies. This includes absorption in the solution cloud, which does not scale as f^2 but follows the curve in figure 4. A discontinuous slope can be noted in these curves at the base of the solution cloud, particularly at lower frequencies. Cool/dense is shown in figure 8. Warm [1] and cool [1] are shown in figure 9.

The effect of departures of the look angle away from zenith will be treated later, after the necessary ray-bending analysis has been covered. For departures less than 45° a secant variation will give and adequate approximation to the increase in absorption.

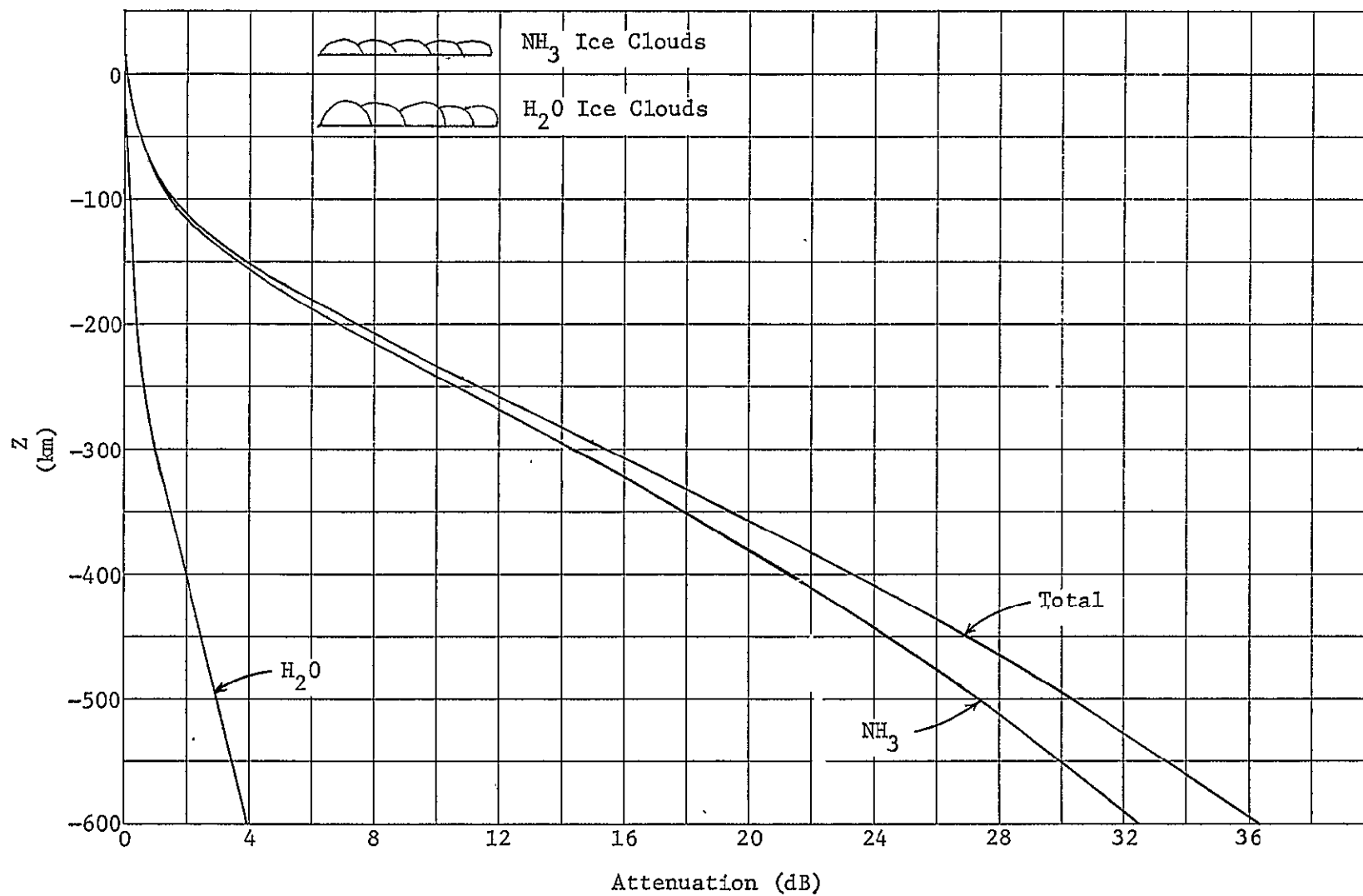


Figure IVK-5 Zenith Attenuation, Nominal Atmosphere, 2.3 GHz

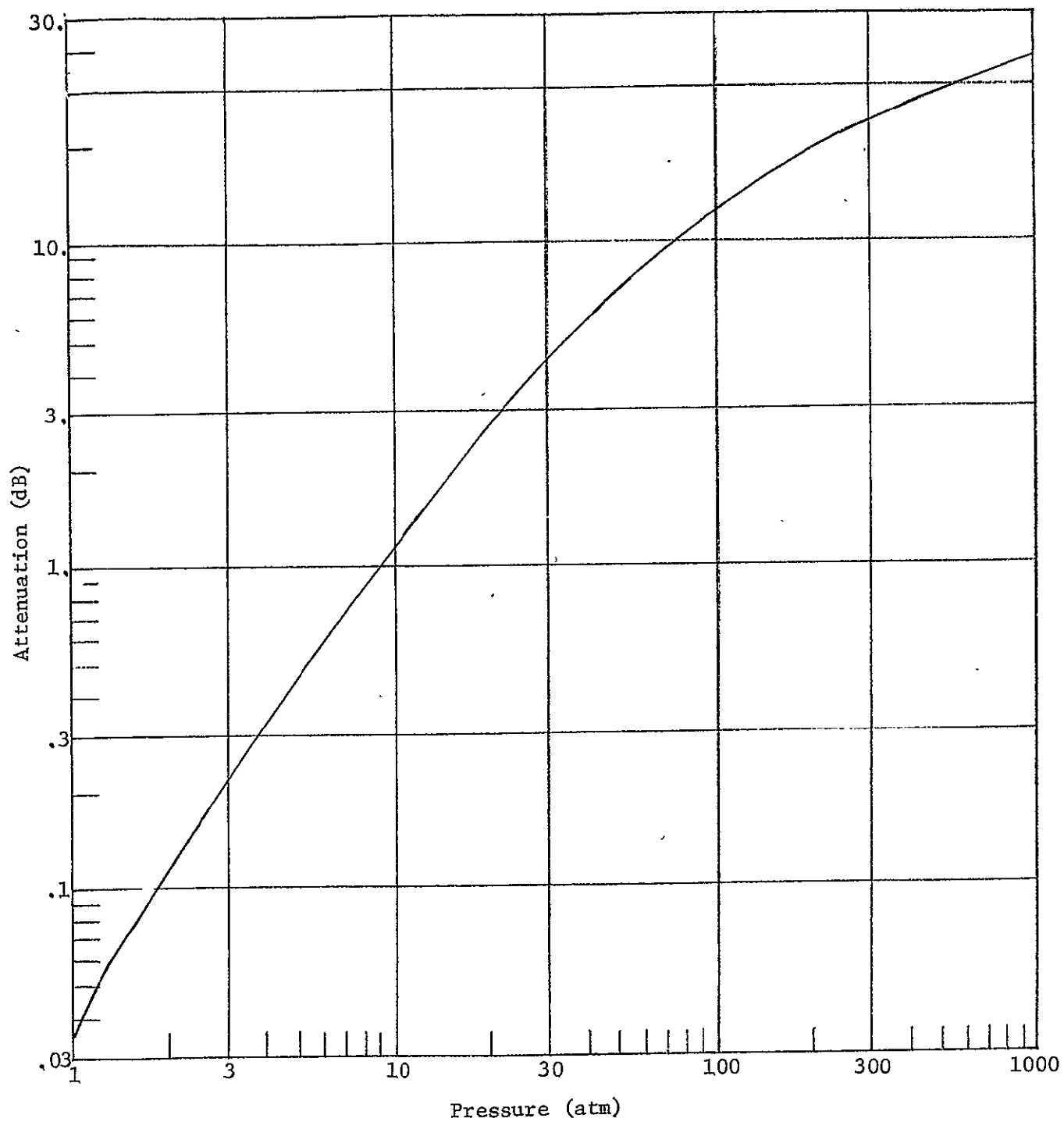


Figure IVK-6 Zenith Attenuation vs Pressure, Nominal Atmosphere, 2.3 GHz

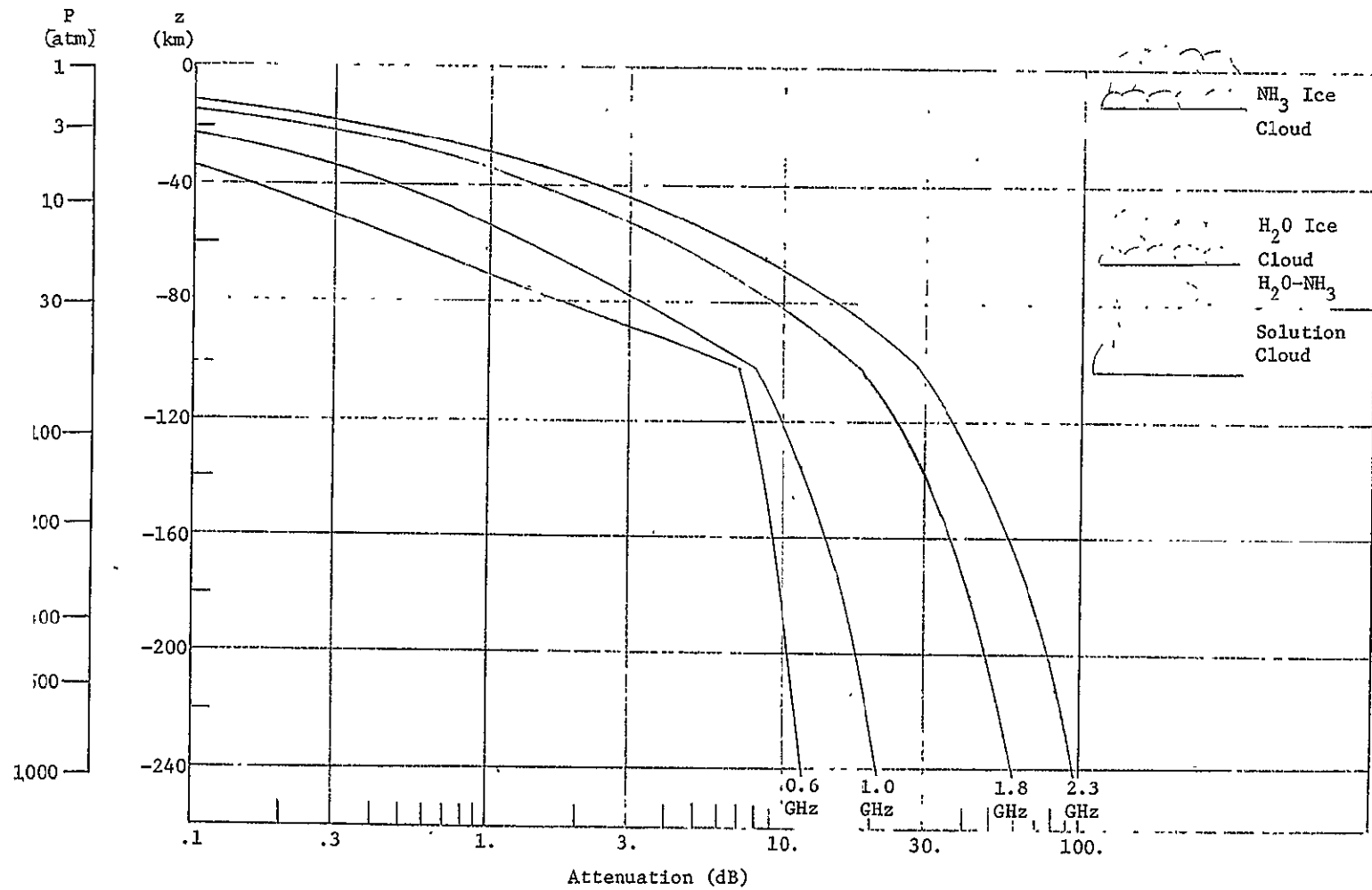


Figure IVK-7 Zenith Attenuation, Cool [2] Atmosphere

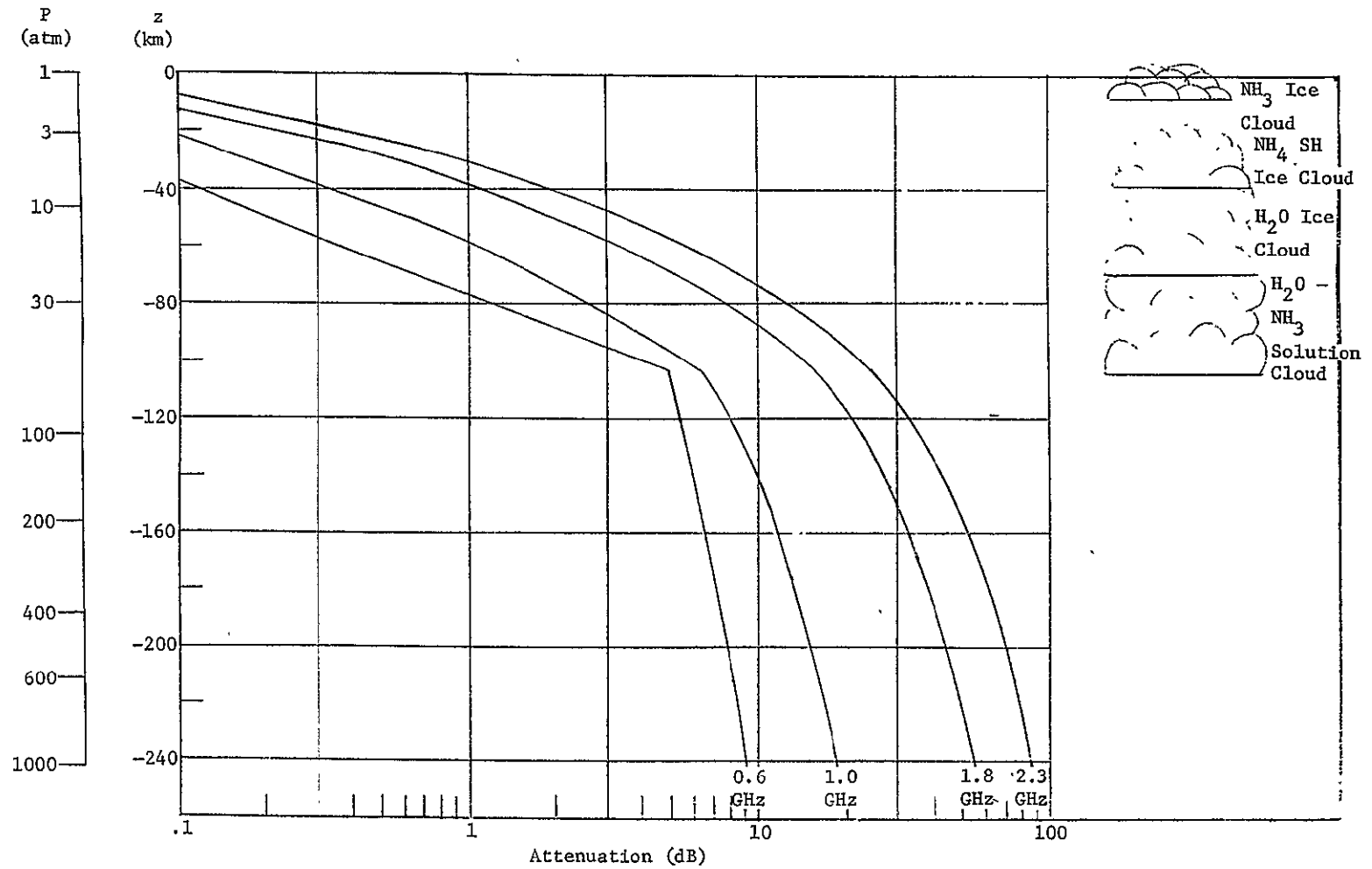


Figure IVK-8 Zenith Attenuation, Cool/Dense Atmosphere

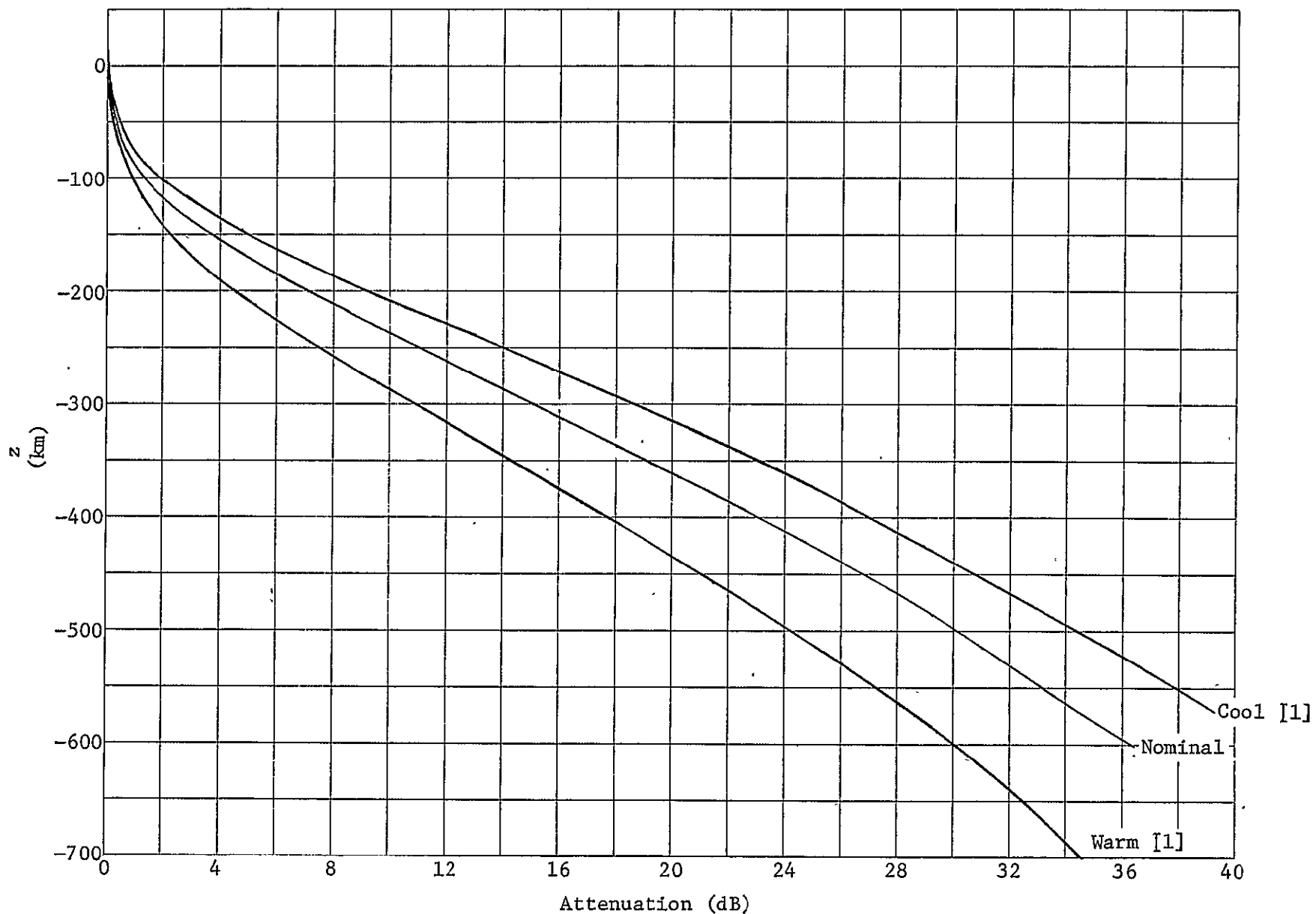


Figure IVK-9 Zenith Absorption, 2.3 GHz, Model Atmospheres from [1], JPL Document 131-10, 12/31/69. (Warm, Nominal, and Cool)

4. Antenna Temperatures

Antenna temperatures seen at any elevation z_0 can be computed from the absorption and temperature profiles. For highly directive narrow-beam antennas the upward, horizontal, and downward-looking temperatures are given by (from [16]).

$$T_V = \int_{z_0}^{\infty} \alpha(z) T(z) \exp \left[- \int_{z_0}^z \alpha(\ell) d\ell \right] dz + T_M \exp \left[- \int_{z_0}^{\infty} \alpha(z) dz \right] \quad (\text{IVK-35a})$$

$$T_H = T(z_0) \quad (\text{IVK-35b})$$

$$T_D = \int_{z_0}^{\infty} \alpha(z) T(z) \exp \left[- \int_{z_0}^z \alpha(\ell) d\ell \right] dz, \quad (\text{IVK-35c})$$

where the integration in each case is along the ray path in the look direction. Similar expressions can be written for any look angle θ . Since α is a function of frequency, these temperatures are also a function of frequency. The magnetosphere temperature T_M , taken from the plot on pg 56 of [17], is replotted and extrapolated to lower frequencies in figure 15. As shown therein, the noise temperature due to the magnetosphere rises very sharply as frequency is reduced into the region of decimetric radiation. Atmospheric absorption favors the selection of lower frequencies for communications, but this decimetric radiation places a lower limit on the frequencies that can be considered. The temperature seen by a low-gain antenna, T_A , can be computed by averaging the temperature $T(\theta)$ over the antenna pattern $G(\theta)$,

$$T_A = \int_0^{\pi} T(\theta) G(\theta) \sin \theta d\theta \quad (\text{IVK-36})$$

Given a vehicle of fixed size, the pattern of a typical low-gain antenna changes with frequency. The front-to-back ratio drops as frequency is reduced and the electrical size of the vehicle becomes smaller. T_A for a down-looking low-gain antenna has been computed a function of z_0 and frequency. Antenna patterns were estimated as a function of frequency assuming a vehicle equivalent to a 24" diameter circular plate. These data are applicable to the down-looking

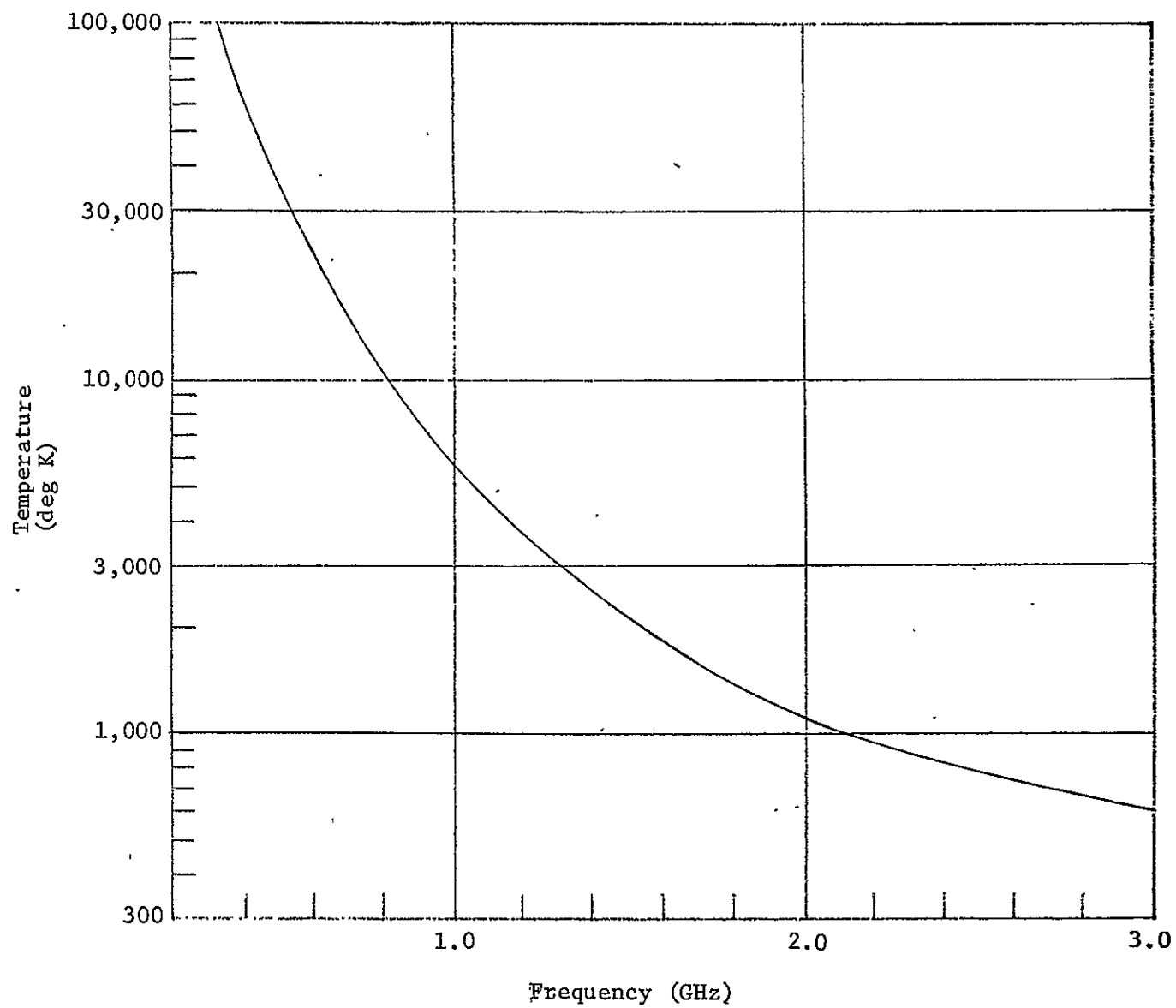


Figure IVK-15 Magnetosphere Temperature

receiving antenna on the upper probe for a split-probe mission. Plots for the nominal atmosphere are shown in figure 16, covering the range of pressures likely to be encountered by the upper probe of a split-probe mission. At these depths T_a becomes nearly independent of depth at the lower frequencies. Figure 17 shows T_a vs f with z_0 set at the 50 atm pressure level for several model atmospheres.

The average disc temperature as seen from a distance (e.g., from earth) can be computed from

$$T_R = 2 \int_0^1 \int_{z_0}^{\infty} \frac{\alpha(z)}{\sqrt{1-r^2}} \cdot T(z) \cdot \exp \left[- \int_{z_0}^z \frac{\alpha(\ell)}{\sqrt{1-r^2}} \cdot d\ell \right] dz dr, \quad (\text{IVK-37})$$

setting z_0 above the atmosphere. This is shown vs frequency for several model atmospheres in figure 18. There are not many earth-based observations in this frequency band because the disc is obscured by the magnetosphere noise. However, Berge [18] infers a T_R of $260^\circ \pm 40^\circ$ at $f = 2.88$ GHz and Branson [19] finds $250^\circ \pm 40^\circ$ at $f = 1.4$ GHz. These two points can be matched reasonably well by doubling the NH_3 in the nominal atmosphere.

The temperature seen by the antenna on the spacecraft that is used to receive signals from the probe depends on the directivity of that antenna and on the location of the spacecraft with respect to the magnetosphere. This location is a function of trajectory. However, for most of the missions examined, the spacecraft will be outside the bulk of the magnetosphere, looking through it, at the end of the probe mission. With this geometry, the spacecraft antenna temperature will be approximately equal to the magnetosphere temperature shown in figure 15. Accordingly, this is the temperature used in our link calculations.

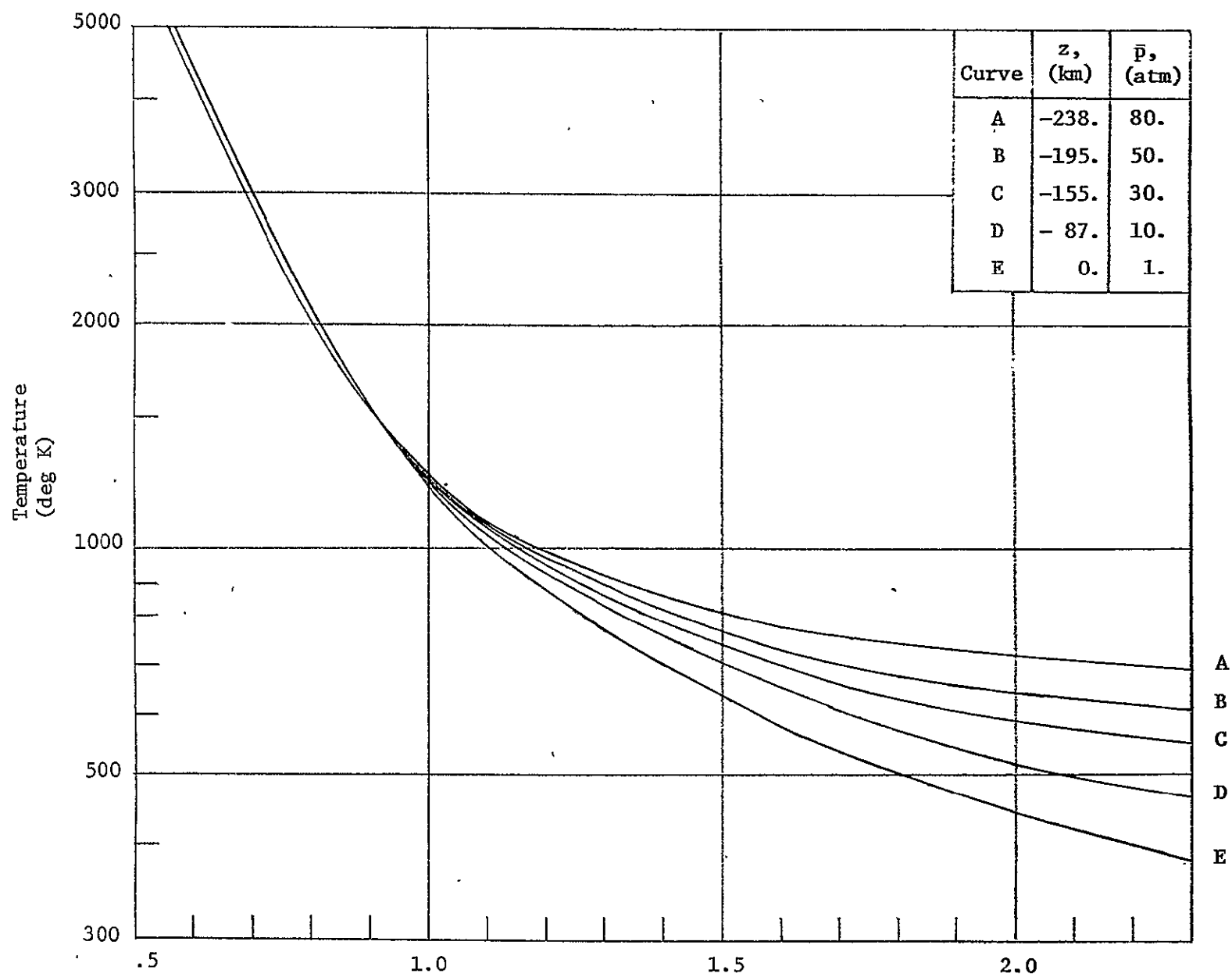


Figure IVK-16 Down-Looking Antenna Temperatures, Low-Gain Antenna, Nominal Atmosphere

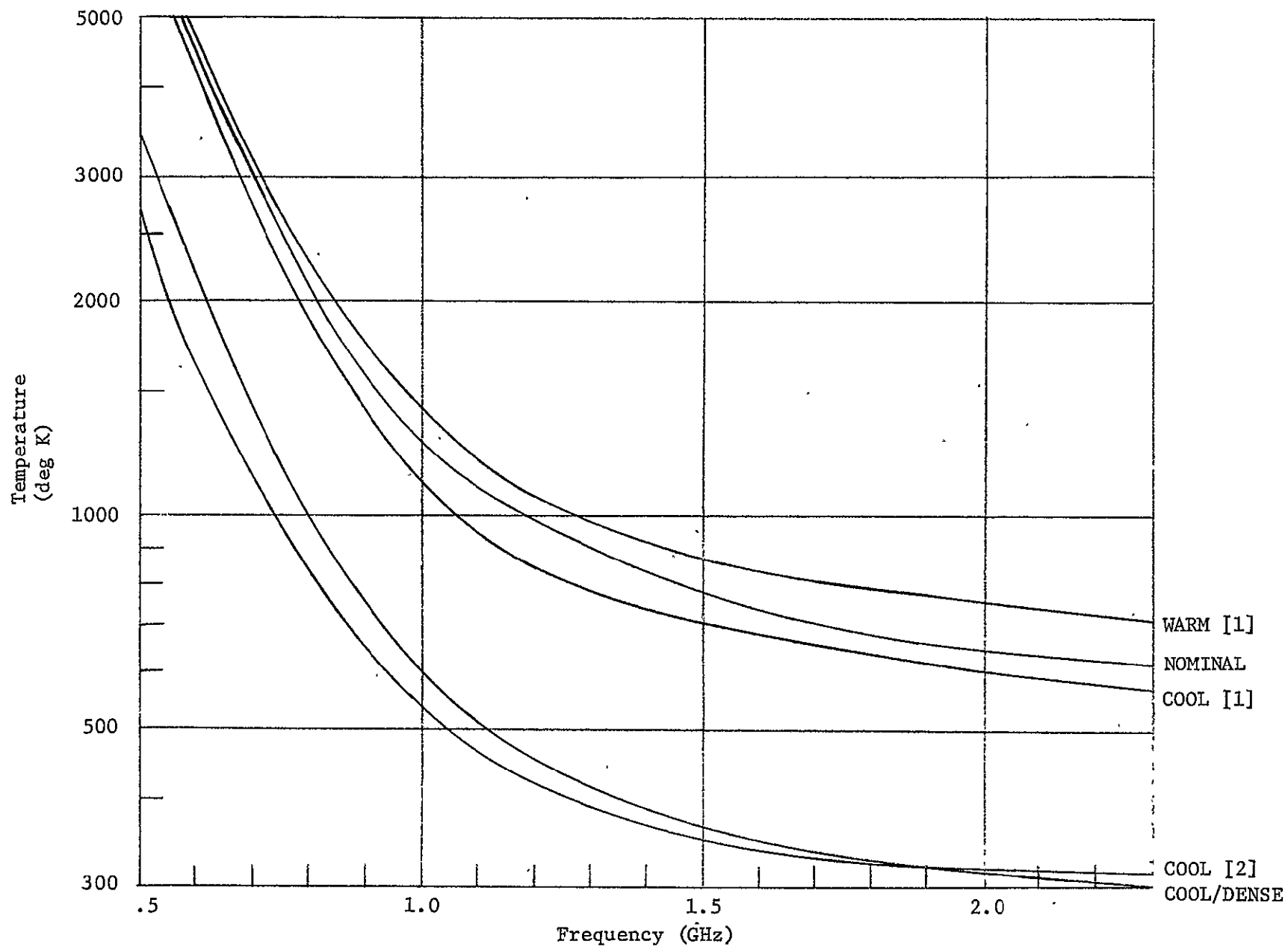


Figure IVK-17 Down-Looking Antenna Temperatures for Several Model Atmospheres at P = 50 atm

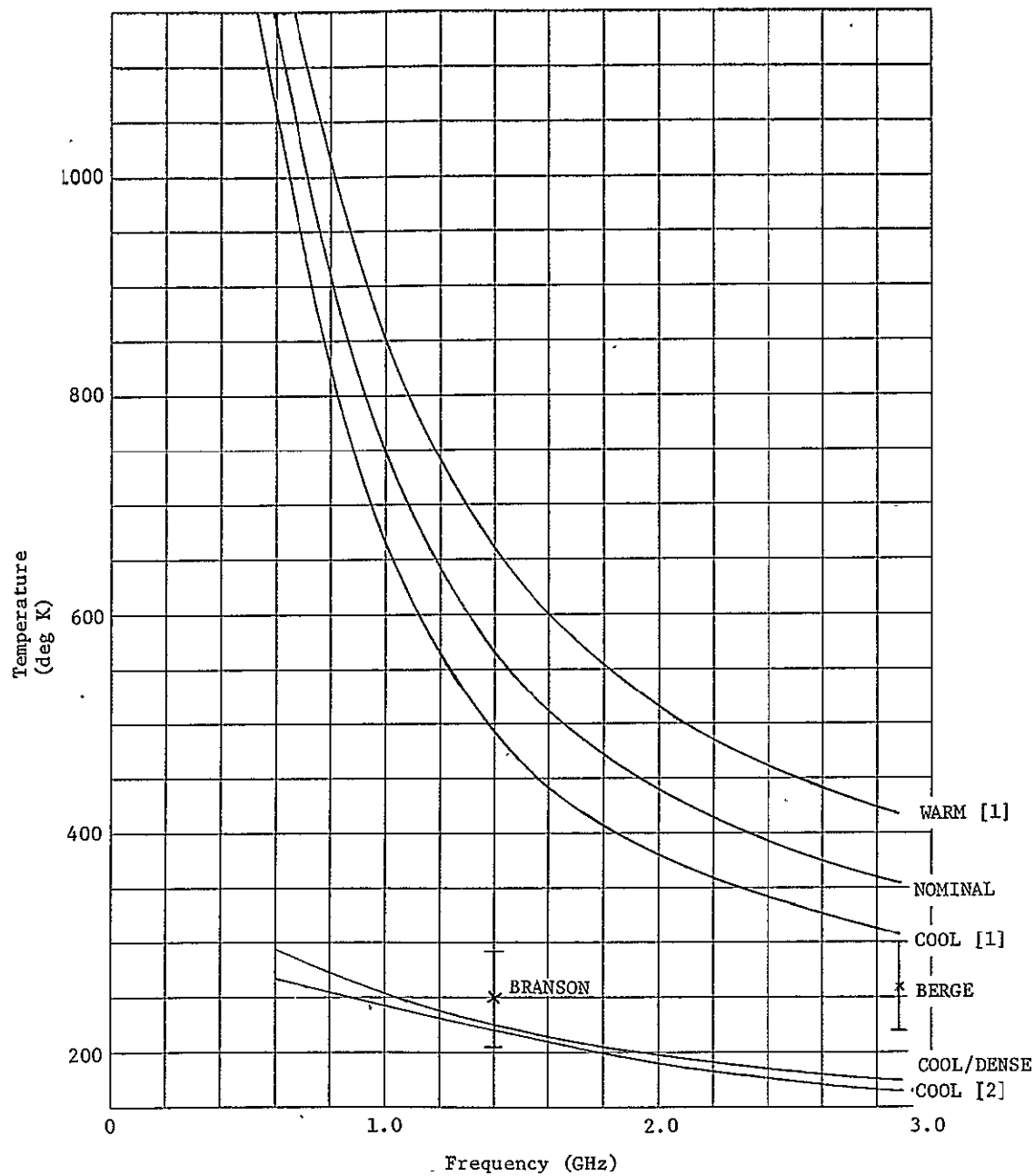


Figure IVK-18 Disc Temperature for Several Model Atmospheres

i. Uncertainties in the Computation of Absorption

The attached memoranda - Vandrey to Ducsay, consider several possible sources of error. The first memorandum considers two phenomena, departures of the gas from the ideal gas law and the likelihood of multiple collisions in the gas. The former is estimated to alter the computed results by not more than 10%, while the latter is found to be negligible. The effect of deuterated ammonia is considered in the second memorandum, and is also found to be negligible. The third memorandum considers conductivity due to ionization in the high-temperature environment at the 1000 atm level. He concludes that this effect would be just perceptible at 1400°K and quite significant at 1600°K or hotter. Since the nominal model just reaches 1400° at 1000 atm, this effect can be neglected in the nominal and the various cooler models but would have to be considered in the warmer models. However, it appears that these warmer models are less believable than the cooler models, so this effect can be assumed to be negligible.

There is some question about the accuracy of the constants used in computing the linewidths, e.g., the differences between Maryott [6] and Wrixon [7], cited earlier. This can only be resolved by further laboratory experiments. Since the values used are based on experimental data, modifications to these results by further experimentation should be small.

By far the biggest uncertainty is in the atmosphere models. For example, the spread in ammonia abundance between warm [2] and cool [2] is 5 to 1. This, together with uncertainties in the temperature-pressure profiles, completely overwhelms any uncertainties in the computation method.

j. Fading due to Turbulence

In view of the uncertainties in any turbulence model for Jupiter, only order-of-magnitude estimates can be made for turbulence-induced fading. De Wolf [20] has studied effects on Venus, particularly the fading observed on the Venera flights. His investigations of fading on Jupiter are limited to some estimates for an occultation experiment, so are not directly applicable to our mission. From De Wolf, the important parameter for fading is

$$\sigma_{\epsilon}^2 = k^2 \epsilon^2 L_i L, \quad (\text{IVK-27})$$

where $[1 - \exp(-2\sigma_{\epsilon}^2)]$ is the portion of the signal power diverted into the fluctuating component,

k is the wave number, proportional to signal frequency

ϵ^2 is the variance in the refractivity N ,

L_i is the scale length of the turbulence,

and L is the path length.

For zenith propagation $L \cong$ the scale height.

Now if we compare these with the values encountered on Venus in the Venera flights, we find:

- k is about the same.
- ϵ is proportional to the eddy input energy, which is at least an order of magnitude lower throughout the Jupiter atmosphere than it is at Venera levels on Venus.
- L_i is hard to estimate, but it is weakly coupled to the shear velocities. These will be lower on Jupiter due to the lower input energy.
- L is about one order of magnitude greater on Jupiter.

Combining all of these factors gives an estimate of σ_{ϵ}^2 that is at least one order of magnitude less than that observed on the Venera flights. Since this observed fading was rather mild, with maximum fading depths of around 1 db, ($\sigma_{\epsilon} \cong .18$ at their frequency of 0.96 GHz), fading due to turbulence on Jupiter should be completely negligible. Again, this is primarily due to the very low input energy (solar plus internal) available to generate turbulence.

3. Effects Due to Refraction

a. Defocusing Loss

The technique used to compute defocusing loss is described in detail in [21]. It is summarized below.

First, the refractivity profile was computed, using

$$N'(z) = \frac{P(z)}{T(z)} (37180.A_{H_2} + 9550.A_{He}) \quad (IVK-28)$$

where the coefficients of A_{H_2} , A_{He} are matched to measured values at $P = 1$ atm and $T = 273^\circ K$. These are $N_{H_2} = 136.1$, $N_{He} = 35.0$, from the International Critical Tables.

$N'(z)$ is defined by $n = 1.0 + 10^{-6} N'(z)$, where n is the index of refraction. In subsequent formulae we use $N(z) = 10^{-6} N'(z)$.

The radius of curvature of a horizontal ray is computed from

$$r_c(z) = \frac{n T(z)}{N \left(\frac{gM}{R} + \frac{dT}{dz} \right)}, \quad \text{where} \quad (IVK-29)$$

g = planetary gravity

M = molecular wt of the atmosphere

R = universal gas constant.

The point at which r_c equals the planetary radius r is the trap radius, and is the maximum depth that can be penetrated by occultation. For $r_c < r$, horizontal rays will be turned into the planet and trapped

The N-profile is then approximated by an exponential,

$$N(z) = N(z_0) \exp \left[-\beta(z-z_0) \right], \quad (\text{IVK-30})$$

by selecting a β that best matched the profile starting from the selected z_0 . β^{-1} is the scale height.

For z_0 below the trap radius, the trap angle ϕ_t can be calculated from

$$\phi_t = \sqrt{2 \left[N_0 \left[1 - \exp(-\beta h_t) \right] - \frac{h_t}{r_s} \right]} \quad (\text{IVK-31})$$

where h_t , the trap height, is the distance below the trap radius, either inferred from the distance below the trap radius determined from (32) or calculated from

$$h_t = \frac{1}{\beta} \ln(N_0 r_s \beta). \quad (\text{IVK-32})$$

ϕ_t is the angle above horizontal at which superrefractivity occurs.

For $\phi > \phi_t$, ray bending (or pointing error) can be computed from the refraction integral. It will be more convenient to measure angles from zenith than from horizontal. Therefore, defining $\theta = 90 - \phi$, the ray launch angle measured from zenith, the pointing error $E(\theta)$ is given by

$$E(\theta) = N_0 n_0 \sin \theta \int_0^\infty \frac{e^{-x} dx}{(1 + N_0 e^{-x}) \sqrt{\left(1 + \frac{x}{\beta r_s}\right)^2 (1 + N_0 e^{-x})^2 - n_0^2 \sin^2 \theta}}$$

The defocusing loss is calculated from

$$L_d(\theta) = \frac{1}{1 + \frac{dE}{d\theta}} \quad (\text{IVK-33})$$

It is independent of frequency, but is a function of z_0 and θ .

It is more convenient to plot L_d vs $\psi = \theta + E(\theta)$, the angle at which the ray emerges from the atmosphere.

L_d is plotted vs ψ for various depths z_o for the nominal atmosphere in figure 10. Plots for warm [1] and cool [1] do not differ greatly from these. Cool [2] is shown in figure 11. This can also be used for cool/dense. Except for angles near horizontal, defocusing loss is small compared to the absorption loss. A plot of ϕ_t vs z is shown in figure 12 for the nominal atmosphere. $\phi_t = 0$ at the trap elevation z_t . Since this is only of incidental interest for this program, ϕ_t was not calculated for the other atmospheres.

b. Absorption vs ψ .

As discussed above, for small departures from zenith, attenuation due to atmospheric absorption $L_a(\theta)$ increases as $\sec \theta \approx \sec \psi$. For larger ψ , ray-bending effects must be considered. As shown in [21], $L_a(\theta)$ is bounded by

$$\begin{aligned} L_a(0) \sec \theta & \quad (\text{lower bound}) \\ L_a(0) \sec (\psi) & \quad (\text{upper bound}) \end{aligned} \quad (\text{IVK-34})$$

A value midway between these bounds gives adequate accuracy for $L_a(\theta)$. As with L_d , it is more useful to plot L_a as a function of ψ . This is done at $f = 2.3$ GHz for various depths z_o for the nominal atmosphere in figure 13. Again, this scales as f^2 . Plots for the cool [2] atmosphere are given in figure 14. These can be used for the cool/dense atmosphere and/or other frequencies by scaling the curves by the ratio of the zenith absorptions.

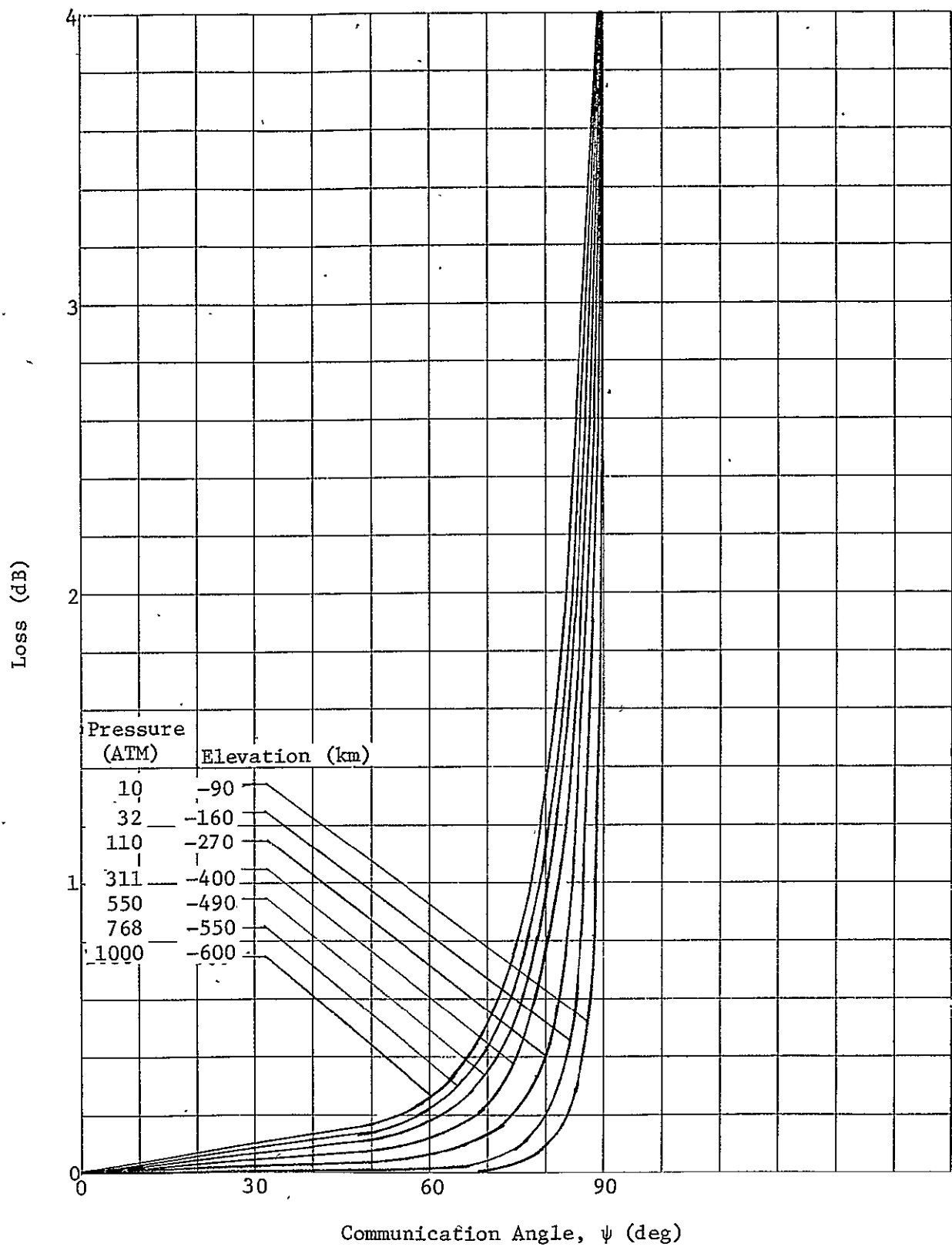


Figure IVK-10 Defocusing Loss, Nominal Atmosphere

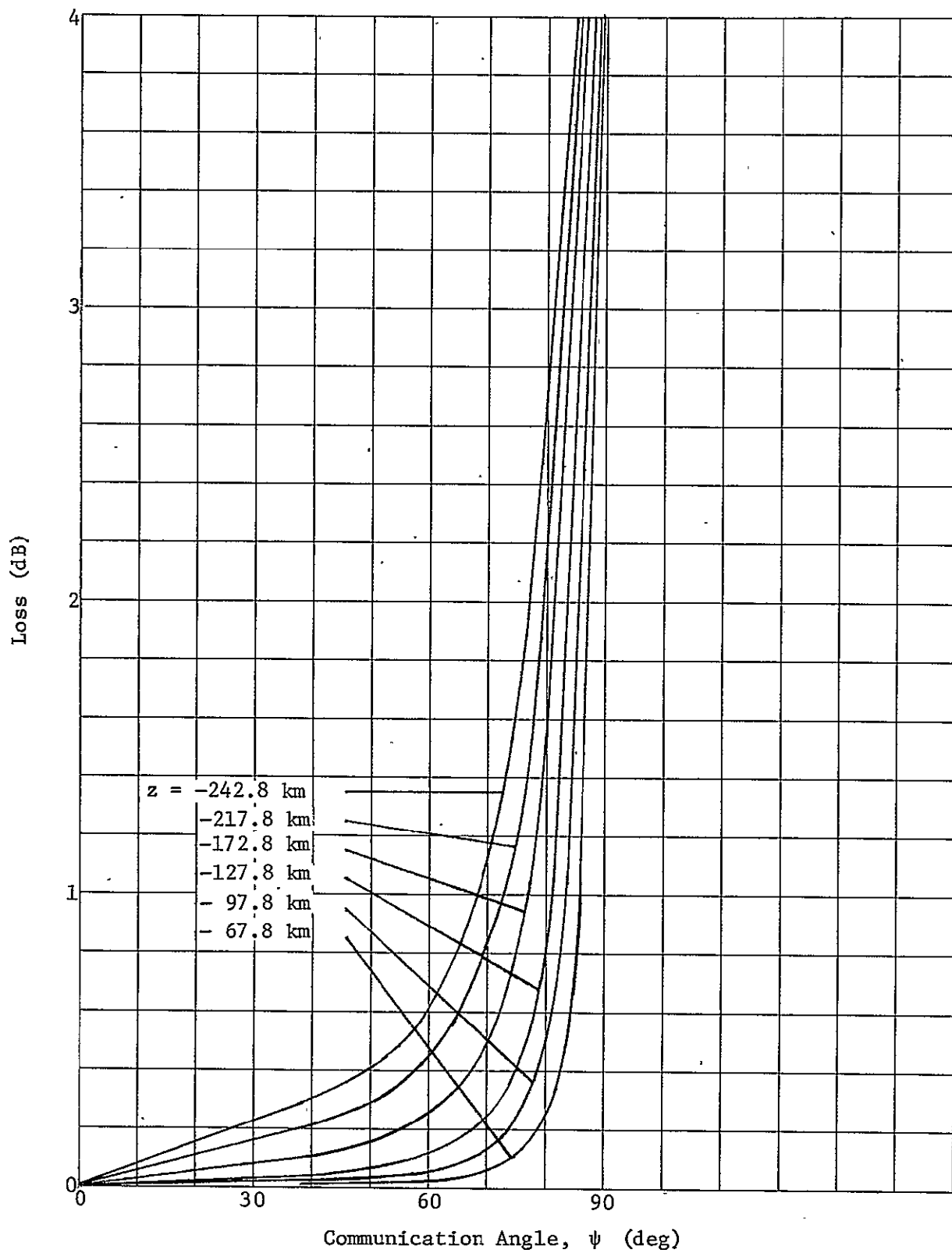


Figure IVK-11 Defocusing Loss vs Communication Angle, Cool [2]
and Cool/Dense Atmospheres

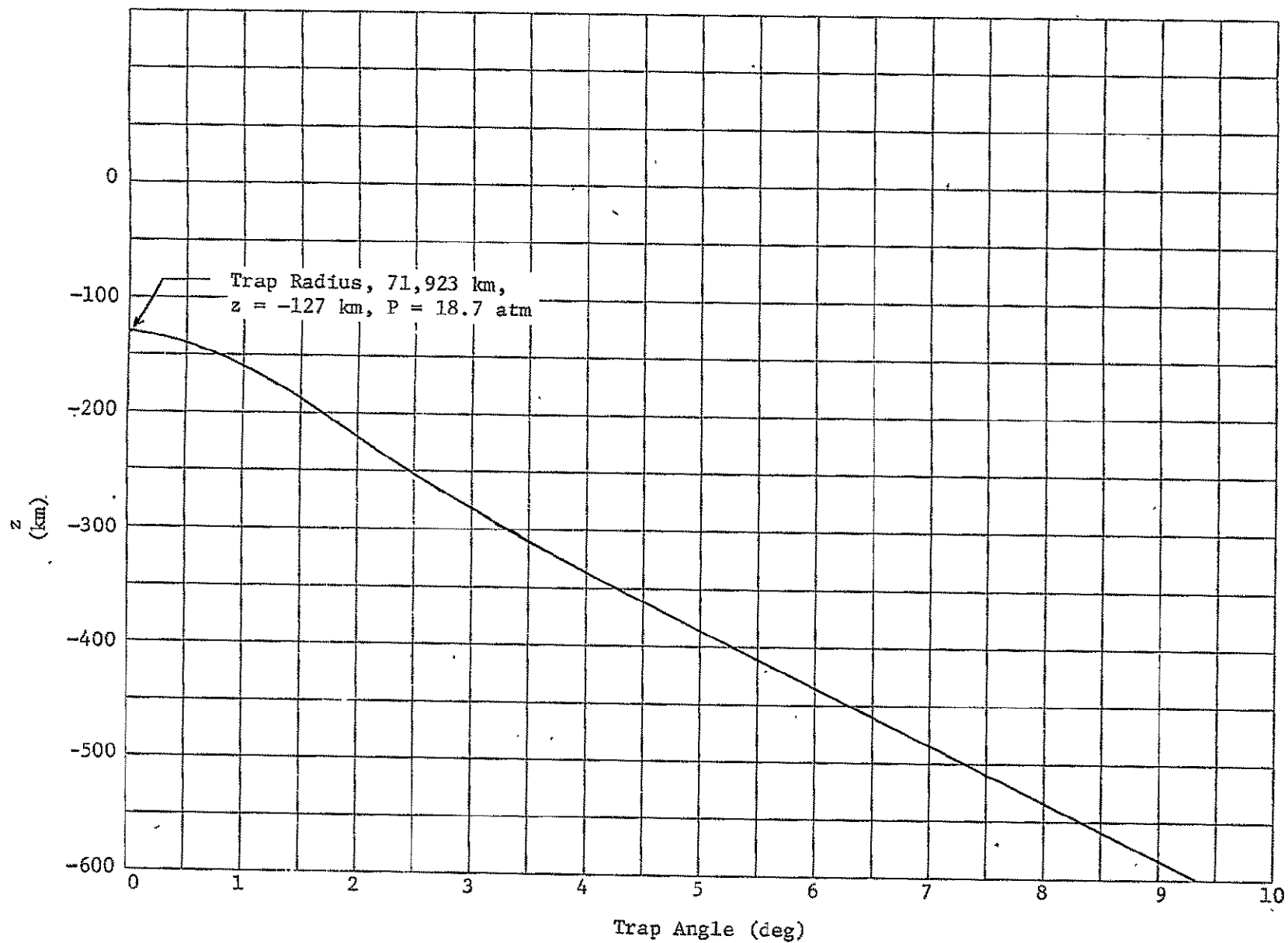


Figure IVK-12 Trap Angle vs Depth, Nominal Atmosphere

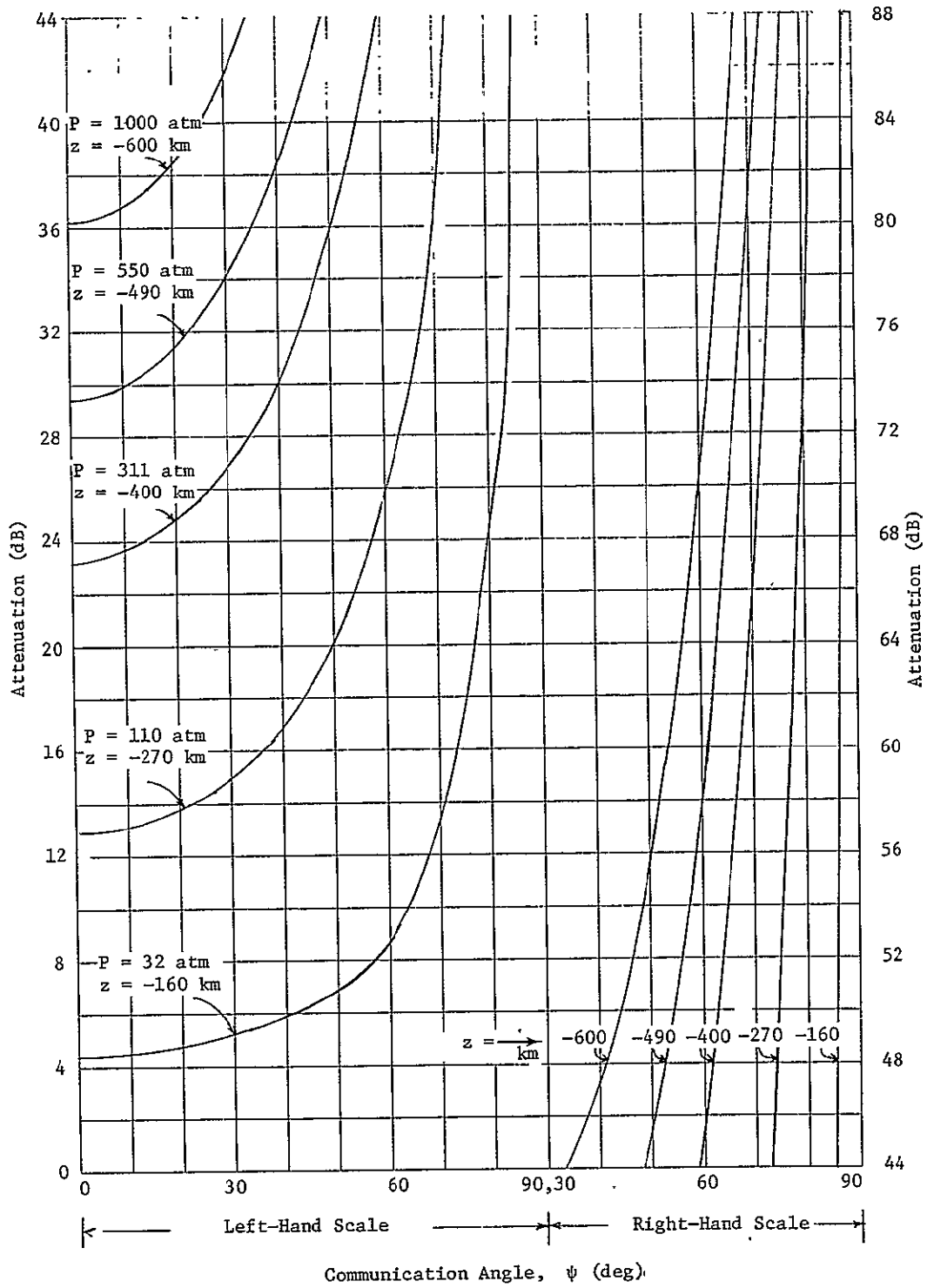


Figure IVK-13 Absorption Loss vs Communication Angle, Nominal Atmosphere, 2.3 GHz

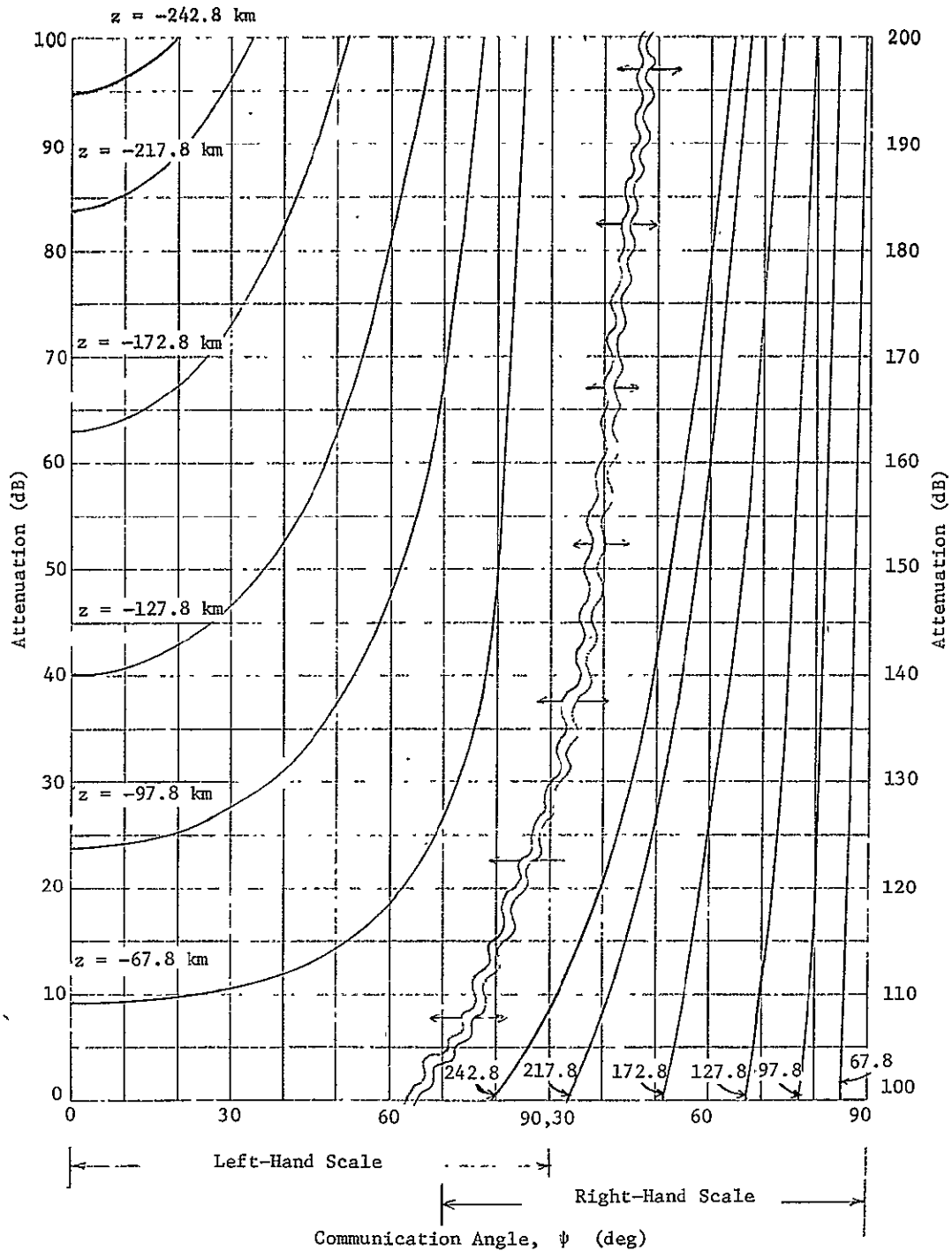


Figure IVK-14 Absorption Loss vs Communication Angle, 2.3 GHz, Cool [2]
Atmosphere

5. Microwave Radiometry

a. Introduction

The possibility that a down-looking microwave radiometer located on a Jupiter descent probe can provide some capability for remote sensing of the atmospheric temperature profile to depths greater than that penetrated by the probe was given a cursory examination. It was concluded that, while some information can be gained from this technique, ability to discriminate between several believable extrapolations of the temperature profile is very limited. The principal limitations are imposed by the directivity limitation on the radiometry antenna and by the very strong decimetric noise generated by the Jovian magnetosphere.

No attempt was made to determine if a given set of radiometry data could be inverted to reconstruct the atmosphere. Rather, a number of different extrapolations of the atmosphere below the observation point was made, and the resulting temperature vs. frequency plots were calculated to see if the radiometer could distinguish between these extrapolations. It is shown that single-frequency radiometry is highly ambiguous, and the additional data provided by swept or multiple frequency readings would be required to reconstruct the temperature profile below the probe.

Investigations were limited to an observation point at a pressure of 50 Atm ($z = -195$ km) in the nominal atmosphere. From this point downward, the nominal atmosphere has a lapse rate of 2.07 deg/km. Other extrapolations considered were;

- A break from 2.07 deg/km to isothermal, with the break located at various distances below the observation point,
- A break from 2.07 deg/km to 1.8 deg/km, with the break located at various distances below the observation point,
- An isothermal step 20 km thick in the 2.07 deg/km lapse rate, at various distances below the observation point, and
- A slow quadratic variation in lapse rate, going from 2.07 deg/km at the observation point to 1.8 deg/km at 1000 atm.

The last of these is the most believable, but it was found that the difference between it and the nominal could not be resolved by the radiometer. The difference between the nominal and the others could be detected for break points some distance below the observation point.

b. Radiometer Sensitivity

Assuming a perfect antenna, the sensitivity of a radiometer is given by [16]

$$\Delta T_{\min} = K(T_R + T_A) (B_{\text{HF}} \tau)^{-\frac{1}{2}}, \text{ where} \quad (\text{IVK-38})$$

T_R = Receiver noise temperature, deg K

T_A = Background temperature, deg K

B_{HF} = Predetection noise bandwidth, Hz

τ = Sample integration time, sec.

K = a constant to account for non-ideal performance.

$K = 1$ for an ideal device and a 1σ uncertainty. For practical systems and a 3σ uncertainty a value of around 10 is more reasonable. Reasonable values for the other variables for a simple system that might be put onto a probe are:

$$T_R = 1200^\circ\text{K},$$

$$B_{\text{HF}} = 10^6 \text{ Hz},$$

$$\tau = 1 \text{ sec}$$

$$\text{This gives } \Delta T_{\min} = 10^{-2} (T_A + 1200). \quad (\text{IVK-39})$$

It would probably be possible to improve somewhat on this performance, but as will be shown below, this is not the crucial limitation on system performance.

c. Antenna Directivity

An ideal radiometer antenna sees only in the direction in which it is pointed, and is not influenced by radiation from other directions. This is not true of real antennas whose directivity depends on a number of factors, one of which is size measured in wavelengths. A typical high-gain antenna not specifically designed for radiometry

or low-noise applications has an optical efficiency of around 50% i.e., when operated as a transmitter, only half of the radiated energy is confined to the 3 db beamwidth. Perhaps 10% of the energy goes into the back hemisphere. This implies that, when used as a receiver, the average temperature of the back hemisphere will appear at the antenna port reduced by a factor of 10. The 210 ft DSN antenna, which represents an extremely careful design, reduces its back-hemisphere temperature by a factor of around 20. A low-gain antenna such as those used on probes for wide-angle communication coverage could have a rejection factor for back-hemisphere radiation as low as 4.

Two antennas were considered in this study. The low-gain antenna on a 24" diameter circular ground plane, originally examined in the previous section in connection with the split-probe missions is one. The other is a medium gain wideband helix in a cone, sketched in Figure 19. The 19" x 22" size of this antenna was selected as the largest that could be reasonably placed on a descent probe. This fixes the low-frequency limit of 800 MHz on the antenna bandwidth. The rejection factor for back radiation was assumed to be 14 for this antenna. Computations were extended to cover frequencies down to 300 MHz in order to determine the value of a larger antenna.

d. The Effects of Magnetosphere Noise

The magnetosphere temperature averaged over the antenna back hemisphere is given by

$$T_{MR} = T_M(f) \int_0^{\pi/2} \exp(-\alpha \sec \phi) \sin \phi \, d\phi \quad (\text{IVK-40})$$

For the selected 50 atm observation point this ranges from 59°K at 2.3 GHz to 6090°K at 0.8 GHz, rising to 131,000°K at 0.3 GHz. This is of course reduced by the antenna directivity factor mentioned earlier.

These very high temperatures would not present a serious problem if $T_M(f)$ were accurately known and remained absolutely constant in time, since in principal it would be possible to subtract them out of the recorded temperature. This would also require accurate knowledge of the absorption coefficient $\alpha(f)$, the radiation pattern of

Frequency, MHz	800	2400
Beamwidth, deg	40	22
Gain, dB	12	17
Sidelobes, dB	<-20	<-23
Weight, 7 lb		

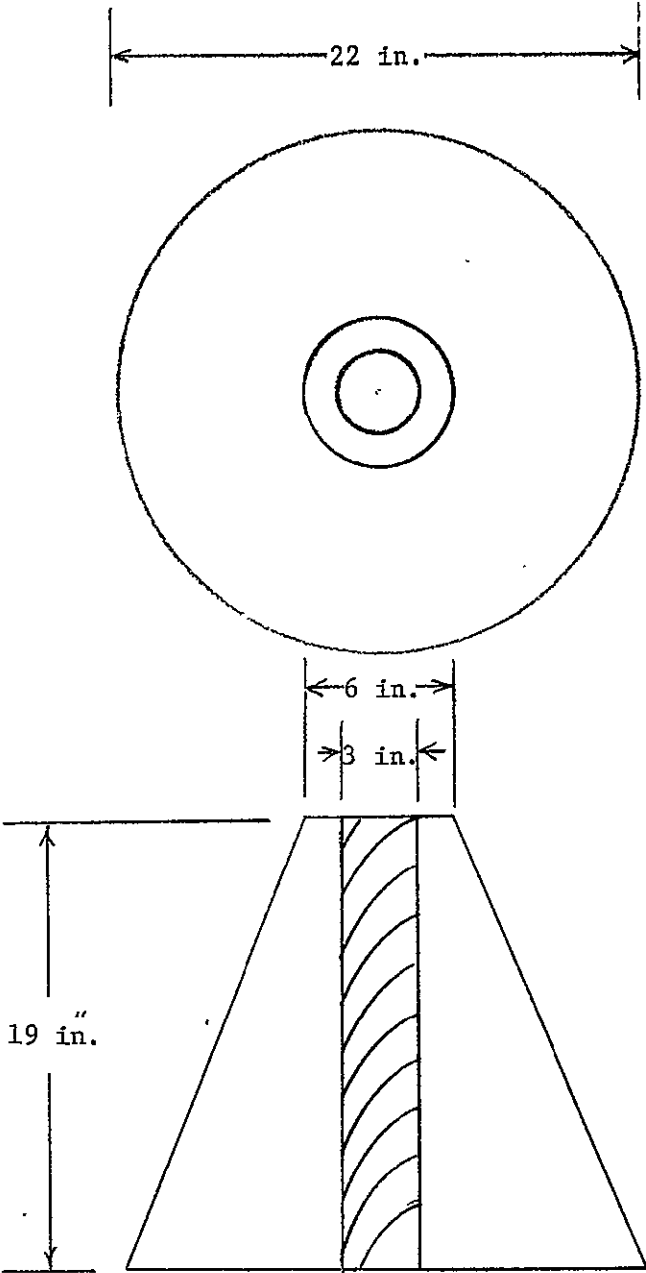


Figure IVK-19, Quad-Filar Helix in a Cone

the radiometer antenna, and swings in vehicle attitude. The phenomena itself is believed to be somewhat variable with time, estimated to vary by as much as 10%* over the period of a mission, about 1 hour. It might be possible to calibrate this out by using a second radiometer with an up-looking antenna. This would be highly sensitive to swings in vehicle attitude. Accordingly, we have assumed a $3-\sigma$ uncertainty due to T_M of 10% of its contribution to the antenna temperature. The RMS sum of this and the instrumentation uncertainty given by (39) is taken as the $3-\sigma$ resolution of the radiometer.

e. Results

Figure 20 shows the temperature vs frequency curves for the nominal atmosphere at the 50 atm observation point, computed for the three antennas, ideal, low-gain, and medium gain. The large departure of the other curves from the ideal in the lower frequencies is due to the magnetosphere temperature contribution.

The balance of the curves were generated using the various modified atmospheres described in the introduction. In each case the temperature difference between the modified and the nominal is shown. The frequency range 0.3 to 2.3 GHz is covered. As noted earlier, the medium gain antenna sketched in Figure 19 does not operate below 0.8 GHz. System temperature resolution is also plotted on these figures.

Figures 21, 22, and 23 cover the isothermal atmospheres, with the break from 2.07 deg/km to isothermal set at various depths below the observation point. Figure 21 shows results for the ideal antenna. Since it rejects all the back-hemisphere noise, resolution is that due to the instrument alone. Note that the spread between resolution and observed temperature difference increases with decreasing frequency. Any curve segment going below the resolution curve is resolvable by the system. The break at 1000 atm, for example, is resolved for any frequency below 1.1 GHz. Figure 22 shows results for the medium-gain antenna. The sharp rolloff of the resolution curve for lower frequencies is caused by the magnetosphere noise coming in from the back hemisphere. The best frequency is the

*Neil Divine, personal communication

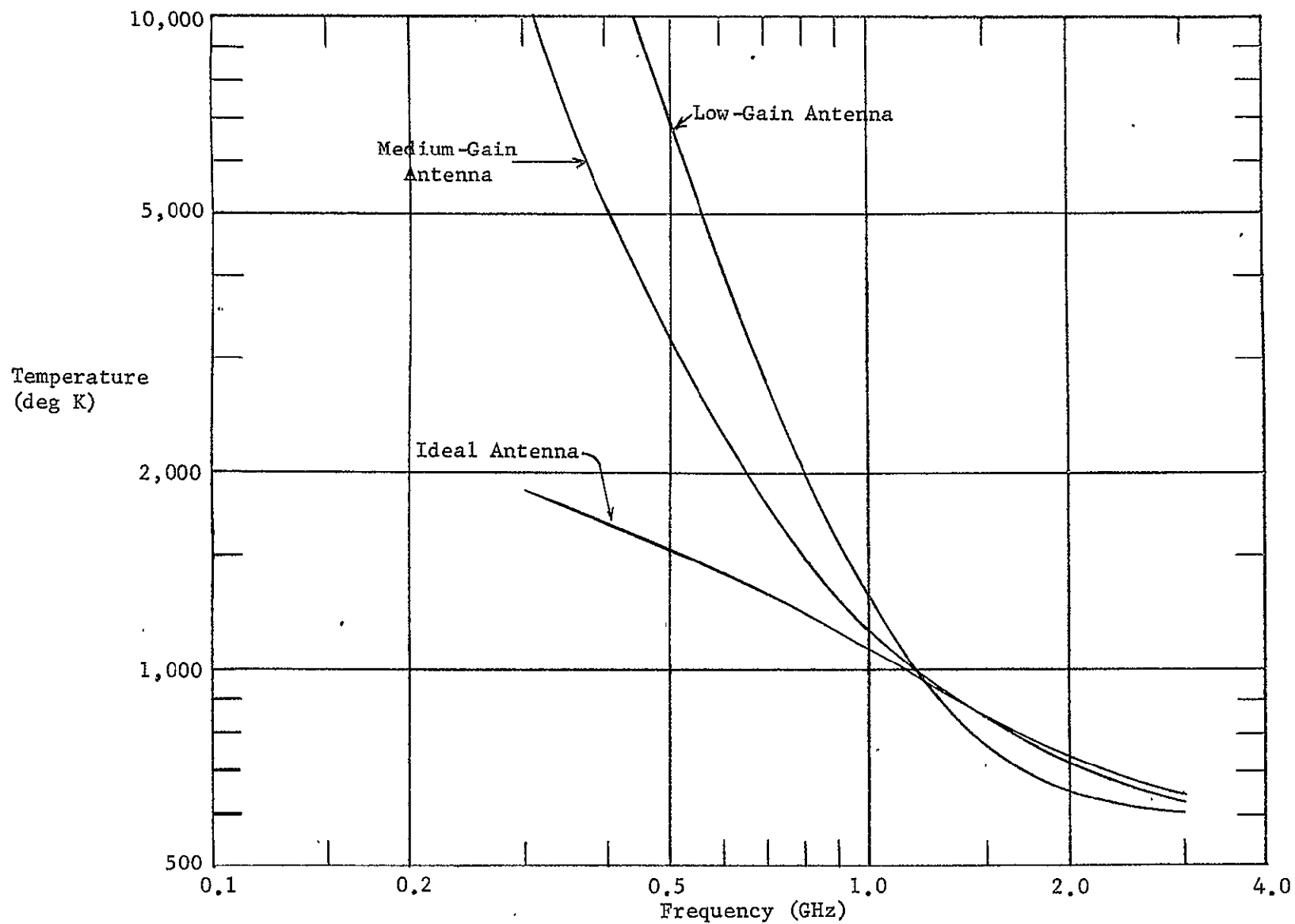


Figure IVK-20 Down-Looking Radiometer Temperatures for Several Antennas,
Nominal Atmosphere, Observation Point at P = 50 atm.

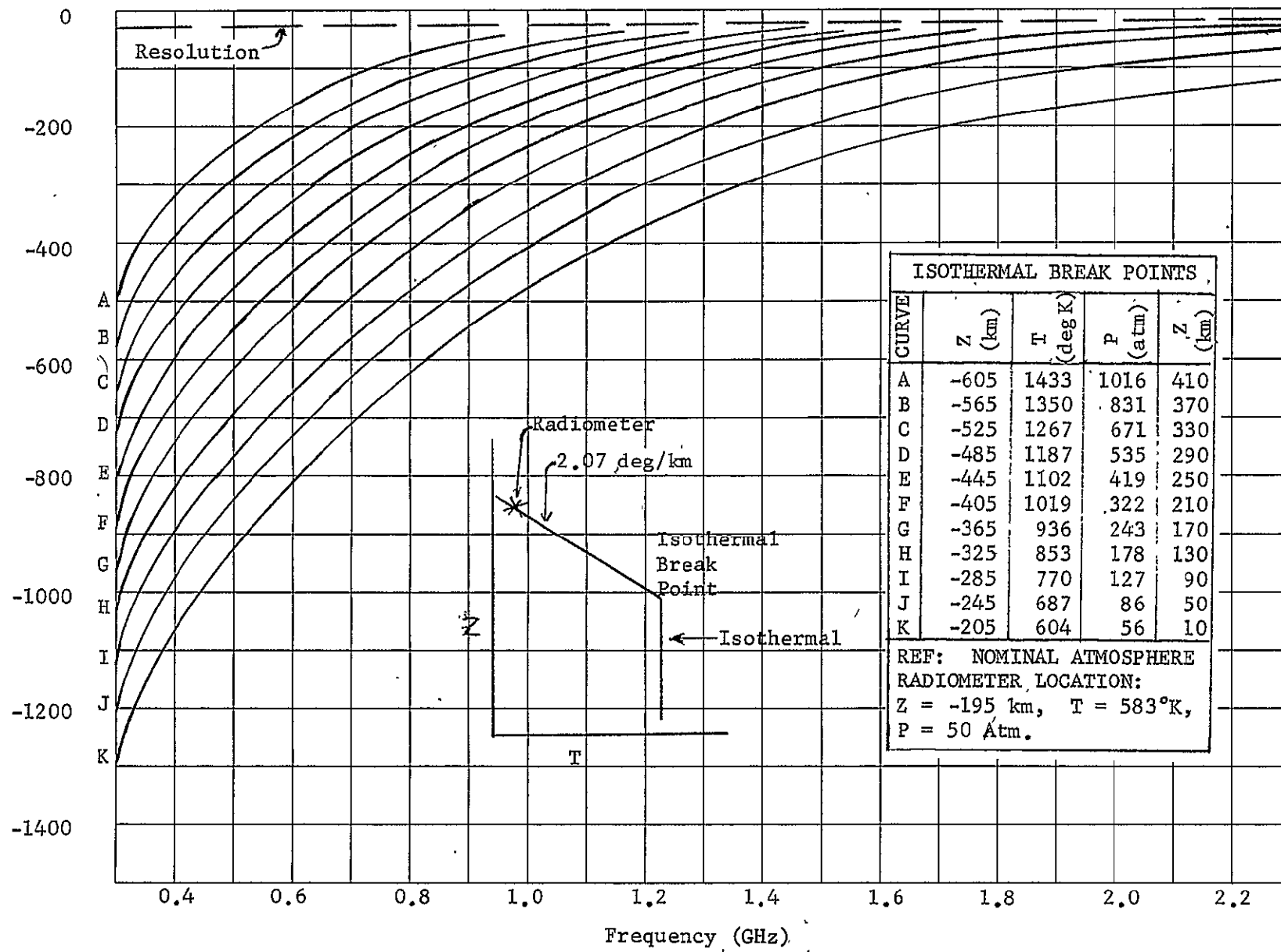


Figure IVK-21 Down-Looking Radiometer Temperature Differences for Several Isothermal Model Atmospheres, Ideal Antenna

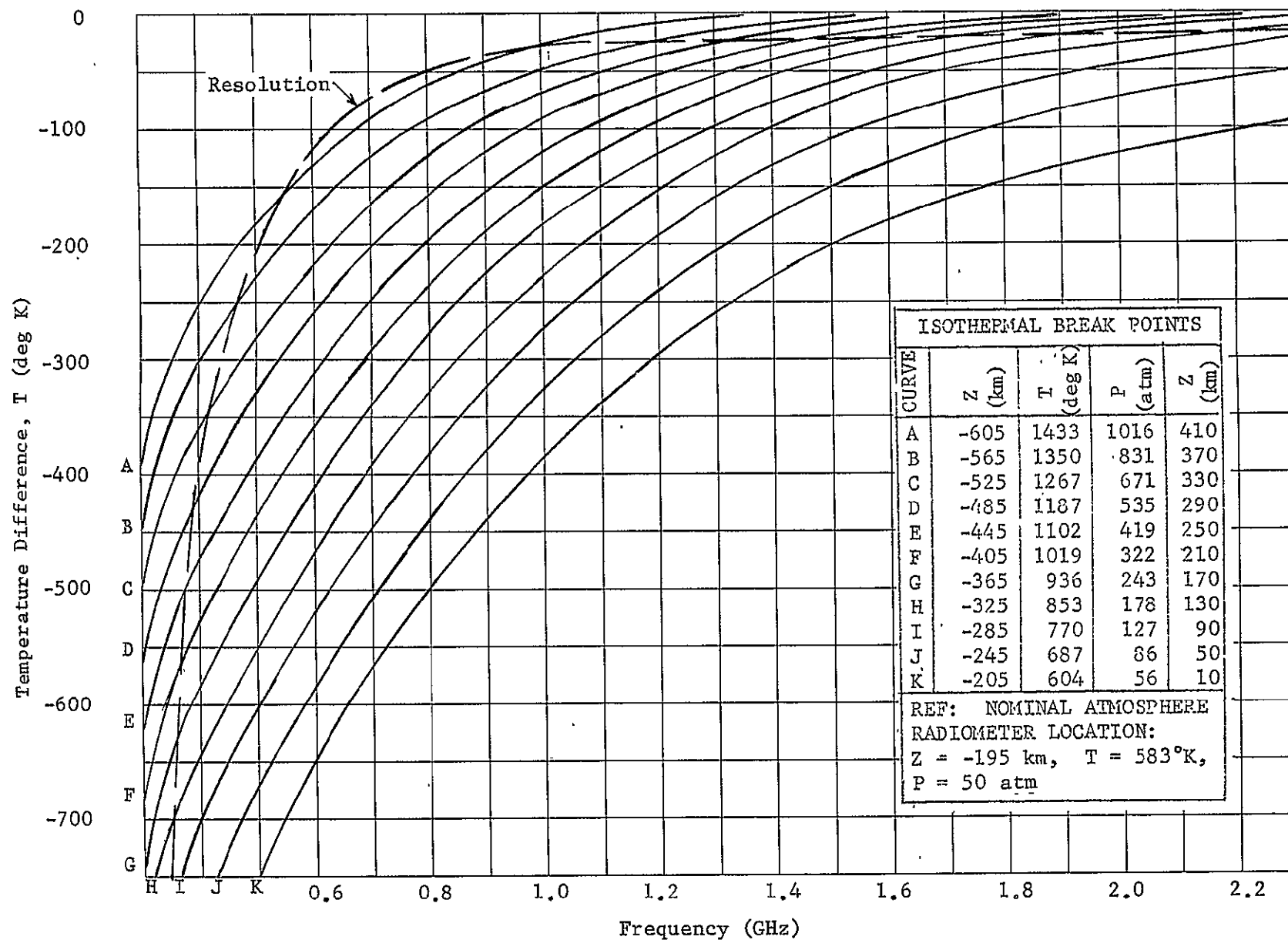


Figure IVK-22 Down-Looking Radiometer Temperature Differences for Several Isothermal Model Atmospheres, Medium-Gain Antenna.

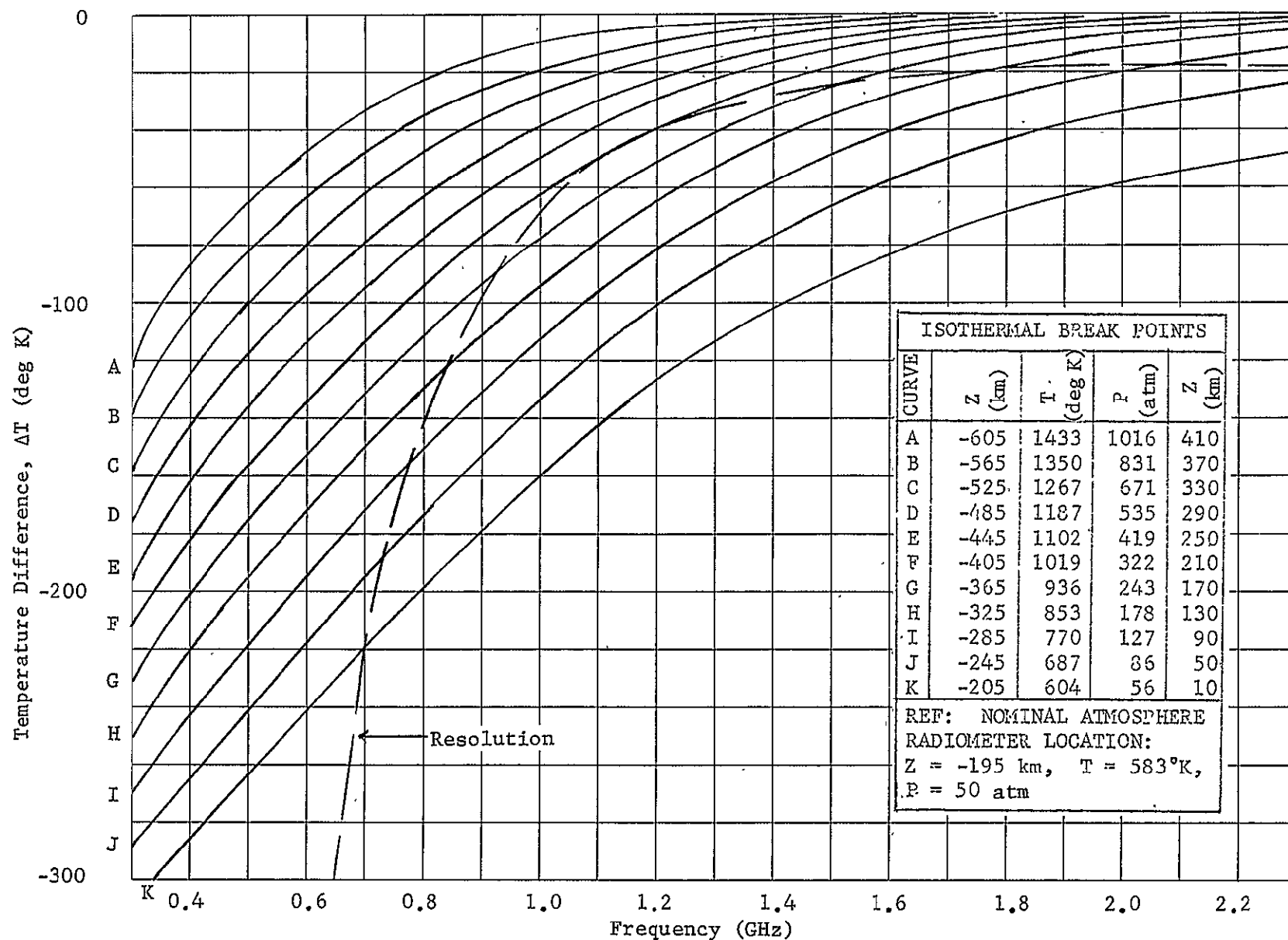


Figure IVK-23 Down-Looking Radiometer Temperature Differences for Several Isothermal Model Atmospheres, Low-Gain Antenna.

region where the 1000 atm break point curve drops below the resolution curve, $0.55 < f < 0.85$ GHz, where this curve is just resolved. Figure 23 shows results for the low-gain antenna. Its best frequency is around 1.1 GHz, where it just resolves curve F, the 322 atm break point curve.

The second class of extrapolation places a break in the lapse rate from 2.07 deg/km to 1.8 deg/km at various distances below the observation point. As shown in Figure 24, the medium-gain system just resolves the atmosphere having a break at 171 atm, at a frequency of 1.05 GHz. It was found that the low gain antenna could not resolve any of these curves, not even curve G, which breaks right at the observation point.

The next model atmosphere has an isothermal step 20 km thick at various depths below the observation point, with a 2.07 deg/km lapse rate above and below this step. As shown in Figure 25, the medium-gain antenna just resolves the break at 138 atmospheres, at a frequency around 1.1 GHz.

Finally, a slow quadratic rolloff in lapse rate from 2.07 deg/km at the probe to 1.8 deg/km at 1000 atm was investigated. This is also shown in Figure 25. It is not resolvable by the medium-gain antenna. The low-gain antenna could not resolve any of the atmospheres shown on Figure 25.

f. Conclusions

While this examination of radiometry was not exhaustive, some general conclusions can be made. First, a low-gain antenna is not effective, and a medium gain antenna having the best possible back hemisphere rejection should be used, consistent with mechanical constraints such as size and weight. Second, it is clear that swept or multiple frequency measurements are required, since any of an infinite number of atmospheres could give the same temperature at one frequency. The different shapes of the curves in Figure 22, 24, and 25 indicate some capability to sort out different atmospheres with swept-frequency measurements. Third, under the assumed conditions (nominal atmosphere, probe at 50 atm), the

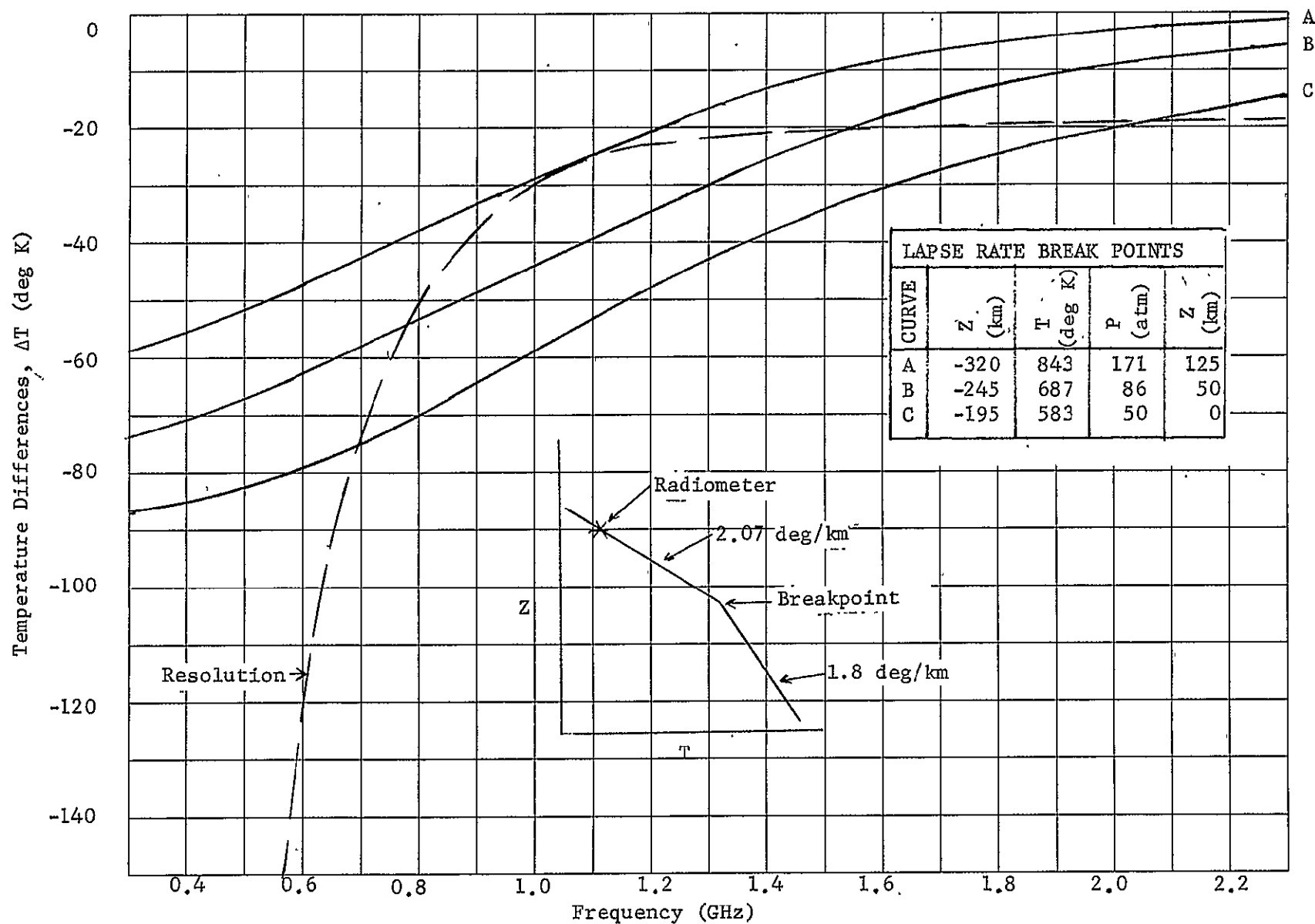


Figure IVK-24 Down-Looking Radiometer Temperature Differences for Several Multiple Lapse-Rate Atmospheres, Medium Gain Antenna

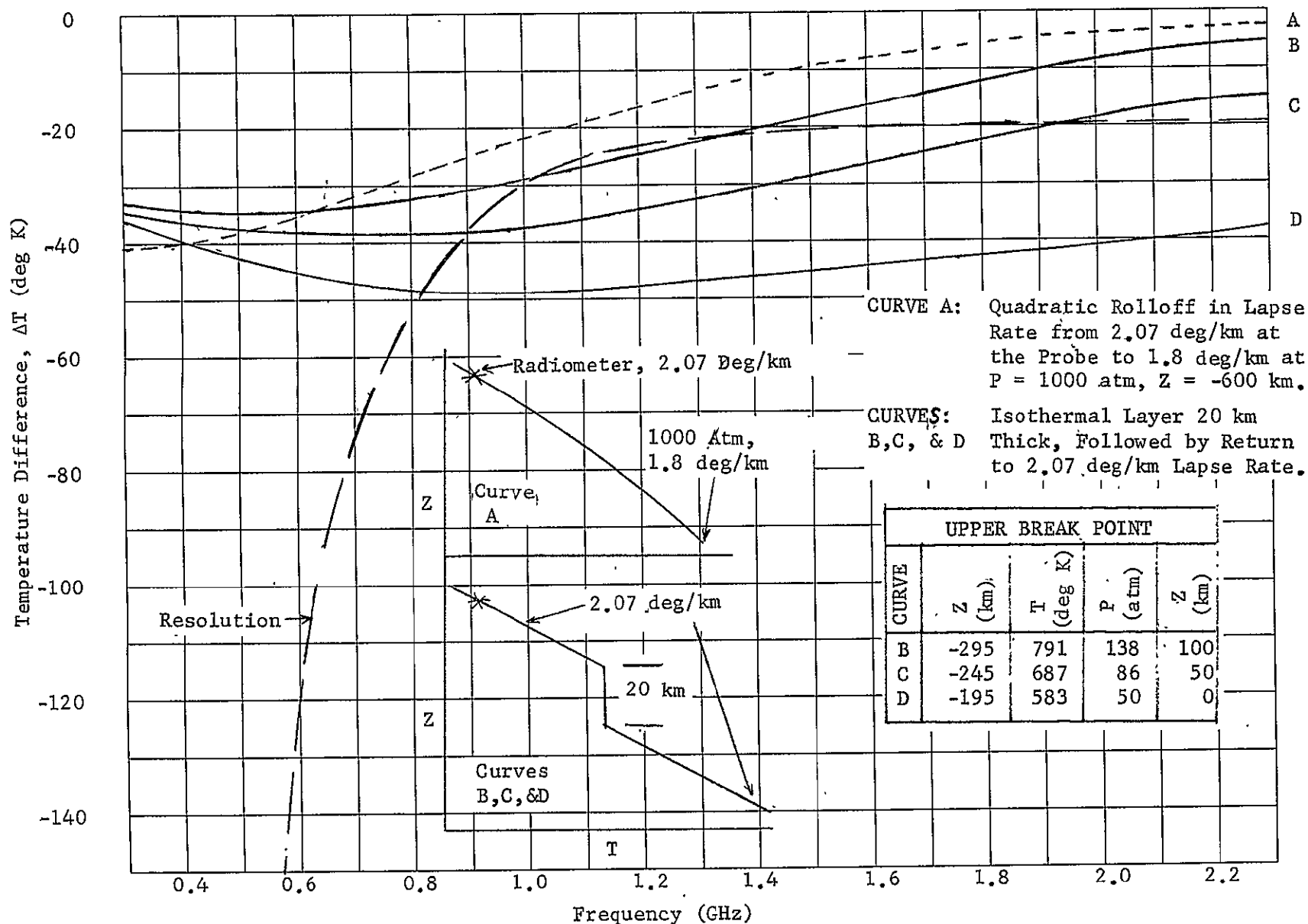


Figure IVK-25

Down-Looking Radiometer Temperature Differences for Several Model Atmospheres, Medium Gain Antenna.

0.8 GHz minimum frequency for the medium gain antenna is adequate, since system resolution is best around 1 GHz for most of these models. Fourth, under the assumed conditions only fairly drastic changes in the lapse rate can be recognized by radiometry. Gradual (and more believable) changes such as the slow quadratic rolloff shown in Figure 25 cannot be resolved.

Some of these conclusions would be altered by changing the assumed conditions. For example, if the observation point were in the cool [2] atmosphere, below the dense solution cloud, this cloud would shield out a substantial part of the magnetosphere noise and resolution would be substantially improved, particularly at the lower frequencies.

In summary, microwave radiometry will give some limited capability for remote sensing of the temperature profile below the probe. It appears that this capability is too limited to warrant inclusion of the large antenna required by the radiometer.

References, Section IVK

- 1 JPL Section Document 131-10 "Preliminary Model Atmospheres for Jupiter, Dec 31, 1976.
- 2 JPL Interoffice Memo, 2947-617, Divine to Long, 8 May 1970
- 3 Lewis, J. S., "The Clouds of Jupiter and the $\text{NH}_3\text{-H}_2\text{O}$ and $\text{NH}_3\text{-H}_2\text{S}$ Systems", Icarus, May 1969.
- 4 Van Vleck, J. H., "The Absorption of Microwaves by Uncondensed Water Vapor", Phys. Rev., 71, P 425-433, April 1947.
- 5 Ben-Reuven, A., Phys. Rev., 145, p 7 (1966).
- 6 Maryott, A. A., personal communication, copy attached.
- 7 Wrixon, G. T., "Microwave Absorption in the Jovian Atmosphere", Tech Report on ONR Contract NONR 222(54), May 25, 1969, U of Calif, Berkeley.
- 8 Bean, B. R., et al, "Weather Effects on Radar", Ch 24 in "Radar Handbook", (M. Skolnik, Ed.), McGraw-Hill, 1970.
- 9 Gallet, Roger, personal communication.
- 10 Condon and Odeshaw, Eds., "Handbook of Physics", McGraw-Hill, 1959, ch 9.
- 11 CRC Handbook of Chemistry and Physics, 46th Editions, pg. E-49.
- 12 Yakovlev, et al, "Propagation of Ultra-Short Waves in the Atmosphere of Venus" English translation, NASA document N69-24128, 5 May 1968.
- 13 Copla, J. P., and J. A. Ketelear, "The Pressure-Induced Rotational Absorption Spectrum of Hydrogen, Part I", Molecular Physics 1, 14-22, 1958.
- 14 Hunten, D. M., "The Upper Atmosphere of Jupiter", Jour. Atm. Sciences, 26-5 Pt 1, p. 831, -3, Sept 1969.
- 15 Hogan, J. S., S. I. Rasool, T. Encrenaz, "The Thermal Structure of the Jovian Atmosphere", Journal of the Atmosphere Sciences, Sept, 1969.
- 16 King, D. D., "Passive Detection", Ch 39 in "Radar Handbook" (M. Skolnik, Ed.) McGraw-Hill, 1970 p 39-5.
- 17 NASA SP-3031 "Handbook of the Physical Properties of the Planet Jupiter." 1967.
- 18 Berge, G. L., "Interferometry of Jupiter in the Decimeter Range". Proc. Cal Tech - JPL Lunar & Planetary Conf., Sept 1965.

References - Continued

- 19 Branson, N. J. B. A.: "High Resolution Radio Observations of the Planet Jupiter." *Mon. Notic. Roy. Astron. Soc.* 139, pp 155-162, 1968.
- 20 De Wolf, D. A., and J. W. Davenport, "Investigation of Line-of-Sight Propagation in Dense Atmospheres: Phase 1 Final Report". NASA CR-73440, May, 1970.
- 21 Final Report, Contract JPL 952534, "1975 Venus Multiprobe Mission Study" April 1970. Chapter VII-A.

M E M O R A N D U M

12 August 1970

To: S. J. Ducsai
From: R. J. Richardson
Subject: Microwave Absorption in the Jovian Atmosphere

This will advise you of some recent outside contacts that I have made to gain more information on microwave absorption due to ammonia and water vapor.

I first contacted James Gallagher of Martin-Orlando. He has been working in microwave spectroscopy. He suggested two prominent workers in the field, A. A. Maryott of NBS - Washington and Lothar Frenkel of DOT - Cambridge. I contacted both of them by telephone. The contact with Frenkel did not provide much information since he is no longer working in this area. However, Dr. Maryott was very interested in our problem and said he would look into it. I received the attached correspondence from him about a week after our conversation. The data contained therein should permit us to compute the absorption due to ammonia vapor for any model atmosphere with adequate accuracy.

I also contacted Roger Gallet of ESSA-Boulder. Dr. Gallet has been studying the Jovian atmosphere and is the author of the model shown on p 99 of NASA SP-3031, "Handbook of the Physical Properties of the Planet Jupiter". The principal item discussed was microwave absorption due to water vapor. It was concluded that the best approach is to simply extrapolate the data that has been collected for water vapor on Earth using conventional relationships for absorption as a function of pressure, temperature, and water vapor abundance. Since absorption due to water vapor is only a small fraction of the total absorption, and errors due to this approach should be negligible.

R. J. Richardson
R. J. Richardson

RJR/dcm

Attachment 1

A. A. Maryott

August 7, 1970

On the NH_3 Microwave Absorption by the Atmosphere of Jupiter.

The microwave absorption of NH_3 may be conveniently separated into two parts

(a) the inversion spectrum consisting of many closely spaced lines centered in the 25 GHz region and

(b) the ordinary rotational spectrum with the first line at about $20 \text{ cm}^{-1} = 600 \text{ GHz}$

$$(\nu_{J+1,J} = 2BJ \text{ where } B = 9.94 \text{ cm}^{-1})$$

In general these two contributions to the microwave absorption will have quite different dependencies on temperature, pressure, and frequency.

(a) Inversion contribution.

$$\epsilon''_{\text{inv}} = \frac{2 \pi N_0 \langle \mu^2_{JK} \rangle F(\nu)}{3kT} = \text{dielectric loss index} \quad (1)$$

where

N_0 = molecular density of NH_3 (molecules per cm^3)

$$\begin{aligned} \langle \mu^2_{JK} \rangle &= \sum_{JK} f_{JK} K^2 \mu^2 / J(J+1) = 0.40 \mu^2 \quad (\mu = 1.47 \times 10^{-18} \text{ esu}) \\ &= \text{mean squared dipole moment matrix element for inversion} \end{aligned}$$

$F(\nu)$ = frequency or line shape factor. This is given by Ben-Reuven, Phys. Rev. 145, 7 (1966); also see Maryott and Kryder, J. Chem. Phys. 46, 2856 (1967).

At high pressures $F(\nu)$ is approximated adequately by the Debye shape factor, i.e., $F(\nu) = 2\nu \Delta\nu / (\nu^2 + \Delta\nu^2) \approx 2\nu / \Delta\nu$ (since $\Delta\nu \gg \nu$)

Then eq. (1) may be expressed by

$$\epsilon''_{\text{inv}} (\text{hi press}) = 1.42 \times 10^{-6} [300/T]^2 (p_{\text{NH}_3})^2 \nu / \Delta\nu \quad (2)$$

where ν is the applied frequency and $\Delta\nu$ is the line width, or relaxation rate.

In eq. (2) the pressure p is in Torr.

Calculations based on the following atmospheric conditions:

Pressure - $p = p_{H_2} + p_{He} = 1000 \text{ atmos}$

Temperature - $T = 1400^\circ K$

Ammonia - $p_{NH_3} / p = 0.00015$

$p_{NH_3} = 0.15 \text{ atmos}$

Frequency - 2.3 GHz

Assume that $\Delta \nu$ is proportional to the partial pressures of the component gases (probably a very crude assumption at these pressures) so that

$$\Delta \nu = k_{NH_3-NH_3} p_{NH_3} + k_{NH_3-H_2} p_{H_2} + k_{NH_3-He} p_{He}$$

where

$$k_{NH_3-NH_3} = 6.0 \text{ MHz per Torr (from J. Chem. Phys. 46, 2856 (1967) data for } NH_3)$$

$$k_{NH_3-He} = 0.24 \text{ MHz per Torr (estimated from unpublished work on } ND_3\text{-He mixtures)}$$

$$k_{NH_3-H_2} = 1.0 \text{ MHz per Torr (estimated from unpublished work on } ND_3\text{-He mixtures)}$$

for a temperature of $300^\circ K$. Also assume that k_{NH_3-He} and $k_{NH_3-H_2}$ vary as

T^{-1} (consistent with data on other systems: Frenkel, Kryder, and Maryott, J. Chem. Phys. 44, 2610 (1966)).

If $p_{H_2} = 750 \text{ atm}$ and $p_{He} = 250 \text{ atm}$ and $p_{NH_3} = 0.15 \text{ atm}$,

$$\begin{aligned} \epsilon''_{inv} &= 2.16 \times 10^{-3} p_{NH_3} [300/T]^2 \nu / \left\{ [(k_{NH_3-H_2} - k_{NH_3-He}) (p_{H_2}/p) \right. \\ &\quad \left. + k_{NH_3-He}] p (300/T) \right\} \\ &= 2.16 \times 10^{-3} (p_{NH_3}/p) [300/T] (\nu / A) \end{aligned} \quad (3)$$

where p is the total pressure and $A = \Delta \nu / p = []$ in denominator above.

Then

$$\epsilon''_{inv} = 2.5 \times 10^{-7} \text{ with above conditions.}$$

To convert ϵ'' to db per km: $\alpha = 2 \pi \nu \epsilon'' / c$ $C =$ velocity of light
 $\alpha =$ absorption per cm
 $\gamma = 10^6 (\log_{10} e) \alpha =$ db per km

So $\alpha = 1.25 \times 10^{-7} \text{ cm}^{-1}$

and $\gamma_{\text{inv}} = 0.054 \text{ db per km}$

Note that in the high pressure limit the absorption is independent of pressure provided the ratio $p_{\text{NH}_3} / p_{\text{total}}$ remains fixed and $p_{\text{NH}_3} \ll p_{\text{total}}$. Also the absorption varies with temperature as T^{-1} , approximately.

(b) Rotational line contribution.

The contribution to the loss index from a given rotational transition, $J + 1$ J , is given by:

$$\epsilon''_{J+1, J} = \frac{2 \pi N_J |\mu_{J+1, J}|^2}{3kT} F(\nu, \nu_{J+1, J}) \quad (4)$$

and the total contribution is

$$\epsilon''_{\text{rot}}(\text{total}) = \sum_{J,K} \epsilon''_{J+1, J}$$

where N_J is number of molecules per cm^3 in the J (and K) rotational state and the dipole moment matrix element,

$$\mu_{J+1, J}^2 = (1 - K^2/J(J+1)) \mu^2$$

The line shape factor $F(\nu, \nu_{J+1, J})$ is given by Ben-Reuven's modification of the Van Vleck-Weisskopf factor. Summing over all lines and as a rough approximation

$$\epsilon''_{\text{rot}}(\text{total}) = 2 \times 1.62 \times 10^{-3} p_{\text{NH}_3} [300/T]^{5/2} [\nu / \nu_c^2] \Delta \nu' (300^\circ \text{K}) \quad (5)$$

where ν_c is the effective centroid frequency of the rotational band and

$\Delta \nu'$ is the effective line width. (Assumed that $\Delta \nu' \sim T^{-1/2} p$)

$$\Delta \nu' = k_{\text{NH}_3\text{-H}_2}' P_{\text{H}_2} + k_{\text{NH}_3\text{-He}}' P_{\text{He}}$$

Let

$$k_{\text{NH}_3\text{-H}_2}' = 3 \text{ MHz per Torr}, \quad k_{\text{NH}_3\text{-He}}' = 0.8 \text{ MHz per Torr, and}$$

$$\nu_c = 60 \text{ cm}^{-1} = 1800 \text{ GHz (very rough estimate).}$$

$$\Delta \nu' = 1850 \text{ GHz} \times (300/T)^{1/2} =$$

Thus

$$\begin{aligned} \epsilon''_{\text{rot}} &= 3.24 \times 10^{-3} P_{\text{NH}_3} [300/T]^{5/2} [2.3 \times 1.85 / 1800^2] P_{\text{total}} \quad (6) \\ &= 1.3 \times 10^{-8} \end{aligned}$$

and

$$\gamma_{\text{rot}} = 0.0027 \text{ db per km}$$

Note: Eqs. 5 and 6 are not strictly valid at the high pressure under consideration since they require $\Delta \nu' < \nu_c$ so that $F(\nu, \nu_{J+1, J}) \simeq \Delta \nu' \nu / \nu_c^2$.

Attachment 2, Section IVK

24 September 1970

To: S. J. Ducsal
 From: J. F. Vandrey
 Subject: Estimate of Compressibility Effects on NH_3 Microwave Attenuation in the Jovian Atmosphere.

Based on unpublished work of A. A. Maryott [1], the writer developed in a preceding memorandum [2] a simple working formula

$$\gamma = 12.5 \frac{\nu^2}{T} (1 + 1.15 \times 10^{-5} \rho^{-2})^{-1} \frac{\text{db}}{\text{km}} \quad (1)$$

for calculating the attenuation of microwaves by interaction with the inversion spectrum of ammonia in the nominal model [3] of the Jovian atmosphere. In (1), ν is the transmitter frequency in GHz, T the temperature of the atmosphere in $^{\circ}\text{K}$, and ρ its density in g cm^{-3} .

Naturally, a formula as simple as eq. (1) can only be obtained by disregarding a number of presumably less important effects in the complex interaction between the NH_3 molecules in the atmosphere and the electric field of the microwave beam under the influence of collisions with the much more numerous H_2 and He molecules around them. In the following, we shall take a closer look at these various simplifications of the problem, and we shall try to assess their effect on the result, as far as this can be done on the basis of our present knowledge of the underlying physical phenomena.

Taking eq. (1) at first as it stands, it is evident that the value of γ can be no better than the atmospheric model ([3], pp. 7 and 15) for which the formula was developed. In the here particularly interesting high pressure region, from about 100 atm and 714 $^{\circ}\text{K}$ at 258 km below the 1 atm reference level down to 1000 atm and 1425 $^{\circ}\text{K}$ at -600 km, one has already to expect some model errors from the fact that an atmosphere of essentially hydrogen (86.6% by number) and helium (13.2%) will already show some deviations in its equation of state from that of a perfect gas.

Writing the equation of state in the more realistic form

$$p = Z(p, T) \cdot \frac{R_0}{M} \rho T \quad (2)$$

one can estimate by extrapolation from published values of the compressibility factor Z for hydrogen and other gases (14, pp. 4 - 117 and 125) that one will have for

p = 100 atm	T ≈ 700°K	Z ≈ 1.027	(3)
300 atm	1000°K	1.07	
1000 atm	1400°K	1.2	

Assuming then that the pressure-temperature relation is still the same as in the original model, one would conclude that the density is up to 20% lower than its value in the model. This assumption is, of course, an unlikely one. More likely is that both T and ρ will be somewhat lower than in a thermally perfect atmosphere at the same pressure level, e.g. both about 10% less at 1000 atm. Numerically, we obtain then from (1) the value of $f = 9.4 \times 10^{-3} \text{ } \nu^2 \text{ db km}^{-1}$ or about 14% more than from the original model values. Most of this difference, by the way, originates from the lower value of the temperature, the density variation has a smaller influence. A maximum error of this magnitude appears to be acceptable in view of the uncertainties about the Jovian atmosphere in general.

A second source of errors in the model, and a potentially more serious one, is in its assumption of the value for the NH_3 concentration in the atmosphere, $p_{\text{NH}_3}/p_{\text{total}} = 1.5 \times 10^{-4}$. A small point is that p_{NH_3} may be somewhat less than this value at the high temperature of the 10^3 atm level, because of beginning dissociation. The general uncertainty about p_{NH_3} which varies between 0.7×10^{-4} and $3.5 \times 10^{-4} p_{\text{total}}$ in the three models of 3 affects the numerical factor 12.5 in (1) which is proportional to p_{NH_3} :

$$f = 12.5 \cdot \frac{p_{\text{NH}_3}/p_{\text{total}}}{1.5 \times 10^{-4}} = 8.33 \times 10^4 \frac{p_{\text{NH}_3}}{p_{\text{total}}} \quad (4)$$

for any model with around 87% H_2 and 13% H_e which contains a small amount of NH_3 . While this is not a compressibility effect, it is one of the major causes of uncertainty in all calculations of the NH_3 microwave attenuation.

We consider now the theoretical background of eq. (1), assuming that it is being used for an errorless atmospheric model of 87% H_2 and 13% H_e with an admixture of 1.5×10^{-4} to 1 of NH_3 molecules by number. Starting from the definition of γ by

$$\gamma = 10^6 \log_{10} e \frac{2\pi\nu}{c} \epsilon'' \text{ db km}^{-1} \quad (5)$$

where c is the velocity of light, and ϵ'' the dielectric loss index of the atmosphere, we see that any errors in estimating γ can only be those involved in ϵ'' . For this quantity, we have in turn

$$\epsilon'' = \frac{2\pi \langle \mu_{ij}^2 \rangle}{3kT} N_0 F(\nu, \nu_0, \Delta\nu) \quad (6)$$

where N_0 is the number of NH_3 molecules per cm^3 , $\langle \mu_{ij}^2 \rangle$ their mean squared dipole moment matrix element for inversion, k Boltzmann's constant, and

$$F = \nu \cdot \Delta\nu \left[\frac{1}{(\nu_0 - \nu)^2 + (\Delta\nu)^2} + \frac{1}{(\nu_0 + \nu)^2 + (\Delta\nu)^2} \right] \quad (7)$$

the frequency shape factor in a here sufficiently accurate form which depends on the natural frequency ν_0 for inversion, on the "line width" or relaxation rate $\Delta\nu$, and also on the applied frequency ν . (For a better form of \tilde{F} , esp. at low pressures, see Ben-Reuven, Phys. Rev. 145, 7, 1966).

In eqs. (6) and (7), $\langle \mu_{ij}^2 \rangle = 8.6 \times 10^{-37} \text{ cm}^5 \text{ g sec}^{-2}$ and $\nu_0 = 2.5 \times 10^{10} \text{ sec}^{-1}$ are characteristic properties of the NH_3 molecules, presumed here to be known with an adequate accuracy from experiments. Our assumption of a perfect atmospheric model implies also that we would know N_0 exactly. It is then evident that any errors in estimating γ can only

originate in errors of the line width parameter $\Delta\nu$, provided we use the form (7) for the shape factor.

Before discussing $\Delta\nu$, we remark that we can simplify (7) in our case to

$$F \approx \frac{2\nu \cdot \Delta\nu}{\nu_o^2 + (\Delta\nu)^2} \quad (8)$$

(which was actually used in (1)), since the typical transmitter frequency of around 2 GHz is an order of magnitude less than $\nu_o = 25$ GHz. One verifies easily by a development in powers of ν/ν_o that the resulting error is inconsequential for the present purpose.

Turning now to the discussion of $\Delta\nu$, we note that the low-pressure formula ([1], p. 2)

$$\Delta\nu = (k_{\text{NH}_3-\text{NH}_3, 300^\circ\text{P}_{\text{NH}_3}} + k_{\text{NH}_3-\text{H}_2, 300^\circ\text{P}_{\text{H}_2}} + k_{\text{NH}_3-\text{H}_e, 300^\circ\text{P}_{\text{H}_e}}) \frac{300^\circ\text{K}}{\text{T}}$$

in which the k 's are certain experimental constants, and P_{NH_3} etc. the partial pressures of the atmospheric component gases (P_{NH_3} is negligible and need not be taken into account) has its theoretical basis in the conventional assumptions of the kinetic theory of gases that only binary collisions are important, and that the duration of a collision is short in comparison with the flight times of the molecules between collisions, so that the individual collisions are still well separated. We will therefore have to check, as far as possible, how well these assumptions are still satisfied in the high-pressure environment.

First, however, we consider another aspect of eq. (9): Its form

$$\Delta\nu = K \cdot \frac{\text{P}}{\text{T}} \quad (10)$$

suggests that the pressures and the temperature are not the really significant physical parameters, but that it is rather the density on which $\Delta\nu$ really depends, so that one should write, omitting the small first term

$$\Delta\nu = (k_{\text{NH}_3-\text{H}_2, 300} \frac{\rho_{\text{H}_2}}{2} + k_{\text{NH}_3-\text{H}_e, 300} \frac{\rho_{\text{H}_e}}{4}) \cdot 300 \text{ R}_o \quad (11)$$

where R_o is the universal gas constant, and 2 and 4 are the molecular weights

of H_2 and H_e , resp. Instead of (11), one can also write

$$\Delta\nu = (k_{NH_3-H_2} \frac{P_{H_2}}{p} + k_{NH_3-H_e} \frac{P_{H_e}}{p}) \frac{300 R_o}{M} \rho \quad (12)$$

where p is the total pressure, M the average molecular weight, and ρ the density of the atmosphere.

This is, in fact, so. From the theory, $\Delta\nu$ comes out as proportional to the total collisional cross-section of the atmospheric gases per unit volume which will then be proportional to the density. Eqs. (11) and (12) show then that any density error in the atmospheric model will affect the value of $\Delta\nu$ with the same percentage. But this is of no concern for the present discussion for which we have assumed a knowledge of the atmosphere without errors. And it is of but little concern for the usefulness of eq. (1), since we have seen that the atmospheric compressibility errors will have only an acceptably small effect on the accuracy.

In fact, the compressibility error of N_o and $\Delta\nu$ will at least partially cancel out in the use of eq. (1), since we can write

$$\mu = 10^6 \log_{10} e \cdot \frac{8\pi^2 \nu^2 \langle \mu_{ij}^2 \rangle}{3 k T c} \cdot \left[\frac{N_o}{\Delta\nu} \right] \cdot \frac{1}{1 + \left(\frac{\nu_o}{\Delta\nu} \right)^2} \quad (13)$$

which makes it evident that the same percentage error in N_o and $\Delta\nu$ will effect only the ratio $(\nu_o / \Delta\nu)^2$ in the denominator which is, by the way, a small quantity at the higher pressures where $\Delta\nu$ becomes much greater than ν_o .

We check now the assumption for the validity of the formula (12) for $\Delta\nu$, that only binary collisions are important. A rough estimate of the frequency of triple collisions (two H_2 molecules hitting the same NH_3 molecule at practically the same time) may be made by considering all the molecules of the gas as elastic spheres with diameters which are not very different (see e.g. [5], pp. 674-75). One obtains then for the ratio of the frequency f_t (H_2, H_2, NH_3) of a triple collision to the frequency f_b (H_2, NH_3) of binary collisions.

$$\frac{f_t}{f_b} = 2 \cdot (1-X) \sqrt{\frac{2m_1 + m_2}{2(m_1 + m_2)}} \cdot \frac{7}{24,600} \cdot \frac{p \cdot 300}{p_o T} \quad (14)$$

where $X = 1.5 \times 10^{-4}$ is the mole fraction of NH_3 , m_1 the mass of a H_2 molecule, m_2 that of an NH_3 molecule, \bar{v} the "incompressible volume" per mole in v.d. Waals' equation of state for the here predominant hydrogen (\bar{v} is 1/3 of the critical volume of 2 g of H_2 , or about 22 cm^3) p is the pressure, T the temperature, and p_0 the standard pressure of 1 atm. Eq. (14) gives then the numerical estimate

$$\frac{f_t}{f} \approx \text{order of } 4 \times 10^{-5} \quad (15)$$

The crudeness of this estimate should be emphasized, a result of the order of 10^{-1} or so would not mean very much. The very low value of less than 1 in 10^4 means, however, that triple collisions with substantial interaction are still very rare at the 10^3 atm, 1400°K level, and that they are therefore most unlikely to affect the validity of eq. (12) for $\Delta\nu$ to any significant degree, in one way or another.

The situation is almost certainly different for more distant interactions between the molecules which should really here be considered as centers of a force field, rather than as elastic spheres. Making a firm prediction of this compressibility effect is, unfortunately, not possible at the present time, since the theory of dense gases has not yet been developed for such more realistic molecular models. It is, however, a common experience that compressibility effects in dense gases are most noticeable at low temperatures, and that the behaviour of a gas tends to approximate that of a perfect one more and more, the higher the temperature, provided that the density is still appreciably less than that which corresponds to the incompressible volume of the gas in question, i.e. around three times the critical density. This is here still the case: the density at the 10^3 atm level in the nominal atmosphere of essentially hydrogen is around 0.02 g cm^{-3} , and $3\rho_{\text{crit}}$ of H_2 is around 0.09 g cm^{-3} . While one cannot be sure of it, one would then expect that the deviation from the low-pressure formula (12) for $\Delta\nu$ will be of a similar magnitude as those in the equation of state, i.e. comparable to some 20% at 10^3 atm, 1400°K , and correspondingly less at the lower pressures. The influence of these deviations on the here mainly interesting integrated attenuation through the entire atmosphere will then

even be less, and probably somewhere around 10 percent. They will therefore be much less than the uncertainty of the NH_3 contents of the atmosphere, so that the calculation of the attenuation with eq. (1) for the nominal atmosphere, and with corresponding formulas for other atmospheric models with different composition and NH_3 contents appears to be justified under the circumstances.

F. Vandrey

J. F. Vandrey

JFV/dcm

References

1. A. A. Maryott: On the NH_3 Microwave Absorption by the Atmosphere of Jupiter. Unpublished Memorandum, N.B.S. August 7, 1970.
2. F. Vandrey: Working Formula for NH_3 Microwave Attenuation in the Nominal Model of the Jupiter Atmosphere.
Memo to S. J. Ducsal September 14, 1970
3. N. Divine: Jupiter Model Atmospheres. J.P.L. Interoffice Memo 2947-617, May 8, 1970.
4. D. Gray, ed.: American Institute of Physics Handbook, 2nd ed.
McGraw-Hill Book Co., Publ. New York 1963
5. F. Rossini, ed.: Thermodynamics and Physics of Matter. Vol. I of High-Speed Aerodynamics and Jet Propulsion.
Princeton Univ. Press, Publ. Princeton, N.J., 1955.

Attachment 3, Section IVK

19 October 1970

To: S. J. Ducsai
 From: J. F. Vandrey
 Subject: Comments on Deuterated Ammonia in the Jovian Atmosphere

In a study of microwave propagation in dense atmospheres, D. A. de Wolf and J. W. Davenport suggested that there may be some communication difficulties for frequencies around 2 GHz, due to the presence of a small amount of ND_3 in the atmosphere, since this very rare ammonia modification has an absorption line near this frequency ([1], p. 14. The exact value is 2.04 GHz, as obtained from the corresponding wave number of 0.068 cm^{-1} , [2], p. 131). The authors suggested a look into this question, in order to see how serious it could be.

If one makes the reasonable assumption that the deuterium abundance in relation to ordinary hydrogen is about the same as on Earth, i.e. about 1 in 5000, it is not difficult to show that there are far too few ND_3 molecules in the Jovian atmosphere to have any appreciable influence on the communication with an entry probe, even if one uses their exact resonance frequency of 2.04 GHz for the transmission of the signals.

For the attenuation parameter γ , one has the general expression

$$\gamma = 5.7 \times 10^6 \frac{\nu^2 N_0 \langle \mu_{ij}^2 \rangle}{kTc \cdot \Delta \nu} \left[\frac{1}{1 + \left(\frac{\nu_0 - \nu}{\Delta \nu} \right)^2} + \frac{1}{1 + \left(\frac{\nu_0 + \nu}{\Delta \nu} \right)^2} \right] \frac{\text{db}}{\text{km}} \quad (1)$$

(see e.g. the preceding memorandum [3]). In this equation, the order of magnitude of γ is essentially determined by the number N_0 of the ammonia molecules with the particular isotopic composition one is considering, i.e.



respectively. The influence of differences in $\langle \mu_{ij}^2 \rangle$, $\Delta \nu$ and ν_0 between them is insignificant by comparison, see below.

Assuming now $N(D) : N(H) \approx 1/5000$ as in terrestrial hydrogen, one obtains from simple probability considerations that eq. (8) of [3] should be modified to

$$\begin{array}{ll}
 N_o = 3.9 \times 10^{19} \rho & \text{for } NH_3 \\
 2.34 \times 10^{16} \rho & NH_2D \\
 4.7 \times 10^{12} \rho & NHD_2 \\
 3.1 \times 10^8 \rho & ND_3
 \end{array} \quad (3)$$

where ρ is the atmospheric density in $g\ cm^{-3}$.

For the four isotopic modifications, one has then (see e.g. [2], p. 131)

$$\begin{array}{ll}
 \gamma_o = 24 \times 10^9\ sec^{-1} & \langle \mu_{ij}^2 \rangle = 8.6 \times 10^{-37}\ \text{e.s.u. for } NH_3 \\
 12 \times 10^9 & 11.6 \times 10^{-37}\ \text{e.s.u. for } NH_2D \\
 5.1 \times 10^9 & 16 \times 10^{-37}\ \text{e.s.u. for } NHD_2 \\
 2.04 \times 10^9 & 24.5 \times 10^{-37}\ \text{e.s.u. for } ND_3
 \end{array} \quad (4)$$

No data are available for the line widths $\Delta \nu$ of the deuterated modifications, but we will not go very far wrong, if we use the line width

$$\begin{aligned}
 \Delta \nu &= (0.76\ p_{H_2} + 0.18\ p_{H_e}) \frac{300}{T} \times 10^9 \\
 &= 7.36 \times 10^{12} \rho\ sec^{-1}
 \end{aligned} \quad (5)$$

for ordinary ammonia, NH_3 , in our estimate ([3], eq. (9)).

Considering then e.g. the 1 atm, 180°K level in the nominal atmosphere with $\rho = 1.5 \times 10^{-4}\ g\ cm^{-3}$, we obtain an attenuation

$$\gamma = 3.5 \times 10^{-12} \frac{db}{km} \text{ due to } ND_3$$

at its resonance frequency of 2.04 GHz. This would have to be compared with the value

$$\gamma = 6.6 \times 10^{-4} \frac{db}{km} \text{ due to } NH_3$$

which one obtains for the same frequency. It is clear that the ND_3 attenuation

is inconsequential even at its resonant frequency, and at low pressures where the line width is small. There is simply not enough of it to cause any trouble.

The situation is somewhat different for the much more abundant modification NH_2D at its resonant frequency of 12 GHz. One obtains then an attenuation parameter of $\mu = 0.004 \frac{\text{db}}{\text{km}}$ from NH_2D at 1 atm which is 10% of the attenuation from ordinary NH_3 at the same frequency.

Conclusion:

Due to their rarity, deuterated ammonia modifications have no appreciable effect on the microwave link between a spacecraft and a Jupiter entry probe. ND_3 is much too rare to disturb the communication even near its resonant frequency of 2.04 GHz (which is fortunate), and NH_2D is still too rare to permit an independent determination of the deuterium abundance by a cooperative e.m. experiment with the spacecraft-probe system at 12 GHz (which is unfortunate, since it would be a help in reducing ambiguities of the mass spectrometer, see e.g. [4], pp. 6-8).

F. Vandrey

 J. F. Vandrey

JFV/dcm

References.

1. D. A. de Wolf and J. W. Davenport: Investigation of Line-of-Sight Propagation in Dense Atmospheres. Final Report. NASA CR 73440, May 1970.
2. W. Gordy et al.: Microwave Spectroscopy
Dover reprint, 1966
3. F. Vandrey: Working Formula for NH_3 Microwave Attenuation in the Nominal Model of the Jupiter Atmosphere.
Memo to S. J. Ducsai Sept 14, 1970
4. Science Criteria for Jupiter Entry Missions
JPL Section Document 131-07, Dec 31, 1969.

Attachment 4

19 October 1970

To: S. J. Ducsai
 From: J. F. Vandrey
 Subject: Order-of-Magnitude Estimate of the Conductivity in the Lower Jupiter Atmosphere.

It was shown in a preceding memorandum [1] that conductivity effects due to thermal ionisation (mainly splitting of molecules with ionic bonds, not separation of electrons) have to be taken into account in the prediction of signal attenuation from a deep probe into the Jovian atmosphere, if the conductivity exceeds around $4 \times 10^{-11} \text{ ohm}^{-1} \text{ cm}^{-1}$ at the lowest level (e.g. 1400°K , 10^3 atm nominal) to which the probe will be designed to penetrate. This value corresponds to a 20% correction of the microwave attenuation predicted from an interaction with the NH_3 inversion spectrum. An increase of the conductivity to $10^{-10} \text{ ohm}^{-1} \text{ cm}^{-1}$ would then lead to a 50% upward correction of the attenuation which would clearly be of concern.

The purpose of the present memorandum is to assess in a very crude way the degree of ionisation which would be needed to cause such conductivities, and the likelihood to encounter it at the 10^3 atm level for a typical range of $\pm 200^\circ\text{K}$ around the nominal temperature of 1400°K .

Quite in general, the conductivity of a fluid with N (for simplicity single-valued) positive and as many negative ions per cm^3 is given by

$$\sigma = N e (U_+ + U_-) \quad (1)$$

where $e = 1.6 \times 10^{-19} \text{ amp sec}$, and where U_+ and U_- are the "mobilities" of the ions, i.e. their velocities in a field of 1 volt cm^{-1} . Typical ion mobilities in air are around $1.5 \text{ cm}^2 \text{ volt}^{-1} \text{ sec}^{-1}$ (see e.g. [2], p. 183), they scale essentially inversely proportional to the viscosity of the fluid (see e.g. [3], p. 419).

Estimating then the viscosity of the Jupiter atmosphere from

$$\log \eta \sim 0.4 + 0.65 \log T \quad (2)$$

with η in micropoise and T in $^{\circ}\text{K}$ ([4], p 11), we obtain with $\eta_{\text{air}} = 1.73 \times 10^{-4} \text{ g cm}^{-1} \text{ sec}^{-1}$ at 273°K

$$U_+ + U_- \sim 2.2 \text{ cm}^2 \text{ sec}^{-1} \text{ volt}^{-1} \quad (3)$$

as a typical value for the 1400°K level in the Jovian atmosphere. This gives then for N the estimate

$$N = \frac{\sigma}{e (U_+ + U_-)} \sim 10^8 \text{ ion pairs cm}^{-3} \quad (4)$$

$$\text{for } \sigma = 4 \times 10^{-11} \text{ ohm}^{-1} \text{ cm}^{-1}.$$

This is a very small degree of ionisation. One finds from the density $\rho \approx 0.02 \text{ g cm}^{-3}$ at the 10^3 atm level of the nominal atmosphere ([4], p. 15), and from its mean molecular weight of 2.30 that only one in about 5×10^{13} atmospheric molecules will be dissociated. Even discounting here the two major atmospheric constituents, H_2 and H_2O , as likely candidates for ionisation, it is only necessary that about one in 5×10^{10} of the more easily ionisable trace component molecules in the atmosphere is dissociated, in order to obtain a conductivity of $4 \times 10^{-11} \text{ ohm}^{-1} \text{ cm}^{-1}$.

Because of this very small degree of ionisation, and because of the fact that the nominal temperature of 1400°K at the 10^3 atm level is close to that of an ordinary candle flame which is known to be somewhat ionized, we try to assess in a very crude way the likelihood to encounter a conductivity of this magnitude in the lower Jupiter atmosphere. We do this by a logarithmic interpolation between the conductivity of an impure gas at ordinary temperature ($\sim 300^{\circ}\text{K}$) which is roughly of the order of $10^{-17} \text{ ohm}^{-1} \text{ cm}^{-1}$, and that of an impure gas with some H_2O , CO_2 , etc. at 2000°K (Bunsen flame) which is roughly of the order of $10^{-6} \text{ ohm}^{-1} \text{ cm}^{-1}$ (from measurements the writer made as a student at the University of Gottingen some 40 yrs ago). This interpolation (which may well give results which are somewhat high) gives us a decrease in the conductivity of around $2/3$ orders of magnitude for a temperature decrease of 100°K .

We obtain then for

T = 1200°K	$\sigma \sim 10^{-11.3} \text{ ohm}^{-1} \text{ cm}^{-1}$
1400°K	$10^{-10} \text{ ohm}^{-1} \text{ cm}^{-1}$
1600°K	$10^{-8.7} \text{ ohm}^{-1} \text{ cm}^{-1}$

These numbers would indicate that a conductivity problem for the communication is very unlikely at 1200°K. The Jovian atmosphere is then still for all practical purposes an "excellent insulator" ([4], p. 11). At 1400°K, the situation becomes marginal. But there is still no real problem, at least not for the nominal atmosphere. The effect is restricted to the very end of the mission, so that its influence on the integrated attenuation through the entire atmosphere is small in comparison with the other uncertainties for which we have to allow in the design of the communication system. Above 1400°K, one will however, be increasingly doubtful about the justification to disregard conductivity effects in the design analysis of the communication system, and one will have to make a more thorough, and unfortunately also much more difficult and time-consuming analysis of the situation, in order to see to which temperature levels one can penetrate (provided that one can tolerate the associated pressure), without running into loss of communication because of the then rapidly increasing ionic conductivity.

F. Vandrey

 J. F. Vandrey

JFV/dcm

References:

1. F. Vandrey: Conductivity Attenuation of Microwave Signals
Memo to S. J. Ducsay
2. J. J. Thomson and G. P. Thomson: Conduction of Electricity through Gases,
Vol. I.
Dover reprint, 1969
3. G. Joos: Theoretical Physics, 3rd ed.
Hafner Publ. Co., New York
4. N. Divine: Jupiter Model Atmospheres
JPL Interoffice Memo 2947-617, 8 May 1970.

V. MECHANICAL SUBSYSTEMS - DESIGN STUDIES AND TRADEOFFS

This chapter contains discussions of the design approaches, analysis methods, subsystem performance and other technical information concerning the areas of:

Thermal Control
Structures and Mechanisms
Heat Shield
Aerodynamics
Guidance and Control and Propulsion

A. Thermal Control

1. Temperature Requirements

Component	Non-Operating Min/Max, °F	Operating Min/Max, °F
Heat Shield	-100/	-
Deflection Motors	- 40/	-
Battery	0/100	40/120
Science	- 65/212	30/175
Power, Telecommunications, Data	- 35/160	50/130*
*Some components can operate as high as 175°F		

Except for the science sensors and antennas, all of the power, telecommunications, data and science subsystems are located inside the pressure vessel. For simplicity, their individual requirements were combined as 125°F maximum operating temperature;

2. Cruise Phase

Thermal control must be provided for the atmospheric entry probe prior to Jupiter entry to ensure that all probe systems are maintained within acceptable temperature limits. This problem can be divided into two separate phases: (1) the pre-separation phase where the probe is being carried by the spacecraft, which it relies upon as a source of power, and (2) the post-separation phase where the atmospheric entry probe has separated from the spacecraft and has been deflected into a trajectory to intercept the planet. Each of these phases is discussed separately below. These analyses are based on the Trial Mission configuration.

a. Pre-Separation

TOPS Spacecraft

It was assumed for this study that 50 watts of power was available from the TOPS spacecraft on a continuous basis and that 100 watts would be available when the TOPS planetary science was not in operation (typically before E-28). Because very little solar input is available during the majority of the cruise time, and power is available from the spacecraft, the lightest weight thermal control system appeared to be a combination of multilayer insulation and thermostatically-controlled resistance heaters. The insulation blanket would be mounted directly on the outside of the heat shield with nylon posts and velcro tape. Since the deflection motors were fired immediately after separation and then jettisoned, this blanket had to be fitted between the motors and the aft portion of the heat shield (see Figure VB-9). In this way the blanket would remain intact and could thus be used to insulate the probe during the post-separation phase. It was therefore assumed that the motors were insulated with a separate blanket. This blanket would be mounted on a light-weight, 3 pound fiberglass frame which would be left behind with the TOPS spacecraft after separation of the probe.

A thermal model of the atmospheric entry probe was made to analyze the interplanetary cruise phase. First view factors between the atmospheric entry probe and the TOPS spacecraft were generated. These were then used in a 41 node thermal model. A multilayer insulation blanket,

fabricated from crinkled 0.25-mil mylar aluminized on one side, was used in the analysis. The insulation properties assumed were a thermal conductivity of 3.33×10^{-5} Btu/hr/ft/°R and a density of 1.5 lb/ft³. The conductivity value does not account for seams, attachments or vent holes, and penetrations are accounted for separately. Penetration conductances were allowed for the spacecraft mounting, the ion mass spectrometer, and an umbilical. Kapton, aluminized on one side, was used as the outer layer of the blanket. Both the Kapton side out, $\alpha/\epsilon = 0.34/0.63$, and aluminized side out, $\alpha/\epsilon = 0.11/0.04$, cases were analyzed.

Figure VA-1 shows the heater power required to maintain the probe at temperatures of -35°F and 50°F as a function of insulation thickness (insulation weight including support structure is also shown) during the pre-separation cruise phase. Curves are shown for both the near-Earth and near-Jupiter conditions for the Kapton side out case, and only near-Earth for the aluminized side out case. The probe would have an equilibrium temperature of 50°F near Earth for this case and would thus not require heater power. The aluminized side out was selected for the TOPS since it resulted in less heater power. Maintaining the probe at -35°F (Table VA-1) of course, requires the least amount of power. This temperature was therefore chosen as the non-operating storage temperature for the probe during the cruise phase. The selection of this temperature also depends on reliability considerations and the TOPS spacecraft power budget during the mission. An insulation thickness of 0.75 inches on the heat shield was selected as the baseline design,* which weighs 5 pounds (including structure) and requires no heater power near Earth and 1.6 watts near Jupiter. This insulation thickness was based on the pre-separation data in Figure VA-1 as well as post-separation considerations discussed below.

The batteries can easily be maintained at their minimum storage temperature of 0°F even if the electronics were at only -35°F.

*The selection of a "baseline" design for either the TOPS or the Pioneer S/C was done for purposes of illustrating how to use the data presented, and does not necessarily represent an optimum design.

This is accomplished by placing the probe heaters on the battery cases and placing a few layers of multilayer insulation around the batteries. It was found that the heat shield material was maintained above its lower temperature limit of -100°F for all insulation thicknesses considered when the electronics were at -35°F .

The heater power required to maintain the deflection motors at their minimum storage temperature of -40°F is shown in Figure VA-2 as a function of insulation thickness (insulation weight including structure is also shown). Again three curves are shown, the aluminized side out case for Earth and both cases for Jupiter. An insulation thickness of 0.33 inches with the aluminized side out was chosen which resulted in a total insulation plus structure weight of 3.5 pounds and no heater power requirements at Earth and 0.7 watts at Jupiter. The motors would have an equilibrium temperature of about 50°F at Earth.

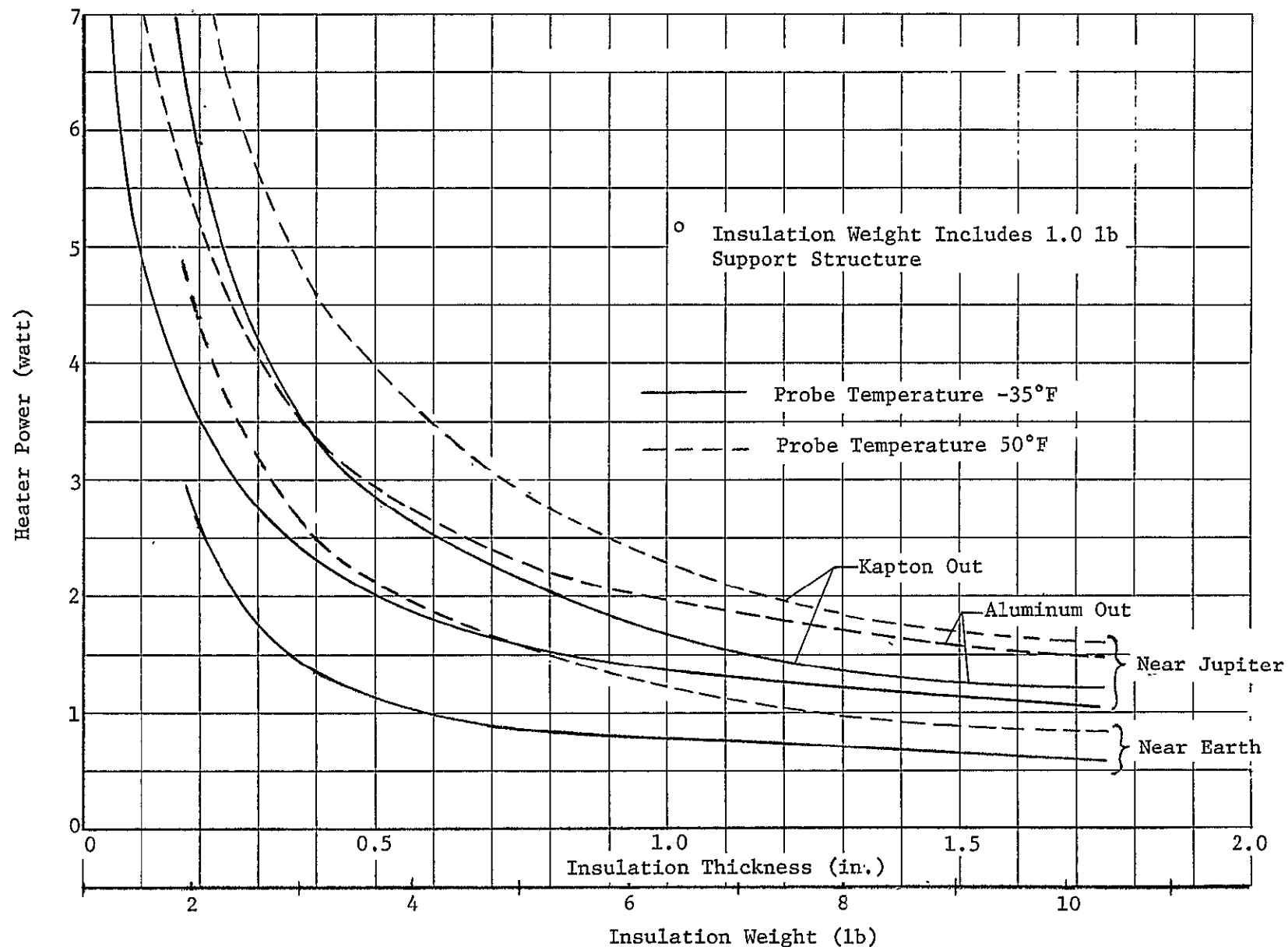


Figure VA-1 Heater Power Required to Maintain Probe Temperature During Pre-Separation Cruise.

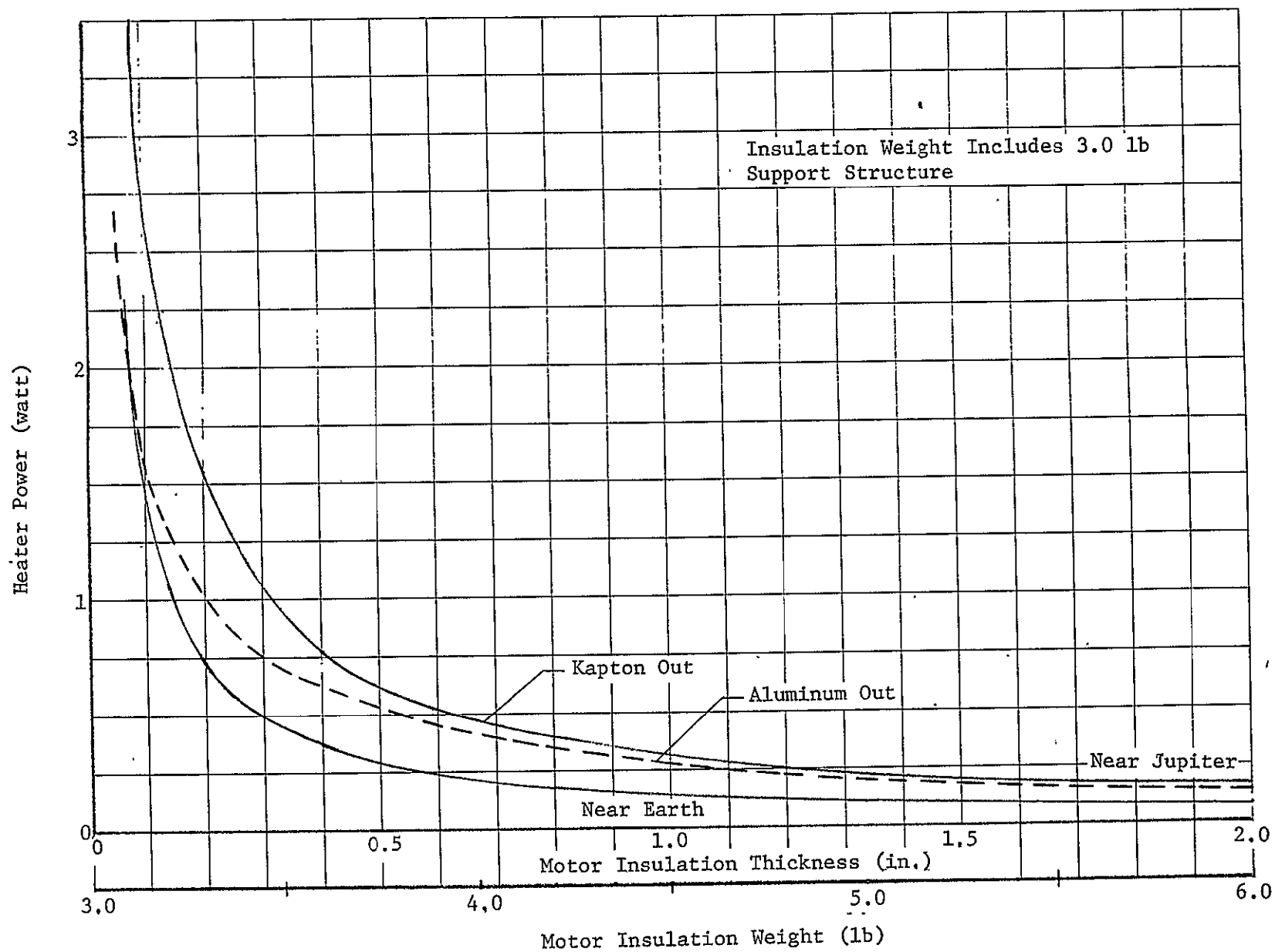


Figure VA-2 Heater Power Required to Maintain Deflection Motors at -40°F During Pre-Separation Cruise.

Insulation and heater power requirements for the probe and motors are summarized in Table VA-2 below.

TABLE VA-2
INSULATION AND HEATER POWER REQUIREMENTS

	Insulation Thickness (in.)	Insulation and Support Structure Weight (lb)	Heater Power at Earth (watt)	Heater Power at Jupiter (watt)
Atmospheric Entry Probe at -35°F	0.75	5.0	0.0	1.6
at 50°F	0.75	5.0	0.0	2.3
Motors at -40°F	0.33	3.5	0.0	0.7
Total	at -35°F	8.5	0.0	2.3
	at 50°F	8.5	0.0	3.0

Pioneer Spacecraft

For the Pioneer spacecraft it was decided to maintain the probe at 50°F during pre-separation cruise, for reasons discussed below in paragraph b. Otherwise the thermal control system would be essentially the same as it would be for the TOPS spacecraft. The insulation blankets (for the motors and probe) would have the same thicknesses but would have to be designed for a different penetration arrangement. If the outer layer of the insulation were aluminized, however, the probe would exceed its maximum allowable temperature near Earth. This is due to the spinning of the Pioneer which causes all sides of the probe to be illuminated while only one side is illuminated in the case of the TOPS. For this reason a lower α/ϵ surface is required for the Pioneer so for purposes of illustration the Kapton side out case was used. Resulting heater power requirements would be 1.1 watts near Earth and 3.9 watts near Jupiter.

b. Post-Separation Cruise

After the atmospheric entry probe has separated from the bus it is spun up and the deflection motors are fired and then jettisoned. The amount of time that the probe coasts before entry depends upon the

trajectory selected. Cruise times from 12 to 36 days were considered with additional emphasis being given to the extremes. Because the descent probe temperature at the end of the entry phase must equal its temperature at the beginning of the descent phase (which was selected as 50°F), the probe's internal temperature at entry must be 50°F. This is also the approximate bulk temperature required by the probe equipment in the operating mode. Planet albedo and IR were ignored.

Two concepts were considered for post-separation thermal control. Both concepts use the multilayer insulation blanket described above to reduce heat losses. This insulation blanket would be jettisoned before the probe entered the atmosphere. Penetration conductances were allowed for the deflection motor mounting, the spacecraft mounting, the ion mass spectrometer, and an umbilical. The first concept uses battery-powered heaters to maintain the probe at 50°F, after spacecraft power is used to heat the probe from -35°F to 50°F. This battery would be mounted on the inside of the aeroshell and would not be part of the descent probe. Figure VA-3 shows the total thermal control weight (battery and insulation) required to maintain the atmospheric entry probe at 50°F as a function of insulation thickness. Curves are shown for 12- and 36-day cruise times for both combinations of surface properties. This concept is not recommended because of its high weight penalties.

The second concept relies on thermal energy stored by the mass of the atmospheric entry probe. The probe is heated to some temperature above 50°F immediately before separation and then slowly cools as it coasts toward the planet. Figure VA-4 shows combinations of initial temperatures and insulation thicknesses (or weights) which yield entry temperatures of 50°F. Curves are shown for both 12 and 36-day cruise times. The 0.75 inch baseline insulation thickness requires initial probe temperatures of 65°F and 100°F for respective cruise times of 12 and 36 days for TOPS and temperatures of 70°F and 115°F for Pioneer (Kapton side out). This insulation thickness in addition to pre-separation cruise requirements above was selected so that a cruise time of 36 days would be possible without heating the probe above its upper temperature limit prior to separation. Insulation requirements are shown in Figure VA-5 as a

function of post-separation cruise time for initial probe temperatures of 70°F and 125°F.

The utilization of the probe's thermal mass as a means of storing thermal energy was selected as the best alternative for post-separation thermal control primarily because of its simplicity and light weight. Both concepts however place a large requirement on the bus power system prior to separation. The first concept requires that approximately 4250 watt-hours of thermal energy be added to the probe to increase its temperature from -35°F to 50°F. For the 36-day cruise time, the second concept requires the addition of 7500 watt-hours to raise the probe temperature from -35°F to 115°F. This would correspond to 100 watts continuously for approximately 3 days, which is compatible with the TOPS power supply for large deflection radii. If less power is available, the pre-heating would have to be applied over a longer time period.

In the case of the Pioneer where this amount of power is not available, pre-heating the probe prior to separation does not look feasible. Both concepts would result in large weight penalties either to the spacecraft or the aeroshell, so it resolves into a choice between maintaining the probe at 50°F (or somewhat higher) throughout the mission until entry, or at -35°F and warming it up to 50°F just prior to entry. Since a 12-day post-separation cruise was used as the baseline for the Pioneer missions and the additional power required to maintain 50°F (see Table VA-2) pre-separation is small, it was decided to use 50°F. Figure VA-3 shows that approximately 33 lb of batteries would be required for post-separation thermal control. These batteries would be located inside the aeroshell.

Another alternative would be to use radioisotope heaters inside the aeroshell, but because the power requirements are small it was decided not to consider them and thus avoid a radioactivity problem.

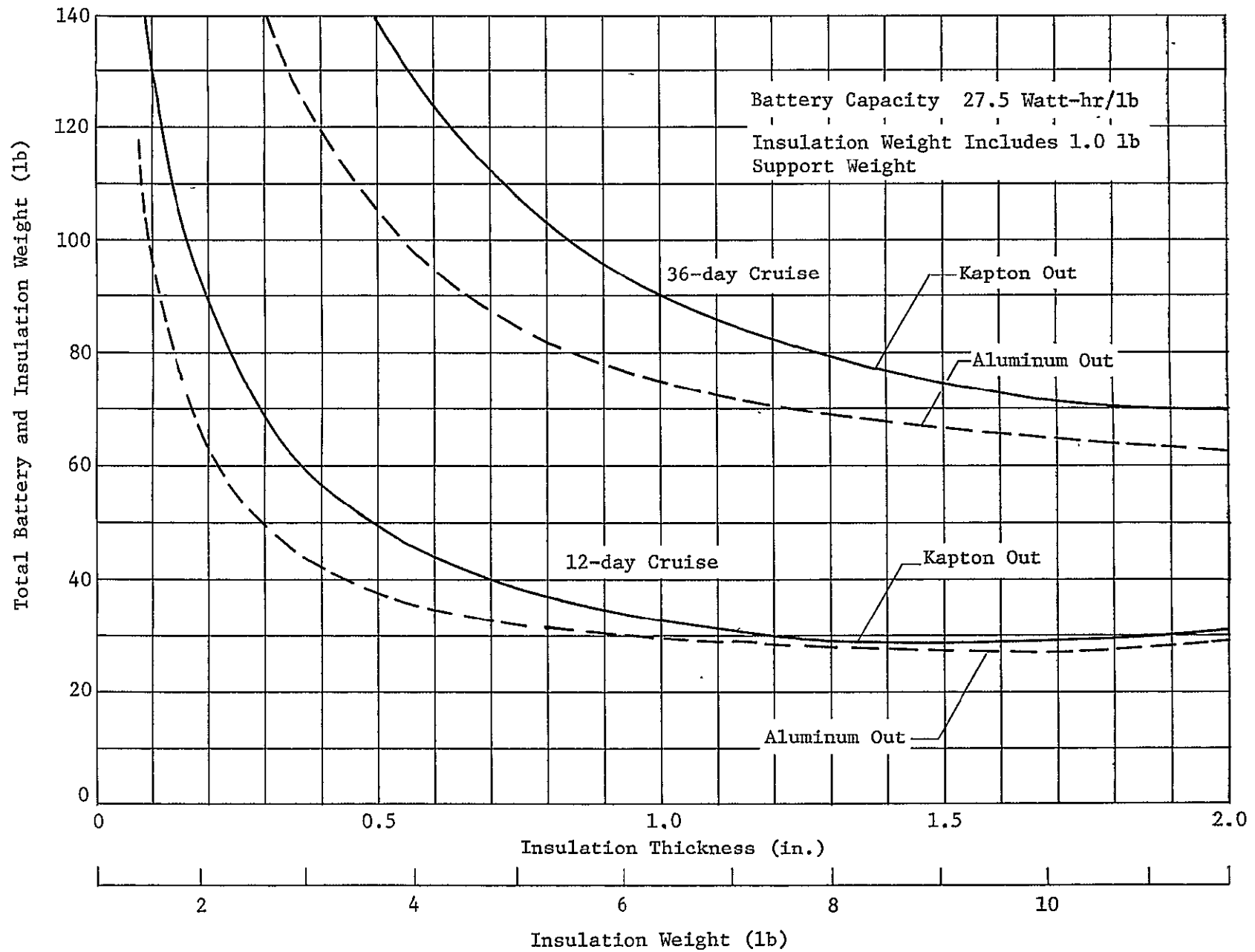


Figure VA-3 Post Separation Thermal Control Weights for Maintaining Probes at 50°F.

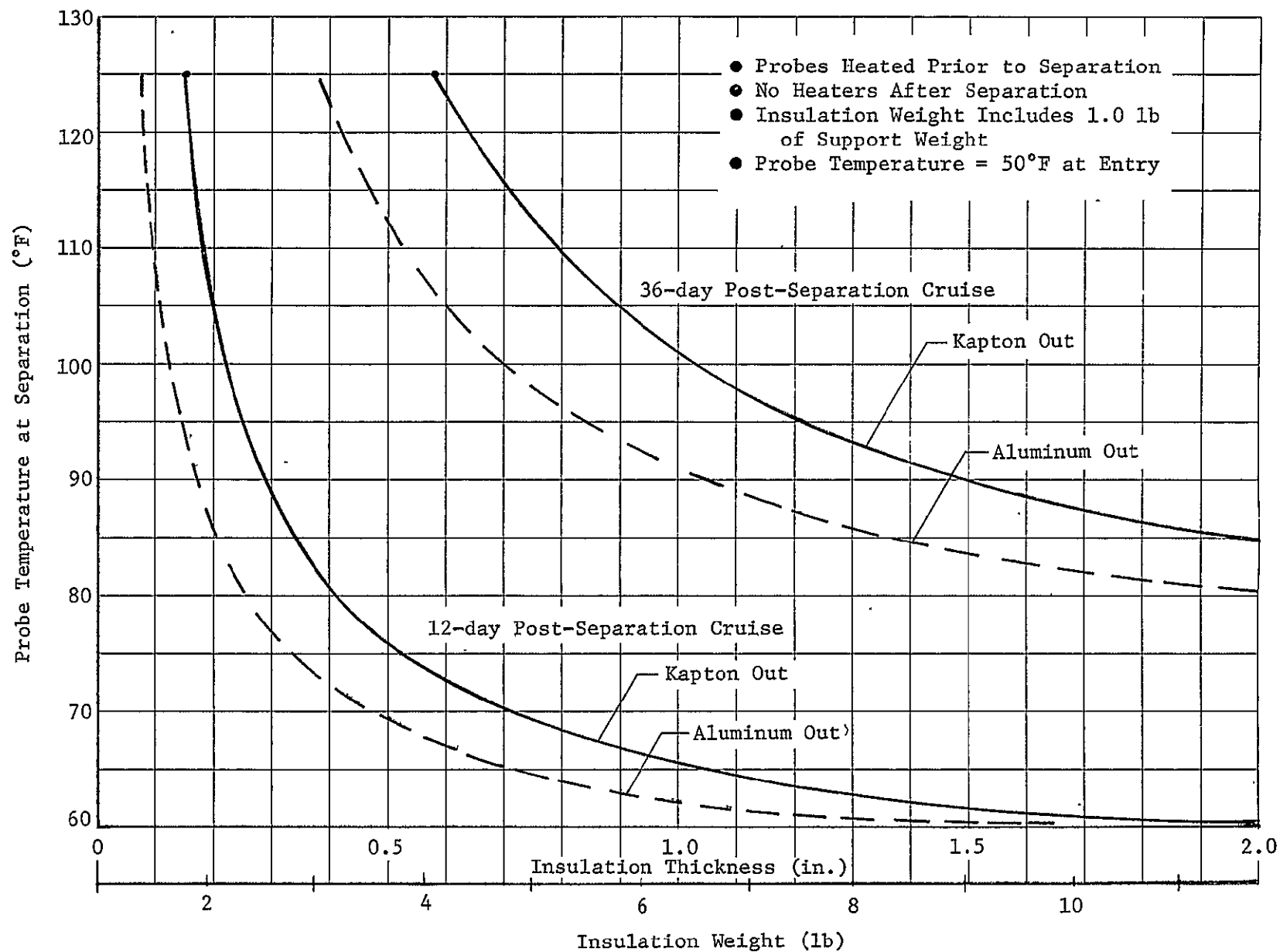


Figure VA-4 Initial Probe Temperature Required for Entry Temperature of 50°F.

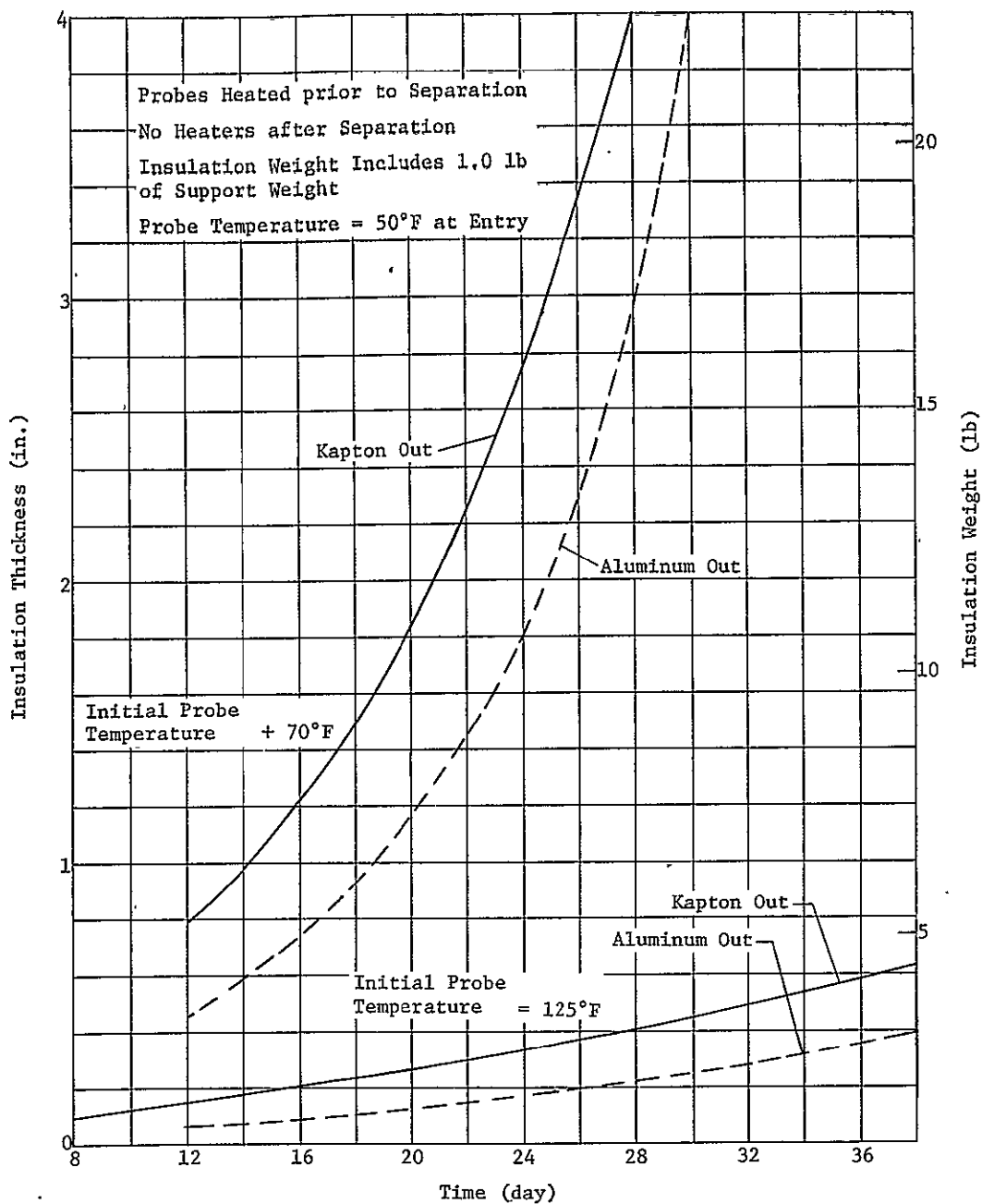


Figure VA-5 Insulation Requirements for Various Post-Separation Time Periods

c. Probe's Impact on the Spacecraft

The thermal control system of both the TOPS and Pioneer spacecraft must be modified to allow for the presence of the probe. The probe is located in a position which partially blocks the louver panel's view to space. Varying amounts of sunlight (depending on the cone angle) are also reflected into the louver panels by the probe.

TOPS

The TOPS spacecraft has louver panels on both +Y and -Y sides of the electronic equipment compartment. The probe is mounted on the +Y axis in front of the +Y louver panel thus reducing its heat rejection capability. This situation can be corrected by incorporating one or more of the following modifications: increasing the size of the +Y louver panel and have the louver blades open in the +Z direction away from the sun; rearranging the equipment so that only low heat dissipation components are located on the +Y side; using heat pipes to transfer heat from the +Y side to the -Y side of the equipment compartment; or relocating the louvers to other surfaces of the compartment.

Pioneer

The Pioneer spacecraft presents a somewhat different problem, since the view of all the louver panels are blocked to some degree. Three different Pioneer antenna configurations were considered with each having a different impact on the thermal control system as discussed below:

The despun dish configuration requires the least modification to the spacecraft since the probe is located at a relatively large distance from the louvers. The main equipment compartment louver panels, however, would still see the probe and antenna mesh. This would require that the louver area be increased and would probably require that the louver blades be oriented with their axes lying circumferentially rather than radially. In this orientation the louvers would open facing outward and would be caged so that the radiating surface could not see the probe.

The wide range despun dish configuration has the antenna located on a boom off the spacecraft axis which allows the probe to be mounted closer to the spacecraft. This would further reduce the heat rejection capability of the louvers and may require that heat pipes be used to transfer heat out to an additional set of louvers located on the scientific instrument compartment. These louvers would be more efficient than those located on the main equipment compartment, since they have a much smaller view of the probe.

The electronically despun phased array configuration would be similar to the wide range despun dish configuration, since the probe would be mounted close to the louvers. Louver performance, however, would be degraded an additional amount by the phased array antenna which would be mounted in front of the louver panels. The antenna elements and mesh ground plane would partially block the louver panel's view to space and may be severe enough to require a more complex thermal control system.

3. Descent Phase

a. Analytical Method

Described in this subsection are the major ingredients of the transient thermal models used to perform all of the descent phase analyses. The number of nodes in each model varied from 4 to 6 and the conductors from 4 to 8. It was determined that heat transfer by radiation was insignificant so it was not considered. Basic inputs include the planet radius vs. time and probe velocity vs. time arrays for the selected mission, and arrays of density, temperature and pressure vs. planet radius for the model atmosphere used. The conductivity, viscosity and specific heat of the atmosphere were input as a function of pressure and temperature.

Determination of the nodal capacitances and conductor values was the most critical step, and was done in the computer program. The pressure vessel material properties were input, as well as the payload weight and packaging density. The pressure vessel dimensions and weight were computed as described below, and the internal structure weight (and capacitance) was computed as a function of entry angle and payload weight.

The model was utilized by assuming PCM weights and insulation thicknesses, limiting the payload temperature to a maximum and forcing the shell temperature to a specified level, and optimizing the thermal/structural weight (the sum of the shell, internal structure, PCM, and insulation). A critical assumption was that the probe internal temperature at the beginning of the descent was 50°F.

Computer Programs - All thermal analysis was done with the use of two computer programs; MITAS, a thermal analyzer, and MTRAP, a radiation analyzer. MTRAP was used to compute black body view factors for the pre-separation cruise phase, and MITAS was used for both the steady-state and transient cruise phase analysis and the transient descent phase analysis.

Atmospheric Thermophysical Properties - The Nominal Jupiter atmosphere is composed of 75.3% Hydrogen (by weight), 23.0% Helium, and 1.7% other constituents. For the purpose of this analysis the composition was assumed to be 75.3% Hydrogen and 24.7% Helium. The Cool-Dense atmosphere was also analyzed. Its composition was assumed to be 50.7% Hydrogen and 49.3% Helium.

Since the atmosphere is composed of a mixture of gases, the properties of the constituents must be combined in order to obtain the properties of the mixture. The properties of Hydrogen and Helium were found from various sources over several ranges of pressure and temperature. The properties for some ranges were not available, but were estimated from available data. This data was then combined according to established empirical relationships. The method and sources used to obtain the properties of the atmosphere are discussed below.

Specific Heat

Specific heat (at constant pressure) data for Hydrogen was obtained for the entire range of pressures and temperatures. The specific heat of Helium is essentially constant at 1.24 Btu/lb/°F over the range of 1 to 170 atmospheres and -260 to 4000°F (111 to 2477°K). Since Helium is a monatomic inert gas, a constant C_p would be expected. It is therefore reasonable to assume that the C_p is also 1.24 at pressures of 1000 atmospheres. Since chemical reactions do not occur between Hydrogen and Helium, it follows from the basic laws of thermodynamics that the C_p of the mixture is equal to the sum of the individual contributions, thus a weighted average was computed at each temperature and pressure.

Viscosity

Viscosity data for Hydrogen was obtained from .07 to 306 atmospheres over the desired temperature range. The data was plotted on semi-log paper, and values for pressures of 1000 atmospheres were obtained by extrapolation. Viscosity data for Helium was obtained from .07 to 170 atmospheres over the desired temperature range. This data was also extrapolated to 1000 atmospheres. The viscosity of the mixture was calculated using Wilke's equation.

Thermal Conductivity

Thermal conductivity data for Hydrogen and Helium were obtained from the same sources as the viscosity data. This data also had to be extrapolated to 1000 atmospheres. The conductivity of the mixture was calculated using Brokaw's Rule for mixtures of non-polar gases.

Convection Heat Transfer Coefficients - During descent heat transfer from the atmosphere to the probe's outer surface is dominated by convection, and the coefficients are so high that the probe's surface temperature only lags the local atmospheric temperature by a few degrees. The correlation used for prediction of the coefficient was:

$$h = \frac{k}{D} (2. + .6 Re^{1/2} Pr^{1/3})$$

where k = atmospheric thermal conductivity

D = probe outer diameter

Re = Reynolds number

Pr = Prandtl number

This equation is for forced convection over a sphere submerged in an infinite fluid.

Phase Change Material Characterization - The PCM was incorporated into the thermal model as a separate node, and its thermal characteristics were controlled by a special subroutine. The required inputs were mass, fusion temperature, heat of fusion, and specific heat of both phases. The significant properties assumed for the PCM were: heat of fusion = 114 Btu/lb, and density = 95 lb/ft³. These properties are representative of available materials and should be realizable through proper design.

Insulation Characterization - Two types of insulation were used in the various probe configurations: multilayer, which requires a vacuum for efficient operation, and Min-K-2000, for applications which involve exposure to the atmosphere. Rather than choose a specific multilayer configuration since the applicable temperature range varies from probe to probe, it was decided to select a representative density and effective conductivity and use these properties for all probes. The selected values were $\rho = 6.0 \text{ lb/ft}^3$ and $k = 0.0004 \text{ Btu/hr/ft/}^\circ\text{R}$, which are quite conservative (penetrations are accounted for separately). This is not an efficient application for multilayer because of the small surface area, the high curvature, and the high ratio of seams and penetrations to total surface area, so spacers would certainly have to be used. Although the mean multilayer temperatures vary from -75 to 600°F, it was felt that the selected conductivity was adequate for this range and was not varied with temperature. Multilayer performance is also discussed in Section b.

For the exposed insulation, Min-K 2000 was selected as the best available material, based on the limited information on hand. The only test data available covers the effects of temperature but not pressure. Because of the nature of the material and of the atmosphere, the conductivity was assumed to be the sum of the vacuum conductivity of the Min-K and the conductivity of the atmospheric gas as a function of pressure and local temperature inside the insulation.

To illustrate the sensitivity of the probe weight to the Min-K conductivity assumed, a comparison was run on a probe mission, first with the vendor data and then with the technique described above. The configuration was a spherical Titanium shell covered with Min-K, and the resultant design details are shown in Figure VA-6. Using the vendor data, the probe required an insulation thickness of 3.25 in., compared to 5.875 in. based on the above assumptions. This type of design is not optimum for Jupiter but the comparison helps demonstrate the need for test data.

Pressure Vessel Calculations - As mentioned above, the thermal analysis of the descent probes was optimized by selecting the design having the lowest thermal/structural weight, as long as it also satisfied the temperature requirements. The pressure vessel weight was a major factor in this total, so it had to be predicted accurately.

The weights were estimated by one of two methods, depending on the combination of design pressure, shell temperature, and material. In both methods the interior volume of the probe was calculated by defining a payload weight and assuming a packaging density (40 lb/ft³). Then the inner radius of the shell envelope was calculated from this volume (assuming a sphere) and the assumed multi-layer insulation thickness, if any.

For example, if Titanium at 125°F were assumed at design pressures below 250 atmospheres buckling criteria was used and the shell thickness was calculated from:

$$t = C(R_i + x)$$

where

R_i = inner radius

x = shell envelope, allowing for stiffening

C = a constant which is a function of Poisson's

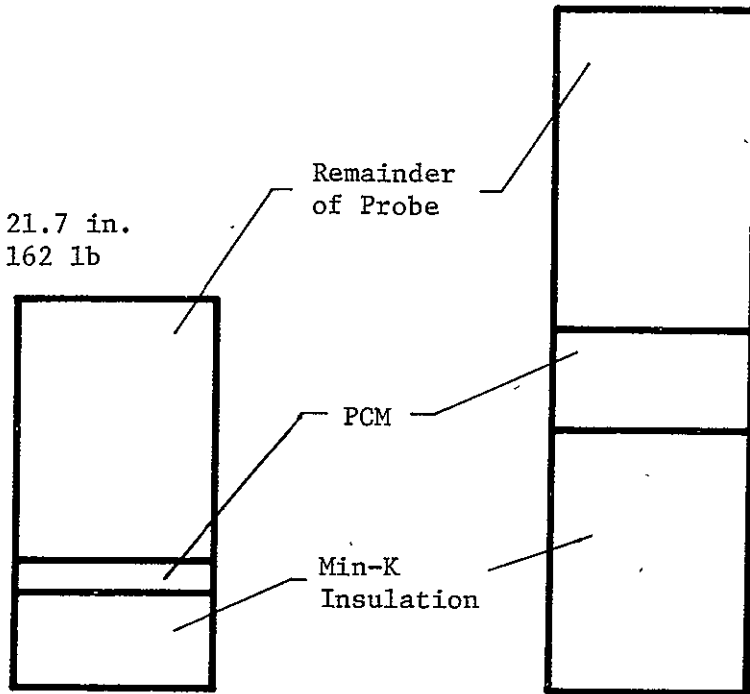
ratio, modulus of elasticity, design pressure, and safety factor.

Configuration
Payload
Time
Design Pres

Min-K/Ti
34 lb, 33 w.
2.57 hr
1000 Atm

Probe OD 28.1 in.
Probe Wt 279 lb

Probe OD 21.7 in.
Probe Wt 162 lb



Vendor Data
Min-K in 1 Atm
 H_2 as a Function
of Temperature

Estimated
Conductivity
Data as a Function
of Local Pres & Temp

Figure VA-6 Sensitivity of Descent Probe Weight to Min-K Conductivity

The shell envelope used was 0.5 inch, and the constant, C, of course varied with the shell material. The shell weight, then, was calculated from t and the outer radius, $R_i + x$. To account for added weight due to closures and penetrations, this bare weight was increased by a factor which is a function of the design pressure.

For the same example at design pressures above 250 atmospheres, thick wall criteria was used. The inner radius was calculated as before and the outer radius was calculated from

$$R_o = R_i (C)^{1/3}$$

where

C = a constant which is a function of the yield stress, design pressure, and safety factor.

In this case no stiffening was provided. The shell weight was then computed from these two radii and the same allowance for closures and penetrations. See section V-B-1 for details on shell calculations.

Penetrations - In a configuration employing multilayer insulation, penetration heat leaks represent the main path of energy transfer into the probe from the atmosphere. In the case of an external insulation, penetration heat leaks are significant although quite a bit smaller than those through the insulation itself. Penetrations result from sampling ports and sensor leads of the science subsystem, and from electrical leads of the power and telecommunications subsystems. The heat leak is proportional to Ak/ℓ , where A is the cross sectional area, k is the conductivity and ℓ is the length. Since ℓ is a variable depending upon the insulation thicknesses, the penetrations are input into the thermal model as an Ak product. Typical values for the sum of these penetrations are 0.0109 Btu-ft/hr/°F for an upper probe and 0.0110 Btu-ft/hr/°F for a lower probe.

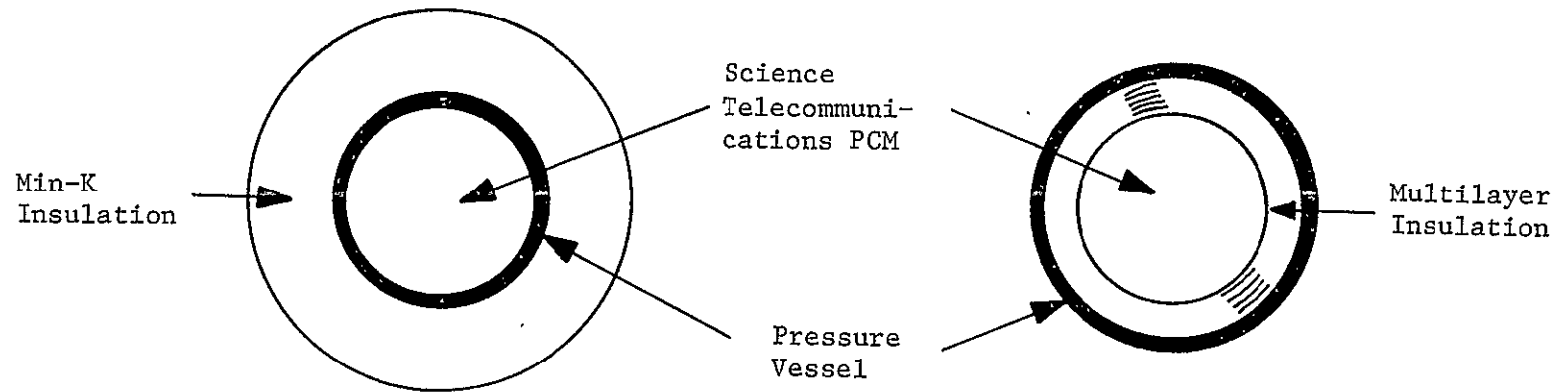
Additional penetrations result from structural supports from the pressure shell to the equipment shell and supports from the external insulation cover to the pressure shell. The Ak product for these supports are input as a function of entry angle (see paragraph c below).

b. Configuration Trade-offs

All of the following analyses utilize the analytical technique described above, including the insulation penetrations.

Pressure Vessels - This subsection deals with the trade-offs performed on the "conventional" planetary descent probe designs, i.e., spherical pressure vessels with insulation. The basic thermal control approach was to introduce a lag in the thermal pulse, since the descent phase was short. Secondly, additional thermal capacitance was built into the probe to absorb energy dissipated by the equipment and energy entering through heat shorts. The thermal lag was provided by multi-layer insulation inside the pressure vessel or Min-K 2000 insulation outside the pressure vessel, or both. The capacitance was provided by phase change material.

Trial Mission Upper Probe - Prior to and during the Trial Mission definition study a trade-off was performed on an upper and lower split probe concept to determine the size and weight comparisons of various thermal/structural designs. The upper probe trade-off was performed at a depth of about 45 atmospheres and 555°F and evaluated on two configurations, an Aluminum shell covered by Min-K and a Titanium shell containing multilayer. The ballistic coefficient was 0.05 slugs/ft², the time 2.57 hours and the power dissipation 99.3 watts. The comparisons are shown in Figure VA-7 and show a decided weight and size advantage for the exposed shell. Previous studies of Venusian entry probes (Reference 1 & 2) have shown the external insulation approach to be weight advantageous, but in this environment the expected Min-K performance is so degraded that the Min-K weight is high and not offset by the shell weight savings, partially



	56.3	Science & Communication (1b)	56.3	
Al	8.8/18.3	Pressure Vessel Wt/Dia (lb/in.)	12.1/18.2	Ti
	17.1	Support Structure (1b)	8.4	
	5.0	Aerodynamic System (1b)	3.0	
	24.7/1.7	Min-K Insul Wt/Thickness (lb/in.)	--	
	--	Multilayer Insul Wt/Thickness (lb/in.)	0.9/0.3	
	20.0	PCM (1b)	2.0	
	131.9	Total Weight (1b)	82.3	
	21.7	Total Diameter (in.)	18.2	

Figure VA-7 Configuration Trade-off - Trial Mission Upper Probe

because of the additional volume required by PCM. Also, the OD of the exposed shell design is smaller which allows a more compact aeroshell.

Pre-Trial Mission Lower Probe - The trade-off for the lower probe was performed at a depth of 987 atmospheres and 2100°F, and considered a third configuration. The third configuration had Min-K outside the shell and multilayer inside, and was evaluated with three different shell materials. Because of the shell mechanical properties at elevated temperatures, in order to minimize weight it was necessary to use Titanium for the protected shell and Columbium B-66 for the exposed shell. For shells with insulation inboard and outboard it was a matter of selecting a design temperature at which the mechanical properties were optimized. The descent profile had ballistic coefficients of 4., 1.75, and 4. slugs/ft², the time was 2.57 hours and the power dissipation was 32.5 watts. The comparisons are shown in Figure VA-8 and include a large range of weights and sizes. The largest variable is the shell weight, of course. The minimum weight configuration is the Inconel 718 at 1100°F, although the Rene 41 design is smaller because of the lower Min-K thickness.

The results of these trade-offs were used to select the configurations in all of the following mission studies. For brevity the configurations are referred to by designating the shell material and insulation type, e.g., Min-K/Inconel/Multilayer.

Alternative Configurations - Several other thermal/structural configurations could be considered if any of the science, power or telecommunications equipment could be designed to withstand the atmospheric pressure, or even better, both the atmospheric pressure and temperature. The objective is to eliminate the requirement for the heavy pressure vessel. These configurations are as follows:

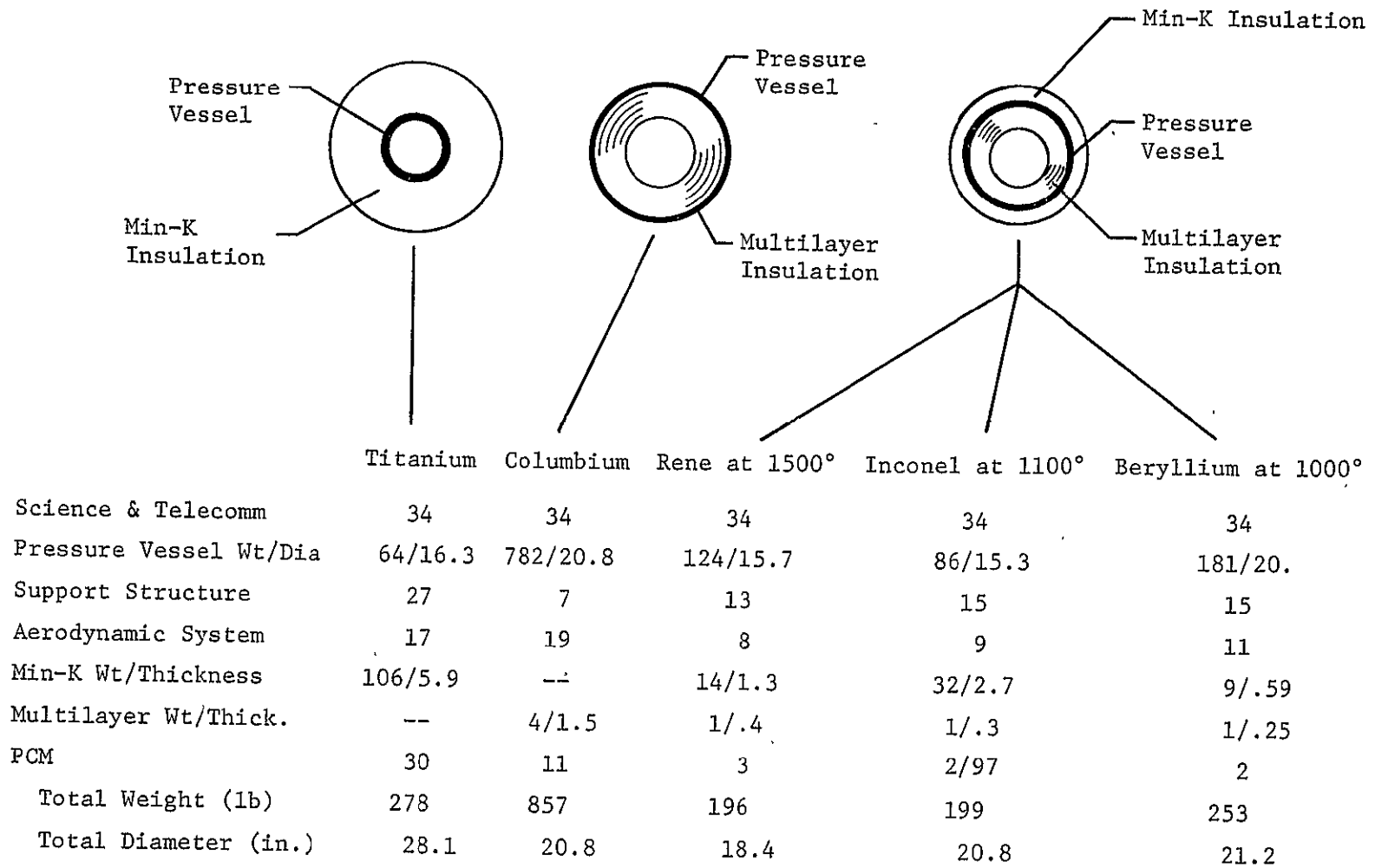


Figure VA-8 Configuration Tradeoffs, Pretrial Mission Lower Probe

- a) An equipment compartment which is vented to the atmosphere, and the incoming atmospheric gas is cooled by a phase change heat exchanger;
- b) A closed system where the atmospheric pressure is transmitted through a bellows to a contained fluid, possibly PCM;
- c) A probe which carries along a gas, stored at high pressure, that is vented inside the probe at a rate which matches the atmospheric pressure increase;
- d) A probe which is internally pressurized to a level at which the shell thickness is minimized between the tension loads when there is no atmosphere, and the compression loads when there is an atmosphere.

All of these configurations become more competitive with the pressure vessel concept as the design pressure increases. Therefore, a preliminary examination of these concepts was done for the 1000 atmosphere depth. The reference design was selected as the Inconel/Multilayer/Min-K probe from Figure VA-8.

The capability of the components to withstand these high pressures is, of course, speculative. In the proposal effort a small feasibility test run to explore this possibility demonstrated that several representative electronic components apparently can operate at 1000 atmospheres. Based on these results and 1975 state-of-the-art, an assessment of the pressure capability (yes or no) of each of the probe components was made. On a weight basis about 40% of the components were assumed to require protection from the pressure above 1 to 2 atmospheres.

With this as a ground rule, comparative weights for concept "d" were approximated. No pressurized design can use multilayer because of the vacuum requirement, which means a 1000 atmosphere delta pressure vessel would still be required. Therefore a pressurized design would have to use the Titanium/Min-K configuration, also shown in Figure VA-8. For this design the increased Min-K weight required to limit the shell to 125°F is already heavier than the shell, so no overall weight savings over the reference design are possible. The optimum internal pressure

would be approximately 410 atmospheres, assuming Titanium at room temperature and a higher safety factor (2.2) in the tension condition due to catastrophic failure considerations. The 64 lb shell could be reduced to 38 lb, but the small 410 atmosphere delta shell for the low pressure components would add back about 10 lb. This would result in a total descent probe weight of about 278 lb, which is still significantly heavier than the reference design (179 lb).

Because none of the other concepts appeared to be weight competitive, a fifth alternative was evaluated. The components that required protection from the pressure were placed inside a small Titanium pressure vessel and the other components were placed on the outside, still retaining a spherical shape.* A 15% weight penalty was assumed for the pressure exposed components to provide individual protection for sensitive parts. An average density of 150 lb/ft³ was used for the external components which resulted in 73% of the equipment volume being void. The PCM was distributed in the same manner as the equipment, with 40% being placed on the inside of the pressure vessel and 60% on the outside. It was assumed that the PCM placed with the equipment on the outside was used for potting this equipment, i.e., filling the void spaces within the equipment. Since all of these voids were not filled for the resulting optimum design, the remaining voids would fill with hot atmospheric gas as the probe descends. This would make the temperature problem more severe, so an additional amount of PCM was added to completely fill these voids.

The probe weight for this configuration was 218 lb which is also heavier than the reference design, although the number of high pressure seals required may be reduced. This configuration is not competitive because of the large weight of Min-K required.

*Min-K was used as the insulation material on the external surface of the probe.

c. Multilayer Vacuum Requirement

The effectiveness of multilayer insulation is highly dependent upon the gas pressure, and ideal performance is achieved at pressures below approximately 10^{-4} torr. As the pressure is increased to 1 atmosphere the apparent thermal conductivity of the insulation is increased by a factor of 300. The actual effect of pressure depends upon the specific multilayer configuration used, however.

Because very small pressure increases result in very large increases in conductivity, the pressure buildup due to outgassing of the equipment during the three year cruise phase had to be considered. As representative conditions, 30 lb of equipment at a mean molecular weight of 40 and a free volume of 1 ft³ were assumed. Even though the temperatures for this phase are low ($\sim 0^\circ\text{F}$), the outgassing loss should be independent of temperature over long periods of time. An outgassing loss of 1% was assumed. The resultant pressure effect, however, is significant only during the descent phase so the pressure was re-evaluated at a mean temperature of 100°F , yielding a pressure of 85.6 torr.

Given the conservative properties used for vacuum conditions, the conductivity still would increase by 50 times for this pressure. Although no quantitative assessment was made, it was obvious that this was significant and a design fix had to be made. Of several possible fixes, it was decided to add a pyrotechnic vent valve in the pressure shell, which would be open during cruise and then be closed prior to entry. The valve assembly weight would be 1.5 lb.

d. Effect of Entry Angle

Entry angle variation affects the probe thermal design through the resultant variation in the structural supports carrying the entry loads from the aeroshell to the probe internal equipment. As the entry angle increases the cross sectional area of the supports increases and therefore the heat transfer into the probe (during descent) increases.

These supports represent the major heat leak into the probe through the multilayer insulation. The supports are in two locations, running from the internal equipment shelf to the pressure vessel, and in designs using Min-K, from the pressure vessel to the insulation outer cover. They are designed to minimize heat conduction by making them out of Titanium and installing them at 30°.

The cross-sectional area of the supports through the multilayer are computed by the equation:

$$A = 1.15 \times 10^{-5} g W$$

where

A = area in square inches

g = entry g

W = weight inside the pressure vessel, lb

The supports through the Min-K were computed in a similar fashion, giving cross-sectional areas that varied from 1.35 in.² at $\gamma_e = -10^\circ$ to 3.45 in.² at $\gamma_e = -50^\circ$.

e. Results - Depth vs. Weight

In order to determine how descent probe weight varied with depth, or design pressure, two descent times were selected and then ballistic coefficients were assumed that would yield a range of convenient depths for that descent time. The payload, or equipment weight inside the pressure vessel, was parameterized on the basis of transmitter size, which affected both the weight and the power dissipation. The transmitter sizes, selected from the trial mission studies, were 20, 40, and 2.5 watts, the latter corresponding to a relay probe.

With these inputs, the configuration types were pre-selected and then analyzed to optimize the thermal/structural weights. Figure VA-9 shows in log-log format this relationship for a 2.5 hour descent time, and Figure VA-10 for a 3.5 hour descent. The pressure vessel material and the insulation configuration vary from probe to probe. In Figure VA-10 at 500 atmospheres the Minimum Size Design refers to a Columbian/Multilayer design and the Minimum Weight Design refers to a Min-K/Inconel/Multilayer design.

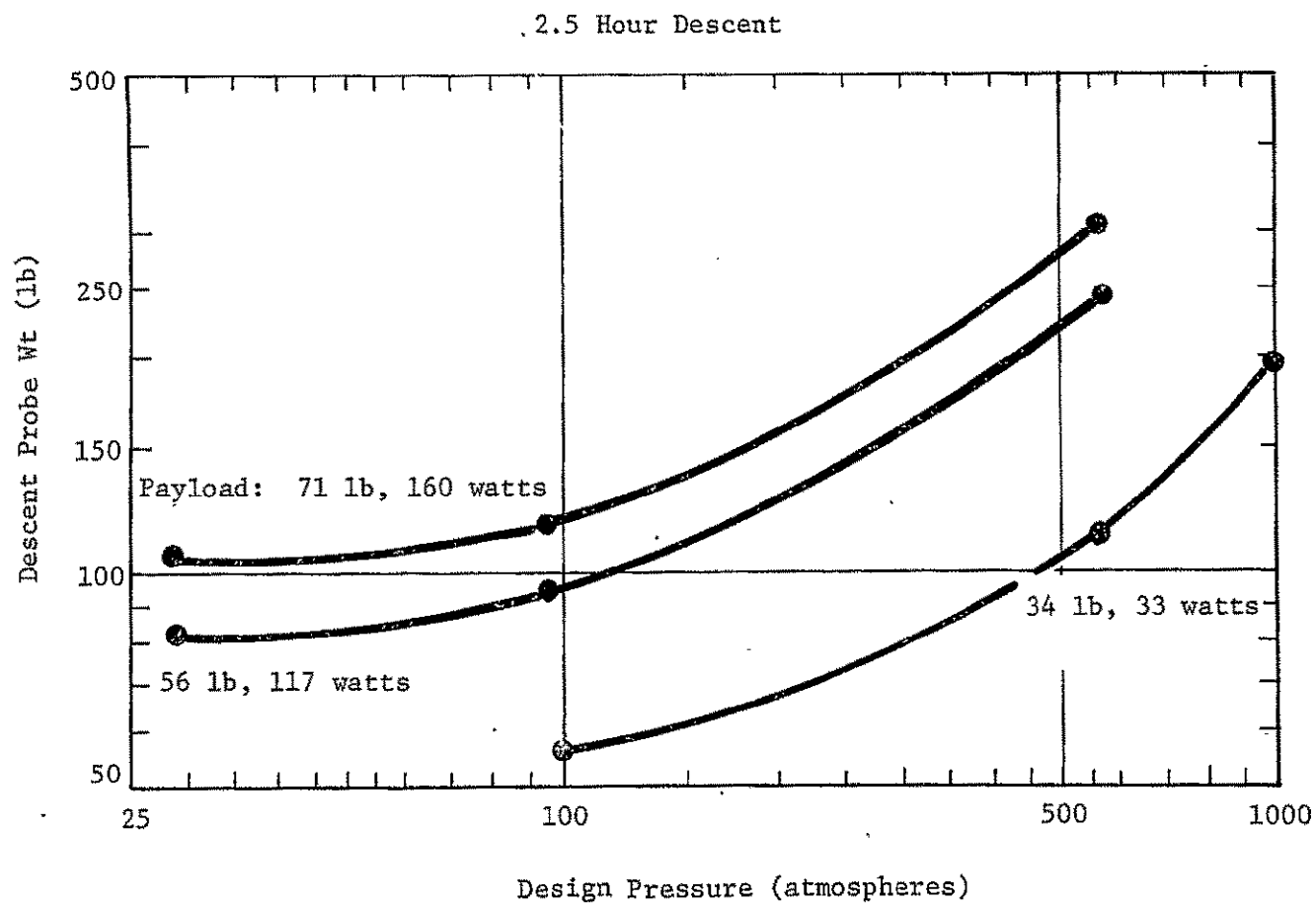


Figure VA-9 Descent Probe Weight vs Design Pressure, 2.5 hours

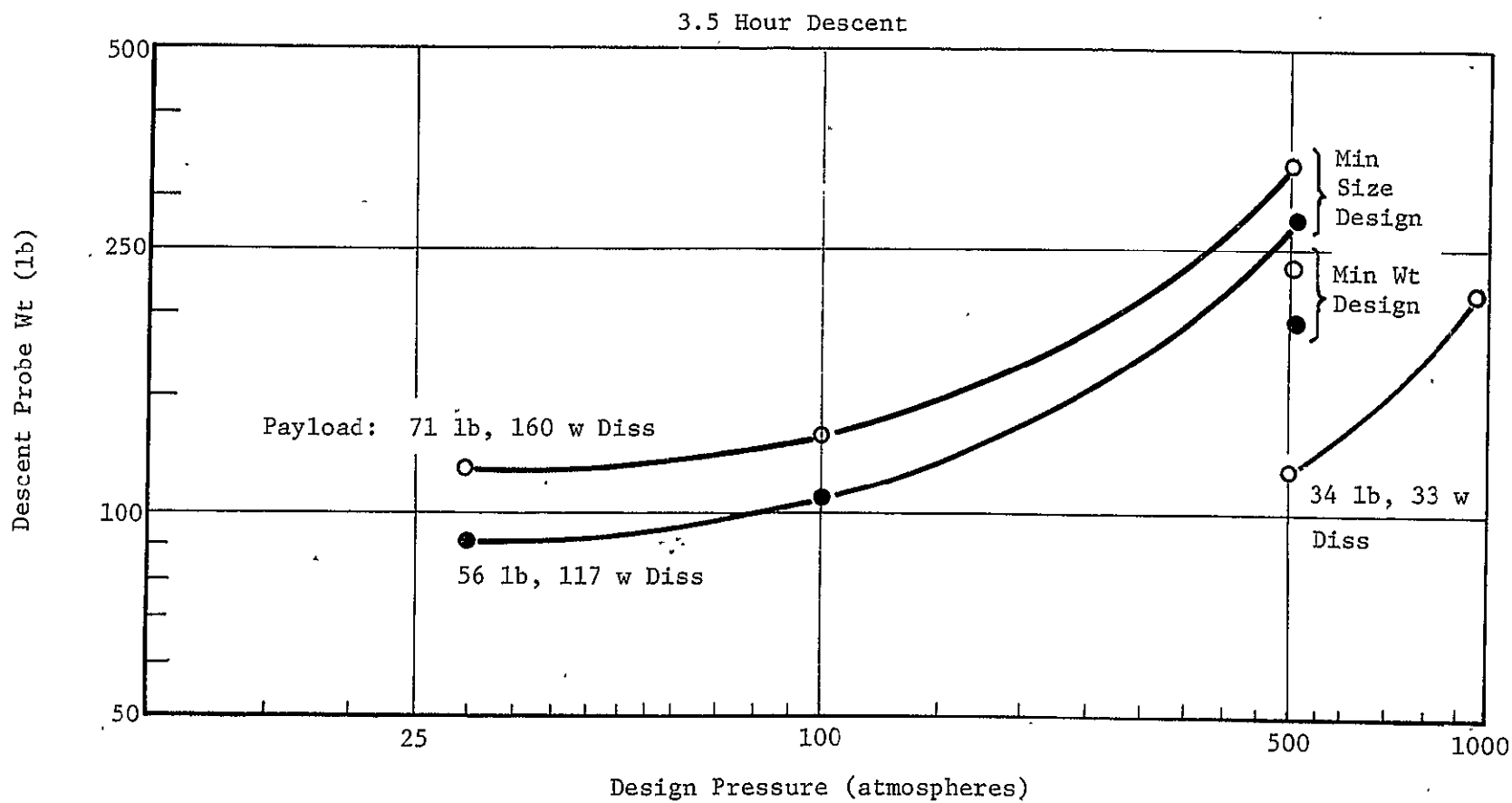


Figure VA-10 Descent Probe Weight vs Design Pressure, 3.5 hours

f. Results - Weight vs. Time for 1000 Atmospheres

Four ballistic coefficients (and corresponding descent profiles) were selected in order to analyze how the descent probe weight varied as a function of the time required to reach a depth of 1000 atmospheres. A single payload, a 2.5 watt transmitter split probe, and a single configuration, Min-K/Rene/Multilayer, were used. Figure VA-11 shows the total descent probe weights on a linear scale, and indicates that the descent probe weight is not as sensitive to descent time as it is to descent depth.

g. Results - Single vs. Split Probes

The data return problems of a single probe descending to the lower depths led to the evaluation of a dual relay, or split probe concept, as discussed in Volume II, paragraph IVB-2. The probe weight comparisons done early in the study showed a definite weight advantage for the split probe concept, and this comparison was repeated in the baseline parametric study. Figure VA-12 shows some of the results corresponding to an $R_p = 2.0$ and $\gamma_e = -20^\circ$. The "Split Probes" curve represents the sum of the upper and lower probes.

h. Results - Sample Missions

Table VA-3 presents the results of the thermal/structural analysis of the Sample Mission probes. Included are the basic inputs such as design pressure, equipment weight, etc.

i. Results - Baseline Parametric Missions

Table VA-4 presents the results of the thermal/structural analysis of the Baseline Parametric probes. The details on the Design Example are repeated in Table VA-5.

j. Results - Effect of Cool, Dense Atmosphere

To evaluate the effects of the Cool, Dense atmosphere on the thermal/structural design, the Design Example from the Parametric Study was selected as the descent probe. Since it was obvious that signal attenuation was the limiting factor (rather than the thermal environment), the Design Example was rerun in the Nominal atmosphere with a 60-watt transmitter instead of 40 watts. The comparative results are shown in Table VA-5.

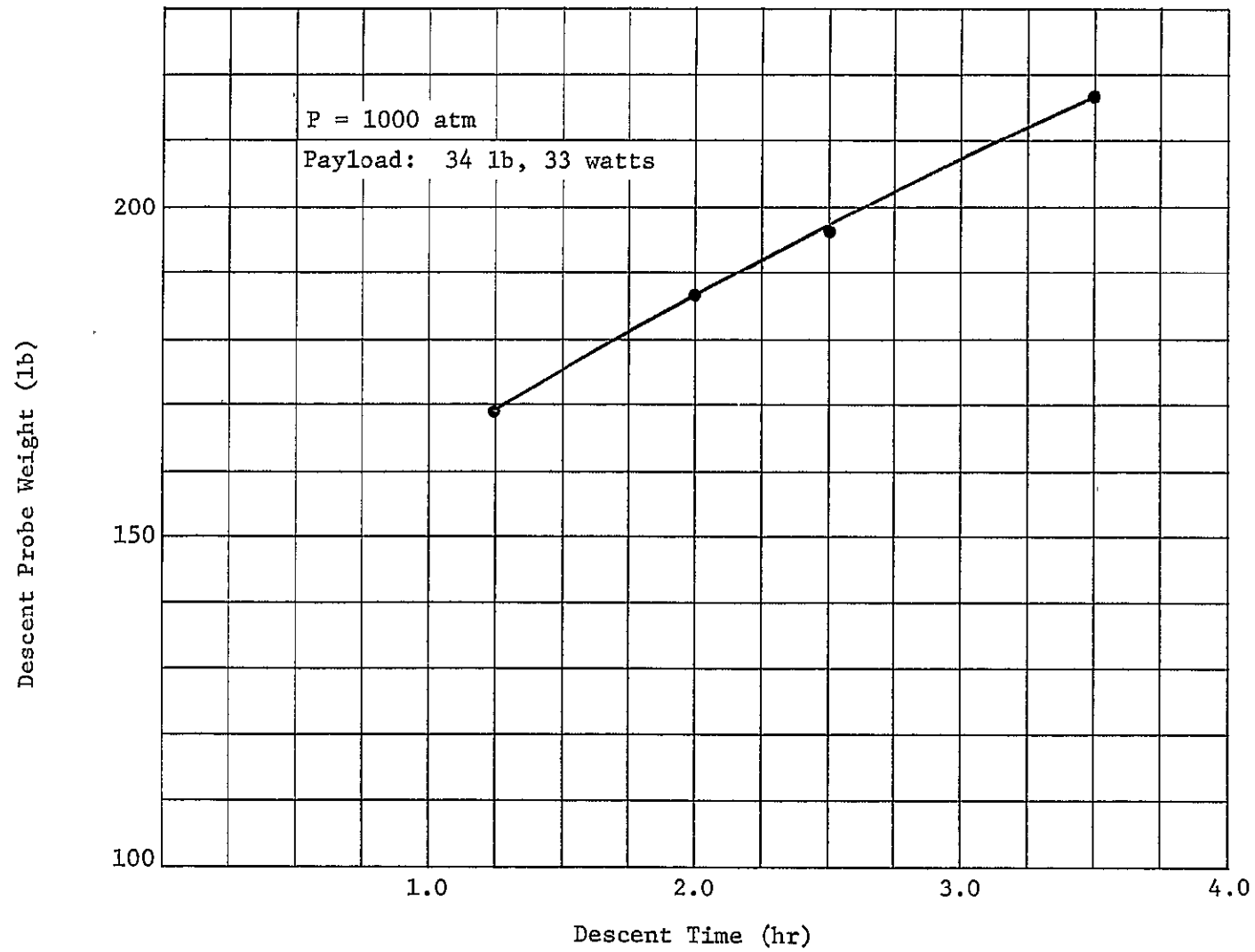


Figure VA-11 Descent Probe Weight vs Descent Time to 1000 Atmospheres

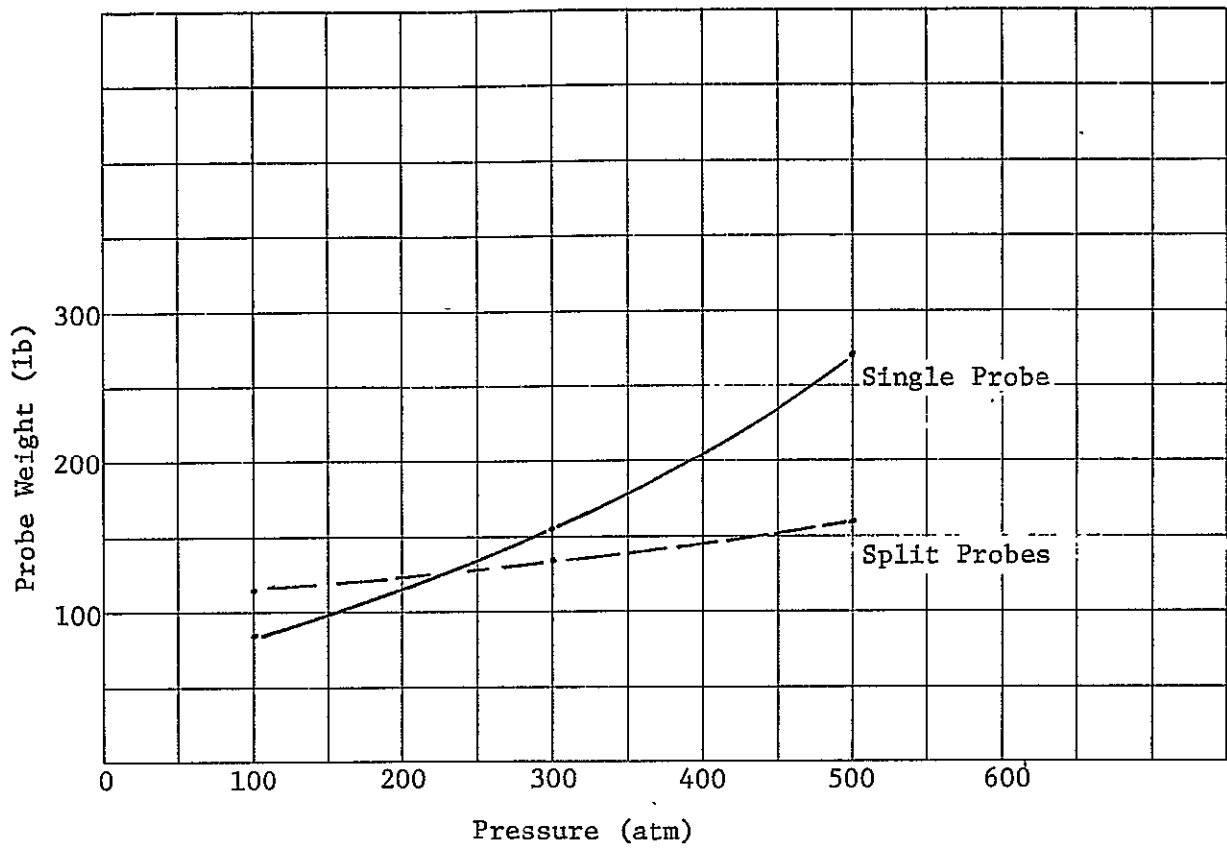


Figure V-A-12

Table VA-3 Thermal/Structural Results for Sample Missions

SAMPLE MISSION.	A -2 *		B	C	D	E
	Upper	Lower				
Design Pressure, atm.	10	100	73	73	17	100
Design temperature, °F	190	833	713	713	293	833
Descent time, hrs.	1	1	1.5	1.5	1.33	1.65
Equipment weight inside pres. vessel, lbs.	54.6	30.4	71.5	71.5	48.5	71.5
Power dissipation, watts	164	29	169	169	141	169
Configuration	T1/M-L	T1/M-L	T1/M-L	T1/M-L	T1/M-L	T1/M-L
Multilayer th., in.	.05	.25	.20	.20	.05	.25
Probe OD, in.	17.6	15.1	19.4	19.4	17.0	19.6
Weight, lbs.						
Pressure vessel	6.6	11.4	19.6	19.6	6.6	24.8
Internal structure	5.6	3.1	11.3	11.3	5.7	7.3
PCM	-	-	-	-	-	1.
Multilayer	0.2	0.5	0.8	0.8	0.1	0.9

*Sample Mission A-1 is the same as the A-2 upper probe

Table VA-5 Effect of Cool, Dense Atmosphere
DESIGN EXAMPLE

Transmitter size, w	40	60
Equipment weight inside pressure vessel, lb	63.6	73.0
Power dissipation, w	145.0	202.0
Configuration	Min-K/Inc/M-L	Min-K/Inc/M-L
Multilayer thickness, in.	0.3	0.3
Min-K thickness, in.	1.1	1.0
Probe OD, in.	20.6	21.3
Weight, lb		
Pressure vessel	49.5	57.3
Internal structure	8.7	10.2
PCM	4.0	7.0
Multilayer	1.0	1.2
Min-K	15.3	15.1

REFERENCES

1. *1975 Venus Multiprobe Mission Study*. Final Report MCR-70-89, Martin Marietta Corporation, Denver, Colorado, April 1970.
2. *Delta Class Venus Probe Mission Study*. Final Report AVSD-0433-60-RR, Avco Systems Division, Wilmington, Mass., October 1969.

PRECEDING PAGE BLANK NOT FILMED

B. Structures and Mechanics

1. Descent Probe

The descent probe is an integrated system that provides, as its primary function, the scientific instruments, communications, electronics, and the power subsystems that it contains with a controlled environment during a specified rate of descent through the Jovian atmosphere. However, prior to its descent phase where it is encountering an increasing pressure and temperature atmosphere, it must withstand the loads associated with launch and boost flight, planetary cruise, and the high G entry loads while captive in the entry aeroshell. In satisfying these requirements, the lowest weight design is usually the primary objective. The ambient pressure conditions impose the most severe design requirement on the descent probe. The probe's aerodynamic shape or auxiliary structure and its packaging in the entry aeroshell also have significant influence on the designs.

The main emphasis is in combining the structural configuration and material with the thermal control provisions to yield the lowest weight. The mechanics of the computer program employed in these evaluations have been discussed in the preceding Thermal Control Section. Structural inputs to the program are based on analysis methods discussed here.

The concept of the descent probe that was selected is essentially an evacuated pressure vessel with insulation, and in some cases phase change material for thermal control. The aerodynamics of the configuration are assessed in Section D and compared with the requirements for meeting the descent rate for science data gathering.

a. Pressure Vessel Design

The pressure vessel design involves material selection, shape and structural arrangement considerations, and determining the appropriate analysis procedure for the given pressure range. The loads due to the entry G's have little effect on the pressure shell design since the entry condition occurs at a time when the ambient pressure is practically zero and the entry dynamic pressure effects are not felt by the shell structure. The support of the pressure

vessel and the equipment within the pressure vessel for entry G's is accounted for and discussed later in this section.

Materials

The pressure vessel materials considered are ones having good strength/weight properties over the various temperature ranges along with good workability and weldability characteristics (with the exception of Beryllium). The yield strength data for the materials considered are shown in Figure VB-1.

In the high pressure range the wall thicknesses of low density materials are large enough to dictate "thick wall" analysis procedures. The resulting thickness penalties result in the normally optimum aluminum alloys not yielding the minimum weight even at very low temperatures, see Figure VB-2.

In intermediate pressure ranges, the normal hoop compression relations apply such that the maximum strength to density ratio materials do turn out to be optimum for any given structural temperature. Finally, at moderate-to-low pressures the Modulus/Density rates ($\frac{\sqrt{E}}{\rho}$) controls the material selection.

To establish the pressure where for any selected material a given stress formula applies, a study was performed and results are plotted in Figure VB-3. The curves define the limits that dictate the selection of the buckling formula, $(t^2 = PR^2 \sqrt{3(1-\nu^2)})/2E$ versus the hoop stress formula ($F_{cy} = PR/2t$). At the points where the curves cross use of either will result in the same wall thickness. On either side of the cross over point, the formula resulting in the larger wall thickness is required since both stress equations must be satisfied. The stress formula, ($F_{cy} = PR/2t$) takes on the thick-walled form ($F_y = P_3 R_o^3 / 2(R_o^3 - R_i^3)$) when the stress increase due to the thick-wall effect reaches a certain value. This point has been arbitrarily selected as when the thick-wall effect increases the stress or weight by 5 percent.

The values plotted include a safety factor and when multiplied by the radius of the pressure shell will yield the weight per square inch of surface area. However, it should be noted that the structural

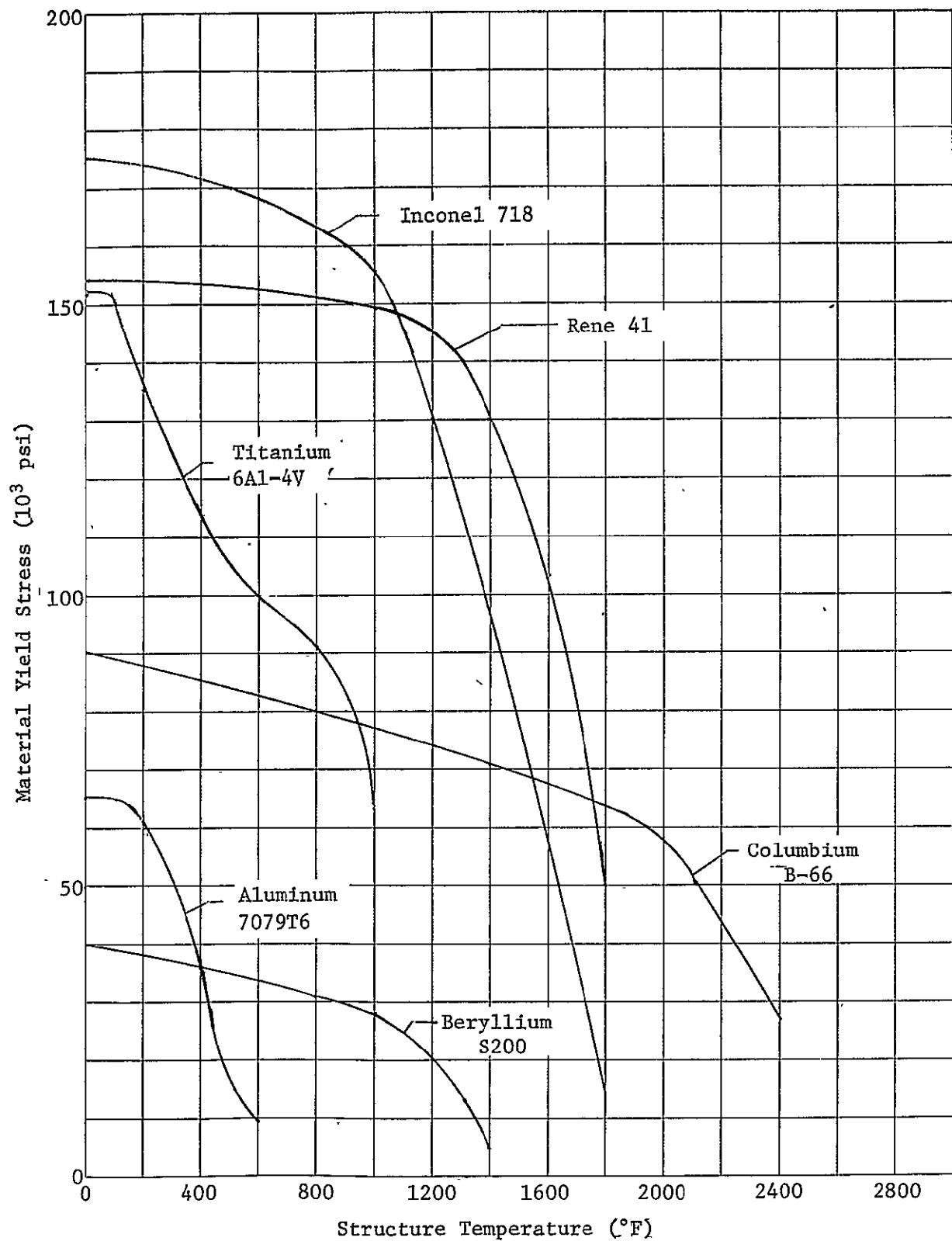


Figure VB-1 Compressive Yield Properties

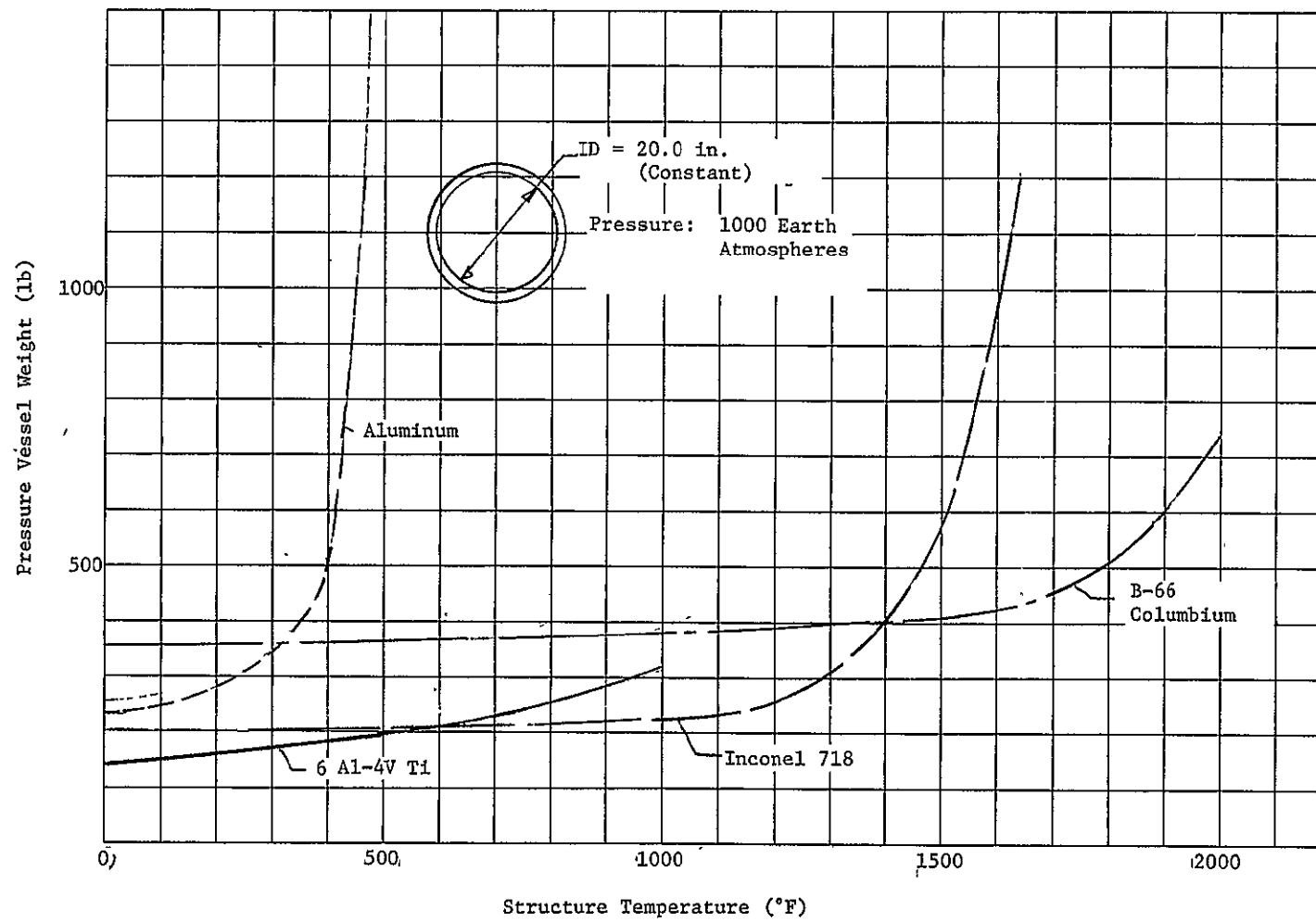


Figure VB-2 Pressure Vessel Weight

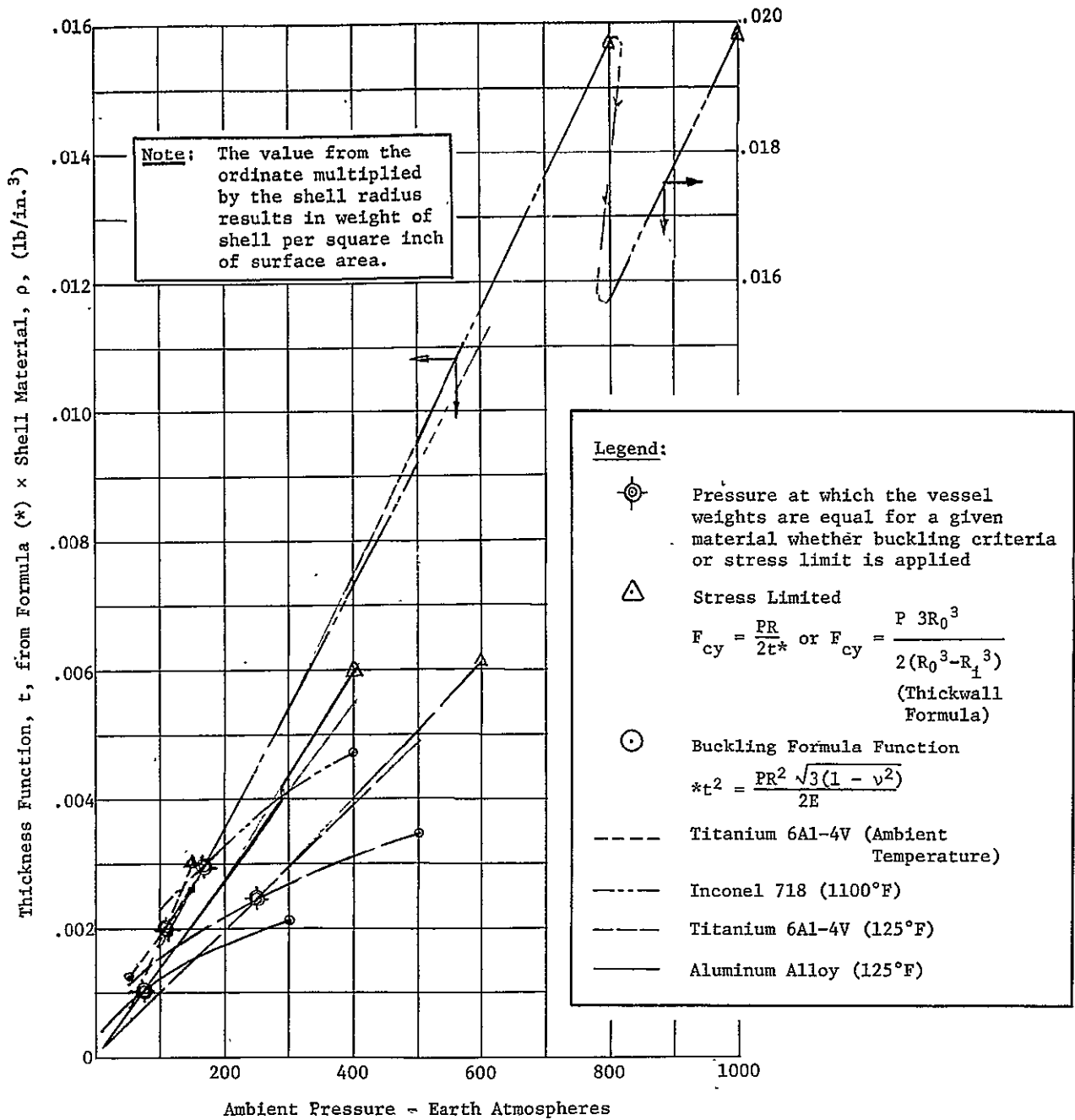


Figure VB-3 Stress/Material Selector

temperatures are different, as indicated, and hence require different amounts of external insulation.

The classical buckling formula, $(t^2 = PR^2 \sqrt{3(1 - \nu^2)}/2E)$ was used to calculate wall thickness in the low pressure range where shell stability was the problem. This calculates a monocoque shell thickness that has been proven by tests to be optimistic. By converting the calculated monocoque shell thickness into a waffle design and using a factor of safety, the weight associated with the use of the above buckling formula is appropriate for study purposes. One-half inch (approximately 5 percent of the radius) is added to the calculated radius of the equipment to allow for a stiffened structural shell.

Safety Factor

A safety factor of 1.25 is applied to the pressure at any condition being investigated to calculate a wall thickness. The use of the buckling formula with this safety factor is still optimistic since the actual pressure vessel will have numerous discontinuities in the shell such as added stiffness at penetration, assembly points, hard points for attachment of instruments, etc. Consequently, allocations of weight for these effects are added to the basic shell weight.

Auxiliary Structure

Allowance for pressure vessel closures and penetrations were made as a weight fraction of the shell weight. These were varied with the ambient pressure having the lowest value at the highest pressure condition.

Allowance for internal mounting structure was made as a weight fraction of the internal equipment and PCM weight since it must support them. These were varied directly with entry angle which is synonymous with entry G's.

The allowance for structure supporting the internal equipment and the pressure shell and penetrating the insulation also varies with entry G's but impacts the thermal design both by mass and as a thermal short across insulation.

The auxiliary structure for aerodynamic shape and stability is dependent upon final descent ballistic factor as well as entry G's. Weight allocations were made in consideration of these factors and had no standard rule of application.

Hydrogen Influence

The high pressure, high temperature hydrogen in contact with the structural materials, e.g., the pressure vessels, causes some concern. The classical H_2 embrittlement phenomenon, i.e., the saturation of the metal lattice structure with hydrogen atoms under pressure and temperature with subsequent precipitation in the dislocations upon cool-down, does not appear to be a problem since no cool down occurs. However, discussions with AMES Research Center Material personnel have indicated that just surface contact of H_2 with metals under tensile stress can cause failure, the mechanism of which is not understood. This phenomenon would not be anticipated to occur with the compressive stress field of the pressure vessels of the Jupiter descent probes, but no data exists to verify this. Also, it may be difficult to totally prevent the existence of tensile stresses in H_2 contact regions.

The uncertainties involved in design and material selection due to the presence of H_2 obviously require additional investigation before a hardware design is effected, but for purposes of this study the standard properties of the candidate alloys have been used.

Creep Buckling

The designs selected for the parametric study and the sample missions have utilized sufficient external insulation to lower structural temperatures to 1100°F or less. Also, total times of descent from 0° to 1100°F do not exceed 2.5 hours. Consequently, creep buckling is not considered to be a significant factor.

b. Integration of the Descent Probe in the Entry Aeroshell

Fitting the descent probes within the entry aeroshells influences the structural/thermal design of the descent probes. Small dimensions are desired for the descent probe in order to minimize the diameter required of the aeroshell. Small aeroshells result in minimum heat shield and aeroshell structure weight even though there is a tendency toward a thicker heat shield and heavier-gage structure with decreasing size (increasing ballistic coefficient) because the reduction in surface area more than offsets the thickness and gage increase. Consequently, in selecting the insulation and structural arrangement for the descent probe consideration must be given to the resulting total diameter.

The geometry of the entry vehicle also is constrained to meet stability requirements; i.e., to achieve a static margin the C_p must be sufficiently aft of the cg and for dynamic stability the roll-to-transverse inertia ratio must be greater than unity. These requirements dictate keeping the axial dimension of the descent probe as short as possible. This is difficult to accomplish in the case of the split probe concept where two separate probes are housed within the same aeroshell.

c. Split Probe Design Consideration

Due to the necessity of maintaining a short axial dimension it becomes desirable for split probes to deviate from the structurally optimum spherical shapes for the pressure vessels. Since the lower probe operates at much higher pressures, re-configuring it would be more costly in weight than reconfiguring the upper probe as can be seen in Figure VB-4.

Figure VB-5 depicts several candidate configurations for the split descent probe, in which the A and B options illustrate the problem of attempting to maintain both as spherical shapes. The result is a major penalty in the aeroshell size and weight and in the case of Option A, dynamic stability as well.

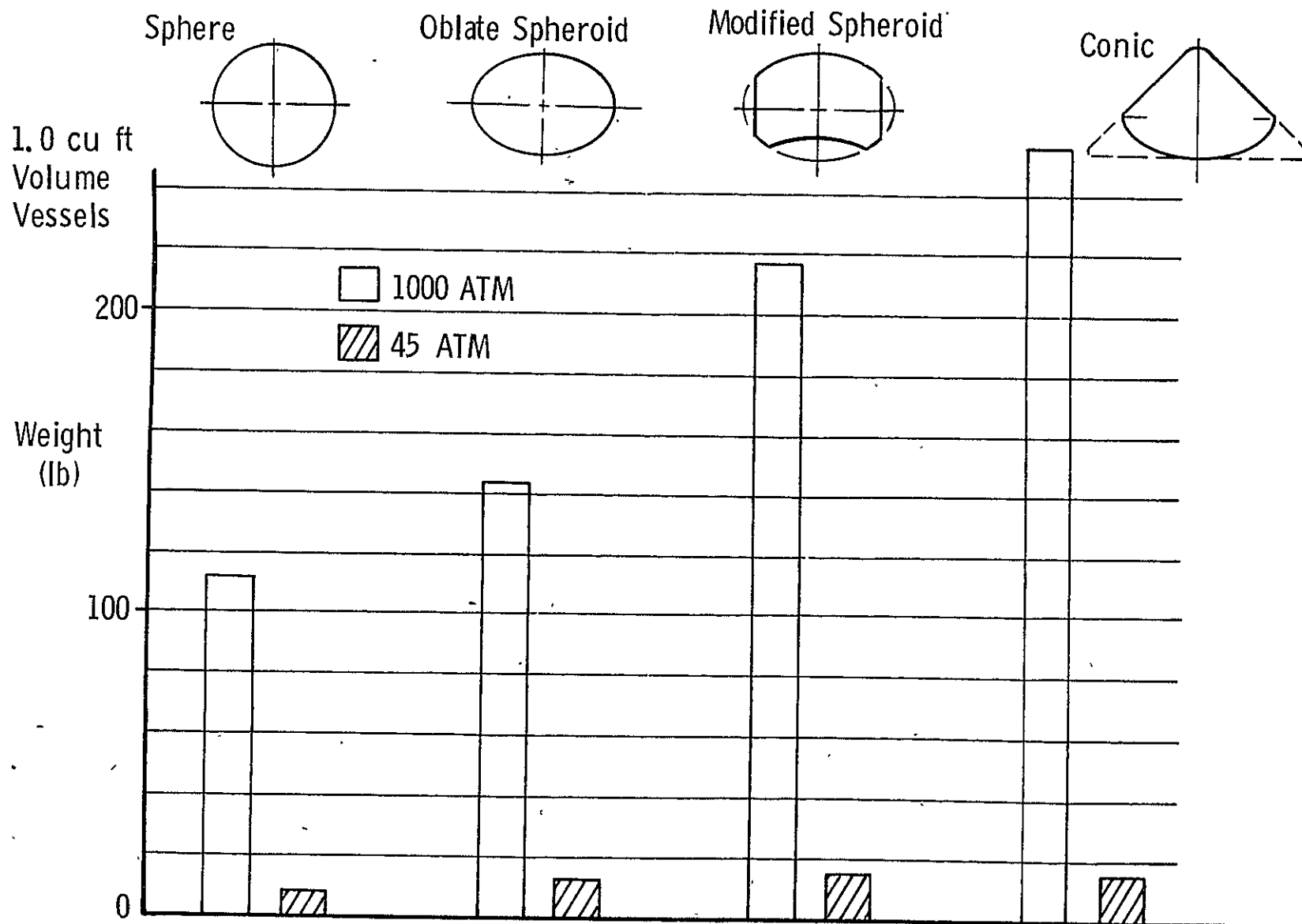


Figure VB-4 Pressure Vessel Shape/Weight Comparison

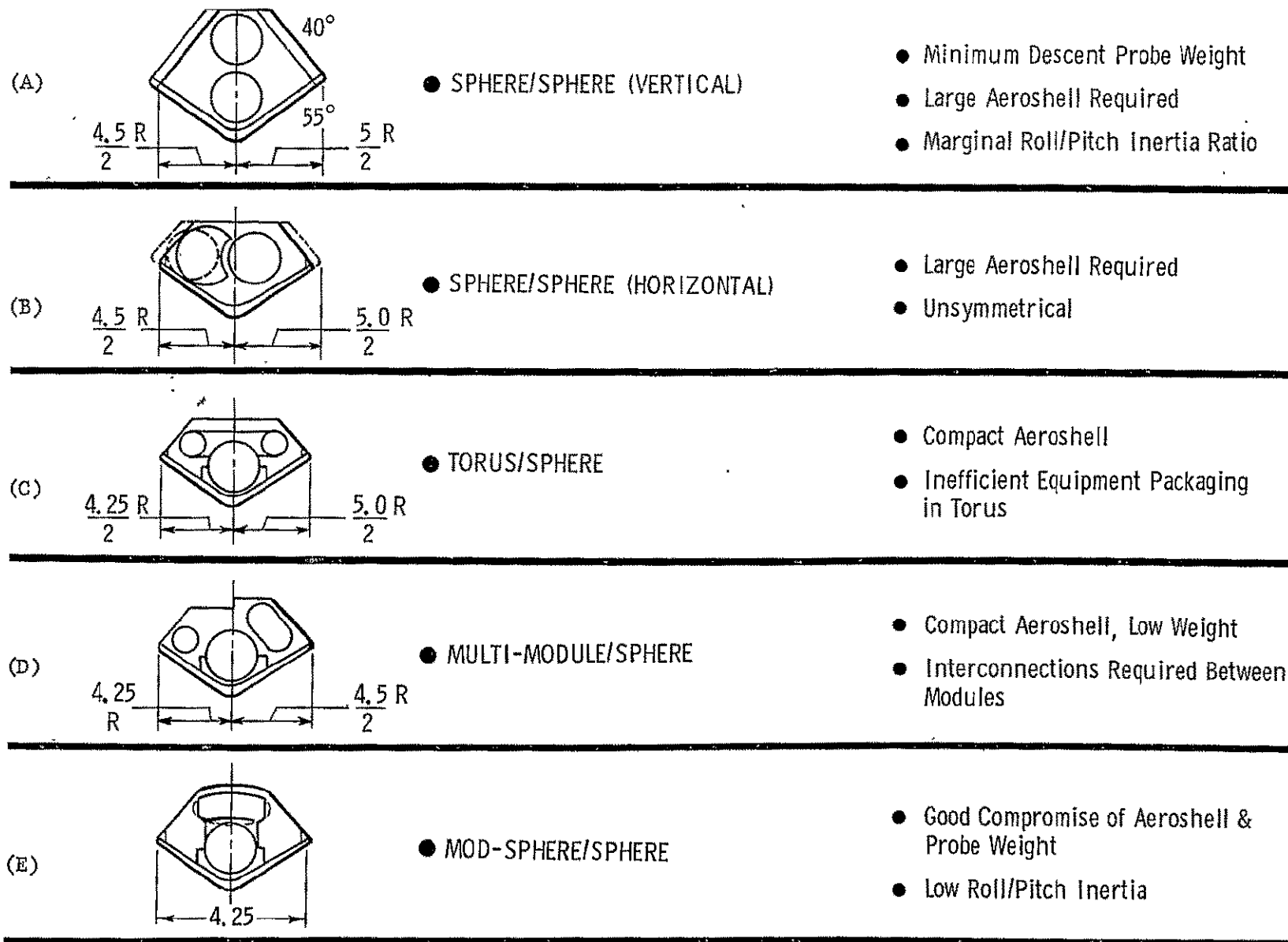


Figure VB-5 Candidate Configurations for Split Descent Probe

Resolving the upper probe volume into a torus shape, Option C, results in the most compact and dynamically stable design, but several problems are generated: 1) insufficient room to build any fixed aerodynamic stabilizing device on the lower probe, 2) a significant weight penalty to the upper probe because of a large surface area to volume ratio, and 3) equipment packaging in the upper probe is less efficient due to the unconventional shape and small cross section size. Because of the much larger surface area, the thermal control problems are also significantly increased. Of these, the major disadvantages stem from the added complexity of closures and the difficulties in installation of equipment within the torus.

Dividing the upper probe into 3 equal modules, Option D, results in a shallow and dynamically stable entry vehicle. Dividing the equipment into three modules does result in more cabling to interconnect the modules. Also, since each of the modules is a pressure sustaining structure, there are more penetrations, complexity of closures and insulation installation, and an interconnecting structure would have to be provided to maintain a rigid mount between the modules.

Utilizing a cylindrical shell as the primary mount for these individual modules as well as for the interconnecting ducts and cabling, antennas, and parachute loads results in the lightest weight. The alternative of nesting the modules in the aeroshell against the cone structure requires a substantial cylindrical shell for payload extraction loads in addition to an appreciable beef-up of the aeroshell due to localized load inputs.

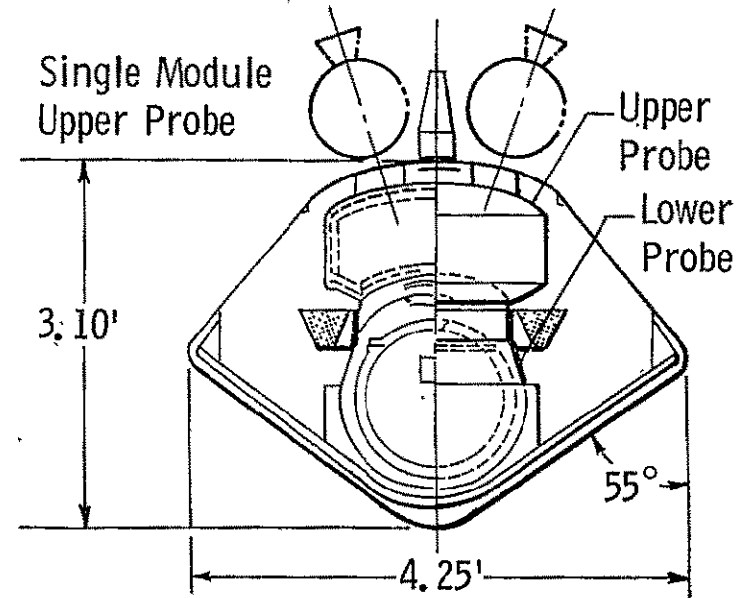
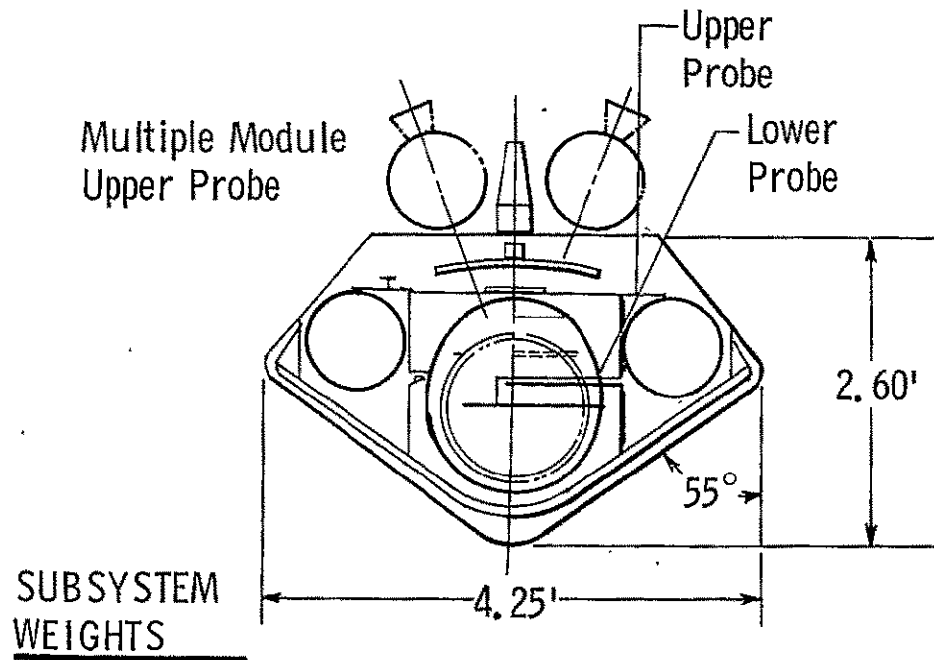
The single-module non-spherical design approach of the upper probe of configuration E causes a minor pressure shell weight penalty as was indicated in Figure VB-4 chart. The remaining structure, thermal control, and incidental weights such as cabling, etc, are minimum however

since the probe shell and equipment make up a compact well arranged design resulting in efficient packaging. A small weight penalty is also incurred in the lower probe in the form of a structural stiffening of the outside cover between its interface with the aeroshell ring beam and where it is extended to provide an adapter for the upper probe. An interconnection is necessary to allow extracting both probes out of the aeroshell with one parachute. Option E is more desirable from the standpoint of its greater simplicity and ease of internal packaging than Option D, however, the probes stacked along the centerline results in a lower ratio of roll to transverse inertia than is the case for Option D. For some situations this ratio approaches 1.0 and Option D becomes marginal.

Both configurations D and E are regarded as acceptable candidates and they result in essentially the same weight, see Figure VB-6. For the Trial Mission, Option D was selected. For the smaller probe of Mission A-2 the single-module version, Option D, was selected due to the exceedingly small diameters which would have resulted if separate modules were to be used and since adequate dynamic stability could be maintained.

2. Aeroshell

The aeroshell structural weights for all configurations are based on parametric curves (Figure VB-7) that show weight as a function of design pressure, cone half angle, and base diameter. The aerodynamic shape is a blunted cone with an initial R_N/R_B of approximately .10. The weights shown are applicable to both 55° and 60° cone-half-angle bodies.



**SUBSYSTEM
WEIGHTS**

Upper Probe	115 lb	101
Lower Probe	199	199
Aeroshell (basic)	75	79
Probe Support Structure	12	18
Heat Shield	263	270
Defl, Approach, and Staging	55	55
Entry Wt.	719 lb	722 lb

Figure VB-6 Comparison of Configurations - Trial Mission

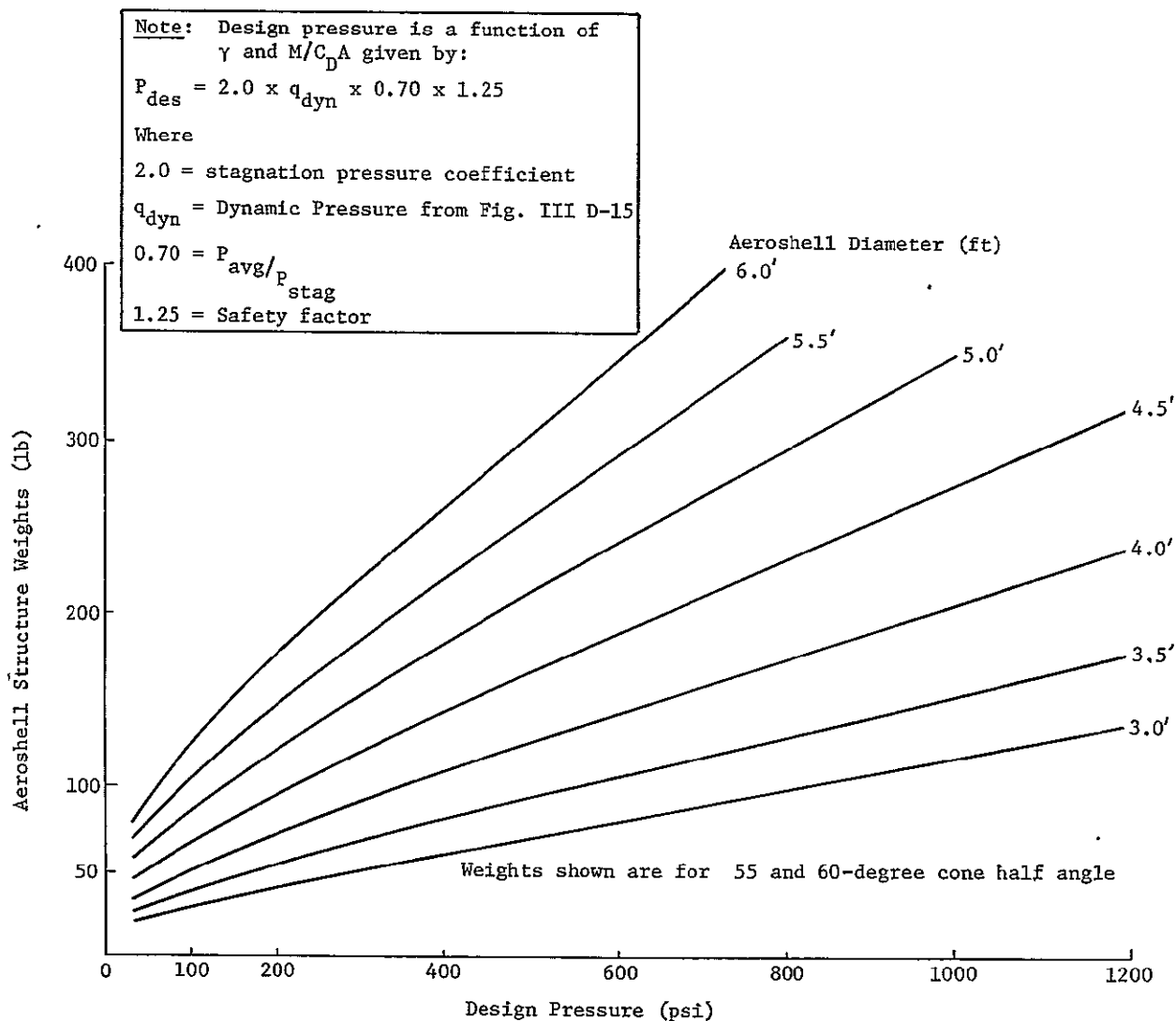


Fig. VB-7 Aeroshell Parametric Weights

The weights are calculated for frame-stabilized aluminum monocoque shell construction. They include allocations for the nose cap, forward cone body, base diameter ring frame, a nominal base cover, and an internal ring beam and adapter to effect a uniform load distribution at its interface with the forward cone. The ring beam allocation is for loads consistent with low, $\gamma = 15^\circ$, entry angle. A ring beam weight increment must be added for higher entry angles to compensate for the higher decelerations generated. This is accomplished for each probe design separately.

The weights of Fig. VB-7 tend to be conservative at higher pressures (higher entry angles) because designs are optimized for moderate pressures ~ 100 psi.

Frame stabilized aluminum monocoque designs have been compared with aluminum sandwich construction designs and the two found to yield approximately the same weights. Titanium sandwich however was found to be approximately 12 percent greater in weight than the aluminum. Since higher temperature capability structures are probably desirable for the Jupiter entry application, titanium sandwich is a likely candidate material. It is estimated that an optimized titanium sandwich shell utilizing the latest technology would result in achieving the weights shown for the aluminum designs. Consequently these data are used in the probe designs of this study. Some conservatism exists since further developments by 1975 could significantly improve the weight picture, e.g., beryllium or carbon fiber composites afford potential weight savings. However, due to the uncertainty of the heat shield design and the resultant aeroshell structural temperatures the use of lighter weights for aeroshell structure is not deemed appropriate for this study.

The aeroshell body is covered over the base but is vented to allow pressure equalization. All probe configurations require staging out of the aeroshell after entry.

The descent probes are mounted symmetrically within the aeroshell in a forward-most position. An aeroshell ring beam provides the transition structure between the aeroshell cone and the probe support to realize a uniform loading at their interface. The probe depth along the roll axis is minimized in an effort to achieve a highest roll to transverse inertias ratio for spin stability. The parachute is centered behind the probes in a

large diameter shallow canister. It becomes deployed when the aeroshell base cover is separated and jettisoned. The entry vehicle attachment to a spacecraft is through attachments at the base diameter ring frame.

The pre-entry communications equipment and power are located within the aeroshell cavity divided into 3 packages so as to promote the desirable inertia ratio. The spin-up and de-spin systems are mounted at the major ring frame on the base of the aeroshell. The pre-entry tracking antenna is aft pointing mounted on the roll axis.

The deflection propulsion module is an integral system mounted on the aft end of the base cover. It is made up of 3 motors to allow positioning concentric around the pre-entry tracking antenna. It separates and jettisons immediately after being spent.

The base cover separates at the major ring frame and is jettisoned by firing pyrotechnic thrusters. The removal of the base cover allows the main parachute to deploy followed by pyrotechnic release of the probe at the ring beam. A lower ballistic coefficient of the probes on parachute as compared to the empty aeroshell effects separation and jettison of the aeroshell from the probes.

Ballistic Coefficient Requirements

The selection of aeroshell diameter is normally based on the smallest diameter which will contain the contents. In the case of steep-entry angles, the resulting ballistic coefficient results in penetration to too low an altitude before the probe slows to a subsonic velocity suitable for staging and instrument deployment. Figure VB-8 shows the required ballistic coefficient as a function of entry angle. The $P = 0.2$ ATM curve of the figure was used to establish ballistic coefficients for the parametric study probes as well as the sample missions.

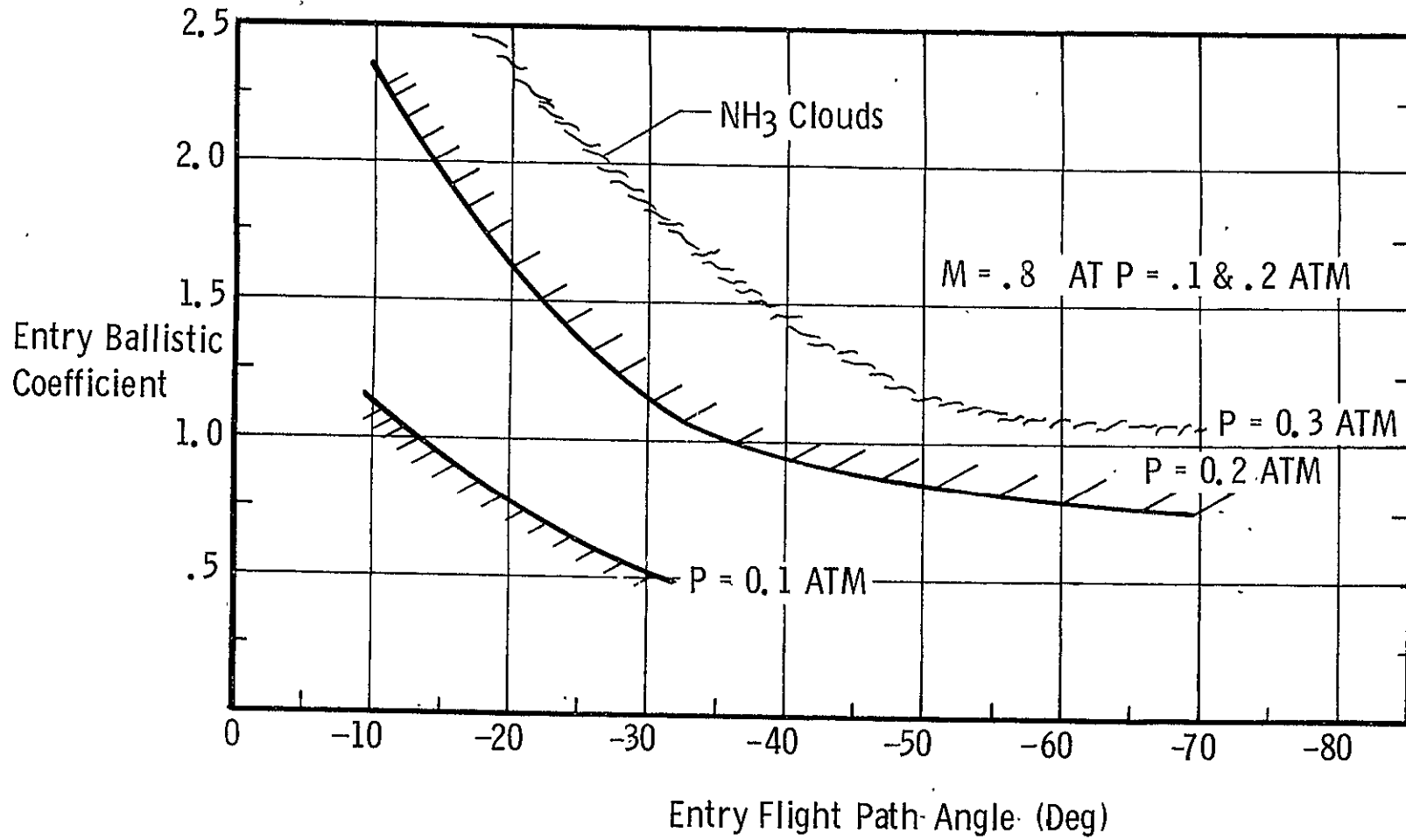


Figure VB-8 . Effect of γ_E On Required Ballistic Coefficient

3. Probe Adaptation to Spacecraft

The general criteria for mounting the probe on the spacecraft are similar for both the TOPS and Pioneer in that the probes should impose little, if any, change to the spacecraft normal mode of operation. However, the two spacecraft are fundamentally different in that the TOPS is a 3-axis stabilized vehicle system while the Pioneer is a spin stabilized system, so the mounting requirements are considerably different. The impact of probe adaptation and systems integration are discussed and summarized for each spacecraft. Figures VB-9 and VB-10 show the integrated planetary vehicle systems with principal design features identified.

TOPS Spacecraft Mounting

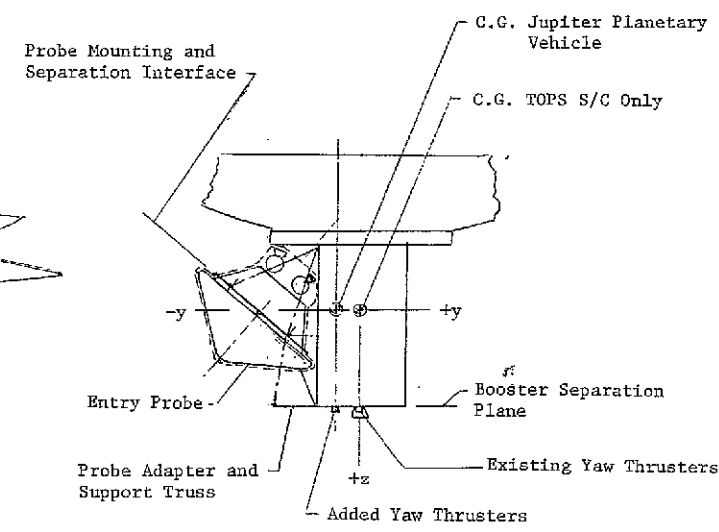
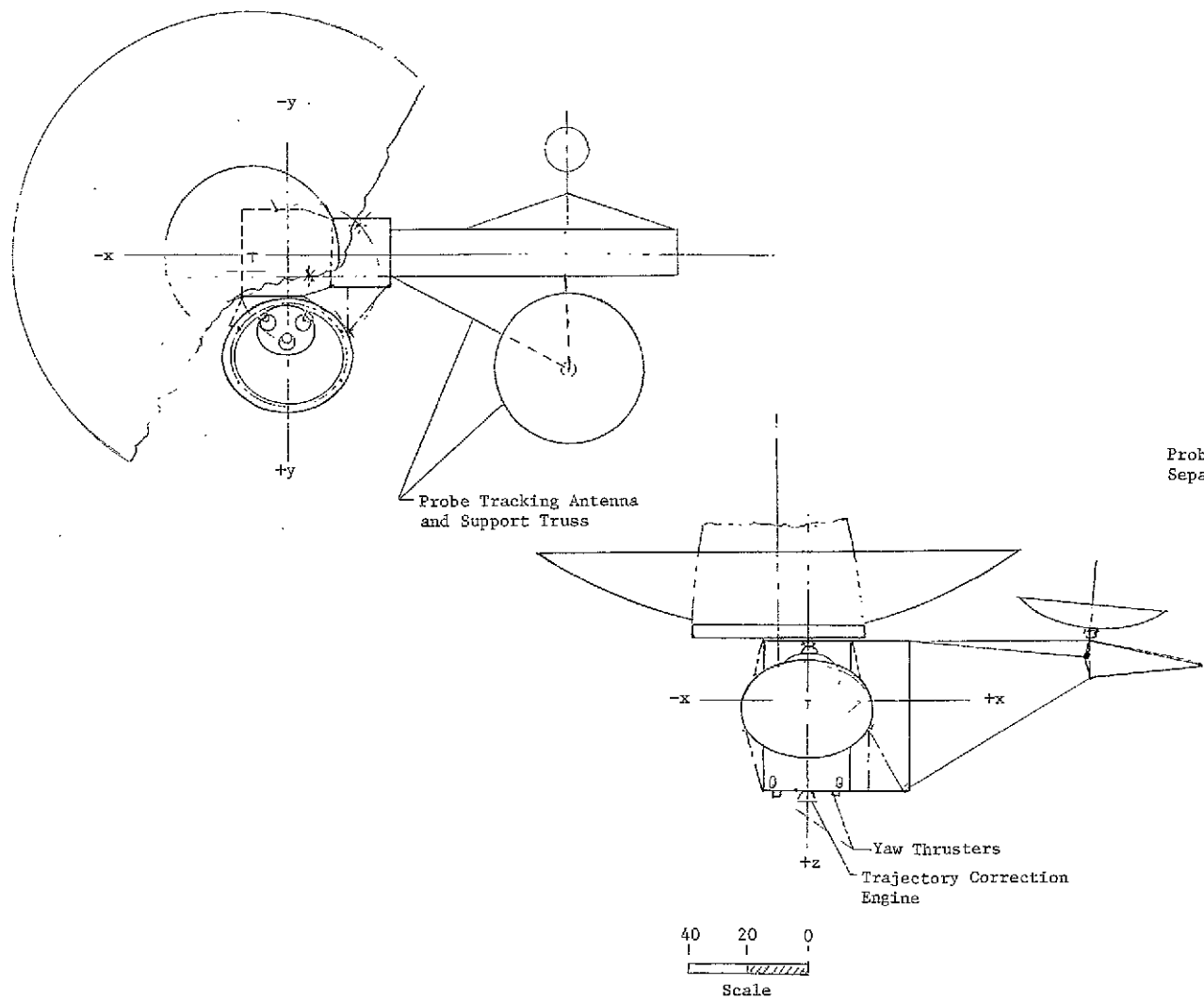
Either side of the spacecraft propulsion equipment compartment is suitable for the location of a probe. The c.g. of the TOPS spacecraft flight configuration is on the Z-Z axis at approximately the centerline of the propulsion compartment. Mounting the probe with its centerline at an angle of 40° with the X-Z plane tilted in a Y-Z plane results in the least offsetting of the planetary vehicle c.g. with respect to TOPS c.g. Moving the plasma wave detector and/or the plasma wave deflector booms out on the RTG truss will also allow nesting the probe up closer to the high gain antenna so that the c.g. shift is only along the Y-Y axis. Figure III-VB-9 shows the geometry and the resulting position. The resultant shift in the c.g. is approximately 7.0 inches for a 3.5 ft diameter 450 pound probe. The trajectory correction motor can be re-aligned to compensate for the c.g. shift.

Attaching and supporting a single small probe may be done by cantilevering off the equipment compartment and would result in less c.g. offset consistent with the size of the probe. Support of dual small probes such as for the multiplanet mission D would result in essentially no c.g. shift for a part of the mission particularly for launch and boost flight when higher loads are experienced. Either both the plasma

wave detector and the plasma wave deflector booms should be moved to the RTG truss to allow locating the probes on the y-y axis, or - neither need be moved in the interest of symmetry by locating the small probes opposite each other in the z-y plane. The trajectory correction engine needs no realignment in either case until an impulse is required after separation of the first probe at Jupiter.

The larger and heavier probes would be mounted in a similar manner with the major objective being to minimize spacecraft c.g. offset. For the Trial Mission where the probe separated weight was 803 pounds, the c.g. offset was 17.0 inches which was large enough to require a relocation or modification of the trajectory correction engine and the institution of additional attitude control sets designed to produce force couples.

The probe mounting structure would include a truss structure extending from the corner and edge members of the equipment compartment where structural stiffness is apparent. The truss system will incorporate a ring frame at the probe interface



FOLDOUT FRAME

Figure VB-9 Planetary Vehicle Config.
(Tops Spacecraft)

FOLDOUT FRAME

2

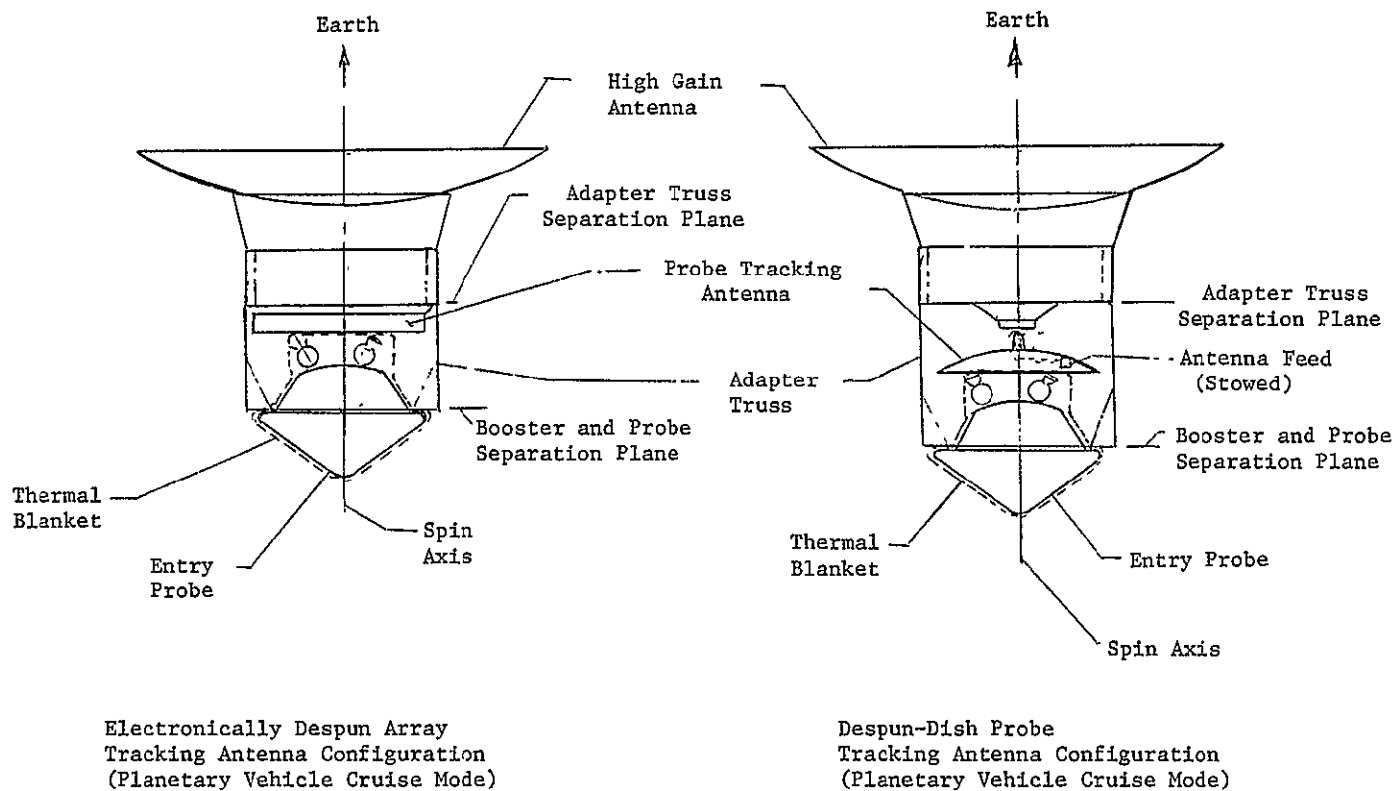


Figure VB-10

to provide for rigid probe mounting and separation mechanisms support. The probe will separate by pyrotechnic release of attachments and be pushed off from the spacecraft by springs. Tip-off is not critical since the probe has an active attitude control system to maneuver the probe into position for imparting the ΔV impulse. The eccentricity of the separation forces on the TOPS will be counteracted by the spacecraft attitude control system.

Pioneer S/C Probe Mounting and Implementation

The probe is mounted symmetrically on the spacecraft spin axis to have the least effect on spacecraft stability. The mounting for the 477 lb probe of mission B is shown in Figure III-V-B10 and is compatible with maintaining the spacecraft spin axis as the maximum inertia axis. For larger probes, the transverse axes tend to become the maximum inertia axes unless shallower, larger-diameter probes are designed (which are not minimum weight probes).

The probe mounts by a truss that also serves as the booster adapter for the spacecraft. In this position the probe intercepts the equipment's line of sight to the deep space for heat rejection through the louvers. Repositioning of the louvers and other modifications to the thermal control system are discussed in Section A.

The probe is pyrotechnically disconnected and separated from the spacecraft while spinning by means of axial compression springs. Probe re-orientation for impacting the deflection impulse will be achieved with its active attitude control system.

The cylindrical adapter truss will be pyrotechnically disconnected and separated from the spacecraft by means of axial springs. It is jettisoned because it would interfere with the probe tracking antennas that operate after separation of the probe.

The asteroid/meteoroid detector instruments and the low gain antenna will require relocation.

4 Spacecraft Structural Modifications

The addition of the probe to the spacecraft to be supported during launch and cruise mode will require some structural redesign and reinforcement of existing structure, particularly in the equipment compartment framework. The addition of a probe tracking antenna poses some mounting problems that were a trade-off with operational capability on the Pioneer mission.

TOPS Probe Tracking Antenna

A 3.4 to 4.9 foot diameter probe tracking antenna is truss mounted on the spacecraft's scan platform inboard truss. The truss deploys from folded position for booster installation, through a rotation about a single hinge axis where it locks for support of science equipment. The antenna in this position with a 2-axis gimbal is capable of scanning in the planet direction in plane of the flyby from the steep angle entry preperiapsis missions to the post-periapsis dark-side probe position. The second degree of freedom allows a transverse scan range to cover the error in trajectory or entry path after separation from spacecraft.

Booster Installation - TOPS

Installation of the planetary vehicle system on the Titan III/Centaur/Viking shroud is shown in Figure III VB-11.

Pioneer Probe Tracking Antenna

Two concepts of a despun antenna system were considered for a specific pre-periapsis flyby/probe mission, Mission B. These included an electronically despun array spanning across the base of the spacecraft body, nested between the body and the probe, and a mechanically despun dish antenna that nests above the probe mounted off the spacecraft body

at the spin axis. These antenna and probe installations are shown in Figure III VB-12. The electronically despun antenna is discussed in Chapter IV. Considerations of weight, complexity and technology development have resulted in the selection of the mechanically despun system as the first choice.

For the range of probe tracking coverage required for Mission B, $\pm 45^\circ$, both antennas mount in the same location but the dish antenna occupies more depth. The antennas become operational when the probes and their adapter trusses are separated to remove direct physical obstacles. The rotating RTG's and Magnetometer also are clear of the antenna field of view for the $\pm 45^\circ$ scan angle coverage.

The concept of despinning a portion of a spinning spacecraft has been proven on various satellite designs such as the OSO series, ATS, and others. The feasibility of this concept is questionable only insofar as the vacuum effects on mechanical design reflect on reliability of performing after a 3-year cruise enroute where the mechanism is locked inoperative. The phenomenon of "cold welding" presents the primary problem with mechanical designs that employ bearings. Consultations with Ball Brothers Corp. personnel who have been active in the design of the aforementioned operational hardware have resulted in the conclusion that it is feasible to employ a mechanically despun antenna system on a Jupiter Probe mission spacecraft. Weight estimates, presented at the end of this section also resulted from the discussions with Ball Brothers Corp.

The mechanical features in question, alternatives considered to their solution, and conclusions with regards to the antenna platform despin mechanism and the antenna gimbals, are discussed in the following paragraphs. The design feasibility is contingent upon the following assumptions and constraints. The despin drive is shown in Figures VB-13 through VB-15.

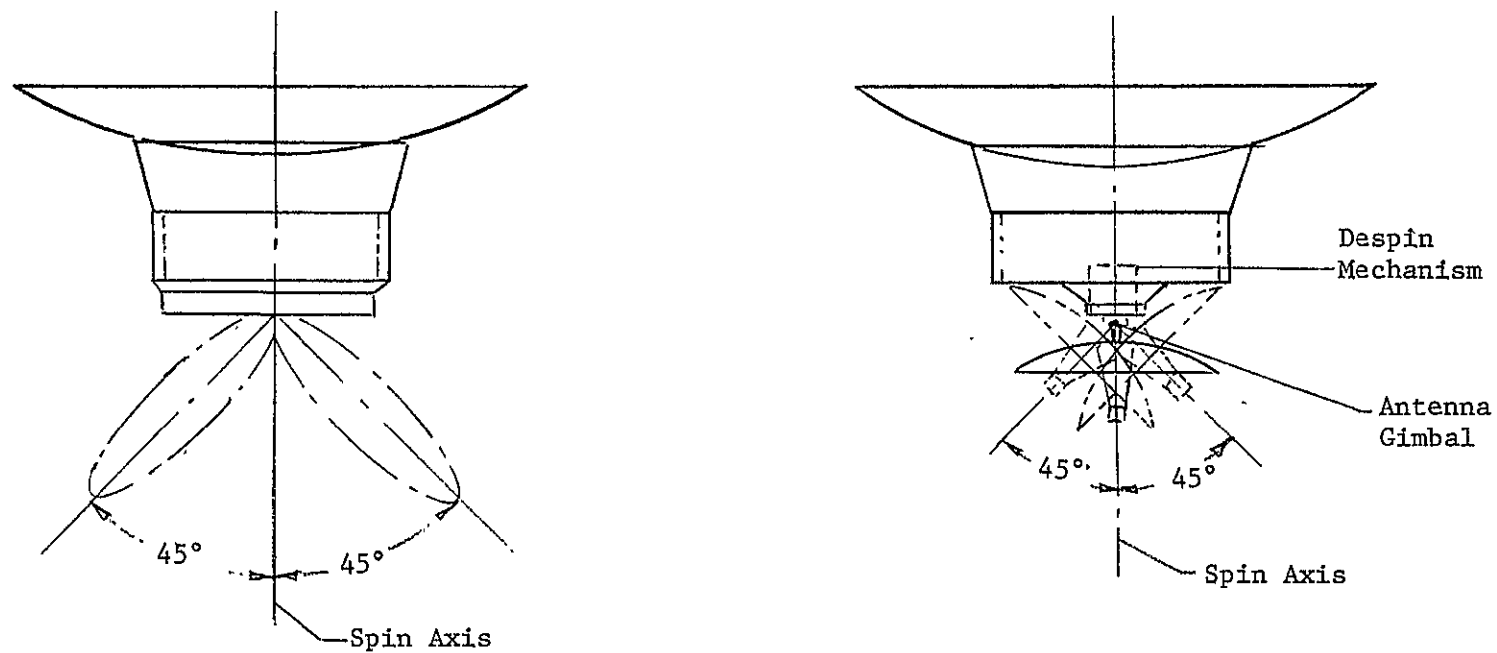


Figure VB-12

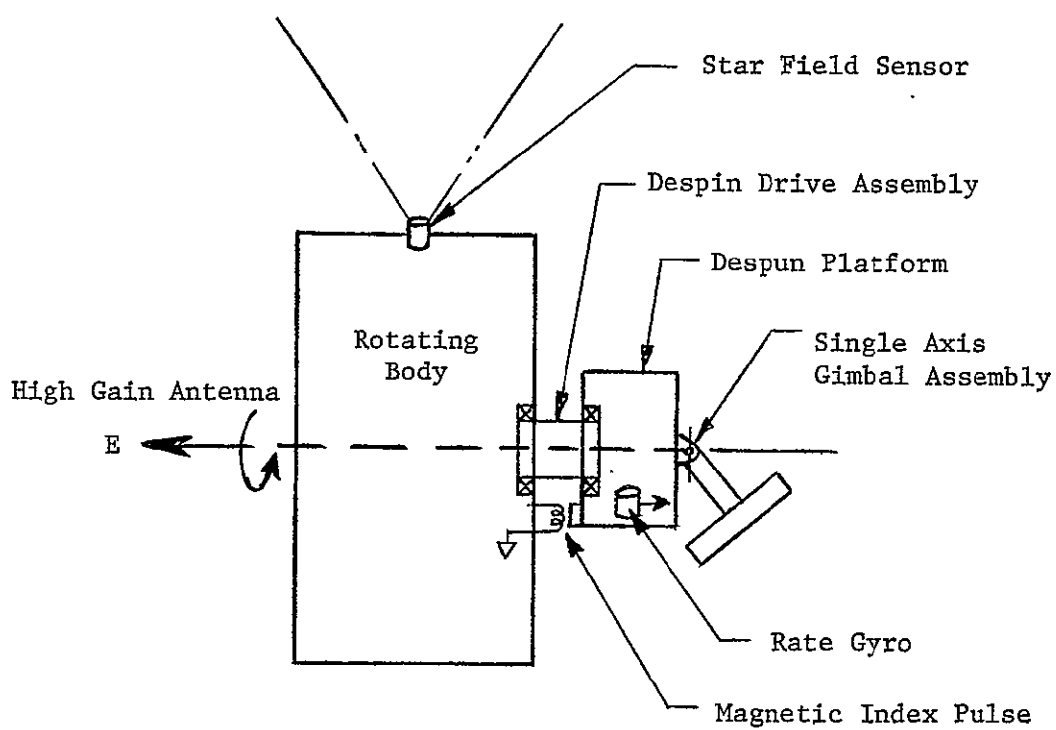


Figure VB-13 Typical Application of Mech. Despun Platform

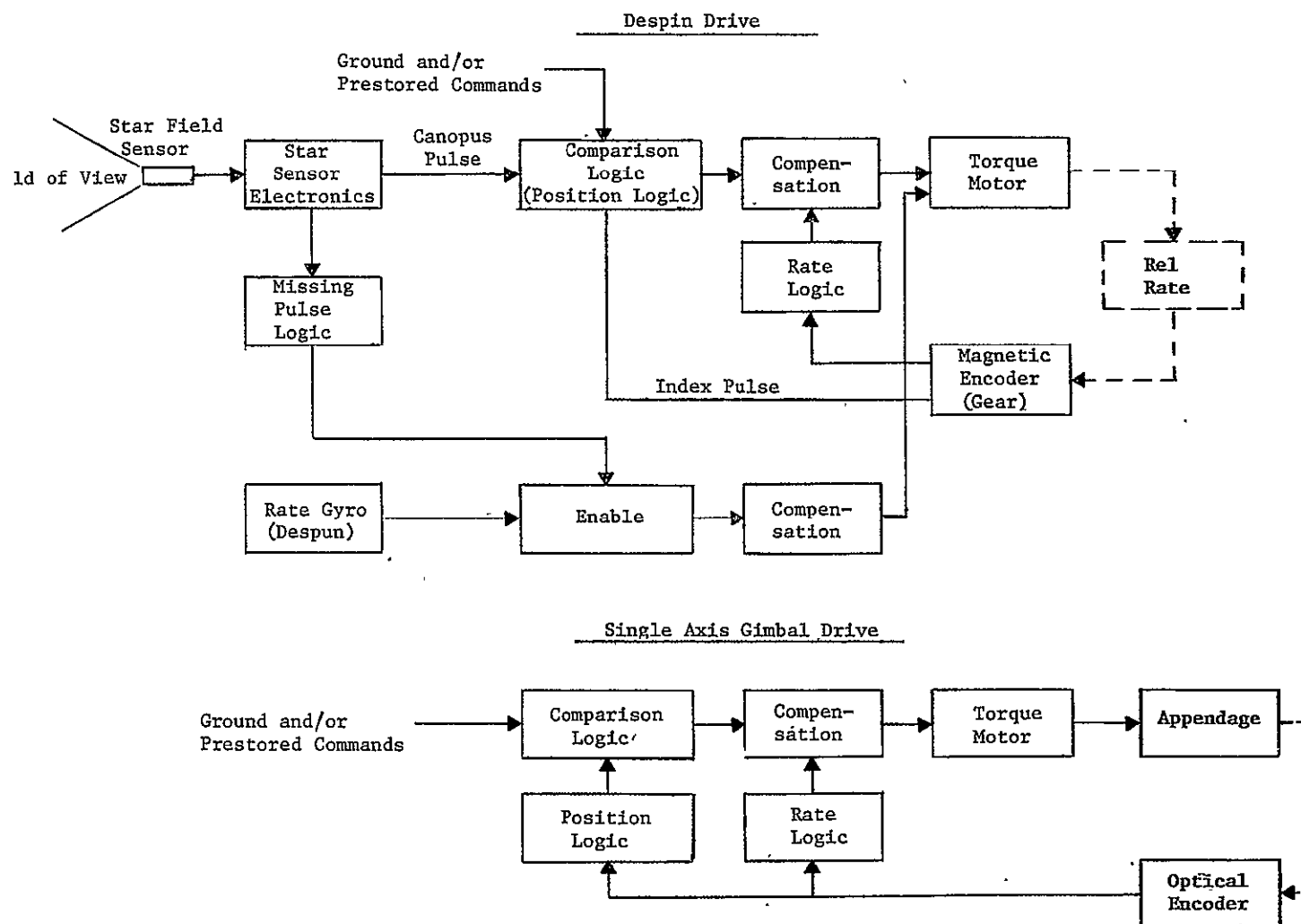


Figure VB-14 Functional Diagram of Typical System

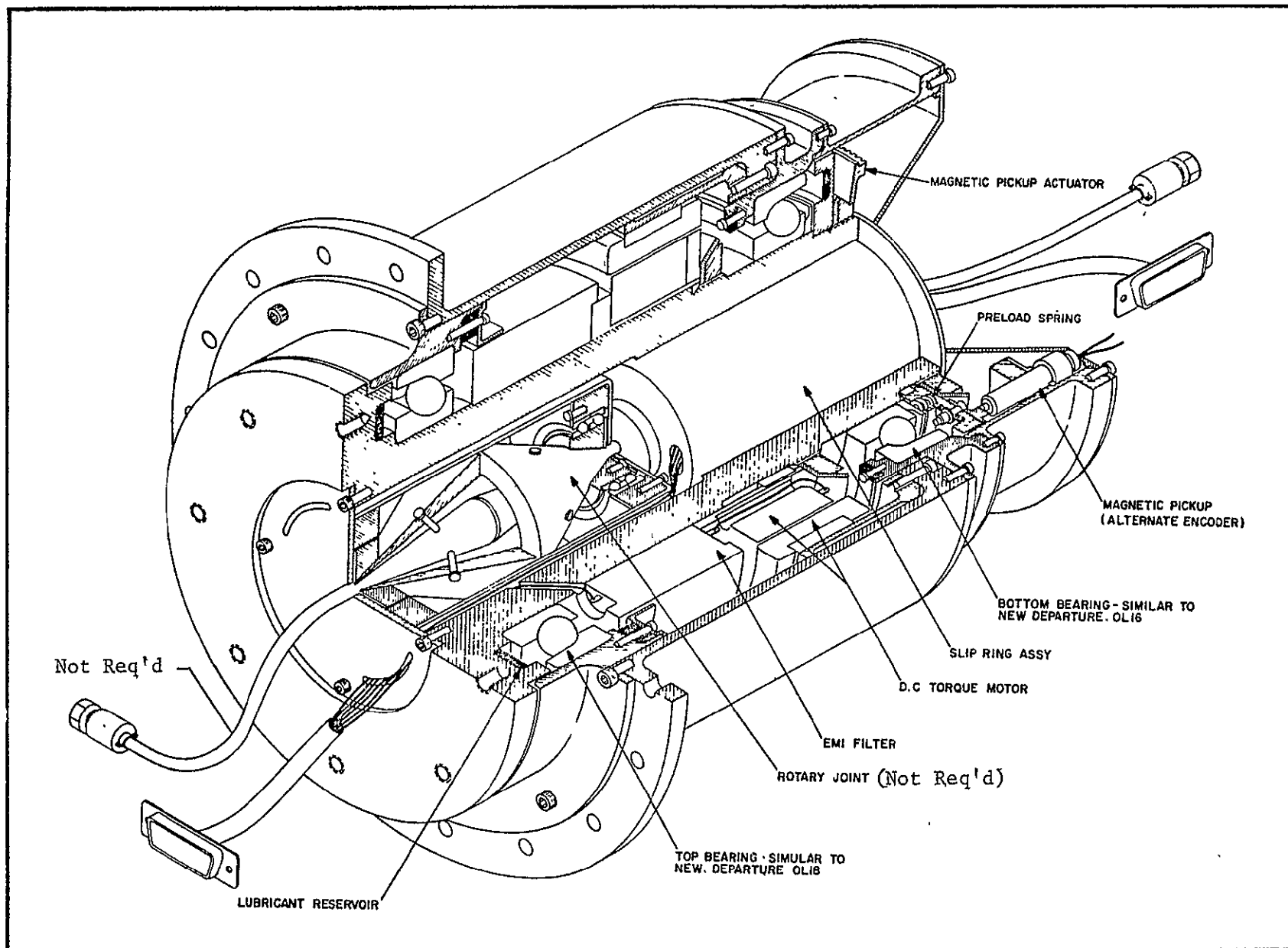


Figure VB-15 Despin Drive Assembly

Assumptions:

The spacecraft is spinning about the maximum inertia axis.

The canopus sensor will always provide a canopus pulse even when Jupiter is in its field of view.

First case, only one single degree of freedom gimbal mounts the antenna to the platform. A second gimbal axis is inherent in the despin axis.

The design considerations should regard the following constraints:

Active single degree of freedom gimbal servo will not be driven (commanded) at the vehicle nutation frequency.

The despun platform inertia cross products will be considered in the despin control loop design.

Total vehicle energy dissipation will be considered to evaluate the need for a passive nutation damper.

Discussion:

The length of the mission time (stored system for 2 to 3 years) and the short operation time required at encounter (approximately 10 to 30 hours) lends itself to a dry film lubricant.

Bearings:

Based on laboratory tests and performance records of satellites in service, dry film lube looks feasible to withstand the launch loads and the static conditions for a 3-year cruise period. Launch loads are low since the bearings are located such that launch acceleration is axial thrust and the weight supported through the bearings is insignificant.

A short term bearing test including loading and vacuum environments would be necessary to demonstrate durability of dry lube system.

Dry film lube is selected because radiation has less effect on a dry lube than any other lube system.

Friction levels of a dry lube system are least affected by temperature (it has no viscosity transients). Laborator experiments have demonstrated the "cold weld-in" phenomenon

Slip Rings:

Metal to metal slip rings could be used. They could be allowed to cold weld then sheared free when operation is initiated.

A commutator brush like material may be used.

Metal compacts in various proprietary formulations that incorporate a conductive self-lubricant are available. In general, some type of self-lubricating systems such as the metal compacts would be preferred.

Motor:

Either brush type or brushless type motors would meet requirements. The brushless type requires more complex electronics. The associated drive electronics may be the basic tradeoff for selection.

Another desirable approach would be to use a continuous electrical cable for passing signals through the interface allowing a loop wrap-up for a free system.

Magnetic Pick-up:

Low spin speeds of 4 to 5 rpm may present a problem to pick up adequate signal.

There are excited magnetic pickups presently being considered specifically for application at low spin speeds.

A harmonic drive could also be considered having the following advantages. It requires lower power than the direct drive; it has an inherent self-lock when a stepper motor is used as a drive source; and it would not require a closed loop servo.

Encoder:

If accuracy is not too stringent, 2° to 4° , an excited magnetic pick-up acting on a 180 tooth gear looks feasible. An optical incremental encoder also looks practical if more accuracy is required.

Conclusions:

The despin drive and a gimballed antenna system are feasible for the $\pm 45^\circ$ scan angle of Mission B within the following weight allocations:

Weight for $\pm 45^\circ$ Scan Range System		
Item	Double Gimbal*	Single Gimbal*
3.5' Dia Dish & Feed	8.0	8.0
Despin Drive	17.0	15.0
Gimbal Drives	14.0	7.0
Servos	4.0	4.0
Antenna and Despin System Support Structure	6.0	4.0
Balance Weight and Mounting	<u>2.0</u>	<u> </u>
	51.0	38.0
*The despin drive provides a degree of freedom equivalent to a gimbal axis; however, for those missions that require scanning through the direct line of sight of the spin axis the double gimbal may be required.		

Full Range Despun Antenna

Subsequent to the above system definition for Mission B based on limiting the tracking scan angle to $\pm 45^\circ$, the possibility was considered mounting the mechanically despun antenna so that the full range of tracking angles required up to 150° for the deepest (longest) missions, could be accommodated. This would permit use of the Pioneer S/C for the broad range of missions covered in the parametric study of Chapter V Vol. II (as limited by probe deflection accuracy considerations with the spinning S/C -- see the following section).

To accomplish the extended angle coverage, the gimballed dish has to be mounted on a boom as shown in Figure VB-16 to clear the main antenna dish. This places the c.g. of the despun mass off the spin axis, unless counterweights are used, but this is acceptable as long as the contribution of the despun mass to the total transverse axis inertia still results in a roll-to-transverse ratio of greater than one. Counterweights of 8-10 lb will bring the c.g. back on the spin axis and this is the recommended approach to permit having the antenna system spin with the spacecraft until needed for probe communications.

Estimated weights for this system (page V-77) indicate that the concept is feasible from a weight standpoint. The practicality from the standpoint of the complexity, accuracy of pointing achievable and the influence of the interference of field of view intermittently by the rotating RTG's and Magnetometer need to be evaluated more thoroughly before finalizing conclusions as to the use of this approach with the Pioneer spacecraft.

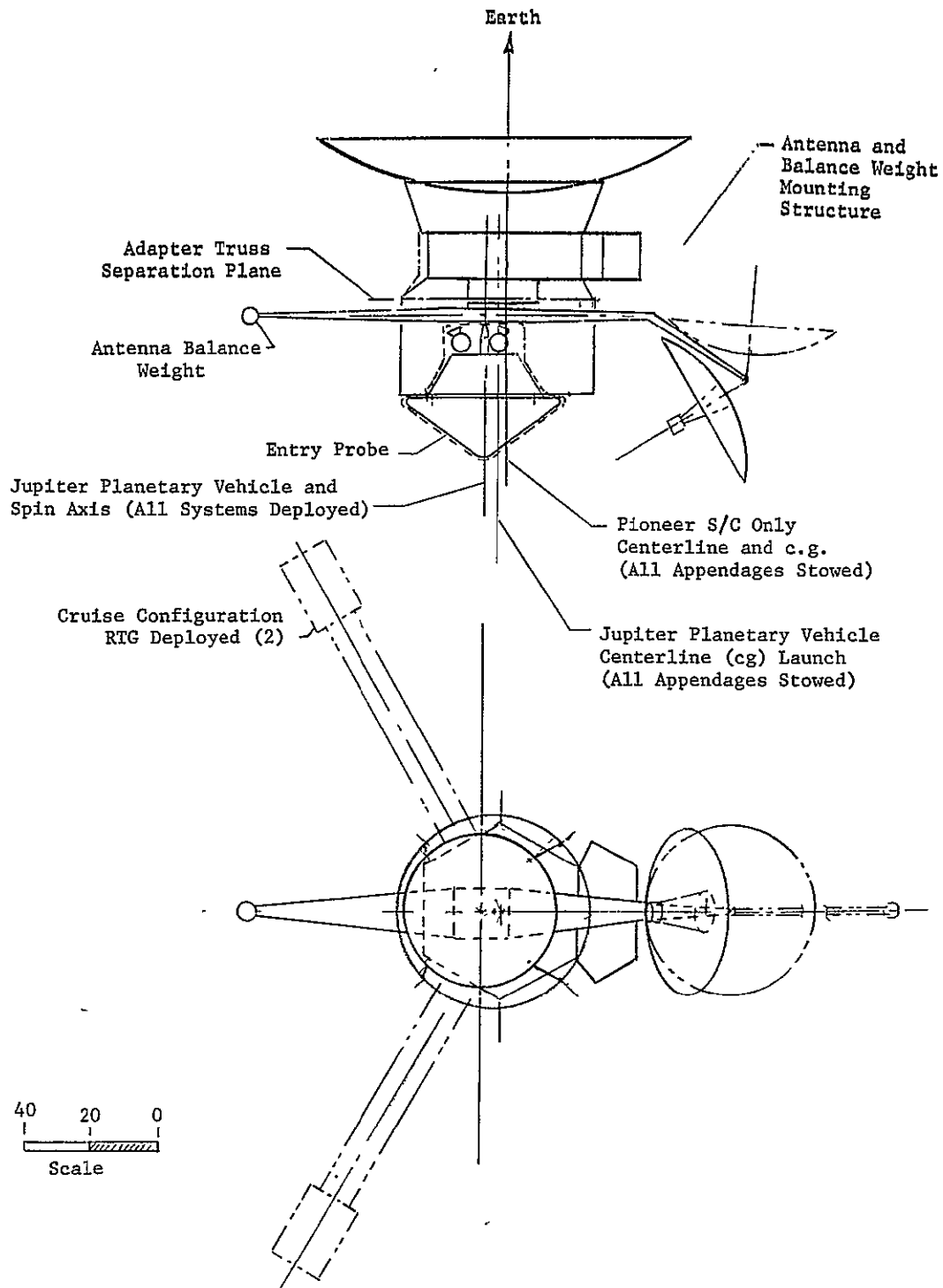


Figure VB-16 Planetary Vehicle Configuration
(Pioneer F&G Spacecraft)

Weight for Full Scan Range Despun Antenna System

Item	Double Gimbal (lb)	Single Gimbal* (lb)
4.2-ft Antenna Dish and Feed	10.0	10.0
Despin Drive	19.0	16.0
Gimbal Drives	14.0	7.0
Servos	4.0	4.0
Antenna and Despin System Support Structure	13.0	11.5
Balance Weight and Mounting	<u>10.0</u>	<u>8.0</u>
	72.0	56.5

Summary of Weight Increases Required to Adapt the Spacecraft
to Carry Probes

TOPS

Table VB-1 shows the breakdown of the added system weights for the TOPS S/C which is based on the JPL analysis* as modified somewhat by differences in the approach used by MMC.

PIONEER

Table VB-2 shows the breakdown of the added system weights for the Pioneer S/C based on the mechanically despun antenna system described earlier. Figure VB-17 shows the Pioneer Spacecraft mounted on the Booster.

*NASA Briefing on TOPS Missions by JPL 6-29-70

TABLE VB-1

Weight Estimates for TOPS Spacecraft Modifications

Item	Weight (Lbs)
Structure	$40.0 \times \frac{\text{Probe Weight}}{400}$
Adapter Beef Up	i.e., 10% of probe weight
S/C Beef Up	
Probe Support Structure	
Boom Relocation	2.5
Antenna for Probe	18.0 for 3.4' dia. dish (24 lb for 4.9' dia. dish)
ACS/APS	2.0
Mechanical Devices	2.0
Temperature Control	5.0
Cabling	5.0
Electronics for Data/Comm System	12.0
Added Propellant for Mid Course Correction (due to extra mass of probe).	0*
*No additional propellant required since propellant currently carried by TOPS for post Jupiter trajectory corrections is more than adequate for Jupiter-only probe missions even with the added weight of the probe.	

TABLE VB-2

PIONEER S/C MODIFICATIONS WEIGHT ESTIMATES
(Weight Additions to Support a 400-500 lb Probe)

<u>Item</u>	<u>Weight (lbs)</u>	
1. Power: a) Battery, Switching and Control for data system during probe spacecraft communications.	13.2	
2. Probe Adaptor System		
Portion of Truss that stays on spacecraft after Probe separation (7")	16.0	
Portion of Truss that jettisons after Probe separation (27")	54.0	
Separation joint at spacecraft (with Pyrotechnics)	2.4	
Probe attachment and separation mechanism (1.2# ea 4 pls)	4.8	
3. Asteroid/Meteoroid Detector Instrument Relocation	3.0	
4. Low Gain Antenna Relocation	1.2	
5. Communications Electronics	11.0	
6. Data Storage System	22.0	
7. Cabling	7.0	
8. Thermal Control Mods	5.0	
	<hr/>	
SUB-TOTAL	139.6	
	<hr/>	
	Full Scan	$\pm 45^\circ$ Scan
	<u>Range</u>	<u>Range</u>
Mechanically Despun Antenna System	72.0	51.0
	<hr/>	<hr/>
	211.6	190.6

NOTE: The above list does not include provision for added propellant weight to handle the extra mass of the probe in mid-course trajectory corrections. If Burner II is used, no added propellant is required since ΔV corrections are reduced. If Burner II is not used, see Section E for added propellant requirements.

* This assumes probe thermal control after separation is handled by a heater system onboard the probe. If the alternative method is used, i.e., using spacecraft power to heat up probe prior to separation (to effect a larger range at separation) 2 RTG's would have to be added to obtain the required power and this would result in about a 70 lb weight increase in the spacecraft.

Forebody Heat Shield Weight Fractions

Figures VC-2 and VC-3 summarize the design values for the fraction of entry weight required for the forebody heat shield. These data are based on an analysis (by AMES Research Center) which includes the influence of the carbon vapor in absorbing and thus reducing the incident radiation, see Appendix C. From the sensitivities of heat shield weight fraction to the entry and geometry parameters as shown in Figure VC-2 and VC-3, the following can be observed:

1. The Weight Fraction increase with γ is negligible at ballistic coefficients near 1 slug/ft² (157 kg/m²) and increases from 35% to 44% in going from $\gamma = -10^\circ$ to $\gamma = -90^\circ$ at $B = .52$ slugs/ft² (83 kg/m²).
2. The optimum cone half angle is 60° , but at shallow entry angles, 55° half angle cones have only 1 or 2% higher weight fractions than the optimum. Below 50° half angle cones the weight fraction becomes quite large regardless of entry angle.
3. Large diameter aeroshells yield larger weight fractions.
4. Below about .8 slugs/ft² (126 kg/m²) for shallow entries and 1.0 slug/ft² (157 kg/m²) for steep ones, reducing the ballistic coefficient results in a substantial increase in the weight fraction.

Afterbody Heat Shield Weight Fractions

A value of 15% of the SD131-12 Forebody values was assumed for purposes of this study. (Afterbody weight fractions calculated for the case of Venus entry in previous studies have been found to be of the order of 15 to 20% of the forebody values.) Jupiter afterbody heating rates have not been determined.

C. Heat Shield

Introduction

JPL Document SD 131-12 states that "Jupiter atmospheric entry heating rate and pressure histories are for the most part outside our present experience. Because of this, the normal analytical tools tend to be very limited in application and where extrapolations are possible they tend to be unverifiable through test. For this reason, a wide variety of opinions are possible as to the heat shielding weight requirements for typical Jupiter missions. In order to constrain these studies to one tier of speculation, JPL has furnished heat shield weight Fraction Data to guide heat shield weight assignment for different probe missions." The data of SD 131-12 is summarized below and Appendix C contains the complete set of information from JPL.

Material

The heat shields are composed of a high-density graphite (ATS-Specific Gravity of 1.75) ablator-insulator backed up by a low-density (0.1 Specific Gravity) carbonaceous insulator.

Heating Rates

Figure VC-1 shows the peak heating pulses for a 60° $1/2$ -angle cone for both a shallow, $\gamma = -15^\circ$, and a steep, $\gamma = -90^\circ$, entry. These values occur at the trailing edge of the cone flank and are higher than stagnation point values by about 70%.

Heat Shield Thickness Requirements

For the two heat pulses shown, the thickness requirements on the 60° $1/2$ -angle cone flank are as follows:

	$t_{\text{dense graphite}}$ (cm)	$t_{\text{low density insulator}}$ (cm)
$\gamma = -15^\circ$	4.50	2.0
$\gamma = -90^\circ$	4.75	2.25

Other values are tabulated in Appendix C.

Note: Data from NASA Ames

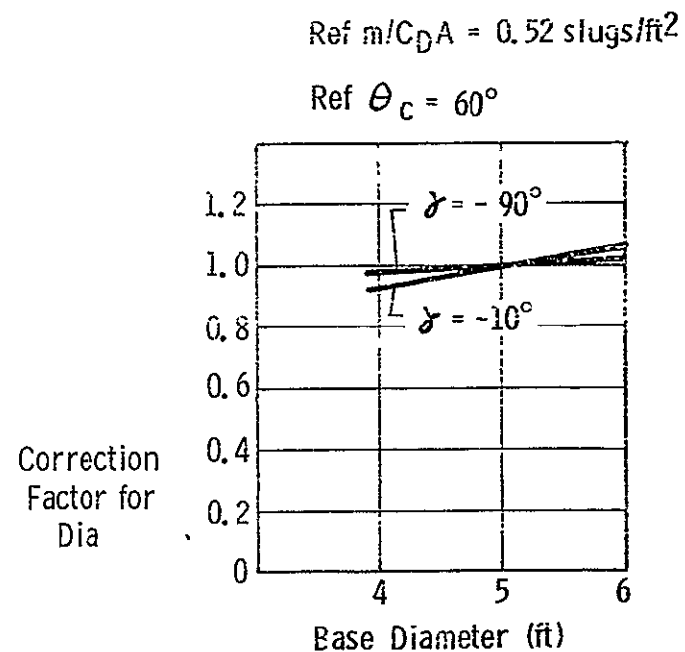
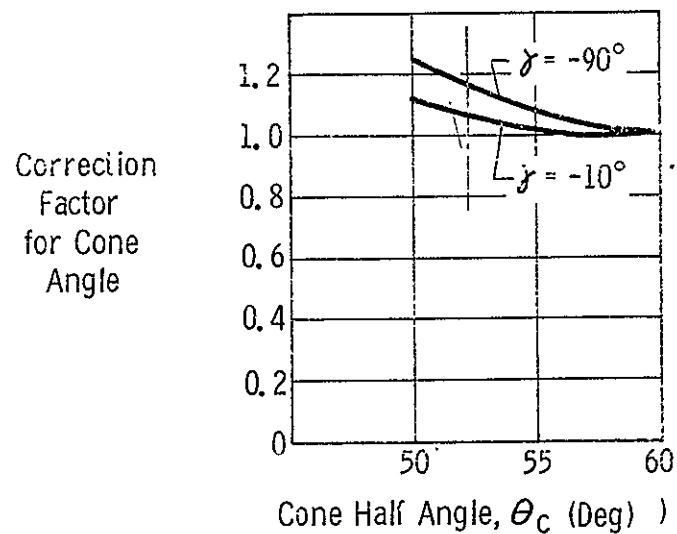
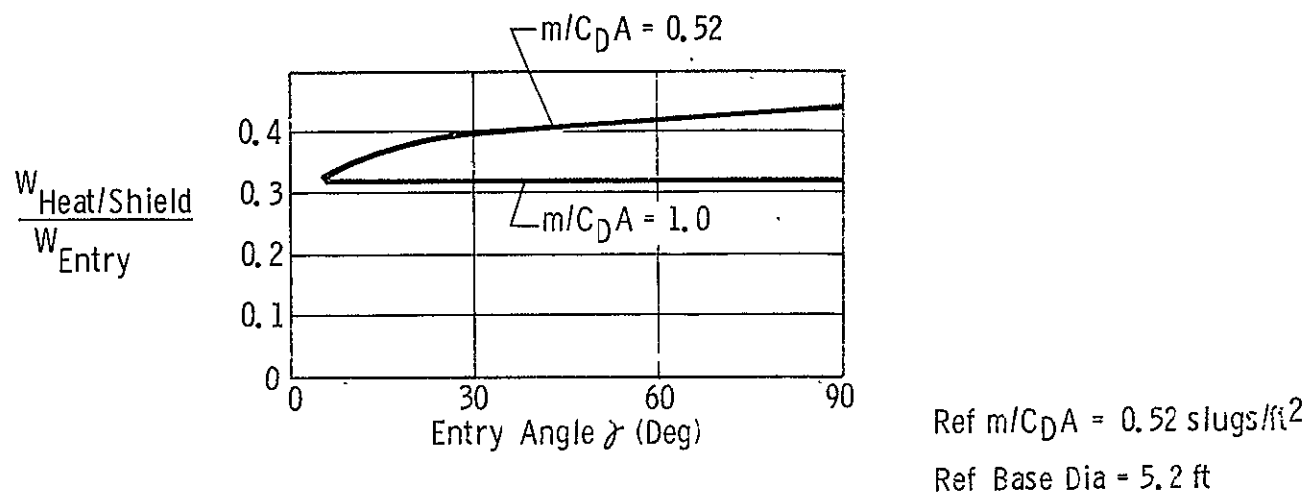
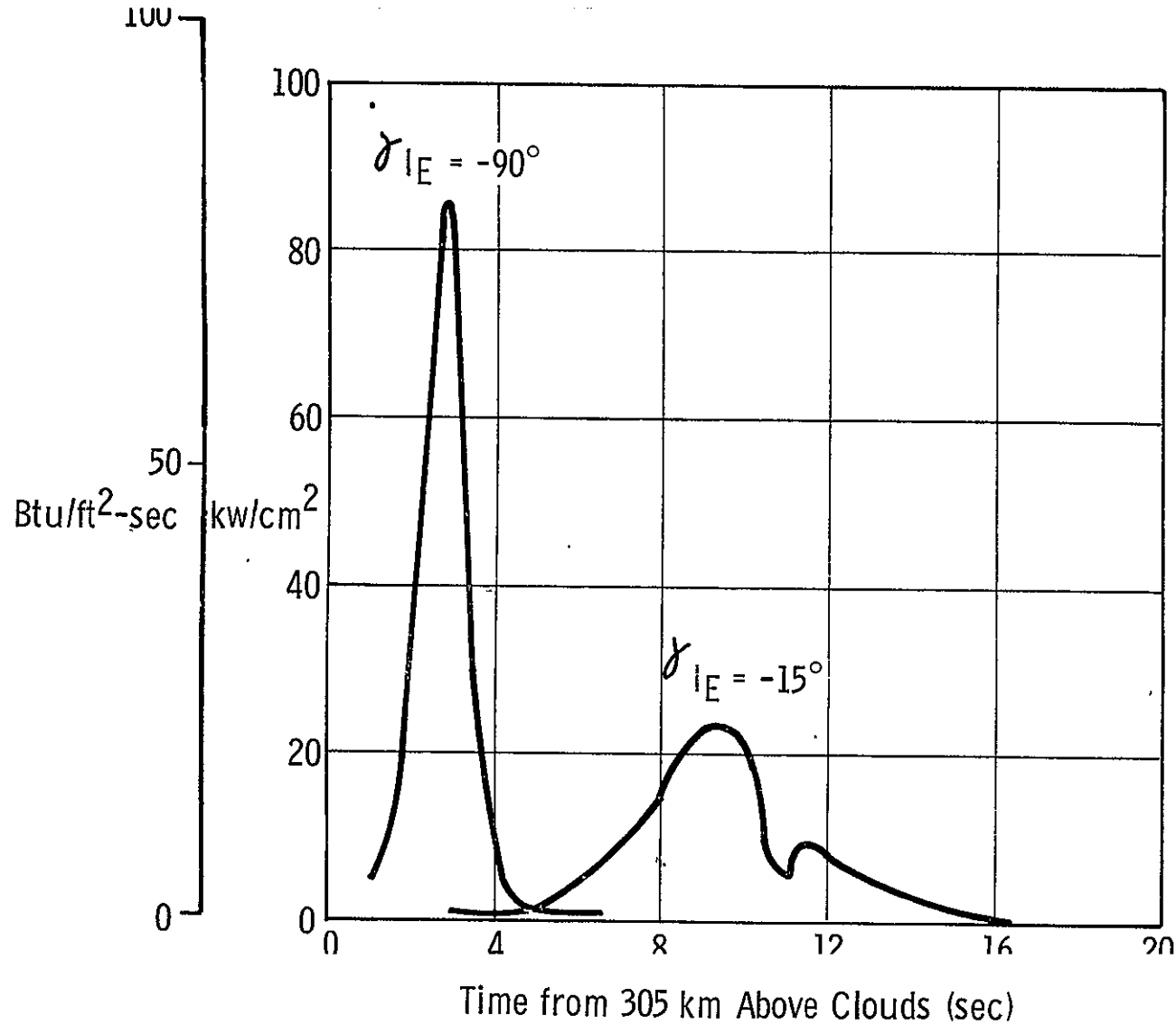


Figure VC-2 Forebody Heat Shield Design Data



$\theta_c = 60^\circ$
 $r_b = 0.80 \text{ m (2.6 ft)}$
 $m_e = 250 \text{ kg (570 lb)}$

NASA Ames Data

Figure VC-1 Heating Pulses

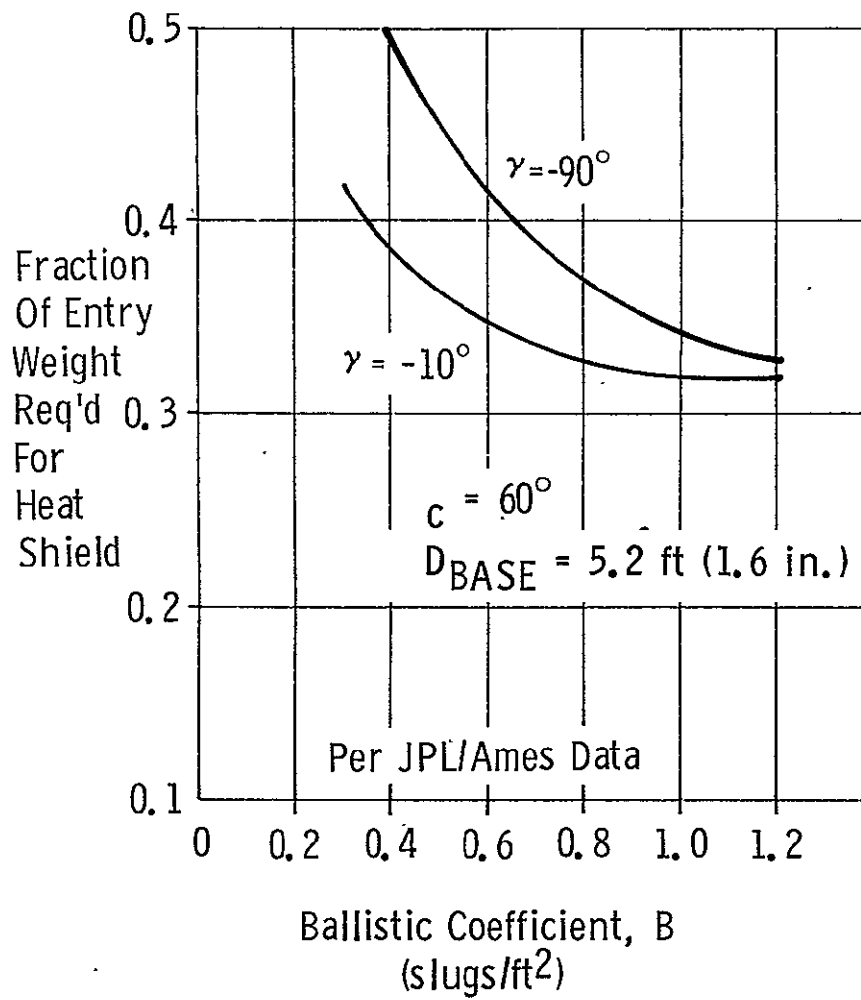


Figure VC-3 Forebody Heat Shield Design Data

D. Aerodynamics

The aerodynamic effort for this study was done in the areas of descent probe aerodynamics and decelerator/parachute design. No general technology problems affecting system feasibility have been identified; however, qualified hardware designs would require some development in the areas of descent probe detailed configuration design, and parachute deployment and survival in simulated Jupiter atmosphere environments.

1. Descent Probe Aerodynamics

The primary aerodynamic design factor for the descent probe is the ballistic coefficient, $m/C_D A$. The science criteria established required descent profiles and corresponding ballistic coefficients. Conventional methods of drag control provide the necessary ballistic coefficient match for the various descent profile segments. Parachutes provide $m/C_D A$ values less than about 0.5 slugs/ft^2 and aerodynamic devices such as fences, skirts or other rigid drag structures provide drag control for $m/C_D A$ values greater than 0.5 slugs/ft^2 . Since it is desirable for probes designed for pressures greater than 50 to 100 atmospheres to use spherical structures to protect the internal equipment, an attempt was made to stabilize and control the drag of a sphere. The aerodynamic characteristics of a cone shape are much easier to predict accurately and the cone shape provided by adding a skirt to the spheres does provide a configuration which is satisfactory for ballistic coefficients of $\sim 1.0 \text{ slugs/ft}^2$. However, for higher ballistic coefficients it becomes difficult to package the resulting conic into an entry vehicle and larger system weight penalties result.

Figure V.D-1 depicts some practical aerodynamic drag and stability modifications for a sphere. The plain sphere has a somewhat erratic wake and essentially neutral stability. In order to assure directional stability so that the antenna will point up, some auxiliary stability device is required. Very little experimental data is available for design purposes; however, by adding fences

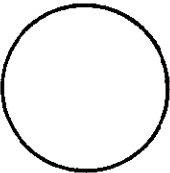
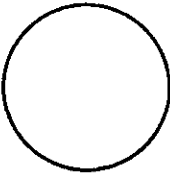
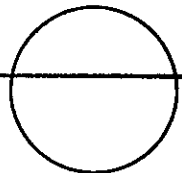
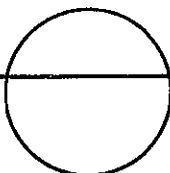
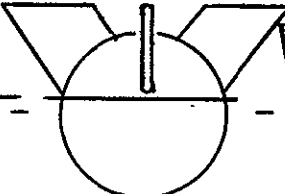
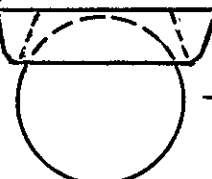
						
COMMENT	LAMINAR FLOW	TURBULENT FLOW	1.1D FENCE	LARGE FENCE	FENCE AND FINS	DRAG RING
DRAG COEFFICIENT, C_D	0.45	0.25	≈ 0.4	$\approx 0.4-.8$.35-.8	.5-1.0

Figure VD-1
Typical Sphere Modifications

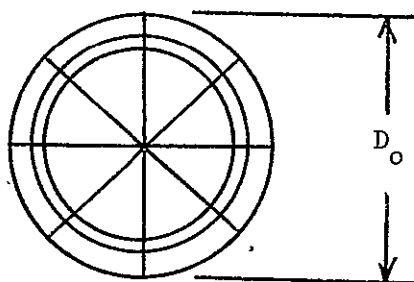
aft of the center of gravity or by shifting the effective C. G. forward by means of external fairings, some stability can be provided. More positive stability devices are fins or a drag ring. Both of these methods cause packaging difficulties but are practical and effective. An inhouse, low speed wind tunnel test program is being conducted at Martin to evaluate a series of fences, fins, and other devices on spheres. Results are not yet available.

It does appear that various practical aerodynamic configuration modifications to the sphere are available for a detail design. Therefore, this concept was the basis for weight estimations and packaging studies for this study.

2. Parachute/Decelerator Design

Conventional parachute designs provide the necessary ballistic coefficient control and deceleration for aeroshell staging. The typical staging conditions are subsonic, $M = .6 - .8$, at dynamic pressures of less than 100 psf and ambient pressures of about 0.2 atmospheres. This pressure is equivalent to about 12,000 ft. of altitude on Earth. Because of the hydrogen/helium atmosphere, the parachute deployment and angular rate damping characteristics will be different from those on Earth. Damping can be expected to be generally degraded on Jupiter. These conditions can be evaluated by analytical techniques and appropriate design changes made if necessary.

Parachutes used in this study are of the disk-gap-band type developed by the G. T. Schjeldahl Company. The disk-gap-band (DGB) parachute has a drag coefficient of $C_{D0} = 0.53$ based on the total constructed diameter, D_0 , including the band (see accompanying sketch).



Although the drag coefficient is reduced from that of solid parachute designs, the DGB parachute provides a very stable descent with rapid damping from angular disturbances. Using parachute weight data based on the Air Force Parachute Handbook and G. T. Schjeldahl data, a parachute weight penalty curve as a function ballistic coefficient, $m/C_D A$ was developed and is presented in Figure V.D.-2. This curve is based on conventional Nylon or Dacron fabric weights. For high temperature drogue chutes, such as those deployed and used from 50 to 300 atmospheres, a glass based material called "S-glass" can be used. Figure V.D.-3 presents a design curve for small S-glass material chutes giving chute weight as a function of payload weight for various ballistic coefficients, B. The insert table gives a correction factor for various temperature ranges; however, the basic curve covers the likely design range of 450-1800°F.

3. Entry Stability

Based on previous Martin calculations with 6-degree of freedom entry simulations, entry disturbances in angle of attack can be expected to converge to about one-tenth of the initial value prior to the maximum dynamic pressure or heating rate condition, if the roll rate is kept below about 0.5 rad/sec. For the higher velocity entry of Jupiter these values may change; however, the trends should remain valid, if the ablation process takes place in a uniform manner. However, due to the massive ablation and blowing (the $m/C_D A$ changes by 30% due to mass loss) the ablation will most likely not take place in a uniform fashion. Very possibly, grooving, cross hatching, and/or regmaglypt recession will occur. Resulting roll rates set up by unsymmetrical shape changes can lead to roll coupling and divergent oscillations which would completely negate the normal convergence trends. Until it is possible to assess the ablation performance more accurately, it is considered that a good design practice would be to require the initial angle of attack to be less than $\pm 5^\circ$ and the initial roll rate to be $\leq .25$ radians/sec. These values are adopted for the probe deflection phase studies conducted in this report.

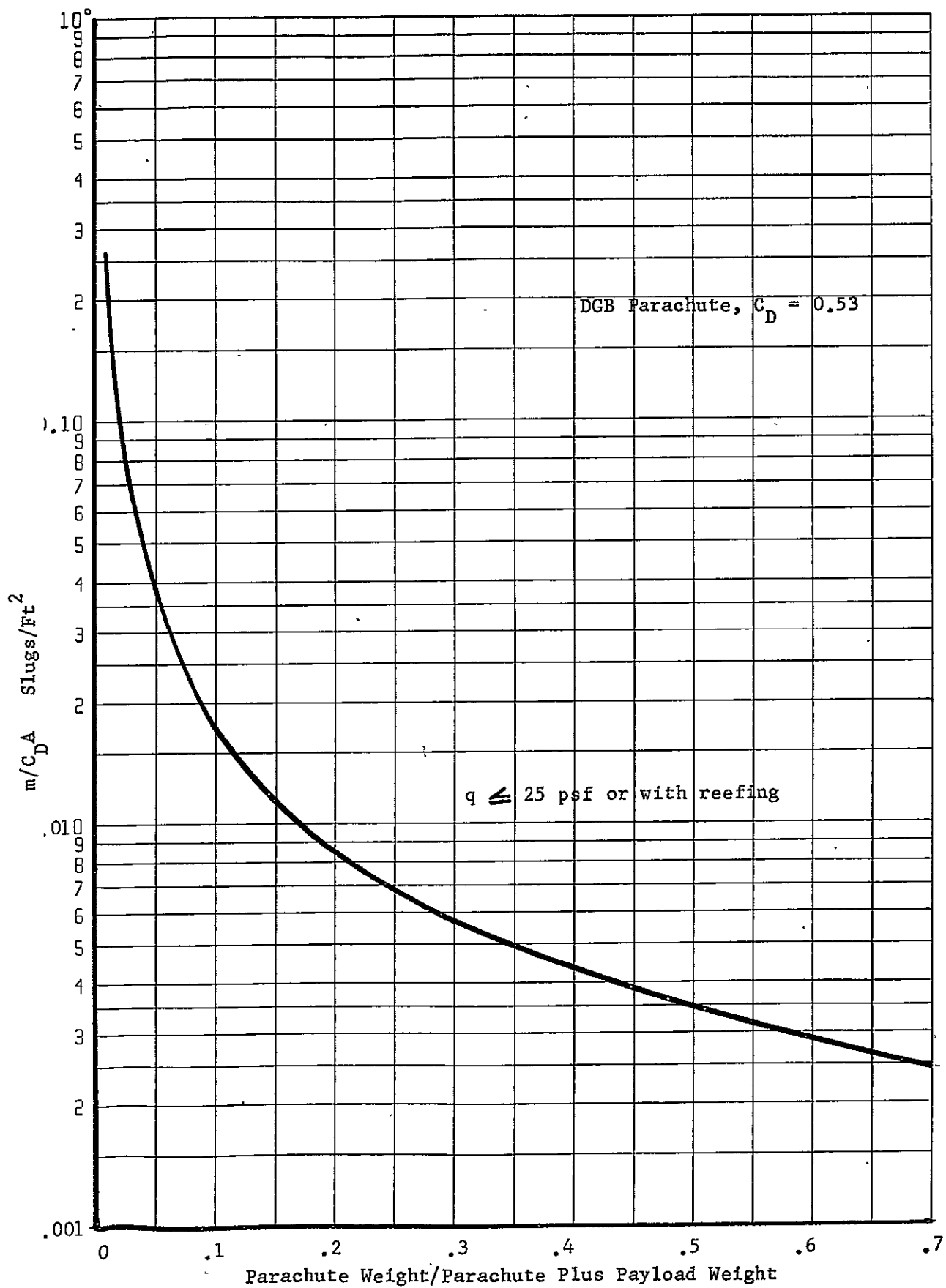


Figure VD-2

 $m/C_D A$ vs Parachute Weight Penalty

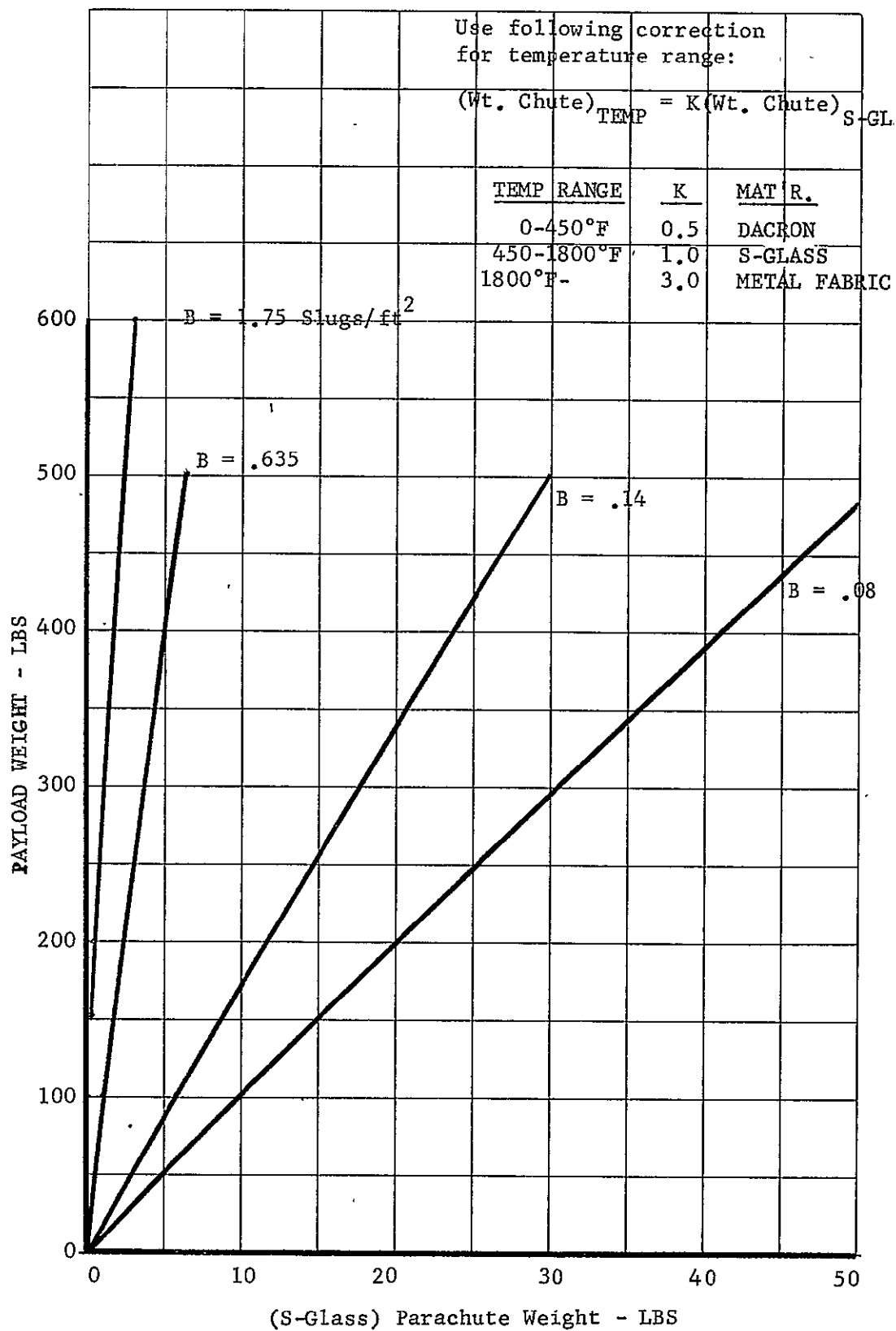


Figure VD-3 Drogue Parachute Weight

E. Guidance and Control and Propulsion Systems

1. Spacecraft Guidance and Control and Propulsion Systems

a. Small and Medium Size Probes on TOPS

For probes up to approximately 450 lbs and 4.0' feet in diameter, it is possible to mount the probe so that the c.g. of the planetary vehicle (combined probe and TOPS spacecraft) stays in the transverse c.g. plane of the original TOPS spacecraft, and to keep the c.g. within 7 inches of the TOPS longitudinal, z, axis. For this situation, the addition of two yaw thrusters, as shown in Figure VB-9, is required to avoid cross coupling. An additional effect of the c.g. shift is to require an increase in the pointing range of the autopilot of the trajectory correction propulsion system from $\pm 5^\circ$ to $\pm 19^\circ$.

Another impact of the probe installation is impingement of the spacecraft roll jets exhaust plumes on the probe. The probe outer cover should not be adversely affected but the plume energy absorption by the probe should be evaluated in terms of its effect on the jet thrust vector.

Also, the hydrazine trajectory correction propulsion system must now be capable of providing approximately 30% more total impulse and the attitude control system (momentum wheels and hydrazine thrusters) must deal with 20 % more inertia to account for the addition of the probe. For Jupiter-only missions this does not impose any added propellant weight since removal of the post Jupiter midcourse corrections, which amount to about 75% of the total impulse required, more than offsets the increase in requirements imposed by the probe mass. For inclusion on Grand Tour missions, a 400 lb probe has been found by JPL,* to require a maximum of 12 lbs additional propellant.

b. Large Probes - TOPS

For larger probes, up to the 800 lb maximum which can be accommodated by the family of launch vehicles, the impact on the spacecraft attitude system and especially on its trajectory correction system is much more pronounced. The c.g. is moved outside

*NASA Briefing by JPL 6-29-70

the propulsion system compartment and up to 17 inches off the TOPS spacecraft axis.

For this case, the attitude control system could be modified by the addition of pairs of thrusters to provide couples such that the thruster location need not surround the c.g. as in the current TOPS thruster arrangement. By the use of couples, the thrusters can all be kept essentially in the existing propulsion compartment.

The trajectory correction engine presents a more difficult situation in that a 30° change in pointing angle would be required (for the 800 lb probes). This would appear to require a major redesign of the system with possible relocation of the remote nozzle to a location outside the present propulsion compartment.

The large probes do not however require additional trajectory correction propellant in Jupiter-only missions due to the availability of impulse capability provided in the existing TOPS spacecraft for post Jupiter midcourse corrections.

c. Probes on Pioneer Spacecraft

Since the probes are mounted on the spin axis of the Pioneer spacecraft, no change is required in the locations for the precession, spinup and trajectory correction thrusters which are mounted in two sites on the periphery of the antenna supporting structure. The total impulse capability of 11,800 lb sec provides for 200 m/s ΔV with an 83 lb total system weight broken down as follows:

Propellant	60 lb
Spin Control	7
Orientation maneuvers	8
Midcourse	48
Leakage	2
System Weight (Tanks, etc)	23 lb

The 200 m/s is based on providing a margin of 1.67 over the 120 m/s that is required with an Atlas 3C Centaur launch vehicle. Since the 120 m/s is reduced to 50 m/s, or 83 m/s using the 1.67 margin, when the Burner II stage is added, the existing 48 lb of midcourse propellant becomes adequate for total spacecraft weights up to ~ 1200 lb. This permits adding a 400 - 500 lb probe without propellant modifications. Still smaller midcourse corrections are required with the advanced Burner II, 20 m/s per AMES personnel, and this value would permit carrying any probe weight within the launch vehicle family capability without adding any propellant.

For the cases where Burner II is not used and thus the existing 200 m/s ΔV requirement is retained, the added propellant weight requirement is approximately the following:

400 lb probe	$\dot{W}_P = 62 \text{ lb}$
600 lb probe	$\dot{W}_P = 77 \text{ lb}$
800 lb probe	$\dot{W}_P = 103 \text{ lb}$

For the 400 and 600 lb probe cases a 22 3/4 inch tank is available which will fit in the same space occupied by the existing tank. A 30" tank is available but it would not fit in the existing space. Again it should be noted that these added propellant requirements only apply in the case where Burner II is not utilized.

Although from the propellant usage standpoint the added probe mass is seen not to be a limiting factor, the influence of the probe mass on roll/transverse inertia ratios does present a limiting situation. The necessary inclusion of a probe tracking antenna between the basic Pioneer and the probe, Figure VB-10, forces the probe mass away from the existing c.g. and results in a strong contribution of the probe mass to the transverse inertia of the planetary vehicle. This can be offset somewhat by designing larger

diameter shallower probes, but if carried very far this results in a significantly off-optimum probe design, i.e, larger A/S structure and heat shield weight fractions are required. Consequently a more reasonable method of maintaining the spin axis as the maximum inertia axis might be to add balance weights or to extend the present RTG booms.

2. Probe Systems

a. Deflection Phase

The ideal criteria for the deflection implementation errors is that they be below 1.0° in angle and 1% in magnitude to prevent constraining the entry angles and communication system design. Three concepts have been considered for placing the probe on the proper trajectory and at the proper attitude for entry. These are:

Method 1

Use of a 3-axis strapdown system on the probe to orient and stabilize the probe during the ΔV burn and subsequently to reorient it for entry.

Method 2

Spin Stabilization of the Probe for the ΔV burn and subsequently precessing it to the entry attitude.

Method 3

Placing the whole planetary vehicle on the probe trajectory and then deflecting the spacecraft into flyby orbit after probe ejection.

The guidance and control and propulsion system considerations for each of these concepts are discussed below. The first is applicable to the TOPS vehicle only, while the latter two are applicable to either the TOPS or Pioneer vehicles. A discussion of the overall operational considerations and comparisons of the three approaches is contained in Chapter IVB on Engineering Concept Evolution.

Method 1 3-Axis System on Probe

In this approach a system similar to that used for control of the deorbit maneuver on the Viking program is used. The main elements of this system include (1) an Attitude Reference Unit (ARU) consisting of three single-degree-of-freedom, pulse-rebalanced strapdown gyros; (2) a Velocity Reference Unit (VRU) consisting of three single-axis pulse-rebalanced strapdown accelerometers; (3) a Guidance and Control Computer (GCC), a digital machine that can have a portion of its memory updated before separation from the spacecraft. These units form a conventional 3-axis strapdown inertial guidance system. Three pairs of thrusters located at the periphery of the probe constitute the 3-axis attitude propulsion system.

In operation, (1) the spacecraft (TOPS) is oriented to the proper attitude for probe ejection, (2) the reference of the probe G&C system is established, (3) the probe is ejected by a spring system at ~ 1 fps, (4) the probe coasts for 1 to 2 minutes to provide enough separation to preclude impingement of the ΔV rocket plume on the spacecraft. While the probe is in the immediate vicinity of the spacecraft the attitude jets can be inhibited to prevent probe/spacecraft interactions. Tipoff rates pose no danger of saturating the gyros since the system uses pulse rebalanced gyros, (5) the ΔV rocket is fired (15 to 60 seconds) with probe attitude and ΔV thrust termination controlled by the 3-axis strapdown system, (6) the probe is then pitched to the attitude corresponding to $\alpha = 0$ at entry, (7) it is spun up to 3 rad/sec to maintain the attitude until entry 13 to 65 days later, and (8) yo-yo's are deployed just prior to entry to despin the probe to a near-zero roll rate. The attitude jets are jettisoned before entry.

This system should provide a deflection impulse error of less than 1° in angle and 1% in magnitude. An error analysis performed by the Viking program on their system yielded 0.9° and 0.9% respectively. Although it might be possible to use the science accelerometers instead of additional ones for the 3-axis system, the system is a fairly complex and heavy one and does not fully utilize the capability of the spacecraft guidance and control system capabilities. Consequently two other methods were considered.

Method 2 Spin Stabilization of the Probe during ΔV Application

With the TOPS spacecraft, the probe is oriented to its ΔV application attitude before it is released (as in Method 1). The ejection is again performed with a spring system but in this method spin-up thrusters are fired just as the probe clears the spring guides. Thus the orientation obtained from the spacecraft is retained until the ΔV burn can be initiated. If the burn time is sufficient to provide at least one period of nutation, nutation errors are averaged out and the main source of error in the deflection angle is misalignment of the ΔV motor relative to the probe

axis. If this geometrical alignment error can be kept very small, it may be possible to keep the angle and ΔV magnitude within the desired tolerances.

In this method, reorienting the probe to its altitude for entry after the ΔV burn is accomplished by precessing the probe using a set of jets fixed to the spinning body and firing them as they pass a certain reference. A phase locked loop is used to time the jets and either the sun or a star sensor provides the crossing reference. The requirements and errors involved in this system are discussed further in Appendix A. At the conclusion of the reorientation the probe remains spin stabilized until just prior to entry when despin yo-yo's are employed.

Deflection accuracy with this method will probably not be as good as with Method 1 but may still be compatible with a $1\frac{1}{2}^\circ$ and 1% criteria. A detailed error analysis is needed to confirm the performance of this approach.

With the Pioneer spacecraft an added step is required of the probe in using this approach. The pointing accuracy with which the pioneer can be reoriented off its earth reference is rather gross, 7% of the angle turned. This means the probe would have to be released while the Pioneer is on its Earth reference and then be precessed into the proper attitude for ΔV application. While the precession procedure would be the same as for the post ΔV attitude correction, the accuracy required is much greater. Again a detailed error analysis, beyond the scope of this study, is required to determine just what accuracy could be achieved by this technique. Depending on the results it may be that Pioneer probe entries using this approach would have to be constrained to steeper entry angles $20-25^\circ$ to avoid skipout of the probe. Lead time errors would also aggravate the probe acquisition problem and affect probe power.

The 3rd method, described next, alleviates the problems of deflection implementation errors but introduces some others.

An alternative to Method 2 is the use of a fixed burn time and controlling the deflection maneuver by the range at

ejection. This has not been studied.

Method 3 Spacecraft Deflection

In this method the spacecraft G and C system places the probe on the proper path for planet encounter and also orients it to the proper attitude for entry (the tolerance on entry attitude, $\pm 5^\circ$, is within the pointing accuracy of the Pioneer as well as the TOPS). After probe ejection, spin jets spin up the probes to maintain the attitude until entry. As before, yo-yo's despin the probes just prior to entry.

After probe ejection, the spacecraft is oriented to employ its trajectory correction motor(s) to place it on the flyby trajectory. This requires more propellant than for the probe deflection in the case of TOPS and also in the case of Pioneer except for very large probes (> 700 lbs), however, this is offset by removing the need for a G and C system on the probe.

Another aspect of this approach is the requirement for a sterile spacecraft if quarantine regulations exist since the spacecraft is targeted initially on an impacting course. Finally, in the case of the Pioneer, one or more additional midcourse corrections are required after the initial deflection maneuver due to the limited accuracy of the spacecraft in achieving the required attitude for deflection.

Weight Comparison of the Three Deflection Methods

Looking at estimates of the weights for the ΔV propulsion and guidance and control systems, the three methods are compared for a 400 lb probe with an Ejection Range of 2.6×10^7 km, a radius of periapsis of $2.0 R_{\oplus}$ and an entry angle of -20° .

System	Method 1	Method 2	Method 3	
			TOPS	PIONEER
ΔV Propellant, 80 m/s (lb)	14	14	52	30
Probe or S/C ΔV Propulsion System Fixed Weight (lb)	10	10	7	4
Probe Attitude Propulsion System (lb)	6	8	3	3
Probe Guidance and Control System (lb)	20*	15**	0	0
Total	50	47	62	37

*Estimated weight for system equivalent to current Viking G&C system. Substantial Development is required to achieve this weight.

**Estimated weight for precession phase locked loop system including roll reference sensor. Development is also required.

For TOPS, Method 1 appears the best selection since it affords good accuracy with a slight weight penalty (assuming the G and C system weight estimate is valid). For Pioneer the weights are a toss-up but the greater accuracy potential with Method 3 might favor that approach if the aspects of quarantine and additional midcourse corrections are acceptable. For this study Method 2 is assumed for Pioneer.

Propulsion System Weights for Probe Deflection Phase

Deflection Propulsion

For a periapsis radius of 2.0 and a probe ejection range of 26×10^6 km the range of ΔV requirements varies from 75 m/s for a -10° entry to 125 m/s for an entry at -50° . Larger R_p values increase the ΔV requirement, e.g., at $R_p = 6.8$; $\gamma = -20^\circ$ the ΔV is 330 m/s. The probe ejection range can be increased up to about 50×10^6 km to reduce ΔV values but this has an adverse effect on accuracy and thermal control system weight.

Probe weights also vary widely, from 200 to 800 pounds, and this combined with the wide ΔV range creates a very wide range in total impulse requirements. Consequently, both solid propellant systems, which are lighter for the low total impulse range due to their smaller fixed weight fraction (higher λ 's), and hydrazine monopropellant systems, were evaluated. Both are compatible with the long time storage and the requirement to achieve precise control over the magnitude of the total impulse.

For the monopropellant systems an I_{sp} of 230 sec was assumed with a 15 lb minimum fixed weight and a mass fraction, λ , varying from 10% to 75% as shown in Figure VE-1. Total system weights are shown in Table VE-1 for a range of probe weights and ΔV values. The results are plotted in Figure VE-2. For the solids, the range of performance achievable is depicted in Figure VE-3 wherein a propellant, with an I_{sp} of 213 sec and a λ of .5 forms the conservation side of the band while an I_{sp} of 285 sec and a λ of .7, which is consistent with performance data for Thiokol's TE-M-541 motor, forms the lower weight bound. For purposes of this study an intermediate system-weight curve equivalent to an I_{sp} of 235 sec and a λ of .6 was assumed.

A comparison of the total deflection system weights for the two systems is shown in Figure VE-3 and 4. The lower of the two values was used in the parametric study of Chapter V, Volume II and for estimating system weights for the sample probe missions of Chapter VI and VII, Volume II. The actual selection of a system would depend on things other than weight, e.g., whether Method 1 or 2 is ultimately selected for implementing the probe deflection maneuver.

Propulsion System for Attitude Control-Probe Deflection Phase

For simply spinning up the probe, small solids which weigh less than a pound each would be the most efficient. For the three-axis control system of Deflection Method 1 (Section E2a) and the precession control pulsing of Method 2, either a cold gas system or a monopropellant system would be required. The TOPS propulsion system study* recommends the hot gas system due to leakage problems with the pressurized cold gas system. This conclusion is based on a longer mission duration and would have to be evaluated for the shorter times involved in the Jupiter-only probe mission. An additional consideration should be whether or not monopropellant hydrazine should be used for the probe deflection. For the precession system the cold gas is preferred due to the greater accuracy achievable in controlling the pulse centroid.

No optimizations of attitude propulsion systems have been attempted in this study, but it appears that existing APS hardware is capable of meeting probe requirements.

*TOPS Spacecraft Propulsion System by L. Eugene Baughman, Astronautics and Aeronautics, September 1970.

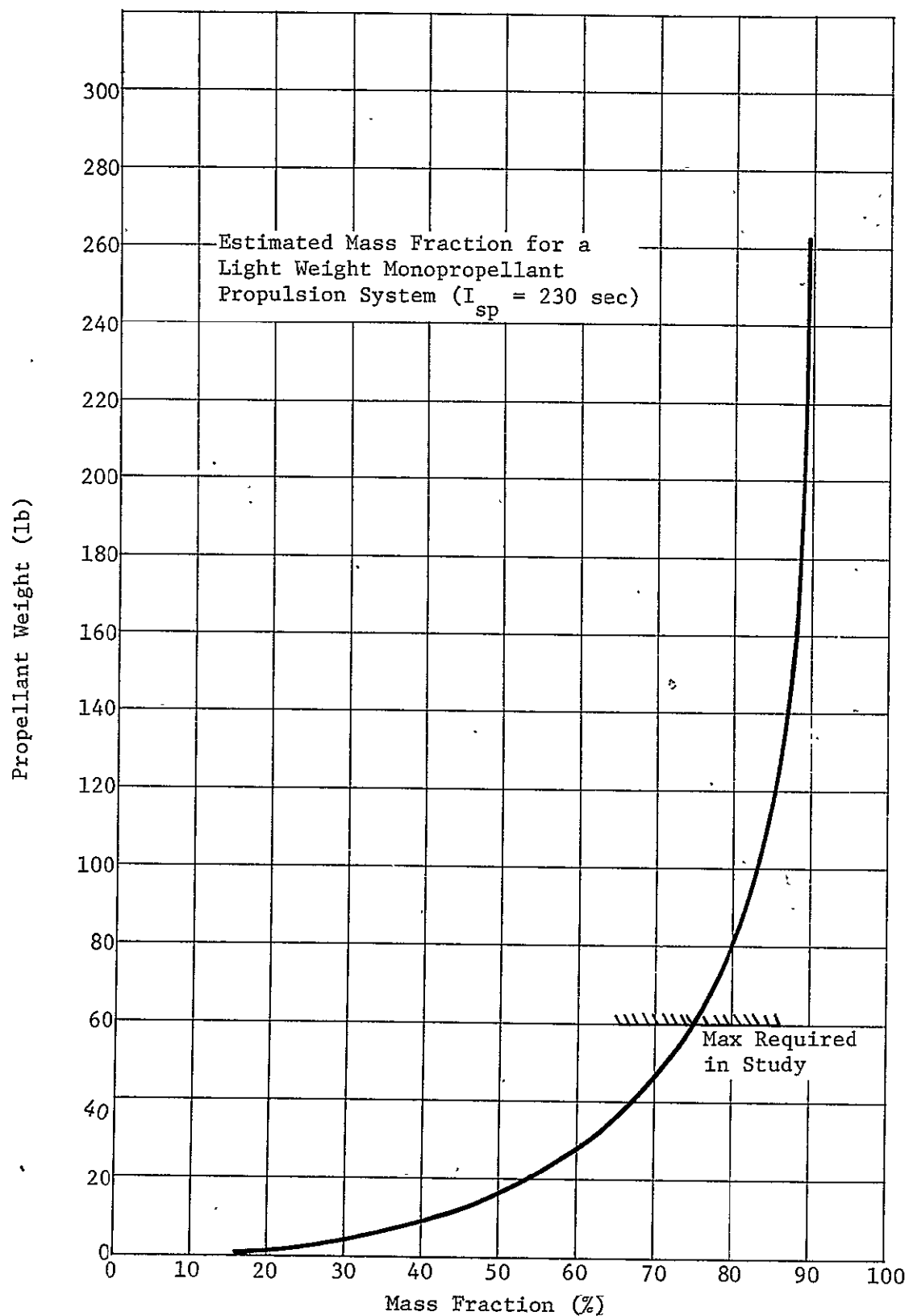


Figure VE-1

TABLE VE-1

$W_{\text{Entry Probe}}$	ΔV	W_{Prop}	W_{Inert}	W_{DS}	M/%
270 lb	197 m/s	26 lb	18 lb	44 lb	59
	125	16	16	32	50
	50	6.5	15	21.5	32
440	298	65	20.5	85.5	76
	225	50	19.5	69.5	72
	75	15	15.5	30.5	49
615	615	201	24	22.5	89.5
	375	116	21	137	85
	150	42	19	61	68.5
650 lb	197	60	20	80	75
	125	33	19	57	67
	50	15	16	31	48
1159	298	170	23	193	88
	225	125	21	146	85.5
	75	40	19	59	68
1936	615	626	70	696	90
	375	358	40	398	90
	150	135	21	156	86.5

Table VE-1 - Continued

Where:

ΔV	= Velocity increment required to achieve (given)	- m/sec
$W_{\text{entry probe}}$	= Estimated Entry Probe weight excluding deflection system - lbm (given)	
W_{prop}	= Calculated propellant weight assuming an I_{sp} of 230 sec - lbm.	
W_{inert}	= Inert, i.e., fixed or hardware weight of deflection system - lbm.	
W_{DS}	= Weight of deflection system - lbm	
$M/\%$	= Mass fraction, i.e., propellant wt/system wt of the deflection system - %	

Sample Calculation

Entry Probe Weight = 650 lb

$$\Delta V = 125 \text{ m/s}$$

$$\Delta V = g_c I_{sp} n (w_i/w_f)$$

$$\ln w_i/w_f = \frac{125 \times 3.281}{32.2 \times 230} = 0.0554$$

$$w_i/w_f = 1.057 \text{ and assuming an inert (fixed) weight of 19 lb,}$$

$$w_i = 1.057 (650 + 19) = 707 \text{ and } w_p = (707 - 669) = 38 \text{ lb}$$

From Figure VE-1, mass fraction = .67 so system weight = $38/.67 = 56.7$
or 57. Inert weight = $57 - 38 = 19 \text{ lb}$ so assumed value agrees.

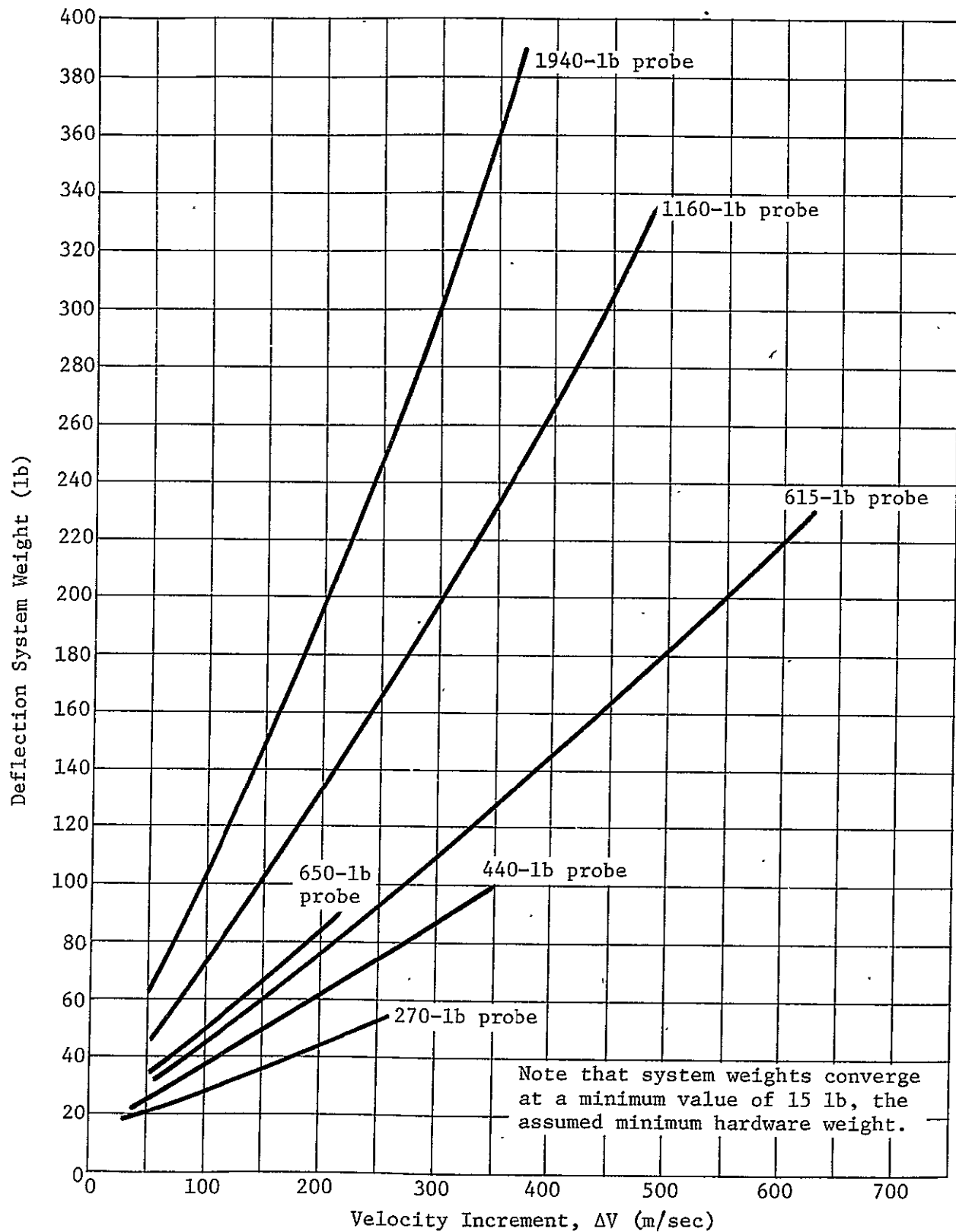


Figure VE-2
Sensitivity of a Monopropellant Deflection System
Weight to Entry Probe Weight and ΔV Requirement

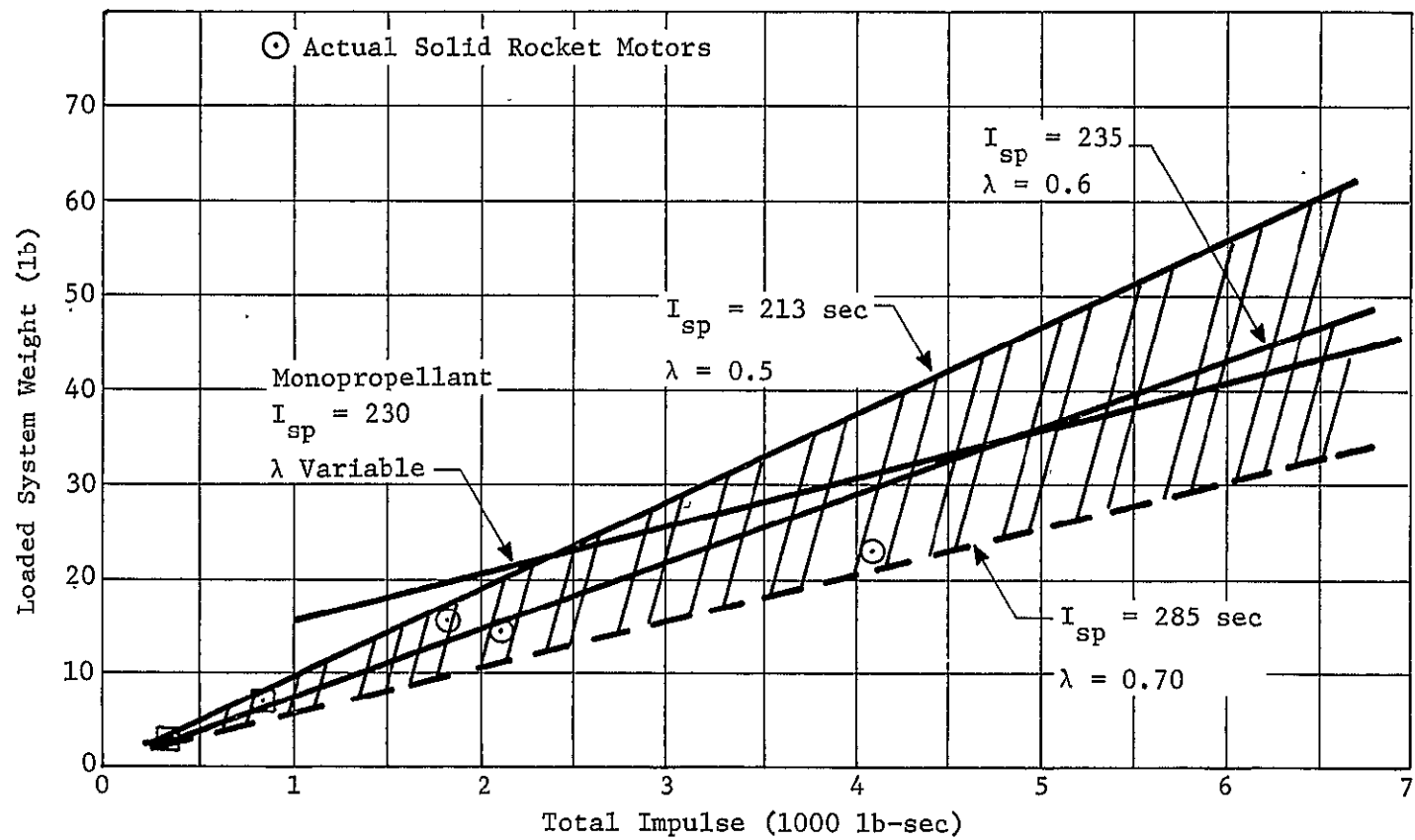


Figure VE-3 Propulsion System Performance Comparison

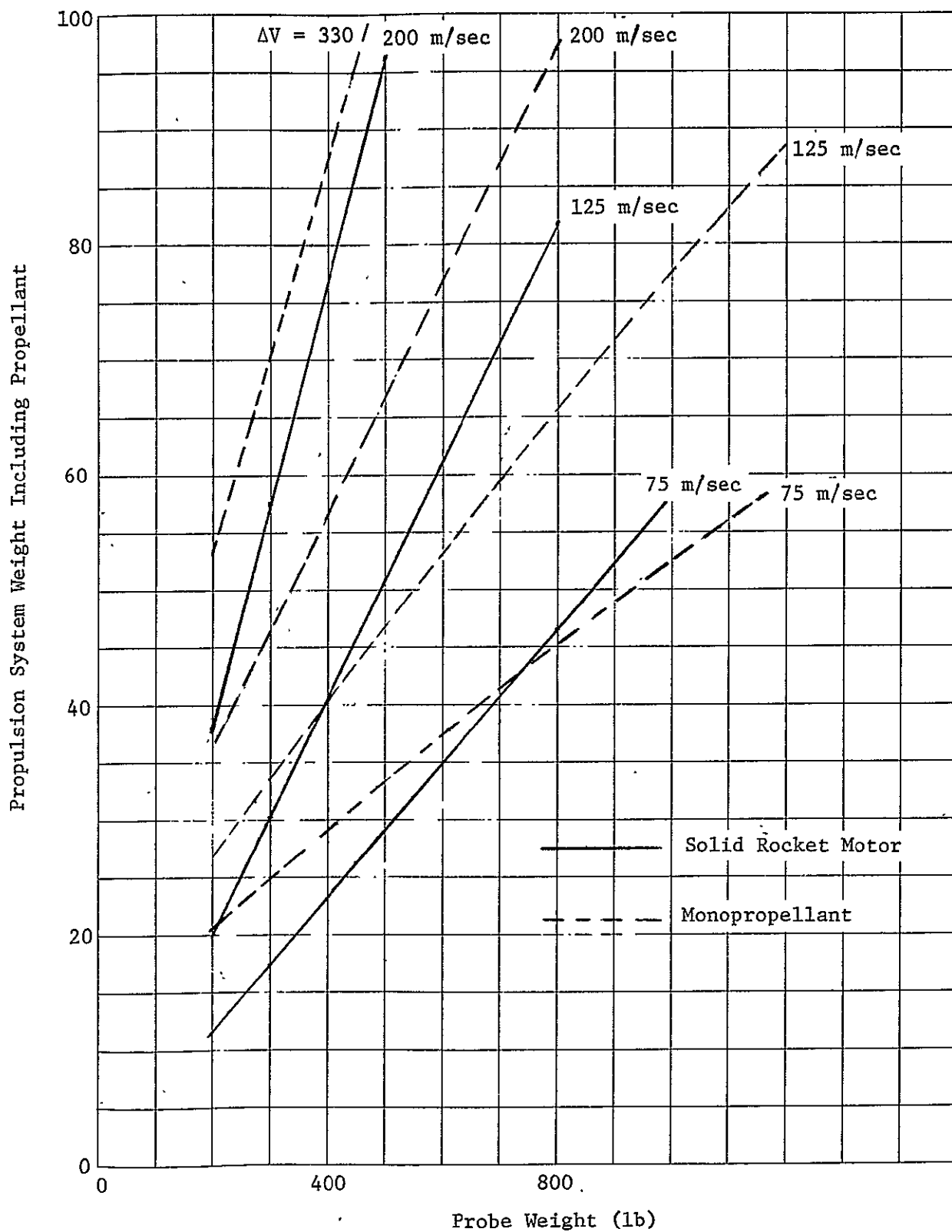


Figure VE-4 Probe Deflection System Weights for Parametric Study

b. Descent Phase Probe Attitude Propulsion Systems

An approach initially considered for alleviating antenna pointing angle variations caused by turbulence during post entry descent was that of an active attitude control system. Consequently a study was conducted to evaluate candidate propulsion systems which could provide the thrust needed to depths of 1000 atm and temperature levels of 2100°F.

It was found that the weights required for such an approach, combined with the evolution of a milder turbulence model than originally anticipated and the concept of the dual relay (split probe) concept which permits the use of broad beam width antennas, indicated that an active ACS system would not be required. However, for future reference, the propulsion system study results are documented herein -- a brief summary is given below and a more detailed account in Appendix B.

Four candidate propulsion systems were identified for operation over a thrust range of from 0.01 to 0.1 lb and over a total impulse range of from 100 to 1000 lb sec. These systems are schematically illustrated in Figure VE-5. Momentum storage devices as well as propulsion systems were considered.

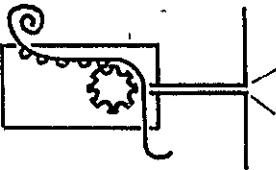
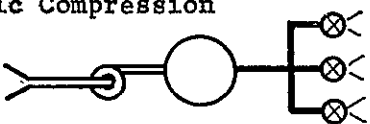
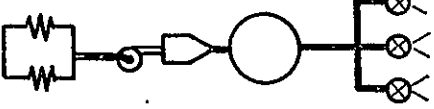
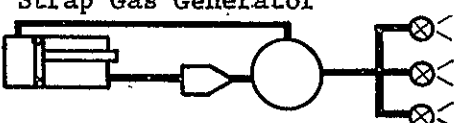
The most significant conclusions from this study are:

1. Use of a conventional monopropellant, bipropellant or stored gas system is impossible for descent probe attitude control because of the extremely high atmospheric pressure and temperature.
2. New technology requirements can be minimized by use of battery powered reaction wheels for attitude control of the descent probe. However, the momentum storage capability of these devices is extremely limited for reasonable system weights, and use of these devices will require that vehicle disturbances be reduced to near zero by design of an effectively neutral aerodynamic shape for the probe.

Figure VE-5

Descent Probe - Active Attitude Control Propulsion System Candidates

V-112

PROPULSION SYSTEM CANDIDATES	ADVANTAGES	DEVELOPMENT REQUIREMENTS	ESTIMATED SYSTEM WEIGHTS	
			100 lb sec .01 lb Thrust	1000 lb sec .1 lb Thrust
CAP PISTOL 	Has Been Demonstrated at Chamber Pressures of 100-200 ATM	<ul style="list-style-type: none"> • Propellant for High Pressures • Nozzle/Cap Seal Problems • Low Thrust Levels 	35 lbs	73 lbs
HOT GAS PLENUM Atmospheric Compression  Pump-Fed Gas Generator  Boot Strap Gas Generator 	Can Get Low Thrust Levels & Relatively High Efficiency	<ul style="list-style-type: none"> • Test Facilities • Valves, Compressors, Pumps, Chemical Reactions, Tanks. 	15	58
			9	31
			9	37
REACTION WHEELS	Internal Installation	Increased Momentum Storage Capability Required	31 lbs will give 2.7 ft-lb-sec per axis storage capability.	

3. The candidate propulsion systems identified here are judged to be the most feasible propulsive approaches for active attitude control of the descent probe. Nevertheless their application will involve a significant weight penalty and will require a major development of new technology; largely because of the reduced performance and added design complexity that will result from operation in a high temperature/high pressure atmosphere.
4. Estimated system weights are shown in Figure VE-6 as a function of total impulse and thrust level. Although no correlations are available between the total impulse required to prevent a given number of probe disturbances due to turbulence, the system weights are quite large relative to the impulse obtained. Consequently an aerodynamically stabilized system would be preferred for all but situations requiring very small pointing angle variations and turbulence models involving few disturbances.

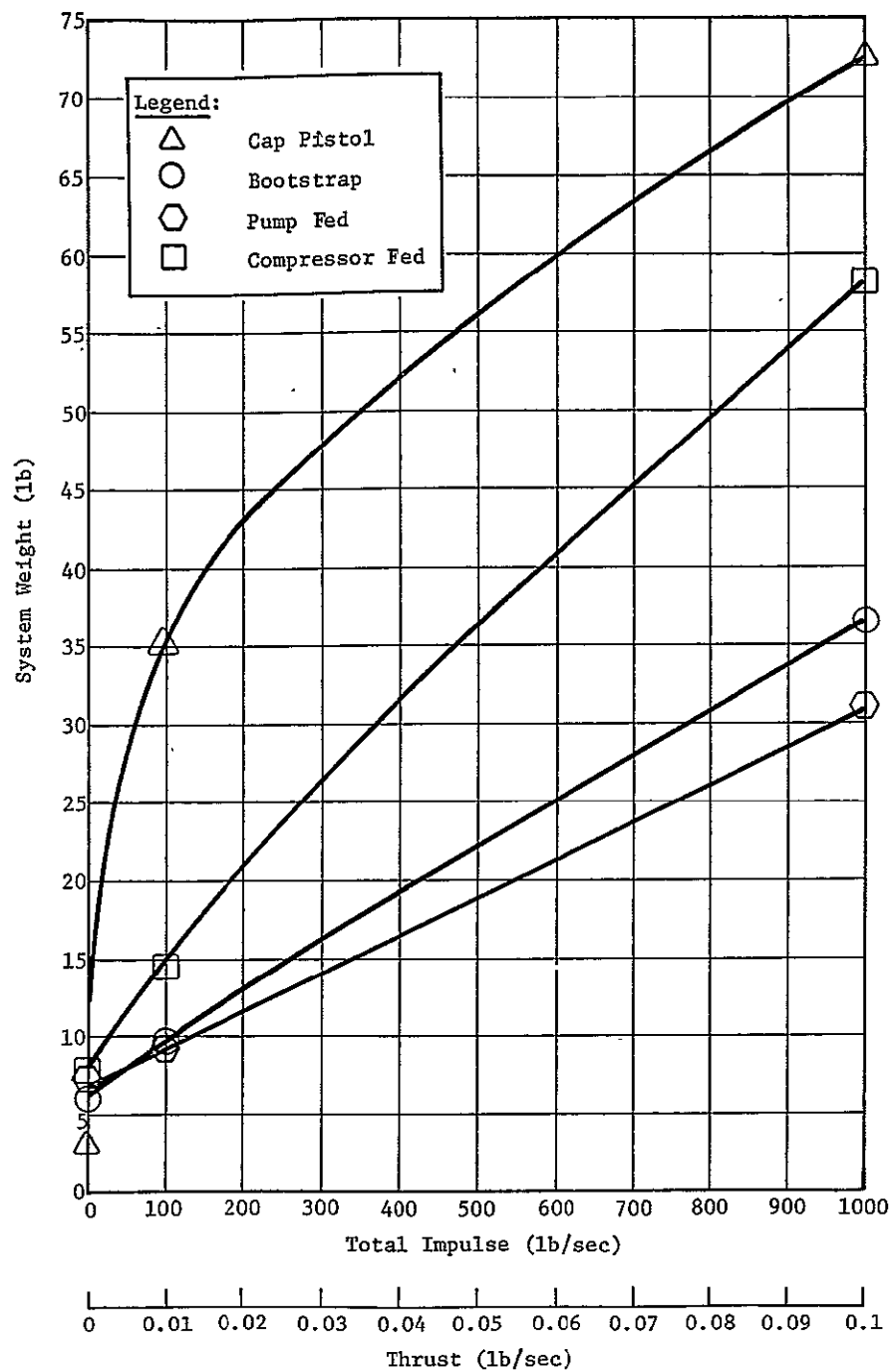


Figure VE-6 Sensitivity of Attitude Propulsion System Weight to Thrust and Total Impulse Capability

VI. MISSION EFFECTIVENESS MODEL

A. Introduction

1. General Purpose of the Model

The Jupiter probe evaluation model is a digital program specifically designed to evaluate the effectiveness with which various competing mission configurations answer the questions which form the science objectives for the Jupiter atmospheric entry mission. The program is written in Fortran IV and arranged such that the IBM 1130 computer with a disk memory and on-line Cal-Comp plotter can be used to insure a rapid turn around time.

A scientific analysis has been made for the sixteen observables which make up the science objectives of the Jupiter atmosphere. This analysis provides, for each observable, the logical arrangement of applicable instruments, the relative value which can be attached to a measurement due to horizontal and vertical location with respect to the planet, and the vertical displacement between measurements. The instrument arrangement forms a part of the model programming, while the value functions are stored in permanent data files, on the computer disk memory.

The mission configuration (probe characteristics and instrument sampling data) is read from card inputs and stored in temporary disk files. An evaluation is made by the model for each observable; during this process, the achieved value for that observable is recorded, for subsequent plotting, as a function of pressure-depth, simulating the probe descent through the atmosphere. The values for different observables are added to give the total value for the mission, as well as a graphical plot of the rate at which it was accumulated during the descent.

A mainline program, sixteen subroutines and an auxiliary program comprise the model. A brief description of the subprograms is given below.

2. Mainline Program - MAJUP

The mainline program sequences the model through the various subroutines and if the option is exercised, plots the summary of the science

value achieved by the configuration as a function of depth and a second plot giving the science value achieved for each observable.

3. Subrouting ZERO

This subroutine initializes the temporary file 1, containing sampling rate and altitude ranges for each of the instruments.

4. Subroutine STARJ

Prints heading for the tabulated output data.

5. Subroutine READJ

When called by the mainline program, this subroutine reads the input data mission, prints out the same information, makes transformations in the units of the input data and finally loads the probe descent profile into temporary file 7 and the instrument sampling data into temporary file 1.

6. Subroutine DRADT

When the plotting option is used, this subroutine provides a reference frame and the proper annotations for the question value versus pressure-height plot.

7. Subroutine DRAVT

When the plotting option is used, this subroutine provides a reference frame and the proper annotations for the question value versus question number plot.

8. Calculation Subroutines CAJ1 thru CAJ9

These subroutines inspect the instruments carried on the probe and determine the extent that the particular observable has been answered. In order to do this, an instrument logic equation (one for each question or observable) is evaluated by using the value established for each instrument. The instrument value is a function of an input value, usually set to unity, and a sampling factor which is a function of the location and timing of the measurements of the particular instrument. Below are listed the observables calculated by the nine calculation subroutines.

Subroutine	Observable Calculated
CAJ1	Q(1) and Pressure-Temperature Reference
CAJ2	Q(2)
CAJ3	Q(3)
CAJ4	Q(4)
CAJ5	Q(5) & Q(6)
CAJ6	Q(7) & Q(8)
CAJ7	Q(9), Q(10) & Q(11)
CAJ8	Q(12) & Q(13)
CAJ9	Q(14), Q(15) & Q(16)

9. Subroutine SAMPJ

This subroutine normally computes the relative value of a given instrument with respect to a particular observable. This relative value is actually a composite sampling factor which modifies the input instrument value. In turn, this sampling factor is the product of five other factors.

a. Sampling Differential Value

This value is the value which can be attached to a measurement due to altitude (in terms of the log of the atmospheric pressure in atmospheres). The value is obtained by the interpolation of the pressure-depth of the probe at the time of the measurement into a differential value profile curve.

b. Sampling Interval Ratio

This factor is the ratio of the permissible interval between successive measurements to the interval resulting from a combination of the probe's descent rate and the instrument's sampling rate.

c. Target Value

This factor is found by interpolating the position of the probe, adjusted for descent time and the rotation of the planet, into a set of target value curves.

d. Probe Reliability

This factor is an input value for each probe and is the probability that the probe will be able to make the measurements it is designed to make.

e. Difference in the Log Pressure - Depth of Successive Measurements

This difference multiplied by the Sampling Differential Value gives the proportion of the total vertical measurement that a given measurement represents. The summation of all possible such products must equal unity before they are modified (reduced) by the factors in b, c, and d.

10. Subroutine FINDJ

This subroutine is a simple linear interpolation routine which is used throughout the program.

11. Auxiliary, File Loading Routine

This is a separate program that has the single purpose of loading the permanent files with data representing the science value functions which should not be changed if evaluations of competitive configurations are to be compared accurately. Therefore, this program is a one-use program.

B. Input Requirements of the Model

1. Science Criteria for the Mission Effectiveness Model

On the following pages, are listed in tabular form, the following information concerning each observable:

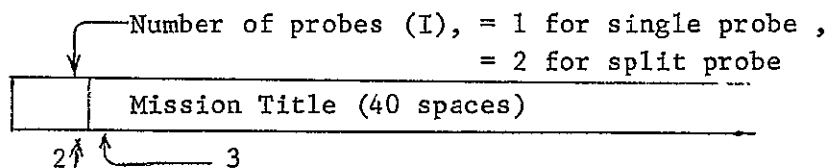
- a. English statement of the question constituting the observable.
- b. English statement describing the logical form of the instrument group applicable to that observable.
- c. For each instrument relating to the observable, reference numbers for a differential value curve, a target value curve, and a measurement interval list are indicated which are applicable for that observable.

- d. The last entry on the table summarizing the science criteria, is an instrument logic equation for that observable.
- e. Following the entries for each observable is a symbol dictionary Table VI-7 which will allow the interpretation of the instrument logic equations.
- f. The last portion of the science criteria is made up of the actual value function curves (Figures VI-1 thru VI-8 and Table VI-8), the differential value profiles, the target value curves and the measurement interval lists.

2. Mission Design Data for the Mission Effectiveness Model

The mission design data can best be understood in the terms of the input data cards, of which there are four separate varieties. Those inputs requiring right-adjusted integers are marked with a (I).

a. Mission Card



- Notes: a. The mission title should be centered in the 40 character field.

Table VI-1 Summary of Science Input Requirements

No.	Observable	Instrument Groups	Potential Value	Applicable Value Curves			Applicable Instrument Logic Equation.
				Pressure-Height Value Curve	Target Value Curve	Sample Interval Value Curve	
0	Determine a pressure and temperature reference at the time of a primary measurement.	Pressure and Temperature	NA	NA	NA	NA	PAT = EX(2)
			NA	NA	NA	NA	= PRESS*TEMP
1	Determine the relative abundances of H and He in the lower atmosphere below the turbopause.	Gas Chrom/Mass Spec	1.	#	#	#	Q(1) = 1-(1-GCMS)
		or Expanded GC/MS	1.	#	#	#	*(1-GCMS)*
		or Neutral Mass Spect.	1.	#	#	#	(1-AMSPC)
2	Determine the isotopic H/D, $^3\text{He}/^4\text{He}$, $^{20}\text{Ne}/^{23}\text{Ne}$, $^{36}\text{A}/^{38}\text{A}$, $^{36}\text{A}/^{40}\text{A}$, $^{12}\text{C}/^{13}\text{C}$ in the lower atmosphere below the turbopause.	Gas Chrom/Mass Spect.	1.	#	#	#	Q(2) = 1-(1-GCMS)
		or Expanded GC/MS	1.	#	#	#	*(1-GCMS)*
		or Neutral Mass Spect.	1.	#	#	#	(1-AMSPC)*
		or H/D Photometer	.3	PV-3	TV-2	SV-1	(1-.3*HDPHO)
3	Determine the atmospheric mean molecular weight and the concentrations of the major contributing gases (i.e., determine whether H_2 or H_E are indeed the only major constituents and, if not, what other gases are.	Gas Chrom/Mass Spect.	1.	PV-1	TV-0	SV-2	Q(3) = 1-(1-GCMS)
		or Expanded GC/MS	1.	PV-1	TV-0	SV-2	*(1-GCMS)
		or Neutral Mass Spect.	1.	PV-1	TV-0	SV-2	*(1-AMSPC)

Table VI-2 Summary of Science Input Requirements

No.	Observable	Instrument Groups	Potential Value	Applicable Value Curves			Applicable Instrument Logic Equation
				Pressure-Height Value Curve	Target Value Curve	Sample Interval Value Curve	
4	Determine concentration profiles of the minor atmospheric constituents (e.g., Ne, A, etc., and CH ₄ , NH ₃ , H ₂ O, H ₂ S, etc.) versus pressure and temperature from above the clouds down to at least several hundred bars.	Pressure-Temperature and at least one of the following	NA	NA	NA	NA	$Q(4) = PAT * TEMP$ $*[1 - (1 - GCMS) * (1 - GCMS) * (1 - .8 * AMSPC) * (1 - .4 * CHPHO) * H3PHO]$
		Gas Chrom/Mass Spec or Expanded GC/MS or Neutral Gas Spec or Methane and Ammonia Photometers and Continuous Temperature Measurements	1.	PV-2	TV-1	SV-3	
			1.	PV-2	TV-1	SV-3	
5	Determine the pressure and temperature profiles from above the cloud tops down to well below the condensation level of H ₂ O with a precision sufficient to determine whether the lapse rate is adiabatic.	Pressure and Temperature or Pressure and Temperature and 10 μ IR Radiometer	$\left. \begin{array}{l} 0.9 \\ 1.0 \end{array} \right\}$	PV-2	TV-1	SV-5	$Q(5) = TEMP * PRES * (.9 + .1 * RAD10)$

Table VI-3 Summary of Science Input Requirements

No.	Observable	Instrument Groups	Potential Value	Applicable Value Curves			Applicable Instrument Logic Equation
				Pressure-Height Value Curve	Target Value Curve	Sample Interval Value Curve	
6	Determine the vertical distribution and structure of the cloud layers with respect to pressure and temperature.	Pressure-Temperature and At Least One of the Following: Nephelometer	NA	NA	NA	NA	$Q(6) = PAT * [1 - (1 - .4 * AEPHO) * (1 - .8 * RADUL)]$
		or Dual Channel IR Radiometer	1.0	PV-2	TV-1	SV-6	$*(1 - ANEPH)]$
		or Aerosol Photometer	0.8	PV-2	TV-1	SV-6	
			0.4	PV-3	TV-2	SV-4	
7	Determine the chemical composition of the cloud particles in each layer.	Pressure-Temperature and At Least One of the Following: Gas Chrom/Mass Spec	NA	NA	NA	NA	$Q(7) = PAT * [1 - (1 - GCMS) * (1 - GCMS)]$
		or Expanded GC/MS	1. } 1. }	PV-2	TV-1	SV-3	
8	Determine the color of each of the cloud layers.	Pressure-Temperature and At Least One of the Following: Nephelometer with Color Filter Wheel	NA	NA	NA	NA	$Q(8) = PAT * [1 - (1 - .5 * COPHO) * (1 - .9 * CONED)]$
		or Photometer with Color Filter Wheel	0.9	PV-2	TV-1	SV-6	
			0.5	PV-3	TV-2	SV-4	

Table VI-4 Summary of Science Input Requirements

No.	Observable	Instrument Groups	Potential Value	Applicable Value Curves			Applicable Instrument Logic Equation
				Pressure-Height Value Curve	Target Value Curve	Sample Interval Value Curve	
9	Determine the intensity distribution of the incoming solar flux at several wave lengths as a function of pressure and temperature from above the clouds down to several tens of bars.	Pressure-Temperature and Solar Photometer	NA	NA	NA	NA	$Q(9) = PAT * SOPHO$
			NA	PV-3	TV-2	SV-4	
10	Determine the thermal radiation (IR) flux profiles at several wave lengths from above the clouds down to at least several hundred bars.	Pressure-Temperature and Up & Down IR Radiometer	NA	NA	NA	NA	$Q(10) = PAT * RADUD$
			NA	PV-2	TV-1	SV-5	
11	Determine whether specific complex molecules are present in the region between the cloud tops and the condensation level of H ₂ O.	Pressure-Temperature and At Least One of the Following: Expanded GC/MS or UV Absorptive Spectrophotometer	NA	NA	NA	NA	$Q(11) = PAT * [1 - (1 - GCMS) * (1 - .8 * UVPHO)]$
			1.0 0.8	PV-3	TV-1	SV-8	

Table VI-5 Summary of Science Input Requirements

No.	Observable	Instrument Groups	Potential Value	Applicable Value Curves			Applicable Instrument Logic Equation
				Pressure-Height Value Curve	Target Value Curve	Sample Interval Value Curve	
12	Determine the frequency of occurrence of electrical discharges and the presence of any thunder as a function of pressure and temperature.	Pressure-Temperature and At Least One of the Following: Lightning Photometer or RF Lightning Detector or RF Lightning Detector and Microphone	NA	PV-2	TV-1	SV-5	$Q(12) = PAT * [1 - (1 - .5 * PHOLT) * 1 - RELIT * (.75 + .25 * EAR)]$
			0.5				
			0.75				
			1.0				
13	Determine the physical characteristics (number density, size distribution) of the cloud particles in each cloud layer -- particularly through the region of the cloud tops.	Pressure-Temperature and At Least One of the Following: Nephelometer or Dual Channel IR Radiometer	NA	PV-2	TV-1	SV-6	$Q(13) = PAT * [1 - (1 - .5 * RADUL) * (1 - .5 * ANEPH)]$
			0.5				
			0.5				
14	Determine the scales and the magnitude and frequency spectra of the atmospheric turbulence from above the cloud tops down to at least several tens of bars.	Pressure-Temperature and Turbulence Accelerometers	0.9	PV-3	TV-1	SV-7	$Q(14) = PAT * .9 * ACCEL$

Table VI-6 Summary of Science Input Requirements (concluded)

No.	Observable	Instrument Groups	Potential Value	Applicable Value Curves			Applicable Instrument Logic Equation
				Pressure-Height Value Curve	Target Value Curve	Sample Interval Value Curve	
15	Determine the magnetic field strength and variations versus depth from above the ionosphere down through the lower atmosphere ($P \sim 1000$ Bars).	Magnetometer	1.0	PV-4	TV-3	SV-3	$Q(15) = \text{AMAG}$
16	Determine the electrical conductivity of the deep atmosphere and clouds.	Electrometer	1.0	PV-4	TV-3	SV-3	$Q(16) = \text{ELECT}$
# For observables 1 and 2, the requirements are for at least four samples to be taken, regardless of the vertical or horizontal position of the measuring instrument. For these two questions, neither the subroutine SAMPJ nor the normal value curves are used for the mass spectrometers.							

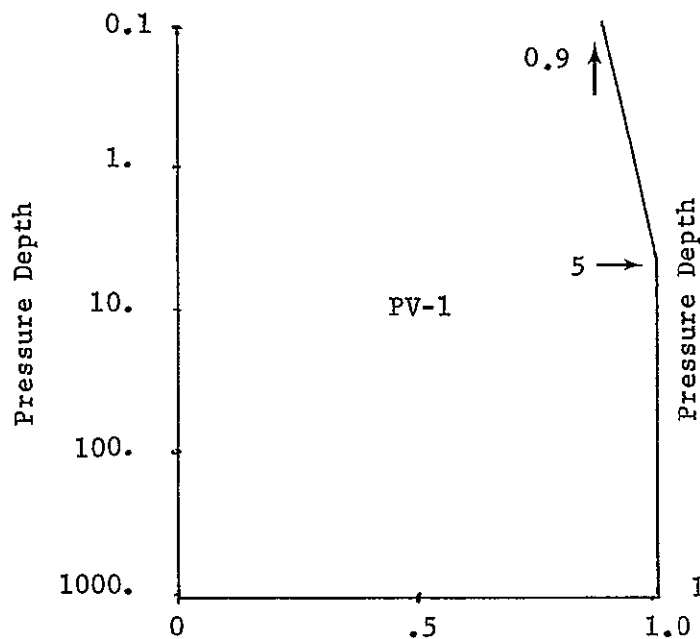
SYMBOL DICTIONARY

TABLE VI-7

<u>Instrument Index</u>	<u>Instrument Description</u>	<u>Program Symbol</u>
1 #	Pressure Sensor	PRESS
2	Pressure-Temperature (has a value of zero if one or both of the instruments are missing and a value of 1.0 if both are present); a calculated rather than an input value.	PAT
3 #	Temperature Sensor	TEMP
4 #	Accelerometer	ACCEL
5 #	Gas Chromatograph / Mass Spectrometer	GC/MS
6 #	H/D Photometer	HDPHO
7 #	Methane (CH ₄) Photometer	CHPHO
8 #	Ammonia (NH ₃) Photometer	N3PHO
9	Expanded GC/MS	GCEMS
10	Photometer with Color Filter Wheel	COPHO
11 #	Aerosol Photometer	AEPHO
12	Solar Photometer	SOPHO
13	UV Absorptive Spectrophotometer	UVPHO
14 #	Lightning Photometer	PHOLT
15	Neutral Mass Spectrometer	AMSPC
16	10 μ IR Radiometer	RADIO
17	Dual Channel IR Radiometer	RADUL
18	Up/Down IR Radiometer	RADUD
19	Nephelometer	ANEPH
20	Nephelometer with Color Filter Wheel	CONEP
21	RF Lightning Detector	RFLIT
22	Microphone	EAR
23	Magnetometer	AMAG
24	Electrometer	ELECT

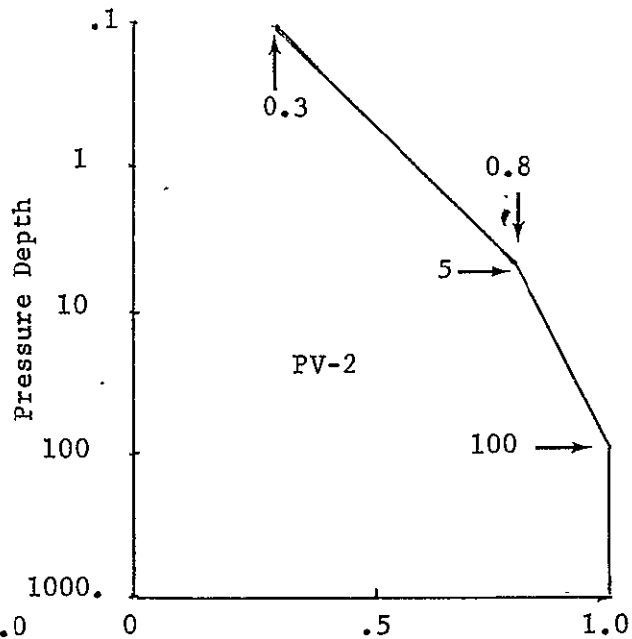
#Instrument is a member of the nominal science payload.

Differential Value Profile



Value of Single Meas.

Figure VI-1 PV-1



Value of Single Meas.

Figure VI-2 PV-2

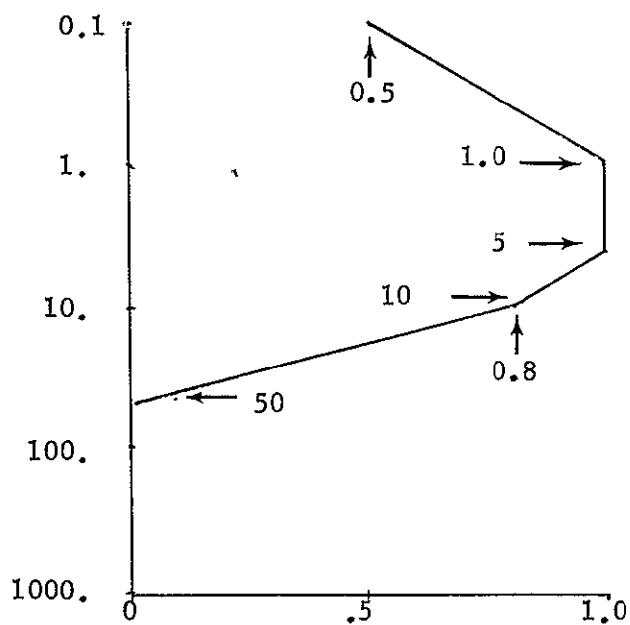


Figure VI-3 PV-3

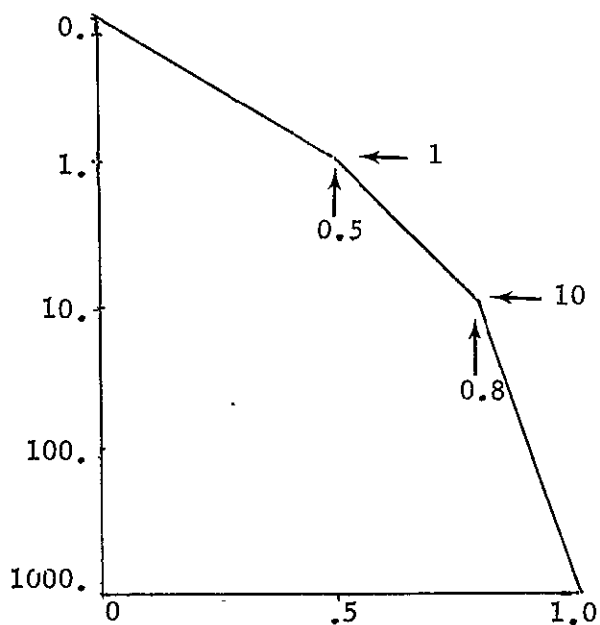


Figure VI-4 PV-4

Target Value Curves

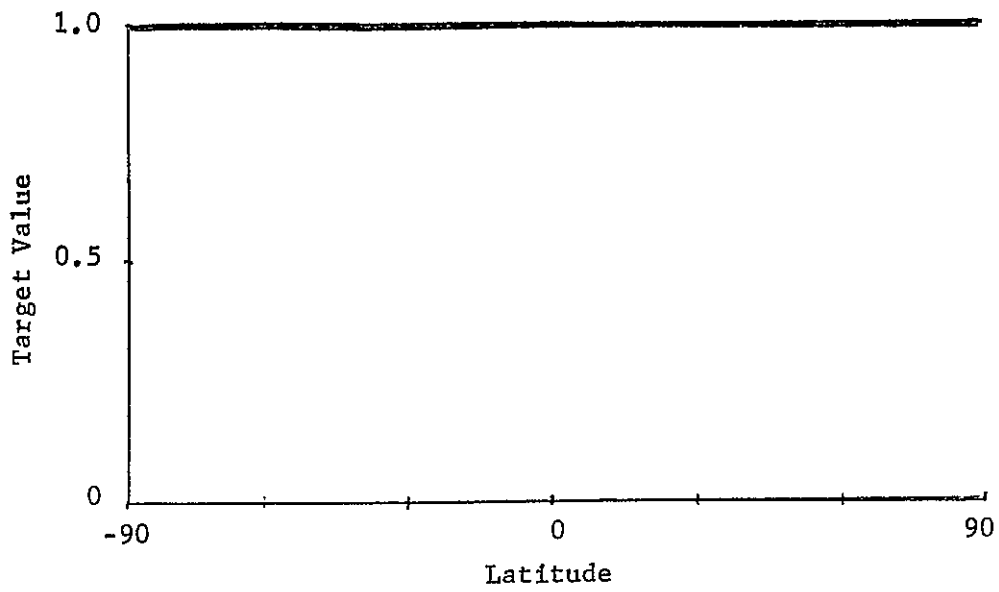


Figure VI-5 TV-0

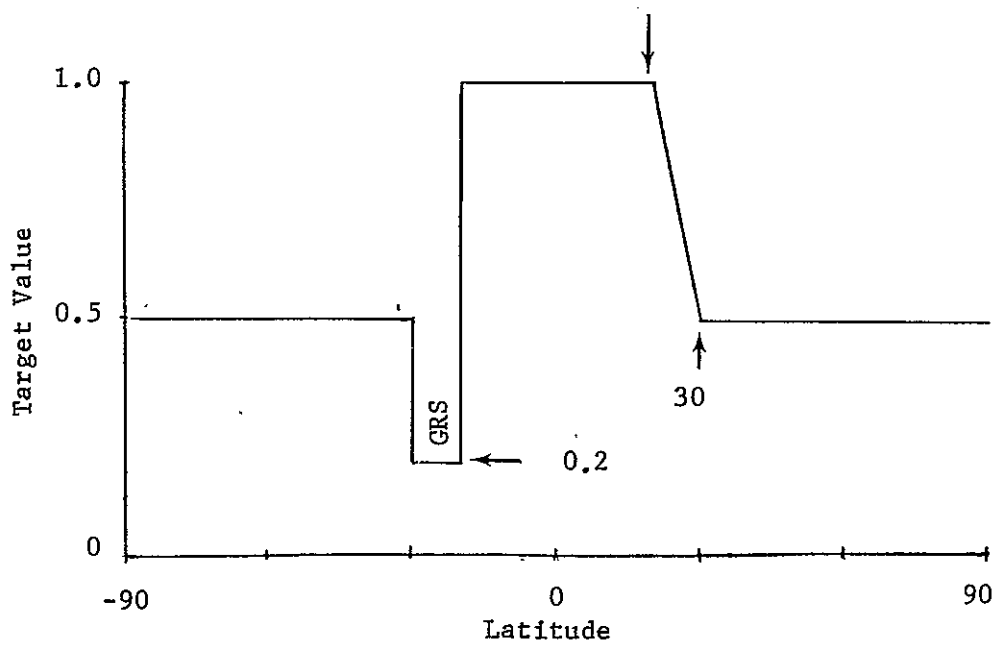


Figure VI-6 TV-1

Target Value Curves

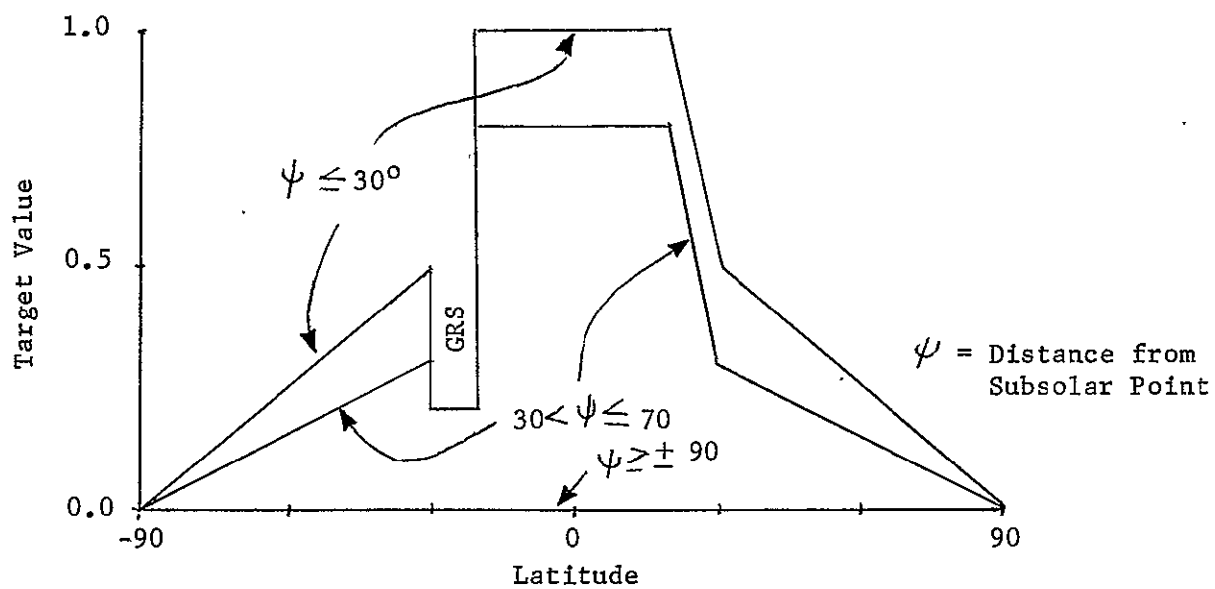


Figure VI-7 TV-2

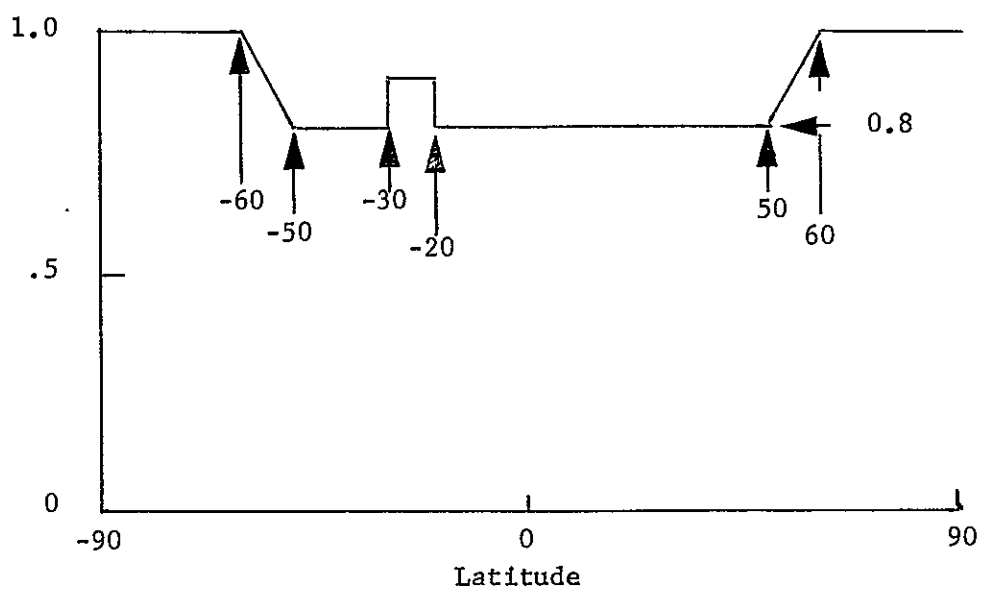


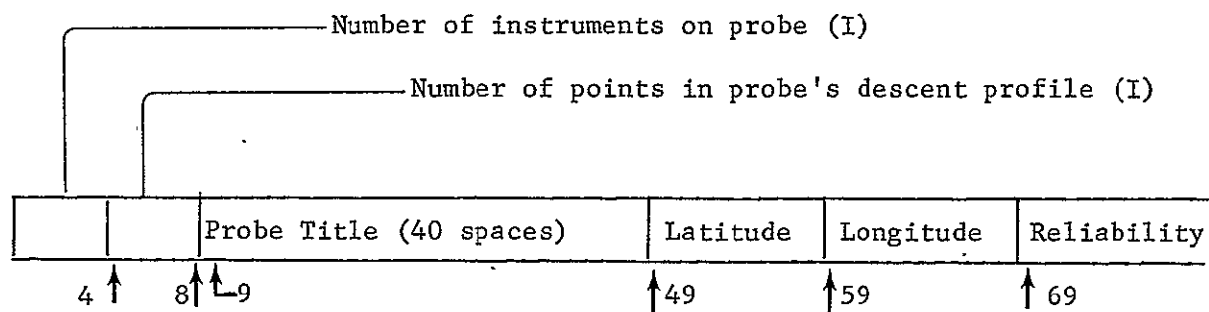
Figure VI-8 TV-3

MEASUREMENT INTERNAL LIST

TABLE VI-8

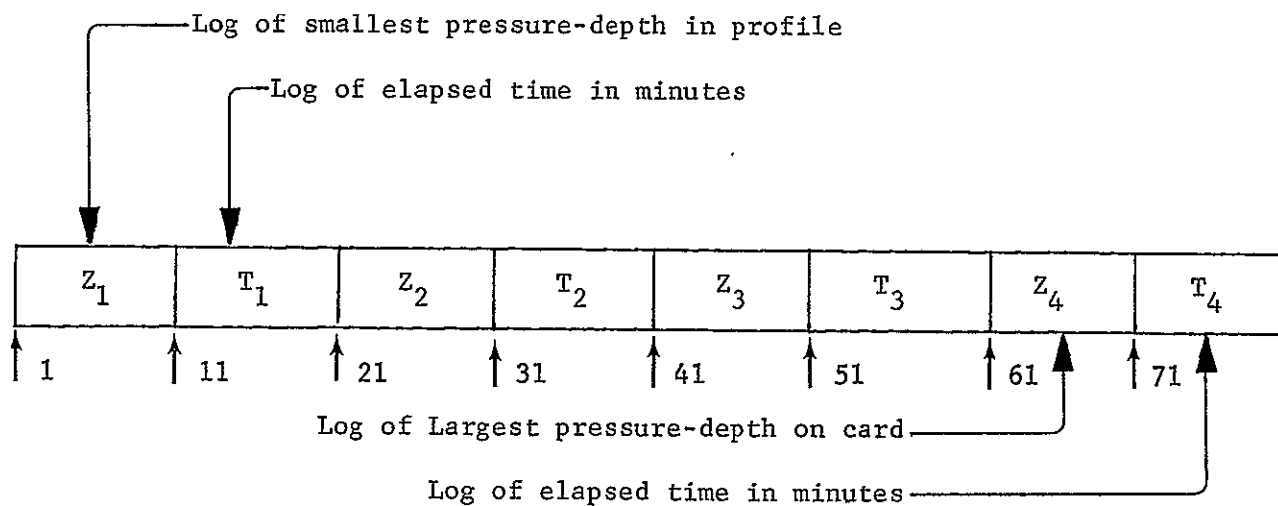
<u>List</u>	<u>Pressure-Depth Range (ATM)</u>	<u>Measurements Per Scale Height</u>	<u>Scale Heights Per Measurement</u>
SV-1	1.0 to 10.0	0.6	1.8
	10. to 50.0	2.0	0.5
SV-2	0.1 to 5.0	1.0	1.0
	5.0 to 1000.0	0.5	2.0
SV-3	0.1 to 100.0	2.0	0.5
	100.0 to 1000.0	0.5	2.0
SV-4	0.1 to 50.0	100.0	.01
SV-5	0.1 to 100.0	50.0	0.02
	100.0 to 1000.0	25.0	0.04
SV-6	0.1 to 100.0	100.0	0.01
	100.0 to 1000.0	50.0	0.02
SV-7	0.1 to 50.0	10.0	0.1
SV-8	0.1 to 50.0	2.0	0.5

b. Probe Data Card



- Notes:
- Core space for a maximum of twenty pairs of points has been provided for the descent profile.
 - The latitude and longitude are given in decimal degrees measured in plus or negative directions from the sub-solar point.

c. Descent Profile Card



Note: The program is limited to 20 pairs of points, four on a card.

d. Instrument Card

The diagram shows an 'Instrument Card' form with the following structure and labels:

- Instrument Index (I)**: Points to the first field (2 characters).
- Number of pairs of points in Design Meas. List (I)**: Points to the second field (4 characters).
- Instrument Title (28)**: A large field for the instrument's name.
- Value Index**: A field for the value index, with an example value of 33.
- Design Measurement List**: A table with 8 columns: P₁, DT₁, P₂, DT₂, P₃, DT₃, P₄, and DT₄. Below these columns are example values: 38, 43, 48, 53, 58, 63, and 68.

Notes: a. The instrument index is a set of arbitrarily assigned numbers as follows:

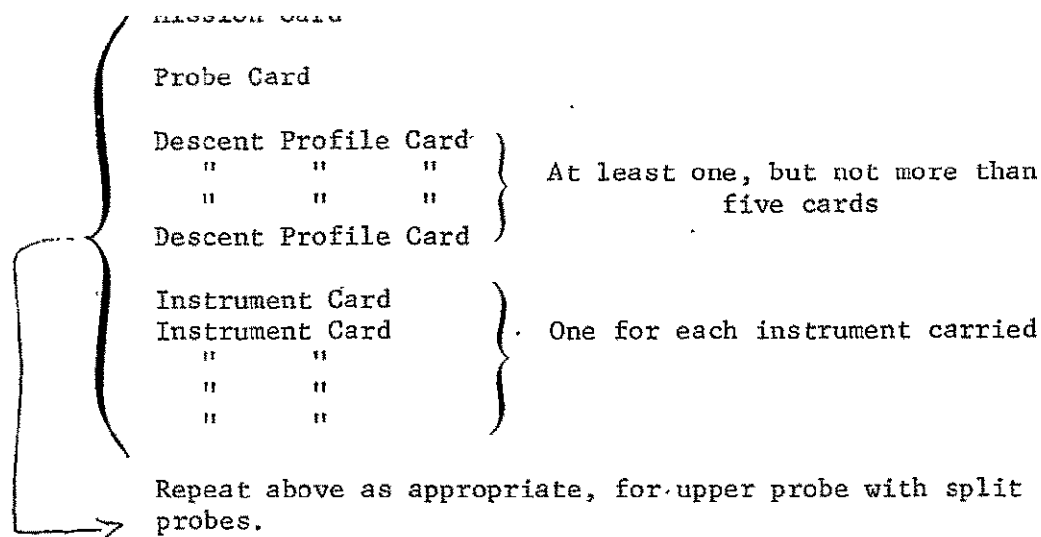
- | | |
|-------------------------------|----------------------------|
| 1. Pressure Sensor | 13. UV Absorb. Spectro. |
| 2. N.A. | 14. Lightning Photomtr |
| 3. Temperature Sensor | 15. Gas Spectrometer |
| 4. Accelerometer | 16. 10 μ IR Radiometer |
| 5. GC/MS | 17. Dual IR Radiomtr |
| 6. H/D Photometer | 18. Up/Down IR Radiomtr |
| 7. CH ₄ Photometer | 19. Nephelometer |
| 8. NH ₃ Photometer | 20. Neph w/Color Wheel |
| 9. Expanded GC/MS | 21. RF Lightning Detector |
| 10. Photomtr w/Color Wheel | 22. Microphone |
| 11. Aerosol Photometer | 23. Magnetometer |
| 12. Solar Photometer | 24. Electrometer |

b. Space is provided for 4 pairs of values in the Design Measurement List. As an example, the Design Measurement List appearing as;

P ₁	DT ₁	P ₂	DT ₂	P ₃
.2	5.	5.	10.	20.

is interpreted as follows, between an atmospheric pressure of two-tenths and five atmospheres, the instrument is sampled every five seconds, and between five and twenty atmospheres it is sampled every ten seconds.

The total data input describing a given mission can be easily assembled;



3. Program Options

The use of console switches can vary the computation and outputs of the effectiveness model. During normal operation, no switches are turned on and the two plots of question value versus pressure-depth and question value versus question number are obtained. The following switch options are available.

a. Elimination of Sampling Factor

With Switch #8 turned on, the determination of how well or how efficiently the measurements are made is eliminated. It should be noted that no plotting information for the question value versus pressure-depth plot is generated with this option.

b. Elimination of Plots

When Switch #9 is turned on, neither plot is generated.

c. Variation of Plotted Function

The use of Switches #1 thru #7 allow the variation of the function plotted in the question value versus pressure-depth plot. In other words, question value is only one of the functions which can be plotted and tabulated versus pressure-depth. Three other functions are available:

TV - Target Value versus pressure-depth

SIR - Sampling Interval Ratio versus pressure-depth

SDV - Sampling Differential Value (integrated) versus pressure-depth

In the following chart, Table VI-9, these switch options can most easily be seen. Switches #1 thru #5 are used to select a given instrument since the plotted function must be tied to a specific instrument.

TABLE VI-9

		Sw #1	Sw #2	Sw #3	Sw #4	Sw #5
Sw #6 On.	Sw #7 On	TV/ TEMP	TV/ ACCEL	TV/ GCMS	TV/ PHOLT	TV/ RADUL
	Sw #7 Off	SDV/ TEMP	SDV/ ACCEL	SDV/ GCMS	SDV/ PHOLT	SDV/ RADUL
Sw #6 Off	Sw #7 On	SIR/ TEMP	SIR/ ACCEL	SIR/ GCMS	SIR/ PHOLT	SIR/ RADUL
	Sw #7 Off	Cumulative Question Value				

There are two exceptions to the options shown in Table VI-9; Questions one and two are formed on a separate logical basis, which eliminates the consideration of target value, Sampling Differential Value or Sampling Interval Ratio. As a result the cumulative Question Value is tabulated and plotted for them regardless of the switch positions.

C. Effectiveness Mode Outputs

The total output of the model consists of two tabulations and two plots. These outputs are best understood by reference to actual outputs annotated with explanations. Figure VI-9 is a reproduction of the

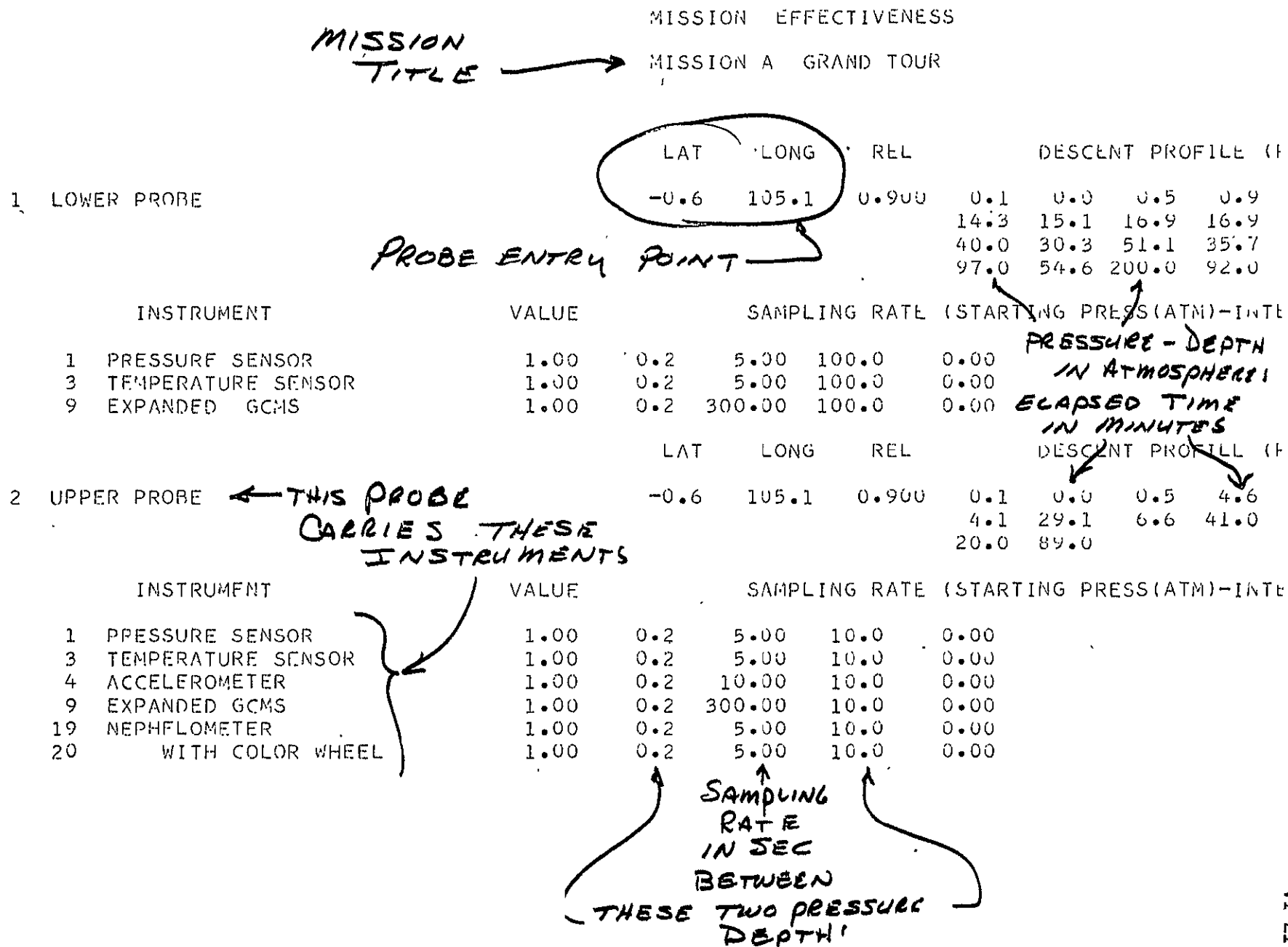


Figure VI-9 Tabulation of Input Mission Data

AT 1.0 ATMOSPHERE QUESTION 3
HAD ACCUMULATED A VALUE OF 0.626

QUESTION VALUE		CUMULATIVE QUESTION VALUE										
		.100	.178	.316	.562	1.00	1.78	3.16	5.62	10.0	17.8	31.6
QUEST 1 =	0.990	0.000	0.399	0.697	0.894	0.990	0.990	0.990	0.990	0.990	0.990	0.990
QUEST 2 =	0.990	0.000	0.399	0.697	0.894	0.990	0.990	0.990	0.990	0.990	0.990	0.990
QUEST 3 =	0.698	0.000	0.332	0.487	0.570	0.626	0.666	0.698	0.698	0.698	0.698	0.698
QUEST 4 =	0.326	0.000	0.006	0.043	0.098	0.150	0.198	0.241	0.279	0.302	0.311	0.319
TOTAL VALUE ACHIEVED FOR QUESTION 4 AT 1000 ATM.												
QUEST 5 =	0.401	0.000	0.014	0.070	0.129	0.180	0.225	0.264	0.312	0.353	0.371	0.387
QUEST 6 =	0.000	0.000	0.000	0.000	0.000	0.000	0.000	0.000	0.000	0.000	0.000	0.000
QUEST 7 =	0.555	0.000	0.095	0.253	0.358	0.433	0.490	0.535	0.555	0.555	0.555	0.555
QUEST 8 =	0.000	0.000	0.000	0.000	0.000	0.000	0.000	0.000	0.000	0.000	0.000	0.000
QUEST 9 =	0.000	0.000	0.000	0.000	0.000	0.000	0.000	0.000	0.000	0.000	0.000	0.000
QUEST 10 =	0.000	0.000	0.000	0.000	0.000	0.000	0.000	0.000	0.000	0.000	0.000	0.000
QUEST 11 =	0.743	0.000	0.238	0.508	0.618	0.677	0.715	0.743	0.743	0.743	0.743	0.743
QUEST 12 =	0.000	0.000	0.000	0.000	0.000	0.000	0.000	0.000	0.000	0.000	0.000	0.000
QUEST 13 =	0.144	0.000	0.016	0.039	0.062	0.078	0.093	0.106	0.127	0.144	0.144	0.144
QUEST 14 =	0.810	0.000	0.389	0.536	0.637	0.705	0.761	0.806	0.810	0.810	0.810	0.810
QUEST 15 =	0.000	0.000	0.000	0.000	0.000	0.000	0.000	0.000	0.000	0.000	0.000	0.000
QUEST 16 =	0.000	0.000	0.000	0.000	0.000	0.000	0.000	0.000	0.000	0.000	0.000	0.000
SUM OF THIS COLUMN												
= TOTAL MISSION VALUE		5.659										

Figure VI-10 Tabulated Model Output

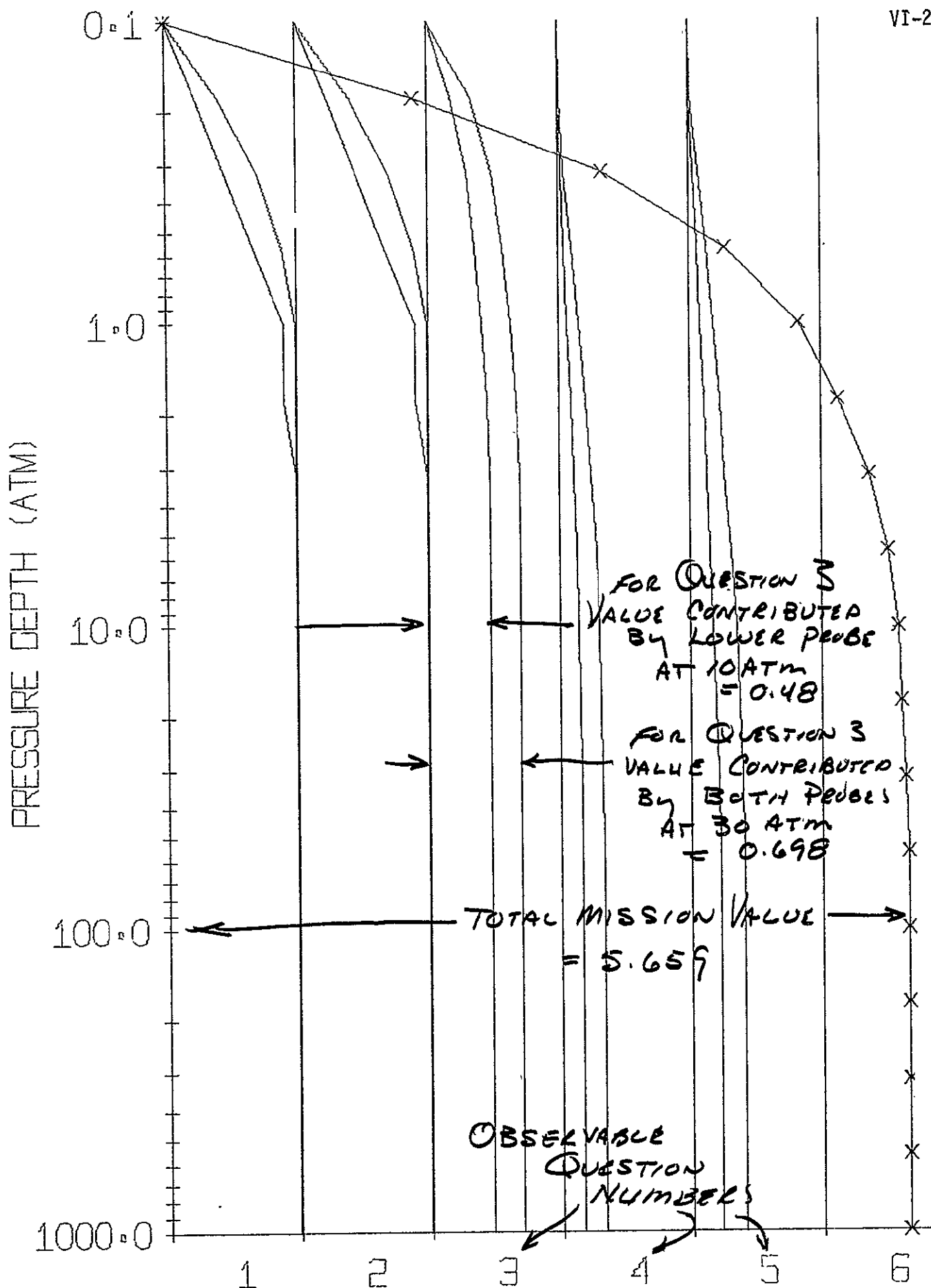


Figure VI-11 Computer Plot of Question Value Versus Pressure-Depth

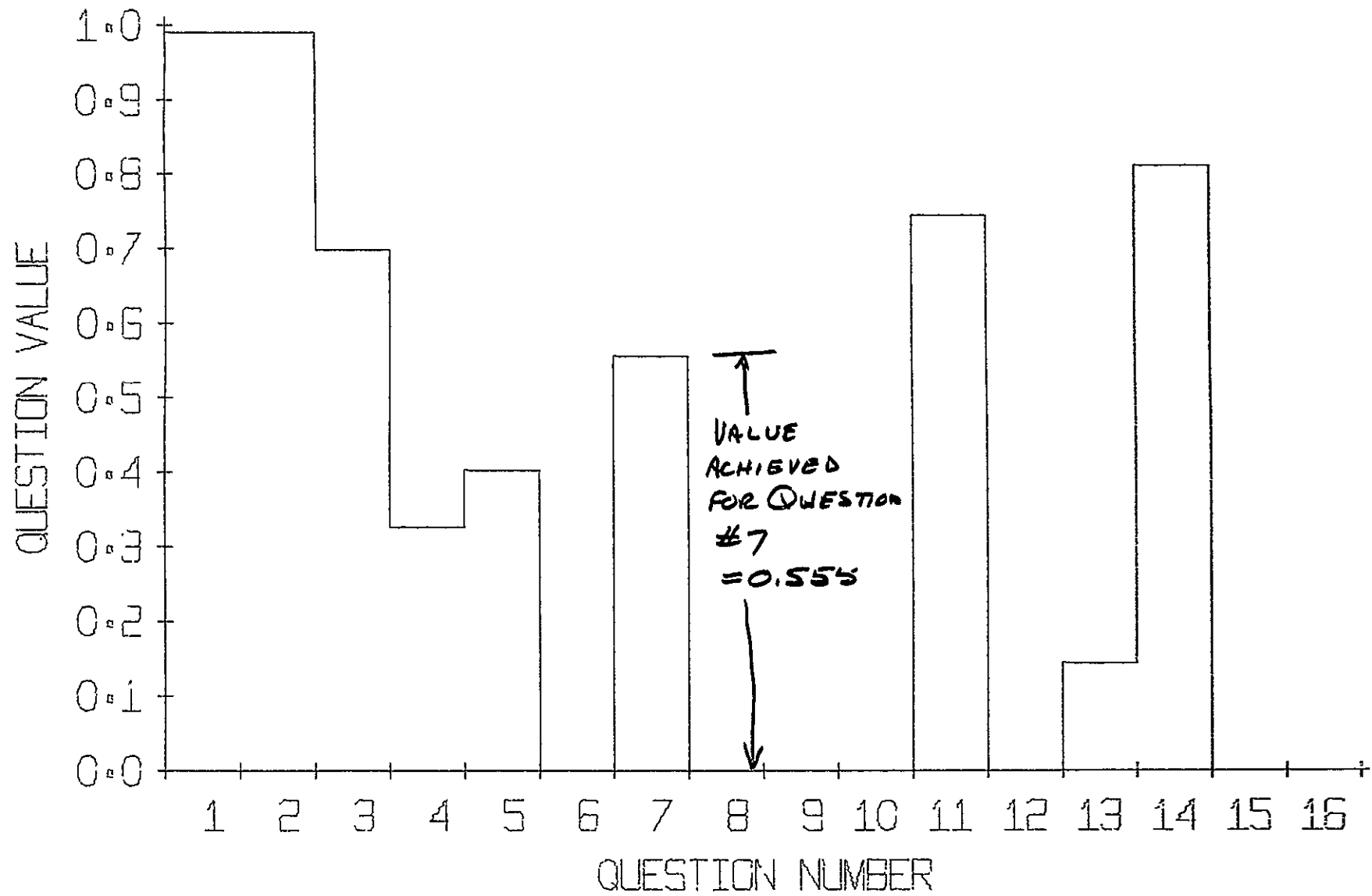


Figure VI-12 Computer Plot of Question Plot Versus Question Number

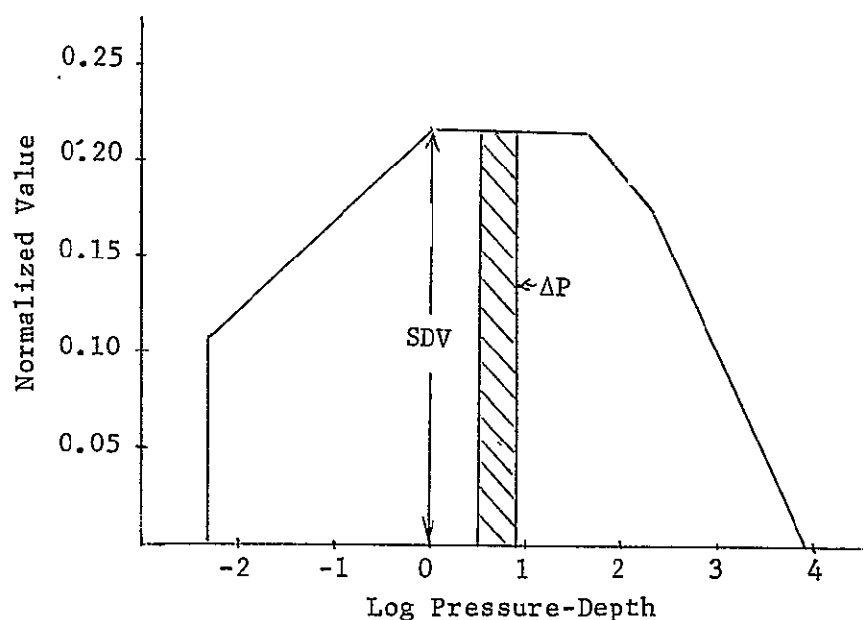
Tabulation of the Mission Input Data. Figure VI-10 is the Tabulated Output Data, here the first number is the observable question number, the second is the total value achieved for that question, and the next seventeen numbers are the values to be plotted on the Question Value Versus Pressure-Depth Plot. Figures VI-11 and VI-12 are the Question Value Versus Pressure-Depth and the Question Value Versus Question Number Plots, respectively.

D. Mathematical Computation Scheme

1. Determination of a Total Measurement for a Given Instrument

The model assumes that a summation of the value achieved by each sample taken by a given instrument will equal unity; providing that the samples are taken at least as often as required, taken over at least as great a vertical range as required and in the most advantageous planet location. The basis of this summation of perfect measurements is the Sampling Differential Value Curve which is keyed for a particular combination of instrument and observable. The actual SDV curves, stored in a permanent disk file and forming a part of the Science Requirements for the Jupiter Probe Mission, were shown in Figures VI-1 thru VI-4. Below Figure VI-13 shows SDV Curve PV-3 after normalization by the File Loading Program so that its total area equals 1.0.

Figure VI-13 Normalized SDV Curve



In general, during the summation for any given instrument, the full value of SDV is not achieved because either the Target Value (TV), the Sampling Interval Ratio (SIR) or the Probe Reliability (REL) do not equal unity. The summation is then

$$\text{Instrument Value} = \sum (\text{SDV} \cdot \text{TV} \cdot \text{SIR} \cdot \text{REL}) \Delta P$$

where TV, SIR and REL lie between the limits of 0 and 1.0.

Each of the above variables is a function of the pressure-depth, and some explanation of their determination is in order. Figure VI-14 is a block diagram showing the overall model operation.

The first step is establishing a Trial Pressure (TP1) which is either the limit set by the design or by the Science Requirements, which ever is the Greater Interpolation of this value into the probe's descent profile provides the time (TO) of the measurement. Incrementing this time by the time interval between samples, provides the time of the next sampling (TOD). This time interpolated into the descent curve gives the pressure-depth of the Next Sample (TP2). With these starting points, the variables required by the summation are easily found.

a. Determine Delta P (TP2-TP1)

Since the Sampling Differential Value is normalized on the basis of the log of the pressure-depth, the appropriate ΔP , the width of the shaded area in Figure VI-13, must be the difference between the logs of the pressure-depth at subsequent measurements; i.e., TP2-TP1.

b. Determine Target Value (TV)

The elapsed time, to which is matched with the first trial pressure TP1, multiplied by the Rotation Rate of Jupiter (0.01056 rad/min) provides a new longitude for the probe with respect to the subsolar point. A triangle solution then provides the requisite angle to the subsolar point from the point of entry, (PSI) as well as the latitude. With these two angles an interpolated Target Value is obtained from the Stored Target Value Curves.

c. Determine Sampling Interval Ratio (SIR)

The ratio of the required scale heights per measurement to the actual ΔP , (TP2-TP1) resulting from the design, is defined as the Sampling Interval Ratio. This ratio like the Target Value is determined for each sample to modify the Sampling Differential Value.

d. Determine Probe Reliability (REL)

The Probe Reliability as shown on Figure VI-14 is an input value reflecting an estimate of probe success including an implementation factor which assesses the technical risks inherent in the technology or analysis or the probe operation or production.

2. Determination of the Question Value

It can be seen on Figure VI-14 that the input instrument value is modified by the summation of values for individual samples termed a Sampling Factor (SF) and the resulting product inserted into an Instrument Logic Equation such as shown in the last column in Tables VI-1 thru VI-6. The total mission value is simply the sum of all sixteen Question Values.

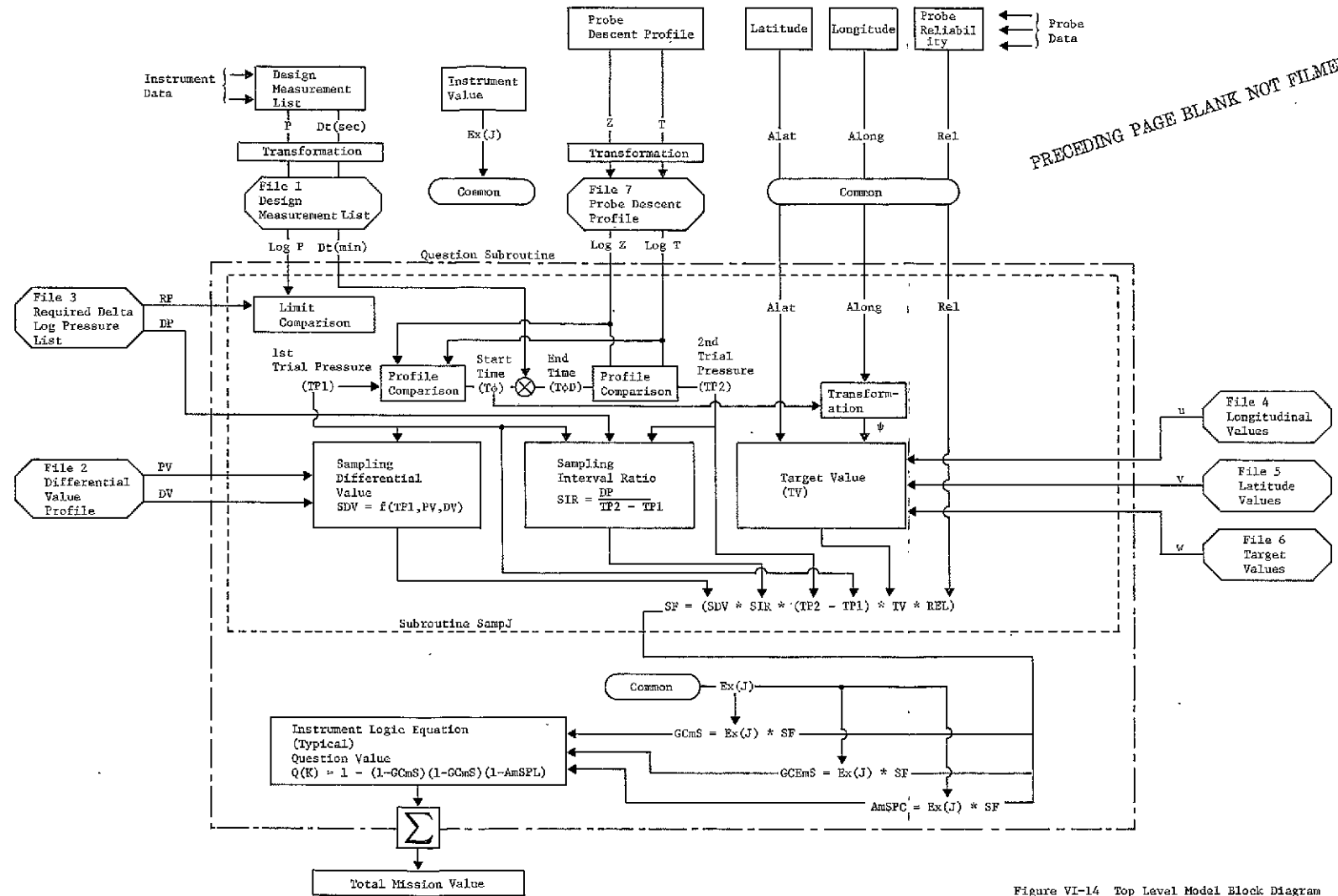


Figure VI-14 Top Level Model Block Diagram

FOLDOUT FRAME

FOLDOUT FRAME 2

VII. TRIAL MISSION DATA

A. Purpose

The purpose of establishing and evaluating a Trial Mission in the first half of the study was to identify the gross bounds on the problem. The trial mission definition task synthesized a preliminary design of a representative mission in order to focus the parametric analysis and tradeoff efforts toward pertinent ranges of study and it provided a method of uncovering critical problem areas.

The Trial Mission, then, was a study tool early in the effort and its description in this section basically only provides a record. The work following the Trial Mission generally supersedes and updates the results.

Basic subsystem parametric data that remained valid after the early study phase has been retained and discussed in the body of the report; however, trades that pertained only to the Trial Mission are reported in this section.

Many of the subsystem design constraints and detailed criteria changed and evolved as the study progressed.

B. Trial Mission Ground Rules, Criteria

The Trial Mission was conducted within the constraints specified in the contract statement of work. These constraints are stated in Volume I of this report and briefly summarized as follows:

1. Use 1978 launch opportunity
2. Use July 1975 state-of-the-art
3. Mission requirements shall be compatible with the DSN capability.
4. Launch energy requirements shall be based on use of the Titan IIID/Centaur family.

The general ground rules established for the Trial Mission study are as follows:

1. Nominal science instruments as specified in the S.O.W.
2. Target - North Equatorial Belt
3. Relay data link - flyby mode
4. TOPS spacecraft (effect of Pioneer was also evaluated briefly)
5. Entry angle, -10 degs
6. Attain 1000 atmosphere depth in 3.5 hours.
7. Stage aeroshell, deploy chute at 0.1 to 0.2 atmospheres.
8. Single planet flyby - Jupiter mission only (this allows consideration of both Type I and Type II trajectories).

C. Trial Mission Description

1. Trial Mission Profile

a. Planetary Vehicle

The Planetary Vehicle for the Trial Mission consists of the TOPS Spacecraft modified to support the Atmospheric Entry Probe during interplanetary cruise, mechanisms and adapters necessary to react the launch loads and achieve the interplanetary configuration, and support equipment that remains with the spacecraft to receive data from the Atmospheric Entry Probe. Figure VII C. 1-1 shows the general relationships and standardized nomenclature. A Jupiter fly-by trajectory will be used.

b. Prelaunch and Launch

Atmospheric Entry Probe systems will be married to the spacecraft as checked out systems and systems tests will be performed to verify functioning of entry science, transmission of data between probe systems, transmission of data to the spacecraft and transmission to earth based ground stations of the Deep Space Net (DSN). Following this marriage testing, the Planetary Vehicle will be installed and mated to the Launch Vehicle. A Launch Vehicle Adapter, will be required to transmit launch loads to the spacecraft and atmospheric entry probe. Environmental control will be provided by ducting conditioned air to selected areas within the nose fairing. No other access will be required on the launch pad. Planetary vehicle systems will be dormant during launch and until separation from the Burner II stage.

c. Deployment of Spacecraft Equipment

After separation from Burner II, the spacecraft RTG, antennas, booms and scan platform will be deployed to the configuration required for interplanetary cruise. Deployment of the antenna for receiving entry probe data will occur with deployment of the scan platform; no probe-peculiar deployment

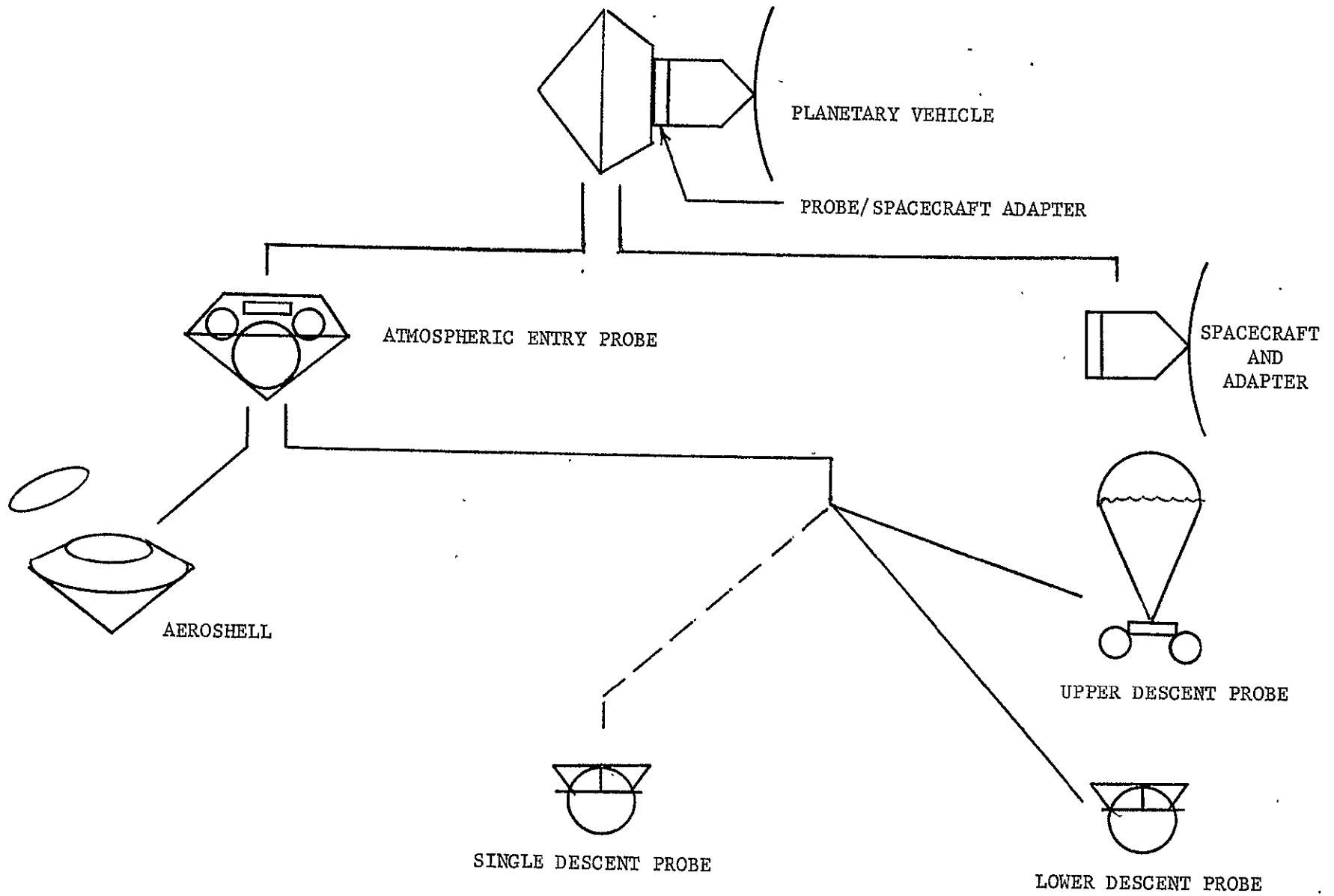


Figure VII C1-1 Standardized Nomenclature

will be required. In order that the spacecraft may attain Sun-Canopus reference in accordance with normal procedures the attitude control torque capability of the spacecraft must be augmented to account for the increases in total mass and moments of inertia over those for the basic TOPS spacecraft.

d. Midcourse Correction

The TOPS spacecraft with a basic weight of 1450 lbs includes midcourse propellant, and a propulsion system with a nominal thrust of 25 lbs applied through the cg and along the z-axis. This thruster must be relocated and the propulsion system augmented to retain the same ΔV capability of 200 meters per second. Design for the trial mission will be based on application of thrust through the cg, but not along the z-axis. This will result in deviation from normal TOPS procedures regarding spacecraft attitude at the time of midcourse correction.

e. Planetary Approach

As the planet is approached, updated trajectory data from DSN doppler instrumentation and updated planet ephemeris data from the spacecraft Approach Guidance Tracker will verify that the entry corridor can be achieved from the approach trajectory with the available deflection impulse contained in the propulsion system of the Atmospheric Entry Probe. Minor trajectory corrections may be required during this period.

f. Probe Separation

Prior to probe separation the probe sequencer/timer will be turned on, probe systems checked out, reference timing will be transferred from the spacecraft to the probe, and the 3-axis attitude control system will be activated.

The separation sequence of the Atmospheric Entry Probe will be controlled by the spacecraft on ground command. The

sequence will include a spacecraft roll maneuver followed by activation of the probe attitude control system to separate the atmospheric entry probe. Reaction forces on the spacecraft due to probe separation (gas impingement, etc.,) will be minimized by selection and location of ACS nozzles.

g. Probe Deflection, Orientation and Spin Up

With attitude control provided by the inertial reference system and the cold gas reaction system, the probe will drift away from the spacecraft with the separation velocity for a period of 20 minutes to reduce the affects of probe deflection on the spacecraft. The deflection rockets (3) will be fired to impart a velocity of 197 meters per second at an angle of -115 degrees to the velocity vector. The probe attitude control system will maintain attitude control during the deflection maneuver and will then orient the probe spin axis parallel to the velocity vector at entry.

The deflection propulsion module will be jettisoned, the attitude control system will be shut down, and the probe will be spun up about the longitudinal axis to a spin rate of approximately 3 radians per second.

h. Coast to Jupiter and Pre-entry Science

The spin stabilized Atmospheric Entry Probe will coast to the planet with all systems dormant except for a timer. The timer will activate the pre-entry science systems (ion mass spectrometer) and radio link to the spacecraft at entry minus one hour (~ 3 planetocentric radii). The receiving antenna on the spacecraft scan platform will acquire the signal in frequency and will be programmed in direction to receive the signal. Pre-entry science data will be transmitted to the spacecraft and relayed to earth at a rate of 100 bits per second. Six minutes prior to entry (as determined on the basis of updated ephemeris data prior to separation) the probe will be despun to a rate of approximately 0.5 radians per second.

i. Atmospheric Entry

Entry is assumed to occur at a planetocentric radius of 71907.7 km. A ballistic coefficient of 1.3 slugs/ft^2 in the nominal atmosphere will give a maximum deceleration of 443 g occurring 41.5 seconds after entry. The maximum dynamic pressure will be $14,755 \text{ lbs/ft}^2$. The entry heating pulse will be absorbed by an aluminum heat shield based on a heat shield allowance of 40% of the entry weight for both forebody and afterbody protection. The heat shield will be staged with the aeroshell at a Mach number of 0.63 (altitude = 33 km) occurring 108.5 seconds after entry. The staging function will be accomplished by a timer referenced to $T = 0$ at entry plus 20.5 seconds when accelerometers will sense a deceleration of 0.1 g. After staging of the aeroshell and heat shield the Upper Descent Probe will have a ballistic coefficient of 0.05. The Lower Descent Probe will have a ballistic coefficient of 4 after aeroshell staging. Acceleration data will be collected during entry and stored for later transmission to the spacecraft.

j. Descent

The Upper Descent Probe will carry science instruments from a pressure of 200 mb to a pressure of 45.4 atmospheres (187 km below the reference radius). The following instruments will be included:

- Pressure sensor (3)
- Temperature sensor (1)
- Accelerometer (1 axially mounted)
- Gas chromatograph/Mass spectrometer (1)
- Photometers (6 channels)

The Upper Descent Probe will carry a radio receiver to receive data from the lower probe and this data will be combined with upper probe data for transmission to the spacecraft at a rate of 42 bits per second. The data rate will be switched to 27 bits per second 35 minutes ($p = 5 \text{ atm}$) after staging, and

will continue at this rate until the design depth is reached at 155 minutes.

The Lower Probe will descend with a ballistic coefficient of 4.0 to a pressure of 30 atmospheres when a decelerator will be deployed to give a ballistic coefficient of 1.75. This will increase the period of time during which the lower probe traverses the region of 30 to 300 atmospheres. At the latter pressure the ballistic coefficient will be changed (by decelerator staging) back to $B = 4.0$ to cause the Lower Descent Probe to descend to 1000 atmospheres in a total mission time of 155 minutes. The lower probe will transmit data to the upper probe (at 9.85 bps) obtained from the following science instruments:

- Pressure sensors (2)
- Temperature (1)
- Gas Chromatograph/Mass Spectrometer (1)
- Accelerometers (3) (Entry data only).

The terminal descent profile is shown in Figure VII C. 1-2.

The communications range to the Earth for the Trial Mission is 6.433 A.U. The probe/spacecraft relay link communications range is shown as a function of time in Figure VIIC1-3. The aspect angles for the probe/spacecraft link and the spacecraft earth link are shown in Figure VIIC1-4.

The sequence of events is shown in Table VIIC2-1. Design parameters for the entire mission are tabulated in Table VIIC2-2.

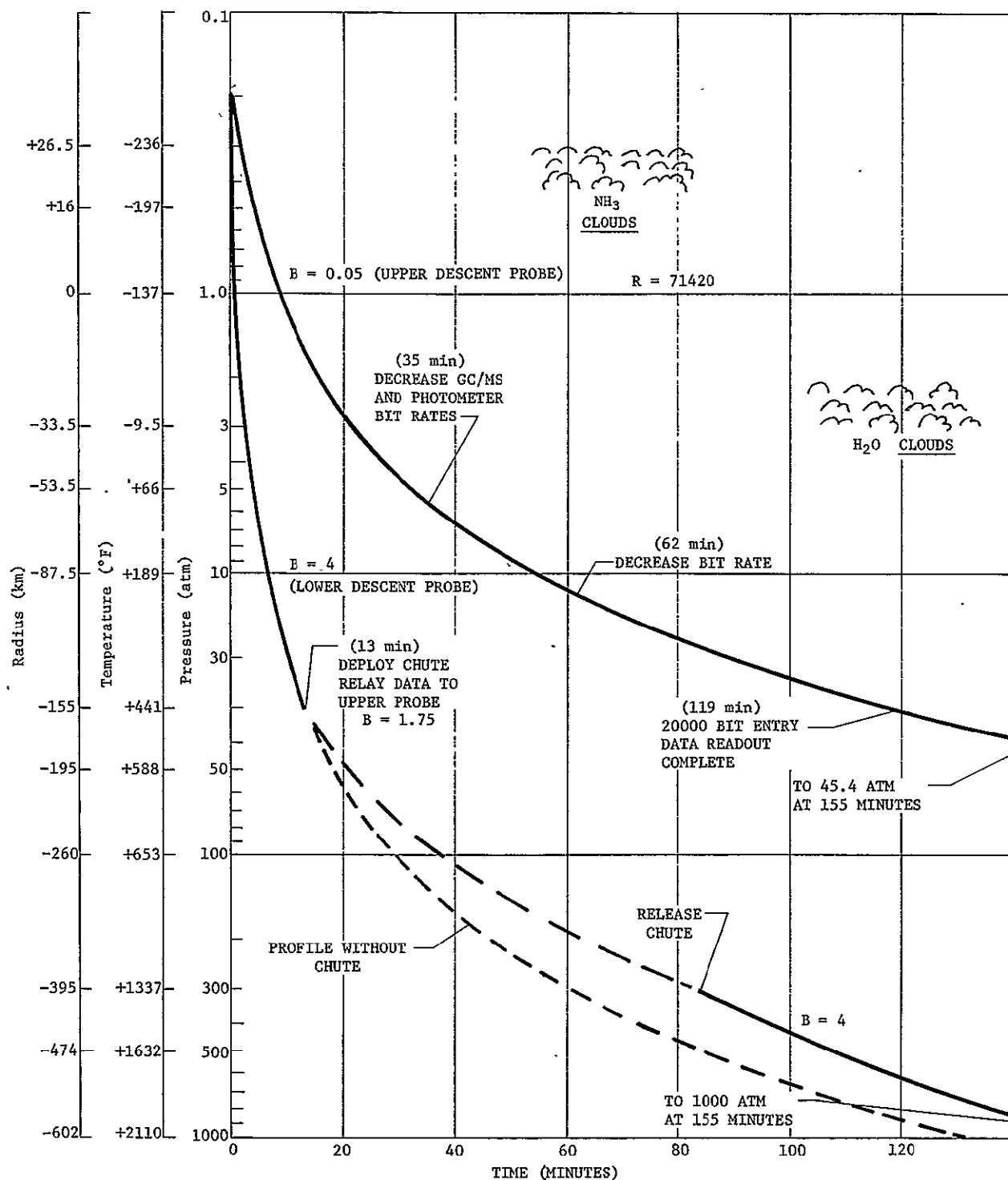


Figure VII C1-2 Trial Mission, Terminal Descent Profiles, JPL Nominal Model Atmosphere

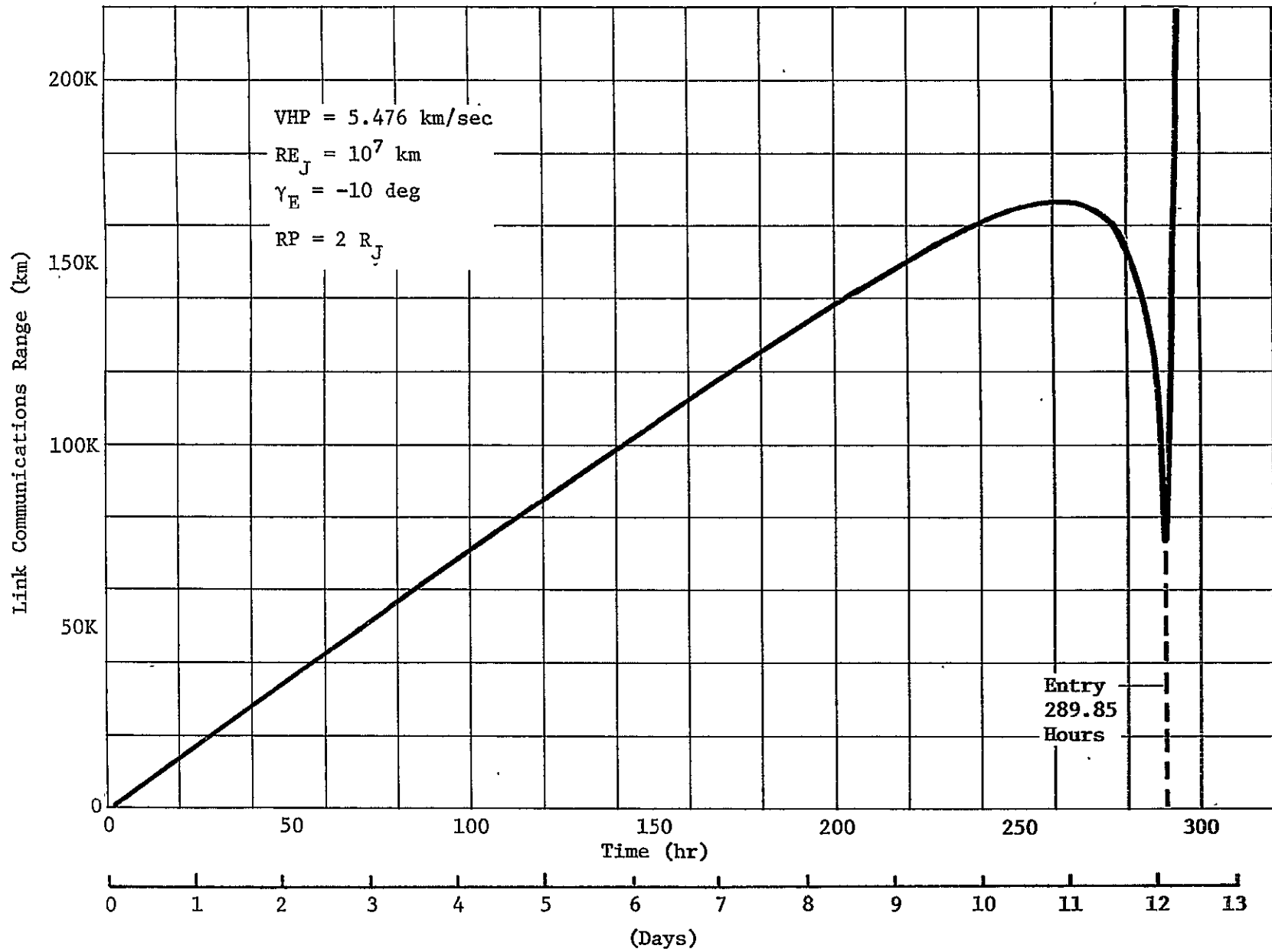


Figure VII C1-3

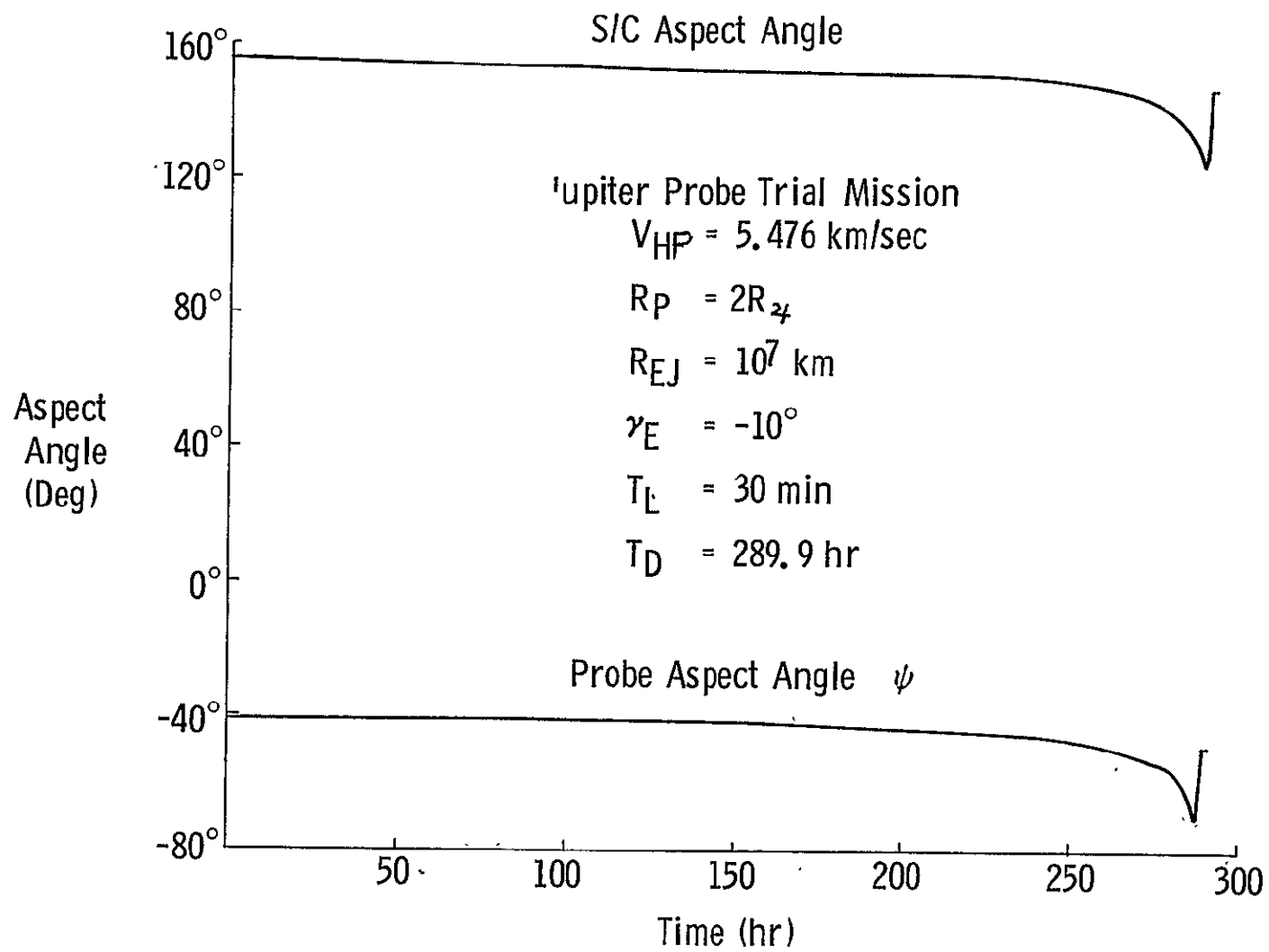


Figure VII C1-4

Table VII C2-1 Sequence of Events
Trial Mission - TOPS Spacecraft

TIME	EVENT	NOTES
E-(290 + T ₁) hrs	Final trajectory observations with DSN doppler and data from the Approach Guidance Tracker. Final determination of deflection velocity, angle, and time of application. Turn on probe systems, check-out, and update. Begin attitude maneuver for probe separation. (Roll about spacecraft sunline or spacecraft earth-line at 1 rph).	Spacecraft downlink to earth through the high gain antenna. Uplink commands are through the forward low gain antenna until attitude maneuvers begin, when the low gain antennas are used.
E-(290.6) hrs	Complete separation attitude maneuver. Transmit reference timing to the entry vehicle. Separate entry vehicle and spin up. Return spacecraft to earth orientation with high gain antenna.	Separation velocity of 1 foot per second. Spin rate of ~ 3 radians per second. (ACS functions)
E-290 hrs	Deflection motors activated by timer. Jettison deflection modules. Precess spin axis to alignment with velocity vector at entry. Switch probe systems to quiescent mode.	$\Delta V = 197$ mps $\gamma'_E = -10$ degrees Attitude sensor and precession impulse with control required.
E-1 hr	Activate ion mass spectrometer and RF link to spacecraft. Transmit stored ΔV data and pre-entry science.	$R = 3 R_J$. Probe support system aboard the spacecraft acquires probe signal in both frequency and direction. Position tracking is programmed at 0.5 deg/second. Data rate from entry vehicle to spacecraft is 100 bps.
E - 6 mins	Despin entry vehicle, jettison weights	Spin rate ~ 0.5 rad/sec
E = 0	Beginning of Entry. Collect entry data and store.	$B_E = 1.30$ sl/ft ² (488 km above 1 atm)

Table VII C2-1 (concluded)

TIME	EVENT	NOTES
E + 20.5 sec	Entry vehicle senses 0.1 g increasing. Shutoff transmitter.	Reference Time: Reset timers in both probes.
E + 108.5 sec ($T_S = 0$)	Deploy decelerator. Stage Aeroshell/Heat shield. Separate and deploy probes. Turn transmitters on. Reacquire upper probe signal to spacecraft. Transmit stored and real time data at 42 bps.	$P = 200 \text{ mb}$ $M = 0.63$ $B_{\text{upper}} = 0.05 \text{ sl/ft}^2$ $B_{\text{lower}} = 4.0 \text{ sl/ft}^2$
$T_S + 13 \text{ mins}$	Deploy decelerator, lower probe. Transmit data to upper probe for relay to spacecraft.	$B_{\text{lower}} = 1.75 \text{ sl/ft}^2$ Link actively transmitting data at $P = 30 \text{ Atm}$.
$T_S + 62 \text{ mins}$	Decrease bit rate, upper probe (27 bps).	$P = 10.5 \text{ Atm}$.
$T_S + 84 \text{ mins}$	Release Chute, Lower Probe	$P = 300 \text{ Atm}$ $B = 4.0 \text{ sl/ft}^2$
$T_S + 126.5 \text{ mins}$	20,000 bit entry data readout complete.	
$T_S + 155 \text{ mins}$	1000 Atm mission complete	

Table VIIC2-2
LAUNCH, INTERPLANETARY CRUISE, AND ENCOUNTER PARAMETERS
FOR JUPITER
TRIAL MISSION

***** LAUNCH PARAMETERS *****

LAUNCH DATE (NOMINAL)	10/2/78
LAUNCH VEHICLE	TITAN III D CENTAUR (7 SEG WITH BURNER II)
LAUNCH PERIOD	30 DAYS
PARKING ORBIT ALTITUDE	100 NAUTICAL MILES
SPACECRAFT	TOPS
SPACECRAFT WEIGHT	1450. LBS
PAYLOAD WEIGHT (INCL S/C)	2420 LBS
FAIRING SEPARATION	CORE 2 IGNITION PLUS 10 SEC
MAX LAUNCH AZIMUTH	115 DEG

***** INTERPLANETARY CRUISE PARAMETERS *****

TRAJECTORY	TYPE II
DECLINATION OF LAUNCH ASYMPTOTE	
DLA	-4.57 DEGREES
RIGHT ASCENSION	111.0 DEGREES
INJECTION ENERGY, C3	98.43 KM2/SEC2
FLIGHT TIME	1096 DAYS (NOMINAL)
SEMI-MAJOR AXIS	3.2257 A.U.
RADIUS OF APHELION	5.46 A. U.
ECCENTRICITY	0.691
INCLINATION TO ECLIPTIC	6.5 DEGREES
CENTRAL ANGLE OF TRAVEL	191.35 DEGREES
TRUE ANOMALY AT DEPARTURE	349.94 DEGREES

***** ENCOUNTER PARAMETERS *****

JUPITER ARRIVAL DATE	10/2/81 (NOMINAL)
TRUE ANOMALY AT ARRIVAL	181.3 DEGREES
EXCESS VELOCITY, VHP	5.476 KM/SEC
DEC OF VHP VECTOR	31.1 DEGREES
RIGHT ASC OF VHP VECTOR	109.1 DEGREES
(WITH RESPECT TO VERNAL EQUINOX, EARTH EQUATORIAL SYSTEM)	
DEC OF VHP VECTOR	7.1 DEGREES
(WITH RESPECT TO EQUATOR OF JUPITER)	
COMMUNICATION RANGE	5.433 A.U.

***** DEFLECTION PARAMETERS *****

BUS TRAJECTORY	FLYBY
PERIAPSIS RADIUS OF BUS	143000. KM
DEFLECTION RADIUS	10,000,000. KM
INCLINATION OF TRAJECTORY	7.5 DEGREES
(WITH RESPECT TO EQUATOR OF JUPITER)	
DEFLECTION VELOCITY	197 METERS/SEC
DEFLECTION ANGLE	-115.0 DEGREES
CAPSULE COAST TIME	12 DAYS
LEAD TIME	29.863 MINUTES
LEAD ANGLE	-15.45 DEGREES

Table VIIC2-2 (Concl)

* * * * ENTRY PROBE DESIGN DATA * * * *

RELATIVE ENTRY VELOCITY	47.1 KM/SEC = 154498 FT/SEC
ENTRY ANGLE	-10. DEGREES (SKIP OUT AT -4 DEG)
ENTRY ALTITUDE (TIME=0)	487.7 KM = 1,600,000 FEET
ENTRY RADIUS	71907.7 KM
ENTRY LATITUDE	5 DEGREES
ENTRY LONGITUDE	58.1 DEGREES
(RELATIVE TO MERIDIAN OF SUN)	

* * * * * *

* * * * AEROSHELL DATA * * * *

ENTRY BALLISTIC COEFFICIENT	1.3 SLUGS/FT ²
TIME TO .1 G POINT	20.5 SECONDS
TIME OF MAXIMUM DECELERATION	
AND MAX DYNAMIC PRESSURE	41.5 SECONDS
MAXIMUM DECELERATION	443. G
MAXIMUM DYNAMIC PRESSURE	14,755 LB/FT ²
TIME OF MACH 1 OCCURRENCE	79.5 SECONDS
AEROSHELL STAGING	
ALTITUDE	33 KM = 200 MB
MACH NUMBER	.63
DYNAMIC PRESSURE	120 LB/FT ²
TEMPERATURE	203.4 DEG R
DENSITY	.00009726 SLUGS/FT ³
TIME (TS)	108.5 SECONDS

* * * * * *

* * * * UPPER DESCENT PROBE * * * *

BALLISTIC COEFFICIENT	.05 SLUGS/FT ²
DESIGN DEPTH	-187 KM = 45.4 ATM
TEMPERATURE AT 45.4 ATM	1020. DEG R
DENSITY AT 45.4 ATM	.00436 SLUGS/FT ³
TIME TO DESIGN DEPTH	TS+155 MINUTES

* * * * * *

* * * * LOWER DESCENT PROBE * * * *

DESIGN DEPTH	-602 KM = 1000. ATM
TIME TO 1000 ATM	TS+155 MINUTES
STAGING DATA	
1 PRESSURE RANGE	200 MB TO 30 ATM (-155 KM)
BALLISTIC COEFFICIENT	4.0 SLUGS/FT ²
TEMPERATURE AT 30 ATM	901. DEG R
DENSITY AT 30 ATM	.00326 SLUGS/FT ³
TIME TO 30 ATM	TS+13 MINUTES
2 PRESSURE RANGE	30 ATM TO 300 ATM (-395 KM)
BALLISTIC COEFFICIENT	1.75 SLUGS/FT ²
TEMPERATURE AT 300 ATM	1796. DEG R
DENSITY AT 300 ATM	.01639 SLUGS/FT ³
TIME TO 300 ATM	TS+84 MINUTES
3 PRESSURE RANGE	300 ATM TO 1000 ATM
BALLISTIC COEFFICIENT	4.0 SLUGS/FT ²
TEMPERATURE AT 1000 ATM	2569. DEG R
DENSITY AT 1000 ATM	.03815 SLUGS/FT ³
TIME TO 1000 ATM	TS+155 MINUTES

4. Probe Configuration Summary - Trial Mission

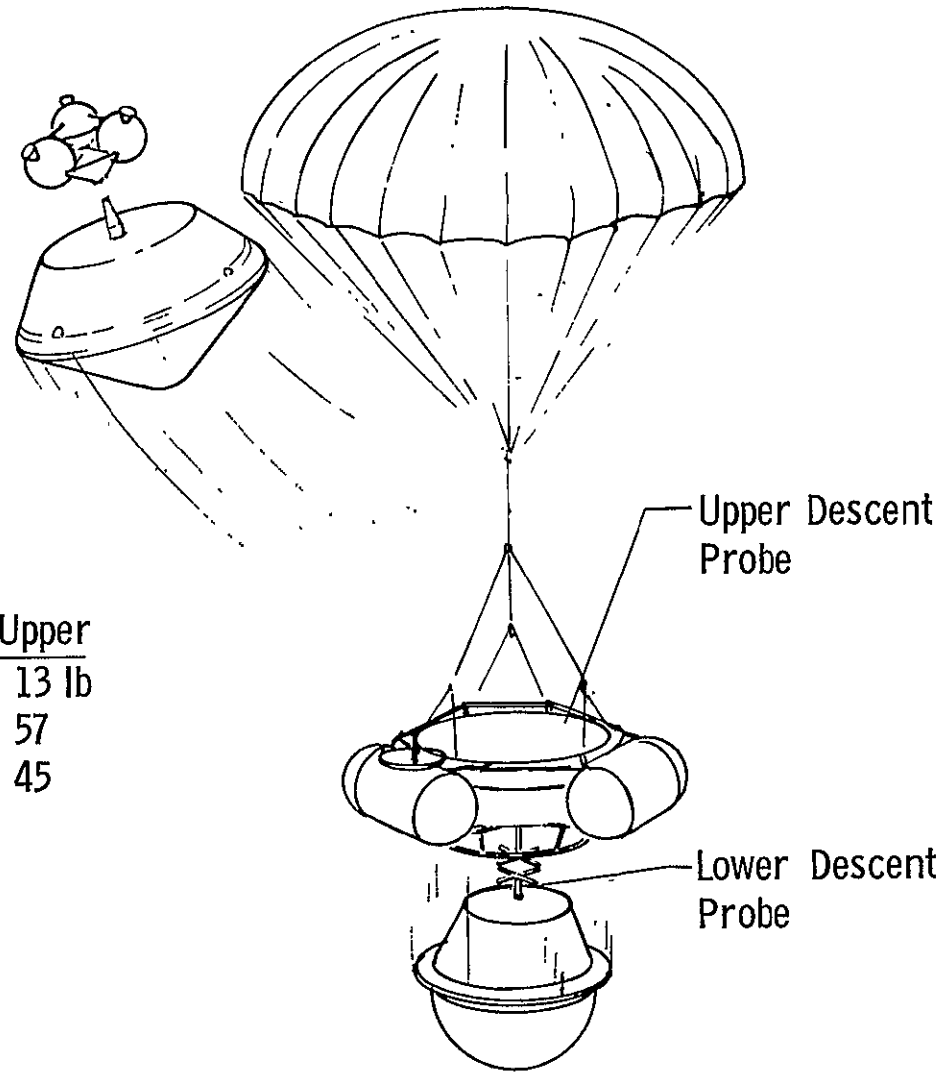
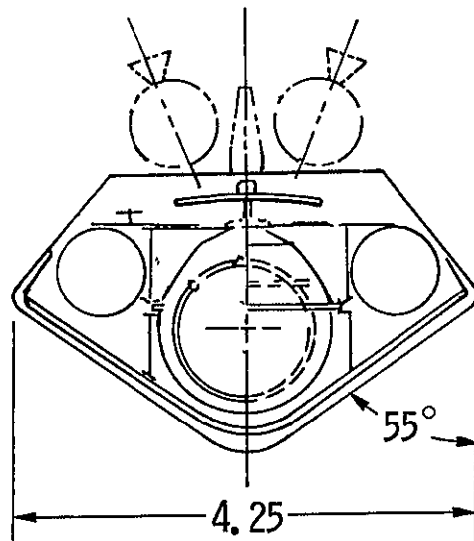
a. Mechanical Systems

1) Probe Systems

The split probe concept shown in Figure VIIC4a-1 was selected to achieve the 1000 bar descent profile of the trial mission. The upper descent probe which relays lower probe data to the spacecraft consists of three small cylindrical canisters to afford as compact an entry vehicle as possible. A parachute is used to stabilize and control the upper probe velocity. The lower probe is nearly spherical and employs an aerodynamic fence for stabilization and descent velocity control. Details of the lower probe are shown in Figure VIIC4a-2 weight summaries for both descent probes and the total entry probe system are shown in Tables VIIC4a-1 through VIIC4a-3. Table VIIC4a-4 shows the science instruments and requirements.

2) Spacecraft Systems

The 4.25 ft diameter 803 lb entry probe and 2.8 ft dish antenna for receiving probe data are mounted on the TOPS spacecraft by utilizing the bulbous launch vehicle fairing, as seen in Figure VIIC4a-3. The total weight of 2403 lb is within the 2420 lb launch vehicle payload capability for the 7 segment TIIC Centaur with Burner II. However, significant modifications to the TOPS trajectory correction propulsion system and attitude correction propulsion system are required to handle the new c.g. location of the combined spacecraft and probe and the increased total mass, e.g., APS thruster location changes and relocation of the trajectory correction motor. The probe antenna must rotate through 130° to maintain contact over a 1.0 hour pre-entry phase and a 2.5 hour descent phase time period and this is accomplished with a gimballed antenna mounted on the TOPS scan platform support structure as shown in Figure VIIC4a-4.



	<u>Lower</u>	<u>Upper</u>
Science	13 lb	13 lb
Communications & Data	22	57
Environmental Protection	164	45
Descent Probe-Subtotal	314	
Aeroshell	97	
Heat Shield	263	
Probe at Entry	719	
Probe at Separation	803	
TOPS with Mods	1600	
Total Launch Weight	2403	

Figure VII C4a-1 Probe Description - Trial Mission

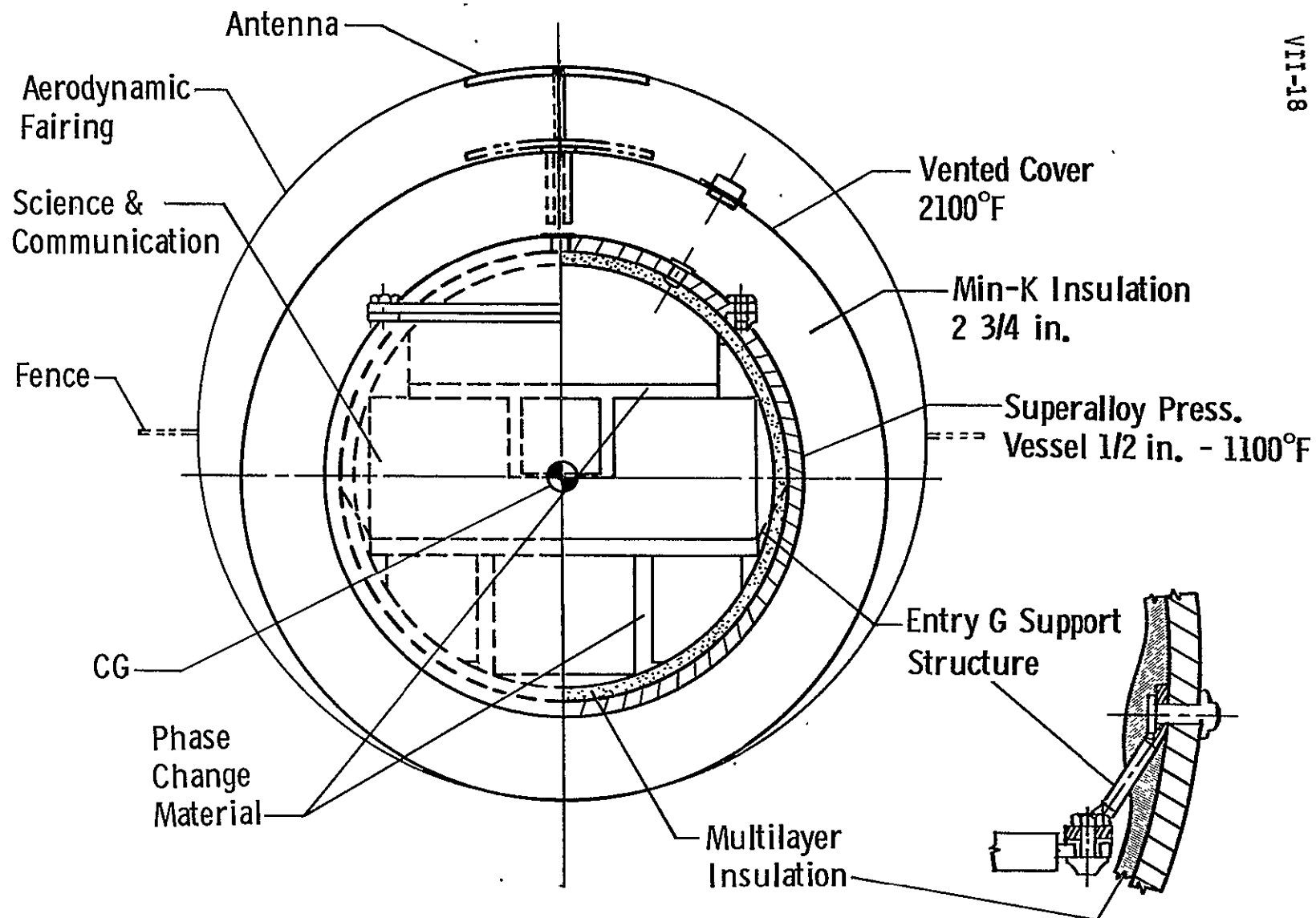


Figure VII C4a-2 Environmental Protection - 1000 Bar Descent Probe

TABLE VII C4a-1

SPLIT PROBE TELECOMMUNICATION/POWER WEIGHT SUMMARY
TRIAL MISSION

		<u>Upper Probe (Relay)</u>		<u>Lower Probe</u>	
		<u>Weight</u>	<u>Power</u>	<u>Weight</u>	<u>Power</u>
		<u>(lb)</u>	<u>(w)</u>	<u>(lb)</u>	<u>(w)</u>
● Antennas					
- Relay to S/C	1.8 GHz	0.5	--	--	--
- Probe/Probe	1.0 GHz	1.4	--	1.4	--
● FSK Receiver		1.5	1.2	--	--
● Modulator/Exciter		1.5	2.0	--	--
● Power Amplifier	20 watts	4.0	65.0	--	--
● FSK Transmitter	2 watts	--	--	1.2	7.0
● Sequencer		4.0	3.0	1.5	2.0
● Data Handling		7.1	8.0	4.0	3.0
● Memory Assembly		3.0	2.0	--	--
● Inverter		4.0	12.0	3.0	2.0
● Battery		10.0	--	2.5	--
● Cabling		<u>6.0</u>	<u>--</u>	<u>5.0</u>	<u>--</u>
Totals		43.0	93.2	18.6	14.0

TABLE VII C4a-2
DESCENT PROBE WEIGHT SUMMARY - TRIAL MISSION

	<u>Lower Probe</u>	<u>Lower Probe</u>	<u>Upper Probe (Tri-Canister)</u>
● Science		13	13
● Comm/Power		21	41
● Pressure Vessel		105	20
● Internal Structure		15	8
● Phase Change Material		2	5
● Insulation		34	2
● Antenna(s) and Mounting			
- S/C Link		--	1
- Probe/Probe Link		1	5
● Intercónnections - Struct/Cabling/Pyro		--	20
● Parachute or Aerodynamic Sys		9	-- Chute Wt is Allocated to Entry Probe A/S Staging
		<u>199</u>	<u>115</u>

TABLE VII C4a-3

ENTRY PROBE WEIGHT SUMMARY -- TRIAL MISSION

Upper Descent Probe	115 lb
Lower Descent Probe	199
Aeroshell (Basic) - 4.25 ft Dia 55° $\frac{1}{2}$ Cone	75
Auxiliary Structure & Mech Systems	12
Staging Parachute System	10
Heat Shield (Including Aft Cover)	263
Approach ACS (Fixed Weight)	15
Deflection Propulsion (Fixed Weight)	15
Telecommunications/Power (Approach Phase)	<u>15</u>
● Entry Weight _____	719
Deflection Propulsion (Expendable)	70
ACS (Expendable)	11
Ion Mass Spectrometer (Expendable)	<u>3</u>
● Separated Weight _____	803 lb

INSTRUMENTS & REQUIREMENTS

<u>Instrument</u>		<u>RFP Sampling Interval (meters)</u>	<u>Bits Per Sample</u>	<u>Recommended Measurements Per Scale Height</u>
Aerometry	Temperature Gauge (Range-Switched)	300	8	50 to 100
	Pressure Gauge (5) (Switched)	300	8	
	Accelerometers (4)	t = 0.2 sec	40	
Ion Mass Spectrometer		1 scan every 2 sec	320	
Gas Chromatograph/Neutral Mass Spectrometer		1000*	600	2 to 5
Photometer (6 Channels)			60	250

*Each Analysis by the Gas Chromatograph Requires from 2 to 5 min. A Minimum of 4 Analyses, at Altitudes Below the Region of Gravitational Separation of Atmosphere Constituents, are Required

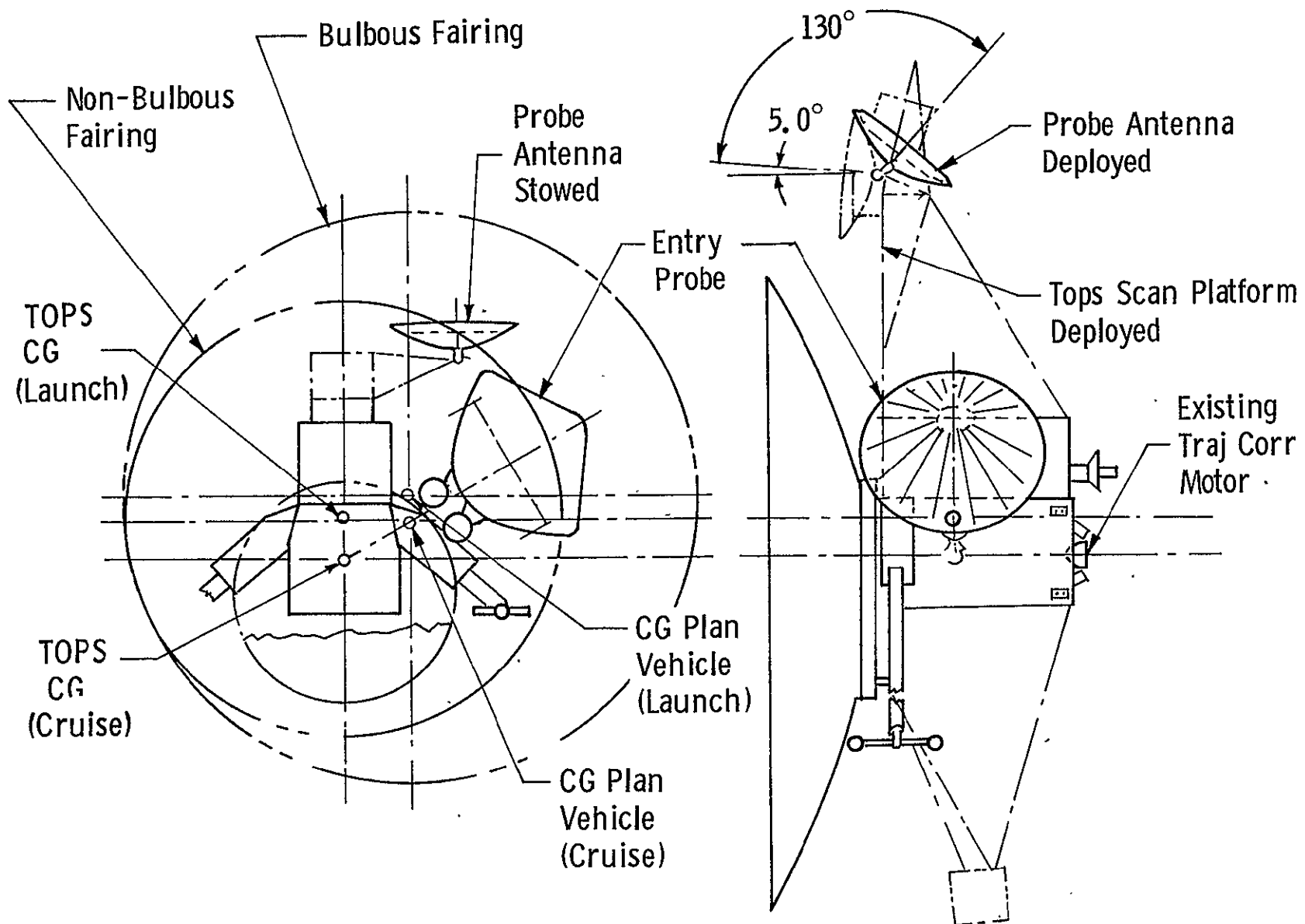


Figure VII C4a-3 Tops Probe Integration

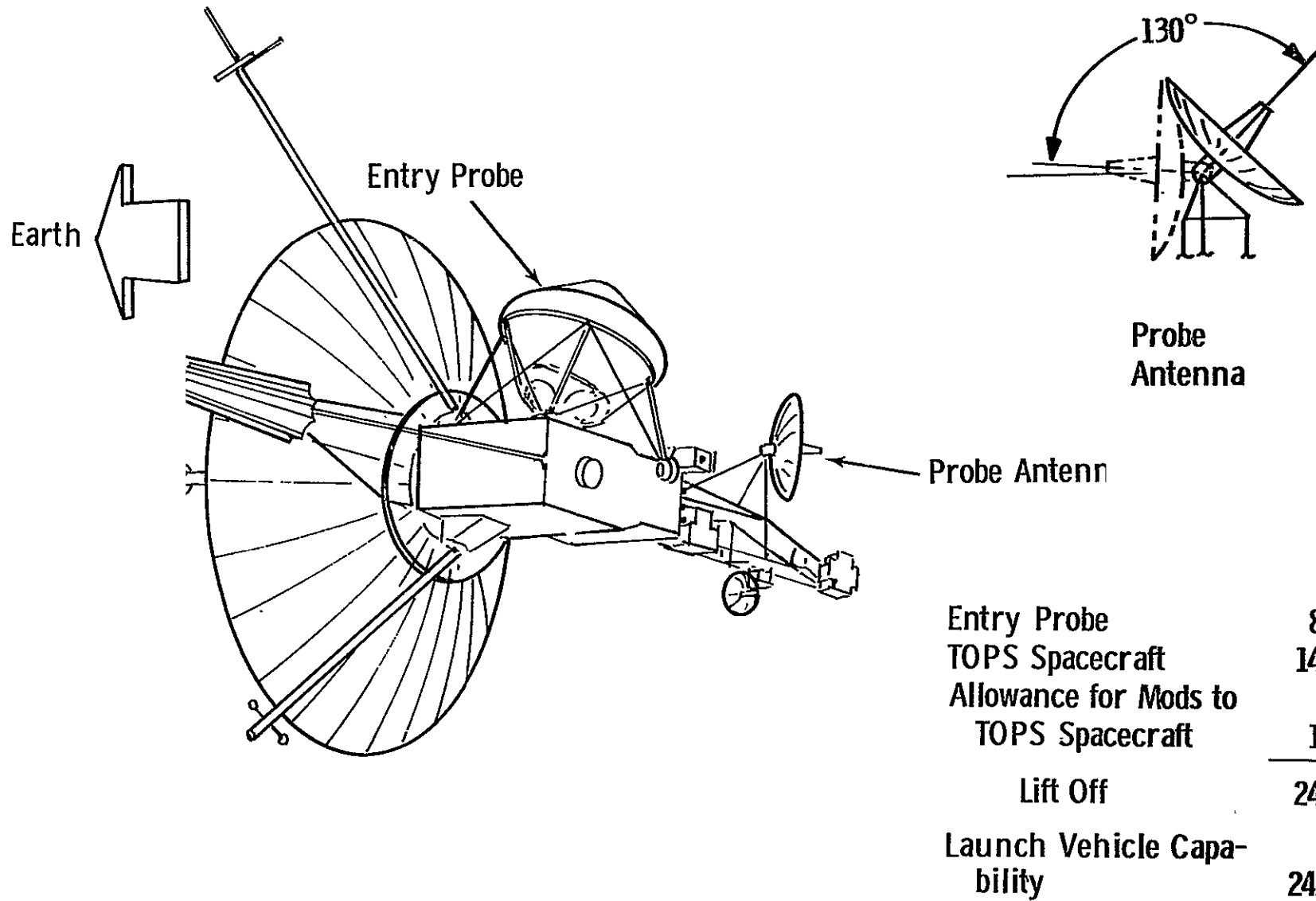


Figure VII C4a-4 Planetary Vehicle - TOPS Spacecraft

b. Telecommunications Data Handling and Power

1) Probe Systems

The Trial Mission requires relay communications from the entry probe to the S/C for a period of an hour prior to probe entry and from the upper descent probe to the S/C for 2.58 hours after entry. Accelerometer data is stored in the upper probe memory during the entry phase and transmitted along with real time data beginning after separation of the probes from the aeroshell.

The lower probe samples the environment at lower depths in the atmosphere than the upper probe and transmits this data to the upper probe for relay to the S/C. Thus, the upper probe data stream for transmission is made up of stored entry data, lower probe data, and upper probe data. The data stream content as a function of time during post entry is shown in figure VIIC4b-1.

Bit rates are 100 bps during the pre-entry phase, 9.85 bps for the lower probe during post entry, 42 bps for the upper probe during initial pre-entry and 27 bps during the latter phases of decent. Bit stuffing in the upper probe is used to compensate for the nonsynchronous lower probe bit rate.

The upper probe to S/C link requires a 20-watt 1.8 GHz transmitter and 2.81 ft. diameter S/C antenna to give the link margin as a function of time as shown in figure VIIC4b-2. Atmospheric losses in this link as well as the probe to probe link are based on the attenuation model that existed when the mission was defined prior to the mid-term contract report, as shown in figure VIIC4b-3. Use of the latest attenuation model (see Chapter IV for discussion) would require increasing link gain by approximately 3 db. at 1.80 Hz. Modulation is PCM/PSK/PM using a square wave subcarrier.

Communications range, S/C antenna aspect angle and probe aspect angle as a function of time are shown in Figure IVC-7,8,9. Communication geometry for the upper probe to S/C link in relation to the planet is shown in Figure VIIC4b-4 in simplified form.

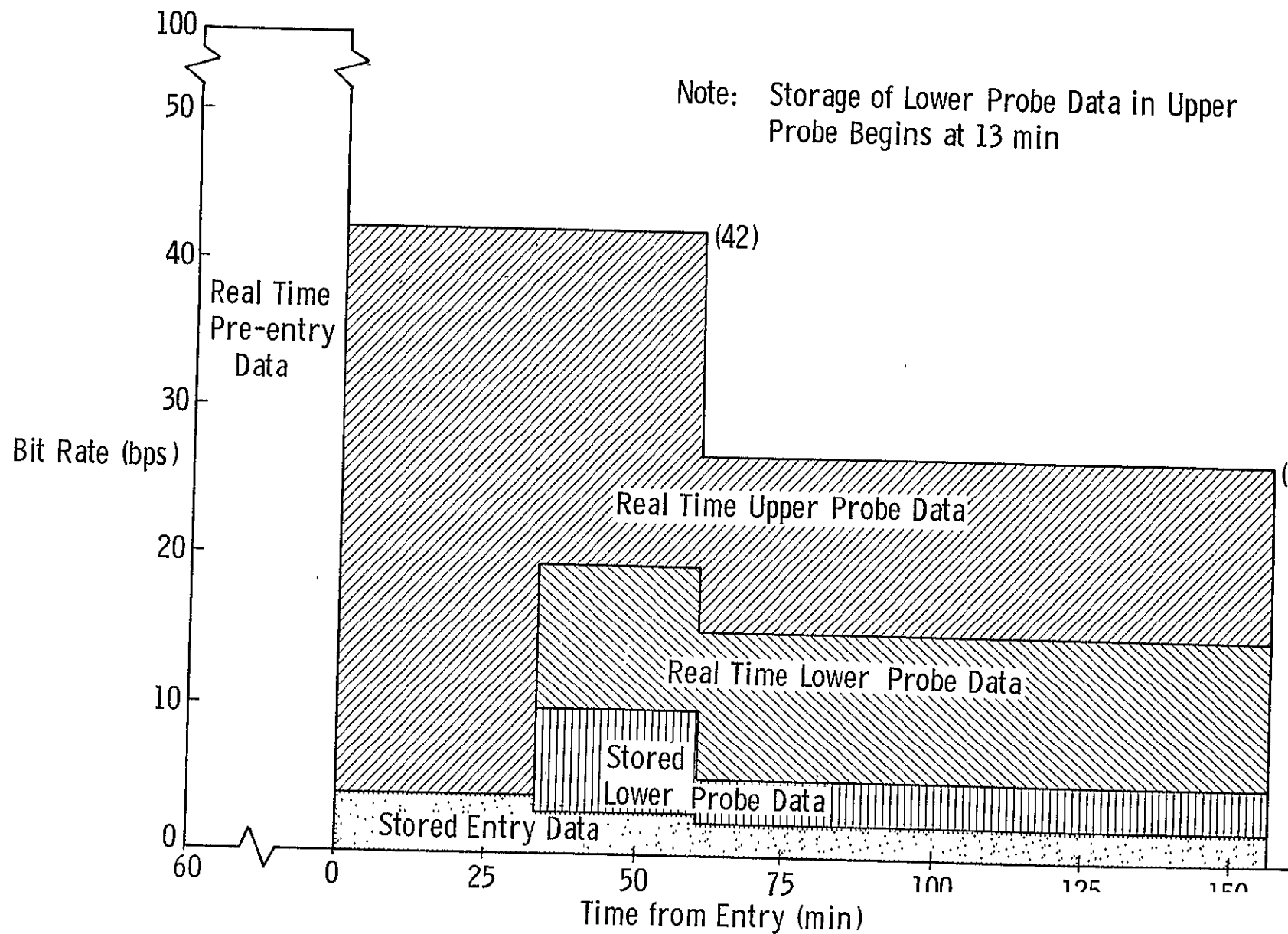


Figure VII C4b-1

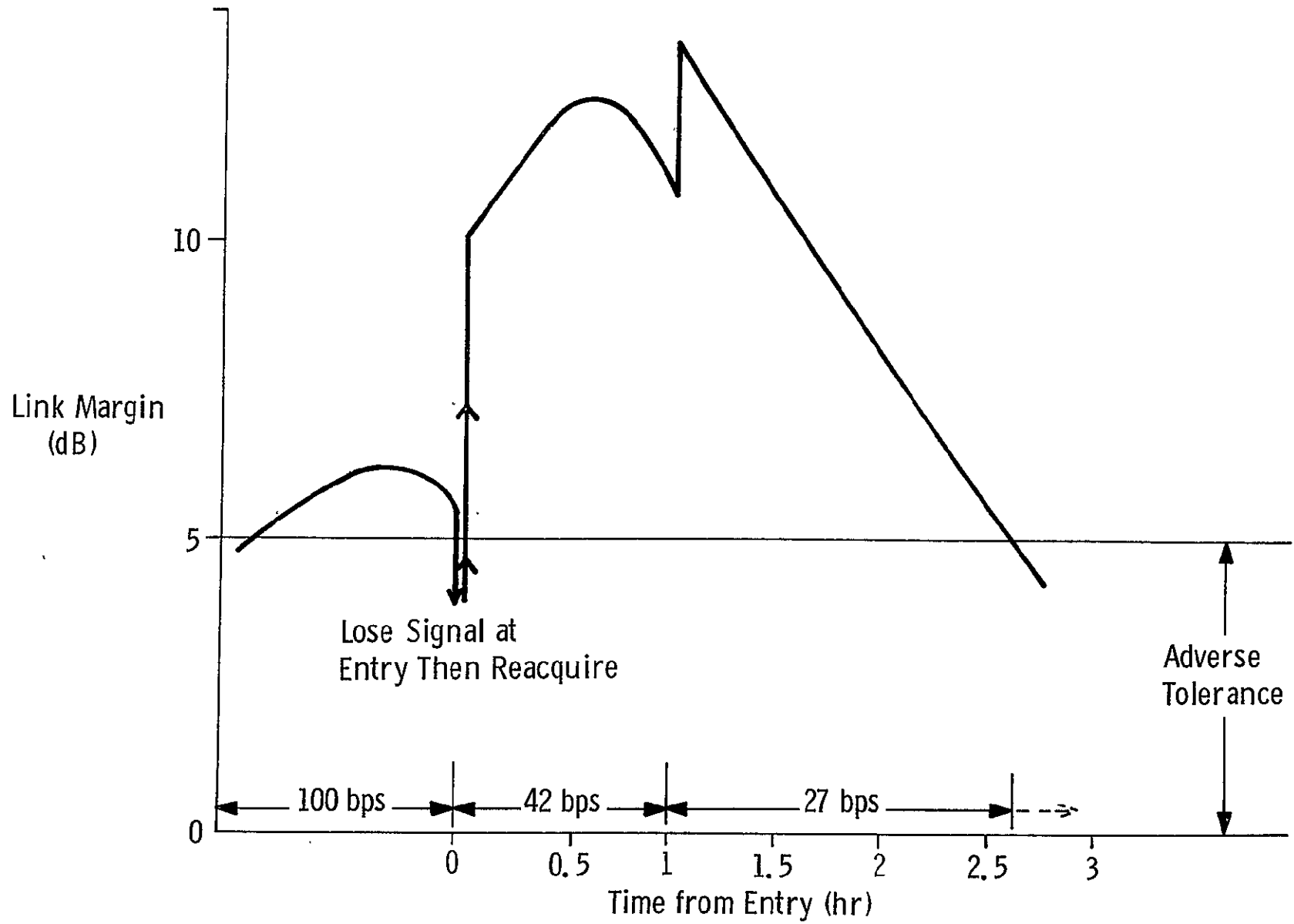


Figure VII C4b-2 Trial Mission - Relay Link Margin Upper Probe to S/C

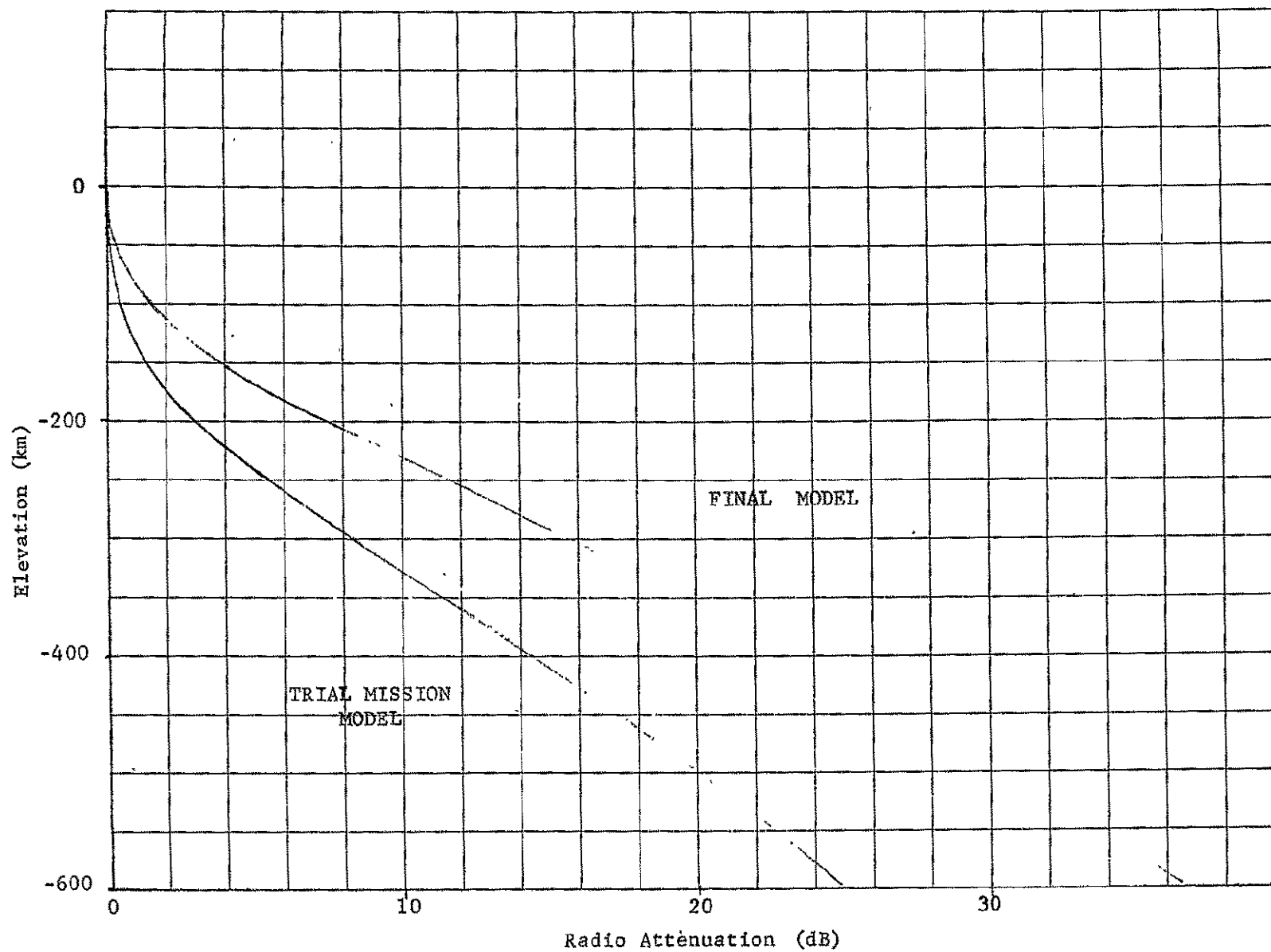


Figure VII C4b-3 Trial Mission Attenuation Model Compared to Final Attenuation Model
Nominal Atmosphere for Frequency of 2.3 GHz

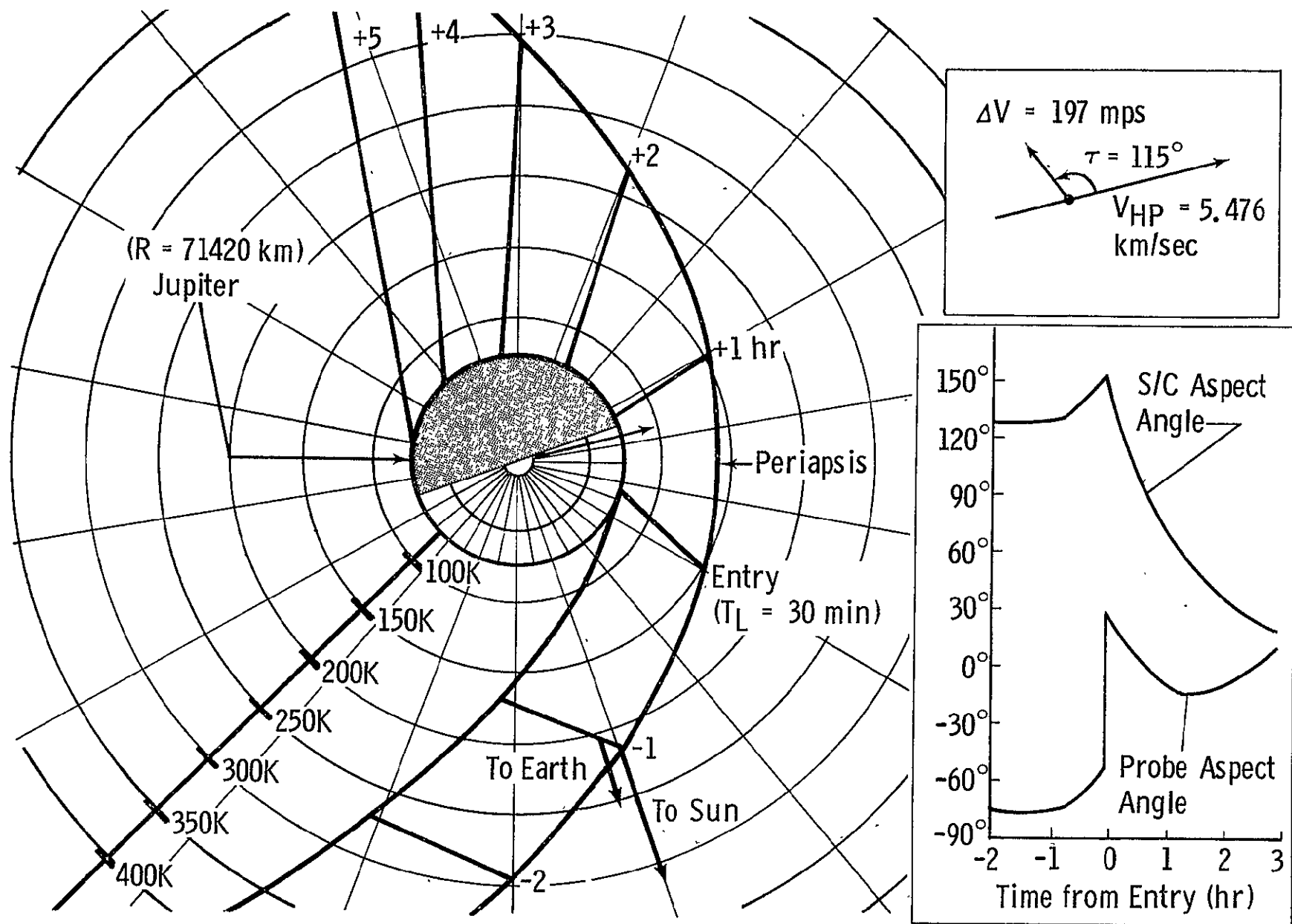


Figure VII C4b-4 Probe/Spacecraft Relative Geometry - Trial Mission

The probe to probe link operates at 1.0 GHz in a wide band noncoherent nonfrequency search FSK mode using a 2.0 watt FSK transmitter in the lower probe and circularly polarized curved turnstile antennas at either end of the link. Margins vs. time for the probe to probe link is given in Figure VIIC4b-5.

A communications design control table for the probe to probe link is shown as table VIIC4b-1. Range for the probe to probe link assumes $\sqrt{2}$ times the difference in relative depths of the probes based on their ballistic coefficients. Antenna noise temperature for the upper probe was computed as discussed in Chapter IVK taking into consideration the fact that the antenna is "looking" down and that the back lobe is looking up toward the non-thermal noise source. Were the atmospheric attenuation corrected to agree with the latest model, an additional 3 db would be required in the link. Reduction of the 8 db adverse tolerance for transmit antenna pointing loss to 5 db rebalances the margin and adverse columns. This reduces the tolerance of the link to wind gusts but the margin is still considered adequate. During the pre-entry phase, pre-entry science and engineering data are fed from the aeroshell mounted equipment to the upper probe data handling system where it is processed for transmission by the upper probe transmitter. The operational antenna during this phase is located on the rear of the entry vehicle. After separation of the aeroshell and probes following entry the upper probe transmitter output is switched to the upper probe antenna. Antennas for the probes are described in Chapter IV.

Sequences for the probes are typically the same as those described for the design example mission and Mission A-2; therefore, they will not be discussed here.

Power subsystems considerations for the probe are typical of other missions described in Volume II and discussed in Chapter IV of this volume.

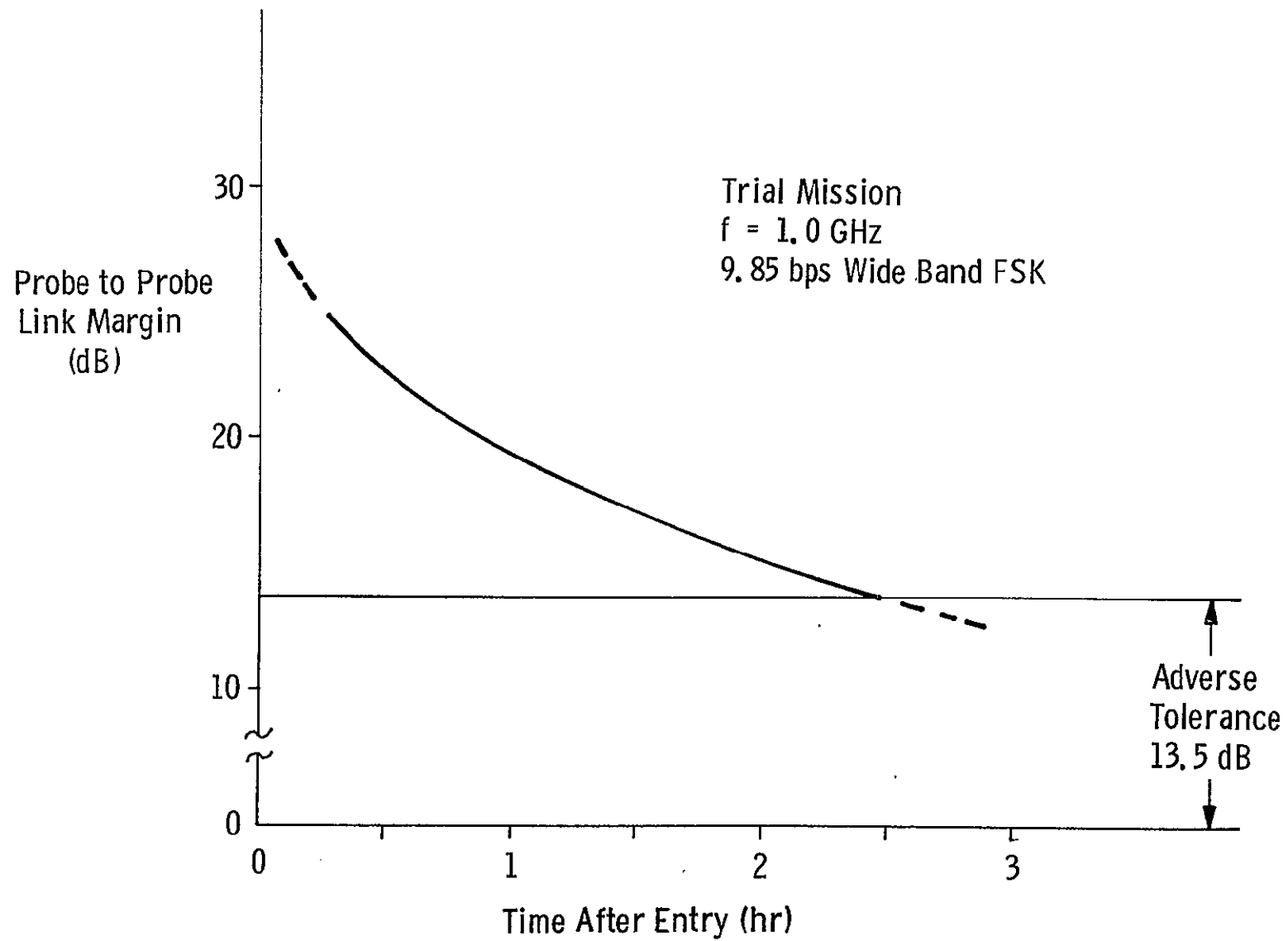


Figure VII C4b-5 Probe to Probe Comm Margin

TABLE VII C4b-1
PROBE TO PROBE COMMUNICATION LINK CALCULATIONS

WIDE BAND FSK		<u>Adverse (db)</u>
Transmitter Power (2 W, 1 GHz)	+33 dbm	0
Transmit Antenna Gain (Max)	+5.0 db	0
Transmit Antenna Pointing Loss(@ 45°)	-1.5 db	8.0
Receive Antenna Gain	+5.0 db	0
Receive Antenna Pointing Loss (@ 45°)	-1.5 db	2.5
Transmit Circuit Loss	-0.5 db	0.5
Receive Circuit Loss	-0.2 db	0.2
Atmospheric Losses	-6.1 db	0
Polarization and Miscellaneous	-1.0 db	0.3
Space Loss (595 km, 1.0 GHz)	-147.9 db	1.0
Total Gains and Losses	-148.7 db	12.5
Received Signal Power	-115.7 dbm	12.5
Receive Noise Power Density (System Temp = 2130°k)	-165.3 dbm	1.0
Filter Bandwidth (13 kHz)	+41.1 db	0
Required Input S/N (Bit Error Probability 1×10^{-5})	-5.0 db	0
Required Input Signal Power	-129.2 dbm	13.5
Margin	+13.5 db	13.5 db

Table VIIC4b-2 shows a list of subsystems components with estimates of power and weight for each.

2) Spacecraft Systems

The spacecraft telecommunications system requires a two-gimbal parabolic reflector antenna 2.81 ft. in diameter with a 1.8 GHz feed. At the time this mission was defined (prior to the mid-term report) it was assumed that the trajectory error analysis which had not been completed would indicate the possibility of relying on a preprogrammed S/C antenna pointing mode without a requirement for an autotrack antenna.

The final results of the analysis show that for the anticipated communications geometry variations due to the deflection strategy and navigation errors, as many as 3 to 4 beam positions would need to be searched in frequency to cover the 3σ pointing uncertainty. Based on the initial estimate, the additional telecommunications equipment to be added to the S/C includes that indicated in Table VIIC4b-3.

Other requirements of the S/C subsystems include programming the operations necessary to accomplish the Probe separation phase, the signal acquisition and reception of the probe relay signal, the storage of the incoming relay data and the retransmission of the data to Earth. Typical requirements including additional S/C power are described in detail in Volume II for similar missions such as the design example mission and will not be dwelled on here. Where a spin stabilized S/C is used for the flyby, special consideration must be given to the S/C relay antenna to provide a despun system. This subject is discussed in detail in Chapters IV and V of this volume.

TABLE VII C4b-2

SPLIT PROBE TELECOMM/POWER WT SUMMARY - TRIAL MISSION

VIT-34

			Upper Probe (Relay)		Lower Probe	
			Weight (lb)	Power (w)	Weight (lb)	Power (w)
● Antennas						
- Relay to S/C	1.8 GHz		0.5	--	--	--
- Probe/Probe	1.0 GHz		1.4	--	1.4	--
● FSK Receiver			1.5	1.2	--	--
● Modulator/Exciter			1.5	2.0	--	--
● Power Amplifier	20 watts		4.0	65.0	--	--
● FSK Transmitter	2 watts		--	--	1.2	7.0
● Sequencer			4.0	3.0	1.5	2.0
● Data Handling			7.1	8.0	4.0	3.0
● Memory Assembly			3.0	2.0	--	--
● Inverter			4.0	12.0	3.0	2.0
● Battery			10.0	--	2.5	--
● Cabling			6.0	--	5.0	--
Totals			43.0	93.2	18.6	14.0

TABLE VII C4b-3
TRIAL MISSION TELECOMMUNICATIONS AND DATA HANDLING
ADDITIONS AND MODS TO TOPS SPACECRAFT

<u>Component</u>	<u>Comments</u>
1.8 MHz Relay Link Data Receiver	Automatic frequency search and acquisition.
S/C Relay Antenna	Preprogrammed pointing 2.81 ft diameter mounted in 2 gimbal base.
Relay Link Pre-amplifier Receiver	Mounted at antenna.
Subcarrier Demodulator and Bit Synchronizer	Single square wave subcarrier recovery of subcarrier reference by frequency doubling.
Viterbi Decoder	1/3 rate, constraint length of 4, quantize symbol to 8 levels (no hard decision).
Data Storage	Use existing TOPS S/C storage. Need 360k bits if stored during pre-entry approximately 300k for post entry data.
Acquisition and Antenna Pointing	Assume use of existing TOPS system.

NOTE: Total additional power allocated for above including thermal is 35 watts during relay communications operations.

5. Supporting Trades

a. Mechanical

Several of the trade studies leading to the Trial Mission Configuration are described below, others are contained in the Engineering Concept Evolution Chapter, Chapter IV, Volume II, and the Mechanical Subsystems Chapter, Chapter V of this volume.

Descent Probe Weight Trade Study

The thermal/structural design of the lower (1000 bar) probe, was arrived at after analyzing the weight and size of systems involving various structural alloys and insulation concepts. Figure VIIC5a-1 shows the resulting tradeoff as a function of pressure vessel structural temperature. At the extreme temperature, 2100°F, the design consists of a columbium alloy vessel with an internal insulation of multilayer. On the low temperature size, the Titanium structural alloy operates at 150°F so that no internal insulation is required and about 5 inches of Min K are used on the outside to reduce the 2100°F ambient temperature to the 150° F level.

It can be seen that the midrange of structural temperatures 1000°F to 1200°F provide the minimum weight, (Inconel is the alloy) and near-minimum size.

Entry Vehicle Weight

The 4.25 ft diameter aeroshell selected to house the upper and lower descent probes is the minimum diameter which provides sufficient volume for the contents. This results in a relatively high ballistic coefficient, slightly greater than 1.0. Consequently a comparison of the weights of lower ballistic coefficient systems, larger diameter aeroshells, was made. The results are shown in Figure VIIC5a-2 from which it is apparent that lowering the ballistic coefficient by increasing aeroshell diameter aggravates the total weight situation. The aeroshell structure goes up slightly since its surface area increases a little faster than the unit thickness or gage, is reduced. The heat shield weight goes up considerably since both its unit thickness and surface area are enlarged by the lower ballistic coefficient and the greater diameter.

Entry Angle Selection

Before selecting the 10° entry angle larger values were considered since they afford longer periods of time on the sun side of the terminator. The dynamic pressure penalty of steeper γ 's is shown in Figure IIIC5a-3 and Figure VIIC5a-4 shows the penalty incurred in the Entry Probe Weight. From this figure it is seen that above $\gamma = -20^\circ$ to -30° the penalty becomes excessive. Even at -20° a 15% weight increase is imposed.

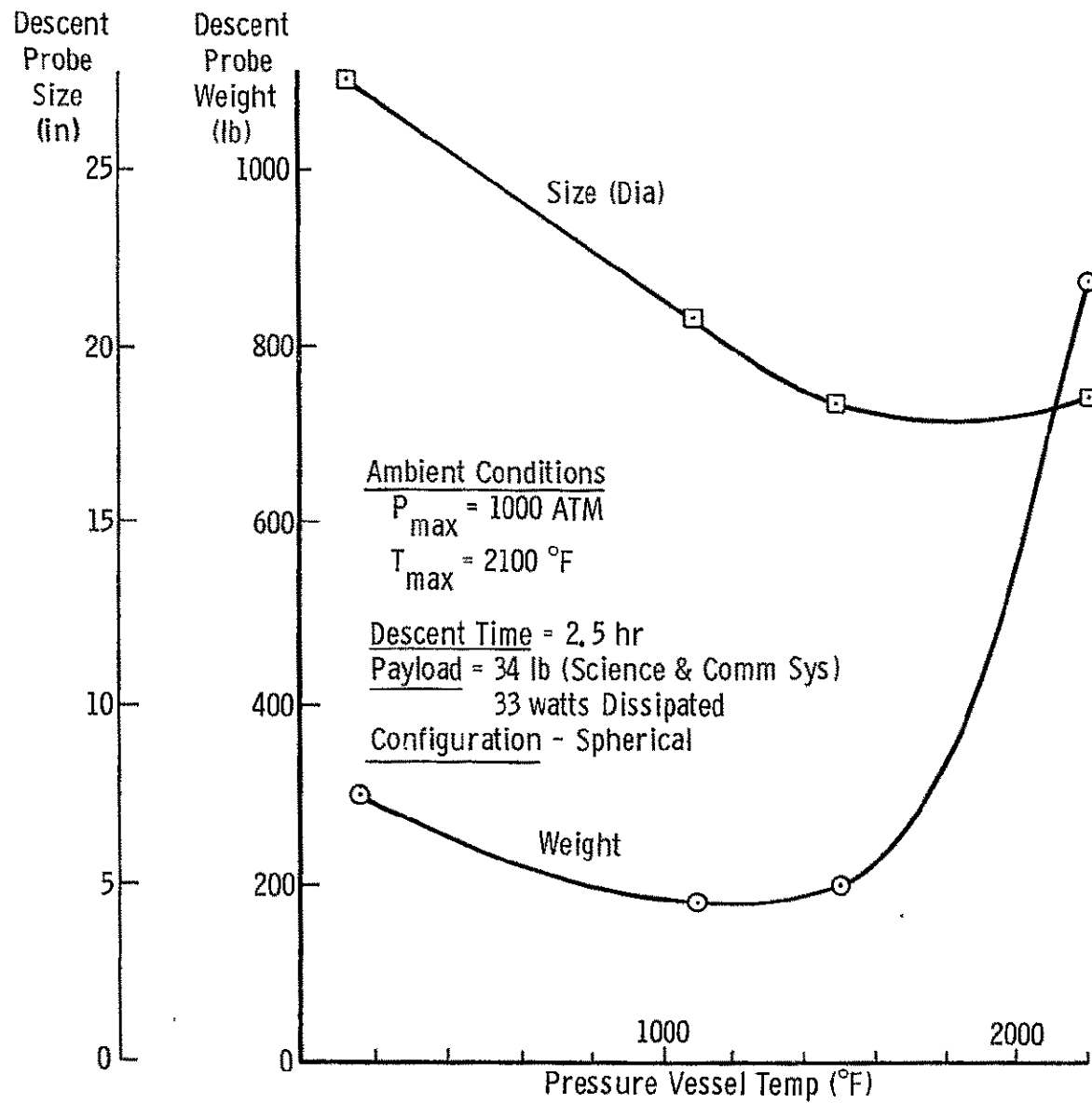


Figure VII C5a-1 Descent Probe Thermal/Structural Weight vs Pressure Vessel Temperature

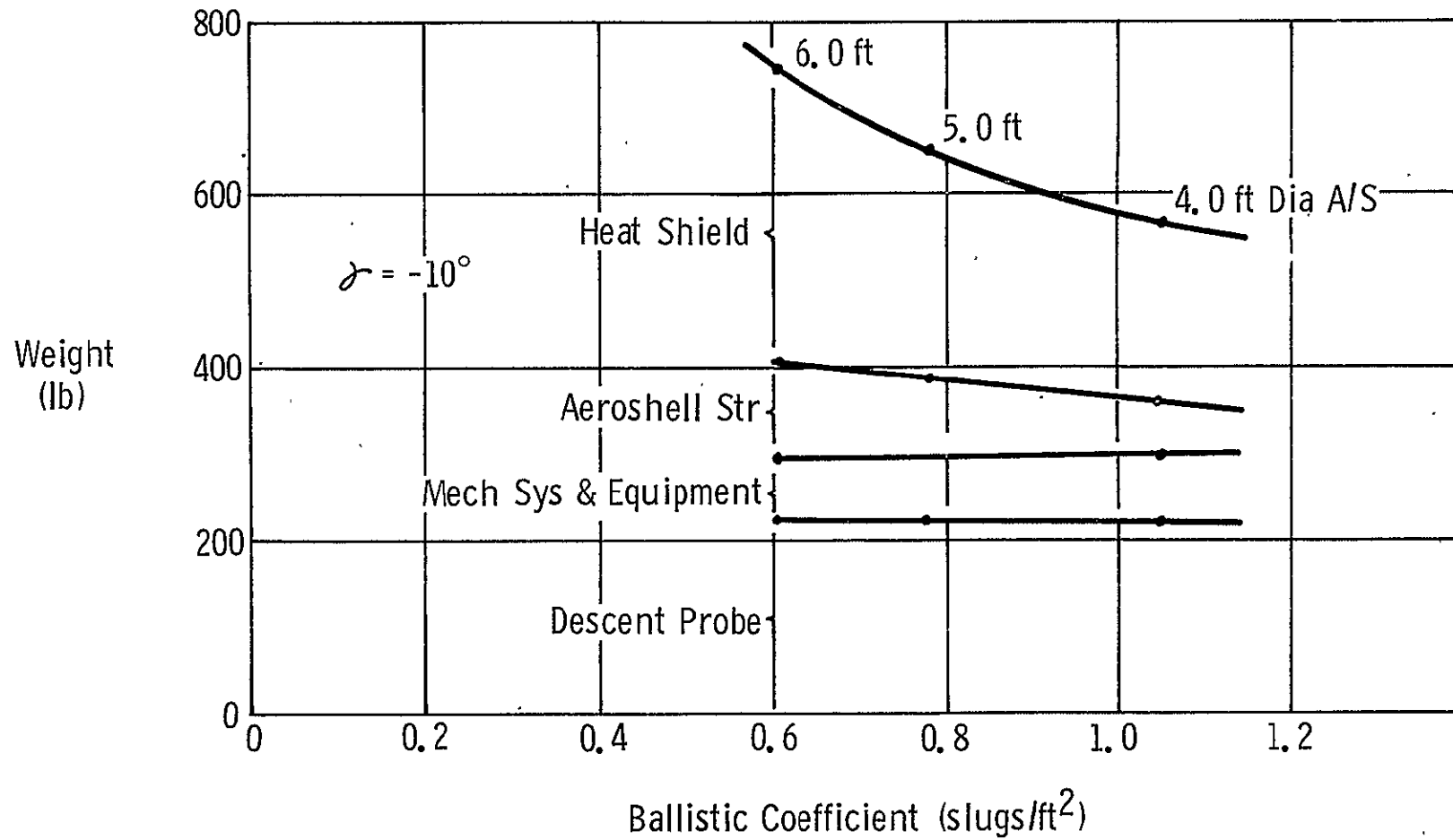


Figure VII C5a-2 Sensitivity of System Weights to Ballistic Coefficient

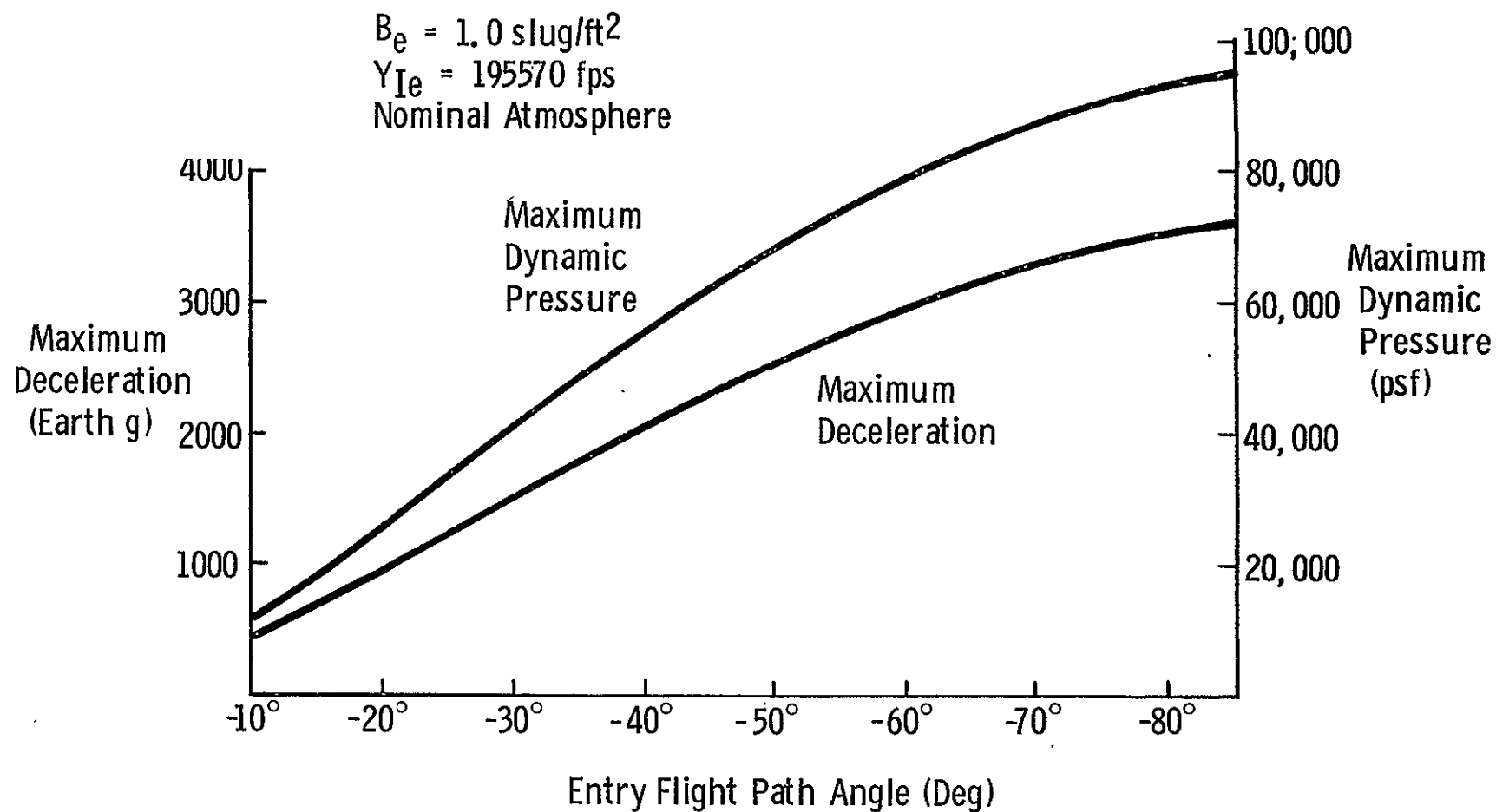


Figure VII C5a-3 Effect of γ_E On Vehicle Loads

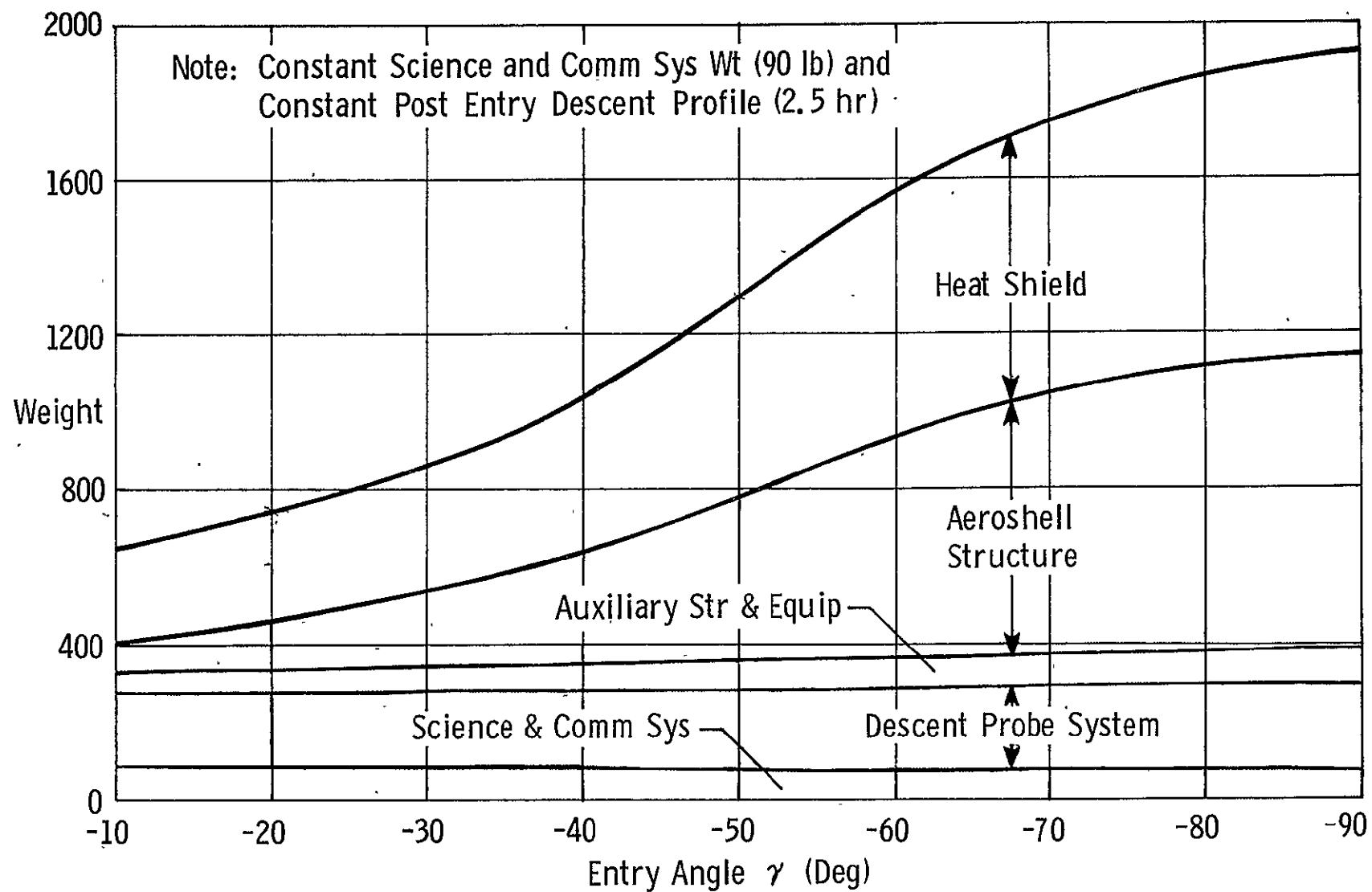


Figure VII C5a-4 Sensitivity of Probe Systems Weight to Entry Angle Variation

b. Telecommunications and Data Handling

Basic tradeoff and parameter selection considerations encountered during the trial mission definition phase of this study essentially correspond to the following:

- Trajectory optimization for relay communications,

- Modulation and coding,

- Frequency selection for relay link,

- Signal acquisition and tracking,

- Single vs. split probe,

- Frequency and modulation selection for probe to probe link.

Tradeoffs and selection parameters applicable to this mission have been discussed in detail in Chapter IV for the first three items on the above list using updated atmospheric attenuation models and, therefore, will not be discussed in detail in this chapter. The fourth item signal acquisition and tracking is also detailed in Chapter IV; however, for the trial mission, unlike the missions studied later, it was assumed that the uncertainty of the location of the probe based on a preprogrammed antenna pointing mode would place the probe within the 3 db beamwidth of a 19.8° half-power beamwidth antenna; therefore, use of an auto track S/C relay antenna was not initially considered necessary. Frequency selection and S/C antenna aperture were then based on maintaining a minimum beam width of 19.8° and at the same time optimizing link parameters to minimize transmitter power. Optimum frequency for the upper probe to S/C link for the attenuation model in use at that time at the final descent depth of 45 atmospheres would have been 2.3 GHz except for the fact that additional antenna aperture was required to attain adequate margin with a 20-watt probe transmitter. The frequency was therefore reduced to 1.8 GHz and the aperture size raised to a 2.81 ft. diameter antenna. Since the frequency tradeoff curves used at that time are now obsolete due to the increased attenuation of the current model, and have been replaced by the latest tradeoff data as given in Chapter IV; the old curves are not shown.

The fifth item in the above list (single vs. split probe tradeoff for the trial mission) has been replaced by data generated in the baseline parametric study which utilizes the latest attenuation model data; therefore, to prevent confusion, the obsolete data will not be presented here.

The equivalent baseline parametric study case for comparison of single vs. split probes using the latest data is a comparison of a single probe to a depth of 1000 bars versus a split probe mission with the upper probe descending to 31 atmospheres and the lower probe descending to 1000 atmospheres. Flyby is at an R_p of $2 R_j$ with entry at a flight path angle of -10° . These and other missions varying in entry depth, trajectory and entry angles are given in Volume II in the baseline parametric section.

Frequency and modulation selection tradeoffs for the trial mission probe to probe data link resulted in use of a 1.0 GHz radio frequency and noncoherent, nontracking wide band FSK modulation. Selection of the 1.0 GHz frequency was based on maximum antenna aperture size constraint since according to the curve of Figure VII C5b-1 were it not for the antenna size even a lower frequency would be appropriate.

Referring to Figure VII C5b-1, the relative required gain in the link as a function of frequency assuming fixed antenna gains on both ends of the link is shown for a range of frequencies from 0.3 to 1.4 GHz. Included for consideration is atmospheric attenuation, upper probe receive system temperature and the ratio of predetection bandwidth to bit rate ratio for a bit error probability of 1 part in 10^{-5} . Atmospheric attenuation in db at a given frequency is the difference between the two curves. Attenuation as shown is based on the old model and a 45° from zenith transmission angle too. The attenuation using the new atmospheric model in db is equal to 1.5 times the attenuation shown. Since the antenna constraint still remains, there is no change in the frequency to be used.

Non-tracking wide band FSK was chosen due to the simplicity of the systems and the relatively low transmitter power resulting from such a choice. Had the transmitter power requirements been doubled or tripled, a more complex system may have been considered.

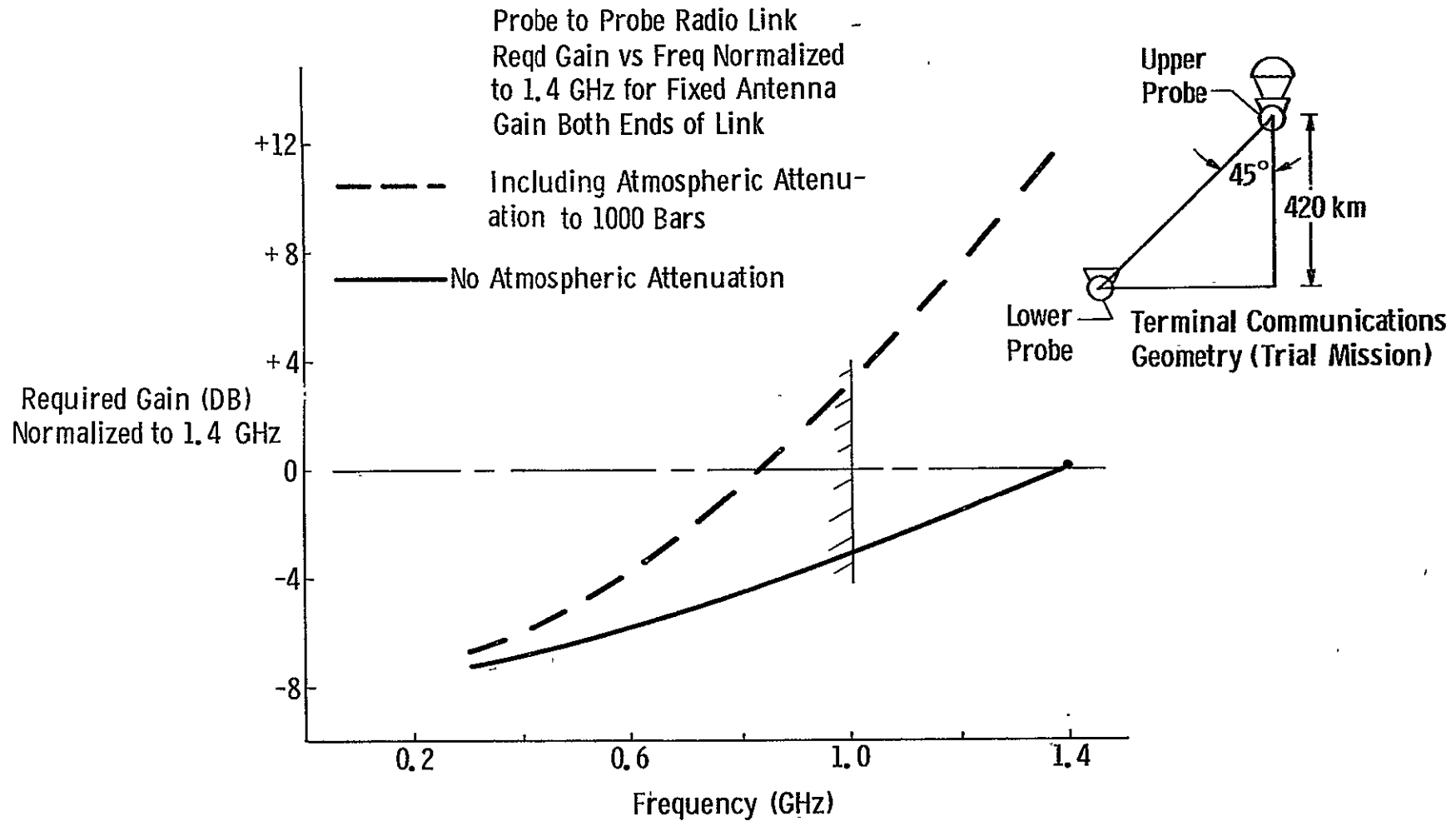


Figure VII C5b-1 Relative Required Power Gain Vs Frequency
Probe to Probe Link

APPENDIX A

PRECESSING OF A SPINNING PROBE

There are two basic methods of precessing a spinning probe. One is to have the jets despun inertially and fire the jets continuously. The other is to have the jets fixed on the spinning body and firing the jets as the spacecraft pass a certain reference. The first is much more efficient, but the latter, the simplest. It is assumed the second is used. Usually the sun is used as a crossing reference and a phase-locked-loop (PLL) is used to time the jets.

There are many error sources, in this report these will be classified as timing errors, propulsion errors, and unknowns in the dynamics. The first two of these are well known. The last contains many subtleties which aren't as well known. These errors will be discussed in the following paragraphs.

Timing Errors -- In this probe the spin axis will cross the sun line, therefore render the sun crossing sensor inoperative. It is fairly close to the sun line to start with $\sim 10^\circ$, and hence may or may not work. A star crossing might work, but a very wide angle must be covered; therefore, a possibility of detecting other stars and/or getting into a position of the sun exists. One may use memory on the PLL, but this depends on the bandwidth, drift rate, and various other parameters of the PLL. One would have to be sure that the passive damper would not change the spin rate sufficiently to render the memory of the PLL useless.

If one used a spin table to spin the probe which was attached to the TOPS, then one could establish the spin rate precisely to a standard clock; then, using this clock to fire the jets. It is easy to show that it would not be too difficult to obtain a clock with sufficient stability, but again possible damping would change the spin speed sufficiently to negate this system.

From a very brief look, it would appear that timing may be a very important problem because it must be updated to the spin speed. The passive damper and its effect on the spin speed will be discussed later.

Propulsion Errors--These errors are due to pressure, temperature, etc., those variations which effect specific impulse of the propellant, also the randomness of the turn-on and turn-off of the jets., i.e., Δh variation. These have been worked and are well known.

Dynamic Unknowns--These errors are due to unknowns in the inertia of the spacecraft, amount of passive damping, and the initial conditions when precession starts. In this section, it is assumed that the classical two-pulse method to precess will be used.

This method is based on knowledge of the inertia ellipsoid (which has equal cross axes inertia) and zero initial conditions on the cross axes rates. If one has these conditions and one jet couple, a jet couple is fired when a cross axis reference is aligned with an inertia reference (i.e., precess in this plane), causing a coning of the spin axis in inertial space (nutation) with a half angle

$$\beta_{1/2} = \tan^{-1} \left(\frac{\Delta H}{H_s} \right). \quad A1$$

Where H_s is the spin axis momentum (total momentum to start problem) and ΔH is the cross axis momentum added by firing the jet. One then waits n integer revolutions of the spin axis and $m+1/2$ revolutions of the inertia coning and then fire the jet couple. If the ΔH is exactly the same the spin axis will be precessed through an angle β and there will be no nutation (inertial coning). Since the coning rate ω_θ is

$$\omega_\theta = \frac{I_s}{I_c} \omega_s$$

the values of m and n can be found as having to satisfy the following:

$$\frac{m + 1/2}{n} = \frac{\omega_\theta}{\omega_s} = \frac{I_s}{I_c}.$$

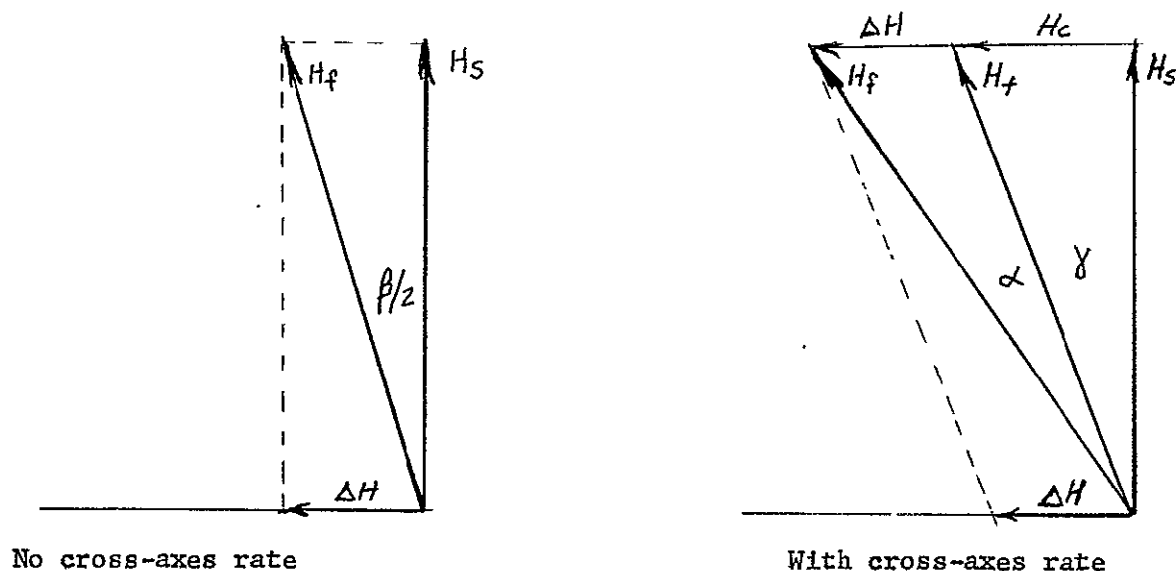
Note that usually n is measured (sun crossing) and m given from knowledge of the inertia ratio. There is always some unknown in this ratio; therefore,

m is in error by the amount the inertia ratio is in error times n .

For large n , one could have large error in m . Hence large nutation build-up. One may require detecting the cross-axis rate and allowing the jet couple to fire only when the cross-axis rate is in proper body coordinates so that the Δh will reduce the cross axis rate or that the cross axis rate is below some level; i.e., this would automatically find m without use of the inertia ratio.

The nutation then comes from three sources in this probe, these are (1) Spin-up or tip-off rate, (2) The ΔV maneuver, and (3) the precessing.

Nutation effects the precessing accuracy primarily in two ways. These are (1) With nutation the spin speed tends to build up; therefore, the spin momentum is greater, hence the cone angle is less than anticipated (see equations (1) and (2) with nutation the change in momentum (Δh) doesn't have as much effect on the cone angle as shown in Figure A1. Nutation in both cases tend to reduce the added cone angle.



NOTE: $\alpha < \beta/2$ for $\gamma > 0$

H_c = Cross-axes momentum projection

Figure A-1 Effect of Cross-axes Momentum (Nutation)

The angle γ varies as its projection on the precession plane; therefore, the angle α varies depending upon the relation of this projection. One is interested in keeping the nutation low because the rate at which the passive damping takes place is proportional to the square of the cross-axes rate.

CONCLUSIONS

Although a number of potential error sources have been identified, a well designed system will take these factors into account. Some of these errors may be negligible. It is assumed that the precession maneuver is to be an open loop maneuver, i.e. preprogramed. Therefore the above errors need to be evaluated quantitatively to obtain an estimate of the accuracy achievable in a reorientation maneuver. Such an analysis is required to establish the feasibility of utilizing precession in the Probe deflection operation.

APPENDIX B ATTITUDE PROPULSION SYSTEM STUDY FOR ACTIVE CONTROL OF A DESCENT PROBE

Introduction - As discussed in Chapter IV, Vol. II, descent probe/planetary vehicle communication requirements favor a coherent link communication system. Loss of signal, even for brief periods, is unacceptable for this design. This factor, plus the anticipated turbulence of the Jovian atmosphere, suggests that active attitude control of the descent probe be considered as an alternate to passive aerodynamic stabilization. This would suggest that an aerodynamically neutral shape be employed in order to minimize aerodynamic disturbances, particularly those resulting from wind shears due to atmospheric turbulence. Consequently a spherical probe shape has been considered in the evaluations of the various candidate control systems. For those techniques requiring mass expulsion the control thrusters are mounted well within the low velocity wake region as illustrated in Figure B-1. This is done in order to avoid disturbance of the wake shape by the thruster exhaust, since interaction with the flow field along the sides of the probe would produce unsummetrically and unpredictable disturbance torques on the probe body.

Selection of Candidate Systems

To provide the torque required to maintain active attitude control to a depth of 600 kilometers into the Jovian atmosphere, several propulsive as well as non-propulsive techniques were considered. It is evident that development of a propulsion system for the descent probe will be strongly affected by the high pressure, high temperature in which it must operate. The high temperatures which will be encountered will greatly influence the materials, components and processes that can be employed, whereas the high ambient pressures will greatly reduce thruster performance. These factors can be expected to have an adverse effect on the weight and reliability of the attitude propulsion system when compared to conventional systems which are designed for operation in a vacuum environment. As an example, Figure B-2 illustrates the anticipated weight effect for a representative performance capability of 0.1 lb thrust and 1000 lb-sec impulse. Weight estimates are shown for both light weight and heavy weight designs at vacuum & 1000 bars:

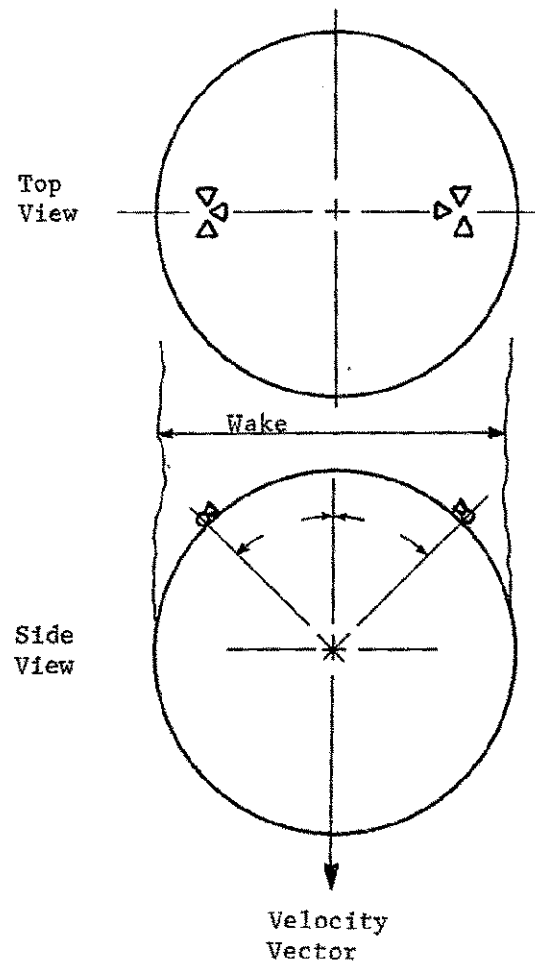


Figure B-1 Descent Probe Reaction
Jet Configuration

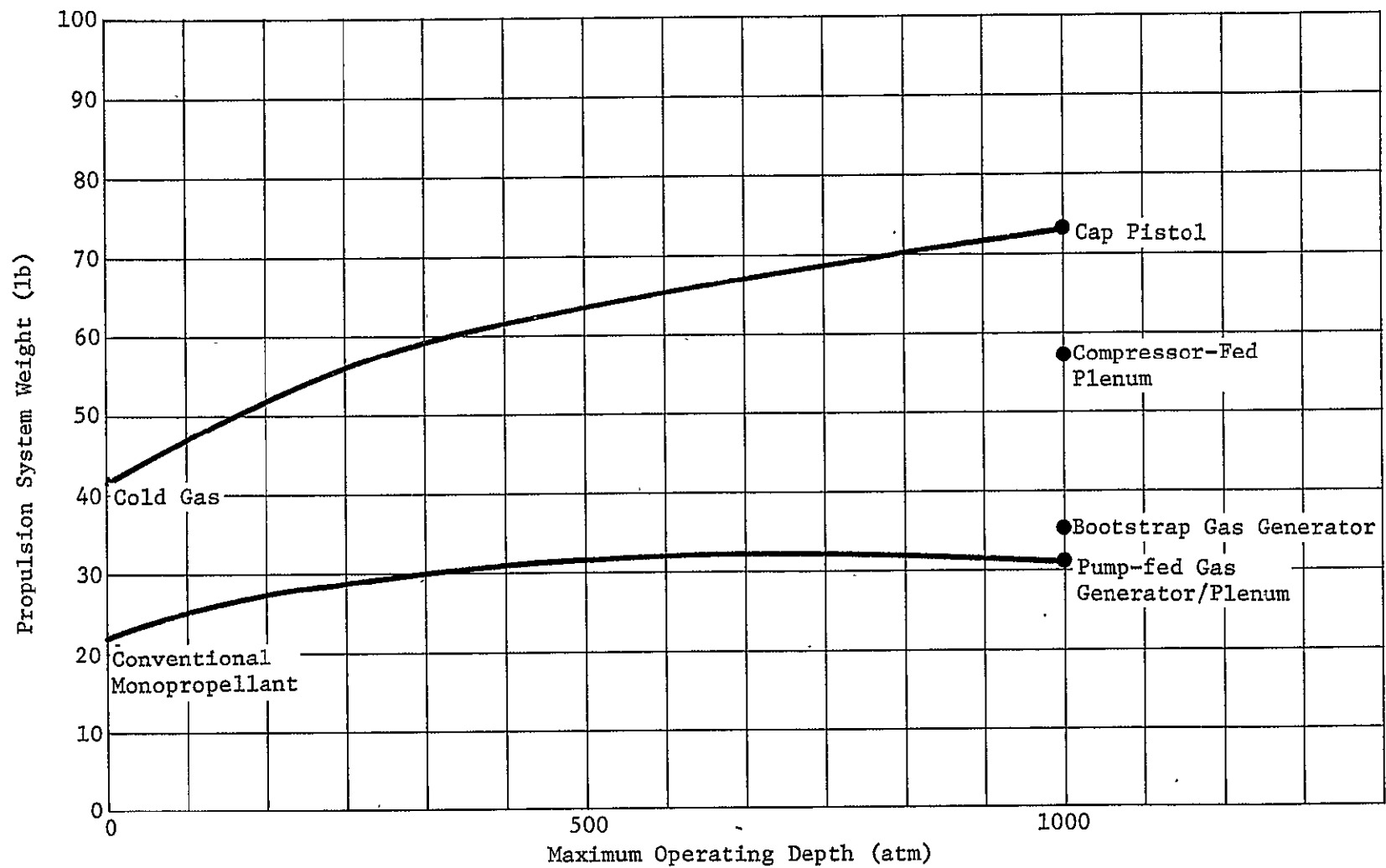


Figure B-2 Sensitivity of Propulsion System Weight to Maximum Operating Depth

Thermal Control

Generally speaking, the use of mass expulsion devices for rocket propulsion requires that a propellant be heated and ejected at high velocity in order to produce thrust.

Systems are generally classified to the energy source used for heating the propellant. Chemical systems, which may store the propellant either as a solid, liquid or gas, produce thrust by a chemical reaction of the propellant; either by combustion as is the case with a bipropellant or dissociation as with a monopropellant. Other heated fluid systems may employ a different agent such as radioisotopes or electric heaters as the energy source. However, since specific impulse, and thus the required propellant weight, is approximately proportional to the square root of the exhaust gas temperature, an attempt is made to maintain the highest gas temperature compatible with the energy source and available material of construction.

In all cases, however, a common factor is the requirement for addition of thermal energy as the means of accelerating and ejecting the propellant mass, and rejection of this thermal energy becomes a major design factor in the development of a conventional mass expulsion system.* This problem of heat rejection will, of course, be greatly increased in the high temperature environment of the descent probe.

For example the use of a conventional bi-propellant or mono-propellant thruster was found to be inapplicable for a 1000 bar descent probe; largely because of their sensitivity to heat soak back to the propellant and propellant valves. As illustrated in Figure B-3, the conventional reaction chamber requires that propellant control valves be installed immediately upstream of the injector and thrust chamber. The close proximity is necessary in order to minimize the propellant volume between the valve and the reaction chamber, which is in turn necessary to achieve the high response, controllable impulse bits required for attitude control. Even

*A notable exception is the cold gas system. It is obvious, however, that this approach is unsuited for high pressure applications such as the descent probe; since for a system using stored gas as the propellant the amount of residual gas, and thus the system weight, is nearly proportional to the required operating pressure.

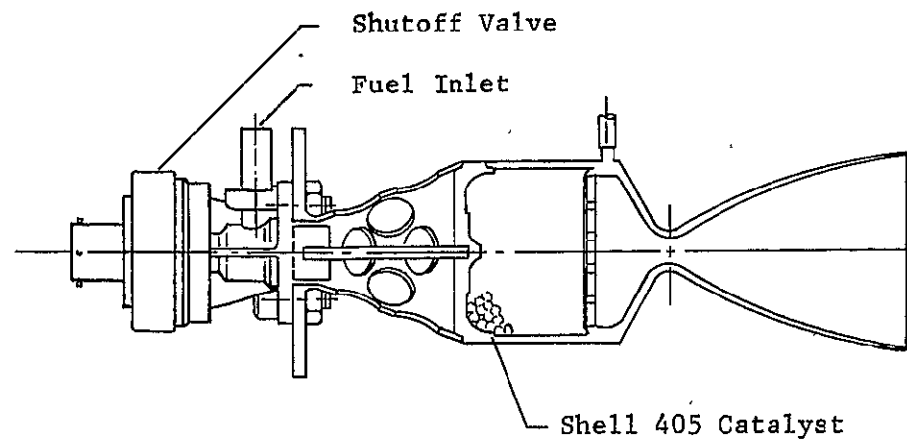


Figure B-3 Typical Monopropellant Reaction Chamber Design

for operation in a vacuum considerable design ingenuity is required to insure controlled injection of the propellant. The propellant valves must be thermally isolated from the injector and chamber body and a means of effectively rejecting heat from the chamber must be provided to avoid excessive heating of the valves and propellant. Although the problem of soak back to the valves is approachable even in this high temperature atmosphere by developing remotely actuated valves, the problem of heat transfer to the propellant is another matter. The propellants must be prevented from vaporizing in the injectors or erratic combustion and unpredictable thrust or possibly engine damage will result. However, in the high temperature/high pressure atmosphere encountered by the descent probe, the exposed engine will be continually heated by the environment even during periods of engine inactivity; thus making effective thermal control of the engine components impractical.

Performance Degradation

Another factor that is peculiar to this application is the reduced performance associated with operation in a high pressure atmosphere. For example, the I_{sp} of the gas generator systems is expected to vary from approximately 150 sec at vacuum to as low as 30 sec at 1000 bars.

For most applications the ratio of thruster chamber pressure to ambient pressure (P_c/P_a) is maintained as high as practicable. This assures sonic flow at the throat and allows the effective use of a divergent section downstream of the throat to increase the velocity of the exhaust gases to supersonic conditions. Since specific impulse is proportional to exhaust velocity, operation in space where P_c/P_a approaches infinity maximizes thruster performance. However, when operating at an ambient pressure approaching 15,000 psi, it is clearly impossible to provide a pressure ratio which will produce sonic flow. Nevertheless, as a means of maximizing performance, the highest possible operating pressure consistent with predicted thruster technology, 1500 psig, was selected for comparison of the various candidate systems; this value being limited by a minimum practical throat diameter of from 2 - 10/1000".

Since the use of conventional monopropellant or bipropellant thrusters is precluded by the thermal environment, the most applicable propulsion systems were found to be the encapsulated solid propellant pulse rocket -- "cap-pistol"--and versions of the gas-generator/plenum system. The most suitable non-propulsive techniques was found to be the reaction wheel system. Thus five candidate systems were selected for evaluation and comparison;

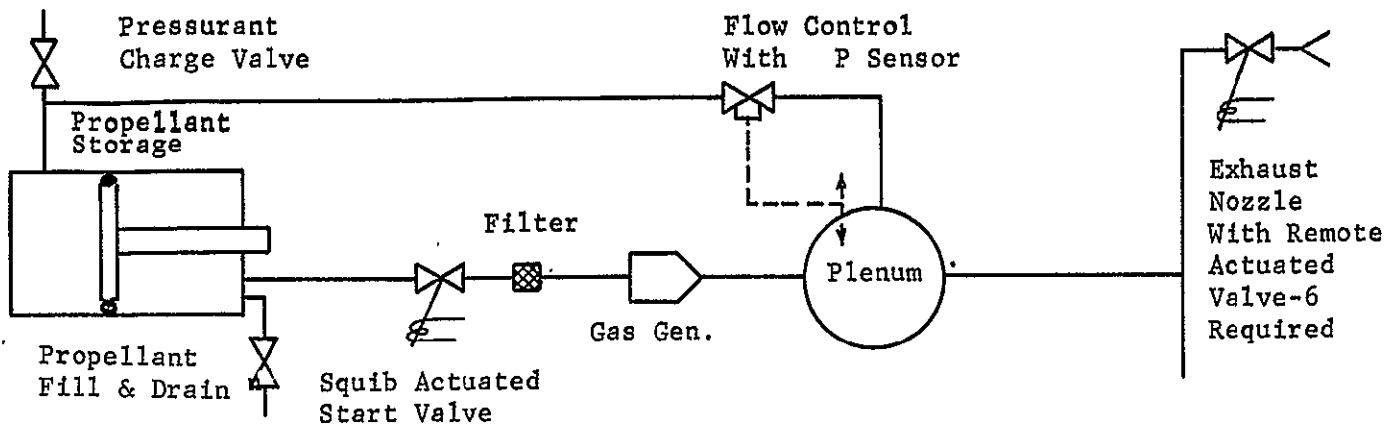
- 1) The cap-pistol,
- 2) A pump-fed gas generator/plenum system,
- 3) A boot-strap gas generator/plenum system,
- 4) A compressed atmosphere/plenum system, and
- 5) A reaction wheel system.

Comparison of Candidate Systems

Each of the five candidates systems are described below, and the propulsion systems are schematically illustrated in Figures B-4 through B-7. Weight estimates are included in the figures for each system over the range of performance capability anticipated for this application. System weights are compared in Figure B-8, and new technology requirements are identified in the following discussions of each candidate system.

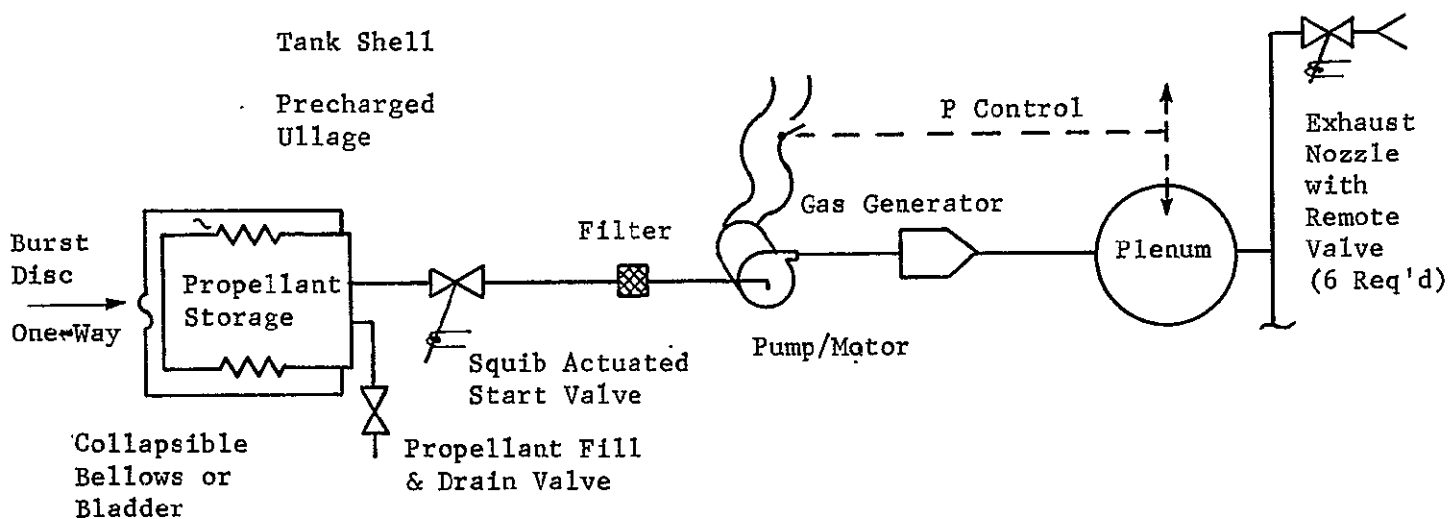
Gas Generator/Plenum Systems

Description - Two approaches to the gas generator/plenum system were considered, one which employs bootstrap pressurization--Figure B-4--and one which is pump-fed--Figure B-5. In both cases high response pulse mode operation is possible without the requirement for a stored gas pressurization system. This is essential in order to avoid the unrealistic requirement for a pressurant storage bottle capable of operating at differential pressures well in excess of 1000 atmospheres.



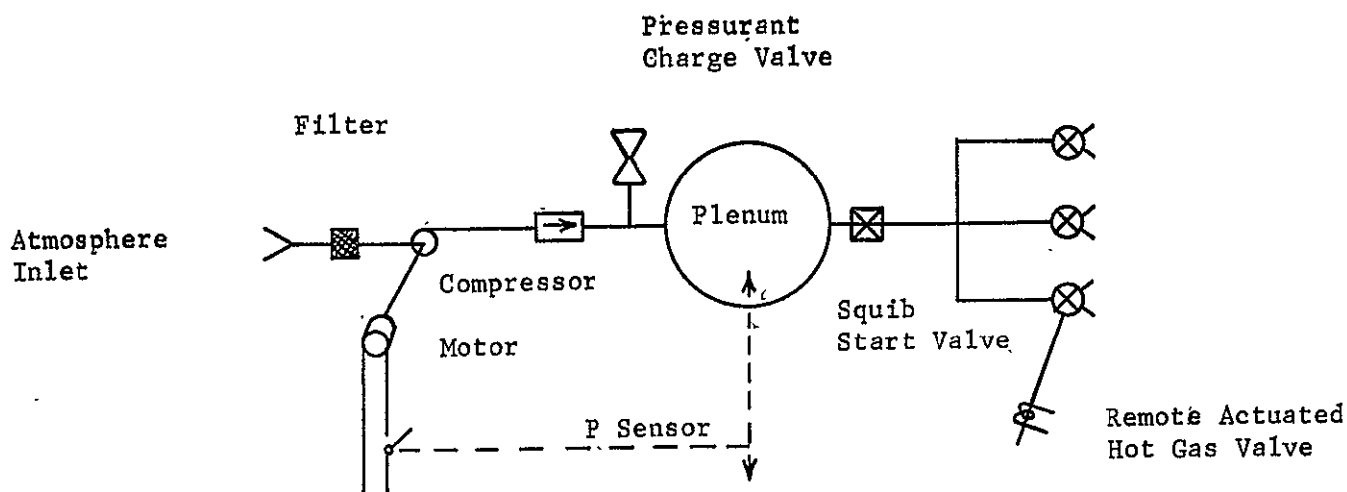
	Weight - lb		Remarks
	0.01 100	0.1 1000	
Thrust / Impulse lb lb-sec			
Propellant/Pressurant	1.6	16.2	Supporting Attachments Estimated at 10% of Total System Weight
Propellant Tankage	1.0	5.5	
Thrusters & Valves	3.0	6.0	
Feed System Components & Attachments	3.7	8.8	
Total System Weight	9.3	36.5	

Figure B-4 Bootstrap Gas Generator System
Configuration and Weight Summary



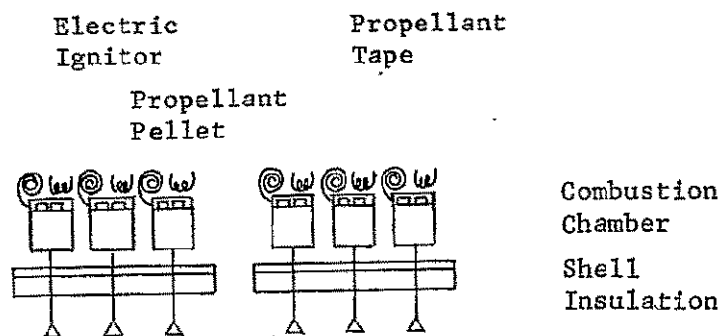
	Weight - lb		Remarks
	0.01 lb	0.1 100 lb-sec	
Thrust / Impulse			
Propellant	1.1	10.7	
Propellant Tankage	0.5	2.0	
Pump/Motor	1.0	4.0	
Thrusters & Valves	3.0	6.0	
Power Penalty	0.1	0.8	Based on Battery Weight of 30 watt-hrs/lb Supporting Attachments Estimated at 10% of Total System Weight.
Feed System Components & Attachments	3.2	7.5	
Total System Weight	8.9	31.0	

Figure B-5 Pump Fed Gas Generator Configuration & Weight Summary



	Weight - lb		Remarks
	0.01 lb	0.1 lb-sec	
Thrust / Impulse lb lb-sec	100	1000	
Compressor/Motor	4.5	18.0	Based on a Battery Weight of 30 Watt-hr/lb
Power Penalty	2.2	22.0	
Thrusters & Valves	3.0	6.0	
Feed System Components and Attachments	4.8	12.0	Supporting Attachments Estimated at 10% of Systems Weight
Total System Weight	14.5	58.0	

Figure B-6 Compressor Fed Plenum System
Configuration & Weight Summary



	Weight - lb		Remarks
	0.01 lb	0.1 1000	
Thrust / Impulse lb lb-sec	100	1000	
Pulser Head & Motors (Two)	3.0	3.5	
Caps	13.0	29.0	
Storage Container	19.0	40.0	
	35.0	72.5	

Figure B-7 Cap Pistol System Configuration
and Weight Summary

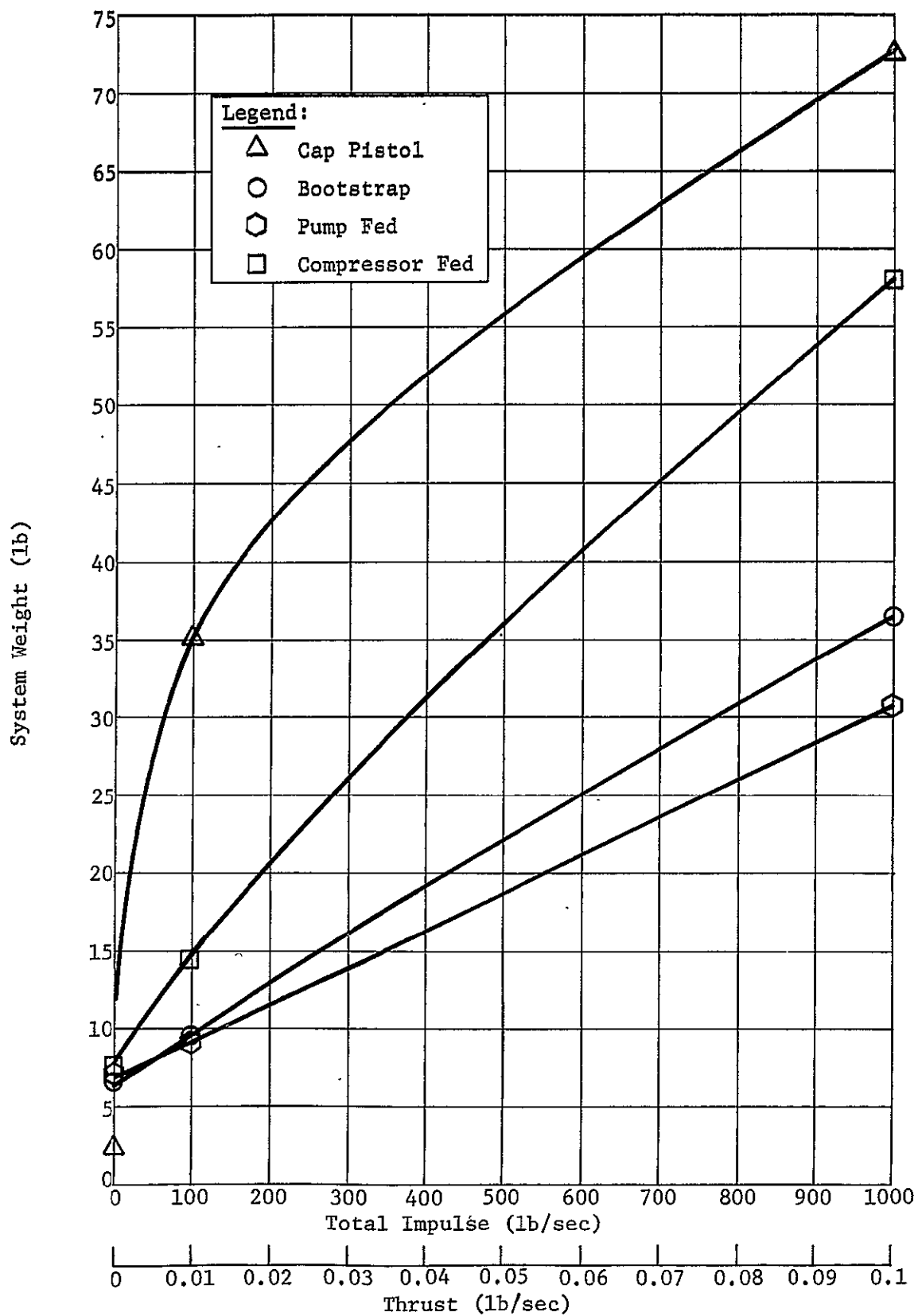


Figure B-8 Sensitivity of Attitude Propulsion System Weight to Thrust and Total Impulse Capability

Several other characteristics are also common for these two systems:

1. The monopropellant is stored as a liquid to minimize system volume and leakage potential--squib actuated start valves are also provided to reduce the possibility leakage prior to system activation.

2. A catalytic gas generator is employed for maximum reliability.

3. Gas generator effluent is stored in a plenum whose operating pressure is controlled at 1500 psig by a differential pressure sensor, thus allowing high response, controlled thrust levels.

4. Hot gas valves installed immediately upstream of each thruster are remotely actuated. This is necessary because of heat transfer from the exhaust nozzles which are exposed to the high temperature atmosphere. (Conventional direct acting thruster valves are limited to operating temperatures of less than 300°F).

5. Both systems are insulated to conserve reaction heat during the early portions of the descent, and thus improve performance, and to protect sensitive components from the atmosphere during the latter portions of the descent.

The pump fed system is battery powered and employs a collapsible propellant storage tank which is exposed to ambient pressure. This means that the pump is required to overcome the difference between operating pressure and ambient pressure (1500 psig) rather the absolute pressure which may be as high as 15,000 psia.

The bootstrap system employs a rigid propellant tank with pressure amplifying device such as the differential area piston schematically illustrated in Figure B-4. Other devices such as multiple or differential area bellows might also be considered, reference a.

Evaluation - Compared to the other candidate systems the major advantage of the gas generator/plenum systems is their relatively light weight, figure B-8, with the bootstrap system somewhat heavier than the pump fed system for impulse requirements greater than approximately 100 lb-sec.

Over the desired range of operation, i.e., vacuum to 1000 bars, the variation in thrust level is expected to be approximately $\pm 20\%$. The

major disadvantage associated with these systems result from their new technology requirements. In addition the pump fed system will be susceptible to instabilities induced by variations in ambient pressure unless it can be sufficiently damped, whereas the bootstrap system will require precise thermal design to achieve acceptable performance without exceeding temperature limits of the propellant and propellant tank components.

New Technology Requirements - If a gas generator/plenum system is to be employed for active attitude control of the descent probe several new technology requirements must be satisfied.

1. In both instances the development of remotely actuated thruster valves will be required because of the high ambient temperatures that will be encountered.
2. Use of a gas generator will require identification of a suitable mono-propellant/catalyst combination and verification of controllable reaction rates at the required operating pressures and temperatures.
3. Design and development of a reliable pressure amplifying tank which will operate at extremely high pressures will be required if a bootstrap system is used.

Compressed Atmosphere/Plenum System

Description - This system is similar to the gas generator/plenum systems in that thrust is produced by compressed gas which is exhausted through remotely actuated hot gas valves. The compressed gas is stored temporarily in a plenum which acts as a surge chamber. Prior to descent to approximately 10 bars, thrust is provided by blowdown of preloaded nitrogen from the plenum. From approximately 10 bars to 1000 bars pressure is maintained in the plenum at a constant value above ambient (1500 psia) by means of a motor driven compressor. Gas is drawn directly from the atmosphere to replenish the depleted plenum as required. The nearly constant gage pressure is controlled by a ΔP sensor and switch operating over a moderate deadband. As with the systems previously described, this assures reasonably controlled impulse bits and thrust levels without requiring that a high response reaction chamber, control valves and propellant be exposed to the high temperature atmosphere.

The compressor is motor driven with power being supplied by storage batteries, a turbine drive being impractical because of the multistart requirement and high discharge pressures that would be required.

Evaluation - The compressor fed plenum system is considerably heavier than either of the gas generator systems. This results largely from the relatively high power and energy levels required to compress the working fluid. Because of the reduced fluid density, these requirements are at least an order of magnitude greater than those for the pump fed system and are reflected directly in the weight estimates for the battery and compressor/motor. The variation in thrust over the desired range of operating pressures will be comparable to that of the gas generator systems; namely $\pm 20\%$.

New Technology - As with the previous approaches, this system also requires a significant development.

1. Development of remotely actuated hot gas valves will be necessary to control the high temperature plenum gases.
2. Development of a compressor that will operate efficiently over a broad range of inlet temperatures and densities will be required.

Cap Pistol

Description - With a "cap pistol" system thrust is produced by individual encapsulated solid propellant rocket motors--caps--which are mounted on a tape and are fed from a storage bin into firing position by a sprocket wheel that is driven by a stepping motor. Figure B-9 illustrates the pulser and motor elements of a multiple nozzle installation. Because of the small impulse generated by an individual cap precise attitude control can be achieved. On the other hand a high cyclic rate of operation (up to 20 cps) also effectively provides a steady state thrust capability for maneuvering or for disturbance correction. Two basic types of motors are available. One type employs a rigid motor case and an integral exhaust nozzle for each cap as illustrated in Figure B-10 and described in detail in reference b; and the second, Figure B-11, employs a flexible case (E-dome) that expands within the sprocket wheel during operation. Reference c describes this design, which allows additional volume for combustion and seals the combustion gases at the interface between the integral nozzle and

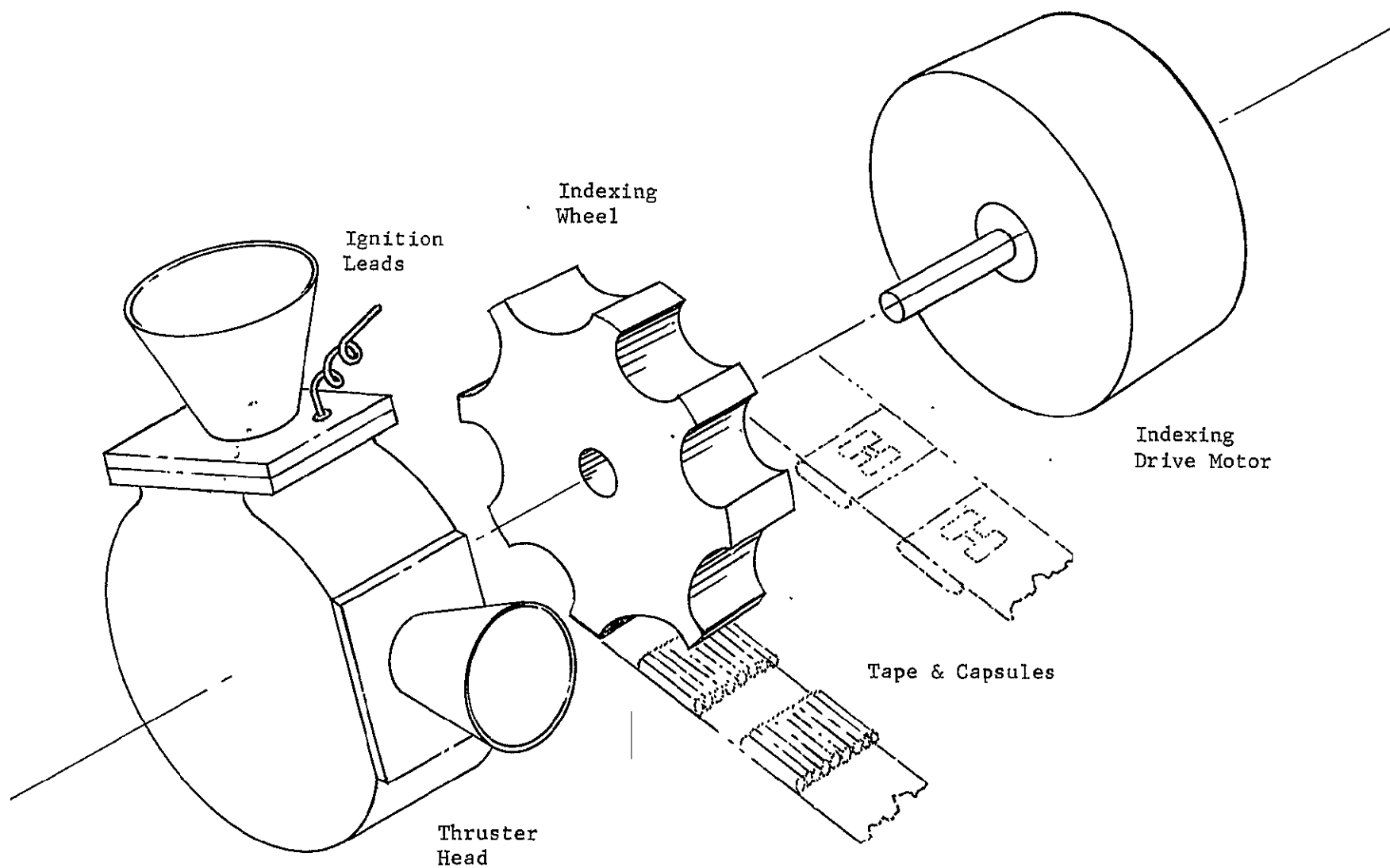


Figure B-9 Cap Pistol Pulser Elements

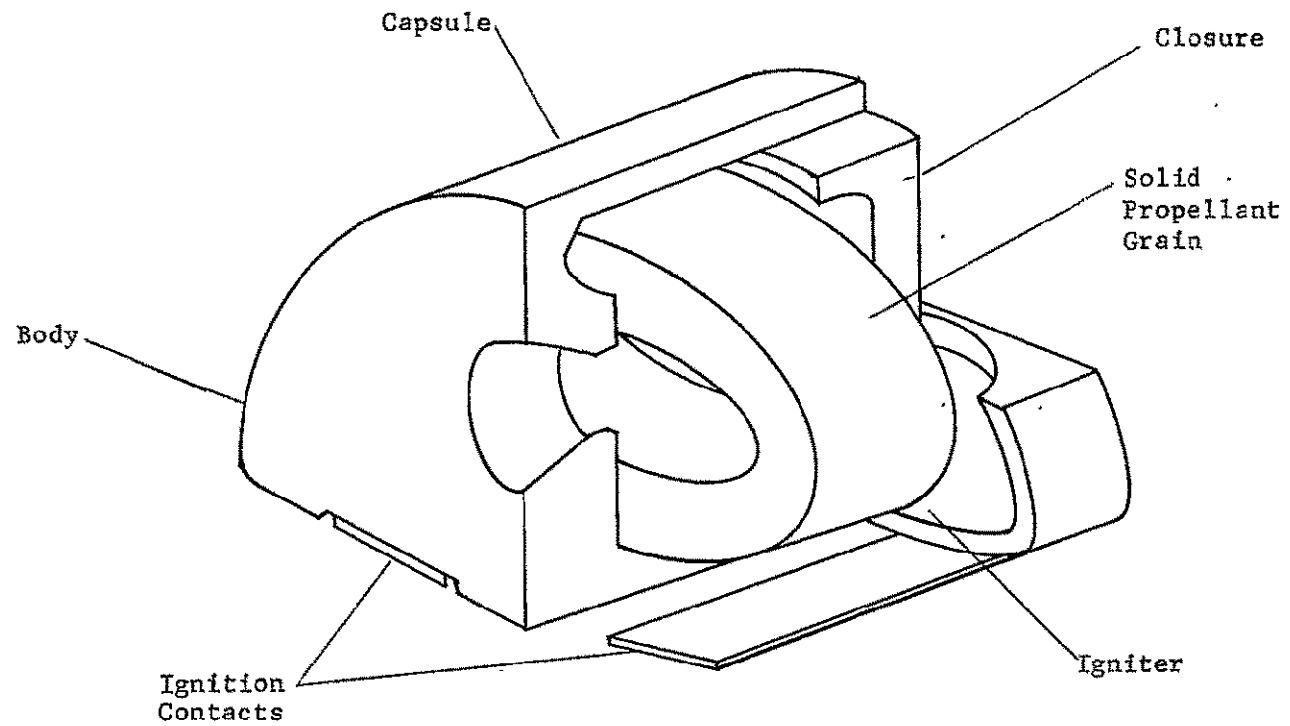


Figure B-10 Cap Pistol Rocket Motor with
Integral Exhaust Nozzle

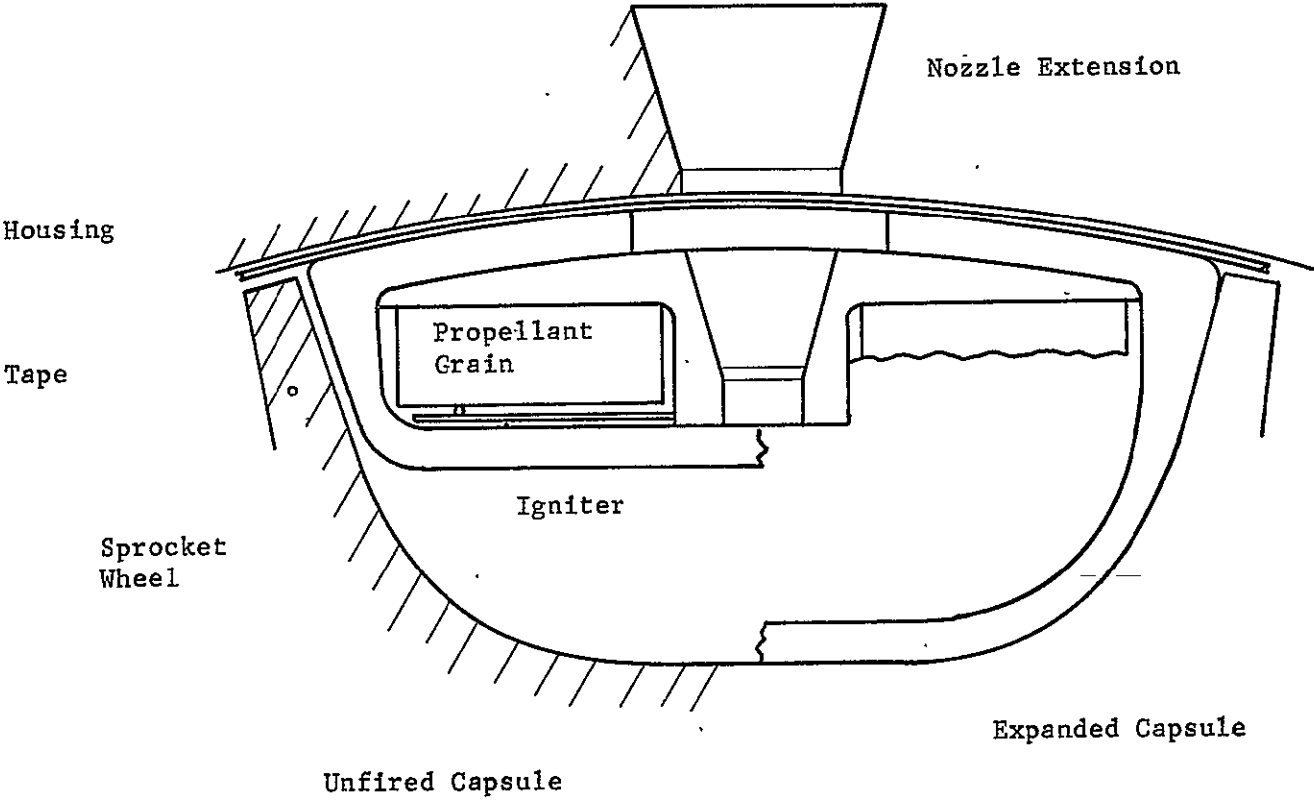


Figure B-11 Dome Cap Pistol Motor

common nozzle extension by expansion of the flexible motor case. After firing the case returns to its original shape and the spent capsule is ejected through an exit chute. In both instances the motor case helps to insulate the pulses from the combustion gases and because the cases are expended after each firing, serves as a means of rejecting residual heat from the combustion process. For application to the descent probe, the E-dome version also has the advantage of allowing a buried installation to protect the pulses from the high temperature atmosphere.

Evaluation - As shown in Figure B-8, the major disadvantage of the "cap pistol" system is its high weight for the range of thrust levels anticipated for the descent probe, 0.01 to 0.1 lb. Because of the inherent requirement for an expendable motor case, ignitor and nozzle for each cap, the motor I_{sp} , Figure B-12, is reduced drastically for small impulse requirements. This factor, in conjunction with the anticipated reduction in performance when operating in a high pressure atmosphere, results in a significant weight penalty for extremely small impulse bit requirements. If, on the other hand, thrust requirements are greater than those indicated in Figure B-8, a cap pistol system will become much more competitive in terms of weight. For example, if the minimum impulse bit were increased from 0.01 to 0.05 lb-sec, the estimated weight of the 1000 lb sec system summarized in table 4 would be reduced from 72.5 lb to approximately 30 lb.

New Technology Requirements - The primary new technology requirement will be the identification, development and demonstration of satisfactory propellant for operation at the required ambient pressures. In addition, some development effort must be anticipated with respect to sealing the exhaust nozzle and adequately rejecting heat from the combustion process.

Reaction Wheel System

The final candidate to be evaluated makes use of a momentum storage device, the reaction wheel, rather than mass expulsion. During the selection of candidate systems, other momentum storage devices such as control moment gyros, were also considered. However, the reaction wheel is simpler and, for the operating range suitable for the descent probe, more efficient.

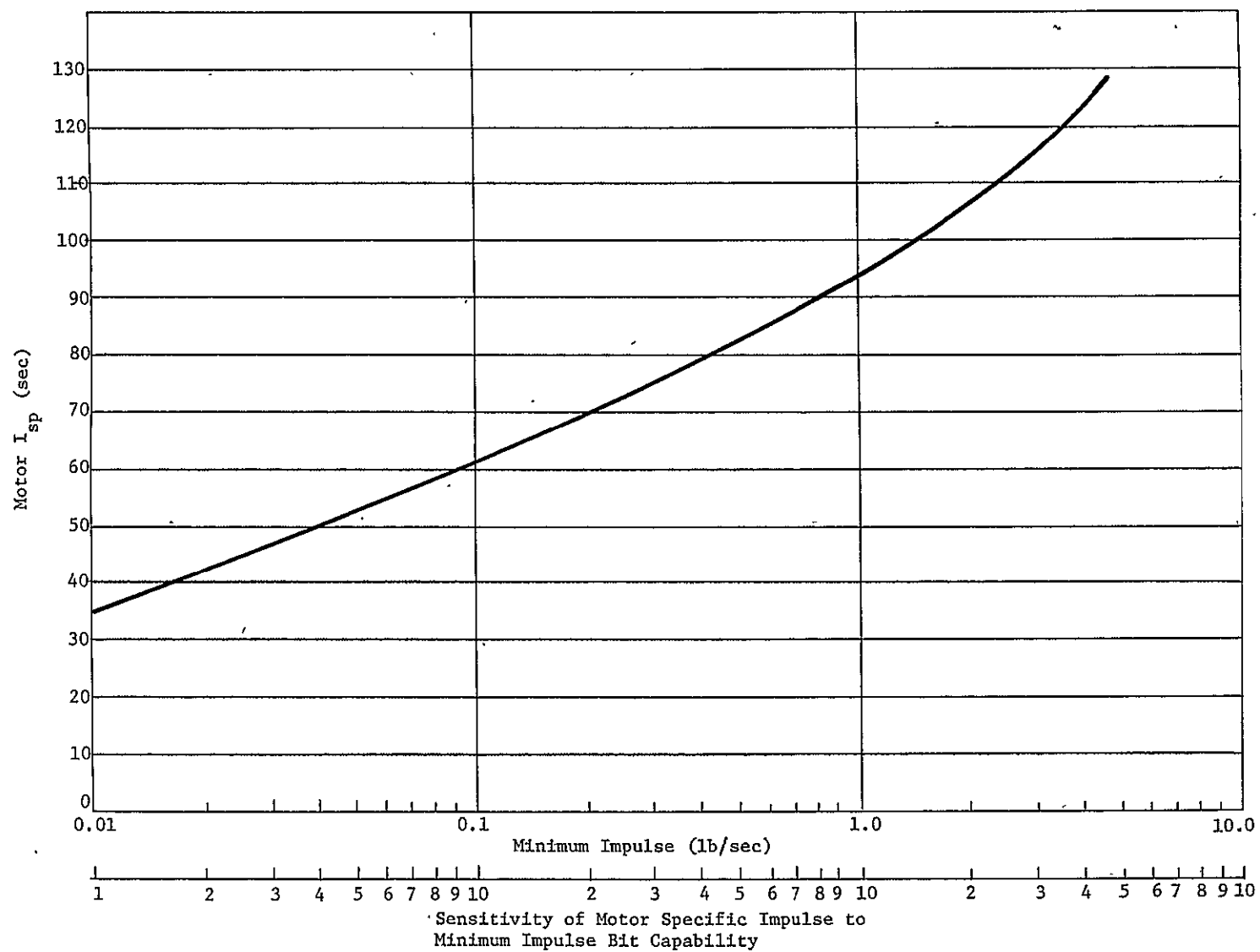


Figure B-12 Sensitivity of Motor Specific Impulse to Minimum Impulse Bit Capability

Description - For this application a conventional three-axis reaction wheel system was considered. As described in "Reaction Wheels for Space Vehicles," reference d, the reaction wheel is essentially a servo motor with a large inertia rotor. On command from the attitude control system, motor torque accelerates or decelerates the rotor, changing its angular momentum. The reaction to this torque is transmitted to the vehicle structure, thus providing the means of attitude control or maneuvering. Each wheel can continue to apply torque in a given direction until a limiting rotor speed is reached. At this speed the wheel is said to be saturated. This point represents the maximum momentum storage capability of the wheel, unless some device such as a reaction jet is provided to unload or desaturate the wheel while still maintaining the desired vehicle attitude.

Evaluation - The weight of a reaction wheel system is primarily established by its momentum storage capability, see Figure B-13. This capability represents the maximum allowable difference between the plus and minus control requirements in each axis rather than the sum of these requirements as is the controlling factor for a propulsion system. Consequently, the weight of propulsion and reaction wheel systems cannot be compared directly without a specified operating duty cycle. Therefore, to provide some basis for comparison, the candidate reaction wheel system was sized to correspond to the minimum weight propulsion system in terms of torque capability and overall system weight. The resultant momentum storage capability was then estimated and is summarized in figure B-13. As can be seen, use of reaction wheels for attitude control of the descent probe would require that the disturbing torques be predominately random in nature. As an illustration the 31 lb system in figure B-13 would only allow what corresponds to 27 seconds of biased engine operation, i.e., $|T_+ - T_-| \leq 27 \text{ sec}$, for each axis. Where T_+ is the total firing time required in the plus direction and T_- is the total firing time required in the minus direction.

In summary, the major limitations associated with a reaction wheel system is its high power to torque requirements, on the order of 2 watts/oz-in, and its high weight for a reasonable momentum storage capability, from 3 to 10 lb/ft lb-sec. Because these systems are so sensitive to torque and momentum storage requirements an accurate prediction of the aerodynamic

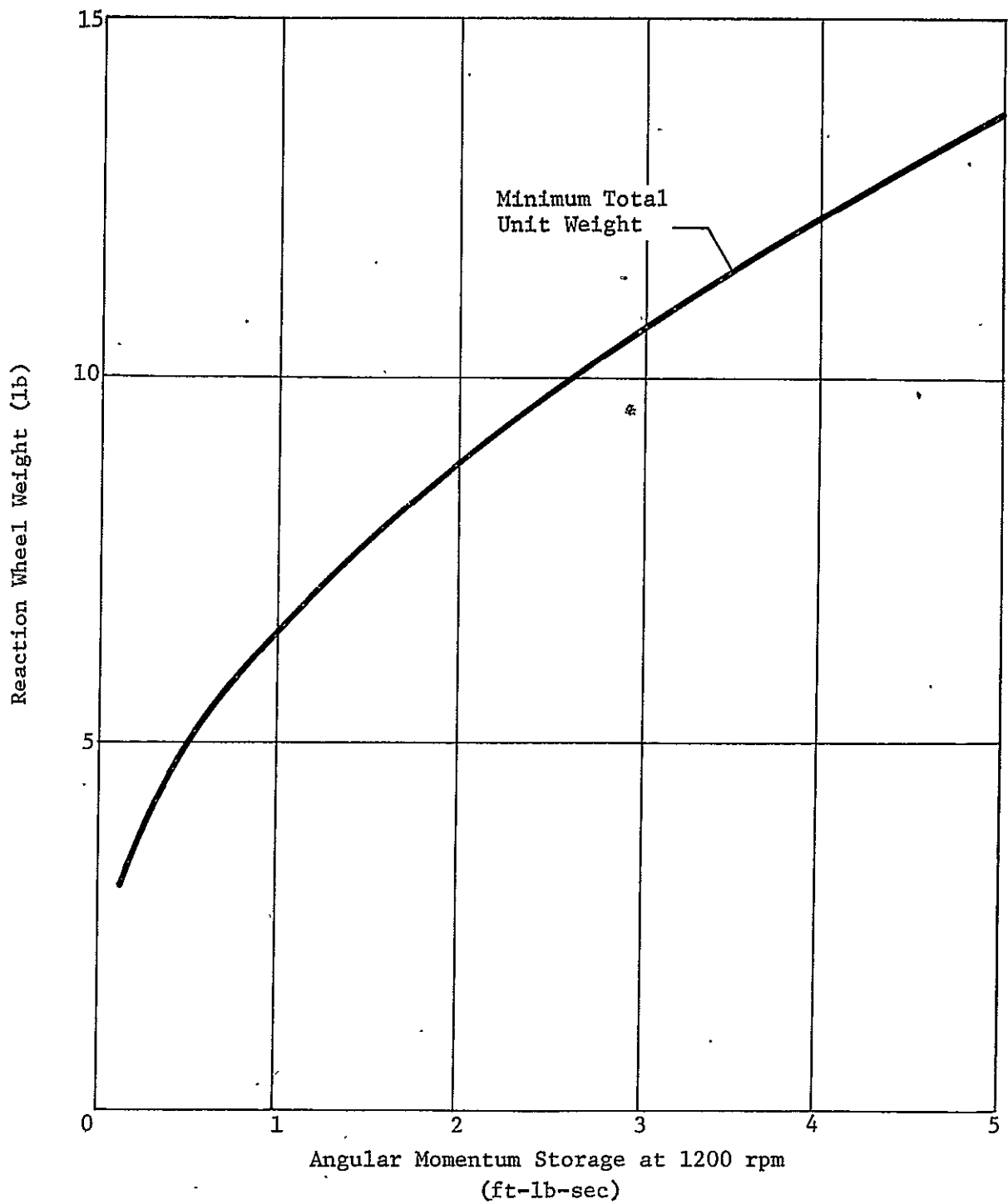


Figure B-13 Reaction Wheel Weight as a Function of Momentum Storage

effects must be available before the feasibility of this approach can be fully evaluated. Also, a continuous controlled roll of the vehicle must be maintained during descent, to minimize biased disturbances caused by atmospheric winds. Nevertheless, if an aerodynamically neutral shape can be maintained and the resultant disturbance torques can be minimized, a straightforward momentum wheel design might be employed. This would allow the entire control system to be buried within the probe body and, by avoiding contact with the extreme environment, allow a completely state-of-the-art approach without any major development of new technology such as must be anticipated if mass expulsion devices are used.

Miscellaneous Systems

Prior to the definition of the above systems and their selection as candidates, the general area of attitude control was reviewed to identify those techniques which could best cope with the extreme environmental conditions that will be encountered by the probe. Those systems that were considered as candidates but rejected are summarized below.

Convention Rocket Engines - As discussed earlier, the conventional mono-propellant and bi-propellant rocket engines were rejected largely because of thermal control problems. Heated fluid systems such as the resistojet and isojet, are also conventional approaches that might be suitable for this range of thrust and total impulse requirements. These systems were also rejected, however, because of their unacceptably high power requirements and/or heat rejection requirements. Use of a stored gas system is also clearly infeasible because of the extremely high operating pressures that would be required.

Atmospherically Heated Liquid - A system was devised to use natural heat from the external environment as the source of energy for vaporizing and ejecting a liquid propellant. Conceptually it consists simply of hot gas valves and nozzles manifolded to a large diameter tube. This tube is warped around the pressure shell at a preselected depth within the external insulation and is used to store a liquid propellant. By properly matching the pressure/temperature of the atmosphere with the vapor pressure of the selected propellant a stable operating pressure is maintained at some level

above atmospheric pressure. Further investigation, however, revealed two apparently unresolvable problems, for a first generation probe. First of all, although a thorough search was not conducted, it does not seem likely that a liquid can be found with a sufficiently high critical pressure so that operation at a 1000 bars will be feasible. For example, the critical pressures of ammonia and water, which are the most frequently considered propellants for vaporizing liquid systems because of their storability and relatively low molecular weights, are approximately 100 and 200 bars respectively. In addition, this approach relies on an accurate knowledge of the atmospheric pressure/temperature correlation, which will probably still be unresolved for a first generation mission.

Hydrogen Burners - A number of schemes were considered for using the atmospheric hydrogen as a fuel. These systems included external burning which was rejected as unsuitable for an aerodynamically neutral shape and several combustion devices that generate and store combustion gases in a manner similar to the candidate plenum systems. These systems were rejected, however, as being more complex than the catalytic gas generators and posing additional heat rejection and combustion control problems.

References -

- a) A. K. Forsythe: Liquid Monopropellant Bootstrap Gas Generators, Rocket Research Corp., Nov. 1966.
- b) Application of the Cap Pistol Concept to the Spin Stabilization Requirements of the TIROS Vehicle, NASA Contract No: NAS5-3586, Curtiss-Wright Corp.
- c) Cap Pistol Propulsion for AMU, CTR-00-304, Wright Aeronautical Division of Curtiss-Wright Corp., Aug. 1965.
- d) Reaction Wheels for Space Vehicles, Engineering Report No. 71-13, Navigation and Control Division of the Bendix Corporation, Nov. 1963.

APPENDIX C
JUPITER ENTRY HEAT SHIELDING REQUIREMENTS

Work by Tauber and Wakefield at NASA-Ames Research Center and Jawarski at Jet Propulsion Laboratory has resulted in heat shield weight Fractions for use in this study. The final version of these weight Fractions as defined in the document "Jupiter Entry Heat-Shielding Requirements - Supplement (June 30, 1970)" by M. E. Tauber and R. M. Wakefield is reproduced for reference in the following pages.

It should be kept in mind that Jupiter heating rates and pressures are for the most part outside our present experience and analytical tools tend to be limited in application and where extrapolations are possible, they tend to be unverifiable by test.

JUPITER ENTRY HEAT-SHIELDING
REQUIREMENTS - SUPPLEMENT (June 30, 1970)

Michael E. Tauber and Roy M. Wakefield
NASA-Ames Research Center, Moffett Field, California

Subsequent to the completion in early April 1970 of the document titled *Jupiter Entry Heat-Shielding Requirements*, new and more sophisticated calculations of shock-layer radiation absorption by ablation product vapors have been made by K. H. Wilson of Lockheed under two contracts, funded by JPL and Ames. These calculations differ from Wilson's previous work (Ref 1) mainly by including the absorption of radiation by molecular species coming from the heat shield. Proper accounting for radiative absorption by these gases at the high pressures experienced during steep entry revealed reductions as great as sevenfold in net radiative flux at the heat shield surface. These effects reduced heat shielding requirements for shallow entry as well, so that recalculation was required. A significant result was that the optimum cone angle increased into the range near 60° as well.

The user of this document should be aware of several major new uncertainties, the effect of which cannot be presently assessed. Among these are:

- 1) Uncertainties in the cross section of some of the molecular species responsible for absorbing significant amounts of radiative energy;
- 2) Wilson's calculations were all made for a stagnation point, yet his results have been applied here to the flanks of a cone;

- 3) No allowances have been made for unpredictable material behavior at high heating rates. For vertical entry, the peak heating rate approaches 100 kw/cm^2 (see Fig. 1a), and may exceed 50 kw/cm^2 for about a second; for shallower entry, 20 kw/cm^2 rates persist typically for several seconds. Maximum heating rates for a range of body weights and sizes are presented in Fig. 2a as a function of entry angle at two points on the body. At the aft end of the cone flank, peak rates range from 10 to 100 kw/cm^2 , while the (ablatant) stagnation point values are about one-half as large. At the high end, these heating rates exceed present experience by at least one order of magnitude.

Complete forebody heat shielding information for 28 direct equatorial entries is presented in Table 1a. Note that a constant cone half-angle of 60° has been used throughout. As shown in Fig. 3a, using a 60° half-angle is close to minimizing the heat shield mass fraction for most entry angles; increasing the cone half-angle significantly beyond 60° would cause a fundamental change in the character of the shock layer from an essentially conical to a blunt body flow field, thus enhancing the radiative heating. The variations of heat shield mass with entry angle are shown in Fig. 4a for three bodies. The fraction ranges from about 0.33 for shallow to about 0.45 for vertical entries. In Fig. 5a, the variation of heat shield fraction with initial ballistic coefficient (before ablation) is shown for one body size. Although the mass fraction of heat shielding decreases with increasing ballistic coefficient, the absolute heat shield weight is

increased since body mass is directly proportional to ballistic coefficient. In Fig. 6a, the effect of varying body size with constant ballistic coefficient is presented and heat shield mass fraction is shown to increase with increasing body size.

The heat shielding requirements for polar-region entry and equatorial entry from a satellite orbit are shown in Fig. 7a for the "nominal" body. For polar entry, the heat shield fraction decreases* from 0.55 for shallow to 0.45 for vertical entry. For the equatorial entry from satellite orbit, the heat shield fraction roughly doubles from shallow (0.19) to steep (.37) entry.

Since up to one-third of the body's initial mass can be ablated, trajectory and time calculations can be strongly affected by ablation. The non-dimensional variation of ablation mass-loss with velocity ratio is presented in Fig. 8a to aid the user with entry-trajectory computations.

The results presented are all for an 85% hydrogen and 15% helium atmosphere (mole fractions). However, preliminary calculations made for direct equatorial entries into a 60% hydrogen and 40% helium atmosphere gave very similar heat shield mass fractions; the radiative blockage results computed by Wilson (for an 85-15 atm) were used.

*In general, for entry bodies experiencing predominantly radiative heating, the total heat input during entry goes up with increasing entry angle (see Table I in original document, for example). However, this is no longer the case if massive absorption of shock layer radiation by ablation product vapors occurs. For posigrade equatorial region entries, however, the total heat input goes up with increasing entry angle, because the entry velocity with respect to the atmosphere increases with increasing entry angle.

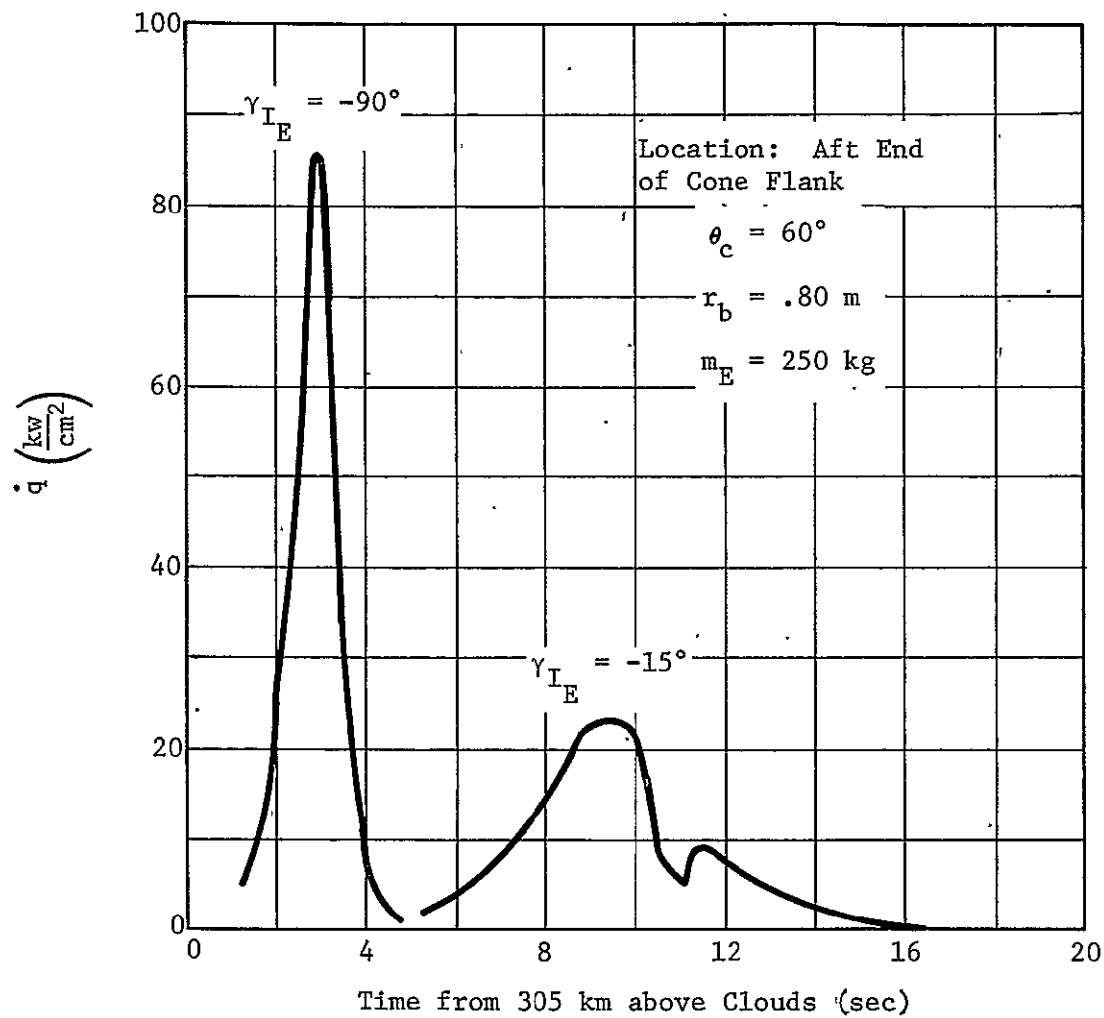


Figure 1a Heating Pulses for Steep and Shallow Entry Angles

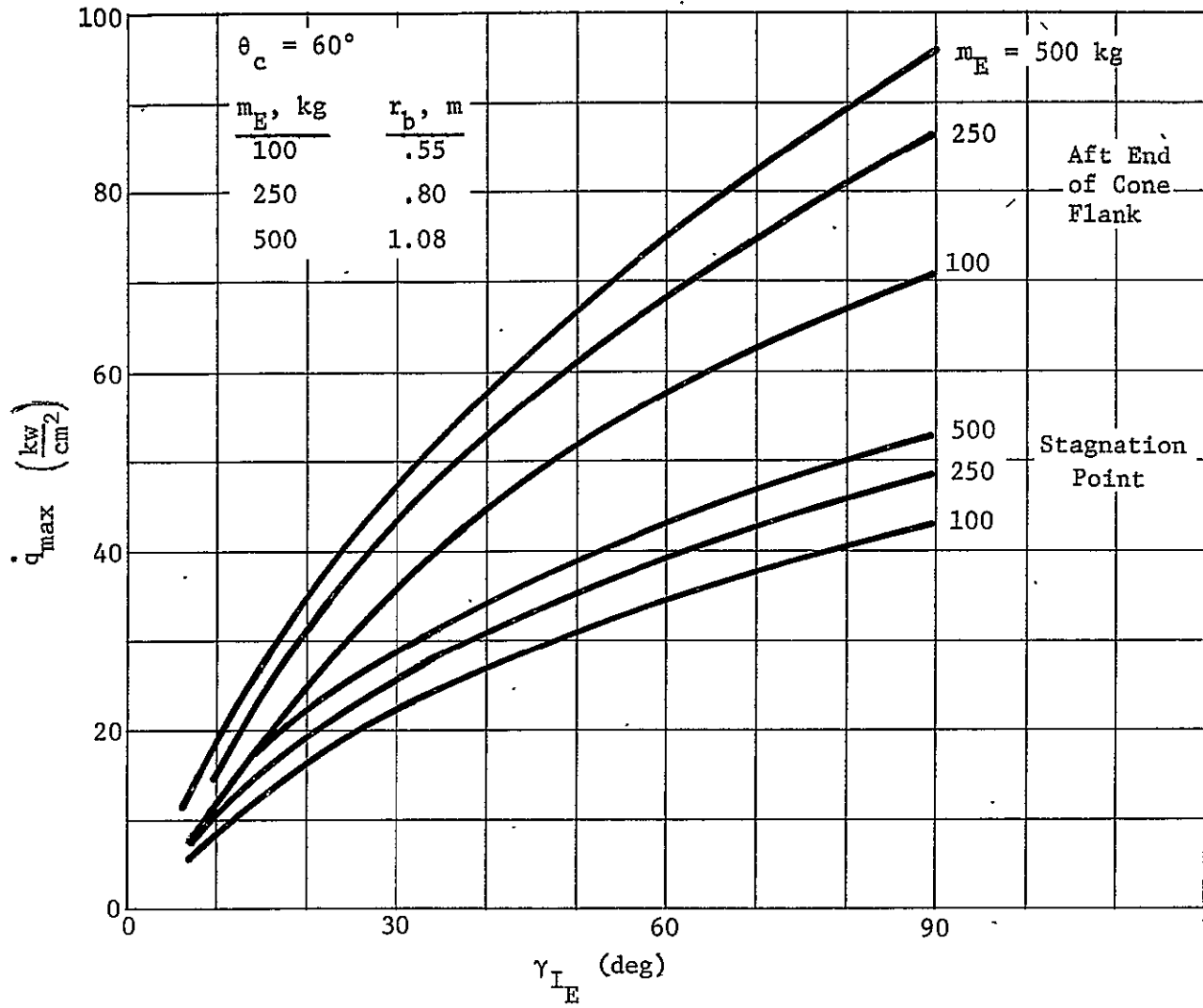


Figure 2a Maximum Heating Rates

Table

	1	2	3	4	5	6	7	8	9	10	11	12	13	14
	v_{r_E}	γ_{I_E}	m_E	r_b	$\frac{m_E}{C_D A}$	θ_c	δ_0 Δ_0	δ_1 Δ_1	δ_2 Δ_2	δ_3 Δ_3	$\frac{m_H}{A_c}$	$\frac{\Delta m_H}{m_E}$ $\frac{m_H}{m_E}$		
1	49.1	- 6.3	100	.55	70.3	60.	1.17	.880	1.04	1.22		.206		
2							4.17	3.38	3.54	3.72	27.3	.327		
3			129		83.		1.48	1.13	1.35	1.62		.208		
4							4.48	3.63	3.85	4.12	32.5	.302		
5			500	1.08	91.1		1.96	1.30	1.67	2.30		.270		
6							4.96	3.80	4.17	4.80	43.0	.363		
7			455		83.		1.80	1.18	1.50	2.06		.265		
8							4.80	3.68	4.00	4.56	39.5	.368		
9	49.8	-15.	100	.55	70.3		1.11	.883	1.14	1.57		.242		
10							4.11	3.38	3.64	4.07	30.1	.361		
11			129		83.		1.40	1.11	1.57	2.02		.247		
12							4.40	3.61	4.07	4.52	36.7	.341		
13			500	1.08	91.1		1.72	1.50	2.03	2.34		.299		
14							4.72	4.00	4.53	4.84	46.3	.392		
15			455		83.		1.59	1.32	1.86	2.14		.300		
16							4.59	3.82	4.36	4.64	43.2	.403		
17	52.0	-30.	100	.55	70.3		1.07	.989	1.45	1.66		.276		
18							4.07	3.49	3.95	4.16	33.1	.397		
19			129		83.		1.32	1.34	1.82	2.09		.270		
20							4.32	3.84	4.32	4.59	39.2	.364		
21			500	1.08	91.1		1.57	1.78	2.10	2.27		.306		
22							4.57	4.28	4.60	4.77	47.2	.399		
23			455		83.		1.46	1.64	1.95	2.11		.311		
24							4.46	4.14	4.45	4.61	44.5	.414		
25	60.3	-90.	100	.55	70.3		1.20	1.46	1.76	1.91		.331		
26							4.20	3.96	4.26	4.41	37.7	.452		
27			129		83.		1.49	1.81	2.14	2.29		.312		
28							4.49	4.31	4.64	4.79	43.7	.406		
29			500	1.08	91.1		1.67	2.11	2.30	2.50		.340		
30							4.67	4.61	4.80	5.00	51.3	.433		

Table 1a Direct Equatorial Entry (concluded)

	1	2	3	4	5	6	7	8	9	10	11	12	13	14
	v_{r_E}	γ_{T_E}	m_E	r_b	$\frac{m_E}{C_D A}$	θ_c	δ_0 Δ_0	δ_1 Δ_1	δ_2 Δ_2	δ_3 Δ_3	$\frac{m_H}{A_c}$	$\frac{\Delta m_H}{m_E}$ $\frac{m_H}{m_E}$		
1	60.3	-90.	455.	1.08	455.	60.	1.56	1.97	2.15	2.34		.348		
2							4.56	4.47	4.65	4.84	48.5	.451		
3	49.1	- 6.3	250.	.80	83.		1.57	1.11	1.36	1.73		.233		
4							4.57	3.61	3.86	4.23	36.1	.335		
5			151.		50.		1.11	.669	.802	.955		.224		
6							4.11	3.17	3.30	3.46	25.6	.393		
7			452.		150.		2.68	1.97	2.68	3.57		.260		
8							5.68	4.47	5.18	6.07	61.5	.316		
9	49.8	-15.	250.		83.		1.43	1.14	1.72	2.01		.277		
10							4.43	3.64	4.22	4.51	40.9	.379		
11			151.		50.		.967	.698	.911	1.23		.266		
12							3.97	3.20	3.41	3.73	28.3	.435		
13			452.		150.		2.29	2.45	3.01	3.41		.272		
14							5.29	4.95	5.51	5.91	63.9	.328		
15	52.0	-30.	250.		83.		1.33	1.51	1.82	2.04		.296		
16							4.33	4.01	4.32	4.54	42.9	.398		
17			151.		50.		.950	.814	1.16	1.34		.310		
18							3.95	3.31	3.66	3.84	31.2	.479		
19			452.		150.		2.01	2.59	2.98	3.19		.265		
20							5.01	5.09	5.48	5.69	62.5	.321		
21	60.3	-90.	250.		83.		1.45	1.82	2.08	2.25		.325		
22							4.45	4.32	4.58	4.75	46.9	.437		
23			151.		50.		1.06	1.21	1.44	1.56		.378		
24							4.06	3.71	3.94	4.06	35.6	.547		
25			452.		150.		2.15	2.98	3.21	3.48		.289		
26							5.15	5.48	5.71	5.98	67.2	.345		
27														
28														
29														
30														

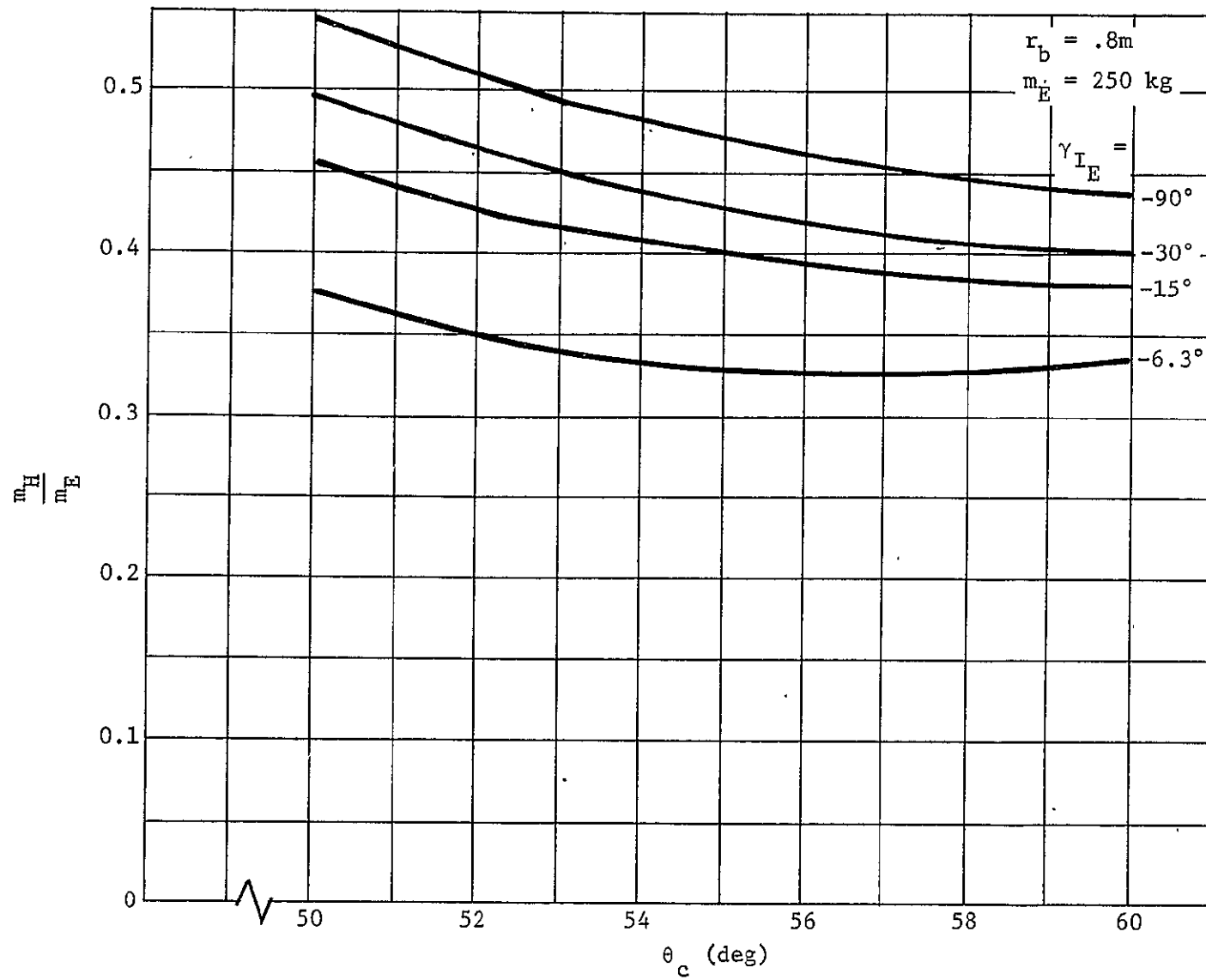


Figure 3a Variation of Heat Shield Mass-Fraction with Cone Half-Angle

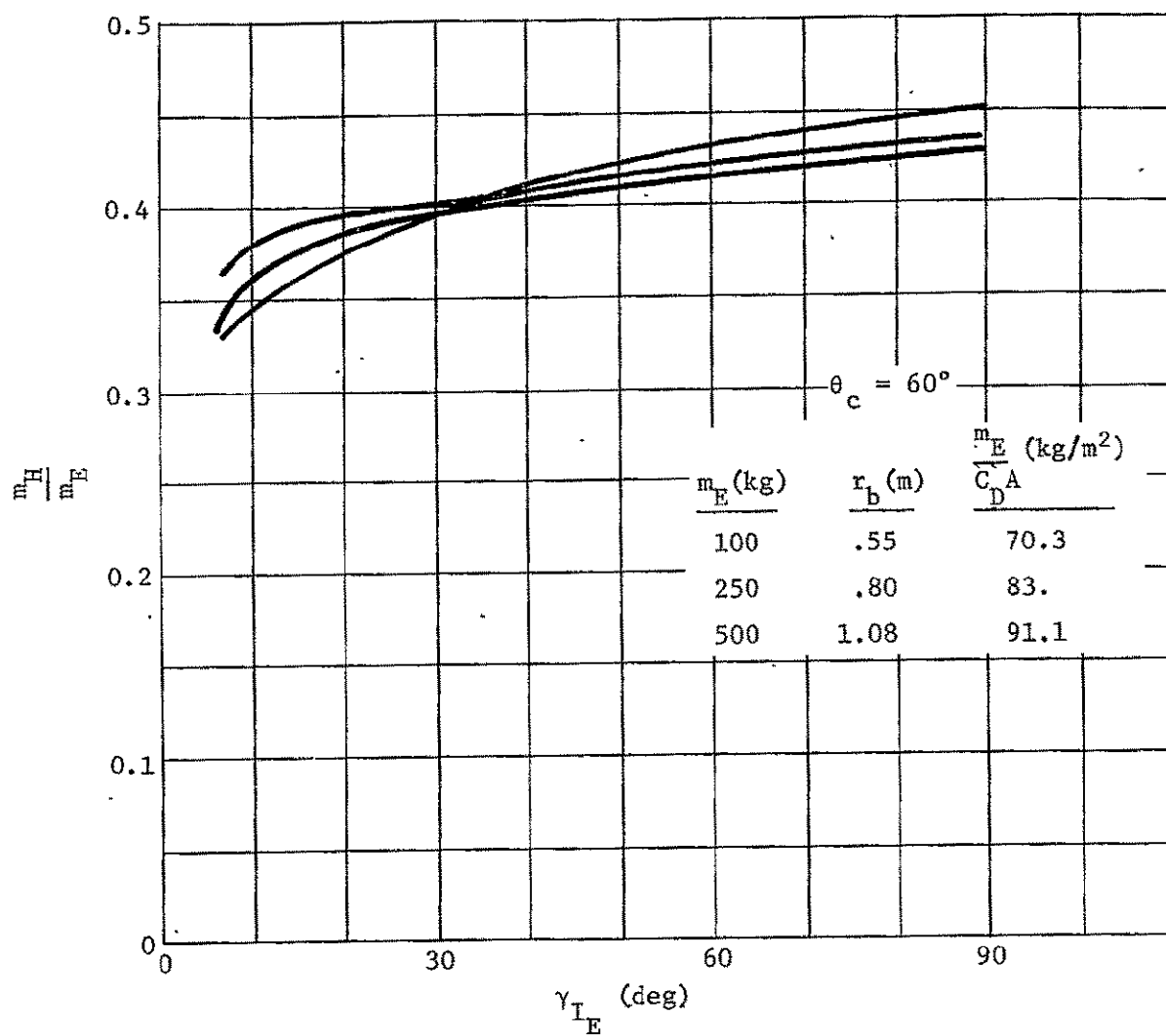


Figure 4a Heat Shield Mass-Fractions

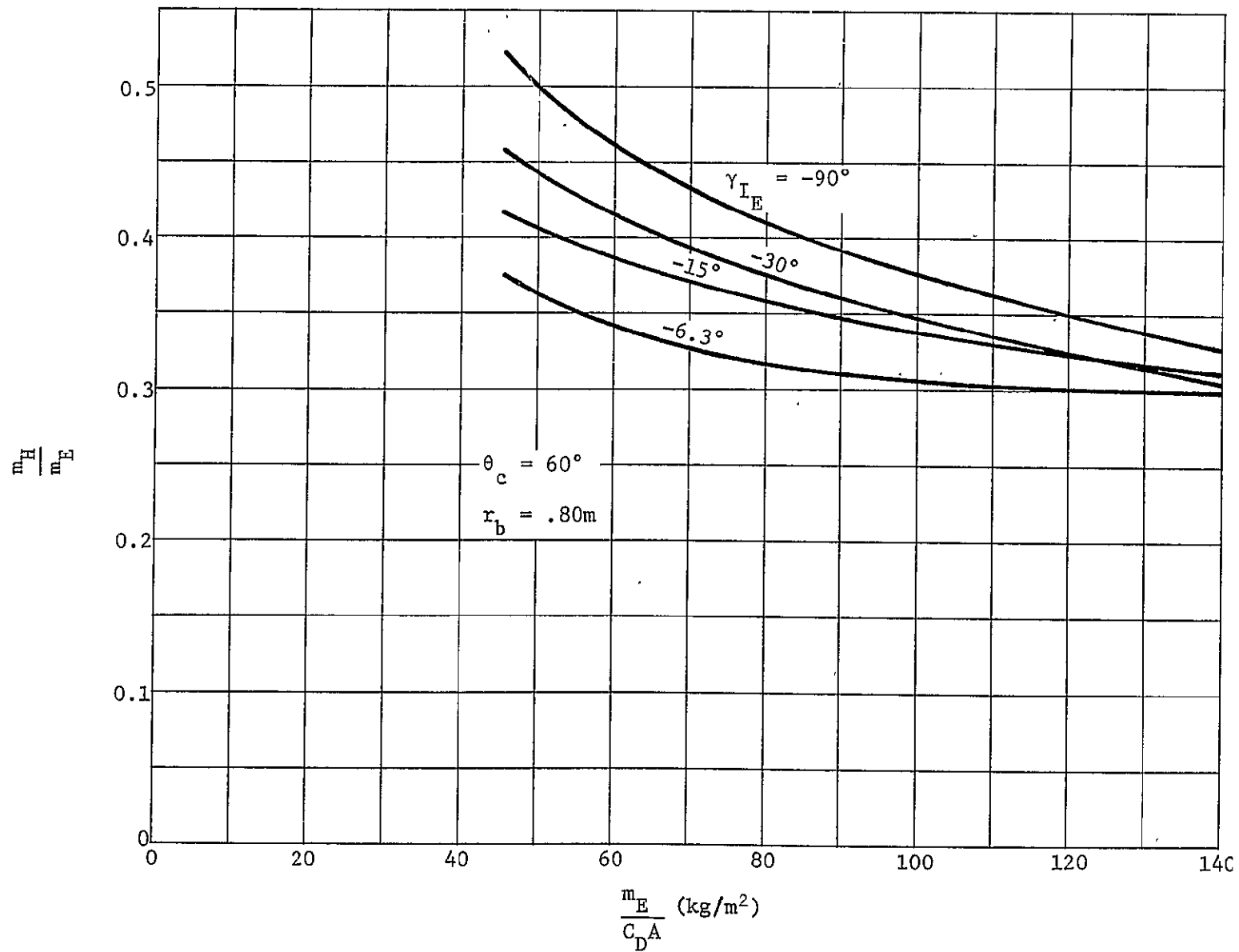


Figure 5a Variation of Heat Shield Mass-Fraction with Ballistic Coefficient

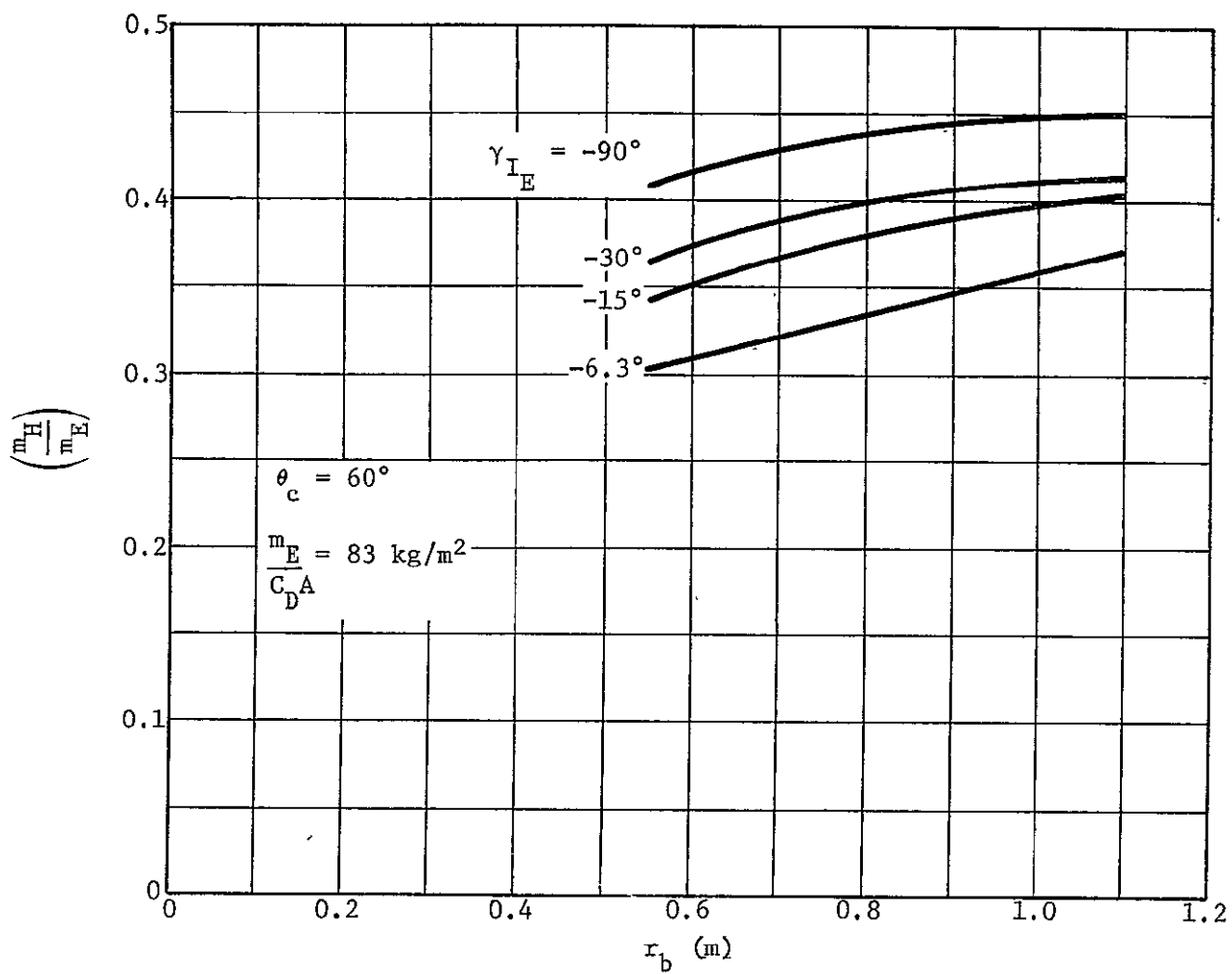


Figure 6a Variation of Heat Shield Mass-Fraction with Body Size

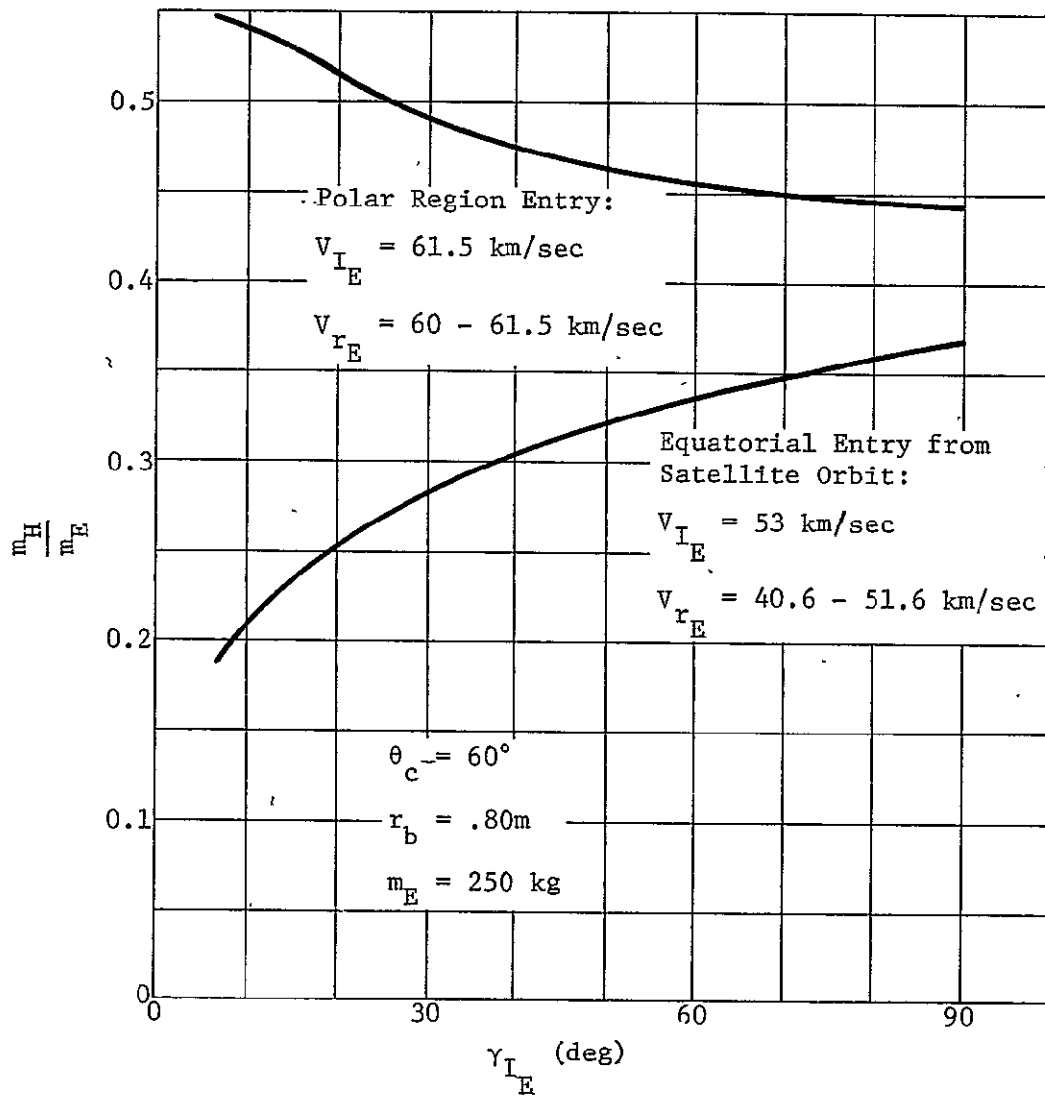


Figure 7a Heat Shield Mass-Fractions for Two Types of Entries

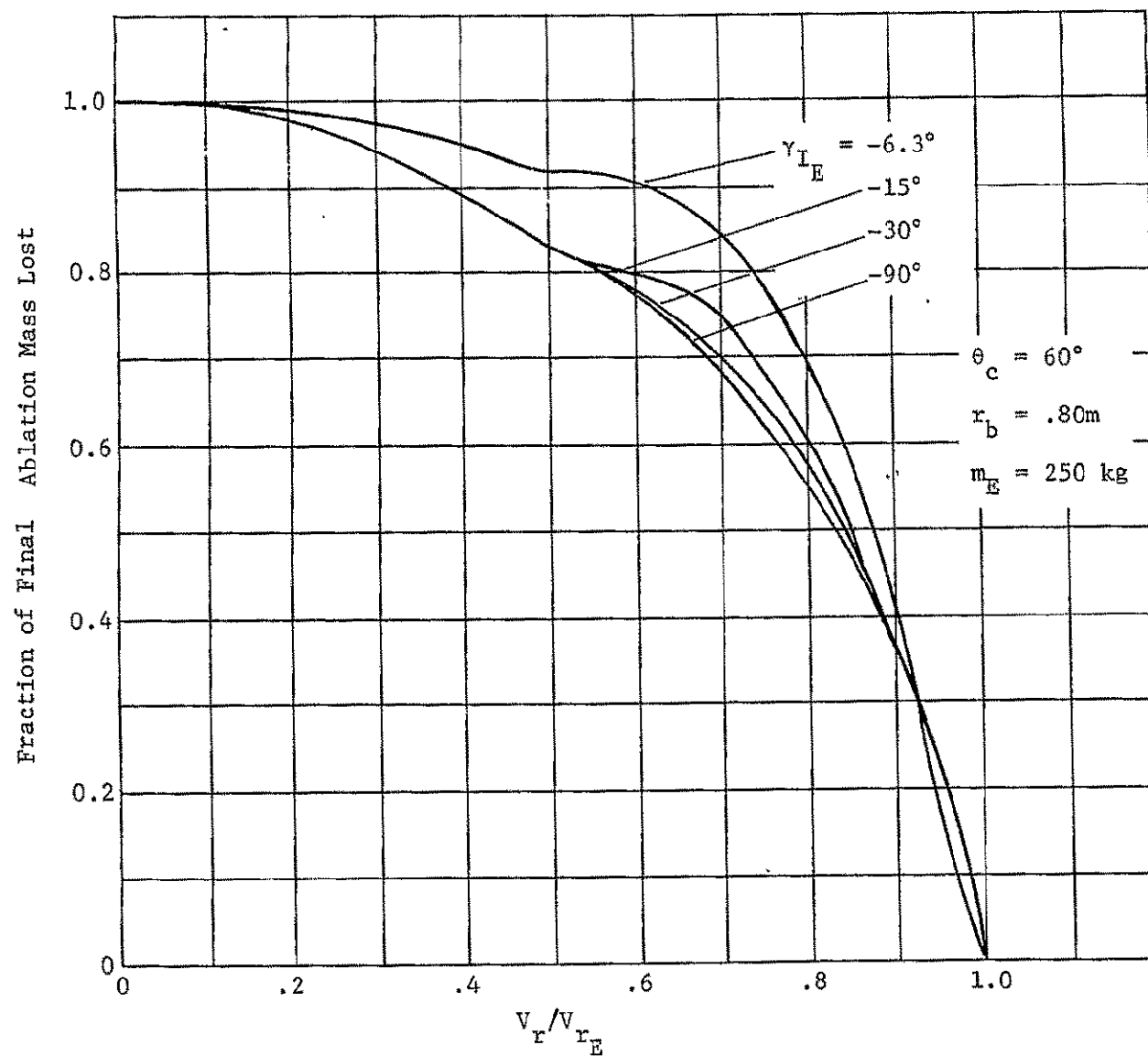


Figure 8a Variation of Mass-Loss with Velocity

APPENDIX D

TECHNICAL MEMORANDUMS PREPARED BY DR. J. F. VANDREY IN
SUPPORT OF THE STUDY ON VARIOUS ASPECTS OF THE JUPITER
ENVIRONMENT.

(These memorandums are in addition to those
referenced in, and included with Section IVK
of this volume).

Low-Turbulence Regions in the Jovian Equatorial Atmosphere

Dose Rates in Jupiter's Van Allen Belts

Desirability of Studies on Real Gas Effects in the Deeper
Parts of the Jovian Atmosphere.

General Comments on the Possibilities to Predict Turbulence
Fading in the Deeper Parts of the Jovian Atmosphere.

Comments on the Thermal Radiation Environment and on Radia-
tion Experiments in the Deepest Accessible Regions of
the Jupiter Atmosphere.

Magnetic Cleanliness Requirements.

1 July 1970

TECHNICAL MEMORANDUM

Low-Turbulence Regions in the
Jovian Equatorial Atmosphere

J. F. Vandrey

Abstract

It is shown from the results of Jupiter observations between 1897 and 1966, from those of existing studies of the cloud dynamics in the Jovian Equatorial Jet, and from general principles of atmospheric dynamics, that the turbulence levels are probably rather low and may even be negligible, in the two regions around $\pm 5^\circ$ of latitude, i.e. midway between the equator and the North or South Equatorial Belts, respectively.

If an entry probe is aimed into the vicinity of either one of these latitudes, it can perform all experiments which are needed to accomplish its scientific mission. It can also obtain information on perhaps occurring thunderstorm-like phenomena in the rising air currents along the equator, by listening for the resulting low-frequency electromagnetic noise.

I. Introduction

One of the many things one has to know for the design of an entry probe into the Jovian atmosphere is the level of turbulence it is likely to encounter when making its measurements above, inside, and below the visible "surface" of the planet.

To be quite honest, this would require a much more detailed knowledge of the dynamics and thermodynamics of the Jovian atmosphere than we can have at the present time. Nevertheless, it seems to the writer that we can use what little we do know about the cloud dynamics in the equatorial regions of the planet, and what we can infer about the processes going on below the visible cloud top level with a reasonable degree of confidence, to identify those regions in the equatorial zone of the planet where the atmospheric turbulence is likely to be a minimum.

The purpose of the present memorandum is to state the case for the writer's contention that we can expect very little atmospheric turbulence in the two regions midway between the equator and the dark North and South Equatorial Belts, i.e. at typically $\pm 5^\circ$ of latitude. It will also be shown that either one of these latitudes is suitable for the scientific mission of the probe.

II. Results from Jupiter Observations

Seen or photographed through our best telescopes, the planet shows on its somewhat flattened disk the so-called cloud belts as its most prominent markings. They appear as dark regular lines parallel to the equator in smaller instruments, but they show a considerable fine structure with brighter and fainter portions, and with knots and divisions in larger instruments. (See e.g. [1], tables XII, XIII). These markings are permanent enough to permit a very exact determination of the rotational period of the planet, and one obtains the result that the cloud tops in the bright equatorial zone rotate appreciably faster than those at higher latitudes.

This so-called "Equatorial Jet" between the very conspicuous North Equatorial Belt at typically $+10^\circ$ latitude and the often less conspicuous and sometimes doubled South Equatorial Belt near -10° has a relative velocity with respect to the remainder of the visible surface of around 100 m sec^{-1} which appears to be rather uniform and changes over a relatively small distance along the two belts over into the slower rotation of the higher latitudes ([2] and [3]).

A far less conspicuous feature of the Equatorial Jet should be mentioned: Many of the better photographs of the planet show a very faint somewhat darker line along the equator.

The general impression one gets from looking at the great number of available excellent photographs of Jupiter's cloud cover is that of a very active atmosphere, with strong prevailing winds in the equatorial zone, and with considerable turbulence on a scale which can be resolved with our telescopes.

This resolution is, of course, rather low in comparison with the scale of turbulence which could be of concern for the design and operation of an entry probe. Our largest telescope, the 200 inch Hale reflector, would give us a linear resolution of a little less than 200 km at opposition when the distance between the Earth and Jupiter is at its minimum of 4.2 AU, if it were diffraction-limited which it is not quite. A more realistic assessment is that most observations of the planet do not have

an actual resolution (including "seeing conditions") which is much better than about 400 to 500 km, and that the smallest features in which we can discern any details have dimensions of 2000 to 3000 km.

III. Analyses of Jupiter Observations and Theoretical Studies of Atmospheric Dynamics.

Using the detailed account of the observations of cloud motions between 1908 and 1958 given in B.M. Peek's book "The Planet Jupiter", A. Ingersoll and J. Cuzzi analysed the observed zonal motion in the equatorial regions under the assumption of a geostrophic balance and a systematic temperature difference between the light and the dark bands [2]. They obtained an excellent agreement between the observed velocities and those calculated from the thermal wind relation, for the case that the light bands are warmer than the dark bands at the same pressure level, and that the bulk of the planet rotates with a uniform angular velocity not very different from that of the higher latitudes. The higher velocity of the bright equatorial zone is then due to a very broad easterly jet stream of unknown, but probably relatively modest depth.

A comprehensive summary of all available visual data on "spot motions" in the Jovian atmosphere between 1897 and 1966 was recently compiled by C. Chapman [3]. It appears from these data that the average easterly velocities of the cloud top region in the equatorial zone has been remarkably uniform over this long period, in the northern half of the zone even more so than in its southern half. The transition from the "Equatorial Jet" to the more slowly rotating clouds in the South and North Equatorial Belts is remarkably sharp, at most equal to the resolution of Chapman's spot motion statistics (around 2° of latitude), and probably even less.

In principle, these transition regions at around $\pm 10^\circ$ latitude would have to be considered as regions of "strong" horizontal wind-shear where one would then also have to expect some turbulence. This may in fact be so. A degree on Jupiter corresponds, however, to a distance of around 1200 km, and the average wind shear for a velocity difference of 100 m sec^{-1} over 10^3 km is only $.1 \text{ m sec}^{-1}$ per kilometer which is not very much. Nevertheless, one would probably prefer to avoid these regions, since the actual local conditions in them may well be somewhat different from the average of rather low resolution observations ($\sim 400 \text{ km}$) over many years.

IV. Tentative Results from Theoretical Studies

The rather extensive theoretical literature on the internal dynamics of Jupiter, and of the Jovian planets in general, was recently reviewed in outline by R. Hide [4]. Most of these studies are based on the governing equations for the flow of an electrically conducting fluid which rotates with constant angular velocity with respect to an inertial frame in the presence of a magnetic field ([4], eqs. 2.1 to 2.8)

These equations permit the use of a very general equation of state

$$\rho = \rho(p, T, \text{chemical composition}) \quad (1)$$

and they allow also for the existence of an internal distributed heat source due to, e.g., a slow gravitational contraction of the planet. They do, however, not include radiative energy transport from the interior to the surface which is likely to be important in some parts of the deeper atmosphere. This omission is, of course, due to the already great complexity of the equations.

The only feasible way to arrive at some practically important conclusions from these equations is then to re-write them in a non-dimensional form with an, unfortunately, rather considerable number of non-dimensional parameters. By means of a necessarily very crude scale analysis, one can then assess the relative importance of the various parameters for a particular problem of the internal dynamics of the planet, and simplify the equations accordingly so that they become more tractable for numerical work.

Of particular interest for us here is the tentative identification of the faster rotating cloud zone near the equator with a "thermal wind" not unlike the Cromwell current in our ocean and the Berson current in our lower stratosphere:

"If the reasonable assumption is made that the essential vorticity balance is between horizontal advection of relative vorticity and effects due to the variation of Coriolis parameter with latitude, then $(UR/2\Omega)^{\frac{1}{2}}$ is an approximate expression for the latitudinal width of a jet of typical flow speed U relative to a rotating planet of radius R ; the expression agrees satisfactorily with observations.: ([4], p. 845).

If this identification of the Jovian Equatorial Jet with a phenomenon not unlike a jet stream in our atmosphere is correct, it would imply a relatively small depth of the jet. Certainly more than the few kilometers which are typical for the jet streams in our atmosphere (see e.g. [5], Figure 8/14 on p. 453, reproduced below as Figure 3 of the present report), but not going into the hundreds or thousands of kilometers. We have to assume that the bulk of the planet's mass is rotating with, essentially, the "radio rotation period" of $9^{\text{h}} 55^{\text{m}} 30^{\text{s}}$ even in the equatorial regions. It implies also that there is a systematic temperature difference between the equatorial zone and the adjacent belts; the faster "rotating" equatorial zone should be warmer than the belts ([3], p. 981) at the same pressure levels.

P. Stone has suggested differential solar heating as the cause of this temperature difference ([6], p. 991). It seems to the writer that this is probably not the only cause, but that convective heating from below may be equally, if not more important. The infrared radiation balance of the planet indicates the existence of an internal heat source which, according to the latest estimates of Trafton and Wildey [7], may have an output of between two and three times the energy the planet receives from the Sun.

This internal heat flow is presumably rather constant over the entire planet at a great depth below the visible surface. Nearer to the surface, one will, however, expect a convective heat flow in a meridional pattern not unlike a Hadley Cell in our atmosphere (see e.g. [8], p. 40). This would then mean that there will be a rising air current along the equator, coming up from a very great depth, and a downward air current along the two dark belts which returns the air to the interior where its heat loss by, ultimately, radiation into space is replenished.

If this plausible interpretation is correct - and the faint dark line often observed along the Jovian equator seems to indicate that something is happening there below the visible cloud top level -, one would also have to expect a condensation of water vapor to clouds to take place in this rising air current at the appropriate temperature level where the water vapor becomes saturated. At this level, the "dry adiabatic"

lapse rate would change over to the smaller "saturation adiabatic rate", because of the liberation of latent heat during the condensation process. This increases then the buoyancy of the rising air, and it is well known that such a situation can lead to instabilities, and consequently to atmospheric turbulence.

It is unlikely that these condensation effects can cause a turbulence in any way as severe as they can in terrestrial cumulo-nimbus, i.e. thunderstorm clouds. The about ten times greater specific heat of the Jovian atmosphere makes these effects far less important (see e.g. [9], p. 11). Considering the about $2\frac{1}{2}$ times greater Jovian gravity, one finds that the buoyancy per unit mass which is due to condensation in a rising air current is only one-fourth of what it would be here under similar circumstances. Nevertheless, it may be wise to avoid the immediate vicinity of the equator as the target area for the first entry probe into the Jovian atmosphere.

V. Analysis of Atmospheric Stability at Intermediate Latitudes in the Equatorial Jet ($\pm 5^\circ$).

We consider now the stability of the Jovian atmosphere in the vicinity of the latitudes $\pm 5^\circ$, midway between the equator and the poleward limits of the equatorial jet.

Of the various causes of turbulence in our atmosphere, the aerodynamic and thermodynamic interaction with the surface of the land and of the ocean is absent everywhere on Jupiter. If there is a phase change in the interior of the planet (metallic hydrogen has been suggested), it would be at such a great depth that we could not care less about it for our purpose. At the particular latitudes we are considering, we have also no large-scale rising air currents which could cause turbulence by condensation of water vapor, and we are far away from the two boundaries of the equatorial jet where turbulence could be generated by the horizontal wind shear.

We have, however, to expect that there are rather appreciable vertical velocity gradients both below and above the jet, and we have to investigate, whether or not they can be causes for significant atmospheric turbulence under the circumstances. In particular, we would here

think of phenomena not unlike the so-called Clear Air Turbulence in our atmosphere which is known to occur sometimes in the vicinity of jet streams in the general altitude range of the tropopause.

At the present time, we are still far from a complete understanding of the CAT phenomenon. The current state of our knowledge on this subject was recently summarized by J. Dutton and H. Panofsky in a survey article in Science [9]. It appears from this paper that the occurrence of severe CAT is most likely in those, usually quite limited, regions of our atmosphere not too far from the tropopause where there are at the same time strong vertical velocity gradients and strong horizontal temperature gradients.

A typical example of such a situation is given in [9], Figure 1, reproduced below as Figure 1 of the present T.M. It appears from this figure that the occurrence of CAT is limited to a very small altitude range, from about 475 down to 350 mb of pressure, or from about 6 to 8 km of altitude above sea level. The ultimate cause for the occurrence of turbulence was here an "internal front" across which there were strong horizontal temperature gradients. Needless to say, the occurrence of such a front in the deep Jovian atmosphere with its predominantly zonal winds is most unlikely.

Figure 2, reproduced from [11], p. 158, gives a schematic cross-section of an advancing Polar Front with the typical difference in the altitude of the tropopause on either side which causes significant horizontal temperature gradients, accompanied by vertical velocity gradients on the north side of a jet stream which is blowing along the front. We may expect the occurrence of CAT on the north side of the jet core, but not elsewhere. Data from measurements of a jet stream cross-section are shown in Figure 3, reproduced from [5], p. 453. They show again the typical drop in the altitude of the tropopause across the jet stream which causes the strong horizontal temperature gradients.

By the way, it appears from the existing statistical evidence that the two conditions of strong vertical velocity and horizontal temperature gradients are not independent of each other. In the free atmosphere, the wind tends to change in the vertical most rapidly when there are strong horizontal temperature changes ([10], p. 939).

To get an opinion on the magnitude of the horizontal temperature gradients which are strong enough to be associated with CAT in our atmosphere, we can use the discussion of the results from 145 research flights with DC-8 Eastern Airlines jet planes in a survey paper by M. London [12] in which atmospheric temperature variations and turbulence were correlated. The highest correlation occurred when a rate of change of $\pm 1^\circ\text{C}$ or more per minute of flight time and a total change of at least 1°C were established as the threshold criteria. We find then from the typical jet plane velocity of 550 mph that this corresponds to a horizontal temperature change of 1°C for about 15 km, or to around $0.07^\circ\text{K km}^{-1}$.

In the latitude regions of the Jovian atmosphere we are considering, we have no reasons to suspect the occurrence of horizontal temperature gradients which could even come close to 70°K for 1000 km, or to around 85°K per degree of Jovian latitude. All existing measurements (with admittedly rather low resolution) are consistent with the assumption that the temperatures at any given pressure level are rather uniform over the observable cloud "surface" of the equatorial jet. They may even be not so very different at the same pressure level in the North and South Equatorial Belts. Some recent measurements with the 200 in. Mt. Palomar refractor gave the result that the temperatures in these regions could be as high as 310°K [13], around 150°K more than for the cloud tops of the equatorial jet. This temperature is, however, most likely to be that from a much deeper part of the atmosphere which becomes visible in the two dark belts because of the absence of the thin ammonia clouds which form the visible "surface" of the bright zones of the planet. Be this, however, as it may. We can still be quite confident that the horizontal temperature gradients at the two latitudes of $\pm 5^\circ$ will be very low, and that the conditions for CAT-like turbulence are not satisfied at these latitudes, if the stability of the Jovian atmosphere against the development of turbulence is not too different from that in our atmosphere.

The controlling non-dimensional parameter for the generation of turbulence by vertical wind shear in a gravitationally stratified atmosphere is now the Richardson number which can be written in the form

$$\text{Ri} = \frac{g}{T \left(\frac{dU}{dz} \right)^2} \left[\frac{dT}{dz} - \left(\frac{dT}{dz} \right)_{\text{adiabatic}} \right] \quad (2)$$

(see e.g. [5], p. 450)

Using then G. I. Taylor's relation

$$q = - C_p A_q \left[\frac{dT}{dz} - \left(\frac{dT}{dz} \right)_{ad.} \right] \quad (3)$$

for the heat flow through the atmosphere ([5], ibid.), and expressing the "eddy heat exchange quantity" A_q by the "eddy viscosity"

$$A_q = m A_t, \quad 1 \leq m \leq 2 \quad (4)$$

([5], p. 265), and

$$A_t = \frac{t}{\frac{dU}{dz}} = \frac{\rho \ell^2}{\left| \frac{dU}{dz} \right|} \quad (5)$$

in turn by L. Prandtl's relation with the "mixing length" ℓ ([5], p. 185), we obtain for the Richardson number the new form

$$Ri = - \frac{qg}{m C_p \rho \ell^2 T \left| \frac{dU}{dz} \right|^3} \quad (6)$$

or, finally, with respect to the equation of state

$$p = \frac{\gamma-1}{\gamma} C_p \rho T, \quad (7)$$

$$Ri = - \frac{\gamma}{m(\gamma-1)} \cdot \frac{qg}{p \ell^2 \left| \frac{dU}{dz} \right|^3} \quad (8)$$

We compare now two situations of possible turbulence with the same Richardson number on Jupiter (subscript 1) and in our atmosphere (subscript 2). The two specific heat ratios are about the same ([9], pp. 2 and 3), and we can also assume that the two empirical constants m_1 and m_2 will not be very different. Moreover, we are here mainly concerned with the general altitude range of the tropopause where the pressures in the two atmospheres are also not very different ($p_1 \sim .21$ atm in the nominal Jovian atmosphere, vs $p_2 \sim .27$ atm on Earth). For the very rough comparison of the two cases which is forced upon us by the lack of detailed knowledge of the Jovian equatorial jet, it will then be good enough to write the condition of equal Richardson numbers, i.e. equal stability against turbulence, in the form

$$\frac{q_1 g_1}{\ell_1^2 \left| \frac{dU_1}{dz} \right|^3} \approx \frac{q_2 g_2}{\ell_2^2 \left| \frac{dU_2}{dz} \right|^3} \quad (9)$$

or

$$\frac{dU_1/dz}{dU_2/dz} \approx \left(\frac{q_1}{q_2} \cdot \frac{g_1}{g_2} \cdot \frac{\ell_2^2}{\ell_1^2} \right)^{\frac{1}{3}} \quad (10)$$

On the right-hand side, we can evaluate the first two terms, since we know the ratio of the gravitational accelerations, $g_1/g_2 = 2.5$, and can find at least representative values for the convective heat flows through the two atmospheres. This leads to the rough estimate

$$\left(\frac{q_1 g_1}{q_2 g_2} \right)^{\frac{1}{3}} \sim \frac{1}{2} \quad (11)$$

Concerning the ratio of the two mixing lengths, we can use Prandtl's idea of assuming ℓ_2 as of the order of the thickness of a typical jet stream on Earth (a few km) as a guide. The mixing length ℓ_1 in the Jovian equatorial jet would then be of the order of its thickness which is, unfortunately, entirely unknown. It is, however, a safe guess that it will be substantially greater than in our atmosphere, and we shall assume it here, for the time being, as around an order of magnitude greater. This means then that the condition of equal stability is roughly

$$\frac{dU_1/dz}{dU_2/dz} \sim \frac{1}{10} \quad (12)$$

This means in turn that vertical velocity gradients in the transition zone above and below the jet will have roughly the same degree of stability on Jupiter as they have above or below the core of a terrestrial jet stream, if they are around an order of magnitude smaller.

But it is now so that the core velocity of a terrestrial jet stream is not very different from that of the Jovian equatorial jet (typically around 70 to 80 m sec⁻¹, [1], p. 84 and [5], p. 453, for a jet blowing along a "front" in temperate terrestrial latitudes vs around 100 m sec⁻¹ on Jupiter). With our assumption that the vertical extent of the Jovian equatorial jet is around an order of magnitude more than that of a terrestrial jet stream, we would then have to expect that the velocity gradients are an order of magnitude less, so that the conditions (12) for a roughly equal stability of the transition regions above and below

the jet streams on Earth and on Jupiter would be satisfied.

. Our preliminary assumption of an at least about ten times greater thickness of the Jovian equatorial jet in comparison with terrestrial jet streams can now be supported by an estimate of the energy balance of the Jovian jet. Its physical nature is that of a thermal wind in a rotating system which is kept blowing by a difference in heating with the latitude ([6], p. 991). But its energy supply is very low by terrestrial standards, and it can therefore continue to exist only, if its energy losses by turbulent dissipation are also very low.

Differential solar heating, as suggested in [6], is probably not the major energy source for the jet. Its total average energy input into the equatorial regions of the Jovian disk is around 10 watts m^{-2} , of the same order as that of the internal heat source. But the difference between the equator and the latitudes of $\pm 10^\circ$ is only in the ratio of $(1 - \cos\phi) \div 1$, or about 1.5 percent, in agreement with the observation that the IR brightness temperature of the bright equatorial band is almost constant at 129°K [14]. And temperature differences of a degree or so across the jet which would be consistent with the accuracy of the observations appear to be inadequate to support the jet ([4], p. 845).

An alternative source for differential heating at greater depth would be the convective heat flow from the interior which rises in the region of the equator and descends again in the regions of the North and South Equatorial Belts. As mentioned before, the average energy output of this heat source appears to be around 20 watts m^{-2} [7]. But not all this energy is available for driving the jet, only the difference in heating at the equator where the heat is convected upwards, and at the two jet boundaries where the gas descends again, after giving up some of its energy to the higher atmospheric levels near the visible disk, and ultimately into space by their IR radiation. Knowing now that the solar differential heating of around $.15 \text{ watt m}^{-2}$ is inadequate to support the jet, and that the total internal heat flow of 20 watt m^{-2} is much more than is available for differential heating, we appear to be as realistic as we can be under the circumstances, if we estimate the average energy supply for supporting the jet as intermediate in order of magnitude between these two limits, or as around 2 watt m^{-2} . Not more than an energy of about this magnitude can be dissipated by turbulence in the transition regions above and below the

jet, or else the jet would very soon stop blowing.

We can now estimate the vertical velocity gradients which can be maintained by the available energy supply from the dissipation function

$$\phi = \eta_e \left(\frac{dU}{dz} \right)^2 \text{ watt m}^{-3} \quad (13)$$

where η_e is the eddy viscosity in turbulent flow. An estimate of η_e in the Jovian atmosphere was given some time ago by R. Hide who argued that the kinematic eddy viscosity

$$\nu_e = \frac{\eta_e}{\rho} \quad (14)$$

in the region of the visible cloud surface should be less than $100 \text{ m}^2 \text{ sec}^{-1}$ [15]. With the typical density of $.1 \text{ kg m}^{-3}$ at this level, one would then have an eddy viscosity of around

$$\eta_e = 10 \text{ kg m}^{-1} \text{ sec}^{-1}, \quad (15)$$

or six orders of magnitude more than the ordinary viscosity of the Jovian atmosphere at this level ([9], p. 6).

In the opinion of the writer, this upper limit is considerably higher than what one would expect the actual eddy viscosity to be under the circumstances, and it will therefore lead to an estimate of velocity gradients which is too favorable. Ratios of η_e/η of the order of 10^6 or even 10^7 do occur in our atmosphere, but only at altitudes of a few hundred meters above the ground under average wind conditions. When the temperature increases with height and the wind is light, a ratio of the order of 10^4 to 10^5 is about what one can have (see e.g. [16], p. 703). For our purpose, we are probably realistic enough, if we estimate

$$\eta_e \sim 3 \times 10^4 \quad \eta \sim .3 \text{ kg m}^{-1} \text{ sec}^{-1} \quad (16)$$

for the altitude range of the equatorial jet in which we are interested.

We can now calculate the combined thickness ℓ of all turbulent shear layers in the Jovian atmosphere which can be supported by an energy input of $E = 2 \text{ watt m}^{-2}$ for a given velocity gradient $|\text{grad } U|$ from

$$E = \ell \phi = \eta_e (\text{grad } U)^2 \quad (17)$$

and we find that we can have a strong gradient of 1 m sec^{-1} per meter for only 6.7 meters, an intermediate gradient of 0.1 sec^{-1} for only 670 m, but a weak gradient of 0.01 sec^{-1} for 67 km. These numbers show clearly that the small energy which is available for maintaining the Jovian equatorial jet is inadequate to support strong turbulent shear layers which would be of concern for the design of an entry probe.

There will, of course, be some turbulence even in this "most quiet" region of the Jovian equatorial jet around the latitudes of $\pm 5^\circ$, since this is needed for the convective transport of heat from below. The average turbulent shear velocities can, however, not exceed the small amount of around 2 cm sec^{-1} per meter, since a stronger turbulence would dissipate more energy than is available for maintaining the equatorial jet.

Addendum

It should be mentioned that the eddy viscosity is substantially lower (only 15 times the ordinary viscosity; [5], p. 180) than assumed in (16) for the limiting case of an "isotropic turbulence", i.e. for the final decay stage at distances from its source which are very large in comparison with its relevant dimension. A typical example is the decay of the turbulence which is caused by a wire grid normal to the axis of a wind tunnel. The isotropic state of the resulting turbulence is then approached at downstream distances which are very large (at least several ten times) by comparison with the mesh size of the grid.

The writer's assessment (16) of the eddy viscosity in the environment of the Jovian equatorial jet was based on the here existing situation that the regions of the most severe turbulence are at distances from the core of the jet which are comparable to its thickness. It is, of course, not excluded that there will be a very wide region of very slowly decaying turbulence at greater distances. But the level of this turbulence will then be too low to be of any concern for the design of the entry probe.

VI. Compatibility of Targeting to $\pm 5^\circ$ Latitude with the Scientific Mission

The scientific questions for Jupiter Entry Missions are defined in the JPL Section Document on Science Criteria for Jupiter Entry Missions [17] in the form of the five questions:

1. What are the relative abundances of hydrogen, deuterium, helium, neon, and other elements, and what are their isotopic compositions?
2. What are the present-day atmospheric composition and altitude profiles of pressure, temperature, and density, and what effect do they have on the radiation balance?
3. What are the chemical composition and vertical distribution of the clouds?
4. Do complex molecules exist in the atmosphere of Jupiter?
5. What are the nature and origin of the colors observed in Jupiter's atmosphere?

It is obvious that a single probe into the Jovian atmosphere cannot be sufficient to obtain complete answers to all of these questions. The most casual look at a color photograph, or even at a black-and-white photograph of the planet shows that the visible surface, i.e. the cloud top layer, is highly non-uniform. There are bright "zones" with generally only faint color differences in mainly whitish blue and blue-green hues, there are darker "belts" with somewhat more pronounced orange or yellowish colors, and there is the Great Red Spot which may at times be quite distinctively reddish, but may at other times fade out to a barely recognizable slightly pinkish region. In addition, there are a great number of transient to semi-permanent smaller features with more or, usually, less distinct colors of their own (see e.g. [1], Table XII and Chapter 11). Presumably, the unobservable deeper layers of the atmosphere will also be somewhat different from place to place, at least up to a very considerable depth where the conditions may be more uniform.

There is also a restriction on the technically feasible target regions for entry missions in the foreseeable future: The probe has to enter into the atmosphere not too far from the equator, and with the direction of the planet's rotation, in order to avoid an unmanageable entry heating problem. Target latitudes up to 10° or even 15° will then not be much more difficult than an entry along the equator, but one would hesitate to select a higher target latitude for the first mission.

Selecting now a target latitude of 5° N or S (preferably 5° N, since the average of cloud observations over 70 years indicates somewhat smaller velocity fluctuations (see [3], Figure 1) will have no great influence on measurements of element abundances. We have no good reasons to suspect that the gaseous components of the main part of the Jovian atmosphere (i.e. below the level of gravitational separation at very low pressures) are not thoroughly mixed, as they are for all practical purposes in our atmosphere up to an altitude of around 75 km above the surface. The same will be true for isotope ratios of the various elements, most probably even more so than for the abundance ratios.

We consider now the second and the third question. It is very probable that there will be differences in the profiles of the state variables vs altitude and in the vertical distribution of the clouds between the rising air current along the equator, the centers of the northern and southern halves of the equatorial jet, and the descending air current in the two dark belts. The conditions at the two midway latitudes of $\pm 5^{\circ}$ are then likely to be more representative of the average Jovian conditions than those at either extremes. For the first entry mission, it is then clearly desirable to target the probe to one of these latitudes (and preferably, as mentioned before, to $+5^{\circ}$). It is then a fortunate coincidence that the turbulence levels at these latitudes are also rather low, and unlikely to cause any great difficulties for the design and operation of the probe.

Concerning the fourth and the fifth questions about the existence of complex molecules and the nature of the colors of the visible cloud top surface, we have to admit that the proposed target latitude of $+5^{\circ}$ is not the most favorable one for experiments on either one of these problem areas. There is not much color anywhere on the surface of the equatorial jet, and a formation of complex, especially organic, molecules is unlikely to occur to any significant degree in a generally quiet part of the atmosphere where the only energy sources would be cosmic radiation and, to a certain extent, also solar UV radiation. The latter, however, cannot penetrate very deeply into the clouds because of scattering. One would expect that its action is limited to the upper, ammonia cloud level where water vapor is practically absent because of the low temperatures. The only elements from which more complicated molecules can be formed are then

hydrogen, the carbon of CH_4 , and the nitrogen of NH_3 . This gives some possibilities, but not as many and as interesting ones as at greater depths where oxygen would be available from water vapor.

Yet, there are likely to be at least some more complex molecules in this part of the atmosphere, formed either locally with cosmic radiation energy, or formed in the perhaps more active immediate vicinity of the equator, and carried into this region by the meridional convection current. If this is so, these molecules are most likely to be adsorbed by the cloud particles (solid ammonia crystals at the highest levels, and solid hydrated ammonia further down). It is likely that one will have a fair chance to find them by an analysis of collected cloud material with a mass-spectrometer of adequate m/e - range, e.g. around 60 as suggested in [17], p. 9, and a gas chromatograph as described *ibid.*, p. 5.

A detection of lightning flashes with a photometer as suggested in [17], p.10 is, of course, quite hopeless, if one selects a target latitude of low atmospheric turbulence for the probe. Thunderstorm clouds are always highly turbulent, due to the condensation instabilities in the atmosphere which create them. The best chance to find them would then be in the rising air currents very close to the equator which, in the opinion of the writer, should be investigated with an entry probe in a later mission.

It is, however, not very difficult to obtain a good idea of the level of electrical activity, and then also an assessment of the atmospheric turbulence in the vicinity of the equator with a probe which enters at $+5^\circ$ latitude. All one has to do is to listen for the resulting electromagnetic noise with e.g. a low frequency broad-band receiver. It is well known that the lightning-generated "spherics" and "whistlers" in our atmosphere can be detected at very great distances from their origin, and sometimes over the entire surface of the Earth with suitable receivers. There should then be no particular problem to determine the level of a perhaps more violent electrical activity along the Jovian equator over the typical distance of around 5000 km between the entry latitude of the first probe and the nearest point on the equator. The writer would like to recommend such an experiment for the first entry probe, both for its own scientific interest, and as a considerable help for the planning of later missions.

VII. Conclusions and Recommendations

The two regions around the latitudes of 5° N and S appear to have the lowest atmospheric turbulence in the Jovian "tropics"; observations of cloud motions in them indicate that the latitude of 5° N is even more quiet than 5° S.

The wind structure of the bright equatorial "zone" between around 10° N and S is probably that of an easterly jet stream of modest, but probably an order of magnitude greater depth (i.e. several tens of km) than the jet streams in our atmosphere. Considering this greater depth, the stability against turbulent decay of the jet (given by the Richardson number) is likely to be not very different from that of terrestrial jet streams. Average turbulent shear velocities appear to be of the order of a few, e.g. 2 cm sec^{-1} per meter. Much greater shear velocities are not compatible with the very low energy which is available for maintaining the jet, at best a few watts per m^2 .

These two latitudes are midway between the equator (where one can have turbulence due to H_2O condensation instabilities, although probably much less severe than on Earth), and the northern and southern boundary of the equatorial jet (where there may be some CAT-like turbulence, although the horizontal temperature gradients in them appear to be too low for any severe CAT to be very probable).

Targeting of the first entry probe to 5° N or S, and preferably to 5° N, is likely to give a good average picture of the structure of the Jovian atmosphere at low latitudes. It is also compatible with the scientific mission to determine the composition of the atmosphere (abundances of elements and of their isotope ratios), the average pressure, temperature and density vs altitude profiles, and the chemical composition and the average vertical distribution of the clouds. There is also a fair chance to detect the presence of complex molecules by an analysis of collected cloud material with a mass spectrometer and a gas chromatograph. Under these circumstances, it is recommended to target the first entry probe to the latitude of 5° N.

The only things which cannot be done in this target region are experiments on the nature of the observed cloud colors (which are most conspicuous in the dark belts and in the Great Red Spot), and a direct

observation of lightning flashes with a photometer which has no significant chance of success with the possible exception of an entry very close to the equator. But one can detect any thunderstorm-like activity near the equator (and probably elsewhere) by monitoring esp. low-frequency electromagnetic noise with a broad-band L.F. receiver. It is recommended to include such an experiment in the scientific payload of the entry probe, both for its own interest, and as an aid for the more detailed planning of later missions.

It is also recommended that two later entry missions should be targeted into the immediate vicinity of the equator and into the Northern Equatorial Belt. Differences in esp. temperature/altitude profiles between the three latitudes of 0° , 5° , and 10° will permit a checking of the theories of internal convection, esp. if combined with magnetic measurements (see e.g. [15]). Vertical distribution of the clouds will probably be appreciably different in the three locations, with thicker and more active H_2O clouds (with lightning? and organic molecules?) at the equator, and with very conspicuous cloud colorations around the 10° latitude. In other words, one needs information from all three locations to obtain a good picture of what is going on below the clouds of Jupiter.

References:

- [1] P. Moore: The Planets
W. W. Norton & Co., Publ. New York 1962
- [2] A. Ingersoll and J. Cuzzi: Dynamics of Jupiter's Cloud Bands
J. Atm. Sci. 26, Sept. 1969, pp. 981-85.
- [3] C. Chapman: Jupiter's Zonal Winds: Variation with Latitude
ibid., pp. 986-90
- [4] R. Hide: Dynamics of the Atmospheres of the Major Planets
ibid., pp. 841-53.
- [5] L. Prandtl: Stroemungslehre, 6 ed.
F. Vieweg & Sohn, Publ., Braunschweig 1965
- [6] P. Stone et al.: Preliminary Results of Experiments with Symmetric Baroclinic Instabilities.
J. Atm. Sci, 1.c. pp. 991-96.
- [7] L. Trafton and R. Wildey: Jupiter: His Limb Darkening and the Magnitude of its Internal Energy Source.
Science 168, 5 June 1970, pp. 1214-15.
- [8] O. Sutton: Understanding Weather.
Penguin Books, Ltd, Publ. Baltimore, Md, 1960
- [9] F. Vandrey: Desirability of Studies on Cloud, Rain, and Thunderstorm Physics in the Jovian Atmosphere.
Memo to S. J. Ducsay, 6 July 1970
- [10] J. Dutton and H. Panofsky: Clear Air Turbulence: A Mystery may be Unfolding.
Science 167, 13 Febr. 1970, pp. 937-44
- [11] E. Reiter: Jet Streams
Doubleday & Co., Publ. Garden City, N.Y. 1967
- [12] M. London: Everybody's Still Trying to Bell the Cat.
Space Aeronautics, June 1970, pp. 34-37
- [13] Dr. H. Greyber, Martin-Denver. (Personal communication).
- [14] R. Wildley et al. Thermal Infrared Emission of the Jovian Disk.
J. Geophys. Res., 70 pp 3711-19, 1965
- [15] R. Hide: On the Hydrodynamics of Jupiter's atmosphere
Mem. Soc. Roy. Sci. Liège, Ser. 5, 7, pp. 481-505.
- [16] D. Menzel (ed.): Fundamental Formulas of Physics, Vol. II
Dover Publ., Inc. New York 1960.
- [17] Science Criteria for Jupiter Entry Missions.
JPL Section Document 131-07, Dec. 31, 1969.

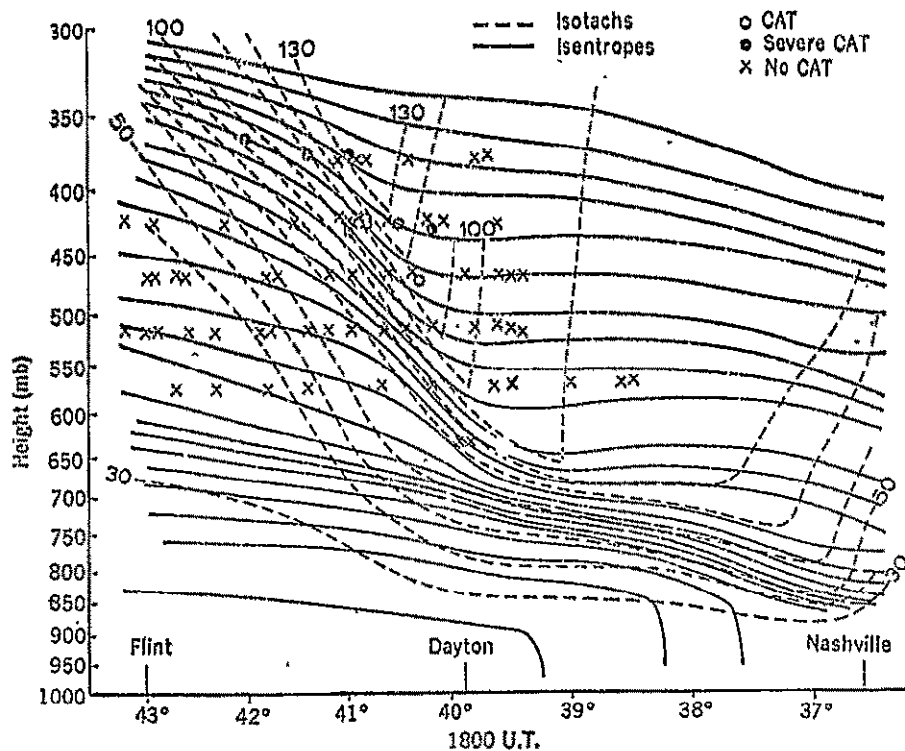


Fig. 1. Cross Section Showing the Relationship of the Occurrence of Clear Air Turbulence (CAT) to the Location of the Internal Front. The Region Shown Extends from Flint, Michigan, to Nashville, Tennessee; the Data were Obtained 23 April 1963 at 1800 Hours GMT. (Dashed Lines) Isotachs at intervals of 10 knots; (solid lines) isentropes at intervals of 2°K ; (open circles) turbulence (solid circles) severe turbulence; (crosses) no turbulence. (reproduced from [9], p 938)

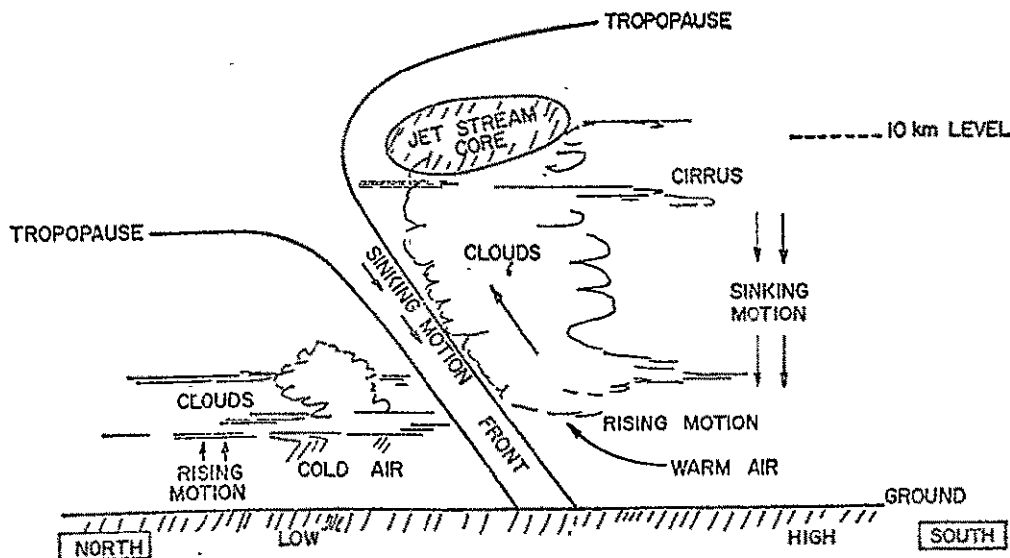


Fig. 2. Polar Front Jet Stream in Cross Section is Pictured Schematically to Show Distribution of Vertical Motions and Clouds (Reproduced from [11], p 158)

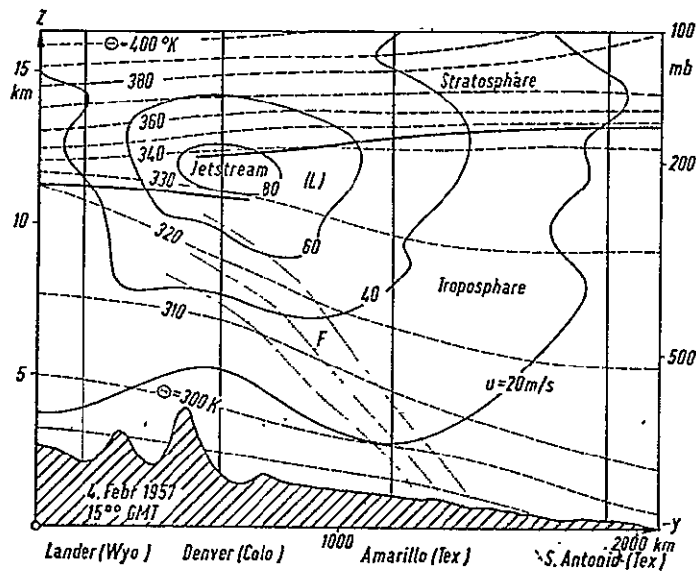


Fig. 3 North-South Section through a Jetstream. Altitudes Exaggerated 100 Times. (reproduced from [5], p 453)

M E M O R A N D U M

1 October 1970

To: S. J. Ducsai
From: J. F. Vandrey
Subject: Dose Rates in Jupiter's Van Allen Belts

On September 30, 1970, the writer attended a seminar lecture on "Electron Energy and Density in the Jovian Magnetosphere" by Prof. D. Beard at the University of Denver.

From all the information which is now available on both the decimetric and the decametric radiation of the planet, it seems now that an equatorial surface field of around 7 gauss, and a polar field of 14 gauss gives the most consistent picture of the situation. An equatorial field as low as 1 gauss is incapable to account for the observations, and a stronger field of e.g. around 15 gauss is equally unlikely.

7 gauss is close enough to the 5 gauss model for which dose rates were calculated by J. W. Haffner in AIAA Journal 7 No. 12, Dec 1969, pp 2305-11. The writer suggests therefore to consider Haffner's 5 gauss model as the nominal one for the purpose of our studies, and both the 2 gauss and the 15 gauss models as (unlikely) limiting cases.

Some small refinements of this nominal model are probably possible with the aid of the new information. Compared with the situation on Earth, the loss of radiation particles by interaction with the atmosphere is probably less important. The scale height in the Jovian thermosphere is considerably less than here. Both thermospheres are essentially hydrogen and helium, but ours is hotter, and our gravity is lower. The main energy loss of the electrons is then by the radiation they emit, and this limits the energy they can obtain in the same way as on Earth. Source of the electrons (with typical original energies of the order of 10^4 ev) is presumably the same for the two planets, i.e. the interplanetary plasma and esp. solar flares. This supply should be much more diluted on Jupiter, because of the greater distance. On the other hand, the stronger and much larger Jovian field is a more effective trap.

Looking at the "envelopes" of the dose rates which Haffner calculated for his three models and which did not come out so very different (figures 6 and 8), it appears unlikely that such refinements will change the picture materially.

J. F. Vandrey

J. F. Vandrey

M E M O R A N D U M

1 October 1970

To: S. J. Ducsay

From: J. F. Vandrey

Subject: Desirability of Studies on Real Gas Effects in the Deeper Parts of the Jovian Atmosphere.

I. Introduction

In a preceding memorandum, the writer had made an attempt to identify a number of problems of Jovian Meteorology, esp. of Cloud, Rain and Thunderstorm Physics under the conditions as we understand them at the present time, where the situation on Jupiter appears to be quantitatively so different from that in our atmosphere that it becomes dangerous to expect a very close analogy between Terrestrial and Jovian meteorological processes [1]. It appeared then that the planning and the design of experiments to be conducted in the clouds of the planet would probably greatly benefit from quantitative studies of Jovian meteorology on the basis of a few typical models of the troposphere of the planet, such as N. Divine's Nominal Atmosphere [2] and several others which have been given in the literature [3],[4].

In the present memorandum, the writer would like to present a case for similar quantitative studies of the deeper parts of the planet's atmosphere, well below the clouds and down to, e.g. the 10^3 atm, 1425°K level in the Nominal Model where various Real Gas-Effects - compressibility, excitation of internal degrees of freedom, condensation of minor constituents, radiative heat transfer, etc., etc. - become of increasing importance, so that a good idea of what one could probably expect in this region would again be very helpful in the planning and the design of scientific experiments for a deep probe into the atmosphere.

II. Structure Theory of Hot and Dense Atmospheres

N. Divine's Nominal Model of the Jovian Troposphere ([2], p. 15) is a classical adiabatic atmosphere of a both thermally and calorically perfect gas in neutral convective equilibrium. As its characteristic feature,

Memorandum - S. Ducsai from F. Vandrey
 1 October 1970
 Page 2

it has a constant temperature gradient (-2.07°K km), and the relations between pressure and density vs altitude have the form of simple power laws

$$p = p_r \left(1 - \frac{Z}{H}\right)^{\frac{\gamma}{\gamma-1}} \quad (1)$$

$$\rho = \rho_r \left(1 - \frac{Z}{H}\right)^{\frac{1}{\gamma-1}} \quad (2)$$

where p_r and ρ_r are the pressure and density at some reference level (here the 1 atm level), H is the altitude above this level up to which a linear temperature profile

$$T = T_r \left(1 - \frac{Z}{H}\right) \quad (3)$$

can be extrapolated in a physically meaningful way ($T = 0$ for $Z = H$), and where γ is the ratio of the specific heats of the atmosphere, both assumed to be constant.

There is no question that such a model will be adequate for analyzing e.g. the dynamics and aerodynamics of a descending probe with a satisfactory degree of confidence. The compressibility factor $Z(p, T)$ in the equation of state

$$p = Z \frac{R_0}{M} \rho T \quad (4)$$

is probably only around 1.2 for H_2 at 10^3 atm, 1400°K (estimated from data in [5], pp. 4 - 117 and 125). The resulting errors should then be of a similar magnitude, and less than the other uncertainties about the atmosphere.

The model will even be adequate for most of the finer points in the design analysis of a probe, e.g. the attenuation of microwave signals due to interaction with the NH_3 inversion spectrum will probably still come out with a fair degree of accuracy [6].

The situation is, however, likely to be different for the scientific aspect of a mission into the deeper parts of Jupiter's atmosphere, one will then need a much more detailed advance knowledge of what can happen for the planning of the experiments, and later for the interpretation of their results.

Memorandum - S. Ducsai from F. Vandrey
 1 October 1970
 Page 3

To illustrate this by a less-known, although elementary fact about polytropic atmospheres: All three relations (1, 2, 3) combined are the consequence of the postulate of a neutral adiabatic equilibrium of a both thermally and calorically perfect gas in a constant gravity field, as shown in every textbook of meteorology and in many elementary physics texts. But it is easy to show that an only thermally perfect gas ($Z(p, T) \equiv 1$) will form a polytropic atmosphere with the pressure and density profiles (1) and (2), and with the polytropic index

$$n = \left(1 + \frac{R_0}{Mg} \frac{dT}{dz}\right)^{-1} \quad (5)$$

instead of $\gamma = C_p/C_v$ in a constant gravity field, if it happens to have a positive or negative constant temperature gradient $\frac{dT}{dz}$ for any reason whatsoever.

It is here suggested to look into these finer points of the theory of atmospheric structure, esp. with realistic specific heats

$$C_v = \left(\frac{\partial h}{\partial T}\right)_v \quad C_p = \left(\frac{\partial h}{\partial T}\right)_p, \quad (6)$$

a realistic equation of state, e.g. the virial equation

$$p \cdot v = A(T) + \frac{B(T)}{v} + \frac{C(T)}{v^2} + \dots \quad (7)$$

and a realistic expression

$$ds = \frac{de + pd\left(\frac{1}{p}\right)}{T} \quad (8)$$

for entropy changes of $H_2 - H_e$ mixtures at high pressures and temperatures.

These studies would also have to include a re-examination of Richardson's stability theory and of such well-known formulas as G. I. Taylor's expression

$$q = -C_p A_q \left[\left(\frac{dT}{dz} \right)_{\text{adiab}} + \frac{dT}{dz} \right] \quad (9)$$

for the turbulent heat exchange flow in the atmosphere (see e.g. [8] p. 450), all of which contain some elements of the theory of ideal gases in their derivation.

Memorandum - S. Ducsai from F. Vandrey
 1 October 1970
 Page 4

III. Radiative Heat Transport from Below

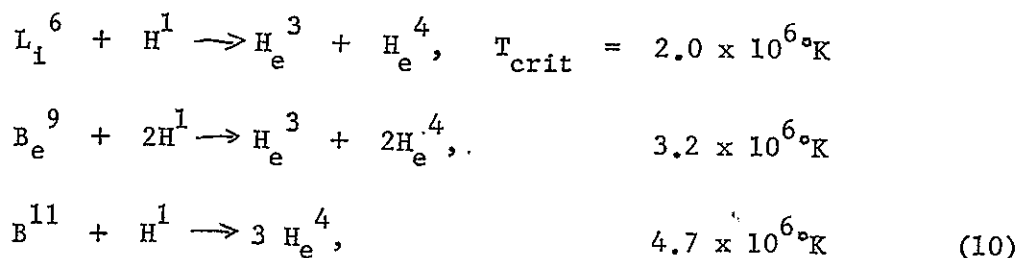
It is suggested to consider the possibility of an appreciable upward radiative heat transport in the deeper parts of the atmosphere where the temperatures become rather high (1400°K). It is conceivable that the most important physical parameter in this radiation problem, the i.r. opacity of the atmosphere, could be quite strongly influenced by impurities, in addition to the absorption properties of the basic hydrogen-helium mixture of the atmosphere (See [2] p. 10 for references on H₂ opacity).

Measuring the upward radiation flux as a function of altitude is not a very difficult experiment. Comparing the result then with a theoretical prediction for the basic atmosphere (with then known amounts of NH₃, CH₄ and H₂O) could give an indication of the presence and abundance of other impurities, at least as a rough bulk number. Such an experiment may be worth doing in the first mission, to get a preliminary idea of "how much is there", and as an aid for the planning of more specific and elaborate experiments in later missions.

IV. Physical Chemistry of the Deep Atmosphere.

There exist some studies of various chemical equilibria and of condensation levels of less volatile trace components than NH₃ and H₂O in the Jovian atmosphere well below the ammonia and water clouds. It has, e.g. been predicted that there will be (probably thin) clouds of silicon and other compounds at certain pressure and temperature levels.

Of considerable scientific interest would be to know the levels below which compounds of the three elements B, Li, and Be can be expected to be gaseous. All three elements are extremely rare, not more than around one part in 10⁹ of the atmosphere is expected. Knowing their abundances, and preferably also their isotopic composition, would, however, give us an idea of how hot the material of Jupiter has ever been, since these elements take part in nuclear reactions which occur with a high probability at already relatively "low" temperatures of a few 10⁶°K. A typical "thermometer" of this kind is given in [9] p. 87, we take from it here



as examples.

Memorandum - S. Ducsai from F. Vandrey

1 October 1970

Page 5

It seems that boron, or at least much of it, will be accessible in the form of BH_3 throughout most of the atmosphere, Li in the forms of Li H or Li OH at a relatively low depth with still moderate ($\sim 1000^\circ\text{K}$) temperature, while Be in e.g. the form of $\text{Be}(\text{OH})_2$ may be marginal even at the deepest (1400°K) level we can hope to achieve with a probe. [10].

But this will only be so, if there are no significant "condensation traps" for these elements in the form of other less volatile compounds at a greater depth, and it might be wise to look at this possibility (boron carbide? lithium silicates?) If there are such partial traps, what gets through them should still have the same isotopic composition, so that one can probably still draw some conclusions with more elaborate instrumentation.

These are only a few of the many physicochemical questions whose investigation would be profitable for planning experiments to explore the depths of Jupiter's atmosphere. The particular example of the three light elements Li, Be, B was here only selected to emphasize that the scientific objectives of Jupiter exploration programs go far beyond the study of the particular object called "Jupiter". We have good reasons to believe that the planet's material is, in its present state, much closer to the original composition of the material from which our solar system was formed than any other material which is accessible to us. By studying it in as much detail as we can, we can therefore hope to obtain some clues on what happened even before our sun was formed as a "second generation star", probably after a "super-nova" explosion of a previously existing one.

V. Thermal Dissociation of Molecules

We consider here only the example of the water molecule to illustrate the typical problems which may arise in the deeper parts of the atmosphere. Even at normal temperatures, ordinary water is to a very small degree dissociated into ions



The familiar statement that " $\text{pH} = 7$ " is neutral, neither acid nor alkaline, means that one H_2O molecule in 10^7 is split into two ions in even the most purified water we can obtain, and that even the purest water has always a very small electrolytic conductivity. It has to be said here that an ionisation as "high" as 10^{-7} at ordinary temperatures is deceptive, since the rate of ion formation is actually much lower than this would suggest. It occurs only, because the re-combination of an H^+ and an $(\text{OH})^-$ ion is extremely difficult in the strongly polar neutral water (dielectric constant around 80!) where every ion is at once surrounded by a "shield" of water molecules which protects it. Yet, there is no doubt that there will be some (and possibly an appreciable) ionisation of H_2O (and of other molecules with ionic bonds) at the more than 10^3°K temperatures in the deepest parts of the atmosphere to which we hope to penetrate, and it is also not unreasonable to expect that a re-combination in an environment containing only a small

Memorandum - S. Ducsai from F. Vandrey
1 October 1970
Page 6


percentage of H_2O will have its difficulties. In other words, we have to expect a small, but possibly not yet negligible, electrolytic conductivity of the densest and hottest regions of the atmosphere in which we are here interested.

If this is so, there may be difficulties with signal transmission from the greatest depths we are presently considering for our deep probes. Not necessarily unsurmountable ones but perhaps enough to increase the transmission frequency beyond present plans. On the other hand, there may be a possibility for a relatively simple experiment to measure the contents of ionizable components in the atmosphere by the resulting d.c. (or low frequency a.c.) conductivity, as long as the conductivity is not yet strong enough to interfere too much with the communication. A thorough study of this question is recommended.

VI. Conclusions

It appears that theoretical and, as far as possible, also experimental investigations of real gas effects in the lower parts of the Jovian atmosphere (down to at least 10^3 atm, $1500^\circ K$), over and above what has already been done in this field, will be of great value for the success of a probe mission which is to penetrate well below the NH_3 and H_2O cloud level.

Particularly urgent from the technical point of view is an investigation of probable ionization effects and of a resulting small electrolytic conductivity in the deepest layers to which we are planning to penetrate, since it may restrict the penetration depth or at least necessitate some changes in the communication system. On the other hand, it may also permit a relatively simple conductivity experiment for measuring the amount of ionizable trace constituents of the atmosphere.



J. F. Vandrey

JFV/dcm

References:

1. F. Vandrey: Desirability of Studies on Cloud, Rain, and Thunderstorm Physics in the Jovian Atmosphere.
Memo to S. J. Ducsal 6 July 1970
2. N. Divine: Jupiter Model Atmospheres
J.P.L. Interoffice Memo 2947-617, 5-8-70.
3. G. C. Goodman: Models of Jupiter's Atmosphere
Ph.D. Thesis, University of Illinois, 1969
4. L. M. Trafton: Model Atmospheres of the Major Planets
Astrophys. J. 147, No. 2, p. 765, 1967
5. D. Gray, ed.: American Institute of Physics Handbook, 2nd ed.
McGraw-Hill Book Co., Publ. New York 1963
6. F. Vandrey: Estimate of Compressibility Effects on NH_3 Microwave Attenuation in the Jovian Atmosphere.
Memo to S. J. Ducsal
7. F. Vandrey: Dynamics and Aerodynamics of Drop Sondes in the Lower Venus Atmosphere.
J. Astronautical Sci XVII No. 2, Sept - Oct '69, pp 95-103.
8. L. Prandtl: Stroemungslehre, 6th ed
F. Vieweg & Sohn, Publ. Braunschweig 1965
9. M. Schwarzschild: Structure and Evolution of the Stars
Dover reprint, 1965
10. F. Vandrey: How Deep?
Memo to S. J. Ducsal, January 30, 1970

M E M O R A N D U M

25 November 1970

To: S. J. Ducsaí

From: J. F. Vandrey

Subject: General Comments on the Possibilities to Predict Turbulence Fading
in the Deeper Parts of the Jovian Atmosphere.

If one uses the computationally relatively simple fading theory of "line-of-sight" communication as in de Wolf and Davenport's analysis of the fading in the lower Venus atmosphere and in the upper atmosphere of Jupiter [1] for an attempt to predict the signal fading from a probe which is to penetrate very deeply (e.g. down to some 600 km below the clouds) into the Jovian atmosphere, one runs into a number of difficulties which are due to the sensitivity of the result to the assumptions one has to make about the level and about the scale of the turbulence deep below the visible surface of the planet.

To see what these difficulties are, and how far they can be reduced if one insists on using the line-of-sight theory with its inherent limitation to the approximation of geometrical optics, we review in outline the calculation procedure.

The basic quantity which is being calculated in this, and in any other fading theory is the variance $\langle (\delta I)^2 \rangle$ of the signal flux intensity I_0 for which one obtains in the line-of-sight approximation.

$$\frac{\langle (\delta I)^2 \rangle}{I_0^2} = 1 - e^{-4 \sigma_\epsilon^2} \quad (1)$$

([1], p. 8) with the governing parameter

$$\sigma_\epsilon^2 = \frac{4 \pi^2}{\lambda^2} \epsilon^2 L_1 L \quad (2)$$

([1], p. 10). In this expression, λ is the wavelength of the signal, and L the propagation distance through the turbulent medium whose characteristics are here

①

Memorandum - S. Ducsay from F. Vandrey
 25 November 1970
 Page 2

assumed to be independent of the altitude, to avoid on unnecessary complexity in the presentation. L_i is an integral scale of the turbulence with respect to its velocity spectrum ([1], p. 27). It is also somewhat dependent upon $L \cdot \lambda$, but de Wolf and Davenport found that the rough estimate

$$L_i \approx 0.186 L_0 \quad (3)$$

or around $\frac{1}{5}$ of the turbulence macroscale L_0 was adequate for their purpose ([1], p. 30). Finally,

$$\epsilon^2 = 4 \langle (\delta n)^2 \rangle \quad (4)$$

is the variance of the dielectric constant of the atmosphere due to random temperature, and then also density variations in the turbulent field. For this quantity, one has the expression

$$\epsilon^2 \approx 25 L_0^2 \frac{(\bar{\epsilon} - 1)^2}{T^2} \left(\gamma_a + \frac{\partial T}{\partial z} \right)^2 \quad (5)$$

where $\bar{\epsilon}$ is the mean dielectric constant of the atmosphere, and γ_a its adiabatic lapse rate. ([1], p. 19).

For the following discussion of these equations, it is useful to express $\bar{\epsilon} - 1$ by the atmospheric density ρ to which it is proportional for all gases as long as they are not too highly compressed (see e.g. [2], p 177), and to express $\gamma_a + \frac{\partial T}{\partial z}$ by the turbulent heat flow q from the interior to the surface which is given by G. I. Taylor's relation

$$q = -C_p A_q \left(\gamma_a + \frac{\partial T}{\partial z} \right) \quad (6)$$

(see e.g. [3], p. 450) and which is valid in the absence of large-scale vertical air motions. In (6), C_p is the specific heat of the atmosphere at constant pressure, and A_q is the "turbulent heat exchange" ([3], p. 259). These two quantities can be combined to an "eddy heat conductivity".

$$K_e = C_p A_q \quad (7)$$

Memorandum - S. Ducsay from F. Vandrey
 25 November 1970
 Page 3

which plays a similar role in turbulent heat transfer problems as the "eddy viscosity" η_e in turbulent momentum transfer problems, and in the eventual dissipation of turbulence into heat. Both K_e and η_e are substantially greater than the corresponding coefficients of ordinary heat conduction and ordinary viscosity, and they are not characteristic of the material of the atmosphere, but characterize rather the degree of turbulence in it (see e.g. [4], p. 668).

We obtain then

$$\left(\mu_a + \frac{\partial T}{\partial z}\right)^2 = \frac{q^2}{K_e^2} \quad (8)$$

and, from refraction data on hydrogen and helium,

$$(\bar{\epsilon} - 1)^2 \approx 1.7 \times 10^{-6} \rho^2 \quad (9)$$

with ρ in kg m^{-3} as a reasonable estimate for the Jovian atmosphere.

Introducing these expressions into (2), we find

$$\sigma_\epsilon^2 \approx 1.7 \times 10^{-3} L_o^3 \frac{\rho^2}{T^2} \frac{q^2}{K_e^2} \cdot \frac{L}{\lambda^2} \quad (10)$$

as a reasonable estimate for the fading parameter within the framework of the line-of-sight theory, with all quantities in MKS units, i.e.,

$$\begin{aligned} L, L_o, & \quad \text{in } [\text{m}]; \quad \rho \text{ in } [\text{kg m}^{-3}] \\ T & \quad \text{in } [^\circ\text{K}] \quad ; \quad q \text{ in } [\text{watt m}^{-2}] \\ K_e & \quad \text{in } [\text{watt m}^{-1} \text{ } ^\circ\text{K}^{-1}] \end{aligned} \quad (11)$$

σ_ϵ^2 itself is, of course, a non-dimensional quantity, as evident from its definition (2).

Supposing now for the moment that we would know all the various quantities in eq. (10) from the outer limit of the Jovian atmosphere down to the deepest

Memorandum - S. Ducsai from F. Vandrey
 25 November 1970
 Page 4

level of e.g. 600 km. below the visible cloud top surface to which our probe will be designed to penetrate, we could very easily calculate $\overline{\sigma}_\epsilon^2/L$ for any atmospheric level in which we are interested, and this would immediately give us the contribution of this level to the turbulence fading within the limits of our theory. This follows quite simply from the physical meaning of $\overline{\sigma}_\epsilon$ (see [1], p. 7): It is nothing else but the expected phase difference between rays which reach the same point on slightly different paths through the turbulent medium. That is, severe fading can be expected to occur, if

$$\overline{\sigma}_\epsilon \approx \pm \pi, \quad (12)$$

since

$$\cos(\omega t) + \cos(\omega t \pm \pi) = 0 \quad (13)$$

The fact is, of course, that we know only some of the parameters in (10) with a reasonable degree of confidence, and have hardly any idea about the others. Using, for instance, the nominal model of the Jovian atmosphere ([5], p. 101), we would have a density of around 20 kg m^{-3} and a temperature of around 1450°K at the 10^3 atm level, about 650 km below the (arbitrary) zero of altitude at $p = 1$ atm which is in the general range of the visible cloud top "surface". We can also estimate the heat flux q from the interior, and we obtain around 30 watt m^{-2} from the recent observations of Trafton and Willey [6] which indicate that Jupiter radiates between three and four times as much energy into space, as the planet receives from the Sun. But we have not much guidance for selecting a plausible range for the eddy heat conductivity K_e deeply below the visible surface, and we have no way at all to support any guess of the turbulence macro-scale L_0 at these depths.

Going ahead anyway, we can relate K_e to some extent to the eddy viscosity η_e of the atmosphere whose dimension is that of the ordinary viscosity, i.e. $\text{kg m}^{-1} \text{ sec}^{-1}$. From the definition (7) of K_e , we find then that the turbulent heat exchange A_q has the same dimension as η_e , i.e. that

$$\frac{A_q}{\eta_e} = m \quad (14)$$

Memorandum - S. Ducsai from F. Vandrey
 25 November 1970
 Page 5

is a non-dimensional number. This does not say very much by itself, but it is a matter of experience that m changes relatively little from one turbulent flow to another, and that it is generally around 2 in regions of "free turbulence" sufficiently remote from any solid boundaries ([3], p. 267). Using this value, we can then write

$$K_e \approx 2 C_p \eta_e \quad (15)$$

in which we can use $C_p \approx 1.3 \times 10^4 \text{ m}^2 \text{ sec}^{-2} \text{ }^\circ\text{K}^{-1}$ as a typical value for the nominal atmosphere (from [5] p. 75 after conversion of units).

Concerning η_e , we can at least make the statement that it should be substantially greater than the ordinary viscosity of the atmosphere for which we have in [5] p. 75 the estimate

$$\log \eta \approx 0.4 + 0.65 \log T \quad (16)$$

with η in micropoise and T in $^\circ\text{K}$. Converting to MKS units, we obtain then

$$\eta \approx 2.5 \times 10^{-5} \left(\frac{T}{1000} \right)^{2/3} \text{ kg m}^{-1} \text{ sec}^{-1} \quad (17)$$

or $3.2 \times 10^{-5} \text{ kg m}^{-1} \text{ sec}^{-1}$ for $T = 1450^\circ\text{K}$ at 1000 atm.

For a guess of how much greater η_e could be than η , we can only resort to the probably somewhat tenuous analogy with the situation in our atmosphere where values of η_e/η between 10^4 and 10^5 seem to be typical in the "free atmosphere" sufficiently high above the ground (see e.g. [7], p. 703). This would then give for η_e the order of $1 \text{ kg m}^{-1} \text{ sec}^{-1}$, and for K_e a value in the general neighborhood of $3 \times 10^4 \text{ watt m}^{-1} \text{ }^\circ\text{K}^{-1}$.

As a check on this guess, we calculate

$$\mu_a + \frac{\partial T}{\partial z} = - \frac{g}{K_e} \approx -10^{-3} \text{ }^\circ\text{K m}^{-1} \quad (18)$$

from (8), and we compare it with the adiabatic lapse rate

$$\mu_a = \frac{g}{C_p} \approx 2 \times 10^{-3} \text{ }^\circ\text{K m}^{-1} \quad (19)$$

Memorandum - S. Ducsai from F. Vandrey
 25 November 1970
 Page 6

where $g \approx 25 \text{ m sec}^{-2}$ is the effective acceleration of gravity in the equatorial regions of the planet into which our probe will be targeted. Subtracting then (19) from (18), we obtain for the temperature gradient in the atmosphere

$$\frac{\partial T}{\partial z} = -3 \times 10^{-3} \text{ } ^\circ\text{K m}^{-1} \quad (20)$$

instead of $-\gamma_a = -2 \times 10^{-3} \text{ } ^\circ\text{K m}^{-1}$ for an adiabatic atmosphere in neutral convective equilibrium with no upward heat flow through it.

It appears thus that our initial guess for γ_e/γ was a lucky one, since it resulted in a $\frac{\partial T}{\partial z}$ only 50% greater than $-\gamma_a$. This is in the right direction, the real temperature gradient in an atmosphere with an upward heat flow has always to be somewhat greater than the adiabatic lapse rate to permit the heat to flow upward by turbulent exchange. From experience with our atmosphere, we would, however, have to say that a 50% excess over γ_a occurs only in rather rare cases of severe instability, and that smaller values of between 10 and 20% are much more common, especially at some distance (a few km) above the ground. Since there is now no ground with strongly non-uniform solar heating on Jupiter, we are lead to a revision of our estimate for K_e , so that it would give us a temperature gradient only around 20% more than $-\gamma_a$. An easy calculation gives then $K_e \approx 7.5 \times 10^4 \text{ watt m}^{-1} \text{ } ^\circ\text{K}$ as our revised estimate for the 10^3 atm level, and generally

$$K_e \approx 7.5 \times 10^4 \left(\frac{T}{1450} \right)^{2/3} \text{ watt m}^{-1} \text{ } ^\circ\text{K}^{-1} \quad (21)$$

for any other level in the atmosphere.

There is still one qualification we have to make with respect to (21), apart from the obvious one that it can be no better than the nominal model of the atmosphere which was used in its derivation. Assuming that K_e is appreciably smaller than in (21) will lead to atmospheric temperature gradients substantially higher than $-\gamma_a$, and this is inconsistent with what we think we know about the thermodynamic behaviour of atmospheres subjected to modest heating from below. But it is quite possible that K_e can be larger than in (21), so that this estimate would give the general region of a lower limit for K_e , rather than a more or less

Memorandum - S. Ducsai from F. Vandrey
 25 November 1970
 Page 7

accurate estimate of its actual value. We revise therefore (21) once more to

$$K_e \geq \sim 7.5 \times 10^4 \left(\frac{T}{1450} \right)^{2/3} \text{ watt m}^{-1} \text{ } ^\circ\text{K}^{-1} \quad (22)$$

so that the use of (21) in calculating σ_e^2 would lead to a result which is too large, i.e. is conservative.

Introducing now our estimate for K_e into our expression (10) for the fading parameter σ_e , we obtain

$$\sigma_e^2 \approx 10^{-9} L_o^3 \frac{\rho^2 q^2}{T^{10/3} \lambda^2} \cdot L \quad (23)$$

as the most reasonable and relatively plausible estimate we can come up with for the somewhat elusive conditions down to 600 km below the visible surface of Jupiter.

The only unknown quantity in this equation is the macroscale L_o of the atmospheric turbulence, i.e. the typical size of its eddies. Since we have no way of assessing its magnitude, not even in the crudest fashion, we have no choice but to make a number of assumptions, i.e. to do a parametric study.

To simplify this task, we introduce into (23) the numerical value of 30 watt m^{-2} for q , and we assume that the probe will have a 10^9 cps transmitter (i.e. $\lambda = 0.3$ m) which is in agreement with present plans. Furthermore, we use the basic assumption for the construction of the nominal model atmosphere, that its lower part is essentially polytropic, to eliminate ρ as an independent variable by

$$\rho = \rho_r \left(\frac{T}{T_r} \right)^{\frac{1}{n-1}} \quad (24)$$

where we can use 20 kg m^{-3} and 1450°K as reference values for density and temperature, and where the polytropic exponent n is not very far from 1.4. We obtain then

$$\sigma_e^2 \sim 6.2 \times 10^{-19} T^{5/3} L_o^3 L \quad (25)$$

for the approximate contribution of any temperature, i.e. also pressure or altitude level in the Jovian troposphere to the turbulence fading parameter for 10^9 cps signals.

Memorandum - S. Ducsai from F. Vandrey
 25 November 1970
 Page 8

To perform now our parametry study with a statistical sample of one, we assume that the probe trasmits from its maximum design depth of 600 km below the clouds, i.e. from the 1450°K level, to an upper relay probe which may at that time be some 50 km below the clouds, so that our transmission length is $L = 5.5 \times 10^5$ m. To obtain then the critical value of $\sigma_{\epsilon}^2 = \bar{\epsilon}^2 \approx 10$ for severe fading, we would need a typical turbulence scale of

$$L_0 = \sqrt[3]{\frac{\bar{\epsilon}^2}{6.2 \times 10^{-19} T_{av}^{5/3} L}} \quad (26)$$

where T_{av} is between the 1450°K at -600 km and around 300°K at -50km. Considering then that the lower and denser parts of the atmosphere will contribute more to the fading than the higher parts with their lower density and temperature, we may estimate $T_{av} \sim 1000^\circ\text{K}$, and we obtain then

$$L_0 < 670 \text{ m} \quad (27)$$

as a, probably even conservative, estimate for the eddy size up to which we would not have to expect any significant difficulties for the communication from turbulence fading.

We would, of course, recommend to make some provision to deal with moderate fading, such as between 5 and 10 dB, in the design of the communication system, but we do not have to anticipate any real difficulties from this source, unless the typical eddy size in the deeper parts of the Jovian atmosphere would be appreciably greater than around 500 m.

This size is an order of magnitude greater than the estimate of $L_1 \approx \frac{1}{5} L_0 \approx 10$ m on which de Wolf and Davenport based their assessment of turbulence fading in the upper parts of Jupiter's atmosphere ([1], p. 18). The physical reason for this is clearly the very low amount of energy which is available to drive the "winds" and their associated turbulence in the lower parts of the planet's atmosphere. In our atmosphere, weather, wind, and turbulence are being driven by an average energy input of somewhere around 20 watts per ton of solar heat which penetrates to the ground, although, admittedly, at a rather low efficiency. On Jupiter, however, we have only around 7.5 milliwatts per ton of energy input into the deeper parts

Memorandum - S. Ducsai from F. Vandrey
 25 November 1970
 Page 9

of the atmosphere where solar radiation, what little there is, cannot penetrate. It helps also that the specific heat of the Jovian atmosphere is around 10 times greater than that of ours, this increases the eddy heat conductivity tenfold over that in our atmosphere for the same value of the eddy viscosity (see eq. (15)).

However, while all this looks quite encouraging, and seems to indicate that turbulence fading may only be a minor problem of the nuisance type for signal transmission from a deep probe into the Jovian atmosphere, we cannot have any assurance that the eddy size in its never observed depths could not be substantially greater than the 670 m limit we had obtained from the "line-of-sight" fading theory.

Fortunately, this theory, while adequate and, in fact, quite good to predict turbulence fading over moderate distances (something like 10 or 20 km for microwaves), appears to become more and more conservative as the transmission distance is increased. As explained in V.I. Tatarski's book on Wave Propagation in a Turbulent Medium, the basic limitation of the line-of-sight theory is in its use of geometrical optics which is no longer applicable over long distances when diffraction effects become important ([8], pp 120-21).

The appropriate criterion for the applicability of the line-of-sight theory to turbulence fading prediction is

$$\sqrt{\lambda L} \ll L_0 \quad (28)$$

or, rewritten for the propagation distance

$$L \ll \frac{L_0^2}{\lambda} = \frac{500^2}{0.3} \approx 800 \text{ km} \quad (29)$$

One can therefore have confidence in the prediction of turbulence fading from the simple theory only up to distances of around 100 km, but the result becomes at least doubtful for a distance of more than 500 km.

And at these long distances, the line-of-sight prediction is likely to give an overestimate of the turbulence fading. It is then no longer so that the "rays", i.e. wave-front normals, arriving at the receiver are only those which have propagated along paths very close to the straight line between the transmitter and the receiver. Since neither the receiver nor the transmitter has an antenna with an "infinite gain", i.e. with an extremely narrow beam, the receiver will

Memorandum - S. DuCsai from F. Vandrey
 25 November 1970
 Page 10

also be influenced by waves which left the transmitter in a different direction, but were partially diffracted to the receiver by the inhomogeneities in the medium between them. These waves, having traveled a longer path than the shortest line-of-sight distance, may have any phase difference with the "direct" signal, and many of them will probably have phase differences which are not exactly multiples of $\pm \pi$. To say the very least, this more complex structure of the pattern of "elementary waves" arriving at the receiver should reduce the probability that all these elementary waves cancel each other at any one time at the receiver antenna, and this is what signal fading is all about. The writer would like to recommend a re-examination of the turbulence fading theory with inclusion of diffraction effects for long-distance communication through a turbulent medium, as a major analytical effort to obtain a better background knowledge for future probe missions into deep planetary atmospheres.

When this effort is undertaken, it should also include a consideration of the fading problem for the communication from a probe deep in a turbulent atmosphere to a receiver at a substantial distance from the planet which is being probed, e.g. the communication from a Venus lander to a receiver on Earth, or the direct transmission from a deep probe into the Jovian atmosphere to a flyby relay spacecraft which may typically be one or two planetary radii away from the surface. The simple line-of-sight theory assumes here that nothing happens anymore to the signal, once it has left the atmosphere. This would be so for a very narrow beam of the transmitter antenna. But not for an antenna with a finite beamwidth. According to Huygen's principle, the receiver will then not "see" a single point transmitter, but a wide area with the diameter

$$D \approx 2 d \cdot \tan \frac{\alpha}{2}, \quad (30)$$

where d is the depth of the transmitter below, e.g. the tropopause in the planet's atmosphere and α the beamwidth of its antenna, which is covered with little transmitters, all sending the same message. The intensity of these transmitters will fall off rather rapidly from the center of the transmitter beam in the outward direction, and they will also be badly out of phase with each other.

Combined, however, their signals would have a low probability to cancel each other out exactly at the receiver and, while one will certainly have to

Memorandum - S. Ducsai from F. Vandrey
25 November 1970
Page 11

expect some random fading, a very severe fading becomes as unlikely as an assembly of all the gas molecules in a container in one of its corners, and for the same reasons of probability which form the basis of the second law of thermodynamics.

An, unfortunately rather complex, analysis of these situations in which L is clearly much larger than L_0^2 / λ may well show that a direct transmission from a deep probe into a planetary atmosphere with a moderately wide antenna beam to a receiver well outside the atmosphere is less affected by turbulence fading than a transmission from the probe to a relay station in the higher parts of the atmosphere with a narrow beam antenna. At any rate, it will be less sensitive to the details of the turbulence which one has to know fairly well (but does not for the Jupiter atmosphere below the clouds) to predict the fading from the line-of-sight theory.

All of the preceding was only concerned with the magnitude of the signal fluctuations, without ever mentioning fading rates. This for the simple reason that their prediction requires a knowledge of the changes of the atmospheric non-uniformities with time, i.e. of winds and wind-shear in the depths of the Jovian atmosphere. This knowledge is non-existent at the present time, and a prediction of fading rates can therefore not be attempted.

This may be enough for the "dark" side of the fading problem. But it has also a "bright" side which should not be overlooked. While fading does introduce noise into the communication link between a deep probe and a receiver higher up in the atmosphere or outside the atmosphere in a flyby spacecraft, an analysis of this noise gives valuable information on the winds and on the turbulent heat transfer down to the depth to which the deep probe can penetrate. And we do have some control over the turbulence fading by selection of the wavelength of our transmitter to which the fading parameter σ_{ϵ} is inversely proportional. To get the data from our probe experiments back with a minimum of fading noise, we should clearly use as long a wavelength as we can under the various restraints (e.g. antenna size for a desired gain, and electrical noise from the Van Allen Belts of Jupiter) of the mission. These restraints lead to the selection of $\lambda \sim .3$ m for the transmission as a probably reasonable compromise. With shorter waves,

Memorandum - S. Ducsai from F. Vandrey
25 November 1970
Page 12

we would get greater fading and more information on atmospheric winds and turbulence. Given some excess capability of the deep probe, we might even consider a deliberate high-frequency fading experiment to obtain this information on the dynamics and thermodynamics of the atmosphere well below the clouds.

Conclusions:

1. Because of the very low energy input from below into the Jovian atmosphere, and because of its high specific heat which permits the transport of substantial amounts of heat by means of very modest mass motions, the turbulence and the associated fading effects are relatively mild even in the deepest parts of the atmosphere to which a probe can be designed to penetrate.
2. The line-of-sight theory is adequate to assure us, as a conservative estimate, that turbulence fading will not be a major problem, unless the average eddy size in the deep atmosphere exceeds about 500 m which is an order of magnitude more than typical for most situations in our atmosphere.
3. Should the typical eddy size be greater than 500 m, there is still a good chance that the fading for long-distance communication remains within acceptable limits, because of diffraction effects which were disregarded in the line-of-sight theory, but are likely to reduce the probability of nearly exact cancellation of all signals arriving at the receiver on different paths more and more with increasing distance between transmitter and receiver.
4. A study of long-distance communication through a turbulent medium, and also out of a turbulent medium to a receiver at a substantial distance, with due regard to the then important diffraction effects, is recommended as a major analytical effort to support deep-probing missions into the atmospheres of the outer planets, and to some extent also into the deep atmosphere of Venus and to the surface of this planet.
5. A positive side of turbulence fading is that its observation gives information on winds and wind-shear, and on the thermodynamics of the atmosphere in general, down to the greatest depth to which a probe can penetrate before failing due to increasing temperature and pressure. The analytical studies suggested in the preceding section should therefore also be concerned with the question of how far one can extract this information from signals over a long-range

Memorandum - S. Ducsai from F. Vandrey
25 November 1970
Page 13

communication link in which diffraction is important.

6. As a practical matter, it is recommended to make some provision for dealing with moderate (5 to 10 dB) fading in the preliminary design of the communication system for the deep probe. It is also advisable to use a probe antenna with a beam which is not too narrow. But this is likely to be necessary anyway, since a narrow-beam antenna for $\lambda = 0.3$ m would simply become too large for the deep probe to be practical.

F. Vandrey

J. F. Vandrey

JFV/dcm

References

1. D. A. de Wolf and J. W. Davenport: Investigation of Line-of-Sight Propagation in Dense Atmosphere: Phase I.
NASA CR 73440 May 1970
2. R. W. Pohl: Optik
J. Springer, Publ. Berlin 1940
3. L. Prandtl: Stroemungslehre, 6. ed.
F. Vieweg & Sohn, Publ. Braunschweig 1965
4. H. Lamb: Hydrodynamics, 6. ed.
Dover reprint, 1945.
5. N. Divine: The Planet Jupiter (1970)
JPL Interoffice Memo 2947-659 October 8, 1970
6. L. M. Trafton and R. L. Wildey: Jupiter: His Limb Darkening and the Magnitude of His Internal Heat Source.
Science 168, June 5, 1970, pp. 1214-15.
7. D. Menzel (ed.): Fundamental Formulas of Physics
Dover reprint, 1960
8. V. I. Tatarski: Wave Propagation in a Turbulent Medium (Transl. from Russian)
Dover reprint, 1967.

M E M O R A N D U M

23 December 1970

To: S. J. Ducsay

From: J. F. Vandrey

Subject: Comments on the Thermal Radiation Environment and on Radiation Experiments in the Deepest Accessible Regions of the Jupiter Atmosphere.

While all the measurements one could make with a probe going as deep as technically feasible into the Jovian atmosphere, e.g. down to the 10^3 atm level with a nominal temperature of 1425°K [1], would be of scientific interest, the only firm requirement for the scientific mission of such a probe appears to be the determination of the deep (p, T) - profile as a boundary condition for an extrapolation into the interior [2]. The purpose of this is, of course, to have an experimentally verified boundary condition for the numerical integration of the governing equations for the internal fluid dynamics of the planet.

As formulated in a recent paper by R. Hide [3], these equations are those for the flow of an electrically conducting fluid in the presence of a magnetic field, when referred to a frame which rotates with a constant angular velocity relative to an inertial one. They do not contain any radiation terms which, by the way, would make them even less tractable than they are already without them.

While this omission appears to be justified under the circumstances, it is, nevertheless, a legitimate question whether or not radiative transfer of energy could play a detectable role at, e.g. the 10^3 atm, 1425°K level, so that one could learn something, in particular on atmospheric impurities, from relatively simple radiation experiments in either the infrared or in the visible part of the spectrum in which there is already some energy at 1400°K (and, in fact, at even lower temperatures), although not enough to count in the overall energy balance.

Memorandum - S. Ducsaï from F. Vandrey
23 December 1970
Page 2

We are thinking here of both active and passive experiments to determine the opacity of the atmosphere at a few typical wavelengths in the near i.r. and in the visible range, with the intent to derive from them some bulk figures on absorbing impurities in an atmosphere which appears to be essentially hydrogen with some admixture of helium, e.g. 87% H_2 and 13% He in the nominal model. Some of these impurities are known or strongly suspected to exist, e.g. CH_4 , NH_3 , and H_2O , these and a number of other likely ones will be determined by an analysis of the atmosphere with a mass spectrometer and a gas chromatograph (which takes, however, some time so that we would not quite get the impurity fractions up to the time when the probe fails due to the increasing pressure and temperature).

Disregarding here this time delay, we could work out from the impurity analysis of the atmosphere what its opacity, due to both absorption and scattering, ought to be, if only the analytically determined impurities were present. An independent opacity measurement would then give an overall check on the analysis. It would also uncover the existence of any absorbing impurities which remained undetected in the analysis for one reason or another, e.g. that they took too long to go through the gas chromatograph, and it would give us at least some quantitative idea of the total amount of atmospheric impurities in the event that the mass spectrometer and/or the gas chromatograph would fail prior to the termination of the mission. In other words, such an independent opacity experiment would be worthwhile to do in a deep probe, if it can be accommodated in the probe without too much difficulty.

On the other hand, we should be clear about its major limitation. While we can get an overall idea of the amount of atmospheric impurities, we cannot hope to identify any of them individually. Any typical absorption bands of particular molecules will be too badly pressure-broadened to permit an identification.

Of the two possible approaches to a measurement of the opacity of the atmosphere for a certain wavelength band of width $\Delta\lambda$ around a central wavelength λ_0 , we consider at first the passive "radiation intensity gradient" - experiment in which we would use the natural thermal radiation of the environment,

Memorandum - S. Ducsay from F. Vandrey
 23 December 1970
 Page 3

essentially a black-body or "hohlraum" radiation at the ambient temperature T , as the source for the radiation. Later, we shall consider the possibility for an active opacity measurement in which we would determine the attenuation of an artificially generated light beam over a given and then, for practical reasons, probably not very long path.

In the passive "radiation gradient" experiment, we would look straight up and straight down from the probe through filters with a pass-band $\Delta\lambda$ around λ_0 . Because of the thermal gradient in the atmosphere, nominally around $2 \times 10^{-3} \text{ }^\circ\text{K m}^{-1}$, we would then see a lower intensity above, and a higher intensity below the probe, and this intensity difference will be proportional to the characteristic length ℓ ($\frac{1}{\epsilon}$) over which the radiation in the selected wave band is attenuated by the factor $e^{-1} \approx 0.37$.

We try to obtain a crude but optimistic estimate for the order of magnitude of ℓ for both infrared and visible radiation, in order to get an opinion on how promising such an experiment could be.

There is certainly plenty of radiative energy around in the environment of the 10^3 atm, 1425°K level, since the intensity of the black-body radiation at this temperature is

$$I = \sigma T^4 \approx 2.3 \times 10^5 \text{ watt m}^{-2} \quad (1)$$

And most of this energy is carried by the infrared, since the wavelength of maximum intensity is

$$\lambda_{\max} = \frac{2.893 \times 10^{-3}}{1425} \approx 2 \times 10^{-6} \text{ m} \quad (2)$$

or 2 microns (Wien's displacement law)

But this intensity changes only very little in the upward direction, because of the low value of the vertical temperature gradient of typically only $2 \times 10^{-3} \text{ }^\circ\text{K m}^{-1}$. Not even enough to carry an appreciable part of the average upward flow of internally generated heat (around 30 watt m^{-2} , according to the latest estimates of Trafton and Wildey, [4]).

Memorandum - S. Ducsai from F. Vandrey
 23 December 1970
 Page 4

To see this, and to estimate the value of \mathcal{L} for infrared radiation in a purposely optimistic way, we consider here only water vapor as the cause of atmospheric opacity, and we disregard all other i.r. absorbers (CH_4 , NH_3 , etc. Even hydrogen has an appreciable i.r. absorption at high pressures, see e.g. [5]).

Assuming then a water vapor fraction of around 10^{-3} by number as in the JPL nominal model, we have 1 atm of H_2O at the 10^3 atm level of the Jupiter atmosphere. At this partial pressure, we find from published data (e.g. [6] p. 170) that a layer of water vapor alone would already have an emittance, and then according to Kirchhoff's law also an absorptance of $e^{-1} \approx 0.37$ for a thickness of only around 2.5 m at 1425°K.

This rather high absorption of i.r. by water vapor permits us to consider the deepest accessible parts of the Jovian atmosphere as "black" so that we can assess the contribution of the radiation to the heat transport through the atmosphere by an equivalent "radiative heat conductivity"

$$\mathcal{J}_r = \frac{16 \sigma T^3}{3 k} \quad (3)$$

where k is the inverse of the length, of in our case 2.5m, over which the radiation is attenuated by a factor of e^{-1} (from the writer's lectures on radiation gasdynamics, [7]). Using then the typical vertical temperature gradient of around $-2 \times 10^{-3} \text{°K m}^{-1}$ in the nominal atmosphere, we find numerically that the radiative energy transport cannot amount to more than

$$Q = - \mathcal{J}_r \frac{\partial T}{\partial z} \approx 4.6 \text{ watt m}^{-2} \quad (4)$$

due to the water vapor absorption alone.

It will then be far less in reality where there are other absorbers, and we can conclude that only an entirely insignificant fraction of the available 30 watts m^{-2} of internal energy can be transported upward to the surface by radiation at the 10^3 atm level. This fraction will be even less at lower pressures where the temperature is also lower, and it is not difficult to show that things do not become much better at greater depth where \mathcal{J}_r does increase with T^3 but where k increases also with increasing density, roughly proportional to $T^{2.5}$. Except at very great depth where there are probably only very low velocities,

Memorandum - S. Ducsay from F. Vandrey
 23 December 1970
 Page 5

so that it does not matter anyway, the omission of radiation terms in Hide's equations appears therefore to be justified.

With respect to our intended radiation gradient experiment, we can also conclude that it will require a very good accuracy of differential radiation temperature measurements. With a typical ℓ - value for infrared of the order of 1m, one will have to measure a difference of the effective radiation temperatures for a certain wavelength band around λ_0 in the upward and downward direction which will be of the order of a few 10^{-3} °K with a background of around 1400°K ambient. Quite unattractive for an experiment in a Jupiter probe, to say the least.

The situation for a passive radiation gradient experiment is somewhat, but not very much better for visible light where one has, of course, considerably less energy available at the still relatively "low" temperatures. As suitable wavelengths for the 10^3 atm level, we have here to consider those below about 0.5 microns, since there are some CH_4 absorption bands near 0.6 microns [8] which will most likely be appreciably pressure-broadened.

We have then, however, already difficulties with Rayleigh scattering from hydrogen molecules which leads to severe extinction over again rather short distances. To estimate the characteristic length for this process, we can use N. Divine's relation

$$k_R \approx 1.8 \times 10^{-3} \lambda^{-4} \text{ cm}^2 \text{ g}^{-1} \quad (5)$$

with λ in microns ([1], p. 9). With a nominal density of around $2 \times 10^{-2} \text{ g cm}^{-3}$ at 10^3 atm, we obtain then

$$\ell_R \left(\frac{1}{\epsilon} \right) = (k_R \rho)^{-1} \approx 17 \text{ m} \quad (6)$$

Again, there will be other contributions to the opacity at 0.5 microns, so that 17 m is an upper bound for ℓ rather than a realistic appraisal of its magnitude. Nevertheless, it would seem that the opacity for visible light is

Memorandum - S. Ducsai from F. Vandrey
 23 December 1970
 Page 6

around an order of magnitude less than in the infrared for the 10^3 atm level on Jupiter. This would then indicate that a passive radiation gradient experiment around .5 microns might be easier to do than at 1 or .2 or 3 microns. But it will still be a difficult thing to measure radiation temperature differences of the order of a few 10^{-2} °K against a background of 1400°K, so that such an experiment is still unattractive for a Jupiter probe. On top of this, one could use the available visible radiation at best near the deepest level to which the probe can penetrate. There is less and less visible light in the thermal radiation at the lower temperatures above, and there will soon not be enough for such an experiment. This follows at once from Planck's radiation law

$$E_{\lambda} d\lambda = \frac{hc^2}{\lambda^5} \frac{d\lambda}{e^{\frac{hc}{kT\lambda}} - 1} \quad (7)$$

or

$$E_{\lambda} d\lambda \approx \frac{hc^2}{\lambda^5} e^{-\frac{hc}{kT\lambda}} \quad (8)$$

for sufficiently low temperatures where the exponential in the numerator of (7) becomes much greater than unity.

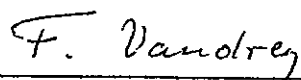
It appears then that, however desirable an independent measurement of the visible and infrared opacity of the deep Jupiter atmosphere may be as an aid to an assessment of its bulk impurity contents and as a check of the more detailed chemical analysis, a passive radiation gradient experiment with the use of the amply available thermal radiation in the probe environment is not the right way to go about it. Our estimates indicate that the opacities will be much too high for any experiments of this type.

This very fact assures us, however, that an active experiment with an artificial light source and suitable band-pass filters will be quite promising. One will, of course, have to chop the light beam at a convenient frequency, either mechanically or perhaps better electrically, to distinguish it from the environmental radiation in the same frequency band. Other experimental details will also have to be incorporated in the experimental apparatus, it will e.g. be

Memorandum - S. Ducsai from F. Vandrey
23 December 1970
Page 7

helpful to work with rather narrow beams for both the light source and the receiver. The main thing is, however, that the opacity is high enough to get away with a relatively modest light path, probably around 1 m, even at lower pressures of perhaps more than 100 atm, for such an experiment.

More work will, of course, be needed on this concept. As far as it could here be determined from crude and preliminary estimates, it looks, however, promising and worthwhile.



J. F. Vandrey

JFV/dcm

References

1. N. Divine: Jupiter model atmospheres JPL-IOM-2947-617, 8 May 1970
2. A. R. Barger: Discussion of Jupiter Entry Probe Science Mission with Dr. S. I. Rasool.
Memo to S. J. Ducsai 9 October 1970
3. R. Hide: Dynamics of the atmospheres of the major planets with an appendix on the viscous boundary layer at the rigid bounding surface of an electrically-conducting rotating fluid in the presence of a magnetic field, Journ. of the Atmospheric Sci. 26 PtI, Sept 1969 pp. 841-53.
4. L. M. Trafton and R. L. Wildey: Jupiter: His limb darkening and the magnitude of his internal heat source.
Science 168, June 5, 1970, pp 1214-15
5. L. M. Trafton and G. Muench: The structure of the atmospheres of the major planets.
J. Atmos. Sci. 26 PtI, Sept 1969, pp. 813-25.
6. J. A. Wiebelt: Engineering Radiation Heat Transfer.
Holt, Rinehart and Winston, Publ. New York 1966
7. F. Vandrey: Introduction into Radiation Gasdynamics. (in German)
Guest Lectures at the University of Gottingen, October 1965, published by W. G. L. 4th Raumfahrt Lehrgang.
8. V. G. Teifel: Molecular absorption and the possible structure of the cloud layers of Jupiter and Saturn.
J. Atmosph. Sci. 26 PtI, Sept. 1969, pp. 854-61.

M E M O R A N D U M

January 7, 1971

To: S. J. Ducsay
 From: J. F. Vandrey
 Subject: Magnetic Cleanliness Requirements

A primary requirement for the probe and its components to be "magnetically clean" exists only, if its mission includes measurements of the Jovian magnetic field during the descent through the atmosphere. The techniques of magnetically clean design are well known, and need not be elaborated upon here.

It may, however, be mentioned that it is probably adequate to conduct any such magnetic measurements in the upper parts of the atmosphere, i.e. in the general region of the visible cloud top "Surface" of the planet. If one uses a split probe, only its upper, more slowly descending, part would have to be magnetically clean, and this is easier to achieve than for the deeply penetrating lower part which will probably need a pressure shell of steel, i.e. be ferromagnetic.

Going much deeper with the magnetic experiment, and in particular down to the deepest technically accessible $[p \sim 10^3 \text{ atm}, T \sim 1400^\circ\text{K}]$ - level some 600 km below the clouds would only be desirable, if one had good reasons to expect already appreciable field distortions from magneto-hydrodynamic effects at this depth.

In our opinion, this is, however, unlikely. It would require that the magnetic Reynolds' number of the atmospheric motions

$$\text{Re}_m = L \cdot U \cdot \mu \cdot \sigma \quad (1)$$

with

Memo - S. J. Ducsai

Page 2

with

$$L = \text{typical length scale, } \sim 10^6 \text{ m}$$

$$U = \text{typical velocity across field lines}$$

$$\mu = \text{magnetic permeability, } \sim 10^{-6} \frac{\text{volt sec}}{\text{amp m}}$$

$$\sigma = \text{electrical conductivity} \quad (2)$$

would already be in some way comparable to unity at a somewhat greater depth, e.g. 1000 or 2000 km below the probe. (See e.g. [1], pp. 4-7, [2], p. 843). But our best "educated guesses" of U and σ 10³ km below the deep probe limit indicate that U is probably less than 10⁻² m sec⁻¹ and σ probably less than the order of 10⁻² amp volt⁻¹m⁻¹ at the still relatively "low" temperature of around 3000°K at this level. We may therefore have magnetic Reynolds' numbers of rather less than 10⁻⁴, so that the field lines would still readily slip through the convective flow with very little distortion.

All other scientific instruments in the probe, namely its

- gas chromatograph and mass spectrometer
- pressure and temperature gauges
- visual photometers
- accelerometers
- nephelometer
- I. R. radiometers
- R. F. lightning detector, and
- microphone

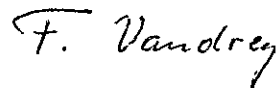
are very little affected by small and spurious magnetic fields, and the same is true for its data processing and transmitting electronics. There is, therefore, no particular requirement for a great magnetic cleanliness of the probe, as far as the major part of its payload is concerned.

Memo - S. J. Ducsay

Page 3

With the exception of the mass spectrometer, the insensitivity of these instruments and of their associated electronics against magnetic fields is even great enough to dispose of a need for particular precautions against interference from the Jovian magnetic field which seems to be about twenty times stronger than that of the Earth (order of 10^{-3} volt sec m^{-2} , or 10 gauss at the surface of Jupiter, see e.g. [3], p. 104.)

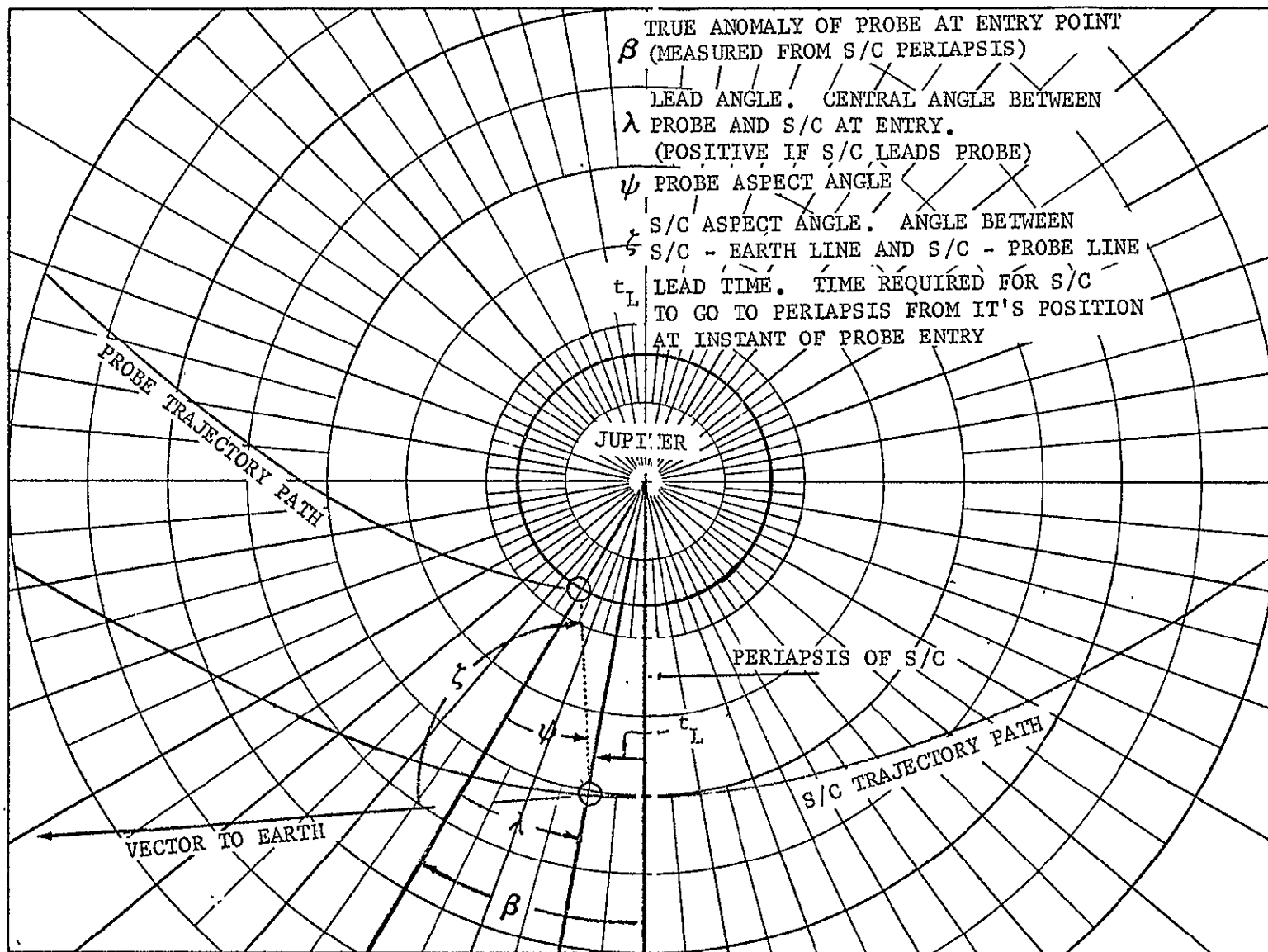
The mass spectrometer will, however, very likely need either some light magnetic shielding of an essentially conventional instrument, or else a special design with stronger and more compact electrical and/or magnetical or, in the case of "Massenfilter," RF-fields, in order to avoid unacceptable defocussing by the gyration of the ions in the magnetic field whose radius is inversely proportional to the field strength (see e.g. [4], Chapter 1 for an outline of the basic theory). Either approach appears feasible. The selection of a particular design is then a question of tradeoffs in weight, complexity, reliability, and development costs.



J. F. Vandrey

References

1. T. G. Cowling. Magnetohydrodynamics - Interscience Publ., Inc.
New York - 1957
2. R. Hide. Dynamics of the Atmospheres of the Major Planets with an
Appendix on the Viscous Boundary Layer at the Rigid Bounding Surface
of an Electrically Conducting Rotating Fluid in the Presence of a
Magnetic Field - J. Atmospheric Sciences, Vol 26, Pt I, September 1969,
pp. 841 - 53.
3. A. Smith and Th. Carr. Radio Exploration of the Planetary System -
Van Nostrand Co., Publ. - Princeton, N. J. - 1964
4. L. Spitzer, Jr. Physics of Fully Ionized Gases - Interscience Publ.,
Inc. - New York - 1956



APPENDIX E

JUPITER ENCOUNTER NOMENCLATURE

APPENDIX F

SYMBOL DEFINITIONS

* * * * *	
REJ	DEFLECTION RADIUS (KM)
DELV	DEFLECTION VELOCITY INCREMENT (M/S)
TAU	DEFLECTION ANGLE (DEG)
VHP	HYPERBOLIC EXCESS VELOCITY IN KM/S
COAST T	COAST TIME FROM DEFLECTION TO ENTRY (DAYS)
RP	PERIAPSIS RADIUS OF SPACECRAFT IN JUPITER RADII
TL	LEAD TIME (TIME REQUIRED FOR S/C TO GO TO PERIAPSIS FROM ITS POSITION AT INSTANT OF PROBE ENTRY)
LEAD ANGLE	CENTRAL ANGLE BETWEEN S/C AND PROBE AT INSTANT OF PROBE ENTRY (DEG)
FPA	INERTIAL FLIGHT PATH ANGLE OF PROBE AT ENTRY POINT (DEG)
BETA	TRUE ANOMALY OF PROBE AT ENTRY, MEASURED FROM S/C PERIAPSIS REFERENCE (DEG)
V REL	ENTRY VELOCITY OF THE PROBE RELATIVE TO JOVIAN ATMOSPHERE (KM/SEC)
PROBE AA	PROBE ASPECT ANGLE AT ENTRY (DEG)
C RANGE	LINK COMMUNICATIONS RANGE AT INSTANT OF ENTRY (KM)
G	DECELERATION IN G S (1G= 32.174 FT/SEC ²)
Q	DYNAMIC PRESSURE, LB/FT ²
ALT	ALTITUDE (FFET)
WT	WEIGHT (LBS)
DLA	DECLINATION OF LAUNCH ASYMPTOTE (REFERED TO EARTH EQUATORIAL SYSTEM)
RAL	RIGHT ASCENSION OF LAUNCH ASYMPTOTE (REFERRED TO EARTH EQUATORIAL-VERNAL EQUINOX REFERENCE SYSTEM)
TAP	TRUE ANOMALY OF S/C AT ARRIVAL (DEG)
C3	LAUNCH ENERGY (KM ² /SEC ²)
TF	HELIOCENTRIC FLIGHT TIME IN DAYS
HCA	HELIOCENTRIC CENTRAL ANGLE (DEG)
ECC	ECCENTRICITY OF HELIOCENTRIC TRANSFER ELLIPSE
INCL	INCLINATION OF HELIOCENTRIC TRANSFER ELLIPSE (DEG)
SMA	SEMI-MAJOR AXIS OF HELIOCENTRIC TRANSFER ELLIPSE (A.U.)
TAL	TRUE ANOMALY OF S/C AT LAUNCH (DEG)
ZAE	ANGLE BETWEEN VECTOR FROM PLANET TO EARTH AND THE HYPERBOLIC EXCESS VELOCITY VECTOR (VHP) (INDICATES DIRECTION OF S/C APPROACH TO TARGET PLANET)
ZAP	ANGLE BETWEEN VECTOR FROM PLANET TO SUN AND THE HYPERBOLIC EXCESS VELOCITY VECTOR (VHP) (INDICATES DIRECTION OF S/C APPROACH TO TARGET PLANET)
VHP	HYPERBOLIC EXCESS VELOCITY AT TARGET PLANET (KM/SFC)
DAP	DECLINATION OF THE INCOMING ASYMPTOTE AT TARGET PLANET (DEG)
RAP	RIGHT ASCENSION OF THE INCOMING ASYMPTOTE AT THE TARGET PLANET (DEG)
RC	JUPITER TO EARTH COMMUNICATION DISTANCE (A.U.)

G. Compendium of Parameters For All Missions

MAX. LAUNCH AZIMUTH	115 DEG
PARKING ORBIT ALTITUDE	100 N M
FAIRING SEPARATION	CORE II IGNITION + 10 SEC
JUPITER HYPERBOLIC	
APPROACH TRAJECTORY	FLYBY WITH ROTATION
DEFLECTION MANEUVER TYPE	NEAR SIDE IN PLANE PROBE DEFLECTION
	ENTRY NEAR EQUATOR, WITH ROTATION
ENTRY ALTITUDE	487.7 KM ABOVE REFERENCE RADIUS
AEROSHELL STAGING ALT	33 KM (200 MB)
REFERENCE RADIUS	71420 KM (PRESSURE OF 1 ATMOSPHERE)
MISSION C	SAME AS MISSION B EXCEPT THAT AFTER PROBE ENTRY THE S/C WILL BE PUT INTO ORBIT ABOUT JUPITER. THIS ORBIT WILL HAVE A PERIAPSIS RADIUS OF 2 RJ, AN APOAPSIS OF 100 RJ, AN ECCENTRICITY OF .96078, AND AN INCLINATION OF ABOUT 7.5 DEGREES. THE VELOCITY INCREMENT REQUIRED WILL BE ABOUT 757 METERS/SEC= 2480 FT/SEC. THE ORBIT PERIOD WILL BE ABOUT 45 DAYS.
MISSION F	SIMILAR TO DESIGN EXAMPLE EXCEPT THAT COMMUNICATIONS IS DIRECT LINK TO EARTH. ENTRY FLIGHT PATH ANGLE IS -49 DEGREES
NOTE	A STAGED PROBE USES A PARACHUTE DURING PART OF THE DESCENT TO SHAPE THE DESCENT PROFILE.

LAUNCH PARAMETERS

MISSION	DESCRIPTION	SPACECRAFT	S/C WT	ENTRY WT	LV P/L CAP	LAUNCH PERIOD
A1 (G/T)	(STAGED)	TOPS	1450	239.0	1900	30 DAY
A2 (G/T)	(SPLIT)	TOPS	1450	367.0	1900	30 DAY
B	(STAGED)	PIONEER	547	457	1550	20 DAY
C	S/C ORBITS J	PIONEER	547	457	1550	20 DAY
D (G/T)	MINI-PROBE (2)	TOPS	(2)	150.5	1900	30 DAY
E (G/T)	(STAGED)	TOPS	1450	353	1900	30 DAY
F	(UNSTAGED)	TOPS	1450	497	2420	30 DAY
DESIGN EX	(STAGED)	TOPS	1450	427	2420	30 DAY
TRIAL MISS	(SPLIT)	TOPS	1450	803	2420	30 DAY

MISSION	TYPE	LAUNCH VEHICLE	LAUNCH	ARRIVAL	TYPE	RP
A (G/T)	JUN	TIID/7/CEN/BI	11-6-79	4-30-81	I	6.8
B (81)	FLYBY	TIID/5/CEN/BI	9-25-78	11/4/81	II	2.0
B (82)	FLYBY	TIID/5/CEN/BI	10-25-78	10-20-82	II	2.0
C	ORBITER	SAME AS B				
D (G/T)	JUN	TIID/7/CEN/BI	11-6-79	4-30-81	I	6.8
E (G/T)	JUN	TIID/7/CEN/BI	10-10-78	3-27-80	I	1.6
F	FLYBY	TIID/7/CEN/BI	9-25-78	11-4-81	II	2.0
DESIGN	FLYBY	TIID/7/CEN/BI	9-25-78	11-4-81	II	2.0
TRIAL	FLYBY	TIID/7/CEN/BI	10-2-78	10/2/81	II	2.0

MISSION	PROBE SYSTEM WT (INCL S/C MODS)	PROBE INSTALLED WT	ENTRY WT	SCIENCE PAYLOAD
A1	399.5	239.	239.	10.
A2	562.5	367.	367.	10.
B	743.0	552.	457.	27.
C	1043.	552.	457.	27.
D	450.	185.	150.5	10.
E	468.	381.	353.	26.
F	617	552.	497.	10.
DESIGN	569.	467.	427.	19.
TRIAL	953	803	719	26

MISSION	PROBE TYPE	ENTRY VEHICLE DIAMETER	SPACECRAFT ANTENNA DIAMETER	DATA RETURN MODE
A1	SINGLE UNSTAGED	3.0	4.5	RELAY
A2	SPLIT UNSTAGED	3.5	4.5	RELAY
B	SINGLE STAGED	3.5	3.5	RELAY
C	SINGLE STAGED	3.5	3.5	RELAY
D	SINGLE UNSTAGED	2.5	4.14	RELAY
E	SINGLE STAGED	3.5	3.4	RELAY
F	SINGLE UNSTAGED	4.0	-	DIRECT LINK
DESIGN	SINGLE STAGED	3.5	4.2	RELAY
TRIAL	SINGLE STAGED	4.25	2.8	RFLAY

INTERPLANETARY CRUISE PARAMETERS

MISSION	DLA	RAL	C3	TF	HCA	ECC	INCL	SMA	TAL
A (G/T)	24.9	139.5	111.7	541	145.1	.8350	2.27	6.0	357.9
B (NOV 4, 81)	6.6	118.4	99.0	1136	200.7	.695	3.6	3.22	342.0
B (OCT 20, 82)	4.87	125.4	86.2	1436	197.7	.705	3.3	3.37	355.3
C (SAME AS B)									
D (G/T)	24.9	139.5	112.0	541	145.0	.8350	2.27	6.0	357.9
E (G/T)	29.65	102.6	112.4	534	141.3	.831	1.76	5.9	1.49
F	6.6	118.4	99.0	1136	200.7	.695	3.6	3.22	342.0
DESIGN EX	6.6	118.4	99.0	1136	200.7	.695	3.6	3.22	342.0
TRIAL MIS	-4.6	111.0	98.43	1096	191.3	.691	6.5	3.22	349.9

ENCOUNTER PARAMETERS

MISSION DESCRIPTION	RC	ZAE	ZAP	TAP	DAP	RAP	VHP
A (G/T)	4.6	161.78	155.26	143.0	6.5	164.7	12.154
B (NOV 4, 81)	6.4	79.91	82.83	182.8	27.4	106.8	5.471
B (OCT 20, 82)	6.3	62.16	58.72	193.0	26.95	109.6	6.344
C (SAME AS B)							
D (G/T) MINI-PROBE(2)	4.6	161.78	155.26	143.0	6.53	164.7	12.154
E (G/T)	4.5	160.46	154.43	142.8	16.54	134.4	11.86
F	6.4	79.91	82.83	182.8	27.4	106.8	5.471
DESIGN EXAMPLE	6.4	79.91	82.83	182.8	27.4	106.8	5.471
TRIAL MISSION	6.4	88.73	86.92	181.2	31.1	109.1	5.476

DEFLECTION PARAMETERS

MISSION DESCRIPTION	RP	FPA	TAU	DELV	VHP	REJ	BETA
A (G/T)	6.8	-15	-126.5	337	12.154	30M	-1.0
B (NOV 4, 81)	2.0	-30	-107.	241	5.471	10M	51.8
B (OCT 20, 82)	2.0	-30	-106.0	242	6.344	10M	51.1
C (SAME AS B)							
D (G/T) MINI-PROBE (2)	6.8	-15	-126.5	337	12.154	30M	-1.0
E (G/T)	1.6	-10	-106.3	44	11.86	30M	13.46
F	2.0	-49	-90.	175.	5.471	26M	89.0
DESIGN EXAMPLE	2.0	-20	-106.5	81	5.471	26M	34.0
TRIAL MISSION	2.0	-10	-115	197	5.476	10M	13.7

MISSION DESCRIPTION	(KM)		TL (HR)	TL (MIN)	RUN NO
	LEAD ANGLE	RP			
A (G/T)	+19.53	483969.04	-1.91	-114.4	R-142.143
B (NOV 4, 81) ARRIVAL	-20.8	143000.	1.63	98.0	R-126.163
B (OCT 20, 82) ARRIVAL	-20.8	143000.	1.63	98.0	R-126.163
C (SAME AS B)					
D (G/T) MINI-PROBE (2)	+19.53	483969.04	-1.91	-114.4	R-142.143
E (G/T)	-23.14	114371.6	.45	27.0	R-105
F	-25.03	143000.	5.26	315.9	
F ANGLE OF ATTACK = 0	-55.03	143000.	27.06	1620.9	
DESIGN EXAMPLE	-16.51	143000.	.95	57.1	R-438
TRIAL MISSION	-15.45	143000.	0.50	29.9	

JUPITER ENTRY PARAMETERS

MISSION DESCRIPTION	V REL	PROBE AA	C RANGE	COAST T
A (G/T)	48.05	-13.05	413000	26 DAYS
B (NOV 4, 81)	49.0	30.2	157113	12 DAYS
B (OCT 20, 82)	49.0	31.4	158800	11 DAYS
C (SAME AS B)				
D (G/T) MINI-PROBE (2)	48.05	-13.05	413000	26 DAYS
E (G/T)	48.0	48	67758	26.5 DAYS
F	52.1			40 DAYS
DESIGN EXAMPLE	47.8	27.3	108563	40 DAYS
TRIAL MISSION	47.1	28.37	166000	12 DAYS

PROBE ENTRY DESIGN DATA

MISSION	S/C RP	FPA		DESIGN DEPTH
A1 (G/T)	6.8	-15.	(STAGED)	-270. (10 ATM)
A2 (G/T)	6.8	-15.	(SPLIT)	-270. (100 ATM)
B	2.0	-30.	(STAGED)	-260. (72.5 ATMS)
C	2.0	-30.	(STAGED) S/C ORBITS JUPITER	-260. (72.5 ATMS)
D (G/T)	6.8	-15.	(STAGED) 2 MINI. PROBES	-195. (17 ATMS)
E (G/T)	1.6	-10.	(STAGED) GRAND TOUR	-270. (100 ATMS)
F	2.0	-49.	(UNSTAGED) DIRECT LINK	-195KM (17 ATMS)
DESIGN	2.0	-20.	(STAGED)	-395KM (300 ATMS)
TRIAL	2.0	-10.	(SPLIT)	-602KM (1000 ATMS)

MISSION	(SEC) TIME TO .1 G	(FT) ALT	(SEC) STAGING	M	Q
A1 (G/T)	12.5	963174.	97	.50	76.8
A2 (G/T)	13.0	952949.	88	.52	83.4
B	6.5	965272	38	.58	102.3
C	6.5	965272	38	.58	102.3
D (G/T)	12.5	963174.	92.4	.50	67.
E (G/T)	19.0	959610	124.0	.52	82.3
DESIGN EXAMPLE	10.	934264.	67.5	.52	81.2
TRIAL MISSION	18.	920025.	108.5	.63	120.

MISSION	(SEC) TIME TO MAX G	LB/FT ² MAX G MAX Q	(FT) ALT	(SEC) T(M=1)	(FT) ALT	MA/MF
A1 (G/T)	26.5	714 15069	297644.	51.5	163358.	0.265
A2 (G/T)	27.0	724 16643	280255.	51.5	158284.	0.265
B	14.5	1514 38000.	229320.	26.5	124797.	0.275
C	14.5	1514 38000.	226320.	26.5	124797.	0.275
D (G/T)	26.5	708 12971	301375.	51.5	170972.	0.260
E (G/T)	40.0	440 11216	321752	79.0	175406	0.250
DESIGN	20.5	976 22518	274087	39.5	146164.	0.268
TRIAL	40.	402 15509	292451.	79.5	152225.	0.265

PROBE ENTRY DESIGN DATA										
MISSION DESCRIPTION	TIME OF DESCENT	TYPE	(KM)	(ATM)	DEPTH	PRESSURE	B1	B2	B3	WT (LBS)
A1 (G/T) (SINGLE)	.93	1	-270	10			0.78	.05		239
A2 (G/T) (SPLIT)	.93	2	-270	100			0.88	.05	1.1	367
B (SINGLE)	1.5	2	-260	72.5			1.09	.05	1.1	400
C (SINGLE)	1.5	2	-260	72.5			1.09	.05	1.1	400
D (G/T) 2 MINI PROBES	.93	1	-195	17			0.71	.10		150.5 (2)
E (G/T) (SINGLE)	1.65	2	-270	100			0.84	.05	1.1	351
F (UNSTAGED)	.93	1	-195 KM	17 ATMS	0.80					497
DESIGN EX (STAGED)	2.47	3	-395 KM	300 ATMS	1.03	.05	1.9			427
TRIAL MISS (SPLIT)	3.5	5	-602 KM	1000 ATMS	1.2	.05	3.5			803

DESCENT PROFILES USED FOR COMMUNICATIONS ANALYSIS FOLLOWS.
NOMINAL ATMOSPHERIC MODEL USED

FINAL PRESSURE	PROFILE	1ST STAGE B	STAGING AT P1 (ATM)	STAGING 2ND STAGE TIME(M)	B	TIME P1-P2	TOTAL TIME
50	1	.05	10	55	1.1	23.5	78.5
100	2	.05	10	55	1.1	56.	99
300	3	.05	15	73	1.9	76.	148.4
500	4	.05	20	89	2.8	90	177.2
1000	5	.05	30	117.3	4.8	107.8	225.1

DESCENT PROFILE NO 1 R2=.05, R3=1.1, T= 78.5 MIN
P2=10 ATM, P3=50. ATM

DESCENT PROFILE NO 2 R2=.05, R3=1.1, T= 99.0 MIN
P2=10 ATM, P3=100.ATM

(KM) ALTITUDE	(SEC) TIME	(TYPE) PROFILE	BALLISTIC COEF	(ATM) PRESSURE
487.68	0.	1 AND 2		
181.28	30.	1 AND 2		
56.37	60.	1 AND 2		
39.00	150.	1 AND 2	.05	
22.5	300.	1 AND 2	.05	
-9.1	900.	1 AND 2	.05	
-40.0	1800.	1 AND 2	.05	
-65.0	27000.	1 AND 2	.05	
-86.943	3300.	1 AND 2	1.1	10.
-116.943	3600.	1 AND 2	1.1	
-182.943	4500.	1 AND 2	1.1	
-195.00	4709.9	1 AND 2	1.1	50.
-235.00	5400.	2	1.1	
-260.00	5941.9	2	1.1	100.
-270.00	6300.	2	1.1	

DESCENT PROFILE NO 3 B2=.05, B3=1.9, T=148.4 MIN
P2=15 ATM, P3=300 ATM

(KM) ALTITUDE	(SEC) TIME	(TYPE) PROFILE	BALLISTIC COEF	(ATM) PRESSURE
487.68	0.	3	1.2	
181.28	30.	3	1.2	
56.37	60.	3	1.2	
39.00	150.	3	.05	
22.5	300.	3	.05	
-9.1	900.	3	.05	
-40.	1800.	3	.05	
-65.	2700.	3	.05	
-85.	3600.	3	.05	
-109.45	4380.	3	1.9	15.
-124.0	4500.	3	1.9	
-205.0	5400.	3	1.9	
-265.0	6300.	3	1.9	
-315.0	7200.	3	1.9	
-360.0	8100.	3	1.9	
-395.0	8904.	3	1.9	300.
-400.0	9000.	3	1.9	

DESCENT PROFILE NO 4 B2=.05, B3=2.8, T=177.2 MIN
P2=20 ATM, P3=500 ATM

(KM) ALTITUDE	(SEC) TIME	(TYPE) PROFILE	BALLISTIC COEF	(ATM) PRESSURE
487.68	0.	4		
181.28	30.	4		
56.37	60.	4		
39.	150.	4	.05	
22.5	300.	4	.05	
-9.1	900.	4	.05	
-40.	1800.	4	.05	
-65.	2700.	4	.05	
-85.	3600.	4	.05	
-103.	4500.	4	.05	
-127.2	5340.	4	2.8	20.
-137.2	5400.	4	2.8	
-225.	6300.	4	2.8	
-293	7200.	4	2.8	
-350	8100.	4	2.8	
-395	9000.	4	2.8	300.
-444	9900.	4	2.8	
-474	10633.	4	2.8	500.
-480	10800.	4	2.8	

DESCENT PROFILE NO 5 B2=.05, B3=4.8, T=225.1 MIN
P2=30 ATM, P3=1000 ATM

(KM)	(SEC)	(TYPE)		(ATM)
ALTITUDE	TIME	PROFILE	BALLISTIC COEF	PRESSURE
487.68	0.	5		
181.28	30.	5		
56.37	60.	5		
39	150.	5	.05	
22.5	300.	5	.05	
-9.1	900.	5	.05	
-40.0	1800.	5	.05	
-65.	2700.	5	.05	
-85.	3600.	5	.05	
-103.	4500.	5	.05	
-121.	5400.	5	.05	
-140.	6300.	5	.05	
-155.	7040.	5	4.8	30
-175.	7200.	5	4.8	
-280.	8100.	5	4.8	
-350.	9000.	5	4.8	
-415.	9900.	5	4.8	
-465.	10800.	5	4.8	
-519.	11700.	5	4.8	
-564.	12600.	5	4.8	
-602.	13502.	5	4.8	1000.

(KM)	(SEC)	(TYPE)		(ATM)
ALTITUDE	TIME	PROFILE	BALLISTIC COEFF	PRESSURE
487.68	0.	6,7,8,9,10		
181.28	30.	6,7,8,9,10		
56.	60.	6,7,8,9,10		
39.	150.	6,7,8,9,10	.05	
22.5	300.	6,7,8,9,10	.05	
-9.1	900.	6,7,8,9,10	.05	
-40.0	1800.	6,7,8,9,10	.05	
-65.	2700.	6,7,8,9,10	.05	
-85.	3600.	6,7,8,9,10	.05	10
-103.	4500.	6,7,8,9,10	.05	
-121.	5400.	6,7,8,9,10	.05	
-140.	6300.	6,7,8,9,10	.05	
-155.	7200.	6,7,8,9,10	.05	30